

DIPAC 2003

6th European Workshop on Beam **D**iagnostics and **I**nstrumentation for **P**article **A**ccelerators

The workshop is a forum for the exchange of the latest experiences in the field of accelerator beam diagnostics and instrumentation world-wide.

It aims at active and efficient participation with a program of oral presentations, poster sessions and discussion groups.

An industrial exhibition and a visit to GSI's accelerator facility are also organised.

5 – 7 May, 2003
Mainz, Germany

Info: www.gsi.de/dipac2003

Programme Committee:

Andreas Peters (Chairman) [GSI]
Peter Cameron [BNL]
Mike Dykes [Daresbury]
Mario Ferianis [Elettra]
Alex Lumpkin [APS/ANL]
Uli Raich [CERN]
Kees Scheidt [ESRF]
Volker Schlott [PSI/SLS]
Hermann Schmickler [CERN]
Mario Serio [INFN/LNF]
Kay Wittenburg [DESY]

Local Committee:

Elke-Luise Pfaff (Secretary)
Peter Forck
Benjamin Hoefler
Tobias Hoffmann
Andreas Peters
Hans-Jörg Reeg
Volker Schaa
Norbert Schneider

hosted by **GSI**

Preface



The Sixth DIPAC (the European Workshop on Beam Diagnostics and Instrumentation for Particle Accelerators) was organised by the Gesellschaft für Schwerionenforschung (GSI), Darmstadt, the heavy ion research centre funded by the Federal Government of Germany and the state of Hesse. The Workshop from 4 to 7 May 2003 was held at Hilton Hotel in Mainz, directly located on the banks of the River Rhine, close to the 2000-year-old city centre. This series of Workshops serves as a forum for the exchange of the latest experiences, results and developments in the field of accelerator beam instrumentation in Europe and worldwide. More than 130 participants coming from 15 different countries attended the Workshop, among these only seven from USA but also three from South Korea. For the first time three fellowships could be given to young scientists from Egypt, Russia and Romania, sponsored by Julien Bergoz and GSI.

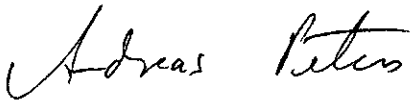
The Programme Committee organised an interesting agenda of 10 invited and 11 contributed talks, as well as 56 posters and three parallel discussion sessions. The talks were grouped into four 'regular' sessions containing invited and contributed talks on Monday morning, Tuesday noon and Wednesday afternoon. As a new idea three sessions including a 30 minutes discussion on Tuesday morning and afternoon, as well as on Wednesday morning were organized. These sessions contained invited and contributed satellite talks on linked subjects. The 30-minutes-discussions with lively contributions from the audience were guided by the session chairmen, a new element in the program which emphasized the workshop character of the meeting. A visit of GSI's accelerator complex in Darmstadt on Monday afternoon and an industrial exhibition on Tuesday rounded off

the Workshop. In addition, the social activities should be mentioned, the reception on Sunday evening as well as the famous banquet with live Jazz during a cruise on the River Rhine.

The success of DIPAC 2003 was the work of many people. First of all, I want to thank the Programme Committee for their contributions during more than a half year of Workshop preparation including two meetings at Mainz and Darmstadt. The second thank goes to all members of the Local Committee and GSI's beam diagnostics group for their large engagement to realise this workshop. In particular, I appreciate the work of the Secretary, Elke-Luise Pfaff. In addition, I would like to thank Ursula Grundinger, Erika Ditter and Carola Pomplun for supporting her. I also want to thank Kathrin Karner for the corporate design of the DIPAC poster and the Workshop accessories, Benjamin Höfler for his efforts on the DIPAC web site as well as Gabriele Otto and Achim Zschau for their work as Workshop photographers.

But the essential part of the Workshop was done by you, the participants: the talks, the posters and discussions, both formal and informal. The proceedings, perfectly arranged by Volker Schaa with assistance of Madeleine Catin from CERN, reflect the quality of all these contributions – thank you all. The online version of these proceedings can be found on the Joint Accelerator Conferences Website (www.jacow.org).

Looking into the future, the Seventh DIPAC Workshop will be held in 2005, organized again by CERN, which carried out the first Workshop of these series in 1993 at Montreux. Please have a look to the CERN beam diagnostics group's web pages (<http://sl-div-bi.web.cern.ch/sl-div-bi/> or <http://ab-div.web.cern.ch/ab-div/Groups/BDI/WelcomeBDI.html>) to get more information about it. I look forward to another exciting Workshop, and seeing many of you again.



Andreas Peters
(Chairman of the DIPAC 2003 Programme Committee)

DIPAC 2003 Time Schedule

Sunday, 4th May, 2003

16:00 – 21:00 Conference Desk open for Registration

18:00 – 21:00 Welcome Reception

Monday, 5th May, 2003

09:00 – 09:15	A. Peters, GSI	Welcome and Opening Presentation
----------------------	----------------	----------------------------------

09:15 – 10:45 Session I — Chairman: Kees Scheidt, ESRF

IT01	W. Henning, GSI	The Future of Nuclear Physics in Europe and the Demands on Accelerators techniques
-------------	-----------------	------------------------------------------------------------------------------------

IT02	J. C. Denard, SOLEIL	Overview of the Diagnostics Systems of SOLEIL and DIAMOND
-------------	----------------------	-----------------------------------------------------------

CT01	M. Gasior, CERN	An Inductive Pick-Up for Beam Position and Current Measurements
-------------	-----------------	-----------------------------------------------------------------

10:45 – 11:15 Coffee Break

11:15 – 13:00	PMxx Different Authors	Poster Session A
----------------------	-------------------------------	------------------

- OTR,
 - Special Measurements Techniques in Synchrotrons,
 - Profile Measurements,
 - Overview Posters, and
 - Miscellaneous
-

13:00 – 14:00 Lunch

14:00 – 18:00	P. Forck, GSI	Visit of GSI: Short introduction talk and tour along UNILAC, ESR, Tumour treatment facility, and HADES experiment
----------------------	---------------	-------------------------------------------------------------------------------------------------------------------

Tuesday, 6th May, 2003**09:15 – 10:45** Session II — Chairman: Volker Schlott, PSI

IT03	R. Jung, CERN	Single Pass Optical Profile Monitoring
CT02	L. Groening, GSI	Single Shot Measurements of the 4-Dimensional Transverse Phase Space Distribution of Intense Ion Beams at the UNILAC at GSI
CT03	G. Mazzitelli, INFN	Beam Instrumentation for the Single Electron DAΦNE Beam Test Facility

Subsequently there is time for a brainstorming and discussion between the speakers and the audience, moderated by the chairman

10:45 – 11:15 Coffee Break**11:15 – 13:00** Session III — Chairman: Mario Serio, INFN

IT04	J. Wenninger, CERN	Challenges for LHC and Demands on Beam Instrumentation
CT04	D. Nölle, DESY	The Beam Inhibit System for TTF II
CT05	P. Michel, FZR	Beam Loss Detection at Radiation Source ELBE
CT06	M. Werner, DESY	Timing Sicknesses in Control Systems: Causes, Cure and Prevention

13:00 – 14:00 Lunch**14:00 – 16:00** **PTxx** Different Authors Poster Session B

- BPMs and Related Electronics,
- Longitudinal Measurements,
- Beam Loss Monitors,
- Current Measurements, and
- Miscellaneous

16:00 – 16:30 Coffee Break**16:30 – 18:00** Session IV — Chairman: Mario Ferianis, ELETTRA

IT05	G. Berden, FOM	Single Shot Electron-Beam Bunch Length Measurements
IT06	P. Krejcik, SLAC	Short Bunch Beam Profiling

Subsequently there is time for a brainstorming and discussion between the speakers and the audience, moderated by the chairman

19:45 – 23:30 Banquet on the River Rhine

Wednesday, 7th May, 2003**09:15 – 10:45 Session V — Chairman: Hermann Schmickler, CERN**

IT07	M. E. Angelotta, CERN	Digital Signal Processing in Beam Instrumentation: Latest Trends and Typical Application
-------------	-----------------------	------------------------------------------------------------------------------------------

CT07	G. Naylor, ESRF	Fast DSP Using FPGAs and DSOs for Machine Diagnostics
-------------	-----------------	-------------------------------------------------------

CT08	M. Dehler, PSI	Capabilities of the ELETTRA/SLS Multibunch Feedback Electronics
-------------	----------------	-----------------------------------------------------------------

Subsequently there is time for a brainstorming and discussion between the speakers and the audience, moderated by the chairman

10:45 – 11:15 Coffee Break**11:15 – 13:00 Parallel Discussion Sessions**

DW01	K. Wittenburg, DESY K. Scheidt, ESRF	Machine Protection And Interlock Systems
-------------	-----------------------------------------	------------------------------------------

DW02	U. Raich, CERN H. Schmickler, CERN	Global Accelerator Network, Control Systems And Beam Diagnostics
-------------	---------------------------------------	------------------------------------------------------------------

DW03	A. Peters, GSI M. Ferianis, ELETTRA	Beam Synchronous Timing Systems
-------------	----------------------------------------	---------------------------------

13:00 – 14:00 Lunch**14:00 – 16:00 Session VI — Chairman: Mike Dykes, ASTeC**

IT08	M. Plum, LANL	Diagnostic Challenges at SNS
-------------	---------------	------------------------------

IT09	G. Kube, DESY	Smith-Purcell Radiation in View of Particle Beam Diagnostics
-------------	---------------	--------------------------------------------------------------

CT09	L. Badano, TERA	SLIM – An Innovative Non-Destructive Beam Monitor for the Extraction Lines of a Hadrontherapy Centre
-------------	-----------------	------------------------------------------------------------------------------------------------------

CT10	S. Brandenburg, KVI	Beam Diagnostics in the AGOR Cyclotron
-------------	---------------------	----------------------------------------

CT11	M. Wendt, DESY	Beam Based HOM Analysis of Accelerating Structures at the TESLA Test Facility LINAC
-------------	----------------	-------------------------------------------------------------------------------------

16:00 – 16:15 Coffee Break**16:15 – 17:00 Session VII — Chairman: Andreas Peters, GSI**

IT10	J. P. Koutchouk, CERN	Advanced Diagnostics of Lattice Parameters in Hadron Colliders
-------------	-----------------------	----------------------------------------------------------------

	A. Peters, GSI	Final Remarks
--	----------------	---------------

DIPAC 2003 – Mainz, Germany



Contents

Preface	i
Schedule	v
Pictures	ix
Contents	xi
Invited Talks	1
IT01 – The Future of Nuclear Physics in Europe and the Demands on Accelerators techniques	3
IT02 – Overview of the Diagnostics Systems of SOLEIL and DIAMOND	6
IT03 – Single Pass Optical Profile Monitoring	10
IT04 – Challenges for LHC and Demands on Beam Instrumentation	15
IT05 – Single Shot Electron-Beam Bunch Length Measurements	20
IT06 – Short Bunch Beam Profiling	25
IT07 – Digital Signal Processing in Beam Instrumentation: Latest Trends and Typical Applications	30
IT08 – Diagnostic Challenges at SNS	35
IT09 – Smith-Purcell Radiation in View of Particle Beam Diagnostics	40
IT10 – Advanced Diagnostics of Lattice Parameters in Hadron Colliders	45
Contributed Talks	51
CT01 – An Inductive Pick-Up for Beam Position and Current Measurements	53
CT02 – Single Shot Measurements of the 4-Dimensional Transverse Phase Space Distribution of Intense Ion Beams at the UNILAC at GSI	56
CT03 – Beam Instrumentation for the Single Electron DAΦNE Beam Test Facility	59
CT04 – The Beam Inhibit System for TTF II	62
CT05 – Beam Loss Detection at Radiation Source ELBE	65
CT06 – Timing Sicknesses in Control Systems: Causes, Cure and Prevention	68
CT07 – Fast DSP Using FPGAs and DSOs for Machine Diagnostics	71
CT08 – Capabilities of the ELETTRA/SLS Multibunch Feedback Electronics	74
CT09 – SLIM (SEM for Low Interception Monitoring) - An Innovative Non-Destructive Beam Monitor for the Extraction Lines of a Hadrontherapy Centre	77
CT10 – Beam Diagnostics in the AGOR Cyclotron	80
CT11 – Beam Based HOM Analysis of Accelerating Structures at the TESLA Test Facility LINAC	83
Posters Monday	87
PM01 – Use of Optical Transition Radiation Interferometry for Energy Spread And Divergence Measurements	89
PM03 – Studies of OTR Angular Distribution on CTF2	92
PM04 – OTR from Non-Relativistic Electrons	95
PM05 – Optical Transmission Line For Streak Camera Measurements at Pitz	98
PM06 – An Improved PLL for Tune Measurements	101
PM07 – Real time management of the AD Schottky/BTF beam measurement system	104
PM08 – Recent Advances in the Measurement of Chromaticity Via Head-Tail Phase Shift Analysis	107
PM09 – Diagnostics for Electron Cooled Beams	110
PM10 – Characterisation of Fast Faraday Cups at the ELETTRA Linac	113
PM11 – Beam Studies Made With The SPS Ionization Profile Monitor	116
PM12 – Cavity Mode Related Wire Breaking of the SPS Wire Scanners And Loss Measurements of Wire Materials	119
PM13 – The PS Booster Fast Wire Scanner	122
PM14 – Upgrade Of The ESRF Fluorescent Screen Monitors	125
PM15 – First Experimental Results And Improvements On Profile Measurements With The Vibrating Wire Scanner	128
PM16 – Wire Scanner Beam Profile Measurement For ESRF	131
PM17 – Development of a Permanent Magnet Residual Gas Profile Monitor With Fast Readout	134
PM18 – Residual Gas Fluorescence for Profile Measurements at the GSI UNILAC	137

DIPAC 2003 – Mainz, Germany

PM19 – Ionisation Beam Profile Monitor at the Cooler Synchrotron COSY-Jülich	140
PM21 – Recent Developments Of The EXCYT Radioactive Beam Diagnostics	143
PM23 – Networked Attached Devices at SNS	146
PM24 – Parasitic Bunch Measurement in e+/e- Storage Rings	149
PM25 – Diagnostics of the PROSCAN beam lines	152
PM26 – A System For Beam Diagnostics in the External Beam Transportation Lines of the DC-72 Cyclotron	155
PM27 – Multifunction Test-Bench For Heavy Ion Sources	158
PM28 – Application of Beam Diagnostics for Intense Heavy Ion Beams at the GSI UNILAC . .	161
PM29 – A Modular VME Data Acquisition System for Counter Applications at the GSI Synchrotron	164

Posters Tuesday 167

PT01 – Beam Position And Phase Measurements Using A FPGA For The Processing Of The Pick-Ups Signals	169
PT02 – Pill-Box Cavity BPM For TESLA Cryomodul	172
PT04 – Advantages Of Implementing Digital Receivers In Field Programmable Gate Arrays (FPGA)	175
PT05 – Experience With Sampling Of 500 MHz Rf Signal For Digital Receiver Applications . .	178
PT06 – Dynamic X-Y Crosstalk / Aliasing Errors of Multiplexing BPMs	181
PT07 – Cavity Beam Position Monitor For The TESLA Energy Spectrometer	184
PT08 – The LHC Orbit and Trajectory System	187
PT09 – Cavity-Type BPMs For The TESLA Test Facility Free Electron Laser	190
PT12 – Beam Phase Measurements in the AGOR Cyclotron	193
PT13 – An X-Band Cavity for a High Precision Beam Position Monitor	196
PT14 – Design of BPM PU for Low-Beta Proton Beam Using Magic Code	199
PT15 – Performance of the ELBE BPM Electronics	202
PT16 – A High Dynamic Range Beam Position Measurement System for ELSA-2	205
PT17 – Impedance-Matching-Transformer for Capacitive Pick-Ups	208
PT18 – Development of a bunch frequency monitor for the preliminary phase of the CLIC Test Facility CTF3	211
PT19 – Transverse Feedback System For The Cooler Synchrotron COSY-Jülich - First Results	214
PT20 – A New Wide Band Wall Current Monitor	216
PT21 – Microwave measurement of intra bunch charge distributions	219
PT22 – Measurement of the longitudinal phase space at the Photo Injector Test Facility at DESY Zeuthen	222
PT23 – Transverse Emittance Measurements at the Photo Injector Test Facility at DESY Zeuthen (PITZ)	225
PT24 – Development of a Bunch-Length Monitor with Sub-Picosecond Time Resolution and Single-Shot Capability	228
PT25 – Fast Tune Measurement System for the ELETTRA Booster	231
PT26 – Cryogenic Current Comparator for Absolute Measurement of the Dark Current of the Superconducting Cavities for Tesla	234
PT27 – A 40 MHz Bunch by Bunch Intensity Measurement for the CERN SPS and LHC	237
PT28 – Current Measurements of Low-Intensity Beams at CRYRING	240
PT29 – Dark Current Measurements at the PITZ Rf Gun	242
PT30 – Ionisation Chambers for the LHC Beam Loss Detection	245
PT31 – Optical Fibre Dosimeter for SASE FEL Undulators	248
PT32 – Beam Loss Diagnostics Based on Pressure Measurements	251
PT34 – DAΦNE Beam Loss Monitor System	254

Discussions Wednesday 257

DW01 – Machine Protection And Interlock Systems	259
DW02 – Global Accelerator Network, Control Systems And Beam Diagnostics	260
DW03 – Beam Synchronous Timing Systems	261

Appendices	263
List of Authors	265
Institutes List	269
Participants List	273
— A —	273
— B —	273
— C —	274
— D —	274
— E —	274
— F —	274
— G —	274
— H —	275
— J —	275
— K —	275
— L —	276
— M —	276
— N —	276
— O —	277
— P —	277
— R —	277
— S —	277
— T —	278
— U —	278
— V —	278
— W —	278
— Y —	279
Vendors List	281
Production Notes	282



INVITED TALKS

THE FUTURE OF NUCLEAR PHYSICS IN EUROPE AND THE DEMANDS ON ACCELERATOR TECHNIQUES

Walter F. Henning, GSI, 64291 Darmstadt, Germany

INTRODUCTION

Nuclear physics has undergone a major reorientation in its research goals during the last decade or so [1]. There are two, or maybe three major reasons for that.

The first one results from the fact that nucleons and mesons, the basic building of nuclei and their fields, have substructure. Understanding the quark-gluon structure of hadrons, how and to what extent this partonic substructure affects the behavior of nuclei and nuclear matter, and to what extent we have a full and quantitative understanding of these features through the theory of strong interaction, quantum-chromo-dynamics (QCD), is at the center of much of the activity in nuclear physics. The length and energy dimensions involved with hadrons and nuclei require the non-perturbative treatment within QCD, and also the extension to finite temperature and chemical potential.

A second important new area has been the development of accelerated beams of short-lived nuclei (sometimes called ‘radioactive’, ‘rare isotope’ or ‘exotic’ beams) at useful intensities. Much of what we know about nuclei comes from nuclear reactions. Consequently these studies have been essentially restricted to stable nuclei where reaction targets could be built and exposed to beams of particles, in particular light ones (protons, deuterons, helium nuclei etc.). Energetic beams of short-lived nuclei now allow to reverse the reaction kinematics and thus, with targets of light nuclei, to study nuclei away from, and up to the limits of stability in nuclear reactions.

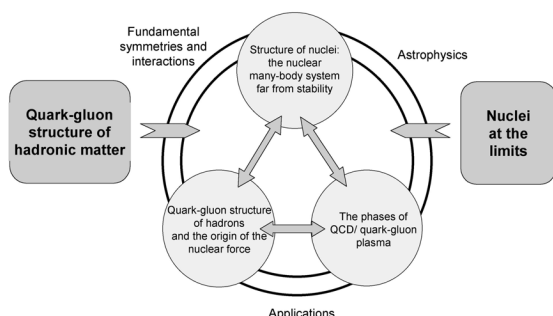


Figure 1: Current research frontiers in nuclear physics.

The third area of interest is the exploration of the limits of the Standard Model. For the strong interaction sector this connects to the QCD discussion above. For the weak sector, the discovery of neutrino oscillations and mass has placed new emphasis on an area which started with Davis’ solar neutrino searches in radiochemical experiments several decades ago [2]. Both solar and

galactic neutrinos as well as neutrinos from high-intensity accelerators are of broad interest now. Rare decays and direct symmetry violation studies requiring intense primary and secondary beams are also pushing accelerator performance and design.

The areas of interest just described have overlap and intersections with each other. One way of summarizing the overall situation could be the schematic shown in Figure 1.

RESEARCH AREAS, FACILITIES AND BEAMS

The new research programs require new experimental capabilities and new facilities and beams, and these then, in turn, define new and very challenging requirements for accelerator instrumentation, in particular beam diagnostics - the subject of this conference.

The substructure of the stable nucleons, protons and neutrons, and of stable nuclei is directly accessible via studies with beams of hadrons, leptons and photons. Other hadrons, mesons and excited baryons, need to be produced in reactions.

Beams of leptons, and in particular electrons, are preferred probes for the ground state structure of nucleons since they are point-like and the electromagnetic interaction is well understood. Structure functions, including in particular spin, have been and are intensely studied. Quark and gluon contributions to the spin are being studied at existing high-energy facilities (HERMES at DESY [3] and COMPASS at CERN [4] for example) but in particular also at the dedicated high-intensity cw electron-beam facility CEBAF at JLAB [5]. Current interest is being focussed on skewed parton distributions and the measurements of DVCS, deep virtual Compton scattering, which promises to provide information on parton correlations and, possibly, structure functions of excited hadrons. These studies, plus the exploration of the transition from perturbative to non-perturbative QCD, are asking for high-duty cycle electron machines up to several tens of GeV laboratory energy. In addition, concepts are being developed for future e-A colliders at tens to 100 GeV center-of-mass energy [6,7].

Facilities for studies of QCD with intense hadronic probes are being developed in Japan and Europe: the Japanese Hadron Facility (J-PARC) [8] with intense proton beams and primary interest in research with secondary beams of kaons and neutrinos; the future facility proposed for the GSI Laboratory in Germany with intense antiproton beams and in particular a high-energy antiproton storage ring with electron cooling [9]. The

goals of these facilities in hadron physics are in tests of the Standard Model and neutrino physics for the J-PARC, and in studies of QCD and chiral symmetry in nuclear matter for the GSI facility.

In addition, the important questions of QCD relating to confinement and chiral symmetry restoration are being pursued in relativistic heavy-ion collisions. Reaching the region of the quark-gluon plasma promises studies of matter fully deconfined and chirally symmetric. Major advances are expected at RHIC at Brookhaven [10] and at the ALICE experiment at the LHC [11] and - to some extent - at the future GSI facility [9].

In Japan (RIKEN [12]), Europe (GSI [9] and EURISOL [13]) and the USA (RIA [14]) there are plans to build new large-scale facilities to provide intense beams of short-lived nuclei. The science interest arises from the fact that this will allow the studies of the nuclear many body system to be extended up to the limits of binding. As in any physical system, pushing it to its limits - here in isospin or neutron to proton ratio - may reveal particular sensitivities. In addition, the paths of explosive nucleosynthesis and thus the generation of all nuclei and chemical elements heavier than iron proceed through the regions of unstable nuclei far from stability. Finally, the high secondary intensities expected from the future facilities promise new and sensitive experiments on fundamental symmetries and features of the fundamental interactions through the use of specific nuclei and their weak decays.

The production of secondary beams of short-lived nuclei proceeds through nuclear reactions, either in flight and in a thin target (projectile fragmentation facilities) or on-line in a thick target with subsequent slow extraction at thermal energies from an ion source (ISOL or isotope separation on-line) and re-acceleration. In the recent RIA scheme, the IGISOL technique, originally developed at Jyväskylä [15], is further expanded [14], allowing for the two approaches being combined to a multi-purpose, powerful future facility.

Use of secondary beams in storage rings has been shown to be particularly powerful for optimising beam quality, for multiple use of the re-circulating beam with an internal target, and precision experiment with cooled beams. Storage rings are envisioned for the RIKEN facility in Japan and for the planned future facility at GSI. Filling the storage rings will probably be more efficient for a synchrotron-injected facility than for a dc primary beam driver such as a cyclotron.

With these facilities it will be possible to reach regions of nuclei far from stability, extending to the rapid neutron capture process (r-process) with useful intensities and the neutron drip line up to medium mass nuclei.

AN EXAMPLE: THE FUTURE FACILITY AT GSI

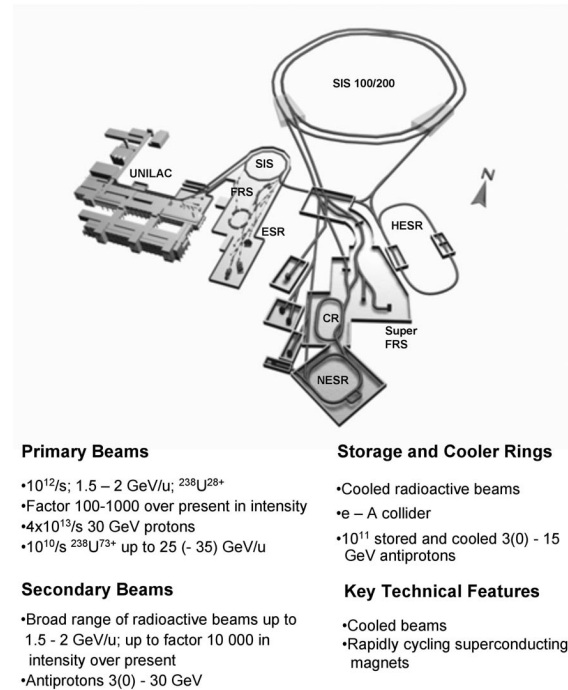


Figure 2: The existing GSI facility (left) with the linear accelerator UNILAC, the heavy-ion synchrotron SIS18, the fragment separator FRS and the experiment storage ring ESR; and the new project (right) with the double-ring synchrotron SIS100/200, the high-energy storage ring HESR, the collector ring CR, the new experiment storage ring NESR, the super-conducting fragment separator Super-FRS and several experimental stations. The present UNILAC/SIS18 complex serves as injector for the new double-ring synchrotron.

From the general overview just given, it is obvious that many important challenges await the construction of advanced beam diagnostics. It is also obvious that this brief overview does not cover the broad range of capabilities of the future facilities anticipated in any detail. We therefore consider one facility as an example: the GSI Future Facility [9]. The conceptual layout is shown in Figure 2, together with some key parameters. Major challenges for beam diagnostics are the very high (primary) beam intensities and the precision use of the secondary beams. In particular the cooling of beams leads to unprecedented precision in momentum spread and physical beam dimensions, requiring new approaches in beam diagnostics. Figure 3 illustrates this with a Schottky noise spectrum of a 'cocktail' of fragment nuclei, electron-beam cooled and circulating in the ESR at the present GSI facility [16]. The Fourier analysis determines precisely rotation frequencies of beams circulating with fixed velocity (namely that of the electron-cooler beam) and thus yields precise mass measurements. This is just one of many examples. For a more detailed discussion of the

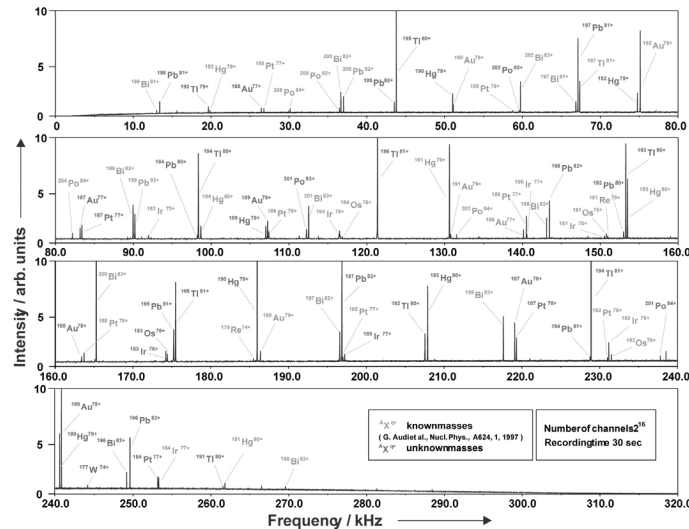


Figure 3: Schottky frequency spectrum of a collection of beams of heavy nuclei circulating in the ESR [16].

GSI Future Facility and its performance characteristics, please see the Conceptual Design Report [9].

OUTLOOK

In this paper a brief summary was given of major facilities under construction or in planning for the field of nuclear and hadron physics. Along one example, the GSI future facility, areas of particular importance for beam diagnostics were indicated. This by no means covers all areas where such future developments are needed. In fact, within the limited scope of this article, many smaller facilities in existence or being planned, could not be covered and often these facilities (with lower beam energies) pose severe demands on beam diagnostics. For example, low-energy beam tracking on a particle-by-particle basis which is desirable for the secondary beams with very low intensity but with possibly strong contamination, may be a major challenge to beam diagnostics. And in all the areas, the clear distinction historically made between beam diagnostics (and accelerator operation) and instrumentation of experiments may become diffuse or often nearly vanish.

REFERENCES

- [1] NuPECC Long Range Plan, in preparation; NSAC Long Range Plan, Opportunities in Nuclear Science; April 2002, Berkeley Lab Technical and Electronic Information Department; NRC Report on Nuclear Physics: The Core of Matter, The Fuel of Stars; National Academy Press, Washington, D.C. 1999
- [2] Davis, Raymond, Jr., Harmer, Don S., Hoffman, Kenneth C., Phys. Rev. Lett. 20 (1968) 1205-1209; <http://www.physicstoday.org/vol-55/iss-10/nobel.html>
- [3] <http://www-hermes.desy.de/>
- [4] <http://wwwcompass.cern.ch/compass/publications/welcome.html>
- [5] http://www.jlab.org/div_dept/physics_division/GeV.html
- [6] Electron-Nucleon/Nucleus Collisions - Joint DESY/GSI/NuPECC Workshop, held at Seeheim, near Darmstadt, March 3/4 1997
- [7] eRHIC: http://www.phenix.bnl.gov/publish/abhay/Home_of_EIC/ WWWW/ EIC: Ya. Derbenev, Proc. of EPAC 2002, Paris, France, p. 314
- [8] J-PARC: <http://jkj.tokai.jaeri.go.jp/>
- [9] GSI: An International Accelerator Facility for Beams of Ions and Antiprotons; Conceptual Design Report, 11/2001; <http://www.gsi.de/GSI-Future/cdr/>; this report is also available on CD. Mail to press@gsi.de to request a copy
- [10] RHIC: <http://www.bnl.gov/RHIC/>
- [11] LHC: <http://lhc-new-homepage.web.cern.ch/lhc-new-homepage/>; ALICE: <http://alice.web.cern.ch/Alice/>
- [12] <http://www.rarf.riken.go.jp/>
- [13] EURISOL: A Feasibility Study for a European Isotope-Separation-On-Line Radioactive Nuclear Beam Facility, EC contract No. HPRI-CT-1999-500001
- [14] RIA: <http://www.phy.anl.gov/ria/w.html>
- [15] IGISOL: <http://www.phys.jyu.fi/research/igisol/>
- [16] Yu. A. Litvinov et al., Hyp. Int. 132, 283-289 (2001)

Overview of the Diagnostics Systems of SOLEIL and DIAMOND

J.-C. Denard, L. Cassinari, SOLEIL, Societ  Synchrotron Soleil, Saint-Aubin, France

e-mail: Jean-Claude.Denard@synchrotron-soleil.fr

M. Dykes, R. Smith, ASTeC, Daresbury Laboratory, Daresbury, UK

Abstract

SOLEIL and DIAMOND are two third-generation light sources in construction in France and in Great Britain respectively. SOLEIL is scheduled to deliver its first photons to its users in 2006 and DIAMOND in 2007. This talk will present the beam diagnostic systems of both projects with emphasizing technological novelties and the instruments that are essential to their performances: BPM system, profile monitors and feedback systems.

Paper not received

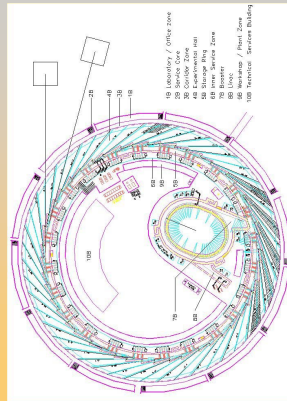
(See slides of talk on
following pages)

Overview of the Diagnostics Systems of SOLEIL and DIAMOND

Jean-Claude Denard and Lodovico Cassinari: SOLEIL
Mike Dykes and Rob Smith : DIAMOND

DIPAC 2003 (IT02)
Mainz, Germany; 4-7 May 2003

DIAMOND



DIPAC2003, Mainz, 4-7 May
Overview of the Diagnostics Systems
of SOLEIL and DIAMOND; Jean-Claude Denard

SOLEIL Site April 2003



DIPAC2003, Mainz, 4-7 May
Overview of the Diagnostics Systems
of SOLEIL and DIAMOND; Jean-Claude Denard

Outline

- Machines
- Status and construction schedules
- Diagnostics challenges
- Beam Stability and BPMs
- BPM electronics
- BPM mechanics
- Other diagnostics

DIPAC2003, Mainz, 4-7 May
Overview of the Diagnostics Systems
of SOLEIL and DIAMOND; Jean-Claude Denard

SOLEIL; Artist view



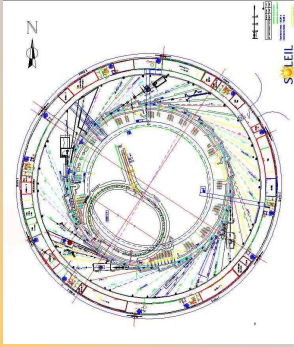
DIPAC2003, Mainz, 4-7 May
Overview of the Diagnostics Systems
of SOLEIL and DIAMOND; Jean-Claude Denard

DIAMOND Site April 2003



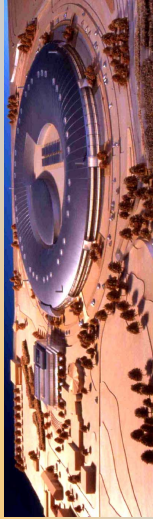
DIPAC2003, Mainz, 4-7 May
Overview of the Diagnostics Systems
of SOLEIL and DIAMOND; Jean-Claude Denard

SOLEIL



DIPAC2003, Mainz, 4-7 May
Overview of the Diagnostics Systems
of SOLEIL and DIAMOND; Jean-Claude Denard

DIAMOND; Artist View



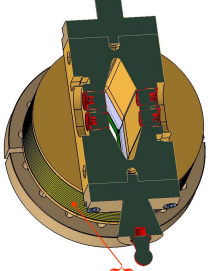
DIPAC2003, Mainz, 4-7 May
Overview of the Diagnostics Systems
of SOLEIL and DIAMOND; Jean-Claude Denard

Time Schedules

Milestones	SOLEIL	DIAMOND
Start LINAC Commissioning	Aug 2004	May 2005
Start Booster Commissioning	Jan 2005	Aug 2005
Start Storage Ring Commissioning	Apr 2005	Jan 2006
Start operation for users	Jan 2006 (10 beamlines)	Jan 2007 (7 beamlines)

DIPAC2003, Mainz, 4-7 May
Overview of the Diagnostics Systems
of SOLEIL and DIAMOND; Jean-Claude Denard

- BPM is the only fixed point of its vacuum chamber section
- Bellow relieves stress from next vacuum chamber section
- Electrode electrical offset calibrated in the lab.
- Mechanical center = center of the 2 end balls
- BPMs fixed on ground (straights) or on Girders (arcs)



Storage Ring BPM cross section

*Overview of the Diagnostics Systems
of SOLEIL and MAXIV, Jean-Charles Duvall*

DPAC2003,
Munich, 4-7 May
SOLEIL
SINCHROTRON

20

Overview of the Diagnostics Systems
of SOLEIL and DIAMOND: Access Channel Demand

DIPAC 2003,
Maurix, 4-7 May

SOLEIL
SINCHROTRON

BPM Survey With Respect to Quadrupoles
Devised by Alain Leclercle

Prism successively moved to the 3 positions

Alignment laser beam

DPAC2003,
Mainz, 4-7 May

SOLEIL

Overview of the Diagnostics Systems
of SOLEIL and DIAMOND, Jean-Claude Deraud

23

Diagram illustrating the components of a beam-based alignment system:

- Reflecting prism
- Inclinometer
- Girdler top

[illegible]

SOLEIL: Other Storage Ring Diagnostics

- 2 Current monitors + life time (Bergoz PCT)
- 1 Fast Current transformer (Bergoz FCT)
- 2 tune measurement systems (redundancy)
- 2 pin hole cameras (profiles at low and high dispersion points)
- Synchrotron radiation monitor in visible:
 - View beam profile
 - Streak camera for bunch length
- Instability interlock
- 32 beam loss monitors
- Bunch purity monitor
- 24 beam lines equipped with photon-BPMs
- Diagnostic undulator (not at commissioning)

SOLEIL DIPAC 2003, Mairix, 4-7 May

Overview of the Diagnostics Systems of SOLEIL and DIAMOND, Jean-Cl  ude Dardard

25

SOLEIL :
Straight Section BPM
Support

Bellows around BPM

Supporting post in steel
(to be later built in invar)

DPAC2003,
Mantex, 4-7 May

SOLEIL
SINCHROTRON
RAYON X

Overview of the Diagnostics Systems
of SOLEIL and DIAMOND, Jean-Claude Denard

21

The diagram illustrates the layout of the SOLEIL and DIAMOND diagnostic systems. It shows a series of vertical components arranged in a row, with dimensions indicated in feet. The components and their dimensions are:

- 320' BUILDING
- 1000' SHEDDING CHIT
- 1000' TEST UNDULATION
- 320' MONITORING CENTER
- 600' TUNNEL
- 600' COLLECTOR
- 600' FT. ELECTROLYTICALLY

The total length of the system is 800' STRAIGHT LENGTH.

SOLEIL
DIPAC2003,
Mainz, 4-7 May

*Overview of the Diagnostics Systems
of SOLEIL and DIAMOND, Jean-Claude Dondard*

24

SINGLE PASS OPTICAL PROFILE MONITORING

R. Jung, G. Ferioli, S. Hutchins, CERN, Geneva, Switzerland

Abstract

Beam profiles are acquired in transfer lines to monitor extracted beams and compute their emittance. Measurements performed on the first revolutions of a ring will evaluate the matching of a chain of accelerators. Depending on the particle type and energy, these measurements are in general performed with screens, making either use of Luminescence or Optical Transition Radiation [OTR], and the generated beam images are acquired with sensors of various types. Sometimes the beam position is also measured this way. The principle, advantages and disadvantages of both families of screens will be discussed in relation with the detectors used. Test results with beam and a possible evaluation method for luminescent screens will be presented. Finally other optical methods used will be mentioned for completeness.

SCREEN MONITORS

Screen monitors are the most popular instruments for single pass profile measurements. A typical monitor is depicted in Fig. 1. It consists of a vacuum vessel with Input and Exit ports for the beam, a mechanism holding several screens, 2 or 3 are usual numbers, a window to extract the light produced by the screen, an optical set-up to image the screen onto a sensor and to control the quantity of light transmitted, and finally a detector to convert the photons into an electrical signal, be it a TV standard signal or a digital acquisition.

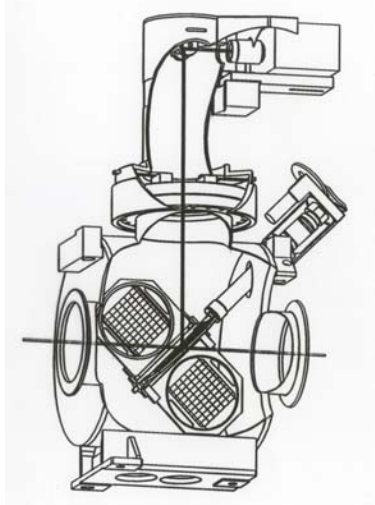


Figure 1: Typical screen monitor.

In the following, we shall review the various types of screens and mention the most important features of the sensors for this type of monitor. The match of these two constituents will largely define the performance of the monitor.

SCREENS

Two types of screens are in general use: Luminescent screens and Optical Transition Radiation [OTR] screens. The first produce light by excitation of the molecules of the screen by the passage of a charged particle beam followed by de-excitation, which is a bulk phenomenon, whereas the second produce light by an electromagnetic phenomenon initiated by the passage of the beam at the interface of two regions with different dielectric constants, and is hence a pure surface phenomenon.

Luminescent screens

When a molecule is excited by an external electromagnetic field, it can emit light via two processes. The first is characterised by a direct jump to the base level with a short decay time constant of a few tens of nanoseconds and will be called fluorescence. In the second process, the de-excitation passes via an intermediate receiver level and takes much longer, typically microseconds to seconds. It will be called phosphorescence. If both processes are present, which is the case with many screens, or in case of doubt, the light emission will be called luminescence.

A first screen type is manufactured from ceramics or glass in which activators have been introduced for controlling the emitted wavelength. The most popular dopant for ceramics is Cr, which results in an emission in the red, well matched to solid-state detectors: see Fig. 8. The concentration of activator, of a few per mil, controls the emitted intensity. Typically, such screens are made from Al_2O_3 powder, with grains of the order of $5\text{ }\mu\text{m}$, to which silica magnesia lime and the activator, here Cr_2O_3 , are added to arrive at a concentration of 99.4% of Al_2O_3 . This powder is mixed and pressed, before being fired to sinter, process in which the glassy phase fills up the voids between the grains. After machining to the final shape and finish, typically to $\text{Ra} \sim 1\text{ }\mu\text{m}$, there is another firing. Microscope observations show large structures, up to $\sim 30\text{ }\mu\text{m}$, in the finished product.

Another type of screen uses crystalline materials, where dopants also control the emitted wavelength. These screens are in general more expensive, but as will be seen later, have a better resolution as well as a higher light yield, i.e. sensitivity. There is experience with two types: Thallium doped CsI [1] and Cerium doped YAG [2].

As the light is generated in the bulk of the material, if the screens are placed at 45° with respect to the beam and if they are not infinitely thin or made of opaque material, there will be a collection of light generated in the depth of the material which will create instrument generated tails [3], in the vertical direction in the case of the Fig.1 set-up. To counteract this degradation, monitors have been built [4] with the luminescent screen perpendicular to the beam

direction and with a light extraction mirror placed at 45° with respect to the screen and the beam direction: Fig. 2. As will be seen later, the mirror will generate OTR, which will add to the luminescence signal, but the generated light levels are sufficiently different so that OTR can be neglected: see Table 1.

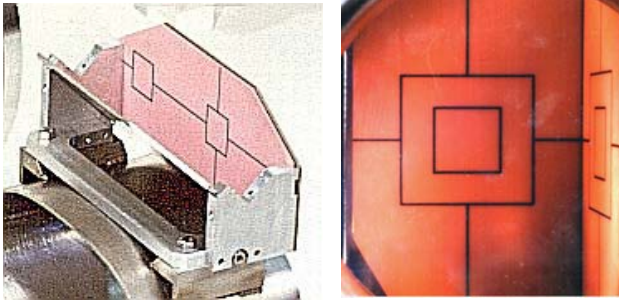


Figure 2: Monitor set-up with perpendicular screen and 45° extraction mirror, with screen at right and mirror at left. Left : actual set-up, right: as seen by the camera.

A recent revival of an old technique where a phosphor layer is put on a metal sheet or a glass substrate [5,6] will also solve this problem. Phosphors of type P40 and P43, the latter with a thickness of 40μm and a grain size of 5μm, have been used. The main disadvantage of these screens is the mechanical fragility of the phosphor layer.

OTR screens

Optical Transition Radiation makes use of the radiation emitted when a charged particle beam goes through the interface of two media with different dielectric constants, like vacuum and a metal sheet. Two light patterns are emitted, see Fig. 3.

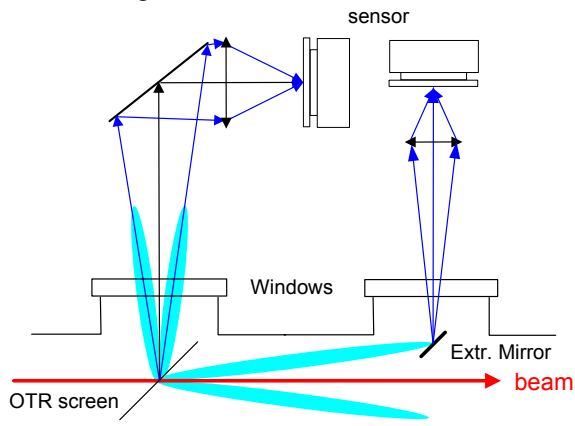


Figure 3: OTR screen monitor, with backward and forward OTR patterns and their imaging schemes.

The most popular use of OTR is for backward production, where the screen produces light in the specular direction. In this case, the image quality depends on the surface flatness of the screen. The photon production between two wavelengths λ_1 and λ_2 , at an angle θ with respect to the specular direction, is given by:

$$\frac{dN}{d\theta} = \left[\frac{\alpha}{2\pi} R^2 L_N \frac{\lambda_2}{\lambda_1} \right] \frac{1}{\theta} \frac{1}{(1 + 1/(\theta\gamma)^2)^2}$$

where γ is the Lorentz energy factor, α the fine structure constant and R the reflection coefficient of the screen. The resulting angular distribution of photons between 450 and 750nm is given in Fig. 4 for a 450 GeV proton.

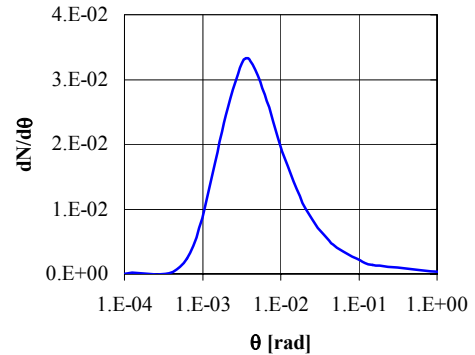


Figure 4: backward OTR photon production between 450 and 750nm for a 450 GeV proton.

The distribution has a central hole and a peak located at $1/\gamma$. For quite some time, this pattern was considered to limit the usefulness of OTR monitors to low γ beams because of diffraction until it was demonstrated analytically [7] and experimentally [8,9] that this was not the case, because most of the emission is spread over the long tail.

For the forward OTR, the light from part of the pattern is extracted at a finite angle, to avoid the particle beam. This type of monitor has to our knowledge only been used at CEBAF [8] with 250nm thick Carbon screens, placed perpendicularly to the beam. Its main advantage is to be independent of the surface flatness of the screen, which allows the use of very thin screens. A quantity that is often quoted in this case is the formation length, given by the formula:

$$l_f = \frac{2\lambda/2\pi}{\theta^2 + 1/\gamma^2}$$

This formation length is small for protons, but can go to large distances, hundreds of metres, for leptons, which was supposed to limit its use. It is accepted that this formation length is irrelevant for imaging applications.

Screen Performance and Test results

Several measurements can be performed to assess the performance of a screen. These measurements are in principle to be made with the beams on which the screen will be used.

The first measurement is that of the screen sensitivity. To compare various materials, it is possible to use a monitor of the type depicted in Fig.1 having a screen holder fitted with different screen types: Fig. 5.

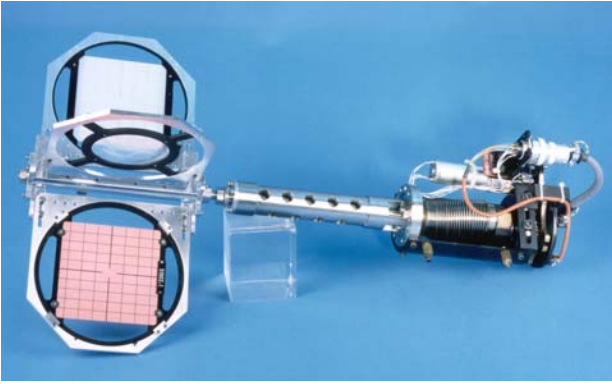


Figure 5: Screen holder with 3 screens (from bottom to top: $\text{Al}_2\text{O}_3[\text{Cr}]$, $\text{CsI}[\text{Tl}]$, Quartz) and one empty position for the free passage of beam.

The results of the measurements obtained with protons in the CERN SPS complex are given in Table 1. It can be seen that the studied screens cover a large dynamic range of $3 \cdot 10^6$. Due to the OTR emission pattern, the sensitivities could be slightly improved with leptons.

Table 1: Screen Sensitivities measured with protons and normalized for images with 7 pixels per beam sigma

Type	Material	Activator	Sensitivity [p]
Luminesc.	CsI	Tl	$6 \cdot 10^5$
“	Al_2O_3	0.5%Cr	$3 \cdot 10^7$
“	Glass	Ce	$3 \cdot 10^9$
“	Quartz	none	$6 \cdot 10^9$
OTR	Al		$2 \cdot 10^{10}$
“	Ti		$2 \cdot 10^{11}$
“	C		$2 \cdot 10^{12}$

Another important parameter for luminescent screens is the emission spectrum. This test can in principle be done with any beam able to excite the luminescence. Given in Fig. 6 are the spectra for different screens, measured with 450 GeV protons in the SPS extraction lines.

The measurement of the duration of the light emission can be performed at the same time for the luminescent screens. This parameter depends on the activator and probably on its concentration. The results are summarised in Table 2. The decay time for YAG[Ce] screens is given to be around 100ns and that of P43 to be equal to 1ms [6]. OTR screens have been able to provide measurements of bunch lengths down to picoseconds [12].

If the screens are under vacuum as in Fig.1, it is difficult to explore the characteristics of many screens in a reasonable time, because of the vacuum interventions. It is easier in this case to use a set-up as developed at ESRF where the screen is in air in a thin-walled tube that can be inserted in the beam line [3]. This could allow testing as many screen types as needed with a minimum of interventions.

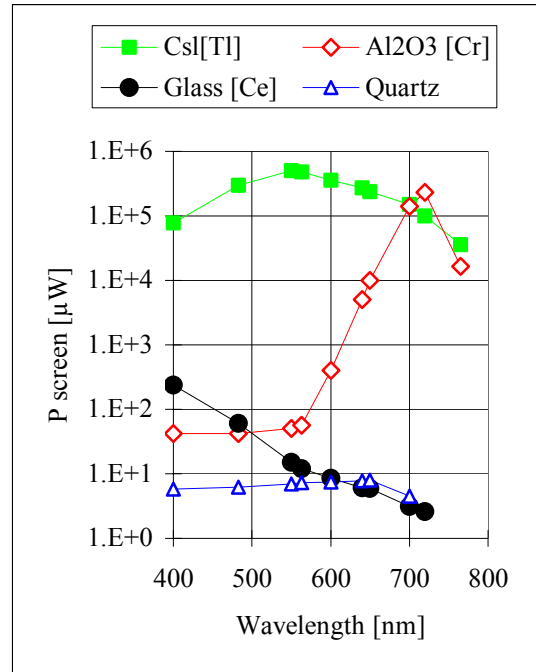


Figure 6: Emission spectra of various luminescent screens normalised for 10^{13} protons at 450 GeV.

Table 2: Decay times of luminescent screens

Screen	Activator	Decay time constant
Al_2O_3	Cr	>20ms
CsI	Tl	900ns
Glass	Ce	100ns
Quartz	None	ns

Whatever the set-up, some measurements are difficult or even impossible to perform with particle beams. This is for instance the case for resolution assessments. So another set-up, independent of an accelerator beam was looked for. An obvious candidate was a laser beam.

Table 3: Comparative Sensitivity Measurements for luminescent screens

Screen	Activator	Sensitivity		
		p beam		UV laser
		Abs.	Rel.	relative
CsI	Tl	$6 \cdot 10^5$	10^4	10^4
P43	Tb			$3 \cdot 10^3$
YAG	Ce			$4 \cdot 10^2$
Al_2O_3	0.5% Cr	$3 \cdot 10^7$	$2 \cdot 10^2$	$3 \cdot 10^2$
Glass	Ce	$3 \cdot 10^9$	2	
Quartz	none	$6 \cdot 10^9$	1	1

Tests were performed with an available UV laser (180μJ with 8ns pulses at 266nm, 10Hz), with high enough photon energy to excite the usual luminescent screens. First, relative sensitivity measurements were done to qualify the method with respect to a beam measurement. The results of this test are given in Table 3. The measurements give results similar to the ones obtained with proton beams, except for the Ce doped Glass which emits in a wide band around 395nm, probably too close to the laser wavelength.

To assess the screen resolution, measurements can be performed in a beam line, but they will be limited by the smallest achievable beam size. This will be easier with a laser beam. In a first test, the laser beam was focused to a small spot, and the beam sizes were measured for the various screens, a method which lacked sufficient precision. To progress further, a “pepper pot” type mask was inserted before the screen, to image onto the screen a pattern of light spots of 210μm diameter at a pitch of 380μm. The Contrast Function of this pattern was measured, and the resolution, expressed as the rms beam size broadening, was deduced from it: see Fig. 7.

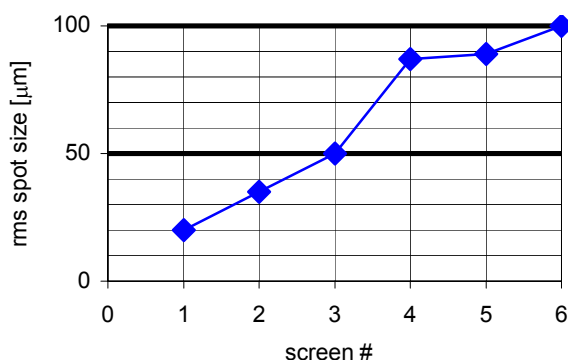


Figure 7: Resolution of different screens: given is the rms spot size for a point beam. The first screens are the P43, CsI and YAG, the others are various Al₂O₃ screens.

A clear separation is visible between the first three screens and the others. It is evident from this plot that the very thin phosphor screen and the crystalline screens will give a better resolution than any ceramic screen. These results were obtained with an IR filter, which improves significantly the resolution while decreasing the sensitivity for the Al₂O₃ screens. The test has shown that the influence on the resolution of the screen material thickness is more important than that of the material granularity.

For OTR screens, the resolution should only be affected by optical phenomena, i.e. defocusing and diffraction. At the high gamma end of the beam energy, the diffraction due to the emission pattern has been considered in the past as preventing the use of OTR. Since then, it has been shown that this doesn't apply, and an estimate for the “blurring” of the spot size of $\sigma \sim 5\lambda$, i.e. 3μm at 600nm, has been published [10] and deduced from experiments

[9]. On the low gamma range, cutting into the OTR distribution decreases the sensitivity and can produce diffraction, see Fig.4 for the angular extension of OTR. But as in this energy range the beams are in general big, this limitation should not be serious. What will be serious is the lack of photons at the detector level. So the optics have to be optimised for the best collection of light.

OPTICS AND DETECTORS

The next items in the chain of a monitor are the optics and the detector. It is important to have reference patterns on at least one screen for precise scaling and geometric references for the whole optical chain: see Fig. 2 and 5.

The optics are non-critical items, except with OTR screens for low gamma beams where the acceptance will have to be maximised.

For the detector [11], the first selection criterion is the local radiation level. If it is high, TV tube cameras have to be used. If the radiation level is lower, solid-state detectors can be used. For not too high levels, CID cameras can be installed. With low radiation levels, CMOS or CCD cameras can be used. The next factor to take into account is the matching of the detector sensitivity to the light emission of the luminescent screens. Given below in Fig. 8, are the emission and sensitivity spectra of various screens and detectors.

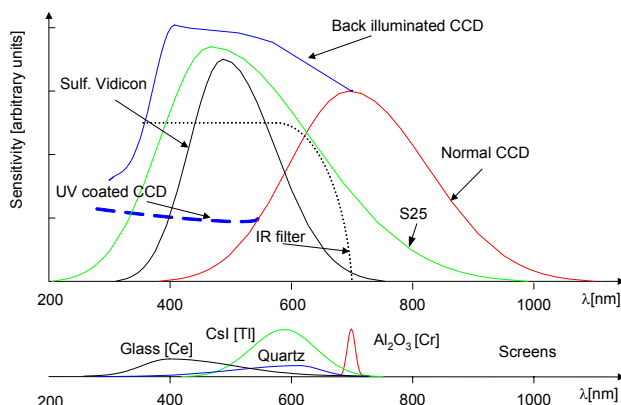


Figure 8: sensitivity and emission spectra of various detectors and screens.

It can be seen that a Glass [Ce] screen is not matched to a normal solid-state camera and that with an Al₂O₃[Cr] screen it has to be checked if the camera is fitted or not with an IR filter, as can be the case for improving camera resolution. The light level generated has to be matched to the detector sensitivity. Table 1 will be of help for this choice. Attention has to be paid to the control of the light level impinging on the detector as a test with the laser beam and an Al₂O₃[Cr] screen has shown. In this test, the beam size was measured either with only the laser beam attenuated to stay below CCD “blooming”, i.e. visible over-exposure on a TV monitor, or with additionally the screen generated light attenuated to stay well below CCD saturation as measured on an oscilloscope: see Fig. 9.

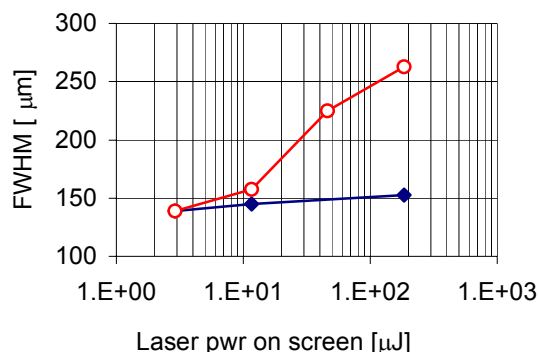


Figure 9: Beam sizes measured with attenuation of the laser beam (top curve) to prevent CCD “blooming” and with additional attenuation of the light emitted by the screen (bottom curve) to stay well below CCD saturation.

It is clear from these curves that the screen is not introducing a beam broadening through “saturation” by more than 7% over nearly two orders of magnitude of laser power, but the camera does, at a level of saturation not visible on a TV monitor. This test shows the importance of being able to control the light level on the sensor by optical attenuators, the aperture control or the integration time of the detector if slow screens are used. If fast profiles are to be acquired, such as beam time structure in transfer lines or turn-by-turn profile information in a circular machine, either OTR screens or fast crystalline screens and specific detectors have to be used. Fast digitised cameras with or without MCP intensifier/shutter, or multi-anode photomultipliers have to be used. Given below in Fig.10 is a sequence of profiles measured at a rate of 10kHz with a MCP gated camera.

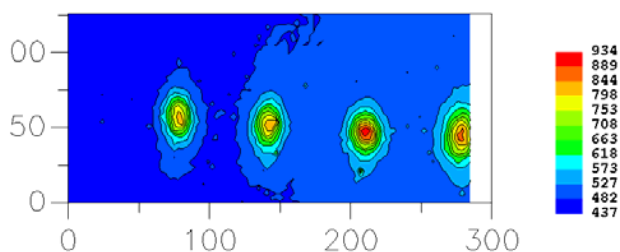


Figure 10: multiturn profile measurements with an OTR screen and a MCP Intensified camera in the SPS ring.

For very fast observations, as for measuring longitudinal profiles of bunches, a streak camera can be used [12].

While CCD detectors capture the beam image over their integration time, normally 20ms in the CCIR standard, before storing it in their memory area, CMOS cameras read their photodiodes sequentially over the 20ms frame time and TV tubes explore sequentially the odd and even lines of the picture. The automatic exposure and gain controls of CMOS cameras can give rise to problems when using fast screens. In certain cases the beam will simply be missed when using the “rolling shutter” asynchronously to the beam passage. In other cases, the

integration time will be pushed to its maximum during the beam off period, which will saturate the detector at beam passage. If position measurements are also to be performed with the screen monitor, attention has to be paid to the sensor type. For a TV type detector, it has to be remembered that a complete image is built from two frames, comprised of the even and the odd lines. A TV tube explores these lines in sequence and in a CCD the two frames are generated from two full scenes shifted on the detector by half a pixel. This will result in a computed vertical centre of charge offset of half a pixel between odd and even frames. This miscalculation will not occur with a CCD working in “progressive scan” mode.

OTHER MONITORS

Other monitors can be used, depending on the beam energy and intensity. Due to lack of space, we can't develop in detail these alternatives.

For high intensity hadron beams, gas luminescence has been used successfully at Los Alamos [13]. While this was considered only useful at low energy, tests in the CERN PS and SPS with Nitrogen and 1 to 450 GeV protons have shown that such monitors can also be used up to high energies [14]. This could be interesting at energies where OTR is not producing light in a reasonably sized acceptance or where small beam sizes at high intensity are a risk for screen survival [15]. The tuning parameter here is the gas pressure, which can go up to atmospheric pressure with separation windows.

For high gamma beams, for instance leptons above a few hundred MeVs, synchrotron light monitors can be implemented using the beam line bending magnets. This will result in a non-interfering profile monitor with an excellent time response, which can be a substitute for OTR screens. Good results were obtained in the MIT Bates transfer line to the South Hall with a 315 MeV electron beam and a 90° bending magnet [16].

Diffraction Radiation may be another method worthwhile considering for a non-intercepting monitor [17].

REFERENCES

- [1] J. Camas et al., PAC 93, Proc. p. 2498, 1993
- [2] W.S. Graves et al., BIW 98, Proc. p. 206, 1998
- [3] B.K. Scheidt, DIPAC 03, Proc. PM14, 2003
- [4] G. Burtin et al., CERN/LEP-BI/89-06, March 1989
- [5] R.L. Wittkover, PAC 95, Proc. p. 2589, 1995
- [6] A. Peters et al., DIPAC 2001, Proc. p. 123, 2001
- [7] R. Fiorito, D. Rule, BIW 94, Proc. p. 21, 1994
- [8] J.C. Denard et al., PAC 97, Proc. p. 2198, 1997
- [9] M. Ross et al., BIW 2002, Proc. p. 237, 2002
- [10] M. Castellano et al., DIPAC 2001, Proc. p. 46, 2001
- [11] R. Jung, BIW98, CERN SL-98-061 BI, October 1998
- [12] A.H. Lumpkin et al., BIW98, Proc. p. 199, 1998
- [13] D. Chamberlin et al., PAC 81, Proc. p. 2347, 1981
- [14] G. Burtin et al., EPAC 2000, Proc. p. 256, 2000
- [15] P. Ausset et al., EPAC 2002, Proc. p. 245, 2002
- [16] R. Jung, Bates Int. Rep., March 1981
- [17] R. Fiorito, D. Rule, NIM B 173, p. 67, 2001

Challenges for LHC and Demands on Beam Instrumentation

J. Wenninger, CERN, Geneva, Switzerland

Abstract

The LHC machine presently under construction at CERN will exceed existing super-conducting colliders by about one order of magnitude for luminosity and beam energies for pp collisions. To achieve this performance the bunch frequency is as large as 40 MHz and the range in beam intensity covers $5 \cdot 10^9$ protons to $3 \cdot 10^{14}$ protons with a normalized beam emittance as small as $3 \mu\text{rad}$. This puts very stringent demands on the beam instrumentation to be able to measure beam parameters like beam positions, profiles, tunes, chromaticity, beam losses or luminosity.

This document highlights selected topics in the field of LHC beam instrumentation. The examples will be chosen to cover new detection principles or new numerical data treatments, which had to be developed for the LHC as well as aspects of operational reliability for instrumentation, which will be used for machine protection systems.

THE LHC MACHINE

The Large Hadron Collider (LHC) is a proton-proton collider scheduled to start operation in 2007. The LHC will be installed in the existing 26.7 km long LEP tunnel. Its nominal operating energy is 7 TeV/c, with injection from the Super Proton Synchrotron (SPS) at 450 GeV/c. The overall layout of the LHC is shown in Fig. 1. The two

chambers that cross in Interaction Regions (IR) 1,2,5 and 8. The two high luminosity experiments are installed in IR1 (ATLAS) and IR5 (CMS). IR3 and IR7 are devoted to beam collimation (beam cleaning). The 400 MHz RF system and most special beam instruments are installed in IR4. The beam dumping system is installed in IR6.

The LHC super-conducting magnets are immersed in a bath of super-fluid Helium at 1.9 K. The nominal operating field of the dipoles is 8.4 T. The main parameters of the LHC for proton operation are summarized in Table 1. Details on ion operation can be found in Ref [2].

Dipole field (at T=1.9 K)	8.39 T
Number of bunches	1 – 2808
Bunch spacing	25 ns
Bunch population	$1.1 \cdot 10^{11}$
R.M.S. normalized emittance $\gamma\epsilon_{x,y}$	$3.75 \mu\text{m}$
Peak luminosity \mathcal{L}	$10^{34} \text{ cm}^{-2} \text{ s}^{-1}$
Number of IPs (high \mathcal{L})	4(2)
Crossing angle at IP	$300 \mu\text{rad}$
Beam-beam tune shift	0.0034
R.M.S. beam size at high \mathcal{L} IP	$16 \mu\text{m}$
R.M.S. bunch length	7.7 cm
Synchrotron rad. power	3.6 kW

Table 1: Nominal proton beam parameters at 7 TeV [1].

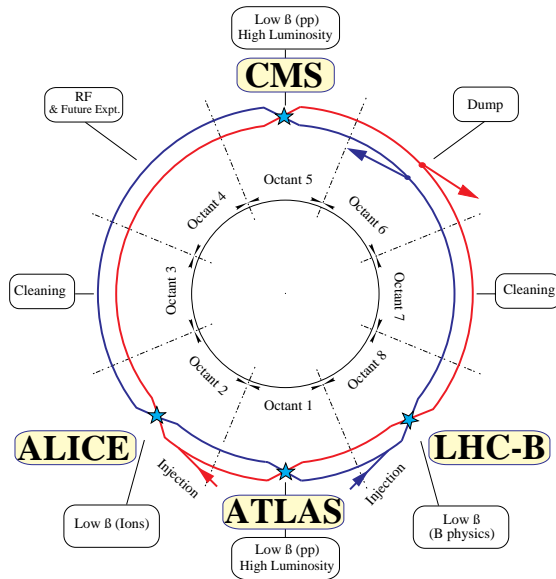


Figure 1: Layout of LHC ring and experiments.

beams (rings) of the LHC circulate in separated vacuum

DYNAMIC EFFECTS OF SUPER-CONDUCTING MAGNETS

The transfer function at low field of super-conducting magnets shows a hysteresis caused by the persistent currents, long lasting eddy currents originating in the super-conducting filaments when they are subject to field changes, i.e. during ramps [3]. The effect of persistent currents is particularly strong at low field and their effects appear on all allowed multi-poles (b_1 (dipole), b_3 (sextupole), b_5 (decapole) .. for dipole magnets).

The field contributions from the persistent currents decay during injection with a time constant of ~ 900 s and result in systematic and random (magnet to magnet fluctuations) effects. Fig. 2 gives an example for the b_3 component of the dipoles. The associated chromaticity change is $\Delta Q' \simeq 80$ units. A field ramp of 20 to 30 mT of the dipole field re-establishes the persistent currents to their original configuration before decay. This so-called 'snapback' occurs therefore in the first tens of seconds of the ramp.

The main consequences of the persistent currents are:

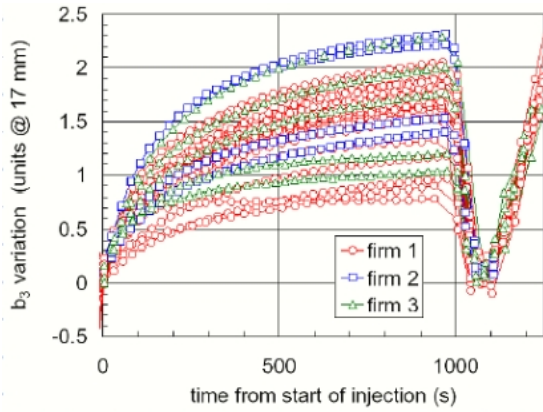


Figure 2: Injection drift of the sextupole field component for a sample of LHC main dipoles due to the decay of the persistent currents [3]. $\Delta b_3 = 1$ unit corresponds to $\Delta Q' = 50$ units. The persistent currents 'snapback' to their value before injection during the first seconds of the energy ramp (time = 1000 s).

- Closed orbit changes of ~ 1 mm r.m.s [5].
- Tune changes of $\Delta Q \sim 0.03$ [6].
- Chromaticity changes of $|\Delta Q'| \sim 80$ units (Fig. 2).
- Large coupling changes due to feed-down of the b_3 components from imperfectly aligned sextupole corrector elements.

It is expected that 80-90% of the changes may be anticipated by operating the machine with a reproducible cycle and by measuring the drifts during the injection decay [3]. Operating the LHC with a reproducible magnetic cycle should allow most of the corrections to be feed forward from one cycle to the next.

TUNE, CHROMATICITY AND COUPLING STABILIZATION

The emittance budget of the LHC is very tight, with only about 10% increase allowed from injection to collisions. To achieve this goal, some key parameters must be stabilized within very tight bounds [4]:

- $\Delta Q \simeq \pm(1 - 3) \cdot 10^{-3}$
- $Q' = 1 - 2$ units
- Coupling $c \leq 5 \cdot 10^{-3}$

To stabilize the tune through the entire cycle, a tune feedback system based on a PLL tune measurement is foreseen. To avoid emittance blowup, a resonant BPM working on oscillation amplitudes of few μm will be used to detect beam oscillations. The chromaticity stabilization is extremely challenging. Measurements based on Head-tail oscillations are foreseen [7], although the required kicks on the beam may affect the emittance significantly. Coupling measurements may be performed with an AC-dipole [8].

PROFILE MONITORS

Precise profile measurements are required to monitor the emittance of the LHC beam throughout the machine cycle. At 7 TeV the emittance of 0.5 nm yields transverse beam sizes of 0.2 – 0.5 mm that should be measured with a relative accuracy of a few percent. Synchrotron light monitors are foreseen as not interceptive devices, with precise wire scanners for cross-calibration. The later can only be used with low beam intensities.

Measurements of betatron function are required to transport the beam profiles to other locations in the ring (collimators): such measurement are based on multi-turn BPM data, the beam excitation being performed with single kicks or AC-dipoles.

BEAM-BEAM AND LUMINOSITY

For collisions the IR betatron function is squeezed from the injection and ramp value of 18 m down to 0.5 m at the high luminosity interactions points. The beams collide at an angle (full opening) of $300 \mu\text{rad}$ to minimize the effects of parasitic encounters in the common beam tube, see Fig. 3. On both sides of the IR, a bunch in the center of a 72-bunch train encounters up to 15 bunches of the opposing beam. The perturbations from those long-range collisions increase the tune spread in the beam and can destabilize particles at amplitudes of a few σ . Bunches at the beginning and end of the trains experience fewer parasitic collisions and are called PACMAN bunches [1, 9]. Such bunches are likely to have lower lifetime and larger emittance.

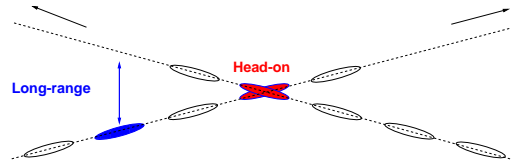


Figure 3: Schematic of long-range collisions.

The effects of the long range collisions depend on the crossing plane combination in the 2 high luminosity IRs [9](both vertical or horizontal, mixed). Fig. 4 shows tune variations along a train due to the long range collisions. The effect on the horizontal beam position at the IR is visible in Fig. 5. Due to the difference in the offsets for the two beams, it is not possible to collide all bunches head-on at the IR. Offsets of $\sim 1 \mu\text{m}$ (for an r.m.s. beam size of $16 \mu\text{m}$) cannot be avoided. A challenging compensation scheme based on a wire located near the IRs is foreseen for the LHC to counteract the side effects of the long-range beam-beam [10].

As a consequence of the parameter variations between bunches, all LHC beam instruments should provide bunch-by-bunch measurements: orbit, tune, lifetime and current, emittance (transverse and longitudinal) and, up to a certain extend, beam losses.

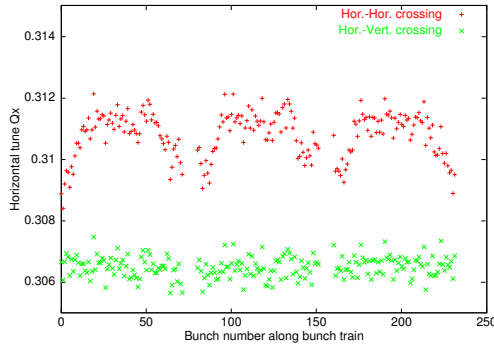


Figure 4: Horizontal tune variation along 3 trains of 72 bunches for the case where the crossing planes are different in the 2 high luminosity IRs (green) and for the case where both crossings are horizontal (red) [9].

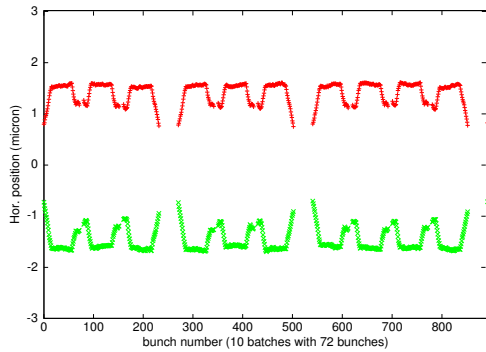


Figure 5: Horizontal beam position variation at the IR along 10 trains of 72 bunches for the 2 counter-rotating beams [9]. The r.m.s. size at the IR is $16 \mu\text{m}$.

The fundamental parameter for machine tuning in physics is the luminosity. Luminosity detectors dedicated for machine operation will be installed in all 4 IRs. Those detectors must cover a dynamic range of $\mathcal{L} = 2 \cdot 10^{26}$ to $10^{34} \text{ cm}^{-2}\text{s}^{-1}$ (nominal). The lowest \mathcal{L} corresponds to collisions of one low intensity ($5 \cdot 10^9$ protons) bunch per beam and un-squeezed optics. In that case, which is likely to be used during the commissioning phase, the integration time is not critical. Bunch-by-bunch measurements, averaged over a few seconds, should be provided to monitor PACMAN bunches. The monitors should also provide background diagnostics at small angles. The technological choice of the detectors, which are installed in an extremely hostile environment in terms of radiation and heat load, has not been finalized: CdTe detectors [11] or ionization chambers [12].

MACHINE PROTECTION

Both the energy stored in the LHC magnets and in the LHC beams are unprecedented. The 8 LHC sectors covering one arc each are powered separately to limit the energy stored in each circuit to 1.3 GJ at top field. The total energy stored in the LHC magnets is 10.4 GJ [13].

Fig. 6 compares the energy stored in the beams of various accelerators. At 7 TeV the 350 MJ stored in each LHC beam exceed the values at existing machines by 2 orders of magnitude. The transverse energy density increases even by 3 orders of magnitude due to the high beam brightness.

The LHC will be protected by over 10000 interlock channels that are managed by a high performance machine protection system [14]. A significant number of those channels are provided by beam instrumentation as will be discussed below.

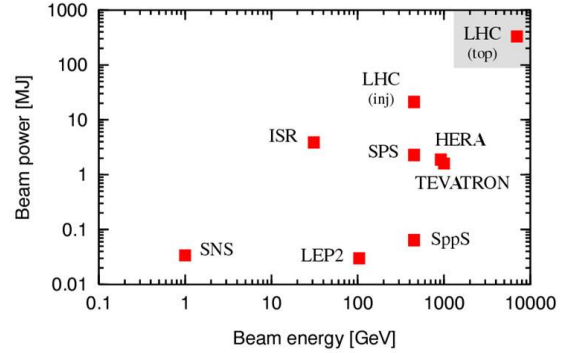


Figure 6: Energy stored in various accelerators.

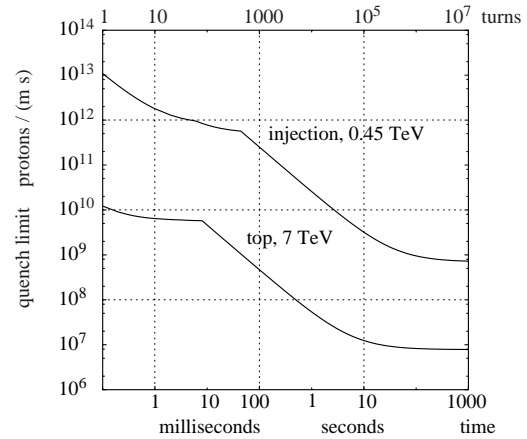


Figure 7: Quench level of the LHC dipoles in lost protons per meter and second as a function of the time scale of the loss.

Beam Collimation

Operating the LHC with beam intensities of 0.5 A or $3 \cdot 10^{14}$ protons per beam requires tight control of the beam losses in the super-conducting magnets. The quench limit of the main dipole magnets is shown in Fig. 7 as a function of beam energy and loss rate. The quench level varies over 6 orders of magnitude from 450 GeV/c to 7 TeV/c and between fast and slow losses. At 450 GeV/c a single low intensity bunch of $5 \cdot 10^9$ protons, the so-called 'pilot' bunch, should not quench the magnets. This pilot bunch will be used to check out and commission the LHC.

Running the LHC requires large beam lifetimes and/or efficient collimation at all stages of operation. With the exception operation at 450 GeV/c with a single pilot bunch,

the collimators must be used in all phases of machine operation [15]. The primary collimator aperture must be set between 5 and 8σ . At 7 TeV the opening is only ± 1.2 mm due to the extremely small transverse beam size, see Fig. 8.

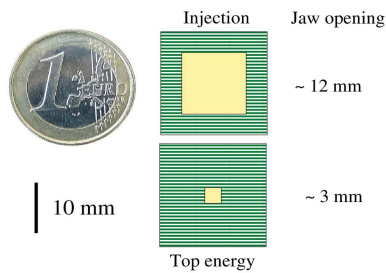


Figure 8: Opening of the LHC primary collimators at 450 GeV/c and at 7 TeV/c. At top energy the opening is equivalent to the size of Spain on the 1 € coin [15].

To maintain a high cleaning efficiency of the collimation system, the orbit must be stabilized to $\sigma/3$ (~ 70 μm at 7 TeV) while the β -beating should not change by more than 5 - 10% [6]. A local (or global) orbit feedback must be operated at all times in the LHC due to the tight aperture, a somewhat unusual fact in a proton machine [5]. Local β -beating measurement must be provided at the collimators and at the location of the emittance devices to determine precisely the beam size at the collimators.

The tight requirements of the collimation system limits the maximum tolerable oscillation amplitude that can be given to the beam to $\sim 0.5 - 1\sigma$ depending on the total intensity. Such limitations put stringent requirements on the beam position monitor resolution for multi-turn measurements (β -beating...).

Beam Loss Monitors

The extremely high beam energy and density can lead to damage of collimator jaws and other machine components. To protect the machine against un-controlled losses ~ 3000 Beam Loss Monitors (BLMs) will be installed around the ring [16]. The BLMs must cover a dynamic range of loss rates that exceeds 8 orders of magnitude, with a minimum loss rate of $\sim 1\%$ of the lowest quench level (see Fig. 7). Two basic monitors types will be used:

- Arc monitors with a typical reaction time of a 2.5 milliseconds will be installed at each quadrupole.
- Special collimator monitors (BLMC) that must have a reaction time of around 1 LHC turn ($89\mu\text{s}$) to protect the collimators or other critical apertures against fast beam losses. The role of those collimators will be extremely important to optimize the collimators settings.

The BLMC monitors will be safety critical devices and operation of the LHC will not be allowed whenever they are not operational. They will be able to trigger a beam dump at any time.

The detectors will be based on ionization chambers (1 liter Nitrogen gas) coupled to a first level electronics

based on Current-to-Frequency conversion that is capable of covering the entire dynamic range. In the LHC arcs separation of the loss signal of the 2 beams will be extremely useful for operation. Detailed simulations of the loss distribution are required to optimize the detector layout.

Beam Abort Gap Monitor

A $3\mu\text{s}$ long beam abort gap free of particles must be provided within the LHC beam to accommodate the rise-time of the beam dump kickers. Un-captured beam (at injection), intra-beam scattering and unavoidable RF noise will populate the beam abort gap [17]. At 7 TeV, the 7 keV/turn energy loss by synchrotron radiation pushes un-captured particles towards the off-momentum collimators and limits the population of the abort gap. Although it is foreseen to clean the abort gap using the transverse damper system, very reliable monitoring of the particle density in the beam abort gap must be provided to ensure that magnets downstream of the dump kickers do not quench during beam abort. The sensitivity of the monitor must be in the range of $2 \cdot 10^5$ protons/m or $6 \cdot 10^4$ protons/ns. This density is 6 orders of magnitude below the peak density inside the LHC bunches.

Beam Dumping System

The limited aperture of the beam extraction septa magnets of the beam dumping system defines a ± 4 mm window on the maximum tolerable orbit excursion around the beam dump area. The position will be stabilized by an orbit feedback, but to ensure that this requirement is always fulfilled, a fast interlock on the beam position will be required. For the fastest magnet/power converter failures, the orbit movement in the dump area will be $\sim 60\mu\text{m/turn}$, thus requiring reaction times of a few turns [13]. The same fast position interlock may be required to complement the BLM system for the fastest failures.

Post-mortem Diagnostics

Post-mortem diagnostics, in the form of turn-by-turn information for the last 1000 turns before a beam abort and in the for a lower resolution (1 - 10 Hz) for the last 20 seconds before beam abort will be required for all critical LHC instruments to diagnose the consequences of beam aborts.

ELECTRON CLOUD

For the 25 ns spacing of the LHC bunches and the vacuum half aperture of 2 - 3 cm the number of electrons may amplify exponentially during the passage of a bunch train, as has been observed in the SPS [18]. This so-called electron cloud can strongly perturb the beam stability [1]. The associated heat load deposited on the vacuum chamber (Fig. 9) may limit the total beam intensity.

The cloud is generated from a small number of primary electrons liberated by gas ionization, beam loss or syn-

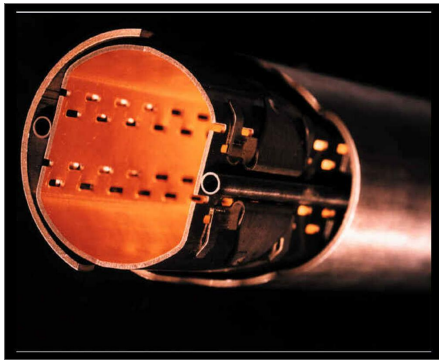


Figure 9: The LHC vacuum chamber and the beam screen (at 4 – 20 K) that shields the cold mass from synchrotron radiation and image currents. In this figure the chamber is rotated by 90° with respect to its normal orientation.

chrotron light impact, see Fig. 10. The key process for cloud amplification is the secondary emission of electrons, and the most important parameter the secondary emission yield, which is typically peaks around 1 to 2.5 for Copper surfaces. The simulated transverse distribution of an electron cloud in the LHC is shown in Fig. 11.

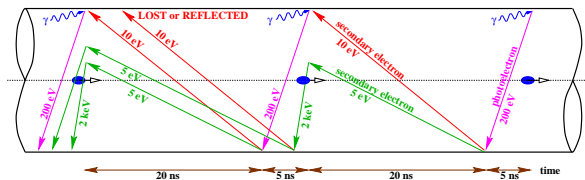


Figure 10: Principle of electron cloud buildup.

Measurements at the SPS [18] have shown a strong dependence of the cloud on the magnetic dipoles field, the filling pattern, the bunch population and the bunch length. Diagnostics is required to monitor the state of the LHC vacuum chamber surface. Measurement devices includes strip detector installed inside the vacuum chamber, special devices to determine in situ the secondary emission yield and the power deposited on the chamber.

For the first two years of LHC operation, the bunch spacing will be increased to 75 ns. For such a spacing no electron cloud effect is expected. Nevertheless beam with 25 ns spacing may be stored at injection energy to clean the vacuum chamber surface in preparation for nominal performance.

CONCLUSION

Reliable and safe operation of the LHC requires excellent beam diagnostics and control during all phases of machine operation. The impact of beam-beam effects requires bunch-to-bunch resolution for most LHC beam instruments. High reliability is required from beam loss monitors, abort gap monitors and beam position interlocks. Stabilization of tunes, chromaticity and coupling without emittance degradation of the high brightness beams are re-

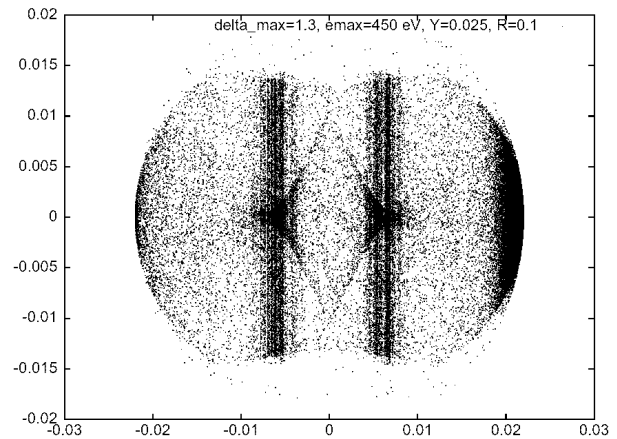


Figure 11: Simulated transverse distributions of electrons due to multi-pacting in the LHC vacuum chamber [1].

quired. Closed loop feedbacks on orbit and tune will be mandatory.

REFERENCES

- [1] F. Zimmermann, CERN-SL-2002-03 (AP).
- [2] K. Schindl, Proc. of the XIIth Chamonix LHC Workshop, CERN-AB-2003-008 (2003).
- [3] L. Bottura, Proc. of the XIIth Chamonix LHC Workshop, CERN-AB-2003-008 (2003).
- [4] O. Bruning *et al*, LHC Project Report 222 (2001).
- [5] J. Wenninger, Proc. of the XIIth Chamonix LHC Workshop, CERN-AB-2003-008 (2003).
- [6] R. Assmann *et al.*, *Time Dependent Superconducting Magnet Errors and their Effect on the Beam Dynamics at the LHC*, Proc. of EPAC02, Paris, France.
- [7] R. Jones *et al.*, CERN-SL-2001-20-BI (2000).
- [8] J.P. Koutchouk, these proceedings.
- [9] W. Herr, LHC Project Report 628 (2003).
- [10] J.P. Koutchouk, CERN-SL-2001-051-BI (2001).
- [11] E. Rossa *et al*, CERN-SL-2002-001-BI (2002).
- [12] W.C. Turner, LBNL-42180 (1998).
- [13] R. Schmidt, Proc. of the XIIth Chamonix LHC Workshop, CERN-AB-2003-008 (2003).
- [14] B. Puccio *et al*, LHC Project Report (2002).
- [15] B. Jeanneret, Proc. of the Xth Chamonix Workshop, CERN-SL-2000-007 DI.
R. Assmann, Proc. of the XIIth Chamonix LHC Workshop, CERN-AB-2003-008 (2003).
- [16] B. Dehning *et al*, *The Beam Loss Detection System of the LHC Ring*, Proc. of EPAC02, Paris, France.
- [17] E. Chapirochnikova, Proc. of the XIIth Chamonix LHC Workshop, CERN-AB-2003-008 (2003).
- [18] J.M. Jimenez *et al*, LHC Project Report 632 (2003).

SINGLE SHOT ELECTRON-BEAM BUNCH LENGTH MEASUREMENTS

G. Berden*, G.M.H. Knippels†, D. Oepts, A.F.G. van der Meer,
FOM Institute Rijnhuizen / FELIX, Nieuwegein, The Netherlands

S.P. Jamison‡, X. Yan, A.M. MacLeod, W.A. Gillespie,
School of Computing and Advanced Technologies, University of Abertay Dundee, Dundee, UK

J.L. Shen§, Dept. of Physics, Capital Normal University, Beijing, China

I. Wilke, Rensselaer Polytechnic Institute, Troy, NY, USA

Abstract

It is recognised by the instrumentation community that 4th generation light sources (like TESLA, LCLS) pose some of the most stringent requirements on beam diagnostics. Of these diagnostics, electro-optic detection of the electric field of electron bunches offers a promising single-shot technique for the measurement of the bunch length and shape in the sub-picosecond domain. The electro-optic detection method makes use of the fact that the local electric field of a highly relativistic electron bunch moving in a straight line is almost entirely concentrated perpendicular to its direction of motion. This electric field induces birefringence in an electro-optic crystal placed in the vicinity of the beam. The amount of birefringence depends on the electric field and is probed by monitoring the change of polarization of a chirped, synchronized Ti:sapphire laser pulse. This paper will provide details of the experimental setup at the Free Electron Laser for Infrared eXperiments (FELIX) in Nieuwegein, The Netherlands, where single shot images of 1.7 ps long electron bunches have been obtained (beam energy 46 MeV, charge per bunch 200 pC). Future upgrading possibilities will be discussed.

INTRODUCTION

An on-going research project at the Free Electron Laser for Infrared eXperiments (FELIX) [1] is the development of methods to measure the longitudinal shape of electron bunches via electro-optic detection of their transverse electric field. The electron bunch shape is measured inside the accelerator beam pipe at the entrance of the undulator of the FEL. A 0.5 mm thick $\langle 110 \rangle$ ZnTe crystal is used as an electro-optic sensor and is placed with its 4×4 mm² front face perpendicular to the propagation direction of the electron beam. The probe laser beam is linearly polarized and passes through the ZnTe crystal parallel to the electron beam.

This paper describes three methods to measure the shape of an electron bunch with electro-optic detection. The electric field-induced birefringence in an electro-optic crystal is probed by

1. sweeping the pulse of the probe laser, with a probe pulse length that is shorter than the electron bunch length, over the electron bunch and recording the intensity of the light transmitted through a the crossed polarizer (analyzer) as a function of time [2]. Although this is not a single-shot method, it can be used for real-time monitoring.
2. using a linearly chirped pulse of the probe laser, with a pulse length longer than the electron bunch length, and recording the wavelength spectrum of the chirped pulse which is transmitted through an analyzer [3].
3. using a chirped pulse of the probe laser, with a pulse length longer than the electron bunch length, and recording the single-shot cross-correlation of the chirped pulse transmitted through an analyzer. An unchirped pulse is used as the reference in the cross-correlator.

DELAY-SCAN METHOD

The probe laser for the “delay-scan method” (method 1) is a femtosecond Ti:Sapphire laser (wavelength 800 nm, pulse energy 5 nJ, repetition rate 100 MHz, pulse length 15 fs) which is actively synchronized to the accelerator rf clock [5] (see Figure 1). The delay between optical pulses and the electron bunches (beam energy 46 MeV, bunch charge 200 pC, micropulse repetition rate 25 MHz or 1 GHz, bunch length ~ 1.5 ps) can be varied with a phase shifter. A balanced detection arrangement was used instead of a crossed-polarizer detection setup in order to increase the signal-to-noise ratio. The laser room, containing the femtosecond laser system and the detection system, is located approximately 30 meters from the FEL cavity. The probe pulse is relayed by means of lenses and mirrors to direct the pulse towards the ZnTe crystal (fibers would stretch the probe pulse). More details on the setup can be found in Refs. [2, 4].

* berden@rijnh.nl

† present address: Picarro, Sunnyvale, CA, USA

‡ also at: University of Strathclyde, Glasgow, UK

§ also at: University of Strathclyde, Glasgow, UK

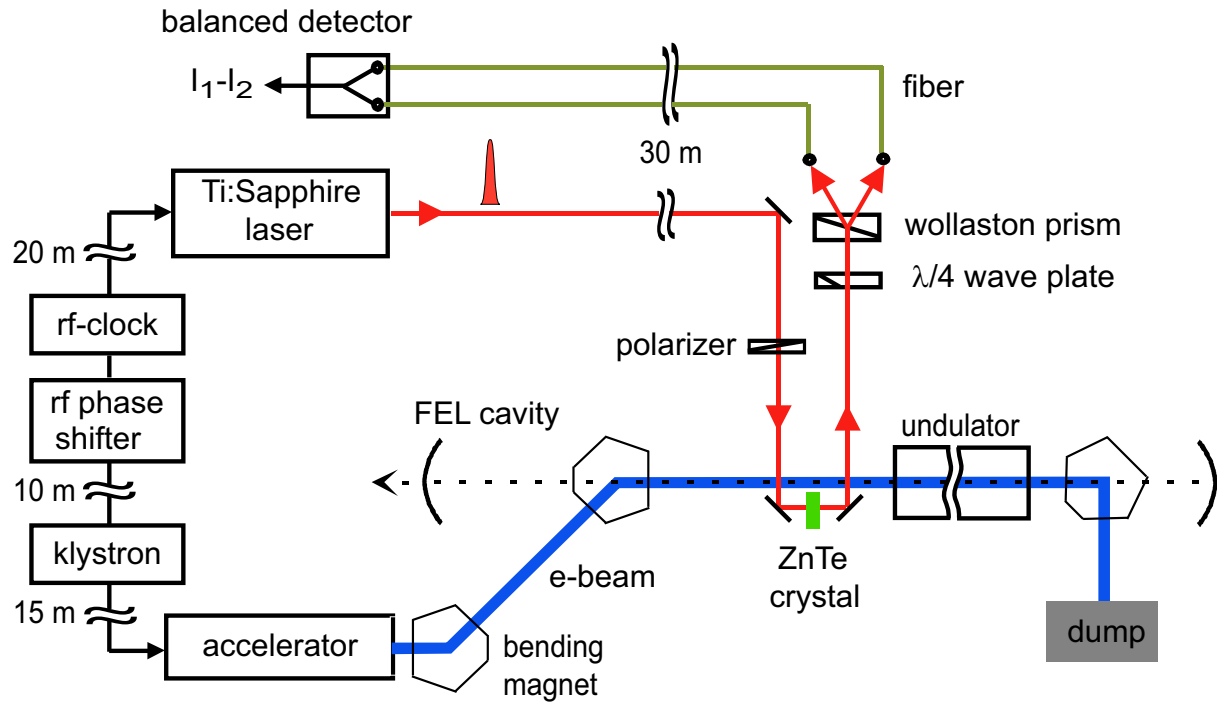


Figure 1: Experimental setup of the electro-optic “delay-scan method” (method 1).

Figure 2 shows a typical measurement. The rf-phase shifter can sweep the probe laser pulses over the electron bunches with a rate of a few picoseconds per microsecond. Since there is an electron bunch every 1 or 40 ns and a probe pulse every 10 ns, this means that the complete electric field profile is measured in a few microseconds. This delay-scan method can therefore be used for real-time monitoring, although the measured profile is sampled from a few hundred individual electron bunches.

The time resolution is determined by:

- the pulse length of the probe laser (in our case 15 fs);
- the time jitter in the synchronisation of the probe pulse to the electron bunch (in our case 50 fs in a few microseconds; on longer time scales 400 fs);

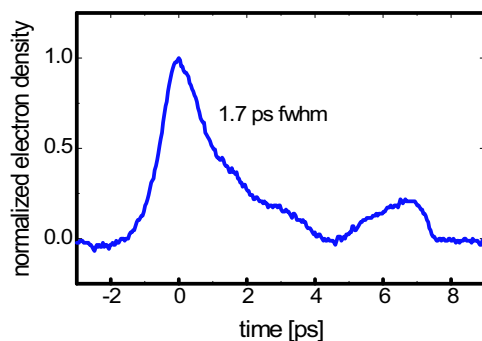


Figure 2: The electric field profile of the electron bunch measured at the entrance of the undulator. The leading edge is on the left. The pulse length is about 1.7 ps FWHM.

- the distance R from the electron beam to the electro-optic crystal, $\Delta t_d \approx 2R/\gamma c$ [6] (in our case $\Delta t_d \approx 0.4$ ps for $R=6$ mm, $\gamma=90$);
- the material and the length of the electro-optic crystal, see below (the cut off for our 0.5 mm crystal is around 350 fs; thus electron bunches shorter than 350 fs are broadened and/or distorted).

WAVELENGTH DETECTION OF CHIRPED BEAM

In the “chirped-pulse spectrometer method” (method 2) a short probe pulse is stretched to a pulse with a linear chirp and with a length longer than that of the electron bunch. In a linearly chirped pulse the instantaneous wavelength is proportional to time. When the electric field of an electron bunch and the chirped optical pulse copropagate in the electro-optic crystal, the various wavelength components of the chirped pulse passing through the crystal obtain different phase retardations, corresponding to different portions of the local electric field. By placing the crystal between crossed polarizers, the phase retardation in the wavelength spectrum is converted into an intensity modulation of this spectrum. Thus, the time profile of the local electric field of the electron bunch is linearly encoded onto the wavelength spectrum of the optical probe beam. This wavelength spectrum is dispersed in a spectrometer and recorded in a single shot with a linear diode array or a CCD camera (see Figure 3).

Figure 4 shows a single-shot image of the electric field profile of an individual electron bunch after on-line data

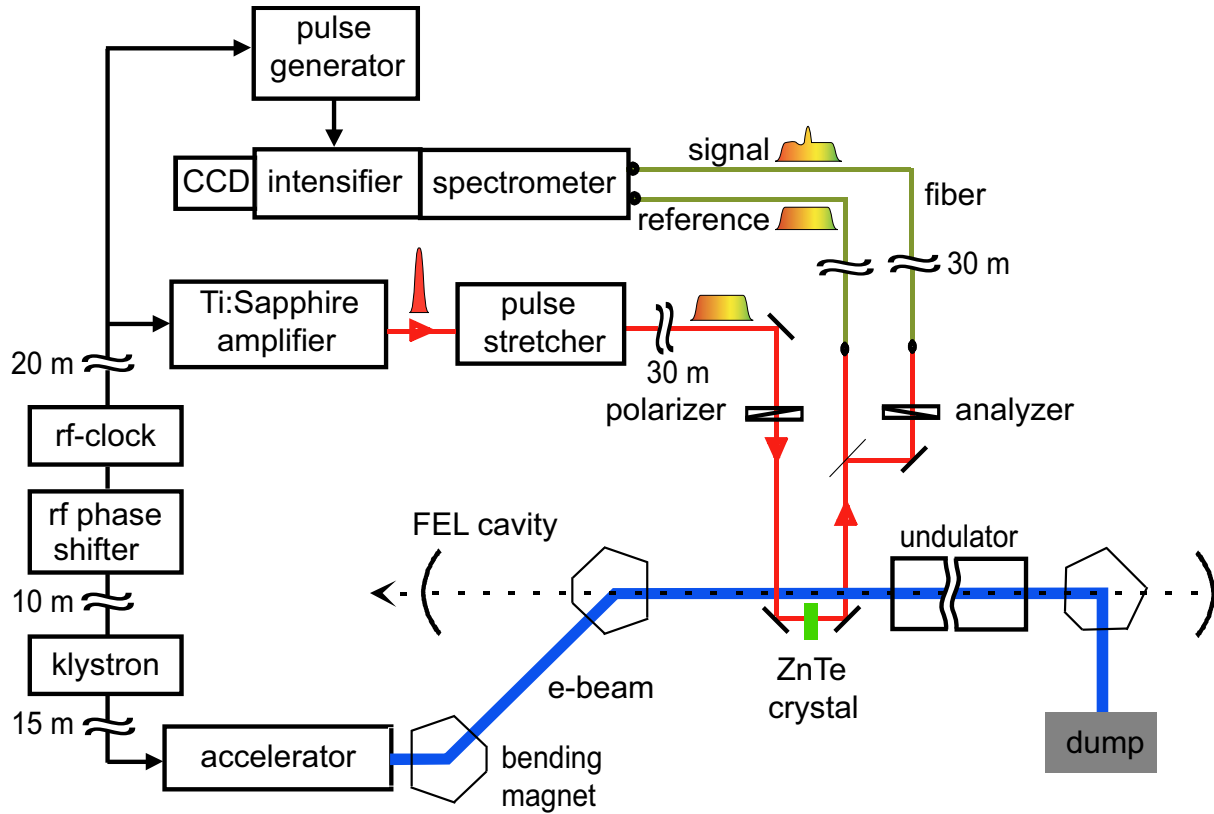


Figure 3: Experimental setup of the electro-optic “chirped pulse spectrometer method” for measuring single-shot images of the electric field profiles of individual electron bunches (method 2).

processing (details on the data processing can be found in Ref. [3]). The time resolution is determined by:

- the pulse length of the probe laser τ_0 and the length of the chirped pulse τ_c . For bunch lengths shorter than $(\tau_0\tau)^{1/2}$ the measured profile will be broadened

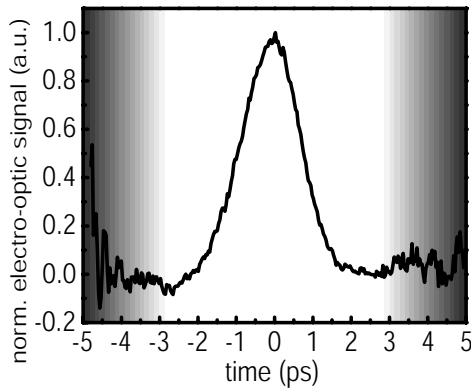


Figure 4: Single-shot measurement of the electric field profile of an individual electron bunch. The leading edge is on the right. The pulse length is about 1.7 ps FWHM. The shaded areas indicate the regions of increased noise introduced by the correction for the wavelength dependent variations in the intensity of the spectrum.

and/or distorted (see below). In our case $\tau_0=30$ fs and $\tau_c=4.48$ ps, which gives $(\tau_0\tau)^{1/2} \approx 370$ fs while the bunch length is ≈ 1.5 ps. The broadening is expected to be less than 100 fs.

- the distance from the electron beam to the electro-optic crystal (in our case $\Delta t_d \approx 70$ fs for $R=1$ mm, $\gamma=90$);
- resolution of the spectrometer and diode array, in the present setup ≈ 300 fs.
- the material and the length of the electro-optic crystal, see below (the cut off for our 0.5 mm crystal is around 350 fs).

Since in our case the electron bunch length is on the order of 1.5 ps, the only improvements in resolution can come from an improvement of the spectrometer/diode-array setup, which can easily be done, and by replacing the crystal with a thinner one.

The time window in which the electron bunch is viewed can be changed as easily as the time scale of an oscilloscope, because the length of the chirped pulse may be altered simply by adjusting the optical path difference in the optical stretcher (which is controlled via one single translation stage). There is however an important limitation in increasing the length of the time-window due to

the intrinsic coupling between the frequency components of the intensity modulation (induced by the electron bunch) and the frequency components of the chirped optical pulse. This coupling introduces additional spectral modifications which cannot by themselves be distinguished from the desired spectral modulation. Experimentally this has been shown by Jamison et al. [7] in the chirped electro-optical detection of so-called optical half cycle pulses (see Fig. 5; theoretically this has been described by Fletcher [8] and more general by Jamison et al. [7]). Very generally, it can be concluded that there are no such problems if a time-window is chosen such that $(\tau_0\tau_c)^{1/2}$ is smaller than the duration of the electron bunch.

CROSS-CORRELATION OF CHIRPED BEAM

The interference effects which can be present in the “chirped-pulse spectrometer method” appear because in the final step of this method the wavelength spectrum of the pulse is recorded. A way to circumvent these problems is to measure the chirped pulse in the time-domain, which is the third method: single-shot “chirped-pulse cross correlation”. In this method the chirped pulse carrying the modulation due to the presence of the electron bunch is cross-correlated with a part of the original optical pulse which has been split off before the optical stretching. Single-shot cross-correlation is based on the temporal to spatial conversion that occurs through the spatial overlap of non-collinear beams in a second-harmonic crystal. The results of such an experiment for a half-cycle pulse are shown in Fig. 5. At the moment of writing this contribution, the first test measurements have been performed on the cross-correlator set-up at FELIX and we have not yet obtained a single shot cross-correlation measurement of the electron bunch. It is clear that the optical alignment of a cross-correlator is more complex than the alignment of a spectrometer. Note that the cross-correlation method does not require a (linear) chirp of the probe pulse. Other related methods have been proposed such as auto-correlation and Frequency Resolved Optical Gating (FROG) measurements [9].

OTHER ELECTRO-OPTIC DETECTION VARIANTS FOR E-BEAM DIAGNOSTICS

Fitch et al. [10] have used the delay-scan method to measure the wake fields in the Fermilab high-brightness photo-injector (charge per bunch: 12 nC, bunch length 4.2 ps). They used a LiTaO₃ crystal as sensor which was oriented in such a way that they were able to probe longitudinal and radial components of the electric field. The measurements were related to the wall impedance.

Srinivasan-Rao et al. [11] proposed a method to encode the electron bunch profile on the *spatial* intensity distribution of the probe laser pulse. In this method the probe laser pulse is focused to form a line focus which is parallel to the direction of the electron beam. A thin electro-optic crystal

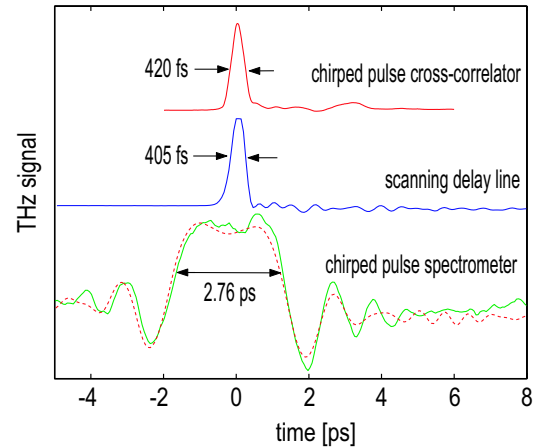


Figure 5: Electro-optic sampling of optical half cycle pulses. The length of the half cycle pulse is ≈ 300 fs, while the length of the probe laser pulse is ≈ 60 fs. The middle curve shows the result of the delay-scan method. The lower curve shows the result of the chirped-pulse spectrometer method, where the time-window (length of the chirped pulse) was 30 ps. If the time-window is too large compared to the length of the electric field, the signal is distorted. The dashed curve is a simulation [7]. The upper curve shows the result of the cross-correlator method, where the chirped pulse duration is also 30 ps.

is positioned at the waist of the laser beam which is directly below the electron beam. The intensity of the light transmitted by the crystal and a crossed analyzer is detected by a linear array. This spatially resolved intensity distribution is a measure of the temporal distribution of the charge in the electron beam. A difficulty in this experiment is the thickness of the crystal. A very thin crystal ($< 30 \mu\text{m}$) is needed because the directions of the electron beam and the probe laser beam are perpendicular to each other. Measurements have not yet been reported.

SOME NOTES ON ELECTRO-OPTIC CRYSTALS

The phase retardation experienced by the probe laser passing through an electro-optic crystal is proportional to the length of the crystal, the electro-optic coefficient (on the order of pm/V) and the local electric field. The actual expression for the phase retardation depends on the orientation of the crystal with respect to the direction of the electric field and the polarization of the probe laser, and can be found in literature (see e.g. [12]). At a first glance the ideal crystal would be a long crystal with a high electro-optic coefficient. There are however a few limitations:

- **Absorptions.** It is clear that the crystal should be transparent for the probe laser, but the ideal crystal is transparent in a very broad THz spectral range as well. The ZnTe crystal has a strong transverse-optical phonon resonance at 5.3 THz, which means that com-

ponents of the electric field with a frequency higher than 5 THz (200 fs) are (partly) absorbed which leads to a distortion of the measured electric field profile of the electron bunch. These absorptions can be modeled and it has been shown that ZnTe crystals can be used to measure frequencies up to 37 THz [13]. Other crystals might be even more suitable; GaP, for example, has a phonon absorption at 8.3 THz (115 fs).

- Dispersion. Two dispersion effects limit the length of the crystal: Group Velocity Mismatch (GVM) and Group Velocity Dispersion (GVD). Due to the wavelength dependence of the index of refraction (dispersion), the optical probe pulse and the electric field travel at a different velocity through the crystal. In the case of a long crystal, this means that the measured electric field profile will be smeared out. For ZnTe the group velocity of the 800 nm probe pulse is identical to that of the 2.3 THz frequency component of the electric field. The second effect, GVD, is a similar effect: the different frequency components of the electric field (but also of the probe laser) have different velocities in the crystal. It is clear that shorter optical pulses and shorter electron bunches require a thinner crystal.

Electro-optic sampling is a technique which originates from THz-science, and many details of this technique (crystal choice, measurement techniques, modelling, etc.) can be found in the literature.

An intriguing point is the effect of the difference in velocity of the electron bunch and the velocity of the electric field propagating through the crystal, which is lower by a factor of almost three. There has to be a region in the crystal where the field lines are not perpendicular to the propagation direction and are stretched over the length (thickness) of the crystal. However, there is still a one-to-one correspondence between the field and the electron density along the (narrow) probe laser path. A more detailed understanding of the propagation of the Coulomb field through the crystal is desirable, although for practical purposes it should be sufficient to probe the electric field at a distance of d/n (d thickness of crystal, n refractive index) from the edge of the crystal.

CONCLUSION

Electro-optic sampling of the Coulomb field of the electron bunch is a promising method for real-time monitoring of the electron bunches. The method is non-destructive (it does not intercept the electron beam) and non-intrusive (although it is expected that the modification of the beamline will slightly influence beam properties, this has not yet been investigated in detail). At FELIX we have measured the length and shape of individual relativistic electron bunches with a subpicosecond time resolution.

REFERENCES

- [1] <http://www.rijn.nl/felix>
- [2] X. Yan, A.M. MacLeod, W.A. Gillespie, G.M.H. Knippels, D. Oepts, A.F.G. van der Meer, and W. Seidel, *Phys. Rev. Lett.* **85**, 3404 (2000)
- [3] I. Wilke, A.M. MacLeod, W.A. Gillespie, G. Berden, G.M.H. Knippels, and A.F.G. van der Meer, *Phys. Rev. Lett.* **88**, 124801 (2002)
- [4] G. Berden, G.M.H. Knippels, D. Oepts, A.F.G. van der Meer, S.P. Jamison, A.M. MacLeod, W.A. Gillespie, J.L. Shen, and I. Wilke, *Proceedings PAC 2003*, Portland (OR), USA, May 2003.
- [5] G.M.H. Knippels, M.J. van de Pol, H.P.M. Pellemans, P.C.M. Planken, and A.F.G. van der Meer, *Opt. Lett.* **23**, 1754 (1998)
- [6] D. Oepts and G.M.H. Knippels, *Proc. 20th International FEL conference*, Williamsburg, 1998 (Elsevier North Holland, Amsterdam, 1999), p. II-45.
- [7] S.P. Jamison, J.L. Shen, A.M. MacLeod, and W.A. Gillespie, *Opt. Lett.* (2003) in press.
- [8] J.R. Fletcher, *Opt. Express* **10**, 1425 (2002)
- [9] P. Bolton, D. Dowell, P. Krejcik, and J. Rifkin, *AIP Conf. Proc.* **648**, 491 (2002).
- [10] M.J. Fitch, A.C. Melissinos, P.L. Colestock, J.-P. Carneiro, H.T. Edwards, and W.H. Hartung, *Phys. Rev. Lett.* **87**, 034801 (2001)
- [11] T. Srinivasan-Rao, M. Amin, V. Castillo, D.M. Lazarus, D. Nikas, C. Ozben, Y.K. Semertzidis, A. Stillman, T. Tsang, and L. Kowalski, *Phys. Rev. ST Accel. Beams* **5**, 042801 (2002)
- [12] L. Duvillaret, S. Rialland, and J.-L. Coutaz, *J. Opt. Soc. Am. B* **19**, 2692 and 2704 (2002)
- [13] H.J. Bakker, G.C. Cho, H. Kurz, Q. Wu, and X.-C. Zhang, *J. Opt. Soc. Am. B* **15**, 1795 (1998)

Short Bunch Beam Profiling

P. Krejcik, SLAC, Stanford Linear Accelerator, Stanford, CA, USA
e-mail: pkrc@slac.stanford.edu

Abstract

The complete longitudinal profiling of short electron bunches is discussed in the context of 4th generation light sources. The high peak current required for the SASE lasing process is achieved by longitudinal compression of the electron bunch. The lasing process also depends on the preservation of the transverse emittance along the bunch during this manipulation in longitudinal phase space. Beam diagnostic instrumentation needs to meet several challenges: The bunch length and longitudinal profile should be measured on a single bunch to characterize the instantaneous, peak current along the bunch. Secondly, the transverse emittance and longitudinal energy spread should be measured for slices of charge along the bunch. Several techniques for invasive and noninvasive bunch profiling will be reviewed, using as examples recent measurements from the SLAC Sub Picosecond Photon Source (SPPS) and the planned diagnostics for the Linac Coherent Light Source (LCLS). These include transverse RF deflecting cavities for temporal streaking of the electron bunch, RF zero-phasing techniques for energy correlation measurements, and electro-optic measurements of the wake-field profile of the bunch.

Paper not received

(See slides of talk on
following pages)



Stanford
Linear
Accelerator
Center

lasing

Dr. Kraljick DIBAC 5.7 May 2003 Mainz Germany

Kraibitz DIPAC 5.7 Mai 2003 Mainz Germany

© KreloK. DIPAC 5-7 May 2003 Mainz Germany

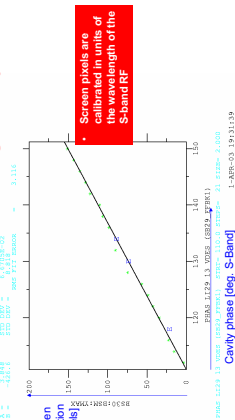
e. Kissick, DIPAC
5-7 May 2003, Mainz, Germany

5-7 Mai 2003 Mainz Games des immatrikulierten Indiens

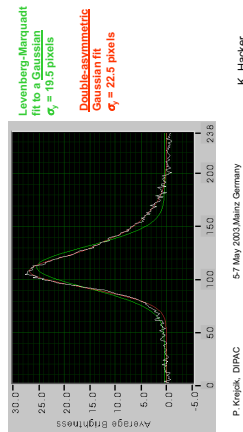
Courtesy Janos Hadju, *Structural Studies on Single Particles and Biomolecules for LCLS*

References

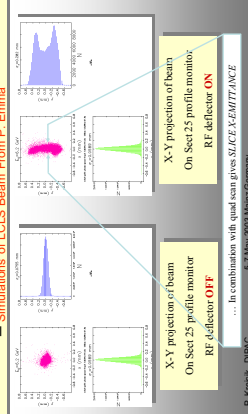
Calibration scan for RF transverse deflecting cavity



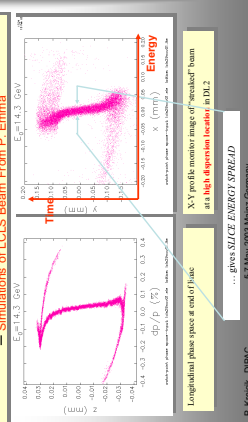
Fitted width to streaked, vertical beam size:



Slice Emittance Measurements in Conjunction With RF Deflector Bunch Length Measurement

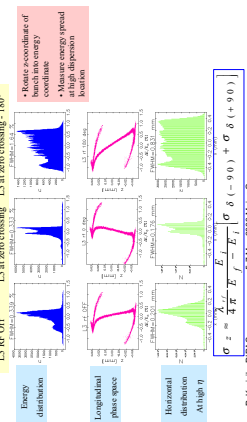


Slice Energy Spread Measurements in Conjunction With RF Deflector Bunch Length Measurement



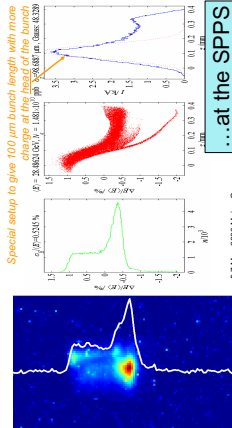
Zero Phase Crossing Measurement of Bunch Length

- LCLS Simulation From P. Emma, Using ELEGANT (M. Borland)

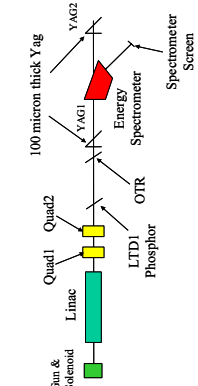


Measured and predicted energy spread of a compressed bunch

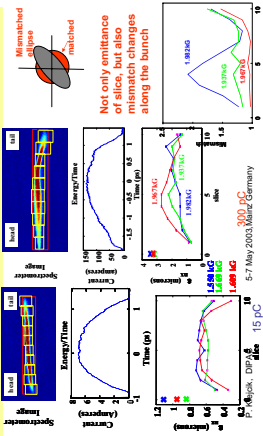
Special setup to give 100 μm bunch length with more charge at the head of the bunch



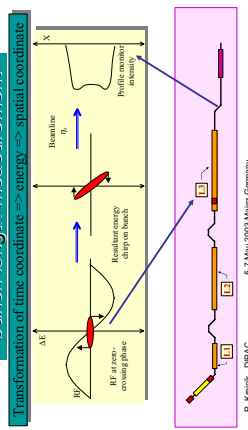
Slice emittance and energy spread
measurement at the SLAC GTF – Dowell et al



emittances for 15 pC and 300 pC bunch charges Dowell et al – GTF Results



Phase zero-crossing bunch length measurement



We can also use the longitudinal RF to measure properties of SLICES along the bunch...

Using the transverse RF deflecting cavity to measure properties of SLICES along the bunch...

Principal of Electro Optic Detection

Electric field from bunch modulates transmission of charged laser pulses

Electron bunch
Laser pump
Laser probe
Spectrometer
Gated spectral signal
Initial laser chip
Beam charge

EO Crystal
Polarizer
Analyzer

5-7 May 2003, Mainz, Germany
P. Keegstra, DIPAC

Electro Optic resolution limits for extremely short bunches

- Bandwidth limited by probe laser pulse to ~5 fs
- EO effect is ~2 fs
- Moving the problem from electron bunch measurement over to measuring a photon pulse
- Different transformations exist to measure photons
- Temporal to frequency domain transformation with chirped laser pulse
- EO crystal
- Slippage between bunch field and probe laser field propagating through the crystal
- Wakefield of the bunch interacting with the EO setup

5-7 May 2003, Mainz, Germany
P. Keegstra, DIPAC

Electric Field from a Relativistic Bunch

10 μm 33 fs

Frequency components

Wakefield bandwidth

$E = 9 \times 10^{10} \frac{2N_e e}{r} \text{ m.k.s units}$

1 nC 10 μm bunch length

$E = 720 \text{ MV.m}^{-1}$ at $r = 1 \mu\text{m}$

5-7 May 2003, Mainz, Germany
P. Keegstra, DIPAC

Electro Optic detection for ultra-relativistic bunches (very large γ)

- $1/\gamma$ is very small, so not resolution limited by distance of crystal to beam
- +/- very high field strengths
- + easily detectable
- higher-order non-linear Kerr effect is added to the Pockels effect

$E = 9 \times 10^{10} \frac{2N_e e}{r} \text{ m.k.s units}$

5-7 May 2003, Mainz, Germany
P. Keegstra, DIPAC

Electro Optic Basics

Polarization
Susceptibility
Electric field

$P = \epsilon_0 [\chi_1 E + \chi_2 E^2 + \chi_3 E^3 + \dots]$

Linear EO effect
Kerr effect

Bandwidth limitation in EO crystals due to optical phonon absorption resonances

6 μm GaAs ~8 THz
GaP ~11 THz

5-7 May 2003, Mainz, Germany
P. Keegstra, DIPAC

Electro Optic Probe Geometry

- Probe laser at a crossing angle to electron beam direction
- Probe laser parallel to electron bunch
- Temporal to spatial
- Temporal to frequency domain sampling

5-7 May 2003, Mainz, Germany
P. Keegstra, DIPAC

Geometry to avoid wakefield perturbation to bunch field

Defining aperture
EO crystal
Probe laser
Beam axis

5-7 May 2003, Mainz, Germany
P. Keegstra, DIPAC

Electric field detection

Rms 50 μm

Note: amplitude and profile changes are cut < 5% max. 11-15 mm target

5-7 May 2003, Mainz, Germany
H. Scharb

SubPicosecond resolution is lost if we try and extract THz radiation from the vacuum chamber:

5-7 May 2003, Mainz, Germany
P. Keegstra, DIPAC

Electric field detection

exit port
mirror
beam
check for 50 μm

Pre-pulse of low frequency generated at the edge of the bunch

5-7 May 2003, Mainz, Germany
H. Scharb

Electro optic spatial profiling of bunch length distribution

End view
Elevation view
Plan view

Pre-pulse of low frequency generated at the edge of the bunch

5-7 May 2003, Mainz, Germany
P. Keegstra, DIPAC

Layout of the 45° EO Crystal Geometry

5-7 May 2003, Mainz, Germany
E. Bong

Limits to Resolution

Slippage between bunch field and probe laser field

$$\Delta t = \frac{L}{c} \left(\frac{n_1}{n_2} - 1 \right)$$

for THz and laser

There is also a transient wavelength shift

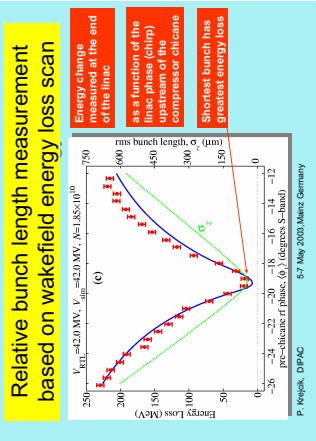
$$\frac{\Delta \lambda}{\lambda} = \frac{L}{c} \frac{dn}{dt} = \frac{L}{c} \frac{1}{2} (n_1^2 - n_2^2)$$

at $V = V_a$

P. Kneip, DIPAC 5-7 May 2003, Mainz, Germany

Relative measurements of the rms bunch length can also be with:

1. Measurement of the wakefield energy loss of the bunch
2. Measurement of the power spectral density of the Coherent Synchrotron Radiation CSR



Aknowledgements

- P. Bolton
- E. Bong
- D. Dowell
- P. Emma
- K. Hacker
- H. Schlarb

P. Kneip, DIPAC 5-7 May 2003, Mainz, Germany

DIGITAL SIGNAL PROCESSING IN BEAM INSTRUMENTATION: LATEST TRENDS AND TYPICAL APPLICATIONS

M. E. Angoletta, CERN, Geneva, Switzerland

Abstract

The last decade has seen major improvements in digital hardware, algorithms and software, which have trickled down to the Beam Instrumentation (BI) area. An advantageous transition is taking place towards systems with an ever-stronger digital presence. Digital systems are assembled by means of a rather small number of basic building blocks, with improved speed, precision, signal-to-noise ratio, dynamic range, flexibility, and accompanied by a range of powerful and user-friendly development tools. The paper reviews current digital BI trends, including using Digital Signal Processors, Field Programmable Gate Arrays, Digital Receivers and General Purpose Processors as well as some useful processing algorithms. Selected digital applications are illustrated on control/feedback and beam diagnostics.

INTRODUCTION

This review addresses latest years' developments in the use of digital techniques in BI. Owing to the large body of data available on this topic, the reader is also referred to the proceedings of various conferences and workshops such as the BIW, DIPAC, PAC, EPAC, ICALEPCS and LINAC, widely available on the web, and to previous reviews on some aspects of this subject [1,2,3].

A "Digital Engineering" perspective is adopted here, through the concept of "Digital Building Block" (DBB). This indicates the smallest digital unit, a chip, which can accomplish a given function. DBBs are now profusely used as part of recent digital systems. There are several DBBs, important for the evolution of the digital signal processing field. The treatment here is limited to only four major programmable DBBs, having great flexibility through programmability, providing multifunctionality hence causing continuing system size shrinkage.

The digital signal processing area has been steadily evolving since the '60s [4]. It is witnessing a slow transition from an all-analogue approach to an analogue/digital balance, primarily in control/feedback applications, with an ever-stronger digital presence.

DIGITAL BUILDING BLOCKS IN BI

Nowadays, digital systems are assembled using a limited number of "miniaturised" DBBs, each accomplishing a range of functions and having a definite place in the signal processing chain (Figure 1). The four DBB considered in this paper, listed as one follows the signal from the detector, are 1) Digital Receiver (DRX), 2) Field Programmable Gate Array (FPGA), 3) Digital

Signal Processor (DSP) and 4) General Purpose Processor (GPP) and GPP-hybrid. DBB major functionalities include baseband translation and initial data reduction (for DRX), fast math-intensive processing (for DSP and FPGA), glue logic (for FPGA), slow processing, data management and high-level interfacing (for GPP). In general, system specification and final goal will influence and modify this generalised chain structure. For example, either the DSP or the FPGA may be absent depending on the type of processing and the time constraints the system imposes. Typically, FPGAs support faster sampling than DSPs. On-site availability of tools and expertise in DSP or FPGA development may tip the chain balance towards either a no-DSP or a no-FPGA implementation. A DBB not covered here is for example the Analogue-Digital Converter (ADC). This will also influence system

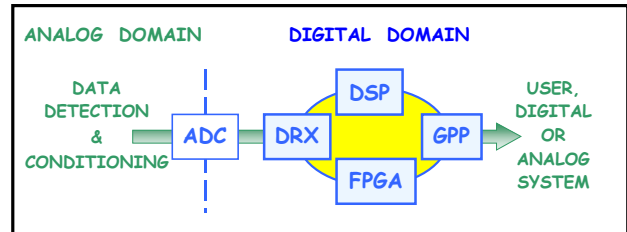


Figure 1: DAQ and processing chain DBBs.

architecture and its evolution will impact digital signal processing in the future. For example, the analogue/digital divide in the system signal chain may move closer and closer to the detector end as ADCs become faster and more powerful. Conceivably, future systems will directly feed the signal to the digitising ADC, without going through intermediate frequency (IF) translation.

Last but not least, developers should provide a digital system with enough diagnostic and troubleshoot access points, to avoid turning the system into a tightly sealed black box.

Digital Receivers

The digital receiver chip, also called Digital Down Converter (DDC), is the evolution of the classical analogue superheterodyne receiver [1]. It extracts a narrow frequency band of interest from a wide-band input by down mixing, filtering and decimation. Figure 2 shows the block diagram for a generic DRX. Its main blocks are the local oscillator (LO), the complex (or I/Q) mixer and the low-pass filter. LO is a direct digital synthesiser generating a quadrature sinusoid, with programmable frequency and phase, from a look-up table. The mixer consists of two digital multipliers and outputs only the

sum and the difference frequency signals, unlike analogue mixers that generate many unwanted mixer products. The third block in Figure 2 performs filtering and decimation.

This kind of digital processing has many advantages. For example, the chip's behaviour can be changed by software, adding flexibility through programmability. Second, the chip is highly linear. Spurious signals are strongly rejected, based on the accuracy of the sinusoidal waves generated by the local oscillator and by the mathematical precision of the mixer. Such rejection is a difficult task if performed by analogue electronics.

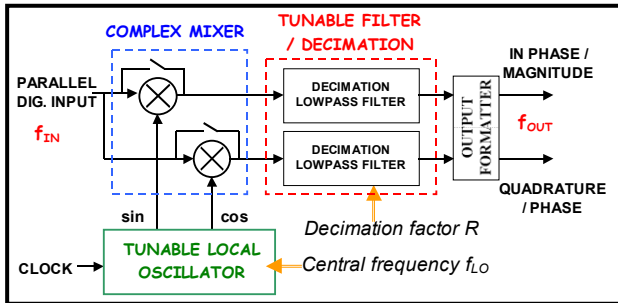


Figure 2: Typical DRX schematic layout, showing its 3 building blocks and two of the control parameters.

Finally the decimation action sensibly cuts down the number of data samples, allowing a subsequent data processing step. DRX are mostly used together with DSPs and/or FPGAs in BPMs [5] and beam parameters measurement systems [6, 7].

FPGAs

FPGAs are high-performance programmable logic devices, i.e. integrated circuits made of an array of logic cells that can be programmed to be interconnected to achieve different designs. FPGAs feature very high capacity (now in the 10^6 gate range) and flexibility. Altera and Xilinx are the two main FPGA producers, their more powerful families being Altera's Stratix and Xilinx' Virtex-II and Virtex-II Pro. FPGAs lead the way to System-On-a-Programmable-Chip (SOPC) technology, which combines in a chip a large amount of programmable logic with memory, a processing engine and possibly additional Intellectual Property (IP) core. FPGAs are limited in that usually the floating-point logic is not easily implemented and its execution is slow. However, some core libraries are on the market now to address this need.

FPGAs are widely used in BI for two main functions: glue logic and very fast data processing. In fact, they support and sustain much faster sampling than afforded by DSPs. Examples of FPGA BI applications are the LHC orbit trajectory system [8], the SNS Front-End low level RF system (FELLRF) [9] and SNS BPMs [10]. In the SNS FELLRF, FPGAs are in charge of fast intra-pulse processing (pulse length is about 1 ms), while inter-pulse slower processing is left to the host processor. In SNS BPMs, FPGAs are again in charge of fast processing, with slower processing left to rack-mounted PCs.

Digital Signal Processors

DSPs first BI applications date back to the '80s [11]. DSPs are microprocessors tailored for fast, math-intensive tasks and may "service" sampling frequencies up to a few MHz. Their architecture, shaped by digital signal processing algorithms, include specialised units for fast execution of mathematical tasks and to keep numerical fidelity. Specialised I/O interfaces and handling schemes, such as Direct Memory Access, ensure fast data transfer without DSP main processor's intervening. The code's predictable execution time and the DSP's low-latency response to interrupts are enhanced by the frequent lack of Operating System (OS), as occurs in interrupt-driven systems. Conventional pre-mid-90s DSP architectures were based on separate data and address buses - the Harvard model [12]. Two main enhanced architectures have emerged since then: Very Long Instruction Word (VLIW) and Single Instruction Multiple Data (SIMD). They increased the execution speed by executing in parallel either different instructions or the same instruction on different data. VLIW is used in TI's 'C6x DSPs and SIMD in the Analog Devices ADSP-2116x family. VLIW and SIMD can coexist in the same DSP, like in Analog Device's TigerSHARC. With these architectures, DSPs are more efficient *but* optimising the associated Assembly code is more complex. This forces developers to write almost entirely C-code and to rely on compiler/optimiser performance. To a higher abstraction level, developers use automatic code-generation tools, such as Matlab Real-time Workshop Embedded Coder and Hypersignal RIDE, allowing code construction by drag-and-drop of pre-defined standard-function boxes.

DSPs are widely used in BI, alone or with other DBBs, typically FPGAs and/or DRX. Usage includes tune, intensity and emittance measurement [6,11]. Beam Position Monitors (BPM) also use DSPs: here the processing carried out is typically signal difference-over-sum plus offset subtraction [5,13]. DSPs occur in Beam Current and Beam Loss Monitors (BCM, BLM), either alone or preceded by a DRX, to perform a differential current loss measurement and often to interface to a fast machine-protection system [14,15]. DSPs roles in feedback/feedforward control systems are beam control, a complex task where beam dynamics is a crucial factor for the control loop design [16] and, less demanding, power converter control and regulation [17].

GPP-based hybrids

GPPs are designed for a variety of computational tasks. From the end of the '80s on, GPPs are mostly Reduced Instruction Set Computers (RISC), characterised by a small set of instructions executable in a single cycle. Examples of RISC-based GPPs are Motorola's PowerPC and Sun's SPARC. GPPs are quite popular in the BI area, since they rely on standard OS and development systems. Typical BI applications use GPPs in master-VME boards to carry out data management and to interface Front-Ends to Control/GUI levels. In such capacity, GPPs depend on

well known Real-Time Operating Systems (RTOS), such as VxWorks, Lynx and, lately, Linux RTAI [18]. Nowadays, the increase in clock speed allows GPPs to carry out data processing and slow control actions, allowing taking over roles once reserved to DSPs [18,19]. This crossover is now even more favoured by the tendency to integrate DSP hardware features and specialised instructions into GPPs, yielding *GPP-hybrids*. Examples are the Pentium with MMX extension and the PowerPC with Motorola's AltiVec extension, the latter's core architecture being shown in Figure 3. The AltiVec 128-bit SIMD unit adds up to 16 operations per clock

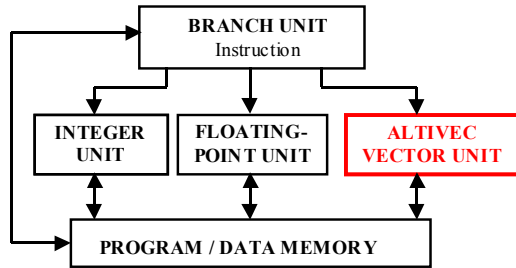


Figure 3: GPP-hybrids. The core of Motorola's PowerPC with AltiVec extension, schematic view.

cycle, in parallel to the Integer and Floating Point units, and 162 instructions to the existing RISC architecture.

DIGITAL SIGNAL PROCESSING IN BI

Of the many techniques useful to BI this paper only covers four: 1) Digital Filters, 2) Wavelets, 3) Spectral Analysis and 4) Algebraic Reconstruction Technique (ART). Of these, 1) and Fast Fourier Transform (FFT) as part of 3), are well-known BI tools. Others, such as 2) and 4), are less frequent and used as off-line post-processing schemes. Still, they show promise for integration in real-time online processing.

Finite Impulse Response (FIR) and Infinite Impulse Response (IIR) filters are widely used to filter unwanted spectral components out of a signal. In adaptive filtering techniques the FIR and the IIR filter parameters are varied in real-time, depending on "system unknowns", to achieve a specific criterion. For example, CEBAF's DSP-based current monitoring system [14], aims at maximising S/N. Digital FIR filters with 2 to 5 taps typically integrate feedback loops. The filter aims to determine a suitable damping action by performing DC rejection and providing a $\pi/2$ phase shift at the oscillation frequency.

Wavelet algorithms expand signals in terms of small wavelike components, i.e. wavelets, with finite energy concentrated in time or space [20]. Suited to approximating data with sharp discontinuities, they are applied to digital filtering [21] and to non-parametric system identification for feedforward control [22].

In spectral analysis a signal is analysed in the frequency domain, splitting it into possibly infinite spectral components, each with a different amplitude and phase. Fourier Series and Transforms and the FFT are the tools of the trade. FFT alone may not guarantee a sufficient

frequency resolution, unless a very large number of data points is used, to the detriment of memory and computation time. Interpolating around the FFT-magnitude peak of interest overcomes this problem. Other methods, such as the Numerical Analysis of Fundamental Frequency [23], allow similar refinements and BI applications abound [24, 25]. A less-known analysis method is Lomb's Periodogram. This is particularly suited to non-equispaced data, as it weighs the data on a "per point" rather than on a "per time interval" basis. Hence, it can resolve frequencies with a number of points insufficient for frequency resolution by standard FFT. Another advantage over the FFT is the lack of constraints on the number of data points. A drawback is the lack of phase information, as only amplitudes are obtained. An application to tune measurements by multiturn beam position analysis is given in [26].

ART is an algorithm used in beam tomography, to reconstruct 2-dimensional images from 1-dimensional beam projections [27], similarly to Computer Assisted Tomography. The difference from the medical application is in the added complexity caused by the beam motion and deformation. A modified ART accounts for this by a particle-tracking algorithm. Figure 4 shows the measured CERN PS Booster injected proton particle density as a function of particle energy and time of arrival at the

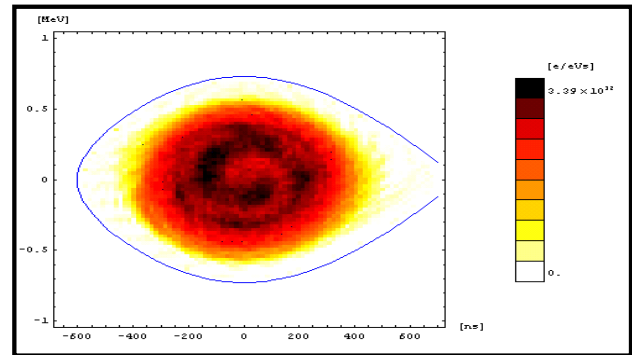


Figure 4: Longitudinal phase space density of a bunched beam during adiabatic capture in the PS Booster [28].

detector [28]. Beam tomography is applied both to the longitudinal [29] and to the transverse case [30, 31].

APPLICATIONS

A small-scale literature search places control & feedback BI applications at the forefront of digital technology, whereas diagnostics *per se* are somewhat lagging behind. This section highlights a few of the main digital applications in diagnostics and control/feedback.

Beam Position Monitors

In BPMs the beam position is determined from the ratio between the difference and the sum of two voltages induced in an electrode [3]. Figure 5 outlines a BPM variation involving DSPs and DRX, developed in jointly by SLS and ELETTRA [5]. Four voltage signals proportional to the beam's horizontal and vertical

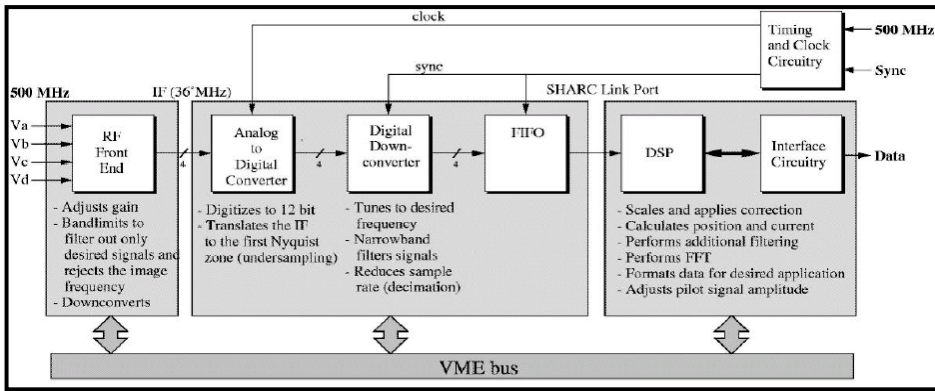


Figure 5: The digital BPM system used on Elettra and SLS – Block diagram [5].

positions are downconverted to IF = 36 MHz and low-pass filtered. They are then sampled, translated to baseband and decimated in the DRX (Digital Down Converter in Figure 5). The DRX bandwidth (BW) is user selectable from a few hundred Hz to over 1 MHz; this allows several measurements modes such as turn-by-turn, feedback, closed orbit and tune modes. When set to low-bandwidth (typically $BW < 10$ kHz) it allows following “slow” aspects of the beam evolution with high precision. An example is the closed-orbit mode, which allows resolution of less than $1 \mu\text{m}$. When BW is wider it is possible to look at “fast” aspects of the beam position with a resolution lower than $20 \mu\text{m}$ (turn-by-turn mode). The DSP can also carry out FFTs to determine the tune from turn-by-turn data.

Other examples of BPM systems include that under development for FNAL’s Recycler Ring [32], the beam position and phase detection system developed for FNAL’s Main Injector/Tevatron/Recycler Low-Level RF [33] and the system developed for KEKB [13].

Control and Feedback

Transverse and/or longitudinal beam oscillations may arise due to various factors and may have to be damped by external means, to prevent beam loss. Damping these

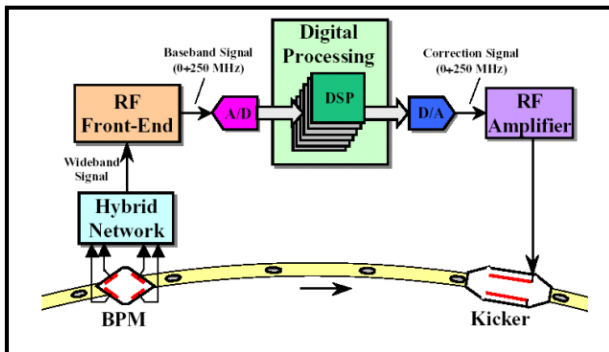


Figure 6: ELETTRA’s transverse multi-bunch feedback system – schematic view [16].

oscillations is the task of the beam feedback system. In addition, the data processing part of a digital feedback system may be a very useful tool to investigate beam instabilities. Feedback systems may be studied from a

frequency-domain or from a time-domain viewpoint (“bunch-by-bunch” feedback). The former approach, the “mode-based feedback”, requires the detailed knowledge of the spectral form of the external forces (forcing and damping), hence is somewhat more complex. Mixed digital/analogue control/feedback systems date back to the early ‘90s [34].

Figure 6 shows ELETTRA’s multibunch feedback system, which deals with 432 bunches 2 ns apart [16]. A baseband signal corresponding to the position error of the bunches passing through the BPM is sampled at 500 MHz by one ADC and de-multiplexed to six COTS DSP boards working in parallel. Each board includes four DSPs, three for feedback tasks and the last working on diagnostic tasks. The three feedback DSPs process data

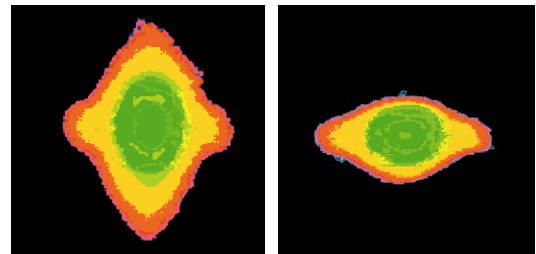


Figure 7: Transverse cross-section of the ELETTRA beam. Left – no feedback, right - vertical feedback [36].

corresponding to 72 bunches per turn. Processing is by a 5-tap FIR filter and corrective actions are applied with a 4-turn delay owing to ADC/DAC delays. The diagnostic DSP can acquire the bunch position for over 200,000 turns, allowing analysing the evolution of transverse coupled multibunch instabilities [35]. Figure 7 is a transverse cross-section of ELETTRA’s beam via a synchrotron radiation profile monitor, showing the effect of the multi-bunch transverse feedback [36].

The longitudinal feedback system developed for PEP II, DAΦNE and ALS [37], also used as diagnostics, is another multi-bunch feedback example. Other feedback applications include RHIC’s beam control and feedback system [38], implementing a state-space technique and BNL’s ABS Booster upgrade, now being developed [39]. Orbit feedback systems are presented in [40,41,42].

Betatron Tune Measurement by PLLs

The betatron tune is among the key machine operation parameters. Several measurement methods are available, differing in the beam excitation used and the processing technique. An important aspect is the excitation strength required to achieve a given tune resolution, keeping in mind that a weak excitation is preferred to avoid emittance growth. The method based on using a Phase-

Locked Loop (PLL) needs usually a continuous excitation with amplitude smaller than needed for standard FFT-based methods. In addition, it provides a continuous measurement of the tune, hence it can be used for feedback. Figure 8 shows PLL-based tune measurement principles. The beam experiences a transverse sinusoidal excitation, with radial frequency ω , generated by a

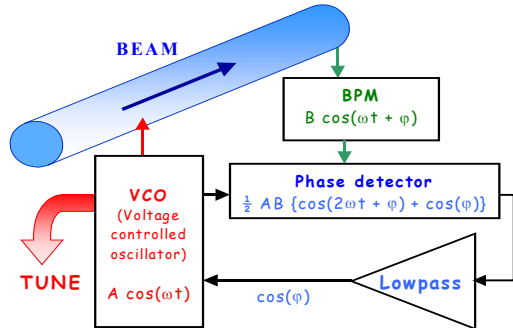


Figure 8: PLL-based tune measurement principles.

Voltage Controlled Oscillator (VCO). A BPM detects the ensuing betatron oscillation; its signal $B \cdot \cos(\omega t + \phi)$, ϕ being the phase difference between beam response and excitation, is multiplied by the excitation signal $A \cdot \cos(\omega t)$ in the Phase Detector module. The result has a component with radial frequency 2ω , which is eliminated by means of a low-pass filter, leaving a $\cos(\phi)$ term. The system changes the excitation frequency until the ϕ equals 90 degrees. At that time the PLL is locked and the betatron tune can be read directly from the VCO as the excitation signal frequency.

In software PLLs (SPLL), features such as the auto-regulation of the excitation amplitude, based on the beam response amplitude, can be added thanks to a DSP. An “intelligent behaviour” may be implemented, with several states and working modes, such as swept mode or PLL-locked/unlocked status. The latter feature is useful when a tune-correction feedback loop relies on the PLL tune. These features make the SPLL state diagram much more complex than that used for BPMs or feedback loop systems. RHIC have been fine-tuning a similar SPLL-based tune measurement system [43].

CONCLUSION

A major transition is slowly taking place in the BI area, from all analogue to mostly-digital philosophies. This sea change imposes a concurrent change of culture. The many advantages of this transition include an ever-decreasing system size, increased flexibility through reconfigurability, the possibility to benefit from other labs’ development and easier inter- and multi-labs collaboration. Digital system development still requires a certain degree of expertise, but is becoming easier thanks to powerful development systems available on the market.

ACKNOWLEDGMENTS

I am grateful to many colleagues at CERN, in particular

to H. Schmickler, F. Pedersen, S. Hancock, M. Giovannozzi, J. Serrano and P. Baudrenghien. Others, from all over the globe, also deserve sincere thanks: P. Cameron and J. DeLong (BNL), J. Crisp (FNAL), L. Doolittle, A. Ratti and M. Placidi (LBNL), C. Hovater (TJNAF), K.T. Hsu (SRRC), M. Lonza and M. Ferianis (Sincrotrone Trieste), M. Plum, A. Regan, J. Power (LANL), V. Schlott (PSI) and R. Ursic (Instr. Technol.).

REFERENCES

- [1] R. C. Kimball, BIW’02, Upton, 2002, p. 79.
- [2] I. Linscott, BIW’00, Cambridge, 2000, p. 61.
- [3] G. Vismara, BIW’00, Cambridge, 2000, p. 36.
- [4] P. Zanella, CERN Computer Newsletter, Vol. 36, Issue 2, April-June 2001.
- [5] M. Dehler et al., PAC’99, New York, 1999, p. 2087.
- [6] M.E. Angoletta et al., PAC’03, Portland, WPPB023.
- [7] C.H. Kuo et al., EPAC’98, Stockholm, 1998, p. 1529.
- [8] E. Calvo-Girardo, CERN, private communication.
- [9] L. Doolittle et al., LINAC’02, Gyeongju, TU428.
- [10] T. J. Shea et al., PAC’01, Chicago, 2001, p. 512.
- [11] K. D. Lohmann et al., CERN/LEP-BI/88-45 (1988).
- [12] S. W. Smith, “The Scientist And Engineer’s Guide To Digital Signal Processing”, California Technical Publishing, ISBN 0-9660176-3-3 (1997), p. 509.
- [13] M. Tejima et al., EPAC’00, Vienna, 2000, p. 1815.
- [14] J. Musson et al., PAC’01, Chicago, 2001, p. 2329.
- [15] D. Barr et al., BIW’00, Cambridge, 2000, p. 242.
- [16] M. Lonza et al., ICALEPCS’99, Trieste, 1999, p. 255.
- [17] J. Carwardine et al., ICALEPCS’99, Trieste, p. 171.
- [18] M. Ferianis et al., DIPAC’01, Grenoble, p. 174.
- [19] K. T. Hsu, SRRC/TLS, private communication.
- [20] M. Vetterli, C. Herley, IEEE Trans. Signal Proc., 40 (1992) 2207.
- [21] Y. Yin et al., PAC’95, Dallas, 1995, p. 2622.
- [22] Y.-M. Wang et al., PAC’01, Chicago, p. 1613.
- [23] J. Laskar et al., Physica D, 56 (1992) 253.
- [24] M. Belgroune et al., EPAC’02, Paris, 2002, p. 1232.
- [25] R. Bartolini et al., PAC’99, New York, p. 1557.
- [26] M.E. Angoletta et al., EPAC’02, Paris, p. 1948.
- [27] D. Raparia et al., PAC’97, Vancouver, 1997, p. 2023.
- [28] <http://tomograp.home.cern.ch>.
- [29] C. Montag et al., EPAC’02, Paris, 2002, p. 1942.
- [30] M. Geitz et al., PAC’99, New York, 1999, p. 2175.
- [31] V. Yakimenko et al., EPAC’98, Stockholm, p. 1641.
- [32] J. Crisp, FNAL, private communication.
- [33] B. E. Chase et al., BIW’02, Upton, 2002, p. 368.
- [34] E. Kikutani et al., EPAC’00, Vienna, 2000, p. 192.
- [35] L. Tosi et al., PAC’01, Chicago, 2001, p. 2066.
- [36] S. N. Thanos et al., BIW’02, Upton, 2002, p. 248.
- [37] J. Fox et al., PAC’99, New York, 1999, p. 636.
- [38] M. Brennan et al., EPAC’98, Stockholm, p. 1705.
- [39] J. DeLong, BNL, private communication.
- [40] J. Carwardine et al., BIW’98, Stanford, 1998, p. 125.
- [41] M. Böge et al., EPAC’02, Paris, 2002, p. 2067.
- [42] B. Podobedov et al., PAC’01, Chicago, 2001, p. 396.
- [43] P. Cameron et al., EPAC’02, Paris, 2002, p. 1855.

DIAGNOSTIC CHALLENGES AT SNS*

M.A. Plum, Los Alamos National Laboratory, Los Alamos, NM, USA;
 T. Shea and S. Assadi, Oak Ridge National Laboratory, Oak Ridge, TN, USA;
 L. Doolittle, Lawrence Berkeley National Laboratory, Berkeley, CA, USA;
 P. Cameron and R. Connolly, Brookhaven National Laboratory, Upton, NY, USA

Abstract

The Spallation Neutron Source now being built in Oak Ridge, Tennessee, USA, accelerates an H^- ion beam to 1000 MeV with an average power of 1.4 MW. The H^- beam is then stripped to H^+ , compressed in a storage ring, and then directed onto a liquid-mercury neutron spallation target. Most of the acceleration in the linac is accomplished with superconducting rf cavities. The presence of these cavities, the high average beam power, and the potential for the e-p instability in the storage ring, provide unique challenges to the beam diagnostics systems. In this talk we will discuss these challenges and some of our solutions, including the laser profile monitor system, the residual gas ionization profile monitors, and network attached devices. Measurements performed using prototype instrumentation will also be presented.

INTRODUCTION

Most of the beam diagnostics [1] at the Spallation Neutron Source (SNS) are fairly standard: beam position monitors, beam loss monitors, wire scanners, beam current monitors, slit and collector emittance stations,

Faraday Cups, etc. However, there are several aspects about the SNS that create some special challenges, such as the superconducting rf cavities, the high beam power, and the potential for the e-p instability in the ring. The high beam power and the superconducting rf cavity challenges have led to the development of a laser profile monitor system that replaces the originally-envisioned wire scanner system in the superconducting linac (SCL). The challenges associated with the e-p instability and the expected beam loss in the ring have led to improvements in the gas ionization profile monitor design. We have also taken advantage of technology developments by basing many of our diagnostics instrumentation designs on the personal computer (PC) platform. A layout of the various diagnostics systems is shown in Fig. 1.

LASER PROFILE MONITOR SYSTEM

The profile monitor system for the SCL was originally envisioned to be a carbon wire scanner system. However, linac designers were concerned about the possibility that carbon wire ablation, or broken wire fragments, could find their way into the superconducting cavities and cause them to fail. A high reliability wire scanner actuator was

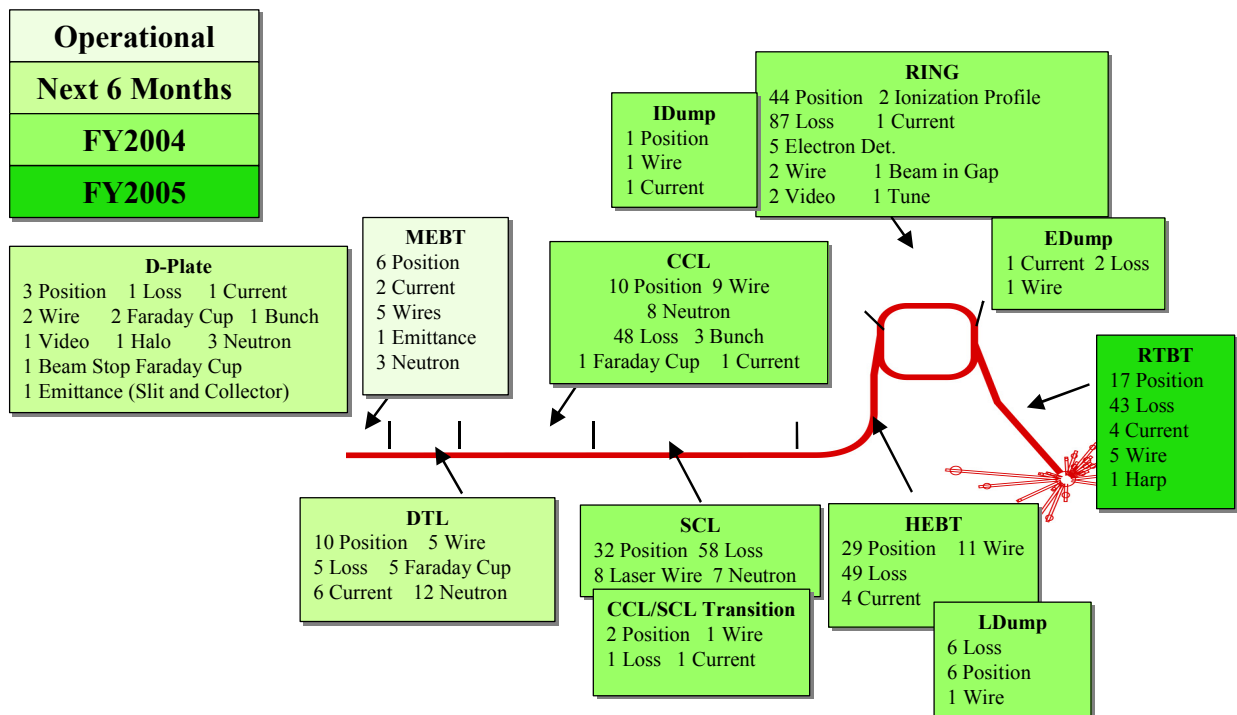


Fig. 1. (color) Layout of the diagnostics in the SNS facility, color-coded to indicate the staged installation dates.

*Work supported by the Office of Science of the US Department of Energy.

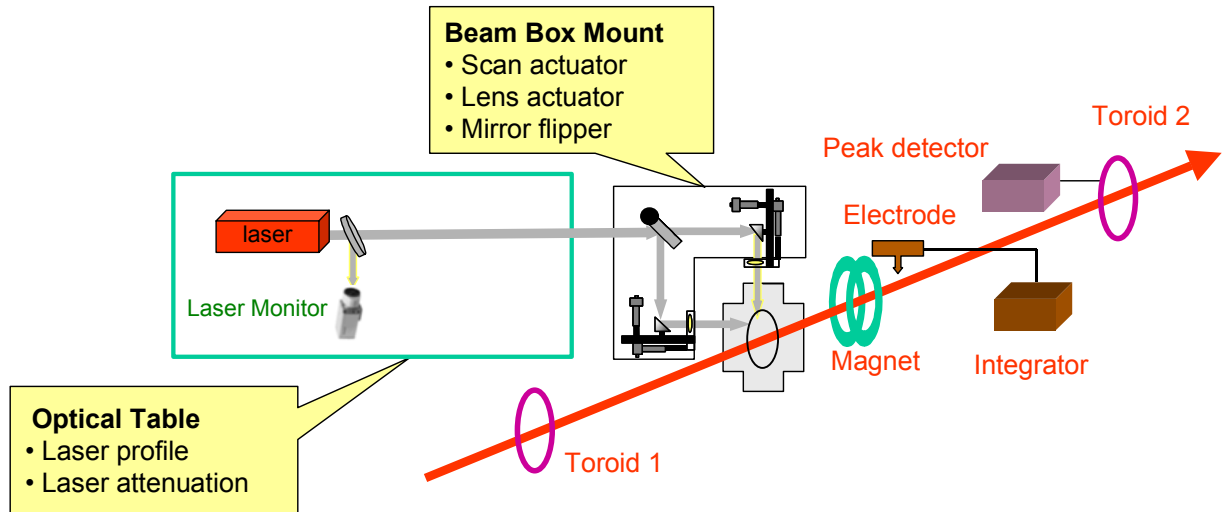


Fig. 2. (color) Schematic layout of a laser beam profile monitor.

developed [2] at Los Alamos National Laboratory (LANL) in tandem with experiments [3,4] using a laser to measure profiles of H^- beams at Brookhaven National Laboratory (BNL).

Once the laser profile monitor concept was proven by experiments at BNL, and subsequently on the SNS MEBT at Lawrence Berkeley National Laboratory, the decision was made to replace the carbon wire scanner system with the laser profile measurement system in the SCL. The

advantages that the laser profile monitor system has over the wire scanner system are: 1) profiles can be measured during normal operations, as opposed to the 100 μ s, 10 Hz duty factor restriction needed to prevent damage to carbon wires; and 2) there are no moving parts inside the vacuum system, thus reducing the possibility of a vacuum system failure. A disadvantage is that the laser is not as rad hard as a wire scanner actuator, but we have overcome this issue by placing the laser far away from the beam line.

The laser profile monitor concept is straightforward: a tightly focused laser beam is directed transversely through the H^- beam, causing photo-neutralization. The released electrons are either swept away by magnetic fields normally present in the linac lattice, or directed by a special dipole magnet to an electron collector that may or may not be part of the laser profile monitor system. The beam profile is measured by scanning the laser beam across the H^- beam and measuring the resultant deficit in the H^- beam current and/or, if the released electrons are collected, by measuring their current. A simple schematic of the concept is shown in Fig. 2.

The advantage of collecting electrons vs. measuring the deficit in beam current are: 1) the signal to noise ratio is better because of the large numbers of released electrons; and 2) the simplicity of the electron collector, since the electron energy is well defined and the electrons are well collimated. The disadvantages are: 1) an external magnetic field is required, 2) an in-vacuum electron collector is required, and 3) the electron collector signal may suffer from interference caused by beam loss. At the SNS linac we will use both methods. Every laser station will have an electron collector, and there will be beam current measurements at the entrance and exit of the superconducting linac.

Recent developments in laser technology have raised laser powers to the point where a low-cost laser that can be easily carried by a person is now powerful enough to

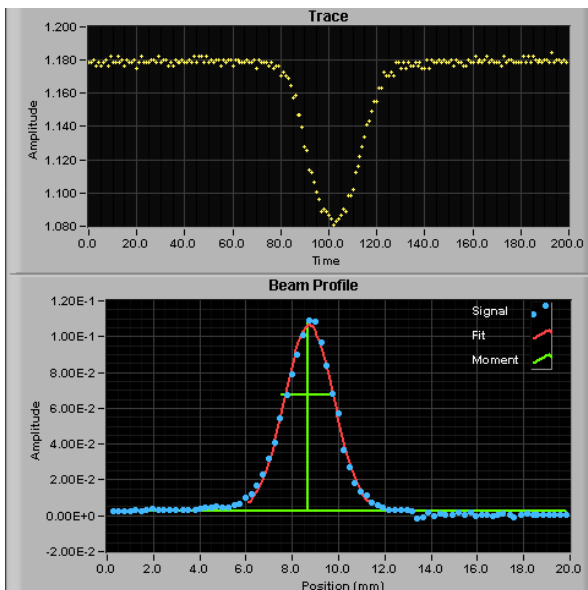


Fig. 3. (color) Horizontal beam profile in the SNS MEBT, measured January 2003. Top: an example of the electron collector signal. Bottom: the results of the measurement, with a Gaussian fit plotted out to 2.5σ .

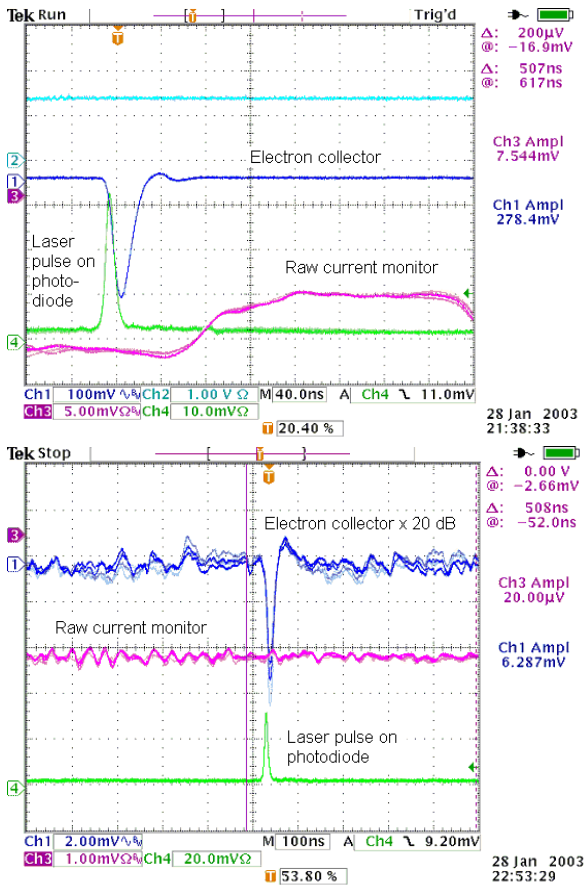


Fig. 4. (color) Some waveforms from the laser profile monitor tests in the SNS MEBT. Top: The laser is fired near the center of the 32 mA peak current beam bunch. Bottom: the laser is fired during the 310-ns gap between the 690-ns minipulses.

almost completely strip all the electrons from the portion of the H^- beam intercepted by the laser. The laser can be mounted directly to actuators on the beam line, and this was in fact the method used for some of the earlier work. However, concerns about long-term radiation damage have led us to install a single laser in a room above the SNS linac, and to transport the laser beam to the profile monitor stations using a system of mirrors.

The laser chosen for the SNS system is the Continuum Powerlite Precision II, 600 mJ, 10 nsec, 1064 nm, 30 Hz ND-YAG laser. The laser beam is transported down through a hole in the ceiling of the beam tunnel at the downstream end of the linac, and then along the length of the linac to the various beam profile measurement stations. Each of the 32 warm inter-segment regions will contain a beam box with fused-silica view ports and an electron collector. However, to contain costs, only the first four inter-segment regions in the medium-beta portion of the SCL and the first four inter-segment regions in the high-beta portion of the SCL will be instrumented with the actuators, the electron deflection magnet, and the electronics needed to make a profile

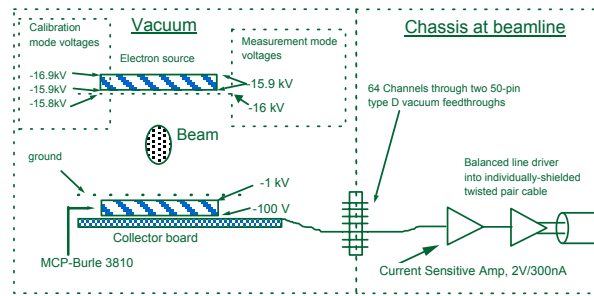


Fig. 5. (color) Schematic of the IPM.

measurement. With this setup, a laser station can be moved or added in an 8-hour shift.

Proof of principle tests were conducted at BNL and on the SNS MEBT at LBNL. The most recent and most complete tests were conducted last January on the SNS MEBT at ORNL. Shown in Fig. 3 is an example of this latest test, where a prototype system was installed at the end of the MEBT using the final-design beam box, dipole magnet, and mirror actuators.

The laser profile monitor can also be used to measure any beam that might be in the gap between the 690-ns long mini pulses. This gap is ideally void of any beam. By adjusting the laser firing time to occur within the gap, any signal on the electron collector must be due to beam in the gap. As shown in Fig. 4, this concept was also tested last January during the MEBT commissioning, and some beam in the gap was in fact detected, with a magnitude of about 2 parts in 1000. We eventually expect to achieve an accuracy of about 1 part in 10,000. We expect to complete the installation of the laser profile system by September 2004.

IONIZATION PROFILE MONITOR

The SNS ionization profile monitor (IPM), to be installed in two (one horizontal, one vertical) locations in the ring, will be based on an improved version of the IPMs installed [5] in the RHIC ring. In fact, some of the improvements have already been tested on the RHIC IPMs.

The SNS (and RHIC) IPMs are based on electron collection in parallel electric and magnetic fields. The electrons are amplified by a microchannel plate and collected on a 64-channel gold-plated printed circuit board. The resultant signals are then transported through the vacuum chamber on 50-pin D-connectors to charge-sensitive amplifiers mounted near the beam line. The signal from each channel is transported to the equipment building using balanced line drivers and individually-shielded twisted pair cables. An electron source has also been added to calibrate the instrument. Some specifications are shown in Table 1, and a schematic is shown in Fig. 5.

The modifications to the RHIC IPM were necessary due to rf coupling to the beam, susceptibility to beam loss, and possible interference from the e-p beam

Table 1. Some specifications of the SNS IPM.

Peak beam current range	15 mA to 60 A
Bandwidth	5 MHz
Profile monitor resolution	± 2.8 mm
Profile measurement accuracy	$\pm 2.5\%$ of nominal beam width
Aperture radius	100 mm
Micro channel plate	Burle 3810
Electron source	Burle electron generator array
Magnetic field	2 kG
Electric field	75 kV/m
Pre amp	Current sensitive, 2 V / 300 nA

instability. Beam loss in the vicinity of the IPM can cause the primary beam and secondary particle showers to pass through the micro-channel plate and the collector board, thus causing large background signals. Also, as demonstrated in the LANL Proton Storage Ring, the e-p instability can create huge amounts of electrons that could be collected by the IPM and possibly swamp the beam profile signal.

To alleviate these concerns the detector components were moved outside the beam aperture by moving the

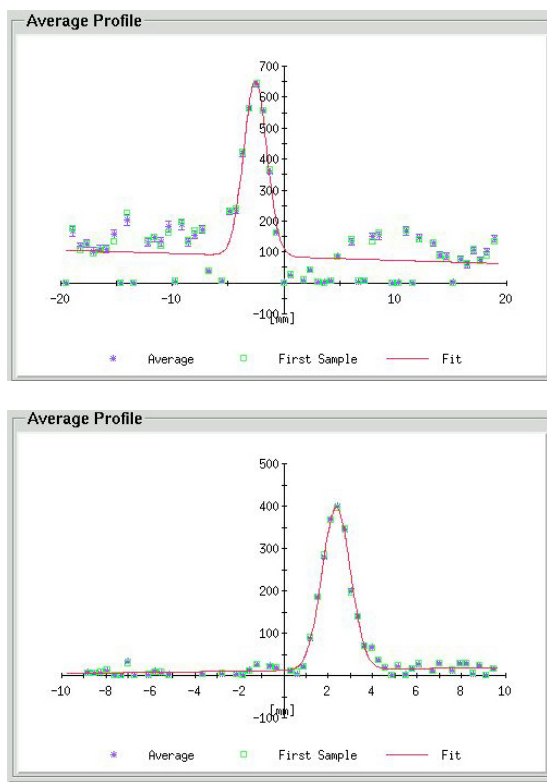


Fig. 6. (color) The RHIC ionization profile monitor measurement before (top) and after (bottom) the modifications.

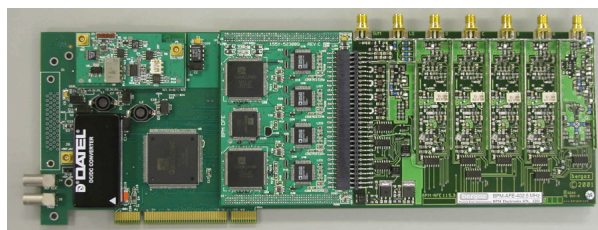


Fig. 7. (color) Photograph of the custom-designed PCI card and Digital Front End for the BPM system. The Analog Front End was designed and fabricated by Bergoz, Inc.

electron sweep electrode and the microchannel plate (MCP) away from the beam centerline and shielding the MCP with a grounded wire grid. The beam pipe in the vicinity of the IPM (in fact all the beam pipes in the SNS ring) will also be coated with TiN to suppress secondary electron creation. Additionally, the IPM's electric and magnetic fields will now extend upstream and downstream of the active volume to prevent electrons created outside the IPM from entering the active volume. Finally, the IPM's strong electric field will prevent electron multipacting within the active volume. To counteract the influence of the IPM's fields on the ring orbit, three electromagnetic dipole magnets will be added to the ring lattice.

The SNS beam intensity will be high enough that it will not be necessary to inject any gas into the IPM. This will make the system simpler, more robust, and will reduce the costs. A 10^{-8} Torr vacuum is expected in the ring, which corresponds to an expected signal level of about 150 electrons collected per turn injected into the ring (a total of 1000 turns will be injected during normal operations). For example, to obtain 5 to 7 profiles along the length of the beam bunch, and to collect at least 200 electrons per profile, we must average over about 10 machine cycles (at 60 Hz during normal operations) to get the profile information for turns 1 – 10. For turns 11 – 1000 no averaging will be required.

The new RHIC IPM, which incorporates many of these design changes, was tested by purposely causing a substantial amount of beam loss by bumping the beam into the beam pipe wall. The test was conducted using gold beam in the yellow ring in March 2003. As shown in Fig. 6, the profile using the improved IPM is much better than the profile measurement using the unmodified unit. The SNS IPMs are scheduled to be delivered to ORNL by May 2004.

NETWORK ATTACHED DEVICES

At the SNS we have chosen to base many of our diagnostics on the rack-mounted personal computer (PC) platform, rather than the more typical VXI, VME, or CAMAC platforms. Instead of implementing many BPMs within, e.g. one VME crate, the Networked Attached Device concept implements each BPM with its own independent resources such as a processor, a timing

decoder, and a network interface. The overall costs stay the same using the cost-effective PC platform but the software is simplified and common failure points are reduced. The standard software suite [6] includes Windows 2000 or XP embedded for the operating system, LabVIEW for the signal acquisition and signal processing software, Input-Output Controller (IOC) core software to communicate with the EPICS-based control system, and a Shared Memory Interface to connect LabVIEW to the IOC. Bench tests on a prototype network attached device demonstrated a 100-element (with 4 bytes /element) waveform update rate of 1000 Hz generated by LabVIEW and communicated over the network to a remote EPICS Channel Access client. The 800-MHz Pentium CPU was less than 5% busy. In some cases (e.g. the beam position monitor (BPM) and the beam current monitor (BCM) systems), custom PCI cards have been designed and fabricated, so that the signal cables are connected directly to connectors on the rear panel of the PC. In other cases (e.g. the wire scanner and the energy degrader / Faraday Cup systems) we use off-the-shelf PCI cards to control actuators and acquire data. For example, shown in Fig. 7 is the PCI card for the BPM system [7], and Fig. 8 shows how the PCI card fits into a rack-mounted PC.

The Network Attached Device concept was first tested with the prototype BPM, BCM, and wire scanner systems on the SNS MEBT at LBNL in February 2002. All these systems were brought on line in one short week, and

performed well during this initial commissioning period. We did however have some difficulties interfacing to the EPICS control system because we did not at this time have the IOC core software installed on the PCs. We plan to have this software ready for the upcoming DTL commissioning.

SUMMARY

A suite of diagnostics instrumentation has been designed to meet the challenges offered by the SNS project. Interesting developments include the laser profile monitor for H⁺ beams, the improvements to the RHIC ionization profile monitor, and the network attached devices based on the PC platform.

To date the SNS facility has been commissioned up through the end of the MEBT at 2.5 MeV using prototype BPM, BCM, wire scanner, and slit and collector emittance systems. All of these systems have performed well, although a few bugs remain to be worked out, like the IOC core software for the PC systems. The laser profile monitor concept was also tested on the MEBT, as well as at a couple different beam lines at RHIC.

The next stage of diagnostics installation is now in progress to prepare for DTL commissioning later this year, followed by CCL commissioning in 2004. The SNS is expected to be fully commissioned by early 2006.

REFERENCES

- [1] T.J. Shea et al., “SNS Accelerator Diagnostics: Progress and Challenges,” proceedings of the 2001 Particle Accelerator Conference, Chicago, Ill, USA, June 18 – 22, 2001.
- [2] R. Hardekopf et al, “Wire Scanner Design for the SNS Superconducting-RF Linac,” proceedings of the 2001 Particle Accelerator Conference, Chicago, Ill, USA, June 18 – 22, 2001.
- [3] R. Connolly et al., “Laser Profile Measurements of an H- Beam,” proceedings of the 2001 Particle Accelerator Conference, Chicago, Ill, USA, June 18 – 22, 2001.
- [4] R. Connolly et al., “Laser Beam-Profile Monitor Development at BNL for SNS,” proceedings of the 2002 Beam Instrumentation Workshop, Upton, NY, USA, 6 – 9 May 2002.
- [5] R. Connolly et al., “Performance of the RHIC IPM,” proceedings of the 2001 Particle Accelerator Conference, Chicago, Ill, USA, June 18 – 22, 2001.
- [6] W. Blokland et al., “Network Attached Devices at SNS,” proceedings of this conference.
- [7] J. Power et al., “Beam Position Monitors for the SNS Linac,” proceedings of the 2001 Particle Accelerator Conference, Chicago, Ill, USA, June 18 – 22, 2001.

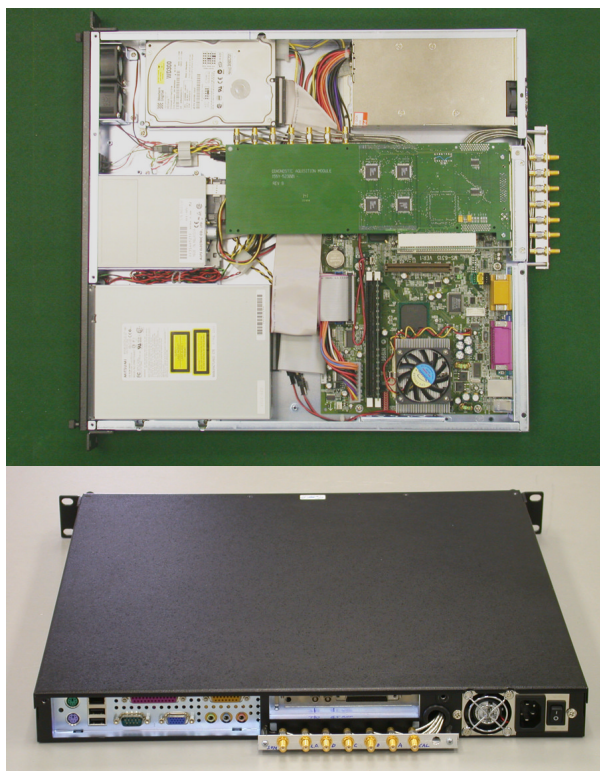


Fig. 8. (color) Photos of the BPM system in a 1U rack-mount PC.

SMITH–PURCELL RADIATION IN VIEW OF PARTICLE BEAM DIAGNOSTICS

G. Kube *, H. Backe, W. Lauth, H. Schöpe, Institut für Kernphysik, Mainz, Germany

Abstract

During the last years Smith–Purcell radiation which is generated when a charged particle beam passes close to the surface of a diffraction grating became topic of interest as non-invasive tool for particle beam diagnostics. In some publications the use of Smith–Purcell radiation for longitudinal as well as for transversal monitoring was already considered. The proposed methods are based on the idea that the relevant beam parameters can be extracted by a comparison of the measured spectral intensity distribution with the theoretical one. In the case of Smith–Purcell radiation this is a non-trivial task because the spectral intensity distribution is strongly influenced by the form of the grating profile, and the theoretical description of the radiation factors describing this dependency require extensive numerical calculations. As consequence a careful choice of the grating is essential or methods are preferable by which the wavelength dependent influence can be minimized. In the case of longitudinal beam diagnostics it should be possible by a proper choice of the form of the grating profile. In the case of transversal beam monitoring it is demonstrated that direct imaging of the beam profile is possible with Smith–Purcell radiation taking advantage of the specific emission characteristics at ultra relativistic beam energies.

INTRODUCTION

The development of the next generation high quality electron beams necessary for future high luminosity linear colliders and short wavelengths free electron lasers presents an enormous challenge for both the diagnostic measurement of beam parameters and the accurate positioning and control of these beams. The existing monitors are based on a number of different physical principles, and one technique is to use the radiation that can be produced by the beam itself. In this context nowadays the beam diagnostics based on optical transition radiation is widely used [1, 2, 3, 4]. However, the transition radiation technique entails the disadvantage of an interaction of the beam with the target leading to either the destruction of the high quality beam parameters due to small angle scattering of the electrons in the target foil or at high beam currents even of the screen. Hence the development of non-invasive, low cost, and compact beam monitors is demanded. Monitors based on synchrotron radiation, while non-invasive, are disadvantageous because they cannot be used in linear beam geometries. Another approach rather similar to the transition radiation technique is to exploit the radiation characteris-

tics of diffraction radiation which is emitted when the electrons pass close to an obstacle [5, 6, 7, 8, 9]. In recent publications beam diagnostics based on resonant diffraction radiation is proposed which originates from electrons moving through an ideally conducting tilted target which is made by strips separated by vacuum gaps [10, 11].

A rather similar and also non-destructive approach is to use Smith–Purcell (SP) radiation as a compact and inexpensive beam profile monitor. The radiation is generated when the electron beam passes a periodic structure like a diffraction grating at a fixed distance close to the surface. The radiation mechanism was predicted by Frank in 1942 [12] and observed in the visible spectral range for the first time by Smith and Purcell [13] using a 250–300 keV electron beam.

Soon after the discovery of the SP effect also potential applications became topic of interest. The possibility to use coherent SP radiation as bunch length diagnostic was proposed in [14, 15] and design studies of bunch length monitors were reported e.g. in reference [16]. The feasibility to use SP radiation for longitudinal bunch shape measurements was recently demonstrated in Frascati [17]. SP radiation as high resolution position sensor is discussed in view of possible applications for ultra relativistic beam energies up to 500 GeV in Ref. [18]. Experimental studies performed at the Mainz Microtron MAMI demonstrated that SP radiation from ultra relativistic energies can be used both as transversal beam size as well as beam position monitor. The investigations presented here were performed in context with the experiment reported in Ref. [19]. SP radiation generated with the MAMI low emittance 855 MeV electron beam [20] was investigated in the visible spectral range. By measuring the spatial intensity distribution emitted perpendicular to the grating surface beam position and beam size in the horizontal plane could be determined.

SMITH–PURCELL RADIATION PROPERTIES

According to the theory of di Francia [21], the emission mechanism of SP radiation can be interpreted in analogy to the diffraction of light as the diffraction of the field of the electrons (virtual photons) which pass the grating at a distance d away from its surface by the grating grooves. One characteristic signature of SP radiation is that it must fulfill the dispersion relation [13]

$$\lambda = \frac{D}{|n|} (1/\beta - \cos \theta \sin \Phi). \quad (1)$$

In this equation λ is the wavelength of the emitted radiation, D the grating period, n the diffraction order, $\beta = v/c$

* corresponding author, present address: DESY, Hamburg, Germany, gero.kube@desy.de

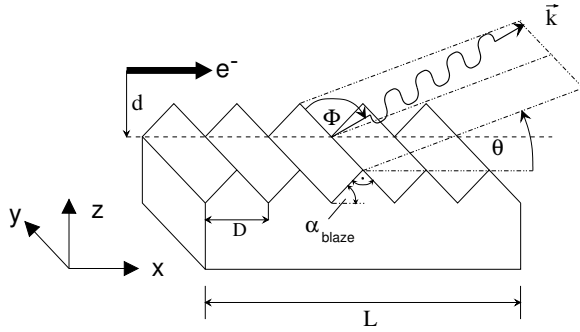


Figure 1: Definition of the geometry. The electron moves with constant reduced velocity $\beta = v/c$ at a distance d parallel to the grating surface in x direction. The grooves, oriented in the y direction, repeat periodically with the grating period D . The blaze angle α_{blaze} characterizes the échelle gratings which were used in the experiment [19]. The direction of the photon wave vector \vec{k} is described in the emission plane resulting from the $z = 0$ plane by a rotation about the y axis by the angle θ . In the emission plane the \vec{k} vector makes an angle Φ with the y axis. The length of the grating is denoted by L .

the reduced electron velocity, and θ , Φ the emission angles as introduced in Fig. 1.

The angular distribution of the emitted power radiated into the n th order is [21]

$$\frac{dP_n}{d\Omega} = \frac{eIn^2L}{2D^2\epsilon_0} \frac{\sin^2\theta \sin^2\Phi}{(1/\beta - \cos\theta \sin\Phi)^3} |R_n|^2 \times \exp\left(-\frac{d}{h_{int}} \sqrt{1 + (\beta\gamma \cos\Phi)^2}\right), \quad (2)$$

with e the elementary charge, I the beam current, L the grating length, ϵ_0 the permittivity of free space, and d the distance of the beam above the grating. The radiation factors $|R_n|^2$ which are analogous to the reflection coefficients of optical gratings are a measure for the grating efficiency. Their properties will be discussed in the following subsection.

According to Eq. (2) the intensity decreases exponentially with increasing distance d between electron beam and grating surface. The interaction length

$$h_{int} = \frac{\lambda\beta\gamma}{4\pi}, \quad (3)$$

where $\gamma = (1 - \beta^2)^{-1/2}$ is the Lorentz factor, describes the characteristic finite range of the virtual photons emitted and re-absorbed by the electrons.

To achieve a good coupling between the electrons and the radiation field via the grating the mean spot size of the electron beam and its distance from the grating should be in the order of the interaction length h_{int} . However, in the experiment of Smith and Purcell [13] the beam spot size of 0.15 mm was much larger than the interaction length which was of order of $h_{int} \simeq 10^{-8}$ m. As a consequence only a

small fraction of the beam could contribute to the radiation emission. At higher beam energies, for instance 855 MeV which is the current maximum energy of the Mainz Microtron MAMI, the interaction length in the optical spectral region amounts to $h_{int} \simeq 70 \mu\text{m}$. Taking, in addition, advantage of the low vertical emittance $\epsilon_z = 1 \pi \text{ nm rad}$ of the MAMI electron beam, a beam spot size as small as a few μm can be achieved, i.e. all electrons contribute to the emitted radiation in nearly the same way.

Furthermore, at ultra relativistic electron energies, according to Eq. (2) the radiation is emitted in a very narrow angular region around $\Phi = 90^\circ$, i.e. in the plane containing the grating normal and the electron beam. For ultra relativistic beam energies the characteristic opening angle (FWHM) can be written as

$$\Delta\Phi = 2 \sqrt{\left(\frac{\ln 2 \lambda}{4\pi d}\right)^2 + \frac{1}{\beta\gamma} \frac{\ln 2 \lambda}{2\pi d}}, \quad (4)$$

i.e. the angular width can be controlled by the beam energy, the wavelength of observation, and the distance between beam and grating surface. Taking additionally into account the distance dependence of the intensity, for an effective coupling the distance d should be in the order of the interaction length Eq. (3). With $d = h_{int}$, Eq. (4) can be rewritten as $\Delta\Phi = 2.733/\gamma$, i.e. the opening angle of SP radiation is slightly larger than the characteristic opening angle $\alpha_c \sim 2/\gamma$ of transition or synchrotron radiation used for particle beam diagnostics. If the restriction imposed on the effective coupling $d \leq h_{int}$ is given up, even $\Delta\Phi$ smaller than α_c can be achieved at the expense of a reduced radiation intensity. For typical experimental parameters $\gamma = 1673$, $\lambda = 360 \text{ nm}$, and $d = 100 \mu\text{m}$ [19], an angular width of $\Delta\Phi = 1.0 \text{ mrad}$ results compared to $\alpha_c = 1.2 \text{ mrad}$. The feature of the strongly collimated emission can be used either to discriminate SP radiation against background components as described in Ref. [19] or for particle beam diagnostic purposes as shown in the present article.

Radiation Factors

In a series of experiments Bachheimer demonstrated that the intensity of SP radiation is strongly influenced by the shape of the grating profile [22]. This dependency is expressed by the radiation factor $|R_n|^2$ which is additionally a function of beam energy and observation geometry.

The radiation factors which are analogous to the reflection coefficients of optical gratings are calculated according to the theory of Van den Berg [23, 24] which is formulated in terms of a boundary value problem for partial differential equations and yields predictions only after extensive numerical calculations. Experiments performed in the low [25] as well as in the high energy region [19] show a satisfactory agreement with the underlying theory.

An alternative approach is based on the interpretation of SP radiation caused by induced surface currents which arise when the beam electrons traverse the grating surface

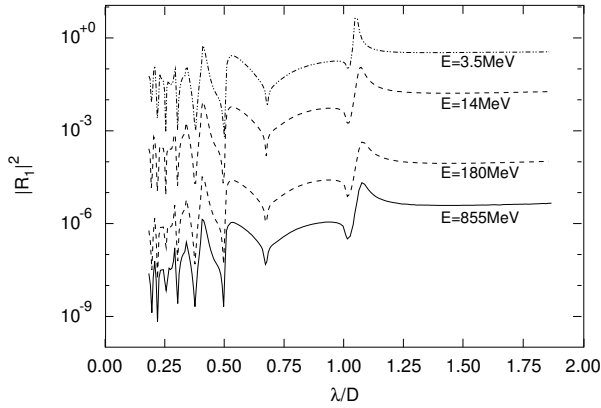


Figure 2: Calculated functional dependence of the radiation factor $|R_1|^2$ on the normalized wavelength λ/D according to Ref. [23] for a grating with $\alpha_{blaze} = 41.12^\circ$ as used in Ref. [19]. The quoted beam energies correspond to the different accelerator sections of the Mainz Microtron MAMI.

[19, 26]. Unfortunately, at ultra relativistic beam energies this kind of model failed to predict the measured intensities by orders of magnitude [19, 27]. Therefore, the subsequent considerations are based on the Van den Berg theory.

In Fig. 2 calculated radiation factors are plotted as function of the ratio λ/D with the beam energy as parameter for experimental conditions accessible at MAMI. The striking feature is that (i) the $|R_n|^2$ exhibit pronounced resonance structures as function of the observation angle (which according to Eq. (1) corresponds to λ/D) and that (ii) the radiation factors are extremely small and scale inversely proportional to γ^2 .

The first aspect known from optical grating theories [28] and usually named “Wood–Rayleigh” anomaly is associated with the passing off of a spectral order. The corresponding “Rayleigh” wavelength at which the anomaly occurs is given by $\lambda_R = \frac{D}{|n|} (1 + 1/\beta)$. As a consequence for beam diagnostic measurements it is to consider that if the beam parameters have to be extracted from a comparison of the measured spectral intensity distribution with the theoretical one, the influence of the anomalies can blur the signature on the relevant parameters as shown in the following section.

The second aspect, i.e. the decrease of the radiation factors with increasing beam energy, was found empirically and a well-founded explanation for the γ^{-2} dependency is still due. Nevertheless as a consequence, for beam diagnostic measurements at ultra relativistic energies the radiated intensity is extremely small. As an example, for the experiment at MAMI the number of SP photons amounted typically $\sim 10^{-9}$ /electron at a distance $d = 100 \mu\text{m}$ between electron beam and grating surface. In comparison to that the intensity of optical transition radiation which originated from beam electrons striking the grating when the beam center was $10 \mu\text{m}$ away from the surface amounted typically $\sim 10^{-5}$ photons per electron [29]. Therefore, for beam diagnostics with SP radiation at ultra relativistic

beam energies extremely clear experimental conditions and a good background suppression are required.

LONGITUDINAL BEAM DISTRIBUTION

Similar to frequency domain techniques based on transition or synchrotron radiation the determination of the longitudinal charge distribution resp. the bunch length via SP radiation is based on the study of the coherent radiation process. Neglecting the influence of transverse beam dimensions the radiated power emitted by a bunch of N_e particles can be written as

$$\left(\frac{dP_n}{d\Omega}\right)_{coh} = \left(\frac{dP_n}{d\Omega}\right)_{inc} \times \left[1 + (N_e - 1) f(\sigma_x, \lambda)\right] \quad (5)$$

with $(dP_n/d\Omega)_{inc}$ the incoherent power emitted by the bunch as given by Eq. (2) and $f(\sigma_x, \lambda)$ the longitudinal bunch form factor which describes the time coherence in the emission process. The form factor is the square of the Fourier transform of the normalized longitudinal charge distribution function $S(x)$ [30, 31], i.e.

$$f(\sigma_x, \lambda) = \left| \int_{-\infty}^{+\infty} dx S(x) e^{i2\pi x \cos \theta / \lambda} \right|^2. \quad (6)$$

For wavelengths in the order of the bunch length σ_x the form factor approaches unity and the radiated intensity is increased by the number of particles in the bunch. Since this number is typically very large (at MAMI up to $\sim 10^6$) the coherent signal is much more intense than the incoherent radiation when the form factor equals zero.

Basis of bunch length diagnostics with coherent radiation is the investigation of the emitted power Eq. (5) as function of the wavelength. From the spectral decomposition of the measured intensity it is possible to determine the bunch form factor Eq. (6) from which $S(x)$ has to be reconstructed. In contrast to transition or synchrotron radiation where usually autocorrelation measurements are performed in order to analyze the spectral content of a polychromatic spectrum, SP radiation is dispersive according to Eq. (1). Therefore, a direct measurement of the spectral intensity distribution has to be done. Due to the dispersion relation the variation of the wavelength corresponds to a variation of the observation angle θ (the detector placed under $\Phi = 90^\circ$). Therefore, a detector which is rotatable in θ direction is required by which the emitted intensity can be measured as function of λ .

In Fig. 3 spectral intensity distributions are plotted as function of θ . The calculations were performed under the assumption of a Gaussian distribution for $S(x)$ with bunch lengths of $\sigma_x = 300 \mu\text{m}$ (which corresponds to the bunch length at MAMI) and of $50 \mu\text{m}$ and a constant radiation factor $|R_1|^2$. A variation of the bunch length results in a shift of the maximum of the intensity distribution, i.e. the angular position of the maximum is a measure for the bunch length. Additionally from the shape of the emitted power as function of the wavelength it is possible to determine the bunch form factor. From that the longitudinal

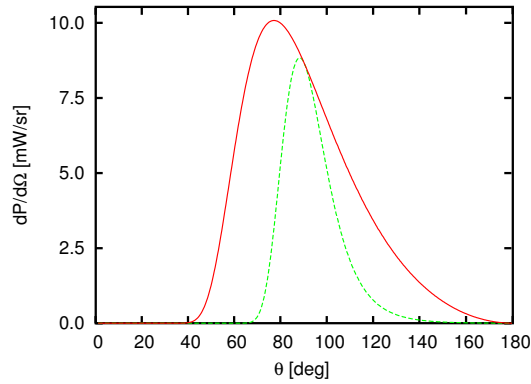


Figure 3: Emitted power in first order as function of angle of observation for a Gaussian longitudinal charge distribution with $\sigma_x = 50 \mu\text{m}$ (solid line) and $300 \mu\text{m}$ (dashed line). The beam energy was 3.5 MeV which corresponds to the output energy of the MAMI injector linac and the beam current $100 \mu\text{A}$ with 10^6 electrons per bunch. Grating: $D = 500 \mu\text{m}$, $L = 5 \text{ cm}$, $|R_1|^2 = 0.3$. Distance between grating surface and beam: 0.5 mm.

beam profile can be extracted by fitting the measured form factor supposing the functional dependency of $S(x)$. Methods based on this principle was proposed in Ref. [14, 15], and in a recent publication the determination of the longitudinal bunch shape was reported with the 1.8 MeV electron beam at the ENEA FEL Facility at Frascati [17] with the result of a triangular beam profile and a bunch length of about 14 ps.

As pointed out before the radiation factors strongly depend on θ . Therefore, in Fig. 4 the same calculated spectral intensity distributions are plotted than in Fig. 3 taking into account the angular dependency of $|R_1|^2$. In this case the maximum of the spectral power is determined by the maximum of the radiation factor. A noticeable influence of the different bunch lengths is only to recognize in the tails where the intensity is already strongly reduced.

As consequence the influence of the radiation factors of

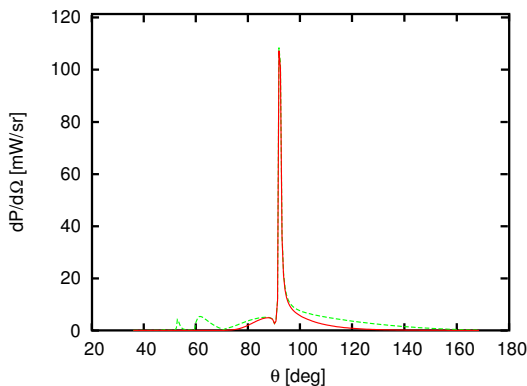


Figure 4: Emitted power in first order as function of angle of observation taking into account the angular dependence of $|R_1|^2$ for the échelette grating of Fig. 2.

the grating can blur the signature on the bunch leading to a misinterpretation of bunch shape and length. Therefore, for beam diagnostic measurements a careful choice of the grating structure should be done. From a comparison of radiation factors of different grating structures it is to conclude that especially gratings with sinusoidal profile seem to be suitable because the influence of the anomalies is strongly reduced [24] while gratings with échelette profiles as used in Ref. [19] show rather pronounced anomalies and thus should be avoided.

Additionally it is to keep in mind that for SP based beam diagnostics $S(x)$ is the induced bunch charge distribution on the grating surface rather than the direct beam profile, which results in an additional broadening, c.f. Ref. [14]. However, this effect can be calculated and therefore taken into account for high resolution beam diagnostics.

TRANSVERSE BEAM DISTRIBUTION

The use of SP radiation as high-resolution position sensor for ultra relativistic electron beams was proposed already in Ref. [18]. The basic idea of the method is that a horizontal displacement of the beam above the grating is connected with a change in the observation angles θ, Φ under which a detector mounted at a fixed position will see the emitted radiation. Therefore, such a displacement will result in a change of the measured intensity.

At the one hand in order to transform the intensity change in a horizontal displacement it is to consider that the radiation factors depend on both observation angles and consequently the calibration requires numerical effort. At the other hand due to the strongly collimated emission of SP radiation the dynamical range of such a monitor would be extremely small, whereby it would make possible to achieve a sensitivity on horizontal displacements in the order of $1 \mu\text{m}$. Anyhow methods are preferable similar to beam monitoring via synchrotron radiation which do not rely on absolute intensities.

At this it is possible to exploit the fact that according to Eq. (4) SP radiation is emitted in a very narrow angular region around $\Phi = 90^\circ$ and to perform a direct imaging similar to beam diagnostics based on synchrotron radiation [32]. In contrast to the latter imaging with SP radiation even would have the advantage that a resolution broadening due to the focus depth can be avoided because the source point for the emitted radiation is the grating surface.

In connection with an experiment at the Mainz Microtron MAMI [19, 27] this fact was used to measure the horizontal beam profile with optical SP radiation at wavelengths of 360 nm and 546 nm. The radiation was generated with the low emittance 855 MeV electron beam focused down to a vertical spot size of $2 \mu\text{m}$ (1σ) which passed over optical diffraction gratings of echelle profiles with blaze angles of 17.27° and 41.12° and with a grating period of $0.833 \mu\text{m}$. In Fig. 5 a sketch of the experimental setup is shown (left). Because no spatial resolving detector was at disposal a $400 \mu\text{m}$ wide slit aperture mounted

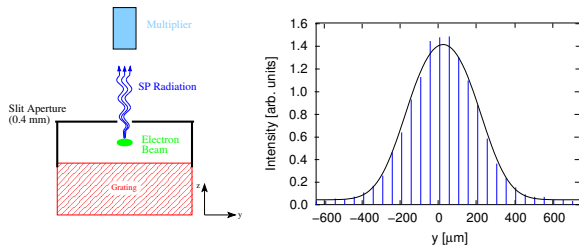


Figure 5: Left: Experimental arrangement for the horizontal SP beam monitor. Right: Measured horizontal intensity profile at observation angle $\theta = 69.8^\circ$ corresponding to $\lambda = 546$ nm, $|n| = 1$. Dashed line: best fit supposing a normal distributed beam profile and a rectangular distribution function for the aperture resolution.

9 mm above the grating and designed originally for background suppression was used to achieve sensitivity on the horizontal (y) coordinate. In the experiment the slit aperture together with the grating was moved in y direction in order to scan the horizontal SP intensity profile which was recorded by a photo multiplier placed under a fixed angle corresponding to a diffraction order of SP radiation. In Fig. 5 (right) the multiplier intensity is plotted as function of the position of the slit aperture together with the best fit which takes into account the horizontal beam profile (normal distribution) and the resolution function of the aperture (rectangular distribution). The result for the horizontal beam width of $\sim 270 \mu\text{m}$ (FWHM) was in accordance with the result from an independent measurement of $\sim 250 \mu\text{m}$ performed with a wire scanner.

By this the proof of principle was done that SP radiation can be applied for beam diagnostic purposes. Nevertheless the problem of the extremely low radiation intensity (typically in the order of 10^{-9} photons per electron) must be overcome before to think about applications of SP monitors in the standard operation mode of an accelerator. Again the question is how to increase the extremely low radiation factors. As pointed out in Ref. [33] based on calculations according to the surface current model large radiation factors can be expected for strip gratings. However, calculations based on the theory of Van den Berg result in values comparable to the ones for echelle-type gratings [34].

CONCLUSIONS

The present article summarizes the main characteristics of SP radiation in view of applications for particle beam diagnostics. It is demonstrated that this radiation mechanism has interesting features which can be used either for bunch length measurements or as transverse beam monitor. Nevertheless the use of SP radiation involves difficulties which are mainly connected with the grating structure. Therefore, the grating properties have to be considered carefully before to apply for standard diagnostic purposes and in addition extensive experimental investigations are required to support the underlying theories.

ACKNOWLEDGMENTS

This work has been supported by the Deutsche Forschungsgemeinschaft DFG under contract Ba 1336/1–3.

REFERENCES

- [1] L. Wartski *et al.*, J. Appl. Phys. **46** (1975) 3644.
- [2] R.B. Fiorito *et al.*, Nucl. Instr. and Meth. A **296** (1990) 739.
- [3] M. Castellano *et al.*, Nucl. Instr. and Meth. A **357** (1995) 231.
- [4] X. Artru *et al.*, Nucl. Instr. and Meth. A **410** (1998) 148.
- [5] M. Castellano, Nucl. Instr. and Meth. A **394** (1997) 275.
- [6] R.B. Fiorito, D.W. Rule, Nucl. Instr. and Meth. B **173** (2001) 67.
- [7] J. Urakawa *et al.*, Nucl. Instr. and Meth. A **472** (2001) 309.
- [8] A.P. Potylitsin, N.A. Potylitsyna, Russ. Phys. J. **43** (2000) 56.
- [9] N. Potylitsyna-Kube, X. Artru, Nucl. Instr. and Meth. B **201** (2003) 172.
- [10] P. Karataev, G. Naumenko, and A. Potylitsyn, Nucl. Instr. and Meth. B **201** (2003) 133.
- [11] P. Karataev *et al.*, Nucl. Instr. and Meth. B **201** (2003) 201.
- [12] I.M. Frank, Izv. Akad. Nauk. SSSR Ser. Fiz. **6** (1942) 3.
- [13] S.J. Smith, E.M. Purcell, Phys. Rev. **92** (1953) 1069.
- [14] M.C. Lampel, Nucl. Instr. and Meth. A **385** (1997) 19.
- [15] D. Nguyen, Nucl. Instr. and Meth. A **393** (1997) 514.
- [16] S.E. Korbly *et al.*, in *Proceedings of the 2001 Particle Accelerator Conference, Chicago*, edited by P. Lucas and S. Webber, p.2347, M.I. Ayzatsky *et al.*, *ibid.* p.2356.
- [17] G. Doucas *et al.*, Phys. Rev. ST Accel. Beams **5** (2002) 072802.
- [18] G. Doucas *et al.*, Nucl. Instr. and Meth. A **474** (2001) 10.
- [19] G. Kube *et al.*, Phys. Rev. E **65** (2001) 056501.
- [20] J. Ahrens *et al.*, Nuclear Physics News **4** (1994) 5.
- [21] T. di Francia, Il Nuovo Cimento **16** (1960) 61.
- [22] J.P. Bachheimer, Phys. Rev. B **6** (1972) 2985.
- [23] P.M. Van den Berg, J. Opt. Soc. Am. **63** (1973) 1588.
- [24] O. Haeblerlé, P. Rullhusen, J.M. Salomé, and N. Maene, Phys. Rev. E **49** (1994) 3340.
- [25] M. Goldstein *et al.*, Appl. Phys. Lett. **71** (1997) 452.
- [26] J.H. Brownell, J. Walsh, and G. Doucas, Phys. Rev. E **57** (1998) 1075.
- [27] G. Kube, Dissertation, Institut für Kernphysik, Universität Mainz, 1998 (in German).
- [28] *Electromagnetic theory of gratings*, edited by R. Petit (Springer-Verlag, Berlin, 1980).
- [29] H. Schöpe, Dissertation, Institut für Kernphysik, Universität Mainz, 1999 (in German).
- [30] J.S. Nodvick and D.S. Saxon, Phys. Rev. **96** (1954) 280.
- [31] Y. Shibata *et al.*, Phys. Rev. E **57** (1998), 1061.
- [32] A. Hofmann and F. Méot, Nucl. Instr. Meth. **203** (1982) 483.
- [33] S.R. Trotz, J.H. Brownell, J.E. Walsh, and G. Doucas, Phys. Rev. E **61** (2000) 7057.
- [34] G. Kube, to be submitted to Nucl. Instr. Meth. B.

ADVANCED DIAGNOSTICS OF LATTICE PARAMETERS IN HADRON COLLIDERS

J.- P. Koutchouk, CERN, Geneva, Switzerland

Abstract

With a beam stored energy exceeding by several orders of magnitude the quench level of the magnets and non-negligible non-linear field components, the control of the beam dynamics and losses in LHC must be very precise [1]. This is a strong incentive to strengthen as much as possible the potential of beam diagnostics. This paper reviews some of the developments in various laboratories that appear to have a large potential. They either allow for a much better access to classical beam parameters or for the measurement of quantities formerly not accessible. Examples are a fast measurement of the betatron tunes, the use of PLL for reliable tune tracking and feedback, new methods or ideas to measure the chromaticity with the potential of feedback systems and similarly for the betatron coupling, the measurement of high-order non-linear fields and resonances and the potential of AC dipole excitation. This list is bound to be incomplete as the field is fortunately very dynamic.

FAST TUNE MEASUREMENTS

The most common method for tune measurement is to Fourier transform the transverse oscillation of a beam after a transverse kick. If observed over N turns, the tune resolution is $1/2N$. The tunes shall usually be controlled to some 0.001, requiring a measurement over 500 turns. This method has limitations. The decoherence due to non-linearities from various sources and the beating effect due to a non-vanishing chromaticity are often significant in the first 500 turns and degrade the accuracy. This is particularly the case when the purpose of the tune measurement is to fix a pathological situation which most often enhances the decoherence.

Methods have been available for some time to either improve the accuracy of the tune measurement for a given observation time or reduce the latter significantly to capture faster phenomena.

Interpolation in the frequency domain

The measurement of the linear parameters like the tunes only requires small amplitude beam oscillations. A simple Fourier Transform does not take advantage of the knowledge that this oscillation is a simple sine wave. It is however possible to re-interpret the spectrum in the light of this hypothesis. This leads to an analytic interpolation between the FFT lines on either side of the true tune, improving significantly the precision [2]:

$$Q_{true} = \frac{1}{N} \left(k + \frac{|\phi_{k+1}|}{|\phi_k| + |\phi_{k+1}|} \right), \quad \text{where } \phi_k \text{ and } \phi_{k+1}$$

are the harmonics of largest amplitude and k/N the FFT approximation of the tune. The tune accuracy improves like $1/N^2$ in the absence of noise.

Cross-correlation in the time domain

Instead of Fourier transforming the data set and interpolating, it is possible to cross-correlate the measured time series with a sinusoidal model using a guessed tune. For continuous signals, the tune difference between the theoretical and measured tunes would simply be given by the abscissa of the peak of the cross-correlation function. For sampled signals, the tune shift is derived from two or more values of the cross-correlation function [3]. The analytical evaluation shows that this algorithm is robust against noise, with an error proportional to $1/N\sqrt{N}$. This method was experimented in LEP.

Windowing in time domain

The transverse beam oscillation signal may be viewed as the product of an infinite sinusoidal signal with a rectangle window of length N . The resulting spectrum is the convolution of a Dirac function with the Fourier transform of the rectangle window i.e. merely the window spectrum shifted in frequency so that its main peak is centred on the tune. The signal power concentrated on the Dirac impulse of the Fourier transform of the infinite sine wave is spread over the main peak and the side lobes of the transform of the rectangle.

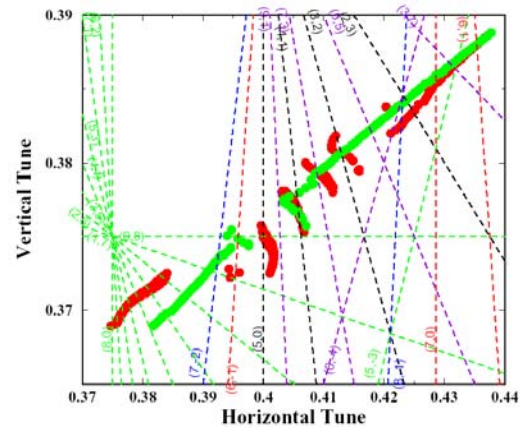


Figure 1: Experimental frequency map of the ESRF [5]

To study the non-linearities in the frequency domain, it is necessary to use the shortest possible window N (e.g. $N < 1000$) and yet to measure the tune to high accuracy (e.g. 10^{-5}). Plotting the tunes for a range of oscillation amplitudes gives a representation of dynamical systems in the frequency space (Fig. 1). The method, developed for celestial mechanics [4] relies on *i*) windowing with a Hanning window of order 2, *ii*) interpolating in the frequency domain *iii*) followed by an iterative subtraction of the identified frequency components. The Hanning window significantly reduces the side lobes. In the

absence of noise the tune accuracy improves like $1/N^3$. This spectacular improvement is somewhat reduced in practice for realistic noisy signals. The simulations [5] show that windowing still improves somewhat the accuracy as compared to a simple FFT. A fast and accurate tune measurement can be used to measure the frequency map (or tune footprint) of an accelerator or investigate the tune diffusion in time. The prominent resonances in ESRF [6] are put in evidence on Figure 1.

CONTINUOUS TUNE MEASUREMENT

The PLL method for tune tracking is certainly not new in its concept but remains a challenge for hadron colliders: The transverse beam excitation shall be small enough to prevent any significant emittance blow-up over long periods of use. The sensitivity of the pickup to transverse signals shall thus be large in presence of a strong parasitic longitudinal signal when the beam is not centered. The lock should not be lost when the beam transfer function

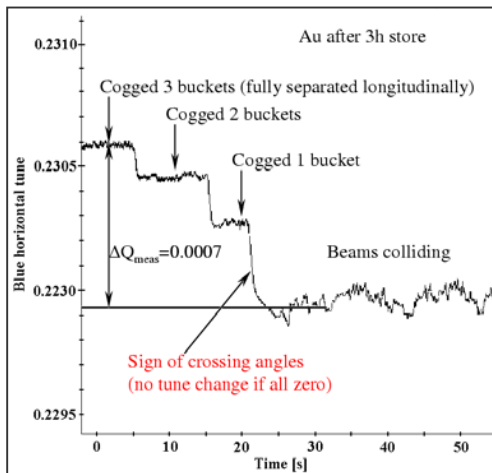


Figure 2: PLL-based beam-beam tune shift measurement at RHIC [7]

suffers significant perturbations e.g. due to a change of the betatron frequency spread or betatron coupling. This is indeed the time where measurements are most useful.

Very interesting results have been obtained e.g. at RHIC [6]. The tune monitoring during the ramp provides a fast response with a moderate resolution (~ 0.001). Smaller loop gains yield a tune resolution of a few 10^{-6} . This is most useful for studies of the tune variations versus slowly (seconds) varying parameters. This principle was used e.g. for studies on the triplet non-linearity (this paper) and the beam-beam tune shift versus beam separation [7] (figure 2: the continuous variation of the beam-beam tune shift versus the crossing azimuth is a signature of a parasitic crossing angle). The PLL system has been found sensitive to variations of the BTF (jump of harmonics), to coupling... An international collaboration on PLL-based tune-meters has been launched [9].

ON-LINE CHROMATICITY MEASUREMENTS

The most natural way of measuring the chromaticity is by measuring the change of tune following a static momentum offset. The method has been upgraded by slowly modulating the RF frequency and tracking the tunes. However, to prevent longitudinal blow-up, the RF frequency modulation is generally very slow (versus the synchrotron period) in order not to interfere with the RF feedback loops. This does not allow tracking the chromaticity at the rate required for the LHC. Indeed, at the beginning of the acceleration ramp, a sudden reorganization of the persistent currents in the superconducting material causes the chromaticity $Q' = \partial Q / \partial \delta$ to change at a rate of 1/s to 3/s. Faster chromaticity measurements (about 10 Hz for LHC) require faster methods for changing the beam momentum.

Measurement of the Head-Tail Phase Shift

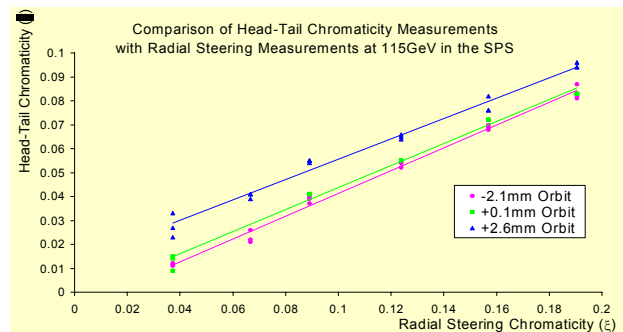


Figure 3: Head-tail versus classical Q' measurement [10]

This elegant method [10] [11] relies on the synchrotron oscillation to change the particle momentum. It is thus much faster than the above-mentioned methods.

Over half a synchrotron period, the particles forming initially the head will become the tail and vice-versa. In this half oscillation, the average momentum deviation of the particles moving from head to tail will be positive (above transition) while it will be negative for the particles moving from tail to head. If the chromaticity does not vanish, the betatron phase accumulated in the two cases will be different. The difference $\Delta\psi$ is proportional to the linear chromaticity and time interval $\Delta\tau$ between head and tail: $\Delta\psi = (2\omega_0/\eta)Q'\Delta\tau$.

In order to detect a coherent signal, the beam must be kicked transversely and the head and tail of the bunch measured separately on a turn-by-turn basis to detect the phase slip. A discrepancy on the value of the chromaticity by a factor of 2.2 with respect to the classical method was lately resolved [11]. Figure 3 demonstrate the consistency with a classical measurement and Figure 4 shows the variation of the chromaticity versus momentum in the SPS. It reveals the presence of a third-order chromaticity. In LHC, this term is expected from the b_5 component of

the main field which need to be corrected to 20% for a well-behaved beam dynamics.

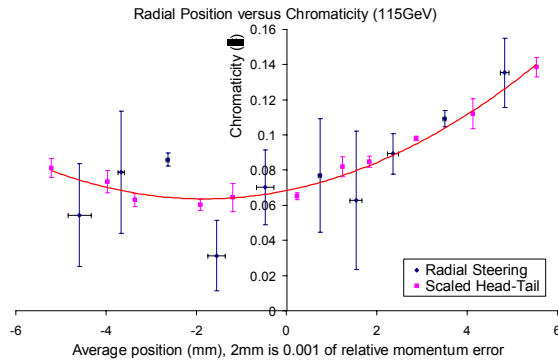


Figure 4: Non-linear chromaticity measured with head-tail oscillation [10]

Measurement via fast RF modulation

Another approach leading to a fast variation of the beam momentum is a fast modulation of the RF phase [12][13]. If this modulation is made outside of the beam frequencies, no dilution of the longitudinal emittance should occur. The modulation depth is limited by the corresponding reduction of the bucket area. This reduction shall not produce a leakage of particles outside the bucket nor create a synchrotron tune spread covering the excitation frequency. For the LHC, the resulting momentum modulation is of the order of $5 \cdot 10^{-5}$ and two times more in an experiment carried out at the SPS, for a modulation frequency close to five times the synchrotron frequency.

While the RF phase is modulated, a high-precision tune meter shall follow the resulting high-frequency tune modulation. The method in [12] assumes a PLL-based tune-meter locked on the beam response. The signal its VCO is Fourier analysed. The amplitude of the harmonic

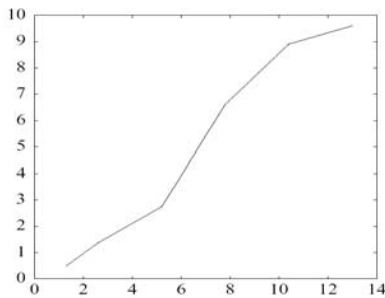


Figure 5: Amplitude of RF line versus set chromaticity [12]

at the RF modulation frequency is proportional to the modulus of the chromaticity. A calibration of the absolute chromaticity scale is possible by modulating the gradient of a quadrupole at the RF modulation frequency. If the amplitude and phase of the quadrupole modulation are adjusted to compensate the modulation due to the machine chromaticity, the signed chromaticity is measured. A first test with an incomplete setup done in

the SPS shows a definite dependence of the amplitude of the transverse spectral line at the RF modulation frequency on machine chromaticity (figure 5). In [13], the beam signal is rather demodulated, filtered and Fourier analysed. The chromaticity sign is extracted from a comparison of an upper and lower sideband.

ON-LINE COUPLING MEASUREMENT

Betatron coupling is most often measured via the closest tune approach. Kick methods can be used as well: the coupling strength can be calculated from the beat period of the exchange of beam amplitude between the horizontal and vertical planes e.g. [14] or, if turn by turn observation is available, by the direct measurement of the resonance driving term [19]. In both cases, the beam must be kicked resulting in some emittance blow-up.

A method better adapted to a continuous measurement and opening the possibility of a feedback circuit is the coupling beam transfer function (BTF) [15]. The principle is to excite the beam over its eigen-frequencies at a very low level in one plane and observe the response in the other. The resulting BTF is proportional to the modulus of the coupling coefficient while its phase can in principle be recovered from the phase of the BTF outside of the beam eigen-frequencies. This method was extensively used in the ISR and other machines. A continuous use for hours would not produce any measurable beam blow-up.

While [15] relied on a simplified approach, a recent

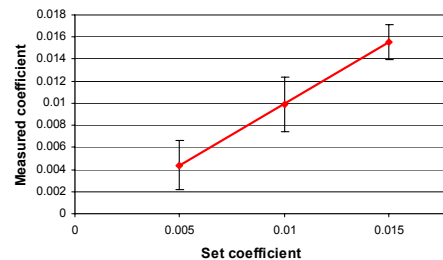


Figure 6: Coupling measurement via the BTF and AC dipole excitation [17]

exact first-order calculation of the single particle transfer function was carried out with the aim of predicting the observables in the general case [16]. This analysis shows that by measuring one or two points of the BTF, on either side of the beam spectrum and outside of it, it is possible to deduce the four parameters of linear coupling (\bar{c}_-, \bar{c}_+) and the local coupling parameters (in case of a local closed coupling bump). The method requires the use of two BPM's on either side of the beam excitor, spaced by a phase advance different from $k\pi$, without quadrupoles between them. Simulations show that an accuracy of 0.001 or better in $|c|$ should be expected. The excitation outside the beam eigen-frequencies should prevent any emittance blow-up. The first test done at the SPS, to be published soon [17] gave already a measurement of the coupling to an accuracy of 0.001 albeit using a non-canonical set-up. A ten times better accuracy is expected when the BTF phase can be measured. The coupling in

the SPS is purely real and the sum resonance very weak. The same test is to be performed in the more difficult environment of a collider. The principle of this measurement seems well adapted to a feedback system.

LOCAL NON-LINEAR FIELDS

The dynamic aperture in superconducting hadron colliders is limited at injection energy by the non-linearity in the arc dipoles and at collision energy by the non-linearity of the low-beta quadrupoles. Multipolar correction circuits are provided. A beam-based correction requires the measurement of the multipoles up to the dodecapole order. The feasibility of measuring high-order multipoles was demonstrated at RHIC[18]: a local closed orbit bump is created at the azimuth of the non-linearity to be measured. The beam displacement in the multipoles creates a feed-down to all lower orders. In practice, the feed-downs either to the orbit or tune order are measured versus the amplitude of the bump. The

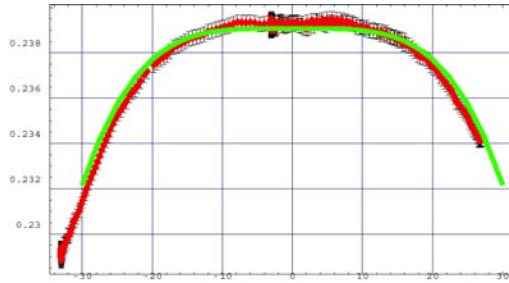


Figure 7: Signature of a dodecapole in RHIC
(tune shift versus bump amplitude [18])

degree of the variation of the tune/orbit with the bump amplitude is used to identify the multipole orders present and a fit provides their respective strengths. Using the PLL Q-meter at RHIC, the feed-down to the tune turned out to be the most accurate observable. The measured tune shift is given by:

$$\Delta Q \propto \int_{bump} \beta \left(\frac{b_n}{a_n} \right) \left(\frac{\Delta x_{bump}}{\Delta y_{bump}} \right)^{n-2} \frac{ds}{R^{n-2}} \quad (1)$$

where n is the multipolar order in the European convention ($n=3$ is the sextupole), R the reference radius.

In the low- β section, the β -function is modulated but the phase hardly advances. Expressing the orbit oscillation as a function of β in (1) shows that the measured tune shift in the plane of the bump is proportional to the 'action kick' $\int \beta^{n/2} b_n ds$, i.e. directly proportional to the quantity to be corrected.

The resolution of the RHIC PLL was found to be $5 \cdot 10^{-6}$. This allowed a very precise measurement of multipoles up to the dodecapole order (figure 7). The statistical error is the % range. Redundant measurements can be obtained using horizontal and vertical bumps and tunes to exclude systematics.

RESONANCE DRIVING TERMS

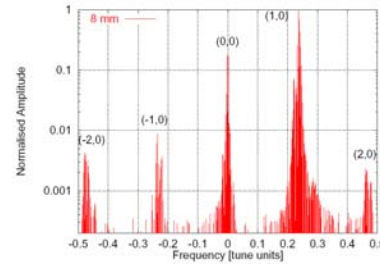


Figure 8: Transverse spectrum from [19]

In presence of non-linearities, the spectrum of the beam oscillation after a kick exhibits harmonics in addition to the main tune lines (figure 8). The method presented in [19] explains how to identify the harmonics with resonance conditions and how to relate their amplitudes with the resonance driving terms. It is summarized below.

To first-order in the non-linearities, the turn-by-turn transverse beam position takes a simple form in normalized complex coordinates:

$$\hat{x}(N) - i \hat{p}_x(N) = \sqrt{2I_x} e^{i(2\pi Q_x N + \psi_0)} - 2i \sum_{jklm > 0} j f_{jklm} (2I_x)^{\frac{j+k-1}{2}} (2I_y)^{\frac{l+m}{2}} \times e^{i[(1-j+k)(2\pi Q_x N + \psi_{x0}) + (l-m)(2\pi Q_y N + \psi_{y0})]} \quad (2)$$

The normalization is done with respect to the local β -function. The momentum is in practice replaced by the beam position measured at a second BPM spaced by 90 degrees. Q_x and Q_y are the betatron tunes and I_x , I_y the actions (normalized amplitudes). The complex coefficient f_{jklm} is directly related to the coefficients h_{jklm} of the expansion of the non-linear Hamiltonian into resonant terms which yields the driving terms.

$$f_{jklm} = h_{jklm} / [1 - e^{-i2\pi[(j-k)Q_x + (l-m)Q_y]}] \quad (3)$$

The expansion of the Hamiltonian, in term of the action-angle variables I and ψ , is itself given by:

$$H = \sum_{jklm > 0} h_{jklm} (2I_x)^{\frac{j+k}{2}} (2I_y)^{\frac{l+m}{2}} \times e^{-i[(j-k)(\psi_x + \psi_{x0}) + (l-m)(\psi_y + \psi_{y0})]} \quad (4)$$

From a comparison between the formula (2) and (4), it comes out that the resonance conditions $(j-k)Q_x + (l-m)Q_y$ appears in the spectrum as the spectral line $(l-j+k, m-l)$. For example, the horizontal third-order resonances $(3,0,0,0)$, i.e. $3Q_x$ appears as line $(-2,0)$. The resonance order is given by $j+k+l+m$.

The modulus of the resonance strength $|h_{jklm}|$ is computed from the amplitude of the spectral line after calibration of the kick. It shows the correct dependence on the amplitude (figure 9). In this formalism, the resonance strength is not Fourier expanded in azimuthal harmonics and thus retains its dependence on the machine azimuth. Its modulus remains constant in the absence of

non-linearity and jumps when a non-linearity is passed. This was used to ‘find’ the SPS sextupoles [19]. The measurement accuracy is limited by the decoherence. The method showed a good accuracy at the third order.

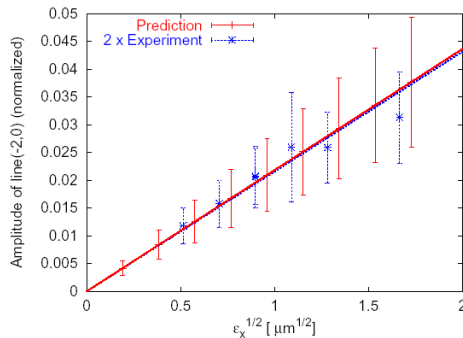


Figure 9: Normalized amplitude dependence of the $3Q_x$ driving term [19]

AC DIPOLE EXCITATION

Most measurement methods, except those based on the Schottky signals, require the beam to oscillate coherently in at least one of its degrees of freedom. The kick methods are easiest and largely used. With the decoherence due to the non-linearities and space charge, the coherent oscillation is transformed into a blow-up of the incoherent amplitudes, i.e. of the emittance.

For the measurement of the **linear** parameters, tunes, coupling... the kick method may be advantageously replaced by a very low amplitude coherent excitation coupled with a proper detection technique such as resonant pick up's, PLL circuit, transfer function... yielding a high signal to noise ratio.

The measurement of the **non-linearities** requires a beam displacement large with respect to the beam size. A beam blow-up can in principle be avoided if the beam is excited outside of its eigen-frequencies. This principle has been formalized in [20] and implemented at RHIC. Various experiments have shown that, provided the excitation frequency is switched on in a progressive manner, Figure 10, (no overlap of the spectrum of the

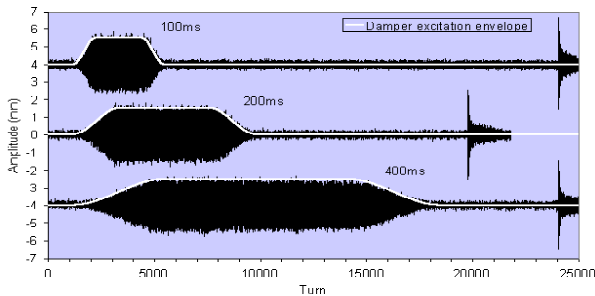


Figure 10: AC dipole excitation from [21]

modulated oscillation with the beam spectrum), the emittance blow-up is indeed in practice negligible for oscillations of the order of the beam size.

Recent theoretical studies show the high potential of this excitation technique in the measurement of the linear optics parameters including linear coupling [16] and in the measurement of the non-linear parameters (detunings and resonance driving terms) [22][23]. Experiments carried out at the SPS in 2002 confirm the potential for the measurement of linear parameters. The measurement of non-linear parameters still appears as a challenge.

REFERENCES

- [1] J. Wenninger, this conference.
- [2] E. Asseo, CERN PS/85-3(LEA), 1985.
- [3] A.M. Fauchet, J.P. Koutchouk, Betatron phase advance measurement in LEP, EPAC'90, Nice, 1990.
- [4] J. Laskar, 'Frequency Analysis for Multi-Dimensional Systems', Physica D67 (1993) 257-281.
- [5] R. Bartolini *et al.*, "Precise Determination of the Betatron Tune", EPAC'96, Sitges, 1996.
- [6] Y. Papaphilippou *et al.*, to be published in PAC'03, Portland, 2003.
- [7] P. Cameron *et al.*, "PLL Tune Measurement During RHIC 2001", EPAC'02, Paris, 2002.
- [8] W. Fischer *et al.*, "Tune Modulation from Beam-Beam", BNL C-A/AP/72 (2002).
- [9] <http://sl-div-bi.web.cern.ch/sl-div-bi/Conf&work/PLL-WORKSHOP/PLL-Workshop.htm>
- [10] D. Cocq, O.R. Jones, H. Schmickler, "Chromaticity via Head-tail Phase Shift", BIF 1998, SLAC, USA.
- [11] N. Catalan, S. Fartoukh, R. Jones, this conference.
- [12] O. Bruning *et al.*, "Chromaticity via RF Phase Modulation", EPAC'02, Paris, 2002, p 1852.
- [13] D. McGinnis, FNAL-PBAR Note 656, 2001.
- [14] P.J. Bryant *et al.*, "Measurement of the coupling resonance $Q_x-Q_y=0$ ", PAC'77, Chicago, 1977.
- [15] J.P. Koutchouk, "Linear betatron coupling measurement in the ISR", HEACC'80, Geneva, 1980.
- [16] S. Fartoukh, "Linear Coupling Coefficients via an AC dipole", CERN-SL-2002-059 AP, 2002.
- [17] N. Catalan, S. Fartoukh, "...", PAC'03, May 2003.
- [18] F. Pilat *et al.*, "Linear/Nonlinear Corrections in the RHIC Interaction Regions", EPAC'02, Paris, 2002.
- [19] M. Hayes, F. Schmidt, R. Tomas, "Measurement of Resonance Driving Terms at SPS", EPAC'02, 2002.
- [20] S. Peggs, PAC'99, New York, 1999.
- [21] O. Berrig *et al.*, DIPAC'01, Grenoble, 2001.
- [22] S. Peggs, C. Tang, "Non-linear Diagnostics using an AC dipole", RHIC/AP/159, 1998.
- [23] R. Tomas, "Normal Form of Particle Motion under the influence of an AC-dipole", Phys. Rev ST Accel. Beams, vol.5 54001 (2002).



CONTRIBUTED TALKS

AN INDUCTIVE PICK-UP FOR BEAM POSITION AND CURRENT MEASUREMENTS

M. Gasior, CERN, Geneva, Switzerland

Abstract

An Inductive Pick-Up (IPU) senses the azimuthal distribution of the beam image current. Its construction is similar to a wall current monitor, but the pick-up inner wall is divided into electrodes, each of which forms the primary winding of a toroidal transformer. The beam image current component flowing along each electrode is transformed to a secondary winding, connected to a pick-up output. Four pick-up output signals drive an active hybrid circuit (AHC), producing one sum (Σ) signal, proportional to the beam current, and two difference (Δ) signals proportional also to the horizontal and vertical beam positions. The bandwidth of these signals ranges from below 1 kHz to beyond 150 MHz, exceeding five decades. Each electrode transformer has an additional turn to which a pulse from a precise current source is applied to calibrate the sensor for accurate beam position and current measurements. The IPU has been developed for the drive beam linac (DBL) of the Third CLIC Test Facility (CTF3) [1]. For that purpose it had to be optimized for low longitudinal coupling impedance in the GHz range.

CONSTRUCTION

The CTF3 DBL beam consists of a $1.5 \mu\text{s}$ train of 2.3 nC , $5 \text{ pS}_{\text{RMS}}$ electron bunches paced at a 1.5 GHz repetition rate [1], as shown in Figure 1. A position monitor for such a beam should have a low cut-off frequency in the kHz range to limit signal droops, a high cut-off frequency beyond 100 MHz to observe fast beam movements and longitudinal coupling impedance Z_C low in the GHz range, containing important beam frequency components, to limit the monitor influence on the beam. These requirements implied significant improvements over the LEP Pre-Injector pick-ups [2] on which this IPU design is based.

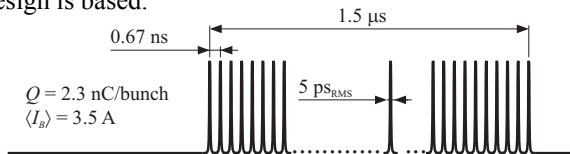


Figure 1: Time structure of the CTF3 DBL beam.

The IPU components and the assembly are shown in Figure 2 and 3 respectively. The 8 electrodes E have an internal diameter only 9 mm larger than the vacuum chamber of 40 mm and cover 75 % of the circumference in order to make the IPU as transparent to the beam as possible to minimize Z_C . The diameter step is occupied by the ceramic tube B of the vacuum assembly A; the tube is titanium coated on the inside. The electrodes are surrounded by the ferrite cylinder F inserted in the body C. The plates H accommodate the PCBs G on which the

transformers are mounted. A screw D passes through each transformer ring, connecting an electrode E to a plate H. The clamps I tighten the plates H with connectors screwed. To achieve good low frequency responses primary circuit parasitic resistances had to be kept below a $\text{m}\Omega$, thus the body C, the electrodes E and the plates H are made from copper. The plates as well as the beryllium copper screws D are gold plated. The electrodes and their supporting plate are machined as one piece to minimize contact resistances between small surfaces and to achieve good mechanical precision.

The four IPU outputs are connected to the AHC, which is followed by amplifiers housed in a common enclosure. The amplifiers, having two remotely switchable gains, amplify Δ and Σ signals to a level suitable to be sent over long cables to an equipment room.

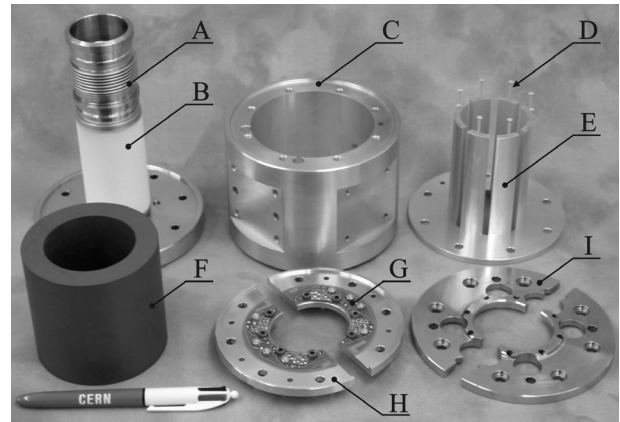


Figure 2: The IPU parts.



Figure 3: The IPU assembled. On the front there are four pick-up outputs and two calibration inputs.

The full beam image current must pass through the transformers, so the IPU can be used for its absolute measurement. To calibrate the sensor for this purpose, each transformer has a calibration turn, used to inject a current pulse of an amplitude known to 0.1 %, which in addition is independent of parasitic resistances of cables, connectors and the like. Similar pulses are used to test the Δ and Σ channels, calibrate their gains and check the common mode rejection ratio (CMRR) by applying identical signals to the transformers of opposite electrode pairs. This is important, since the AHCs are only one meter away from the beam and they are exposed to some radiation.

A MODEL AND RESULTS

The low frequency behavior of two opposite pairs of electrodes, forming one IPU plane, can be modeled by the circuit shown in Figure 4. Components of the beam image current I_B flow through four 1: n electrode transformers, which are combined in pairs so that each sees half of the secondary winding load R_S . The output Σ signal voltage

$$V_{\Sigma} = \frac{R_S}{2n} I_B \quad (1)$$

decays with the time constant set by $R_p = R_S/2n^2$, representing R_S transformed to the primary winding, and inductance L_{Σ} of the loops built from electrodes and the body walls; the loops are filled with the ferrite. Taking into account parasitic connection resistances R_C of primary loops yields the Σ signal low cut-off frequency

$$f_{L\Sigma} = \frac{1}{2\pi L_{\Sigma}} \left(\frac{R_S}{2n^2} + R_C \right) \quad (2)$$

provided that the transformer low cut-off is still smaller.

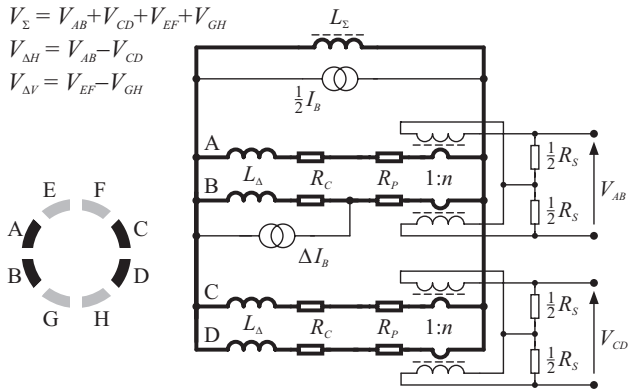


Figure 4: IPU low frequency model for one plane.

Similarly, the current ΔI_B resulting from the beam displacement decays with the time constant set by the sum $R_p + R_C$ and electrode inductance L_A . The corresponding low cut-off frequency is

$$f_{LA} = \frac{1}{2\pi L_A} \left(\frac{R_S}{2n^2} + R_C \right) \quad (3)$$

The number of turns n was a trade-off between four parameters: the low cut-off frequencies $f_{L\Sigma}$ and f_{LA} proportional to n^{-2} , the voltage V_{Σ} changing as n^{-1} and

high cut-off frequencies, degrading with increasing n . The low cut-off frequencies were also reduced by lowering R_S at the expense of decreasing V_{Σ} . Since $L_A \ll L_{\Sigma}$ resulting in $f_{LA} \gg f_{L\Sigma}$, only frequency f_{LA} was lowered by another decade using extra low frequency gain in the Δ signal amplifier. Parameters of the model of Figure 4, the IPU and a channel IPU-AHC are listed in Table 1.

Table 1. Parameters of the IPU and of its electronics.

IPU	Electrical centre position error	< 0.1 mm
	Range of linearity to 50 μ m	± 5 mm
	Transformer load R_S / turn number n	7 Ω / 30
	L_{Σ}/L_A inductances / ferrite μ_r	$\approx 5 \mu$ H / 70 nH / 100
	Primary winding resistance R_p	4 m Ω
	Primary parasitic resistance R_C	≈ 0.5 m Ω
	Transresistance V_{Σ}/I_B	0.1 Ω
	IPU electrode high cut-off frequency	300 MHz
	IPU Σ low cut-off frequency	150 Hz
	IPU Δ low cut-off (without the slope)	10 kHz
IPU + AHC	Titanium coating end-to-end resistance	10 Ω (i.e. 15 Ω/\square)
	Coupling imp. Z_C @ 1.5 / 3 GHz	9 + j2 / 10 - j0.5 Ω
	Beam pipe / electrode inner diameter	40 mm / 49 mm
	Length with bellows / body diameter	168 mm / 130 mm
	Position sensitivity	10 mm $\times \Delta\Sigma$
	Overall Σ signal bandwidth	300 Hz – 250 MHz
	Overall Δ bandwidth (without slope)	800 Hz – 150 MHz
	Δ equivalent noise @ $\langle I_B \rangle$ 3A / 0.3A	< 5 μ m _{RMS} / < 50 μ m _{RMS}
	Σ equivalent noise, low / high gain	< 3 mA _{RMS} / < 3 mA _{RMS}
	Σ signal amplifier gain low / high	5 / 25 dB
IPU + AHC	Δ signal amplifier gain low / high	15 / 35 dB
	AHC CMRR @ 1 / 100 MHz	> 60 dB / > 50 dB
	Calibration current pulse	300 mA 0.1 %, 150 μ s

The transformer load R_S is as small as 7 Ω making the secondary winding circuit very sensitive to parasitic series inductances. To minimize them, R_S is built from 6 chip resistors and connections between components of the secondary winding are made by sections of low impedance microstrip lines.

Frequency characteristics of the IPU with the AHC are plotted in Figure 5. The measurement was done with a wire method, where beam is simulated by the central conductor of a coaxial line which the IPU was a part. The Σ signal is flat to 0.5 dB over 5 decades. The Δ signal, originating in a small central conductor displacement, has a 3 dB slope for some 4 decades, which can be explained by a frequency dependence of the ferrite permeability and electrode current surface distribution.

The PCB layout of the AHC module was carefully designed to obtain sufficient CMRR at high frequencies. Note that the achieved CMRR of better than 50 dB at 100 MHz is equivalent to 0.1 pF of parasitic asymmetry of a 50 Ω line.

The IPU displacement characteristic is linear to 50 μ m for excursions up to ± 5 mm, most important for the DBL. The linearity error, shown in Figure 6, was measured with the wire method, where a thin wire was displaced diagonally through the pick-up aperture.

The IPU longitudinal coupling impedance Z_C was estimated by a wire method measurement shown in Figure 7. It can be seen that the components beyond

1 GHz flow essentially only over the titanium coating, so its resistance of about $10\ \Omega$ limits the Z_C , hopefully also beyond 3 GHz. Above this frequency waveguide modes were observed in the setup and the measurement did not yield meaningful data.

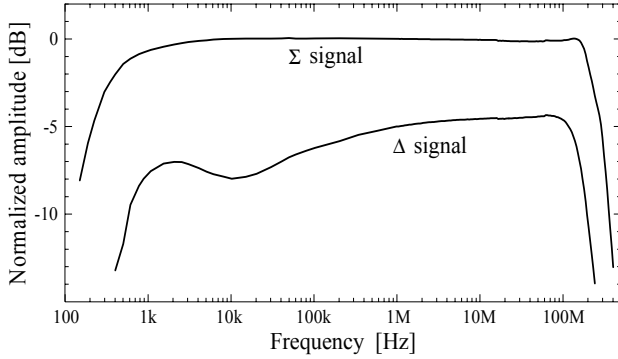


Figure 5: Characteristics of the IPU with its AHC. Measured with a $50\ \Omega$ coaxial line setup (wire method).

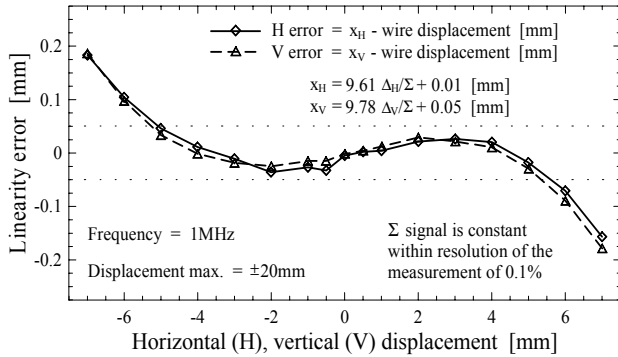


Figure 6: IPU linearity error. Measured with a wire of diameter of 0.2 mm displaced diagonally.

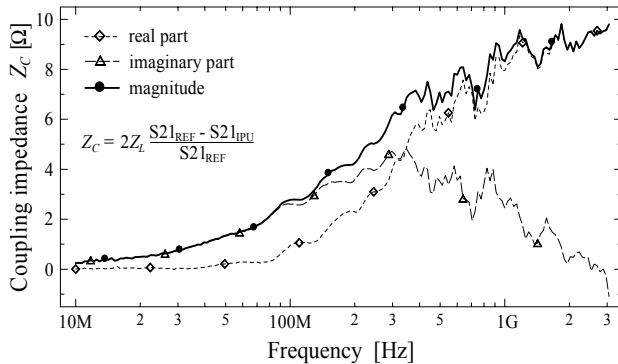


Figure 7: Longitudinal coupling impedance Z_C measured with a coaxial setup of $Z_L = 50\ \Omega$ (wire method). For the $S_{21_{REF}}$ reference measurement the IPU was replaced by an equivalent length of a straight tube.

The IPU influence for the beam may also be deduced from a Time Domain Reflectometry (TDR) measurement shown in Figure 8. For high frequency components the electrode diameter step is not visible, as they flow over the coating. For lower frequencies an impedance increase

of about $6\ \Omega$ is seen, corresponding to the electrode diameter step for the most part occupied by the ceramic insertion (alumina, $\epsilon_r \approx 10$).

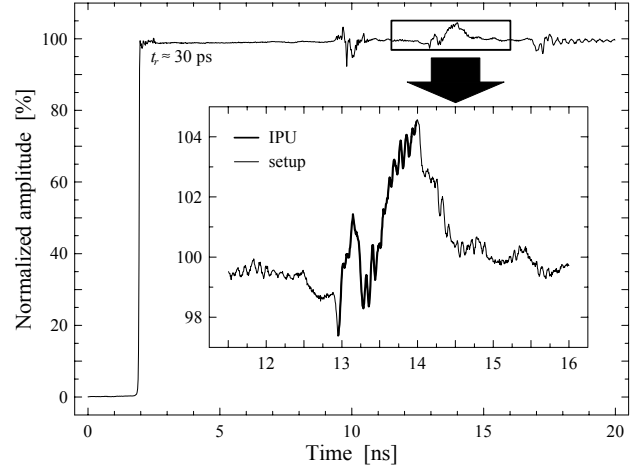


Figure 8: IPU TDR measurement with a $50\ \Omega$ coaxial setup (wire method) and TDR module Agilent 54753A. Ripples in the magnified region originate in setup waveguide modes and the irregularities outside the region result from setup imperfections, especially of the conical adaptations.

CONCLUSIONS AND THE FUTURE

An inductive pick-up and a dedicated active hybrid circuit were designed for the drive beam linac of the CTF3. They allow to measure beam position with a bandwidth of 5 decades and absolute beam current over 6 decades. The IPU with its AHC can be tested and calibrated in place with precise current pulses. Neither the IPU nor the AHC contain adjustable elements. The pick-up longitudinal impedance was limited to about $10\ \Omega$ in the GHz range. The pair IPU-AHC has been tested with a beam in the CTF2. Two monitors have been installed in the CTF3 for the startup in June. An acquisition system [3] based on 12-bit fast digitizers is being developed. In the future some 20 IPUs will be installed in the facility.

ACKNOWLEDGMENTS

I would like to thank all members of my AB/BDI/PI section for their help, especially to J. Belleman, J. Durand, J.L. Gonzalez, J.P. Potier and L. Søby. I am also grateful to Y. Cuvert for the superb mechanical design and to J.L. Chauvet for excellent PCBs.

REFERENCES

- [1] G. Geschonke et al., "CTF3 Design Report", CTF3 Note 047, CERN, May 2002.
- [2] S. Battisti et al., "Magnetic Beam Position Monitors for LEP Pre-Injector", Proceedings of the 1987 IEEE PAC, Washington, March 16-19 1987, pp. 605 – 607.
- [3] M. Gasior, "Hardware of the CTF3 Beam Position Measurement System", CTF3 Note 053, CERN, February 2003.

SINGLE-SHOT MEASUREMENTS OF THE 4-DIMENSIONAL TRANSVERSE PHASE SPACE DISTRIBUTION AT THE UNILAC AT GSI

W. Barth and L. Groening, GSI, Darmstadt, Germany

D. Liakin, ITEP, Moscow, Russia

Abstract

The UNILAC is used as an injector for the synchrotron SIS. It is designed to fill the synchrotron up to its space charge limit. The upper limit for the useful beam emittance of the UNILAC is given by the finite acceptance of the SIS during the injection process. In order to remain within this acceptance the emittance growth during beam acceleration and transportation due to space charge effects must be minimized by applying an appropriate beam focusing. Therefore, the influence of the magnetic focusing strength on the beam emittance growth was investigated experimentally for different beam currents. Measurements of transverse phase space distributions were performed before and after the Alvarez accelerator with a periodic focusing channel, respectively. In order to perform such a wide parameter scan within a reasonable time with respect to machine stability, the pepper pot technique was applied. The pepper pot method allows for single-pulse measurements. For comparison several measurements using the slit-grid technique, which averages over many pulses, were performed. Both transverse planes were measured simultaneously. Using two pepper pot devices more than 60 single shot measurements of the full 4-dimensional transverse phase space distribution were performed within 8 hours. In this paper we report on the results of the measurements and we compare them to beam dynamic simulations and we give an outlook on further developments on pepper pot devices.

INTRODUCTION

The High Current Injector (HSI) of the UNILAC (Fig.1) comprises a RFQ and two IH-structures operated at 36 MHz. It accelerates intense ion beams generated by a MUCIS- or MEVVA- ion source to an energy of

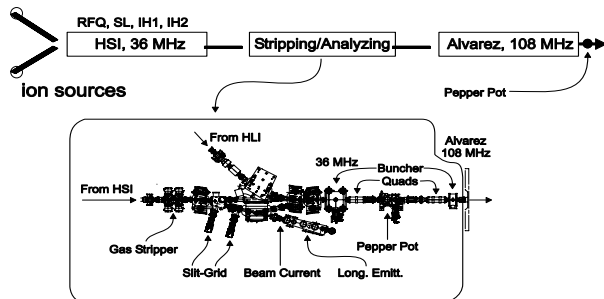


Fig. 1: Schematic overview of the Universal Linear Accelerator UNILAC at GSI.

1.4 MeV/u. After the HSI the ion charge state is increased by passing the beam through a gas jet stripper. A subsequent charge state separator selects the charge state for further acceleration in the Alvarez DTL (108 MHz) to 11.4 MeV/u. To match the periodic transverse focusing in this section, the beam size must be reduced significantly in all three dimensions. This leads to a strong increase of the space charge forces, which scale with the space charge parameter SCP [1]

$$SCP \sim I_p \cdot q^2 \cdot \beta^{-1} \cdot (XYZ)^{-1},$$

where I_p is the particle beam current, q is the ion charge state, β is the relative velocity, and (XYZ) is the bunch volume. As shown in Fig.2 the SCP has two maxima

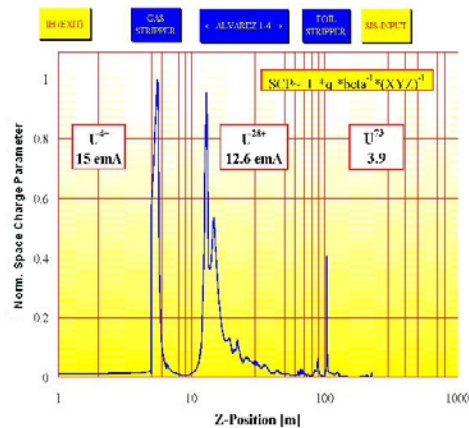


Fig. 2: The space charge parameter SCP along the UNILAC.

during the stripping process and at the entry to the Alvarez section, respectively. During acceleration it decreases due to the increase of β . For a given beam current the emittance growth along the section depends on the transverse focusing strength. According to theory the growth should be reduced by a stronger focusing. We aimed on the experimental investigation of this dependence for three different beam intensities.

EXPERIMENTAL SET-UP

Figure 1 shows the set-up of the experiment. Beam currents were measured before and after the Alvarez section. The 4-dimensional transverse phase distributions were measured during single-shots using a pepper pot device before and after the DTL, respectively. Additionally, a horizontal slit/grid set-up was employed,

which serves normally to optimize the charge state separation. A detailed description of the diagnostics at the UNILAC can be found in [2].

The beam focusing along the DTL was set to a transverse zero current phase advance σ_0 of 39° . By variation of the stripping gas pressure the current of the $^{40}\text{Ar}^{10+}$ beam was set to 10 emA for the first measurement of the parameter scan. The five quadrupole lenses before the DTL were set in order to maximize the beam transmission. Beam emittances and currents were measured before and after the DTL using the pepper pot devices. Beam intensity reduction (1 emA, 5 emA) was done by varying the stripping gas density. This method preserves the shape of the phase space region occupied by the beam. These three measurements were repeated for phase advances σ_0 of 45° , 51° , and 59° , respectively. In total 12 measurements on emittance growth were performed including more than 60 measurements of the full transverse 4-dimensional phase space distribution. This scan could not have been accomplished using slit/grid set-ups within a reasonable time with respect to machine stability. Additionally, for each current one measurement of the horizontal phase space distribution was performed with the slit/grid set-up (Fig.3). The results confirm that the shape of the distribution did not change significantly with the beam intensity.

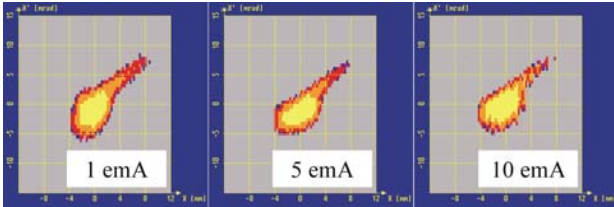


Fig. 3: Measured horizontal phase space distribution for three different ion currents using a slit/grid set-up before the Alvarez section.

EXPERIMENTAL RESULTS

Figure 4 shows the horizontal phase space distributions after the DTL measured with a pepper pot device for different currents and phase advances. For a σ_0 of 45° and 51° compact distributions were observed. In case of 39° and 55° large tails of lower density occur, which increase the emittance. The measurements were used to extract the normalized beam emittances for both transverse planes. Figure 5 summarizes the obtained emittances after the Alvarez DTL together with the beam transmission through the section. As already seen qualitatively on the pepper pot images, the extracted horizontal emittance is lowest for $\sigma_0=51^\circ$, which is 10% higher than the phase advance of 45° used so far in routine operation of the UNILAC for intense beams. This behaviour of the horizontal emittance fits to the measured transmissions, which were highest at 51° as well. The vertical emittance

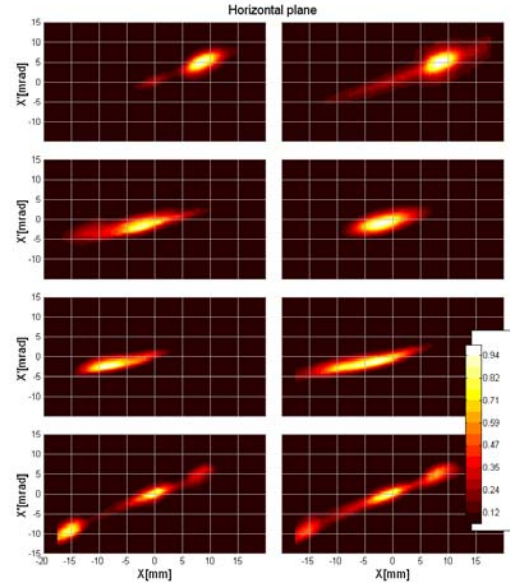


Fig. 4: Horizontal projections of single-shot measurements of the phase space distributions after the Alvarez section using a pepper pot device. Shown are the results for currents of 1 emA (left) and 10 emA (right) for transverse phase advances σ_0 of 39° , 45° , 51° , and 59° (top to bottom).

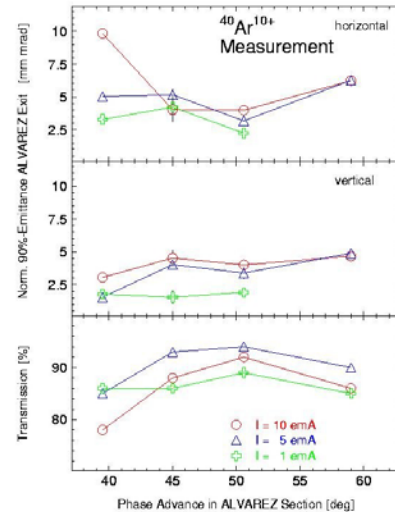


Fig. 5: The measured normalized horizontal and vertical emittances after the Alvarez section. The values refer to 90% of the particles. The bottom part shows the transmission through the Alvarez DTL.

after the DTL as function of σ_0 did not show a conclusive behaviour. It was observed to be constant within the accuracy of the data reduction. Additionally, the measured emittances before the Alvarez DTL showed a strong dependence on the beam size at the pepper pot for all beam currents as shown in Fig.6. The emittance before the DTL should not depend on the beam focusing especially for very low currents of 1 emA. The measured rms emittance shows a linear dependence on the beam size. The slope is about 2.7 mrad. Besides the beam size

the rms beam divergence was evaluated and found to be larger than 2 mrad for all beam sizes being comparable to

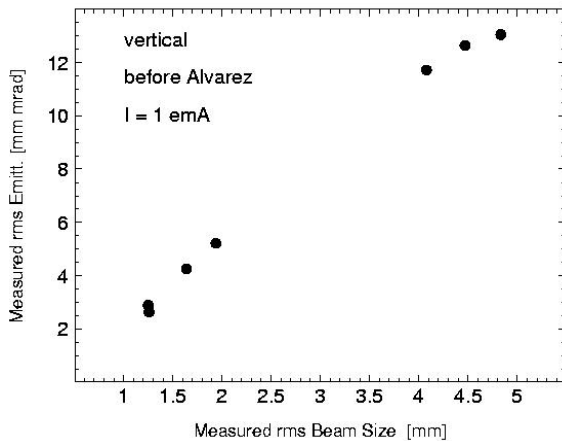


Fig. 6: The measured horizontal rms emittance for different horizontal beam spot sizes on the pepper pot. The ion beam parameters are identical for all measurements.

the slope of 2.7 mrad mentioned before. This observation can be understood, if the angular resolution of the pepper pot devices before the DTL, i.e. at 1.4 MeV/u, is about 2 mrad. These linear dependences at low currents were observed for both planes before and after the DTL. At higher ion energies of 11.4 MeV/u the angular resolution seemed to be about 1 mrad. Starting from the phase space distributions measured with the slit/grid set-up we expect rms beam divergences, which are about half of the angular resolution estimated from the measurements with the pepper pot devices. However, the quantitative results of the pepper pot measurements clearly showed that most compact phase space distributions could be obtained if the DTL phase advance σ_0 for high intensities is set close to 50° .

SIMULATIONS

In order to model the initial 6-dimensional distribution, the measurements with the slit/grid set-up, with the pepper pot devices, and with various beam profile monitors before the Alvarez DTL were used. Additionally, previous measurements of the longitudinal phase space distribution were taken into account [3]. Using the obtained distribution as an input for PARMILA the simulations showed consistency with all measurements before the DTL. However, the correlations between the longitudinal and transverse distributions were not accessible by measurements but they influence considerably the beam dynamics in the subsequent DTL. This must be kept in mind for the interpretation of the simulations.

Using the reconstructed initial 6-dimensional distribution before the DTL, the experimental scan was simulated. The results showed a decrease of the emittances after the DTL as function of σ_0 for all beam currents. The smallest emittances were calculated for the strongest focusing. For σ_0 up to 51° this is in agreement with the experimental observations. But the experimentally observed increased emittance growth for the strongest focusing of $\sigma_0 = 59^\circ$ with respect to the minimum at 51° was not reproduced in the simulations. The calculated beam transmission was 90% and did not depend on the beam current and on the focusing strength. However, this value fits within the measured transmissions ranging from 80% to 93%.

SUMMARY AND OUTLOOK

Using two pepper pot devices before and after the Alvarez DTL the emittance growth in the DTL was measured qualitatively as function of the beam intensity and of the beam focusing strength. The results showed that the emittance growth is smallest for a zero current phase advance between 45° and 55° . Due to the limited angular resolution of the devices no quantitative measurements could be done so far. The resolutions were found to be about 2 mrad at an ion energy of 1.4 MeV/u (before DTL) and about half of this value at 11.4 MeV/u (after DTL). In order to scope with the typical beam parameters at the UNILAC the angular resolutions should be increased by a factor of five. However, the experimental results strongly suggest an increase of the currently used zero current phase advance of 45° to 50° for routine operation of high intensity beams. For the heaviest ion species $^{238}\text{U}^{28+}$ this requires an update of the power supplies of all quadrupoles along our Alvarez DTL. The implementation of horizontal and vertical slit/grid set-ups before and after the DTL is foreseen for this year. Future experiments will thus allow for comparing measurements using pepper pot devices and slit/grid set-ups.

REFERENCES

- [1] W. Barth, et al., High Current Transport and Acceleration at the Upgraded UNILAC, Proc. of LINAC98, Chicago, p. 454, (1998).
- [2] W. Barth, et al., Beam Diagnostics for Intense Heavy Ion Beams at the GSI UNILAC, these Proceedings.
- [3] P. Forck, et al., Measurement of the Six Dimensional Phase Space at the New GSI High Current Injector, Proc. of LINAC2000, Monterey, p. 166, (2000).

Beam Instrumentation for the Single Electron DAΦNE Beam Test Facility

G. Mazzitelli*, F. Sannibale, P. Valente, M. Vescovi
 Laboratori Nazionali di Frascati dell'INFN, Frascati, Italy
 P. Privitera, V. Verzi
 Dipartimento di Fisica & INFN Roma II, Roma, Italy

Abstract

The DAΦNE Beam Test Facility (BTF) has been successfully commissioned in February 2002, and started operation in November of the same year. Although the BTF is a beam transfer line optimized for single particle production, mainly for high energy detectors calibration, it can provide electrons and positrons in a wide range of multiplicity: between $1 \div 10^{10}$, with energies from a few tens of MeV up to 800 MeV. The large multiplicity range requires many different diagnostic devices, from high-energy calorimeters and ionization/fluorescence chambers in the few particles range, to standard beam diagnostics systems. The schemes of operation, the commissioning results, as well as the beam diagnostics are presented.

DESCRIPTION OF THE DAΦNE BTF

The Beam Test Facility (BTF) is a beam line optimized for the production of a pre-determined number of electrons or positrons, in a wide range of energies (up to 800 MeV) and multiplicity. The facility is particularly suitable for particle detector testing purposes, such as energy calibration and efficiency measurements, in single electron mode; while beam diagnostics devices and detector aging can be studied at higher intensities.

The BTF is part of the DAΦNE accelerator complex, consisting of a double ring electron-positron collider, a high current linear accelerator (LINAC), an intermediate damping ring (Accumulator) and a system of 180 m transfer lines connecting the four machines. The LINAC delivers electrons with energy up to 800 MeV, with a typical current of 500 mA/pulse, or positrons with energy up to 550 MeV, with a typical current of 100 mA/pulse; the pulse duration can be adjusted in the range $1 \div 20$ ns with a maximum repetition rate of 50 Hz. When injecting for operation of the main rings at the ϕ resonance, the beam energy is 510 MeV.

Since the minimum LINAC beam current that can be conveniently measured by the DAΦNE current monitors is $I \approx 1$ mA, the corresponding number of electrons (positrons) is $\approx 10^8$ /pulse. It is thus necessary to strongly reduce the number of particles to reach the few particles range. The reduction of the particle multiplicity can be achieved with different methods, the one chosen for the BTF operation is the following[1]: first the LINAC beam is

intercepted by a (variable depth) target in order to strongly increase the energy spread of the primary beam; then the out-coming particles are energy selected by means of a bending magnet and slit system. The energy selector only accepts a small fraction of the resulting energy distribution, thus reducing of the number of electrons by a large and tunable factor. The target is shaped in such a way that three different values of radiation length can be selected ($1.7, 2.0, 2.3 X_0$) by inserting it at different depths into the beam-pipe. The attenuated beam is transported by a ≈ 12 m transfer line to the BTF hall, where the experimental setups can be installed. The dipole magnet, together with a downstream collimator, selects the momentum of the particles. At the end of the BTF line a second bending magnet allows to use two separate test lines: one directly from the straight section, the other from the magnet at 45° .

Due to the momentum dispersion introduced by the bending magnet, the relative energy spread $\Delta E/E$ is essentially determined by the magnet/collimators configuration[2]; in the standard BTF operation for a wide range of slit apertures a resolution better than 1% can be obtained.

The number of transported electrons (or positrons) can be adjusted in a wide range, down to single particle, and is well below the sensitivity of any standard beam diagnostics device, so that many different particle detectors have been used to monitor the beam characteristics.

BEAM COMMISSIONING AND DIAGNOSTICS

During 2002 the BTF has been successfully commissioned and started operation, delivering beam to the first user experiments, from Nov. 2002 to May 2003[3]. The facility has been operating both in the single electron production scheme and the high multiplicity operation mode, according to the different user requirements.

At low multiplicity a calorimeter has been used as main diagnostic device. The detector is a lead/scintillating fibers calorimeter of the KLOE type[4], with single side photomultiplier readout. The main features are a sampling fraction of $\approx 15\%$, a good energy resolution, $\sigma_E/E = 4.7\%/\sqrt{E(\text{GeV})}$, and excellent timing resolution, $\sigma_t/t = 54\text{ps}/\sqrt{E(\text{GeV})}$.

The LINAC setting has been optimized to provide a 510 MeV energy, $4 \div 5$ mA intensity beam. The repetition rate of the LINAC was 24 Hz (+1 shot to the spectrometer line

* giovanni.mazzitelli@lnf.infn.it

for LINAC energy measurement), and the pulse duration was the same as for injection in the accumulator, ≈ 10 ns. The typical collimator settings were 2 mm of total aperture, both for the upstream and downstream slits: with the attenuator depth set to $1.7 X_0$ only a few electrons reach the diagnostic detectors.

Due to the good energy resolution of the calorimeter, $\approx 7\%$ at 500 MeV, the number of produced electrons can be counted simply by measuring the total deposited energy E : $n = E/E_1$, where E_1 is the energy deposited by a single electron. An example of ADC spectrum (pedestal subtracted) is shown in Fig. 1, for a selected energy of $E_{\text{sel}} = 471$ MeV: the individual peaks corresponding to $0, 1, \dots, n$ electrons can be easily identified. The total number of events in each peak should represent the probability of producing n particles: by fitting the distribution of the number of events in each peak with the Poisson function, the average number of particles can be determined (see the inset of the figure).

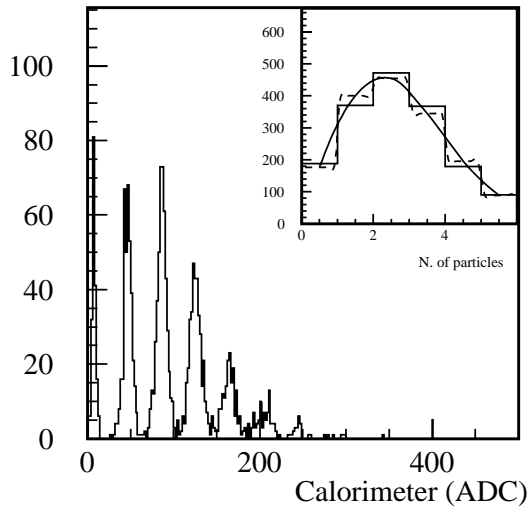


Figure 1: Counting electrons in the calorimeter: charge spectrum for $E_{\text{sel}} = 471$ MeV (in the inset: the number of particles in each peak is fitted with the Poisson function, mean value $\bar{n} = 2.3$).

The most effective way to change the average number of particles in the beam is to change the selected energy E_{sel} ; in particular, at the **same** LINAC energy and intensity and with the **same** collimator settings, the multiplicity increases by decreasing the chosen E_{sel} . In addition, the multiplicity can be tuned by changing the aperture of the upstream and/or downstream collimators. In this case the energy resolution of the selector will be also affected, but by a relatively small amount, in any case well below the intrinsic resolution of our calorimeters. In particular, the measured multiplicity increases by increasing the slits aperture until the intrinsic beam spot size is exceeded.

There are two intrinsic limitations to the particle counting with calorimeters. Since the absolute width of the peaks increases as \sqrt{n} , increasing the average multiplicity the

peaked structure in the energy distribution gradually disappears, approaching a Gaussian shape. In this case the number of particles in the beam cannot be measured *event by event*, but only the average multiplicity \bar{n} can be statistically estimated. Another intrinsic limitation to the particle counting performed by means of the total energy measurement in a calorimeter is the detector saturation, *i.e.* when the signal begins to be no longer proportional to the number of particles. This is in general due to one or more of the following factors: saturation of the ADC scale, of the photomultiplier gain or the scintillation light yield.

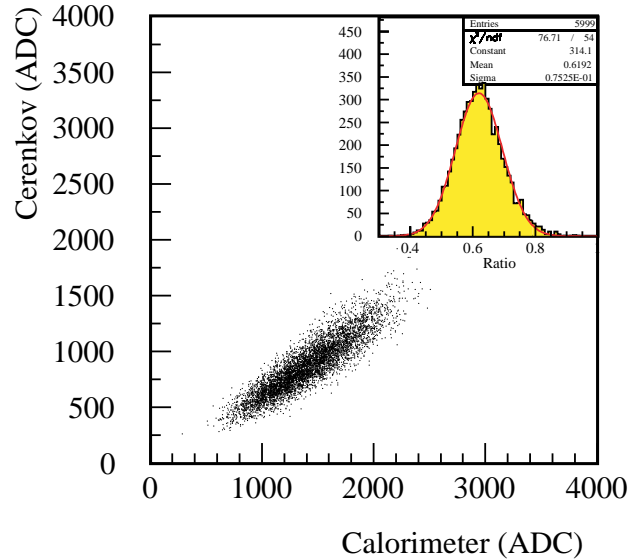


Figure 2: The signal in the Cerenkov counter as a function of the total energy in the calorimeter (in the inset the ratio between the two measurements is fitted with a Gaussian).

Above ≈ 20 particles the calorimeters are no longer effective due to saturation effects. In order to have a diagnostic device in the $\bar{n} = 100$ -1000 range (and higher), a different detector has been developed and tested in collaboration with the AIRFLY group [5]. It is essentially a counter based on the Cerenkov light emission in a PLEXIGLAS radiator when crossed by relativistic electrons (which in the BTF energy range is always the case). The light is then extracted by properly shaping the end part of the radiator itself and collected by a photomultiplier, without optical connection: this gives the possibility of interposing a calibrated optical filter between the radiator and the PMT, in order to attenuate the Cerenkov light by a known factor, thus extending the dynamical range of the counter. The Cerenkov light yield, and in turn the phototube analog signal, should be proportional to the number of electrons crossing the radiator; this phenomenon should be linear up to a very high number of electrons. The Cerenkov counter signal shows a good correlation with the energy deposited in the calorimeter, as shown in Fig. 2, with a suitably low multiplicity beam; using the cross-calibration between the two detectors, the Cerenkov counter has been used to monitor the beam multiplicity up to ≈ 1000 .

The above described devices are fully remotely controlled by the DAΦNE control system. The Data Acquisition System is based on VME bus, equipped with a VMIC 7740 controller CPU, running Red Hat 7.3 Linux and National Instruments LabView. The splitted analog signals are properly delayed and fed to CAEN V792 ADCs, and discriminated and fed to CAEN V775 TDCs. The DAQ trigger and gate signals are driven by the digital pulse of the LINAC gun provided by the DAΦNE timing system.

Another important parameter is the beam energy, that can be chosen by changing the current of the energy selector dipole magnet. The average measured energy of the single electron signal in the calorimeter is proportional to the incoming beam energy E_{sel} as shown in Fig. 3.

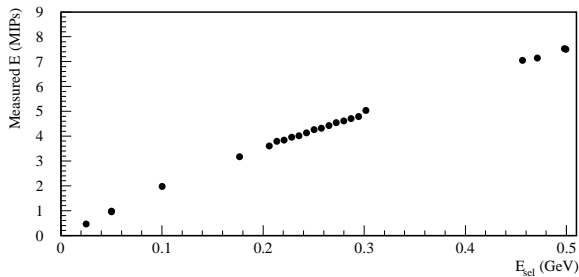


Figure 3: Total energy deposited in the calorimeter by a single electron as a function of the selected beam energy E_{sel} .

Many user experiments were carried out since Nov. 2002 in the two main different operation modes of the BTF facility:

- high multiplicity in a wide range of energies: the AIRFLY experiment measuring the air fluorescence yield, in the widest accessible energy range for the BTF beam, with the air fluorescence detector chamber in a fixed position; and the DIAMANTE2 beam intensity monitor;
- single electron for a number of energy points, full coverage of the detectors (moving them across the beam): LCCAL electromagnetic calorimeter calibration, CAPIRE collaboration RPC efficiency tests, LHCb gas detectors efficiency tests, AGILE silicon tracker tests.

Profiting of the high spatial resolution of the silicon micro-strip detector, a beam profiling chamber has been installed in collaboration with the AGILE group[6], in order to monitor the beam spot size (at low multiplicities). An example of the beam spot measured by the silicon microstrip monitor is shown in Fig. 4. The device is a single-sided, AC-coupled, 410 μm thick, 9.5 cm side square silicon strip detector with a readout pitch of 242 μm and one floating strip with polysilicon bias voltage resistors. Three 128-channel analog-digital, low noise, self-triggering ASICs, with multiplexed analog readout are used.

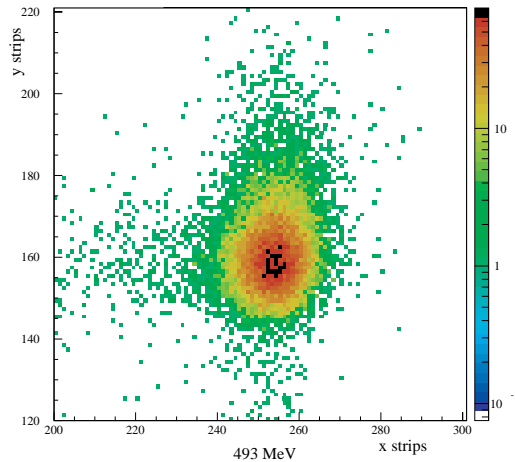


Figure 4: Beam spot measured by the AGILE silicon tracker (242 μm strip pitch): $\sigma_x \approx \sigma_y \approx 2 \text{ mm}$.

CONCLUSIONS

Since the beginning of operation, the BTF has demonstrated to be easily tunable both from the point of view of the desired particle multiplicity (from single electron mode to ≈ 1000) and energy setting. In order to overcome the present limitations imposed by the DAΦNE collider experiments operation and to largely improve the duty-cycle, we plan to upgrade the facility [7]; a complete separation between the DAΦNE transfer lines to the Main Rings and the BTF channel will allow to operate in the BTF mode with the only limitations of the LINAC switching time and the time spent for filling the Main Rings.

More diagnostic systems, especially devoted to high multiplicity measurement and beam energy resolution, are under development in order to improve the characterization of the beam quality.

Finally, an upgrade of allowed radio-protection dose up to 10^{10} particles/s, will permit to use the BTF also for testing of standard beam diagnostics devices.

REFERENCES

- [1] L. Rinolfi *et al.*, *Single electron beams from the LEP pre-injector*, in Proceedings of PAC 89, Chicago (1989) 298.
- [2] F. Sannibale, G. Vignola, DAΦNE Technical Note **LC-2** (1991).
- [3] G. Mazzitelli, P. Valente, *Commissioning of the DAΦNE Beam Test Facility*, LNF-03-003(P).
- [4] M. Adinolfi *et al.*, Nucl. Instrum. Meth. **A482** (2002) 364.
- [5] P. Privitera *et al.*, *AIRFLY Letter of Intent*, INFN Gr. V, unpublished.
- [6] M. Prest *et al.*, Nucl. Instrum. Meth. **A501** (2003) 280.
- [7] G. Mazzitelli *et al.*, DAΦNE Technical Note **BTF-1** (2003).

The Beam Inhibit System For TTF II

D. Nölle, P. Göttlicher, R. Neumann, D. Pugachov, K. Wittenburg, M. Wendt, M. Werner, H. Schlarb, M. Staack, DESY, Hamburg, Germany
 M. Desmons, A. Hamdi, M. Jablonka, M. Luong, CEA, DAPNIA, Saclay, France
 e-mail: dirk.noelle@desy.de

Abstract

The new generation of light sources based on SASE Free-Electron-Lasers driven by LINACs operate with electron beams with high beam currents and duty cycles. This is especially true for the superconducting machines like TTF 2 and the X-RAY FEL, under construction or planning at DESY. Elaborate fast protections systems are required not only to protect the machine from electron beams hitting and destroying the vacuum chamber, but also to prevent the machine from running at high loss levels, dangerous for components like the FEL undulator.

This paper will give an overview over the different protection systems under construction for TTF 2. The very fast systems, based on transmission measurements and distributed loss detection monitors, will be described in detail. This description will include the fast electronics to collect and to transmit the different interlock signals.

INTRODUCTION

The TESLA Test Facility phase 2 (**TTF 2**) is currently under construction at DESY in Hamburg. This machine has two main objectives [1]:

- serve as a test facility for accelerator components for the future TESLA and X-RAY FEL [2],
- operate as a 4th Generation Light Source to provide SASE FEL radiation in the range between 100 and 6 nm.

In order to demonstrate the requirements for the large machines for high luminosity in case of the collider and high peak and average brightness in case of the SASE light source, the TTF 2 is capable to run a 800 μ s long beam pulse at 10 Hz rep. rate with a 9 MHz bunch frequency. With the design charge of 1 nC this yields currents of 9 mA averaged over the bunch train, or a total average current of 72 μ A.

Although the average current of TTF II is rather small compared to a typical conventional 3rd generation light source, the intrinsic energy of this system is much higher (Table 1).

Table 1: Comparison of power and energy stored in the beam and losses for LINAC and storage ring driven light sources.

	Storage Ring	TTF 2
Average Current	200 mA	72 μ A
Circumference/Length	200 m	250 m
Beam Lifetime	10 h	-
Energy	2 GeV	1 GeV
Avg. Beam Power	400 MW	72 kW
Energy (Beam/Pulsetrain)	0.26 kJ	7.2 kJ
Loss Level	10^{-7} (Undulator only)	$2 \cdot 10^{-11}$ (total, 1/Turn)

Therefore, effective protection systems are required to prevent the machine from serious damage due to the operation. These systems have to protect the machine from different damage mechanisms resulting in different damage levels at different time scales, e.g.:

- Beam hitting a part of the vacuum chamber. The beam has to be stopped as fast as possible. In the worst case less than 10 bunches can cause damage. Therefore, the reaction time of the system has to be as short as possible, and is mainly determined by signal transmission times.
- Beam halo or dark current is (partially) lost in the machine. Such losses would result in increased activation of components. In the undulator accumulated losses can degrade the performance of the magnets substantially. Therefore, losses have to be observed down to a level of 10^{-7} .
- Invasive beam diagnostics or even obstacles are present in the beam pipe. Such an event has to be recognized by a protection system, to restrict the number of bunches within a bunch train to a number given by the sensitivity of the inserted object.

In order to allow safe machine operation, TTF 2 will have monitoring as well as interlock systems. There will be rather slow monitoring system based on Dosimetrie, using conventional Thermo-Luminescence-Dosimeters crystals and optical fibres. The fibre-based system can provide information about high dose rates in the machine with good spatial resolution and update rates of some minutes [3].

The active part of the protection system is taken by the Beam Inhibit System (**BIS**). This system was redesigned based on the experience with a predecessor system at TTF 1.

THE BEAM INHIBIT SYSTEM

In order to deal with different machine settings a number of operation and beam modes are defined.

Operation modes define the path the electrons have to take, like gun mode (beam stopped by a Faraday cup before the first module), undulator and bypass mode.

The beam modes determine, whether short, long or even only single bunch operation is allowed. These modes depend on the machine setting, e.g. if a screen is inserted only single bunch mode is allowed. Furthermore, they depend on the performance of the machine, i.e. the beam mode is switched back from long to short pulse or even to single bunch in the case the losses get too high or transmission gets too bad.

These actions are taken by the BIS system automatically depending on the settings of the machine.

The BIS is a PLC based system to collect all interlock relevant information and to use this information to block risky or dangerous operation modes. The interlock signals taken by the BIS are divided into two categories. Slow signals like screens, power supplies or valves are connected directly to the BIS. The reaction time to this information is 100 ms determined by the maximum pulse rep. Rate of the machine.

Fast signals, i.e. signals that require switching off the beam immediately within a bunch train, are collected by the **Fast Beam Inhibit System**. Signals connected to this system are the transmission based interlock system as well as the beam loss monitors. Furthermore, the fast acting valves and some fast RF signals are connected.

THE FAST BEAM INHIBIT SYSTEM

The fast beam inhibit system is a kind of distributed logical **OR**. It is built from beam concentrator units (**BIC**) with well-specified I/O channels, concentrating 16 input channels to 1 interlock output. The units can be cascaded and will be used to set up a tree like topology to collect the interlock signals (Fig.1) to one signal acting on the drive laser of the photoinjector. The reaction time is of the system about 2-3 μ s, depending on type and location of the interlock source. It is dominated by the signal delay in the cables and the time of flight of the electron bunches from the gun to the detector.

In order to deal with different modes and also special situations during the operation, the parameters of the fast system are controlled by the BIS. It is possible to mask individual interlock channels by software for special machine operations. The interlock status of the system is provided to the control system on a shot to shot basis.

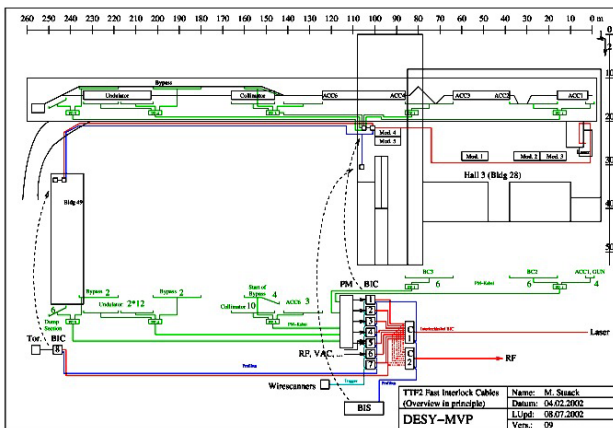


Figure 1: Topology of the BIC System.

The Beam Interlock Concentrator

The BIC modules (Fig. 2) are the central hardware to concentrate all fast interlock signals. 16 input channels are reduced to 1 output using a logical OR comparison with a processing time of 100 ns. In addition to the fast interlock output, there is a second output line to the BIS.

As this system is a central safety system apart from speed redundancy is an essential requirement. Therefore, the hardware operates with 2 independent circuits, one based on discrete logics, the other on digital signal processing implemented in a FPGA. In addition to the basic processing, the FPGA provides additional features like a Profibus interface to the BIS with the possibility to

- Read back the status of the interlock inputs
- To two kinds of masks via the BIS; “hard-masks” in order to disable interlock channels permanently (for more than one bunch train) and “soft-masks” to disable them for a single bunch train only.

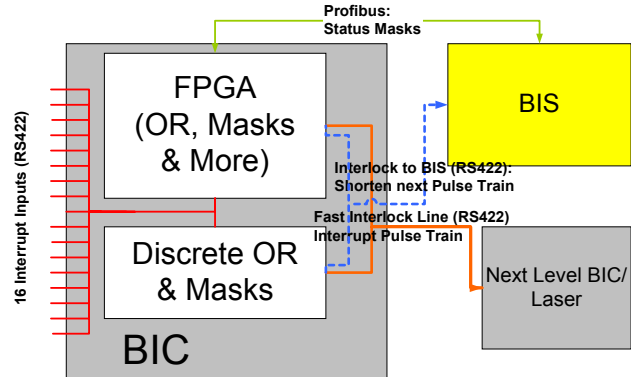


Fig. 2: Block Diagram of a BIC module and its interfaces.

In order to avoid problems due to ground loops all input channels have galvanic isolation. A differential communication line (RS422) is used for both input and output, with the levels chosen in a way that power failures and cable breaks will block the beam.

The Transmission Based Interlock System

In order to run the machine with high charge and high duty cycle, the transmission from gun to dump has to be close to 100%. The transmission is measured as a charge difference using pairs of charge monitors (toroids), as listed in table 2. Each toroid provides a signal with a bandwidth of about 100 MHz (single bunch resolution) with an accuracy of about 1%. Two pairs have been defined for the two operation modes: undulator and bypass operation. As the path length of an upstream and a downstream toroid can be up to 250 m, the minimum reaction time of this system cannot be faster than about 1 μ s. Including the signal processing and transfer time of the fast interlock system to switch off the laser this will add up to about 3 μ s.

The toroid signals are transmitted to the protection system, located in a building at about 1/2 of the length of the machine. The electronics consists of fast ADCs and a digital signal processor per pair, to calculate the charge difference ($Q_d - Q_u$) between downstream and upstream monitor and to compare it on different time scales and with different alarm thresholds (T_{Qi}):

- Charge Validation:
If $Q_u < T_Q$; $T_Q \approx 0.05$ nC; Input charge at upstream toroid not valid
- Single Bunch Transmission Threshold:

$$\left(\frac{|Q_u - Q_d|}{Q_u} \right)_i > T_{sgl}; T_{sgl} \cong 25 \%$$

The single bunch mode detects single bunch losses, if the threshold T_{sgl} is exceeded an interlock is released.

- Slice Averaged Transmission Threshold:

$$\sum_{j=i-l}^i \frac{|Q_u - Q_d|}{Q_u} > T_{Slice}; T_{Slice} \cong O(1\%)$$

In this mode the transmission in the bunch train is measured over a slice of bunches ($i=O(100)$) “moving” over the train. As soon as the averaged loss reaches the threshold T_{Slice} an interlock is released. Due to the averaging the resolution of the system will improve compared to the single bunch resolution. Slice resolutions down to 10^{-3} are expected.

- Pulse Integrated Transmission Threshold:

$$\sum_{i=0}^n |Q_u - Q_d| > T_{int}; T_{int} \cong O(10 \text{ nC})$$

The integration mode sums the losses over the whole bunch train. An interlock is released as soon as the threshold is reached. A threshold of 10 nC corresponds to $1 \cdot 10^{-4}$ of the nominal charge within a bunch train.

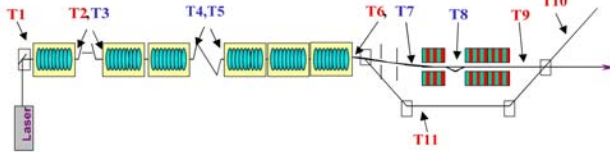


Figure 3: Sketch of TTF 1, showing of charge monitors along the machine. Devices indicated in red serve as input for the protection system.

Table 2: Toroid Pairs for the Protection System

Toroid 1	Toroid 2	Purpose
T ₁	T ₉	Undulator Mode
T ₁	T ₁₁	Bypass Mode
T ₂	T ₁₀	Transmission to the dump (undulator beam path)
T ₂	T ₁₀	Transmission to the dump (bypass beam path)

The Beam Loss Monitor System

The beam loss monitor (BLM) system is based on measurements of radiation due to the electromagnetic showers produced by lost electrons. The monitors are located at positions that are rather radiation sensitive. Compared to the global acting transmission based protection system, it has much higher, but localized sensitivity ($O(10^{-7})$) [4]. Thus both systems complement each other, providing high redundancy and safety for the machine.

Beam losses will be measured by 49 photomultipliers (PMs) equipped with scintillator and 18 secondary emission multipliers (SEMs) equipped with Al cathode.

The multipliers will deliver a 20 ns long pulse with an amplitude of up to 100 mA. As the reaction of the PM system depends only on the input of a single sensor, the reaction time of the system is dominated by the cable length from the detector to the laser. Thus it can be significantly faster than the toroids ($< 2\mu\text{s}$). Fig. 3 gives a schematic view of the BLM distribution along the accelerator. Scintillator plates (40 x 40 cm and 10 x 10 cm) are foreseen to be installed along the linac, long scintillator rods (220 x 5 cm) will be placed parallel to the undulator vacuum chamber. SEMs will be placed in locations like collimator and dump sections, where rather high radiation levels have to be expected.

The readout of the BLMs will be done by a special VME based electronics. These VME-systems will also control and monitor the high voltage (HV) of the multiplier units and are able to generate test pulses. Each loss monitor will release alarms for immediate beam pulse interruption to the BIC in case of exceeding thresholds due to high losses from the beam or dark current (distinguishing between these two loss sources) or if the HV is missing.

For recording of the data the losses are integrated over a time period of 9 bunches and the time of the following bunch is used to digitise and reset the integrator. The loss profile of course is the main tool to optimise the performance of the machine.

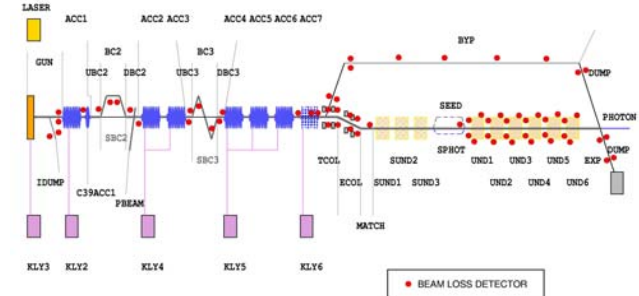


Figure 4: Sketch of TTF 2; the red dots indicate the position of the BLMs along the machine.

References

- [1] TESLA-FEL Report 2002-01, DESY 2002
- [2] TESLA; Technical Design Report & XFEL Supplement, DESY 2002/2003
- [3] M. Koerfer et al., Optical Fibre Dosimeter for SASE FEL Undulators, this proceedings
- [4] H. Schlarb et al., Expansion of the Fast Linac Protection System for High Duty Cycle Operation at the TESLA, EPAC 2002, Paris

Beam Loss Detection at Radiation Source ELBE

P. Michel, J. Teichert, R. Schurig, H. Langenhagen
Forschungszentrum Rossendorf (FZR), Dresden, Germany

Abstract

The Rossendorf superconducting Electron Linac of high Brilliance and low Emittance (ELBE) delivers a 40 MeV, 1 mA cw-beam for different applications such as bremsstrahlung production, electron channeling, free- electron lasers or secondary particle beam generation. In this energy region in case of collisions of the electron beam with the pipe nearly all beam power will be deposited into the pipe material. Therefore a reliable beam loss monitoring is essential for machine protection at ELBE. Different systems basing on photo multipliers, compton diodes and long ionization chambers were studied. The pros and cons of the different systems will be discussed. Ionization chambers based on air-isolated RF cables installed some cm away parallel to the beam line turned out to be the optimal solution. The beam shut-off threshold was adjusted to 1 μC integral charge loss during a 100 ms time interval. Due to the favourable geometry the monitor sensitivity varies less than $\pm 50\%$ along the beam line (different shielding conditions).

Introduction

The Forschungszentrum Rossendorf is constructing a superconducting Electron Linac with high Brilliance and low Emittance (ELBE) which can deliver a 1 mA cw beam of 40 MeV. The electron beam is used to generate infrared light (Free Electron Lasers), X-rays (electron channeling), MeV-bremsstrahlung, fast neutrons and positrons. [1] The safe and reliable operation of the accelerator is essential for a user facility like the ELBE radiation source. The machine should run over many shifts and for long periods with constant and reproducible parameters. The facility must be able to be operated by a minimum number of trained operators. Because of the high beam power (max. 40kW) and the electron energy range of 15-40 MeV the prevention of beam losses in the beam line plays a special role. Due to the average electron penetration depth at these energies approximately the full beam power can be deposited into the vacuum pipes. Apart from the production of ionizing radiation and activation, the vacuum pipes can be melted. It is inevitable that the vacuum system,

and in particular the superconducting accelerator cavities, would be contaminated. The result would be long down-times and substantial costs for repairs.

Detectors

Multiple detectors for the measurement of the beam loss were tested at the ELBE beam line. These were photomultipliers (PM), Compton diodes (CD) [2] and long ionization chambers (LIC) [3] constructed from air-filled high frequency cables.

Photo Multipliers: Photomultipliers (Electron tubes P30P) were installed approximately 3m away from the beam line. The detector shows very short response time (~ 1 ns) and is able to detect extremely low levels of radiation (~ 10 nA beam loss). Due to the nonlinear behaviour of the PM signals saturation effects in the PM problems appear at very high dose rates. At very fast increasing and extremely high beam losses the PM saturate before the necessary signal level for the accelerator shut-off is reached. In addition, the continuous monitoring of the beam pipe can be guaranteed only when a large number of detectors (\sim one PM per meter) is used due to the strong dependence of the monitor signal on the distance between PM and the location of the beam loss.

Compton Diodes: Compton diodes were installed similar to the PM's. They showed a very good linear behaviour up to extremely high beam loss levels. The Compton diodes exhibit an angle dependent signal and thus a directional characteristic based on the geometry of the detector. This can be used in order to supervise certain segments of the beam line with increased sensitivity. Nevertheless, the crucial disadvantage remains the same as for the PM. A complete beam line monitoring with approximately constant sensitivity is attainable only with a very large number of detectors.

Long Ion Chambers: Air-filled high frequency cables of the type Andrew HJ5-50 (diameter 22.2mm) were mounted approx. 20cm away parallel to the beam pipe. The cables were operated as ionization chambers applying a high voltage to the outer conductor and

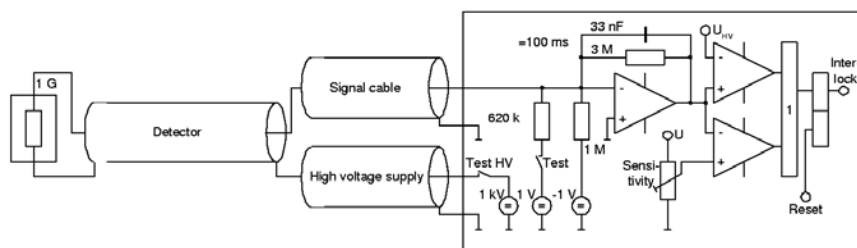


Figure 2: Block diagram for the cable ionisation chamber electronics.

measuring the ionization current. The detector showed a very good linear behaviour up to the maximum possible beam loss. The sensitivity to low beam loss levels is approximately 100 nA . The perfect geometry of this detector permits the installation parallel to the beamline. Thus a uniform sensitivity for all potential beamloss locations is reached. The response time of all three detectors is sufficient for fast shut-off system (<1ms).

The ELBE BLM system

The LIC was chosen because of the ability to monitor the entire beamline with the same shut off level and the small number of electronics that is required for such a system. The Andrew HJ4-50 (diameter 12.7mm) Heliax cable was selected for the ionization chamber. The system was segmented corresponding to the logical sectioning of the ELBE beamlines, adding some segments with special shielding conditions (e.g. large chicane vacuum chamber). The cable is covered with a plastic tube to prevent damage and to provide high voltage insulation. It was mounted as closely as possible (approx. 200mm) to the beamline. The cable was installed within the iron yoke of the dipole magnets to avoid their shielding effect. Fig.1 shows the BLM signal of various

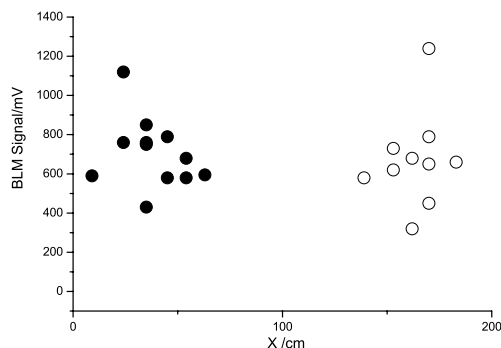


Figure 1: BLM signal from the same beam loss current at different locations along the beam line. Full and open circles are measured with different cable sections. The open circle section belongs to the chicane vacuum chamber.

detector sections with artificially produced beam loss at different locations along the ELBE beam line. Due to the ideal geometrical constellation, the BLM signal varied approximately only 50% along the beamline, which is caused by the inhomogenous distribution of attenuating material (magnets, flanges ect.).

In order to prevent damage to the system, all the electronics was installed outside of the accelerator enclosure. A self check system monitors the high voltage and signal acquisition. Fig. 2 shows the layout of BLM readout electronics. The beam shut-off threshold of the system in the present stage (limited beam energy) was set on $1\text{ }\mu\text{C}$ loss charge integrated over 100 ms. In consideration of all fluctuations of the signal a maximum beam loss current of $10\text{ }\mu\text{A}$ in CW operation at 12 MeV beam energy is tolerated. In the worst case 120 W of thermal power are deposited into any beam line components. Thus, a safe operation of the accelerator is ensured.

Outlook

Since the system very sensitively measures beam loss currents of few μA a second system for on-line monitoring the beam transmission during accelerator operation is under construction. This system is divided into sections with a length of 0.5m and a special serial read out electronics is under development [4]. Fig. 3 shows schematically the layout. Thus a position resolved measurement of the beam loss becomes possible. The operator will be able to judge and correct the quality of beam transmission while running the machine in high beam power mode.

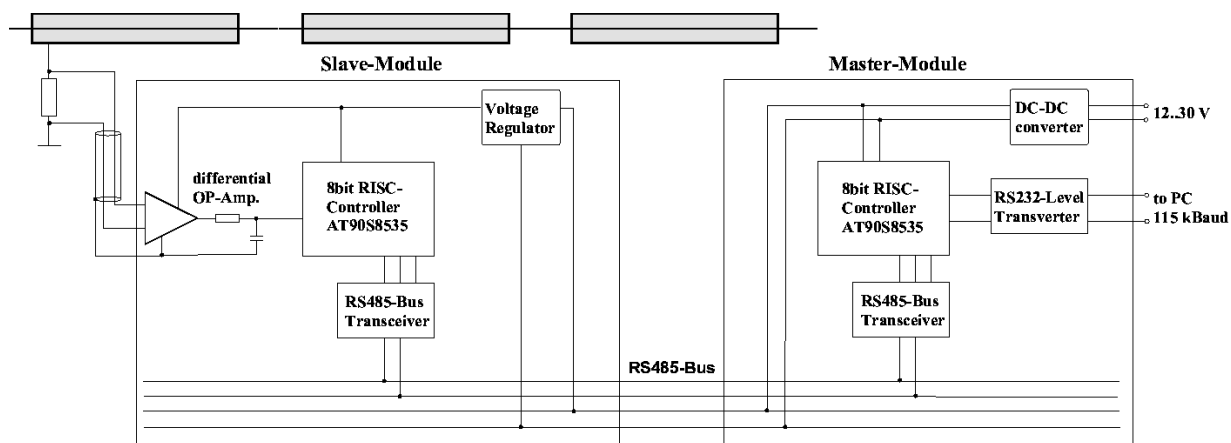


Figure 3: Acquisition electronics for segmented BLM system with longitudinal resolution.

References

- [1] F.Gabriel et al., The Rossendorf radiation source ELBE and its FEL projects , NIM B 161-163 (2000) 1143-1147
- [2] M.Brunken et al. Latest Developments from the S-DALINAC, FEL Conference, Hamburg, (1999)
- [3] J.Roelfe et al. SLAC-PUB-4925, 3/1989
- [4] R.Schurig, P.Michel , A Beam Loss Monitor with Longitudinal Resolution, ELBE Annual Report 2002, 11

TIMING SICKNESSES IN CONTROL SYSTEMS: CAUSES, CURE AND PREVENTION

M. Werner, DESY, Hamburg, Germany

Abstract

In some cases, Trigger Generators or Data Acquisition Systems used for Beam Diagnostics show undefined or unreliable timing behavior. This presentation identifies common reasons, ways to fix the problems and some general rules to avoid them from the beginning. Examples will be given to discuss causes for e.g. double bunches and timing and trigger jumps, periodic as well as randomly. It will be discussed, how proper layout, timing calculations and timing measurements can avoid these inconvenient effects in advance.

TRANSMITTING MEDIA

Copper Cable

Copper cable is good for short and medium distances. Many electronic devices have **coaxial** input and output connectors and use TTL or NIM voltage levels.

Alternatively a signal can be transmitted **differentially over twisted pair** lines, decreasing the sensitivity to common mode noise. Two examples are **RS-422/RS-485** with a common mode immunity of at least $\pm 7V$ or **LVDS** for high speed applications.

Glass fibre

A **monomode** fibre works well for high speeds over long distances, while **multimode** fibres are suited for medium distances - look carefully on jitter specifications!

ERROR SOURCES

Noise

Noise is a major concern to limit the timing precision of a system. It ranges from the small electronic noise of every cable receiver, 50/60Hz ground noise and switching power supplies up to big spikes produced by switching electric devices like motors.

Reflections

Some amount of reflection is always present on a cable transmission, but with proper topologies and proper termination it can be minimised.

Digital Trouble

Digital trouble often shows up as jumps of the timing. The reason can sometimes be found in an improperly constructed module itself (e.g. asynchronous design not considering all conditions) or in a setup-/hold time violation, see below.

ANALOG SICKNESSES

Figure 1 shows some examples how an analog signal (e.g. at the end of a cable) can be distorted:

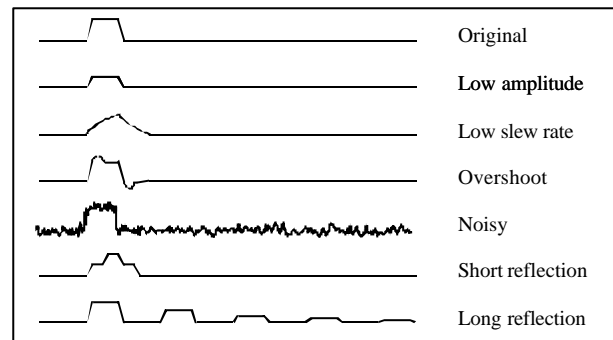


Figure 1: Analog sicknesses

DIGITAL SICKNESSES

At a digital output, bad signals could look like this:

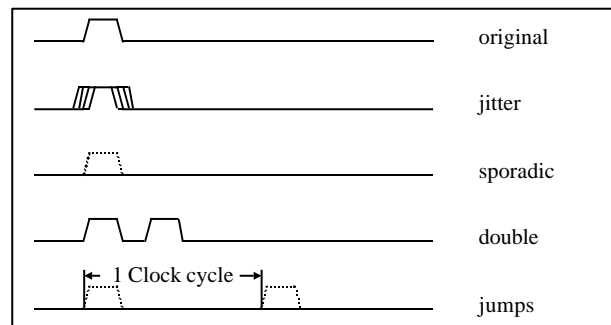


Figure 2: Digital sicknesses

HOW TO CHECK SIGNALS

Some poor methods to check a signal on a cable

- Dividing the signal with a 6dB power splitter, one output going to an oscilloscope (50 Ω input). This will attenuate the signal amplitude by 50%.
- Inserting a "T-piece" into the line, connecting one end by a short cable to an oscilloscope (1M Ω input). This will produce strong reflections on the main line for a fast signal.
- Looping the signal to an oscilloscope (1M Ω input). But the extra cable will give extra delay.
- Opening the destination module and checking at the input connector with an oscilloscope probe. For

this you have to open or even extract the module from the crate.

A better way: The Signal Sampler

Avoiding all the previous disadvantages, the Signal Sampler can just be inserted into a cable connection. It is an unsymmetrical line splitter which couples out only a small portion of the signal, leaving the main signal almost unchanged (amplitude decrease < 4%, delay < 1ns). The self-made device shown in the schematic below works from 0 to >300MHz, and commercial devices are available for a range of at least 0 to 5 GHz.

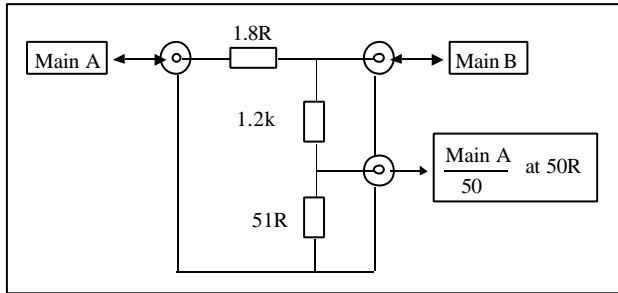


Figure 3: A Signal Sampler

PULSE JITTER VERSUS NOISE

The basic relation between pulse jitter and noise is:

$$jitter[s] = \frac{noise[V]}{slewrate[V/s]}$$

...At receiver threshold

For RMS values of the noise voltage (e.g. considering random noise), the result is also in “seconds RMS”, whereas for peak-to-peak voltages (e.g. considering the noise introduced by the 50/60Hz mains) also the resulting jitter is given in “seconds peak-to-peak”.

The relation is obvious if you look on the big arrow on the following graph, pointing into a triangle where the sides are made up of noise amplitude (vertical), jitter amplitude (horizontal) and slew rate:

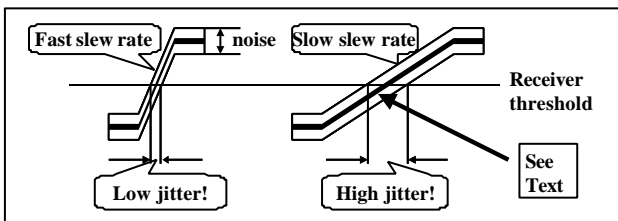


Figure 4: Jitter as function of noise and slew rate

Slow slew rates can be caused by slow transmitters or too long or lossy cables.

THRESHOLD CROSSING

Two things are important for the threshold of a cable receiver:

- The threshold must be well within the signal range
- The slew rate at the threshold must be high enough

Consider the following examples:

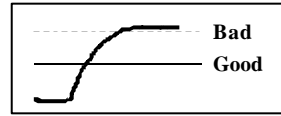


Fig. 5: Signal after cable

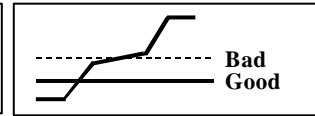


Fig. 6: Signal with reflection

In Fig. 5 (signal after cable) the “bad” threshold is very close to the upper signal range limit. A small change could lead to total failure, and the jitter is big because at the threshold the slew rate is rather low. This will happen if the transmitter output power is too low or the cable is too long and the receiver threshold cannot be adapted. A good threshold would be in the centre of the signal range. In Fig. 6 (cable reflection), the best threshold is not at the centre of the signal range because there the slew rate is rather low. Naturally it is better to remove the reflection than to adapt the threshold in this case!

REFLECTIONS

In the following drawings, “Tx” means Transmitter, “Rx” means Receiver and “T” means Termination Resistor.

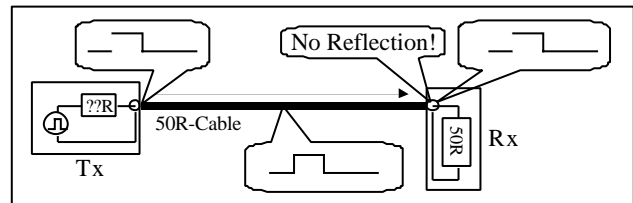


Fig. 7: Termination at Receiver at end of the cable

Fig. 7 shows the standard method: The source impedance of the transmitter is not very important, because the cable is terminated at the other end, so almost no reflections come back to the transmitter. The pulse shape is the same everywhere on the cable.

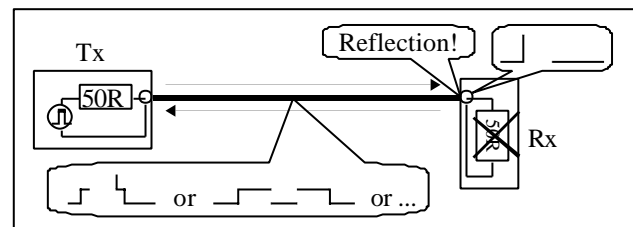


Fig. 8: No termination at receiver - only at transmitter

In the case of Fig. 8 the signal will be reflected at the end of the cable because of missing termination. The transmitter must absorb the reflected signal by a correct 50Ω termination. The correct pulse shape is only present

at the Receiver point, everywhere else original and reflected signal are overlaid, so no receivers on stubs are possible.

GOOD TOPOLOGIES

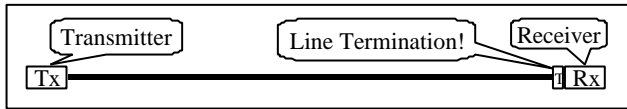


Figure 9: Point-to-point connection

Fig. 9 shows the standard way to connect one transmitter to one receiver; termination at receiver only.

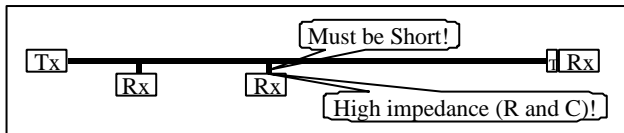


Figure 10: Bus line topology

Fig. 10: Like “point-to-point”, but additional receivers with high impedance inputs are placed between transmitter and receiver, connected with **short** stubs to minimise reflections. As every additional receiver adds signal distortion on the line, check signal integrity !

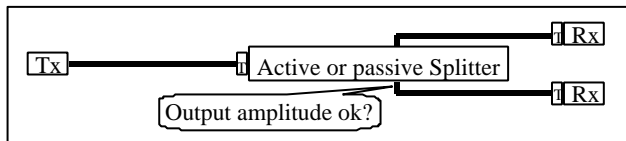


Figure 11: Using a splitter

Fig. 11: While a passive splitter decreases the amplitude (adjust receiver threshold!), an active splitter can split a signal to any number of outputs. It can even improve signal stability by amplifying weak signals before they are sent through another long cable.

CRITICAL TOPOLOGIES

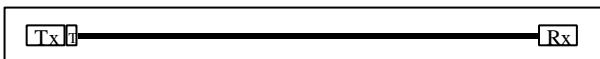


Figure 12: Termination at Transmitter

Fig. 12: See above in chapter “REFLECTIONS”. This topology is critical because the source impedance of many signal sources is below 50Ω or even undefined and no additional receivers can be connected on short stubs.

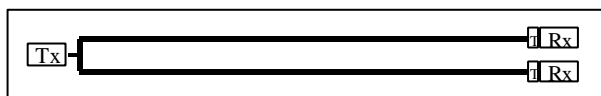


Fig. 13: Forking at transmitter

Fig. 13: As this loads the transmitter with two cable loads, it could destroy the transmitter, or the amplitude could be decreased. See transmitter datasheet.

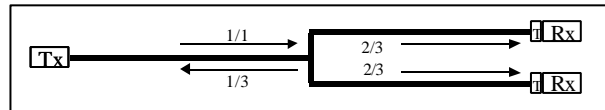


Fig. 14: Forking “somewhere”

Fig. 14: The amplitude at the receivers is reduced to 2/3, and 1/3 of the signal is reflected to the transmitter, partly reflected back again from there.

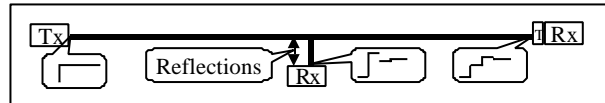


Fig. 15: Long stub

Reflections bounce between the ends of the long stub, thereby distorting the signal.

SETUP-/HOLD TIME VIOLATION

Let us consider a Digitiser Module, digitising an analog bunch signal (e.g. from a current monitor), using the bunch clock as digitising clock and a “Bunch 1” signal as Trigger. The active edge of “Bunch 1” marks the first bunch of a bunch train in a Linear Accelerator.

It is obvious that the time relation between the Clock and the Analog Bunch signal has to be adjusted so that the Analog Signal is sampled at its top value.

But it is also important to keep the “Bunch 1” trigger in a certain time window relative to the Clock to make sure that the correct Clock edge samples the first pulse. See figure 16: No active trigger edge is allowed from T_Setup before the active Clock edge until T_Hold after it. So, the “Bunch 1” trigger must be delayed if necessary.

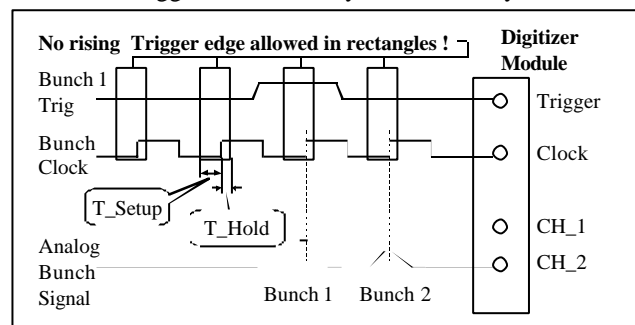


Fig. 16: Setup-/ Hold Time Violation

A violation of this condition may result in a changing mapping of the bunch numbers in the Digitiser Module. The same applies for pattern generators producing the bunch pattern for the electron gun or for bunch counters.

ACKNOWLEDGEMENT

I want to thank all the colleagues who gave me valuable information and contributed to this paper by telling me their experiences.

FAST DSP USING FPGAs AND DSOs FOR MACHINE DIAGNOSTICS

G.A.Naylor, ESRF Grenoble France

e-mail: naylor@esrf.fr

Abstract

Digital signal processing using digital signal processors is now a mature field for machine diagnostics, giving significant benefits, in particular when used to analyse BPM signals for tune measurement and fast feedback systems. We discuss here digital signal processing using Field Programmable Gate arrays (FPGAs) with large gate counts and intelligent oscilloscopes. These offer great potential for the analysis of very fast signals to maximize the information extracted from high bandwidth sensors.

i) FPGAs allow data to be filtered numerically and treated at the speed of data collection of A/D converters in the 100MHz range. Parallel, fast and continuous treatment of BPM and FCT signals is possible. Examples are given of injection efficiency, turn-by-turn injection efficiency, turn-by-turn beam position, amplitude and phase calculation with averaging over each turn or many turns.

ii) Modern oscilloscopes include much computational power. In-built DSPs can perform correlations on the traces allowing the application of FIR filters. Some oscilloscopes incorporate a PC and allow on-board manipulation of the data using MATLAB. An example is given using an FIR applied to a 5GHz oscilloscope to extend its time response to measure electron bunch lengths less than 100ps with 1ps resolution.

PLATFORMS FOR PERFORMING DIGITAL SIGNAL PROCESSING

- Digital Signal Processor boards
- Digital Storage Oscilloscopes with processing capabilities (in-built maths operations and or PC with Matlab)
- Field Programmable Gate Arrays (FPGA)

The use of DSP boards for treating signals from diagnostic sensors is now well established (eg for feedback systems). The increase in acquisition speed of Analogue to Digital converters coupled with the large memory capacity of recent generation oscilloscopes puts a heavy demand on the network bandwidth and on post-processing. At such speeds pre-treatment of the signal with a view to extracting the useful information and reducing the bandwidth of the data to be exported becomes all the more important. The latest generation of fast intelligent oscilloscopes offer interesting possibilities for the pre-treatment of fast signals. For the ultimate in pre-treatment data bandwidth, FPGA boards may also be used.

DIGITAL STORAGE OSCILLOSCOPES

Figure 2 shows the layout for a system using a 12GHz photo receiver [1] and a high bandwidth digital storage oscilloscope [2]. Modern digital storage oscilloscopes provide means for exporting waveform data to on board software running on the internal PC. Pre-processing of the waveform data may also be performed using standard maths library functions on the Oscilloscope DSP. Further processing on the PC part of the oscilloscope may be performed using analysis packages such as Matlab. By

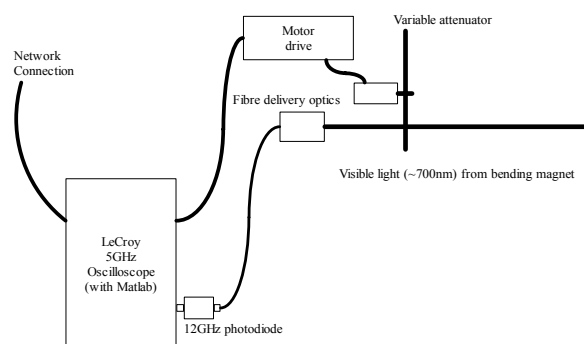


Figure 1 Optical Layout of bunch length measurement

programming custom functions using Matlab it is possible to perform tasks such as:

- bunch length measurement by deconvolution of the instrument response
- beam phase monitoring (both fast and slow drift).

In order to perform deconvolution of the instrument response (to extend the effective bandwidth) it is important to process very clean, noise free, waveforms of high precision (10-12bits). Such waveforms should be recorded by averaging many repetitions of the waveform. A very stable trigger is required in order to maintain resolution when averaging. Using this technique, we have been able to measure pulses as short as about 95ps, see figure 2. A trend of the bunch length is shown in figure 3 during operation in a high bunch charge filling-mode, which suffers charge dependent bunch lengthening. This technique provides means of permanent monitoring of the bunch length without the continuous operation of a streak camera [3].

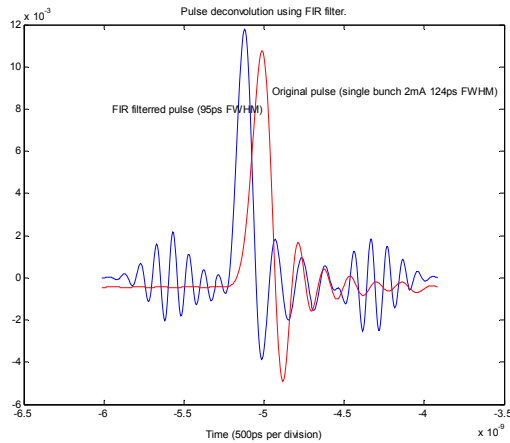


Figure 2 Reduction of pulse width by deconvolution of the instrument response

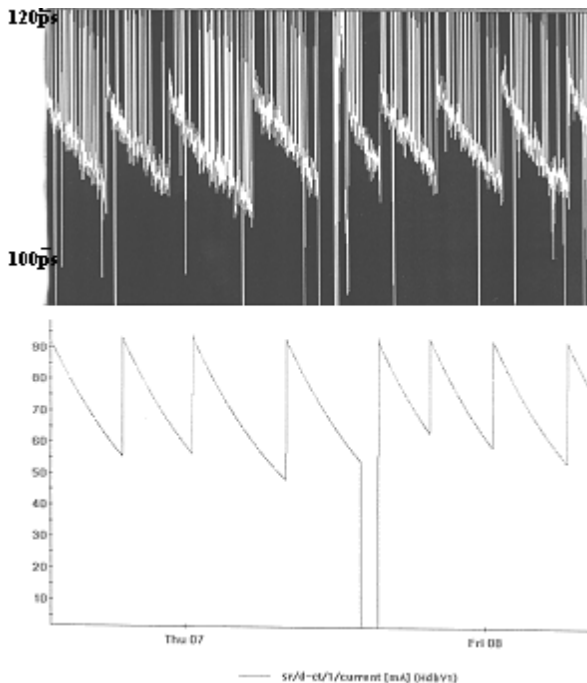


Figure 3 Monitored pulse length (upper trace) and beam current (lower trace)

Other applications of pre-processing of oscilloscope waveforms are:

- i) Turn by turn beam current determination from fast current transformer signals.
- ii) Bunch purity measurement using single photon counting of synchrotron radiation.

FIELD PROGRAMMABLE GATE ARRAYS (FPGA)

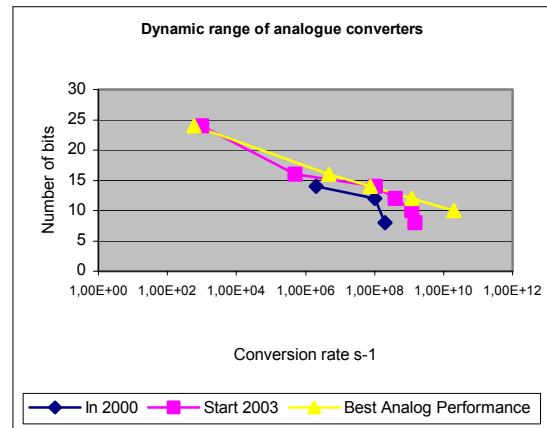


Figure 4 performance of A/D converters

The current performance of analogue converters is shown in figure 4. The data rate produced by modern high speed A/D converters exceeds the capacity of even the fastest of DSPs. As can be seen from the table below however, these high data rates can be processed using modern FPGA chips.

Function ^a	Industry's Fastest DSP Processor Core ^a	Xilinx Virtex-II Pro Platform ^a
8x8 Multiply-Accumulate (MAC) ^a	4.8 Billion-MAC/s ^a fclk = 600-MHz ^a	1 Trillion-MACs/s ^a fclk = 300-MHz ^a
FIR Filter ^a -256 Taps, Linear-phase ^a -16-bit data/coefficients ^a	9.3-MSPS ^a fclk = 600-MHz ^a	300-MSPS ^a fclk = 300-MHz ^a
Complex FFT ^a -1024-point, 16-bit data ^a	10-μs ^a fclk = 600-MHz ^a	1-μs ^a fclk = 150-MHz ^a
Viterbi-Decoding Throughput ^a	Five hundred channels at: 7.95 Kbps for a total of 3.9 Mbps ^a	155-Mbps (OC-3 rates) ^a
Reed-Solomon-Decoding Throughput ^a	4.1-Mbps ^a fclk = 600-MHz ^a	10 Gbps ^a (OC-192 rates) ^a fclk = 85-MHz ^a
Turbo Convolutional Decoder Throughput ^a	Six 2-Mbps data streams ^a *(6 iterations) ^a	5.4-Mbps ^a *(6 iterations) ^a

Table 1 Comparison of DSP and FPGA performance. Courtesy Xilinx

Though the programming of FPGAs has in the past been quite difficult, the recent development of high level programming tools combined with the ability to simulate the target application has made the process much easier.

Figure 5 shows a graphical programming environment for FPGAs using toolbox System Generator from Xilinx [5], which runs under Simulink (Mathworks).

Injection Efficiency

The current signal from fast current transformers installed on the transfer line into the storage ring and on the storage ring itself are converted using 12 bit ADCs at 22.7MHz. This sampling frequency represents 64 measurements per turn (see fig 6). The signals from the two current transformers can be compared using a cross-

correlation technique, summing the product of corresponding signal values over 1 turn.

$$Injeff_n = \frac{\sum_{i=1}^{64} I_{TL2} \times (I_{SRafter-n} - I_{SRbefore})}{\sum_{i=1}^{64} I_{TL2} \times I_{TL2}} \quad (1)$$

Equation 1 is used to calculate the percentage of the charge added to the storage ring after turn n. This calculation may be performed over several turns in order to monitor the injection efficiency during the capture process as shown in the graphical application (figure 7).

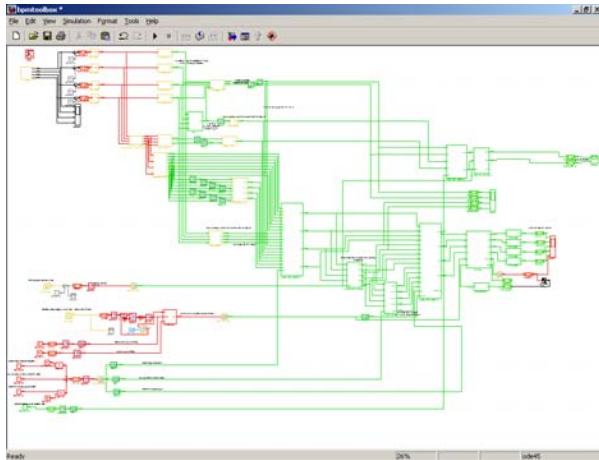


Figure 5 Development of processing algorithm using Simulink

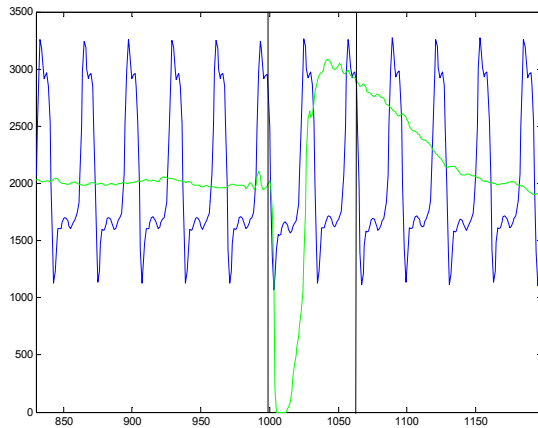


Figure 6 Data converted from 2 Fast Current Transformers

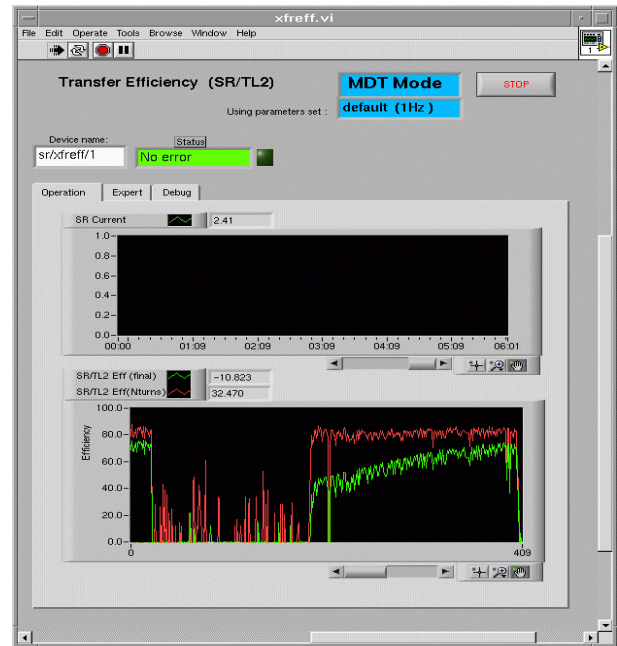


Figure 7 Injection efficiency after 10 turns (upper trace) and after 2000 turns (lower trace)

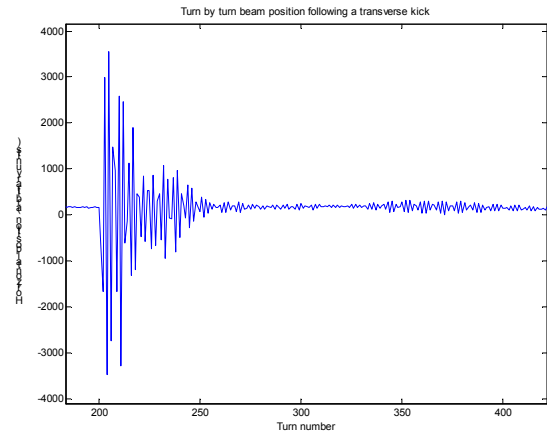


Figure 8 Turn by turn measurement of beam position using an FPGA

ACKNOWLEDGEMENTS

This work was made possible by the following:
Christian Herve, Jacques Cerrai, Gerard Goujon, Gonzalo Penacoba, Jean-Marc Koch, Eric Plouviez, Francis Epaud and Pascal Verdier

REFERENCES

- [1] <http://www.newfocus.com/>.
- [2] <http://www.lecroy.com/>.
- [3] EPAC 1996 Sitges paper TUP031L Scheidt, K. p1621
- [4] Beam Position and phase measurement using FPGA for the processing of the pick-ups signals Paper PT01 DIPAC 2003 Mainz.
- [5] <http://www.xilinx.com/>

Capabilities of the ELETTRA/SLS Multi Bunch Feedback Electronics

M.Deidler, R.Kramert, P.Pollet, Paul Scherrer Institut, CH-5232 Villigen PSI, Switzerland
 M.Lonza, D.Bulfone, Sincrotrone Trieste, Trieste, Italy
 e-mail: Micha.Deidler@psi.ch

Abstract

Following the cessation in the production of the commercial ADC/DAC boards adopted by the ELETTRA/SLS digital multi-bunch feedback systems, a new family of 500 MS/s data conversion boards with an 8 bit resolution has been developed. The ADC and DAC circuits are separate modules containing analog and digital electronics providing a data rate of 500 MSample/sec using 250 MHz DDR clocking techniques. The following stage being a common design to both ADC and DAC reduce the data rate to 125 MS/sec, allows data recording and play back using on board RAM and allows freely programmable multiplexing/demultiplexing up to ratios of one to twelve. The digital data streams flow via Front Panel Digital Ports (FPDP). A special design criterion were low system latencies ensuring a high feedback efficiency. Apart from lab tests, we report on feedback system test and describe additional hardware applications.

INTRODUCTION

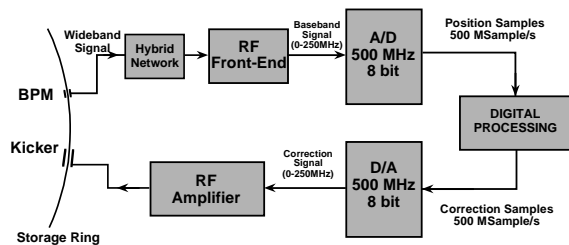


Figure 1: System Layout for the transverse multi bunch feedback

The ELETTRA/SLS Multi-Bunch Feedback System is a wide band feedback correcting the positions of individual bunches, spaced 2 ns apart (Figure 1). Wide band position signals coming from button type BPMs get converted to baseband (DC-250 MHz), followed by sampling with a fast 8 bit, 500 MS/s Analog to Digital Converters (ADC). A digital filter calculates correction kicks, which are getting reconverted via 8 bit, 500 MS/s Digital to Analog Converter (DAC). For the transverse feedback, the signals are directly fed via broad band power amplifiers and strip line kickers to the beam, in the longitudinal plane, a Lower Single Side Band (LSSB) modulator mixes the signals up to the 1.25-1.5 GHz band, where they get amplified and fed to a longitudinal kicker [1] [2].

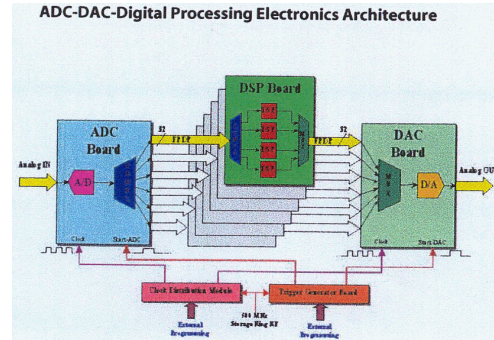


Figure 2: Digital filter structure

The digital filter (Fig. 2) consists of the ADC itself, which is followed by a first one to four demultiplexing stages. A second one to six demultiplexing reduces the data rate to approximately 20 MS/s, The six Front Panel Data Ports (FPDP) each feed a quad processor board containing TI-TMS320C6201 Digital Signal Processors (DSP). Three processors per board concurrently calculate the correction kicks, whereas one DSP takes all the data from the FPDP port and is used for on-line beam diagnostics.

The system described has been shown to work (e.g. [1]) and two systems are in routine operation on the vertical and horizontal planes at ELETTRA. A show stopper in setting up a feedback for all planes proved to be the cessation of production of the ADC and DAC boards, which were planned to be used. Following that, it was decided to launch our own development of ADC and DAC boards, at the same time trying to improve on the suitability for feedback and other accelerator applications. The main specifications of the boards are given in table 1.

ELECTRONICS

The similarities in the functionalities of ADC and DAC boards shows up also in the layouts in figures 3 and 4 and was exploited to simplify the development process. Both boards consist of three functional blocks, the first being a dedicated mezzanine in 50 Ω matched technology and containing the pure ADC or DAC circuitry. Common to both layouts is the main board containing the VME interface, a Xilinx Virtex II FPGA and (as of now) eight MBytes of ZBT RAM. The third block, also common in terms of hardware to both ADC and DAC, is the FPDP connector card. For both main board and FPDP board, only the FPGA firmware and the mezzanine card (ADC or DAC) attached determine the difference in the functionality.

Sampling Rate	200-500 MHz
Resolution	8 bits
Input Impedance	50 Ω
Coupling	AC
Analog Bandwidth (3 dB)	5kHz - 500 MHz
In-band Phase Rotation	< 10°
Input Level(ADC)	0 dBm
Output Level(DAC)	6 dBm
Signal/Noise + Distortion Ratio (Total Dynamic Distortion)	> 40dB
External Clock	Sine Wave/DECL
Clock Programmable Shift	Range > 2ns, steps < 100 ps
External Trigger	DECL
Total Jitter from Clock Input to Analog I/O: VME interface	< 10 ps VME64x compatible A32/D32 (base address geographic or switch selectable) ANSI/VITA 17 Single Ended TTL, 80 pin connector
FPDP Interface	1 to 12 8 MByte
Number of FPDP Ports	
Memory Size	

Table 1: Main ADC and DAC specifications

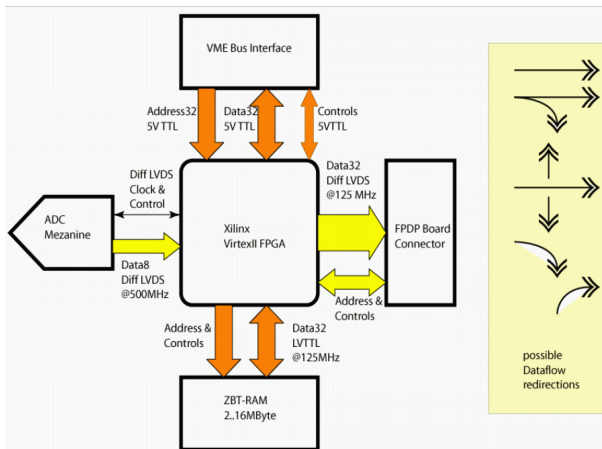


Figure 3: Layout and data flux for the ADC board

The ADC communicates with the main board at a 500 MS/s data rate via the LVDS bus. In the main board FPGA, the eight bit data is demultiplexed with a ration of 1 to four to produce a 32 bit wide internal data rate at 125 MHz. The data passes a Gray to Binary decoder and a 2 ways data redirector, which may send the data either to the FPDP board for further demultiplexing or the ZBT memory, which is configured as ring memory, or to both. For hardware debugging purposes, the ZBT memory can also be written via the VME interface and used to generate data streams at the FPDP ports. The FPDP board takes the 125 MS/s data from the main board and does an additional de-

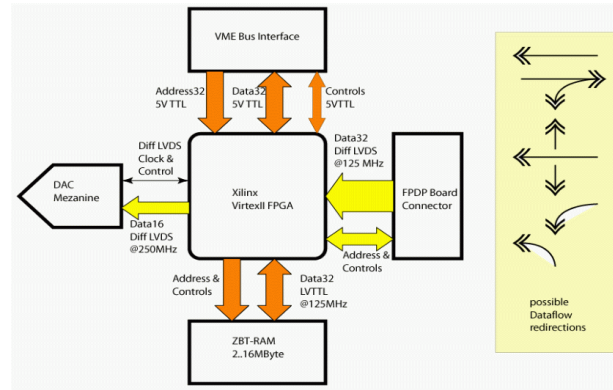


Figure 4: Layout and data flux for the DAC board

multiplexing with a programmable ratio of one to five to one to twelve, which are sent out to the FPDP ports. For demultiplexing ratios in the excess of 6 an additional board is necessary purely to carry the required connectors. The board can be triggered either via a software trigger or an external DECL trigger signal. A photo of the main board is shown in figure 5.

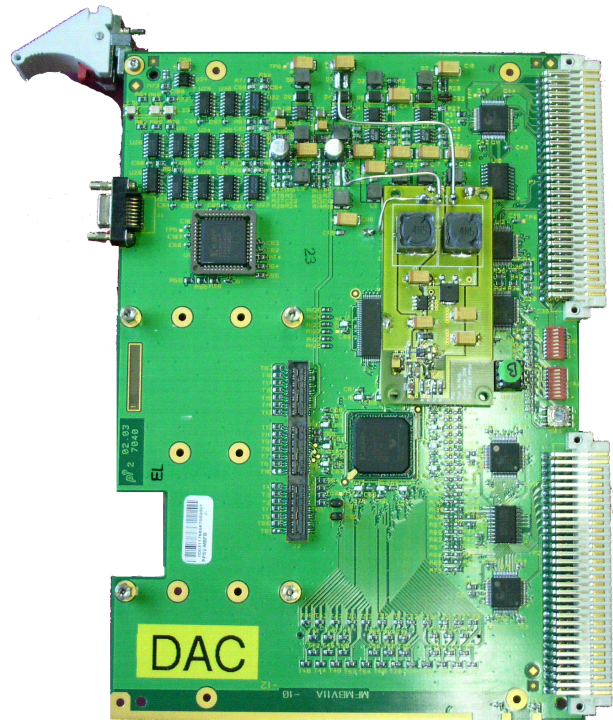


Figure 5: Photo of ADC/DAC main board.

The DAC works in the reverse manner. The FPDP board, being triggered via the Data Valid (DVALID) line of the FPDP ports, multiplexes the input data into a 32 bit 125 MS/s data stream for the main board FPGA, where it is buffered into an internal FIFO register. A START_DAC trigger (external DECL or software) launches the second one to four multiplexing stage in order to produce the 500 MS/s data for the DAC circuit. Analog to the ADC, a 2

ways data redirector is incorporated into the chip, which allows storing FPDP input into the internal RAM and even using the DAC for data playback, where a signal written into the ZBT RAM is fed to the DAC.

An important parameter determining the efficiency of any feedback application is the latency of the data throughput, which was reduced to a total of 88 ns for ADC and DAC board combined.

BEAM TESTS

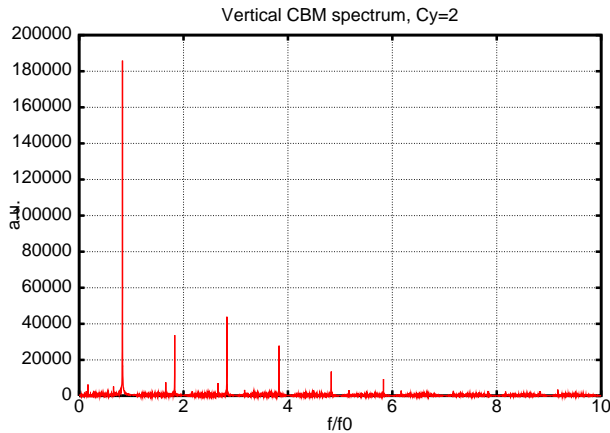


Figure 6: Vertical coupled bunch mode spectrum, 75 mA beam current with all buckets filled, vertical chromaticity set at three times the standard chromaticity.

With laboratory testing for the ADC board completed, a first commissioning for the front end part of the transverse multi bunch feedback has been started. The system consists of the RF front end, the new ADC board used with a demultiplexing ratio of one to six connected to the six DSP board. Equally included was another new development, a four channel 500 MHz DECL clock generator/shifter. Without the DAC, the system was used as a passive diagnostic device, reading out bunch by bunch vertical position data via the diagnostics DSPs.

For testing, we used a non standard homogeneous fill with out any gap with an average current of 75 mA. Since there is no gap in the fill pattern, coupled bunch modes due to daisy chain like effects as resistive wakes and ions will show up quite clearly despite the comparatively low current. Varying the chromaticity of the ring produces a mix of combinations of these effects.

With a high chromaticity setting just below the stability threshold at three times the nominal value, the spectrum in figure 6 was obtained, showing high peaks a $Q = -1, -2, -3 \dots + Q_y$, $Q_y = 0.17$ typical of an instability dominated by resistive wakes. Lowering the vertical chromaticity further to the nominal value leads the CBM spectrum in figure 7, where resistive wall instabilities are still recognizable, but the beam motion is dominated by other effects, probably of the ion type.

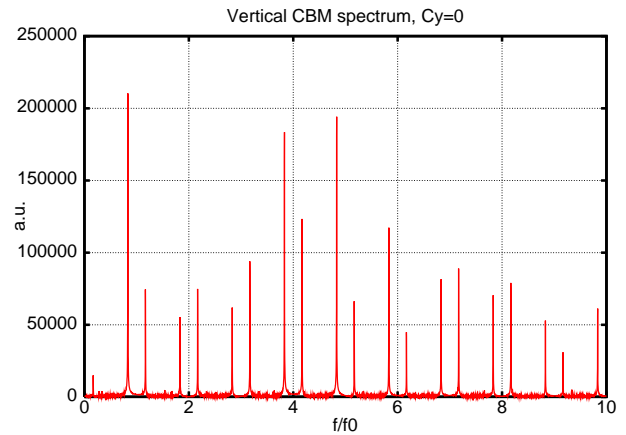


Figure 7: Vertical coupled bunch mode spectrum, 75 mA beam current with all buckets filled, vertical chromaticity set to standard chromaticity.

OUTLOOK

As also the Digital to Analog Converter boards will become available in the near term, the main application for the new boards will be to commission and get into operation the bunch by bunch feedback systems for all three planes at SLS and for the longitudinal plane at ELETTRA (Two systems are in operation for now.). Extremely interesting is the strongly reduced latency of the new development in comparison to the original boards, which will allow to reduce the latency of the overall digital filter by one whole bunch circulation period (960 ns in the case of SLS), so that higher efficiency and better performance can be expected.

Another system planned now is a bunch by bunch current feedback, optimizing the behavior of the SLS top up system [3]. The feedback RF front end together with a stand alone ADC board is going to be used to read out the sum signal of a BPM pickup. This information will be used for selective refilling of empty buckets in order to have a highly controllable fill pattern.

A third application will be taking bunch by bunch data from the wide band BPM and microwave front end installed in the SLS storage ring, which will allow to measure intra bunch charge distributions for individual bunches within a multi bunch filling [4].

REFERENCES

- [1] D. Bulfone et al, "The ELETTRA Digital Multi-Bunch Feedback Systems", proc. of EPAC 2002, Paris, France, June 2002.
- [2] M. Dehler, "Kicker design for the ELETTRA/SLS longitudinal feedback", proc. of EPAC 2002, Paris, France, June 2002.
- [3] T. Korhonen, B. Kalantari, personal communication.
- [4] M. Dehler, "Microwave measurement of intra bunch charge distributions", this conference.

SLIM (Sem for Low Interception Monitoring) AN INNOVATIVE NON-DESTRUCTIVE BEAM MONITOR FOR THE EXTRACTION LINES OF A HADRONTHERAPY CENTRE

L. Badano*, O. Ferrando, M. Pezzetta, Fondazione TERA, Milan, Italy
G. Molinari, CERN, Geneva, Switzerland

Abstract

Real time monitoring of hadrontherapy beam intensity and profile is a critical issue for the optimisation of the dose delivery to the patient carcinogenic tissue, the patient safety and the operation of the accelerator complex. For this purpose an innovative beam monitor, based on the secondary emission of electrons by a non-perturbative, sub-micron thick Al target placed directly in the extracted beam path, is being proposed. The secondary electrons, accelerated by an electrostatics focusing system, are detected by a monolithic Silicon position sensitive sensor, which provides the beam intensity and its position with a granularity of 1 mm at 10 kHz frame rate. The conceptual design and the engineering study optimised for hadrontherapy, together with the results of the preliminary tests of the first system prototype, will be presented.

INTRODUCTION

The rationale for the SLIM project

Hadrontherapy is the use of hadron beams to irradiate tumours. In its most advanced form, the intense end-of-track Bragg ionization peak, together with variations in beam profile and energy, are used to deliver an optimum, shaped dose to the tumour that minimizes the damage to nearby normal tissues [1]. Patient safety, accelerator operation, and that optimum dose delivery would all benefit if the beam intensity and profile could be continuously monitored during treatment, rather than just during the set-up. This has not been previously possible, since existing interceptive monitors interfere with the beam, considered that the therapeutic beam kinetic energies varies in the range (60 – 250) MeV for protons and (120 - 400 MeV/u) for carbon ions and that non-interceptive instrumentation is not sensitive enough to detect average beam intensities from few pA to few nA, with spill duration ~ 1 s. For this purpose an innovative beam monitor, named SLIM (Sem for Low Interception Monitoring), capable of providing beam intensity and profile during the treatment, has been conceived and developed in the framework of the SUCIMA (Silicon Ultra fast Cameras for electron and gamma sources In Medical Application) project. SUCIMA has been funded by the European Commission with the primary goal of developing a real time dosimeter based on direct detection in a Silicon substrate.

* laura.badano@cern.ch; the authors research is supported by the European Commission under the contract G1RD-CT-2001-00561

SLIM beam monitor principle and requirements

A thin Al - Al₂O₃ - Al foil set at an angle to the beam serves both as a source of secondary electrons (SE) and as an electrode with electric field lines from the foil surface that guide the emitted electrons to a pixel/pad detector beyond the beam volume. A schematic layout of the beam monitor is shown in Figure 1.

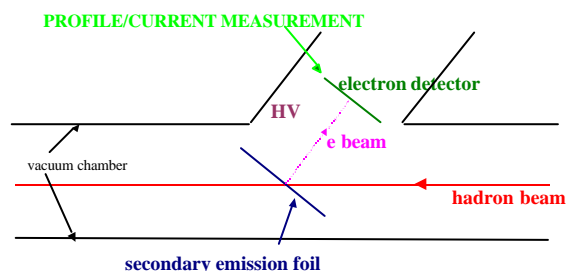


Figure 1: Schematic principle of the SLIM beam monitor.

The thin foils are produced following a technique consolidated at CERN [2] and consist of a support of 0.1 - 0.2 μm of Al₂O₃ coated on each side with 0.01 - 0.05 μm of Al for a maximum diameter of about 65 - 70 mm. As secondary emission is a surface phenomenon, it will concern just the most superficial aluminium layers. The emittance blow-up induced by the foil has been evaluated with a Monte Carlo programme for plural scattering [3] and goes from 2% to 10% according to the beam divergence at the foil for a 60 MeV proton beam (worst case). Experimental validation of the model results are foreseen during the first measurements on hadron beams.

The optics for the collection of the SE, the type, size and pitch of the electron detector, the front-end electronics and the read-out system have been designed on the base of the key requirements on the performances of the SLIM beam monitor summarised below:

- real-time (during the treatment of the patient)
 - stigmatic optics (demagnifying or proximity) to preserve the information on the beam profile
 - thin foil diameter $\Phi = 70$ mm (beam on $10 \times 10 \text{ mm}^2$)
 - profile granularity 1 mm
 - vacuum compliant ($10^{-6} \div 10^{-7}$ Torr)
- and of the requirements specific for the SE detector and related electronics:
- active surface subdivided in cells (pads or pixels)
 - 5000 cells or more
 - sensitive to low-energy (~ 20 keV) electrons
 - large dynamic range ($3 \div 9 \cdot 10^3 \text{ e}^-/\text{pixel} \cdot 100 \mu\text{s}$)

- 10 kHz frame rate (to guarantee ± 2 % dose uniformity [4])
- no dead time

Last but not least, the monitor will be installed in a hospital-based facility: it should, therefore, be easy to operate and maintain, reliable and have a limited cost. Previous attempts to use the secondary emission from thin foils as a mean to measure the main beam parameters can be found in Refs. 5 - 8.

The secondary electron detectors

Two solid-state detectors (named PAD or pixel detector, according to the cells/sensor size) and a commercial detector (to test the performance of the focalization system) are foreseen for the SE detection:

- a commercial detector consisting of a micro-channel-plate (MCP effective diameter 32 mm) for SE amplification followed by a phosphor screen and a CCD camera;
- a Silicon PAD detector [9] with a sensitive area of 30.8 mm and a pitch of 1.4 mm for the first prototype and a sensitive area of 50 mm and pitch of 1 mm for the final prototype, bonded to a commercial integrating chip [10];
- a monolithic CMOS Silicon detector [11], developed in the framework of the SUCIMA collaboration, with a sensitive area of 17 mm and a pitch of 200 μm .

SLIM BEAM MONITOR DESIGN

Physics aspects of secondary emission

The main aspects of secondary emission necessary for the design of the SLIM in terms of SE energy and angular distributions and yields are summarised below. The low energy (below 50 eV) part of the SE spectrum does not depend on the primary beam kinetic energy. For proton on Al targets the distribution is peaked around 2.1 eV with a FWHM (that contains the 85% of SE) of 8.2 eV [12]. The integrated angular distribution, i.e. the number of SE with low energies emitted from the surface in the solid angle, follows a cosine-law peaked around the normal to the foil [13]. The number of SE emitted per impinging protons have been evaluated using Sternglass theory [14] with Borowski correction [15] for the C-ions and are summarised in Tables 1 and 2 (f and b refer to the forward and backward emission respectively).

Table 1: Calculated yields (proton beam)

p energy [MeV]	γ_{total} [%]
60	4.4 (γ_b : 2.0, γ_f : 2.4)
250	1.6 (γ_b : 0.7, γ_f : 0.9)

Table 2: Calculated yields (C-ion beam)

C-ion energy [MeV/u]	γ_{total} [%]
120	78
400	27

The energy and angular distributions illustrated above make possible the transport of the SE preserving the

information on the beam profile (see next Section). The number of electrons produced, evaluated on the base of the data of Tables 1 and 2, goes from 3 (0.3 if the 2 sigma beam edge is considered) to $9 \cdot 10^3$ e⁻/pixel·100 μs for both proton and C-ion beams.

Focalisation system (FS) design

Different optics have been studied to match the electron detectors sizes and pitch. The final solution for the CMOS detector, simulated with SIMION 3D Ion Optics Programs [16], has been designed adapting the optical scheme of an image intensifier tube [17] to the beam monitor needs. Figure 2 shows the final prototype and its cross section inserted in the vacuum chamber. An arc of 60 degree of the cage cylinder is covered by 25 tungsten wires of 40 μm diameter (99% beam transparency) to allow the passage of the hadron beam. In blue are the SE trajectories and in red the electrostatic potential lines, while the green arrow represents the hadron beam. On the right are the values of the electrodes polarizing voltages.

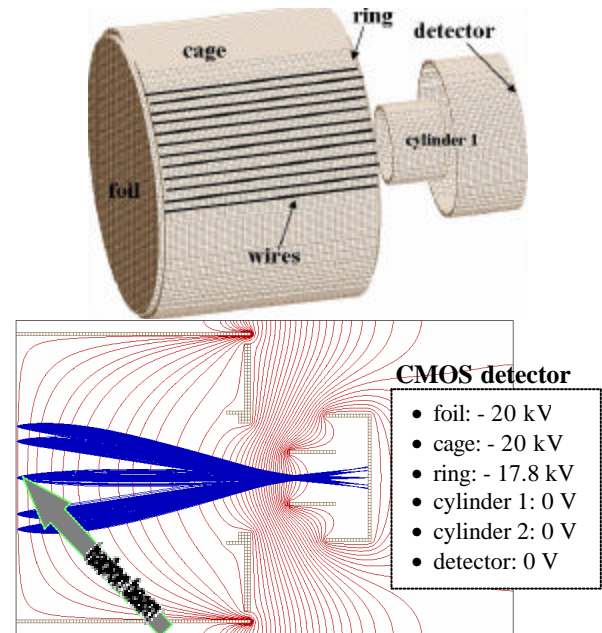


Figure 2 The final FS prototype (wire spacing 4 mm, wire diameter 40 μm , wires arc 60°).

As shown in Figure 2, the image is demagnified of a factor 5 to match the CMOS detector size. The flat emitting surface and the wider SE energy and angular spread in respect to photoelectrons causes aberrations larger than in the image intensifier tubes that inspired the FS design. Nevertheless simulations with a gaussian hadron beam proved that the spatial resolution is within the requirements also for off-centred beams.

Vacuum chamber (VC) design

Different vacuum systems with different geometries have been studied [18]. The final design is represented in Figure 3 where the green arrow on the right represents the hadron beam hitting the FS cage on the wire side (the flange-to-flange longitudinal occupancy is 460 mm). A

CCD camera is mounted on the right smaller flange to detect the light emitted in the interaction of the phosphor screen on the FS (see below) with the focalised SE.

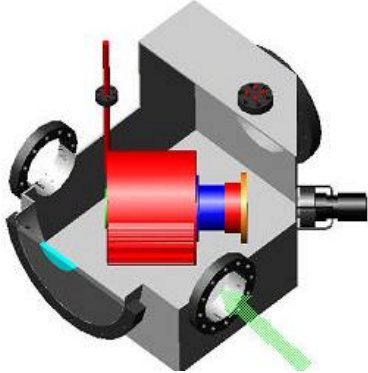


Figure 3: Inside view of the VC with the FS.

THE SLIM PROTOTYPE

A prototype of the SLIM beam monitor has been constructed and is shown in Figures 4 (focalisation system) and 5 (integrated system). In Figure 4 the detector mounted on the FS (left side) for the first tests is a phosphor screen (P47).

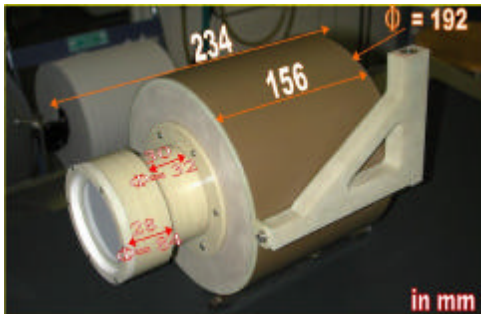


Figure 4: FS prototype (sizes in mm).



Figure 5: Integrated system in the laboratory.

Thermo-ionic electrons emitted from a biased tungsten wire replace the SE in the first laboratory tests of the FS performances. Results are qualitative (the CCD video signal was observed on a monitor), but promising. No discharges have been detected neither between FS and VC, nor between the FS electrodes for polarization voltages up to 30 kV and $5 \div 6$ kV differences between the cage and ring electrodes at a residual gas pressure of $\sim 5 \cdot 10^{-5}$ Torr. A blue spot rising from the interaction of the thermo-ionic electrons with the phosphor P47 was clearly detected: it corresponds to a demagnified image of the tungsten wire (5:1) that changes size and position varying the FS polarization voltages. The first simulations indicate that a small shift (~ 2 mm) of the image can be ascribed to the tungsten wire magnetic field. Further tests with a MCP for electron amplification and lower wire currents (and therefore lower B-fields) and development of the frame grabber software for more quantitative measurements are in progress.

CONCLUSIONS

An innovative beam monitor based on secondary emission by a sub-micron thick foil for real time diagnostics in the extraction lines of a hadrontherapy centre has been constructed. A prototype, including thin foils, vacuum, focalisation and slow control systems, has been realised. Integration and laboratory tests are on progress: the preliminary results are qualitative, but promising. Test on hadron beams are foreseen by the end of 2003.

REFERENCES

- [1] U. Amaldi and B. Larsson (eds.), "Hadrontherapy in Oncology", Proceedings of the First International Symposium on Hadrontherapy, Como, Excerpta Medica, Elsevier International Congress Series 1077 (1994).
- [2] G. Molinari, CERN, private communication.
- [3] M. Pullia, TERA Foundation, private communication.
- [4] L. Badano et al., Proton-Ion Medical Machine Study – Part I, CERN/PS 99-010 (DI) (1999).
- [5] C. Fernandez-Figueroa, G. Molinari, Proceedings of the Third European Particle Accelerator Conference, EPAC92, Berlin (1992).
- [6] C. Chianelli et al., Nucl. Instr. and Meth. A237 (1988) 245.
- [7] R. W. Odom et al., Nucl. Instr. and Meth. B44 (1990).
- [8] J. Bosser et al., SPS/ABM/Note/87-06, CERN (1987).
- [9] A. Braem et al., Nucl. Instr. and Meth. A478 (2002) 400.
- [10] VA-SCM2, produced by IDEas, www.ideas.no.
- [11] G. Deptuch et al., IEEE Trans. Nucl. Sci. 49 (2002) 601.
- [12] Hasselkamp D., Rothard H. et al., Particle Induced Electron Emission II, Springer-Verlag (1992) 63.
- [13] Abbot R.C., J. Appl. Phys. 30 (1959) 871.
- [14] Sternglass E.J., Phys. Rev. 108 (1957) 1.
- [15] Borovsky J.E., Nucl. Instr. and Meth. B36 (1989) 377.
- [16] David A. Dahl - SIMION 3D - Version 7.0 - Idaho National Engineering and Environmental Laboratory.
- [17] Illes P. Csorba, Image Tubes, Howard W. Sams (1985).
- [18] L. Badano, O. Ferrando, M. Pezzetta, Engineering Design Study for the SLIM Beam Monitor, SUCIMA Int. Note.

BEAM DIAGNOSTICS IN THE AGOR CYCLOTRON

S. Brandenburg, W.K. van Asselt, H. Post, H.W. Schreuder
 Kernfysisch Versneller Instituut, 9747 AA Groningen, the Netherlands
 B. Launé
 Institut de Physique Nucléaire, 91406 Orsay CEDEX, France

Abstract

Using the superconducting cyclotron AGOR at the KVI as an example the beam diagnostics equipment in modern multi-particle, variable energy cyclotrons for research in nuclear physics is reviewed. The experience obtained with the extensive set of diagnostics tools integrated in the design since the start of operation in 1996 is discussed.

INTRODUCTION

The AGOR cyclotron at the KVI is a multi-particle, variable energy AVF-cyclotron [1, 2]. It accelerates ions with charge-to-mass ratio Q/A in the range $0.1 \leq Q/A \leq 1$. The maximum energy per nucleon is, depending on Q/A , determined by either the bending limit $E/A = 600 (Q/A)^2$ MeV or the vertical focusing limit $E/A = 200 Q/A$ MeV. The magnetic field, in the range 1.7 to 4T, is produced by two superconducting maincoils, fifteen trimcoils and three fully saturated iron polesectors. The beams from the external ion sources (ECR for heavy ions, multi-cusp source for light ions and atomic beam source for polarised protons and deuterons) are axially injected. The extraction system consists of an electrostatic deflector, two electromagnetic deflectors with dipole and quadrupole windings and a quadrupole channel.

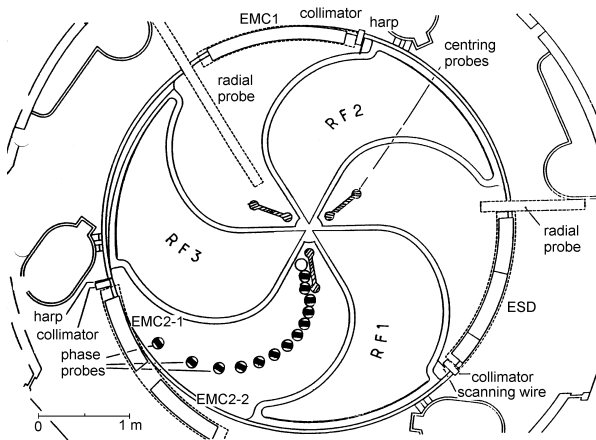


Figure 1: Layout of the AGOR median plane, showing various diagnostic tools and the position of the different extraction elements.

ESD: electrostatic deflector, EMC: electromagnetic channel

Besides the radial probe, the basic diagnostic tool in almost any cyclotron, an extensive set of diagnostics has

been integrated in the design (see figure 1) to allow a proper optimisation of beam centring, isochronism and alignment of the beam along the extraction path [4].

BEAM CENTRING

Because of the high magnetic field along the injection path the beam has to be injected exactly on axis. This implies that the orbit of the injected beam is off axis by about 15 mm. The major part of the centring error is corrected by the geometry of the acceleration electrodes in the central region of the cyclotron. The remaining centring error (1 – 2 mm) is corrected with a first harmonic of the magnetic field produced with two of the inner trimcoils [4].

Minimising the centring error is essential to obtain high extraction efficiency and to minimise the radial emittance of the extracted beam. Because of the large phase acceptance (around 30°) the number of turns needed to reach extraction radius varies by about 20, corresponding to several precession periods of the coherent radial betatron motion associated with the centring error. The resulting precession mixing causes a significant increase of the emittance of the beam at the entrance of the extraction system. This leads to reduced extraction efficiency and increased emittance of the extracted beam.

To verify the centring three probes have been installed at azimuths 120° apart to measure the radial turn pattern just beyond the central region of the cyclotron. The use of these probes to optimise the beam centring has turned out to be complicated:

- The observation of the individual turns requires the magnetic field to be tuned such that “turn” focusing is achieved: the number of turns required to reach a given radius has to be independent of the injection phase of the particles. The large phase acceptance allows this to be achieved only approximately, resulting in a small radial intensity modulation rather than separated turns.
- The centring error to be corrected can be as large as the radius gain per turn due to acceleration. Together with the weak turnseparation this makes it difficult to link the turn patterns from the three probes and extract the centring error from the data.

These complications preclude automatic calculation of the centring error from the measurement and thereby its use for the routine operation of the accelerator.

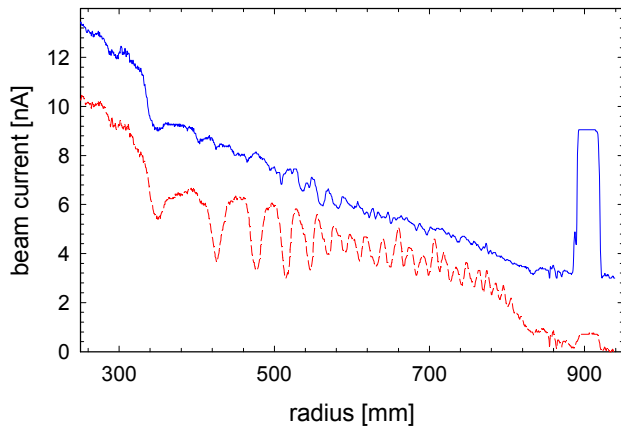


Figure 2: Radial oscillation pattern measured with the radial probe before (dash) and after (full) optimisation of the beam centring. The full curve has an offset of 3 nA. Note the strong influence of beam centring on extraction efficiency (peak at 900 mm).

An alternative method has been developed, which uses the main radial probe in the cyclotron. In front of the probehead a 0.5 mm tungsten wire has been mounted, which intercepts a fraction of the beam just before it hits the stopping block of the probe. In this way information on the current density is introduced in the scans. The precessional motion induced by the centring error leads to variations in the current density at larger radii, where the turns are no longer separated. The amplitude of these variations is a measure of the centring error and can thus be used to optimise the first harmonic (figure 2).

ACCELERATION REGION

Because of the absence of phase stability the main concern in the acceleration region is to maintain isochronism. Apart from ensuring acceleration up to extraction radius isochronism is important for the extraction process, which uses a precessional motion excited at the passage of the $v_r = 1$ resonance. The optimum tuning of this first harmonic strongly depends on the beam phase at the resonance passage and its further evolution in the fringe field up to the entrance of the extraction system.

The radial probe is used to tune the magnetic field such that the beam is accelerated all the way up to extraction. This typically requires an overall field correction $\Delta B/B < 3 \times 10^{-4}$ with respect to the calculated settings. This correction is made with the main coils. For the final optimisation with the trimcoils the beam phase is measured as a function of radius using 13 capacitive pick-ups. Strong perturbations from the RF system have so far made it impossible to do this in a systematic way. Thanks to the complete saturation of the iron hill sectors the magnetic field has good reproducibility, thus alleviating the need for beam phase measurements during routine operation. A new system has been successfully tested and will be implemented in the near future [5].

The radial probe in the AGOR cyclotron runs along a straight track. This greatly simplifies the mechanical design as compared to the “train”-probes running along a track following a symmetry axis of the cyclotron, which have been installed in other superconducting cyclotrons. The consequences of this choice are:

- No measurement can be performed during the first fifty turns. We do not consider this a handicap, except for the study of vertical beam motion.
- The angle of incidence of the beam on the probe head varies by some $\pm 10^\circ$ with respect to the optimal right angle. Consequently the efficiency of the current measurement varies with radius. For high energy proton and deuteron beams very little signal is left close to extraction, which seriously complicates tuning. This problem has been partly cured by making the tangential edge of the probe head parallel to the beam direction close to extraction. Comparison of the scans of figures 2 and 3, made with the original and modified probeheads respectively, clearly shows the effect of this.

A good vertical alignment of the beam is important to minimise coherent vertical betatron motion, in particular for beams close to the vertical focusing limit. Like the radial oscillations this leads to reduced extraction efficiency and increased emittance of the extracted beam. The vertical beam position is measured with the radial probe, which can be equipped with a layered head.

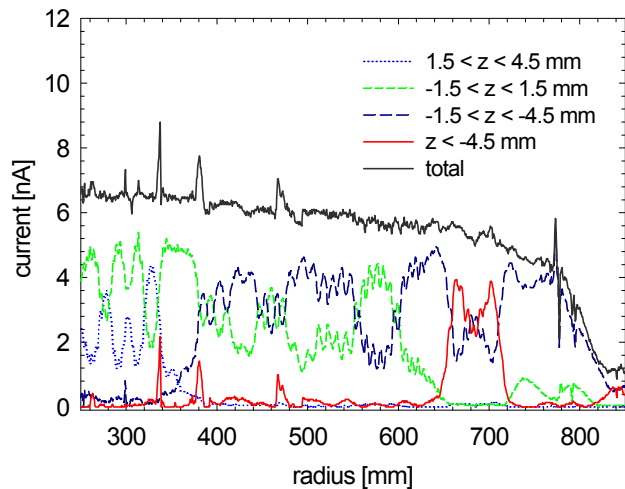


Figure 3: Vertical beam motion measured with the radial probe. Coherent vertical betatron motion caused by off-midplane injection and large-scale motion caused by coil misalignment are observed.

The measurements of the vertical beam position have been crucial for understanding the behaviour of beams close to the vertical focusing limit. Localised vertical beam losses and large vertical excursions of the beam have been observed (figure 3). Comparison of the measurements with calculations showed that the most likely cause of these excursions is a vertical misalignment of the superconducting coils by about 0.6 mm, despite the

fact that the alignment of the coils was made on the basis of field measurements.

EXTRACTION

In superconducting cyclotrons the extraction system has to guide the beam through an extensive fringe field region with large gradients. Consequently the extraction system extends over almost 360° and consists of several elements. These elements provide bending and horizontal focusing along the extraction path but also perturb the beam motion in the acceleration region, in particular near the $v_r = 1$ resonance. As this resonance is used to properly position the beam at the entrance of the extraction system, the field perturbations of the extraction elements have to be compensated with correctors integrated in the different elements.

The extraction system of the AGOR cyclotron consists of electrostatic and electromagnetic elements (figure 1), in contrast to other superconducting cyclotron where also magnetostatic elements are used. A quadrupole doublet (QP) in the beam exit port of the magnet is not displayed. The position of all elements can be adjusted to the extraction trajectory of the various beams. For the ESD also the curvature can be adjusted. In total the extraction system (exc. QP) has 18 adjustable parameters. Optimisation in this large parameter space is only possible thanks to detailed tracking calculations for some twenty typical beams throughout the operating range.

To verify the proper settings diagnostics measuring the radial beam profile all along the extraction path is needed, starting at the entrance of the first extraction element.

At the entrance of each element a beam profile monitor (either scanning wire or harp) and a collimator with current readout have been installed. The profile monitors do not operate satisfactorily for the high-energy proton and deuteron beams, which make up for almost 80 % of the beamtime:

- The strong magnetic field (up to 4.1 T) in which they are placed suppresses the delta electron emission, which normally strongly increases the signal, despite the fact that the wires have been tilted with respect to the magnetic field.
- The typical beam current of ≤ 10 nA is at least one order of magnitude lower than anticipated during the design stage. This is due to the good beam quality and the large acceptance of modern experimental set-ups, resulting in higher transmission and lower luminosity.

The collimators, however, provide a workable alternative. When the beam "touches" the walls of the collimator (20 mm tungsten) the current on the collimator strongly increases due to delta electron emission, thus allowing the optimum setting of the preceding element to be found rather easily.

At the exit of ESD, EMC1 a beam current measurement is made with a radially scanning probe intercepting the

beam. This measurement is used to optimise the transmission through the extraction system.

At the exit of EMC2 no current measurement has been installed, the measurement at the machine exit, beyond the quadrupole channel was considered sufficient. Operation experience has shown that a beam intensity measurement at this location would be very helpful as a diagnostic tool. The installation of such a measurement is planned. However, the compactness of the cyclotron complicates the design.

CONCLUSION

In the design of the AGOR cyclotron a complete set of beam diagnostics has been integrated to allow optimisation of all the relevant tuning and beam dynamics issues: beam centring, isochronism, radial and vertical motion and extraction settings. At the beamintensities foreseen in the design these operate well after minor modifications, with the exception of the phase probes. Exploitation of the results from the centring probes has turned out to be impractical for routine operation; an alternative using the main probe has been developed. At the actual intensities, at least one order of magnitude lower than anticipated, operation of the beamprofile monitors along the extraction path is insufficient for light ions. A satisfactory work-around for this problem has been found.

ACKNOWLEDGEMENT

This work has been performed as part of the research programme of the "Stichting voor Fundamenteel Onderzoek der Materie" (FOM), with support of the "Nederlandse organisatie voor Wetenschappelijk Onderzoek" (NWO).

It has been supported by the Rijks Universiteit Groningen (RuG) and by the European Union through the Large-Scale Facility program LIFE under contract number ERBFMGE-CT98-0125.

REFERENCES

- [1] S. Galès *et al.*; Proc. ICCA XI, Tokyo (Japan), eds. M. Sekiguchi, Y. Yano and K. Hatanaka, p. 184 (Ionics, Tokyo, 1986)
- [2] H. W. Schreuder *et al.*; Proc. ICCA XIV, Capetown (South Africa), ed. J.C. Cornell, p. 6 (WSP, Singapore, 1996)
- [3] B. Launé *et al.*; Proc. ICCA XIII, Vancouver (Canada), eds. G. Dutto and M.K. Craddock, p. 487 (WSP, Singapore, 1992)
- [4] J.P. Schapira, A. Le Goff and R. Brizzi; Proc. ICCA XII, Berlin (Germany), eds. B. Martin and K. Ziegler, p. 335 (WSP, Singapore, 1991)
- [5] T. Nijboer, W.K. van Asselt and S. Brandenburg; Proc. DIPAC2003, paper PT12

BEAM BASED HOM ANALYSIS OF ACCELERATING STRUCTURES AT THE TESLA TEST FACILITY LINAC

M. Wendt, S. Schreiber, P. Castro, A. Gössel

Deutsches Elektronen Synchrotron (DESY), Hamburg, Germany

M. Hüning, Fermi National Accelerator Laboratory (FNAL), Batavia IL, U.S.A.

G. Devanz, M. Jablonka, C. Magne, O. Napoly, CEA, Saclay, France

N. Baboi*, Stanford Linear Accelerator Center (SLAC), Stanford, U.S.A.

Abstract

The beam emittance in future linear accelerators for high energy physics and SASE-FEL applications depends highly on the field performance in the accelerating structures, i.e. the damping of higher order modes (HOM). Besides theoretical and laboratory analysis, a beam based analysis technique was established [1] at the TESLA Test Facility (TTF) linac. It uses a charge modulated beam of variable modulation frequency to excite dipole modes. This causes a modulation of the transverse beam displacement, which is observed at a downstream BPM and associated with a direct analysis of the modes at the HOM-couplers. A brief introduction of eigenmodes of a resonator and the concept of the wakepotential is given. Emphasis is put on beam instrumentation and signal analysis aspects, required for this beam based HOM measurement technique.

INTRODUCTION

Well controlled electron beam parameters are essential in future linear accelerators, like linear colliders for high energy physics or SASE-FEL driver linacs for applied science. The transport of very low emittance beams through the entire accelerator requires low transverse *wakepotentials* and therefore well damped *higher order modes* (HOM) in the accelerating structures. At the TESLA Test Facility (TTF) linac a series of beam based HOM measurement experiments has been performed [1, 2, 3]. Beam instrumentation, in terms of a broadband beam position monitor (BPM) and HOM-couplers, was used to characterize beam excited dipole modes of the accelerating structures.

An intensity modulated bunched beam was used, which causes tunable sideband at frequencies

$$f_{\text{side}} = n f_b \pm f_{\text{mod}} \quad (1)$$

where f_b is the bunch repetition frequency, f_{mod} is the modulation frequency and n is an integer. Resonant modes are excited if $f_{\text{side}} = f_{\text{HOM}}$. A beam bump offsets the beam trajectory in the accelerating structure by an amount δx to ensure the excitation of dipole modes. Two measurements are required to find and analyze HOM's:

1. On a downstream located broadband BPM an automatic

routine searches for beam excited dipole modes by analyzing its transverse kick proportional to $(R/Q) \delta x$.

2. A measurement on the HOM-couplers of the accelerating structures is required to identify mode frequency and Q-value.

HIGHER ORDER MODES

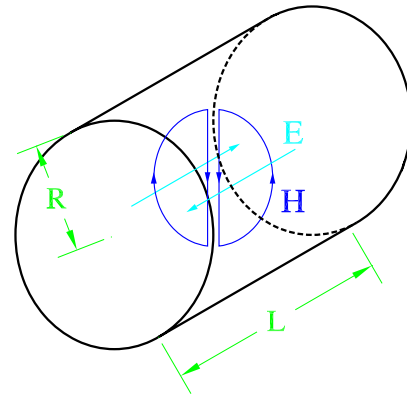


Figure 1: Cylindrical “pill-box” cavity, shown with the field lines of the TM_{110} dipole mode (horizontal polarized).

A cylindrical cavity (“pill-box” cavity) forms a simple single-cell accelerating structure (Fig. 1). By neglecting the vacuum chamber ports the resonant behavior in terms of the eigenmodes can be derived analytically, which results in an infinite number of eigenfrequencies at:

$$f_{npq}^{\text{TM(TE)}} = \frac{1}{2\pi R \sqrt{\epsilon\mu}} \sqrt{x_{np}^{(r)2} + \left(\frac{q\pi R}{L}\right)^2}$$

where x_{np} and x'_{np} are the zeros of the n^{th} -order Bessel-function respectively its derivative.

Each mode behaves equivalent to a parallel resonant circuit, driven by a current source. The fundamental TM_{010} mode is used for particle acceleration and driven by the rf-transmitter. All other *higher order modes* (HOM) are unwanted, but may be excited by the beam itself. Due to the finite conductivity of the cavity walls, power P_d is dissipated which limits Q-value of the resonances:

$$Q_0 = \frac{2\pi f_0 U}{P_d} = \frac{f_0}{\Delta f} \quad R_0 = \frac{V^2}{2P_d}$$

* On leave from NILPRP, Bucharest, Romania

(U : stored energy, V : voltage gain of a resonant mode)

Each deflecting mode is characterized by the quality factor Q_0 and the beam-coupling impedance $R_0 = 2 R_{sh}$ (R_{sh} : shunt-impedance). The normalized impedance R/Q depends only on the cavity geometry, and can be evaluated in most cases by computer simulation. The eigenfrequencies f_0 and Q-factors are measured in the laboratory (network analyzer). The “strength” of the mode, i.e. its ability to kick off the bunch train in a linac at resonance, is then proportional to $R = (R/Q) Q$.

HOM effects can be reduced in several ways, like: Optimizing the cavity shape or absorbing HOM power (with special coupling antennas – so-called HOM-couplers – or through the vacuum chamber, which acts as a waveguide port).

Dipole modes, as well as all other higher modes, have a so-called polarization axis. In practice this axes orientates along imperfections, e.g. coupler ports, HOM-couplers, etc. This requires two HOM measurements with horizontal and vertical beam displacement, particular in our multicell, multi-cavity configuration with all the exotic effects (trapped modes, propagation modes,...).

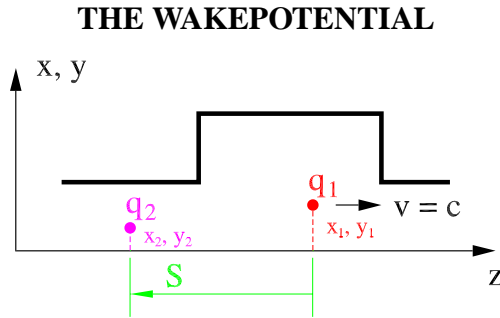


Figure 2: Wakefields are generated by q_1 and seen by q_2 .

Consider a test charge q_2 , which follows a point charge q_1 at a distance s and some displacement under relativistic conditions (see Fig. 2). Due to the discontinuities in the vacuum chamber, here a simple cavity, the electromagnetic fields of q_1 act on the test charge with the Lorenz force:

$$\mathbf{F} = \frac{d\mathbf{p}}{dt} = q_2(\mathbf{E} + c \mathbf{e}_z \times \mathbf{B})$$

The *wake potential* of the point charge q_1 is defined as:

$$\mathbf{W}(x_2, y_2, x_1, y_1, s) = \frac{1}{q_1} \int_0^L dz (\mathbf{E} + c \mathbf{e}_z \times \mathbf{B})_{t=(z+s)/c}$$

Transverse and longitudinal components of the wake potential are connected (*Panofsky-Wenzel* theorem). For beam emittance issues only transverse wakefields are of concern. In case of cylindrically symmetric structures a multipole expansion is made to describe the wake potential. The n -pole transverse wake potential is given by the sum of the

eigenmodes of same kind of the structure:

$$W_{\perp}^{(n)}(s) = c \sum_i \left(\frac{R^{(n)}}{Q} \right)_i \sin\left(\frac{\omega_i s}{c}\right) \exp\left(\frac{-\omega_i s}{2(Q_{ext})_i c}\right)$$

Depending on the shape of the structure the damping time $\tau \approx 2 Q_{ext}/\omega$ of the eigenmodes varies. In case of low damping *long range wakefields* can act over the bunch-to-bunch distance in a train of bunches. Due to the kicks of the dipole wakefields ($n = 1$) a cumulative beam-breakup instability (BBU) can be driven. Therefore the HOM measurement experiments are focused on the observation of dipole modes.

BEAM BASED HOM MEASUREMENTS

Experimental Setup

Fig. 3 shows the experimental setup for the beam based HOM measurements performed at TTF. The laser driven rf-gun was modified to generate bunches with 18.5 ns spacing ($f_b = 54$ MHz). The length of the macropulse was in the range 300...500 μs with a repetition rate of 1 Hz. A GPIB-controlled rf-source was used to modulate the intensity of the laser beam and therefore the charge of the electron bunches. The modulation frequency could be varied ($0.5 < f_{mod} < 27$ MHz), the modulation depth was set to 80 %. For the excitation of dipole modes a “dog-leg” magnet was used to give the required displacement of the beam trajectory in the accelerating structures. *Device under test* (DUT) were different types of 1.3 GHz superconducting TESLA accelerating structures:

- 9-cell standard structures
- Pairs of weakly coupled 7-cell structures (so-called “superstructures”)

Two kind of signals were used for the HOM measurements:

HOM signals delivered from the HOM-couplers of the accelerating structures are switched on a spectrum analyzer via a GPIB-controlled coaxial relays.

BPM signals delivered from a downstream, broadband BPM (re-entrant cavity type) are fed via a passive Δ -hybrid on another spectrum analyzer.

Measurement of the BPM signal

The deflection caused by a dipole mode is measured by analyzing the difference signal of a broadband, re-entrant cavity BPM. The bandwidth of the BPM and the passive Δ -hybrid is sufficient to resolve a single bunch position measurement in the 18.5 ns frame. For the analysis a external triggered spectrum analyzer was used in the zero-span mode as AM-receiver. The passband (center) frequency was set to $12 \times 54 \text{ MHz} \pm f_{mod}$, as the BPM offers the highest sensitivity around 650 MHz. The first part of the macropulse is intensity modulated, trying to excite a dipole mode; while

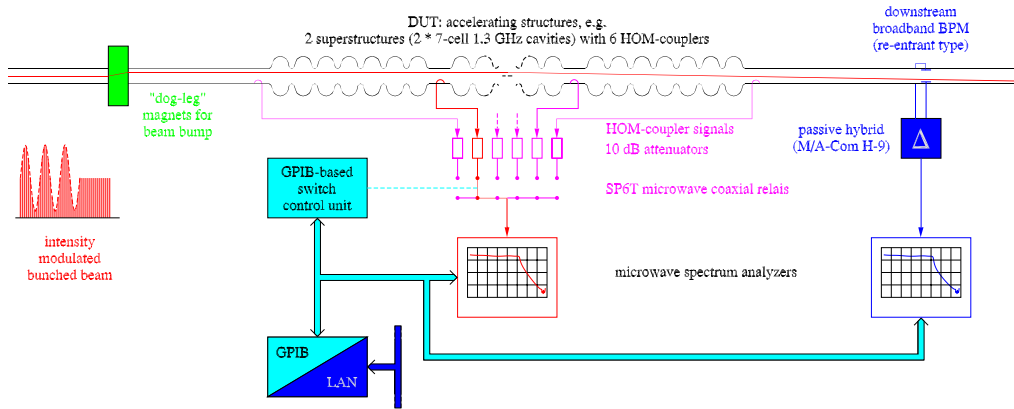


Figure 3: Experimental setup for the beam based HOM measurements at TTF.

the unmodulated second part was used to analyze its decaying deflection effect sensitively in absence of a common mode beam signal ("pump-and-probe" technique).

Fig. 4 shows BPM signals of two different resonances, one with low, the other with high Q-value. By calibration of all related components (beam current and energy, DUT-to-BPM drift, BPM characteristic, etc.) the R/Q of the mode can be estimated. A fully automated search routine (*Lab-View*) scans f_{mod} in steps of 1 kHz by analyzing the second part of the BPM signal for HOM effects. Dipole modes can be distinguished from other mode types by testing for a linear response of the BPM deflection signal to a variation of the beam displacement in the accelerating structure.

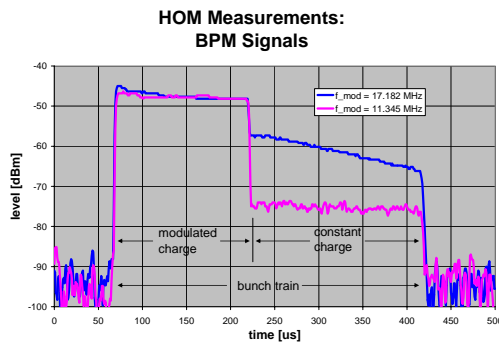


Figure 4: BPM signals at presence of higher order modes.

Measurement of the HOM signal

For each modulation frequency f_{mod} , where a HOM effect at the BPM was observed, the associated eigenfrequency of the mode f_{HOM} has to be determined. Therefore the complete macropulse is modulated with this frequency f_{mod} . Again the spectrum analyzer is used in zero span mode, but now scanned through the signals of the HOM-couplers of the accelerating structure. With a semi-automatic routine (*VEEPro*) center frequencies according to (1) are scanned ($n = 26 \dots 54$ and both signs), by observation of the spectrum analyzer signal. The mode is identified, if the signal shows a decaying slope after the actual

macropulse, i.e. the beam excited resonance continues to oscillate in the cavity (Fig. 5). The Q-value of the resonance is determined from the decay-time of the slope. Its physical location can be estimated by the HOM-coupler in which the signal appears. Detuning of individual cavities can give further details.

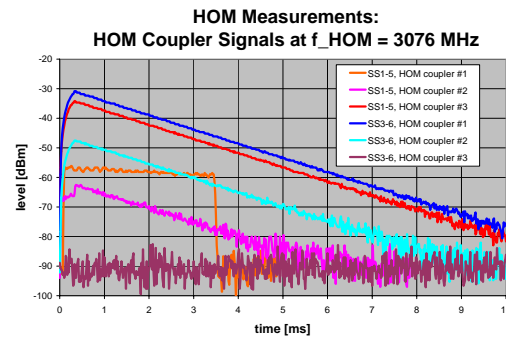


Figure 5: HOM-coupler signals of a high-Q mode.

CONCLUSIONS

This beam based HOM measurement technique led to the finding of unexpected, harmful dipole modes on TTF, which could not be forecast by computer simulations or network analyzer measurements in the laboratory. One consequence of these experiments is the modification of the HOM-coupler orientation in the TESLA accelerating structures. An interesting aspect for beam instrumentation is the use of HOM-couplers as beam monitor, which may result in new BPM's, located inside the accelerating structures.

REFERENCES

- [1] S. Fartoukh, et.al., Proc. of the 1999 Particle Accelerator Conference, New York, U.S.A., pp.922-924.
- [2] Ch. Magne, et.al., Proc. of the 2001 Particle Accelerator Conference, Chicago, U.S.A., pp.3771-3773.
- [3] G. Devanz, et.al., Proc. of the 2002 European Particle Accelerator Conference, Paris, France, pp.230-232.



POSTERS MONDAY

USE OF OPTICAL TRANSITION RADIATION INTERFEROMETRY FOR ENERGY SPREAD AND DIVERGENCE MEASUREMENTS

R. B. Fiorito and A.G. Shkvarunets, Institute for Research in Electronics and Applied Physics,
University of Maryland, College Park, MD 20742, USA

Abstract

OTR interferometry (OTRI) has been shown to be an excellent diagnostic for measuring the rms divergence and emittance of relativistic electron beams when the fractional energy spread $\Delta\gamma/\gamma$ is less than the normalized rms divergence $\sigma = \gamma\theta_{\text{rms}}$. This is the case for most beams previously diagnosed with OTRI. To extend this diagnostic capability to beams with larger energy spreads, we have calculated the effects of all the parameters effecting the visibility of OTR interferences, V ; i.e. energy spread, angular divergence, the ratio of foil separation to wavelength ratio, d/λ and filter band pass. We have shown that: 1) for a given $\Delta\gamma/\gamma$, the sensitivity of V to σ is proportional to the observation angle θ_0 , the fringe order n and the ratio d/λ ; 2) the sensitivity of V to $\Delta\gamma/\gamma$ is independent of θ_0 and n but is proportional to d/λ . Thus, by adjusting d/λ , and choosing the appropriate fringe order, one can separate out and measure *both* the energy spread and divergence. However, the filter band pass must decrease with θ_0 and n . Results of our calculations will be given for various beams of interest.

INTRODUCTION

A conventional optical transition radiation interferometer [1] consists of two parallel thin foils, oriented at 45 degrees with respect to the electron beam. A charged particle or particle beam produces forward directed OTR from the first foil and backward directed OTR from the second foil, which is usually a mirror. Interferences between the two radiations will be seen near the direction of specular reflection when the distance between the foils, d is comparable to the vacuum coherence length, L_v , the distance in which phase (ϕ) of field of the electron and the OTR photon differ by π .

The component of intensity of OTR interferences parallel to the plane of incidence can be written as

$$\frac{d^2 I_{\parallel}(\gamma, \lambda, \theta)}{d\omega d\Omega} = \frac{4\alpha}{\pi^2 \omega} \frac{\theta_x^2}{(\gamma^{-2} + \theta^2)} |1 - e^{i\phi}|, \quad (1)$$

where $\phi = d/L_v$ and $L_v(\theta, \gamma, \lambda) = (\lambda/\pi)((\gamma^{-2} + \theta^2)^{-1})$, α is the fine structure constant, γ is the Lorentz factor of the beam, λ is the observed wavelength, $\theta = (\theta_x^2 + \theta_y^2)^{1/2}$ is the observation angle measured with respect to the direction of specular reflection, θ_x is the x component of θ projected onto a plane perpendicular to the direction of specular reflection and ω is the angular frequency of the observed photon.

We have developed a useful rms beam divergence diagnostic using OTR interferences [2]. In this method one focuses the beam to a waist. Then the visibility of the interference pattern is primarily a function of the rms beam divergence, θ_{rms} provided that the energy spread of the beam is less than the normalized divergence, $\sigma = \gamma\theta_{\text{rms}}$. This is the usual case observed for high energy beams. Also, if one observes perpendicular and parallel polarized OTR interferences, i.e. by inserting a variable polarizer into the optical path, the corresponding components of the divergence can be measured.

Since the visibility is also affected by the optical bandwidth of the observation, one must take care to make this narrow enough so that the change in visibility due to the divergence can be seen. The inter foil distance and the filter band pass must be designed to produce the required number and spacing of the fringes for a given range of divergence. This is typically done with the aid of a computer code, which calculates the OTR interferences, for example, Eq. (1) convolved with a Gaussian distribution of particle trajectory angles and a given filter transmission function. The fit of measured to calculated interferences give the beam energy via the position of the fringes to about 1% precision and the rms divergence to about 10 % precision [2].

Recent theoretical studies have considered use of OTR from a stack of multiple dielectric foils as a beam energy distribution diagnostic [3]. In this study the effect of divergence is neglected. We are currently planning to measure divergence and transverse emittance of a low energy beam (8 MeV) where nonlinear space charge forces create a large energy spread on the beam (1- 10 %), and the normalized divergence $\sigma = \gamma\theta_{\text{rms}} \sim 0.03$, which is comparable to the energy spread. For this application a careful analysis of the effects of all beam and measurement parameters and a strategy for separating out the effects of divergence and energy spread is required.

APPROACH

Our approach to this problem is twofold:

1. Calculate of the effect of variations of beam angle (divergence), energy spread and wavelength (filter band pass) on the difference in phase between OTR photons produce at each foil. It is this phase that determines the fringe visibility and corresponding capability of OTR interferometry (OTRI) to diagnose beam parameters with good sensitivity and precision.
2. Develop estimates and computer codes which convolve variation effects with OTRI patterns to determine and define parameter ranges needed to separate out effects of energy spread and beam divergence.

Calculation of the phase and its variation

To illustrate our method we will calculate the phase of forward directed photons produced at each foil of an OTR

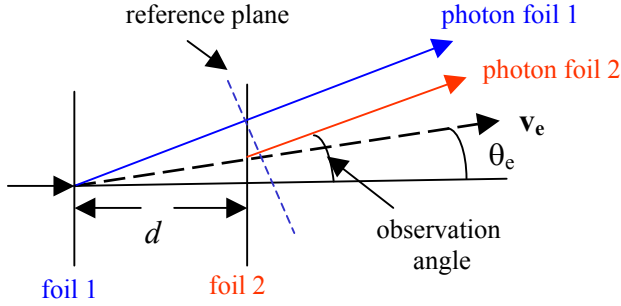


Figure 1: Diagram of an ideal forward directed OTR interferometer.

interferometer observed *in the plane of incidence*, i. e. the plane formed by the average velocity vector of the beam and the observation direction as shown by the arrows in Figure 1. A similar analysis pertains to forward-backward OTRI, and can be extended out of the plane of incidence.

The phases of the OTR photons generated at foils 1 and 2 are given respectively by:

$$\begin{aligned}\psi_1 &= kd / \cos \theta_x \\ \psi_2 &= kd / (\beta \cos \theta_e) + kd (\tan \theta_x - \tan \theta_{ex}) \sin \theta_x\end{aligned}\quad (2)$$

where k is the wave number of the photon, d is distance between the foils, θ_x is the x component of the observation angle in the plane of incidence, θ_e is the trajectory angle of the electron, and θ_{ex} is the x component of this angle. In the limit of small angles and relativistic energies, the phase difference at the interference maxima is given by $\Delta\psi = 2n\pi$ or:

$$(\gamma^2 - 1)^{1/2} / \gamma + \theta_x^2 - \theta_x \cdot \theta_e - 1 = n\lambda / d \quad (3)$$

where n is the fringe order and λ is the observed wavelength. The total variation of Eq. (3) gives:

$$\Delta\gamma / \gamma^3 + \theta_x \Delta\theta_{xe} - (2\theta_x - \theta_{xe}) \Delta\theta_x + \Delta\lambda n / d + \lambda \Delta n / d = 0 \quad (4)$$

where the term $\Delta\xi$ refers to a finite variation or spread in the associated variable ξ .

We choose $\Delta\theta_x = 0$, i.e. a fixed angle of observation; and $\theta_e = 0$, i.e. the beam direction along the axis. Note that if $\Delta n = 0$, the fringes are 100% visible and if $\Delta n \sim 1$, they are washed out (0% visibility). We estimate that $\Delta n = 0.5$ as the value of highest sensitivity to a given variable variation. Then Eq. (4) becomes:

$$\Delta n = 0.5 = (d / \lambda) [\Delta\gamma / \gamma^3 + \theta_x \Delta\theta_e] + n \Delta\lambda / \lambda \quad (5)$$

From this fundamental equation we can estimate how variations in energy spread $\Delta\gamma$, angular divergence, $\Delta\theta_e$ and filter bandwidth, $\Delta\lambda$ affect the visibility of OTR interference fringes.

By setting the variation of two of the three variables on the right hand side of Eq. (5) equal to zero, we can determine the dependence of the remaining variation on θ_x , γ , λ and d . For example, if we set the variations $\Delta\theta_e = \Delta\lambda = 0$, and fix d/λ , we conclude that the effect of energy spread, $\Delta\gamma$ on the fringe visibility decreases as γ^{-3} but is independent of θ_x . Similarly if $\Delta\gamma$ and $\Delta\lambda$ are neglected, the effect of $\Delta\theta_e$ on the visibility is proportional to θ_x but is independent of the energy, γ . Also, the effect of bandwidth is proportional to the fringe order n but is independent of the beam energy.

These dependences can be used to advantage to diagnose either the energy spread or the divergence. However, control of the bandwidth is necessary for both diagnostics. We can experimentally adjust d and λ to optimize the number of fringes for a given range of divergence or energy spread.

Table I. Design Parameters for OTR Interferometer

E MeV	$\Delta E/E$	d mm	$\Delta\theta_e$ mrad	$\Delta\lambda/\lambda$	Δn	$\gamma\theta_x$
95	0	25.4	0.6	0	0.25 0.75	1 3
95	0	25.4	0	0.11	0.13 1.17	1 3
95	< 0.1	25.4	0	0	< 0.1	
50	0.003	1000	0	0	0.5	
50	0	162	0.2	0	0.5	1
50	0	54	0.2	0	0.5	3
50	0	54	0	0.007	0.5	3
8	0.01	9.5	0	0	0.5	1
8	0	9.5	0	0.006	0.5	1
8	0	1.5	1.8	0	0.5	0.5
8	0	1.5	0	0.04	0.5	0.5

RESULTS OF VARIATIONAL ANALYSIS

Consider a measurement of the energy spread $\Delta\gamma$. The analysis given above shows that lower order fringes, which are minimally affected by $\Delta\lambda$ and $\Delta\theta$, are most useful to measure $\Delta\gamma$. On the other hand for maximal sensitivity to divergence it is useful to employ higher order fringes.

Estimated design parameters for an OTR interferometer are presented in Table I. for various beam energies, energy spreads and divergences. We include parameters for 95 MeV for which the divergence was actually measured.

COMPUTER CALCULATIONS

We have developed a series of computer codes, which convolve the OTR intensity, e.g. Eq. (1) with energy, angle and filter distribution functions. The results are shown in Figures 2-5 for a fixed beam energy, $E = 8$ MeV. Parameters d and λ are chosen to optimize the fringe pattern for a measurement of either energy spread or divergence.

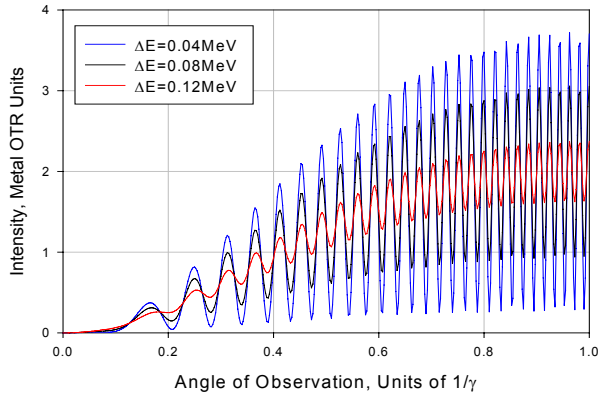


Figure 2: Effect of energy spread on OTR interferences; $\lambda = 650$ nm, $\Delta\lambda = 0$, $\Delta\theta_e = 0$, $d = 10$ mm.

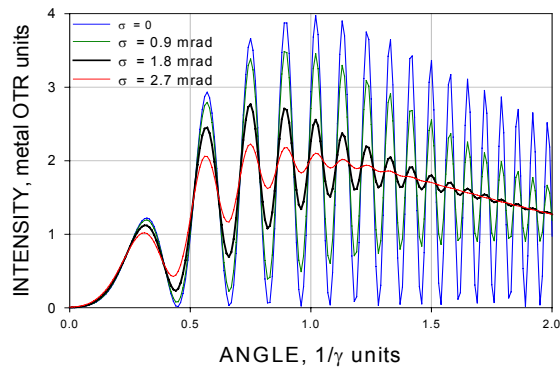


Figure 3: Effect of divergence on OTR interferences; $\lambda = 650$ nm, $\Delta\lambda = 0$, $\Delta E = 0$, $d = 1.5$ mm.

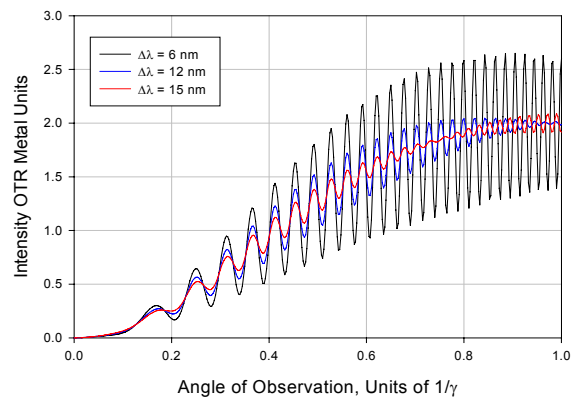


Figure 4: Effect of bandpass on energy spread measurement; $\lambda = 650$ nm, $\Delta E = 0.08$ MeV, $\Delta\theta_e = 0$, $d = 10$ mm.

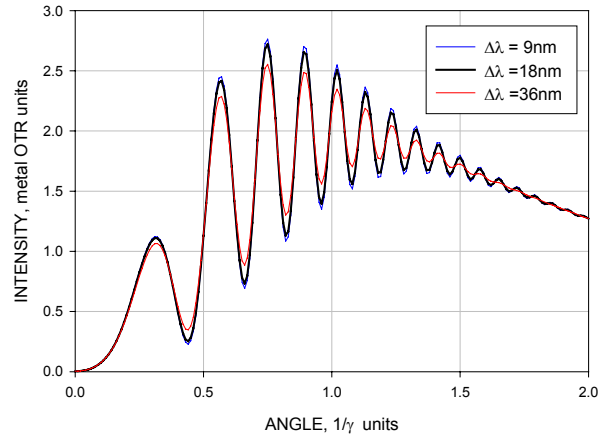


Figure 5: Effect of bandpass on divergence measurement; $\lambda = 650$ nm, $\Delta\theta_e = 1.8$ mrad, $\Delta E = 0$ MeV, $d = 1.5$ mm.

Figure 2. e.g. shows that effect of the energy spread on fringe visibility is independent of angle. Comparatively, Figure 3. shows the angular dependence of the visibility for different beam divergences, i.e. that a larger divergence washes out the fringes at higher orders more rapidly than a smaller divergence. Figure 4. shows the effect of band pass on energy spread measurements and that lower fringe orders should be used to measure energy spread to avoid the effect of $\Delta\lambda$. Similarly Figure 5. shows the effect of band pass on divergence measurements.

CONCLUSIONS

Variational analysis has resulted in a number of simple conclusions affecting the ability of OTRI to measure beam divergence and energy spread: (a) the effect of energy spread on OTRI is independent of observation angle and the fringe order and falls off as γ^{-3} ; (b) the effect of divergence is proportional to the observation angle; (c) the effect of bandwidth is proportional to the fringe order; (d) the scaling of energy spread and divergence effects depends on d and λ , which can both be adjusted for diagnostic purposes.

The above results have been verified by more exact analysis using computer calculations and are further verified by experimental data.

We are using these results to design OTRI diagnostics to separate out and measure both energy spread and divergence.

REFERENCES

- [1] L. Wartski, et.al., J. Appl. Physics, 46, 3644 (1975).
- [2] R. B. Fiorito and D.W. Rule, AIP Conf. Proc. No. 319, R. Shafer ed., 187 (1994).
- [3] X. Z. Qui, et. al. Nuc. Instrum. and Methods A, 363, 520 (1995).

STUDIES OF OTR ANGULAR DISTRIBUTION ON CTF2

E. Bravin and T. Lefèvre, CERN, Geneva, Switzerland

Abstract

Optical Transition Radiation (OTR) is widely used in beam diagnostics. The most common application is the acquisition of the transverse and longitudinal beam profiles. Other beam parameters, like divergence and energy, can also be deduced from the angular distribution of the OTR emission (“Doughnut”). In order to investigate the possibilities and the limits offered by this technique we have performed a test on the 48MeV, 1nC electron beam of the CLIC Test Facility 2 (CTF2.). Beam divergences between 2 and 6mrad were measured with an accuracy of a few percent. A good agreement was also found between the energy measurements obtained with a classical spectrometer and the OTR based technique. We conclude by describing some possible applications of OTR based diagnostics for CLIC.

1 INTRODUCTION

Optical Transition Radiation [1] has become a familiar tool in accelerator diagnostics for beam imaging [2]. Its success resides in its simplicity, only requiring a conducting foil and an adequate optical system, providing thus a robust and cheap instrument. The perfect linearity of the light intensity versus the number of particles is a significant advantage compared to scintillating screens, which are subjected to saturation. Its femtosecond time resolution [3] allows accurate bunch length measurement, limited in most cases by the performance of the camera. Using the so-called ‘quadrupole scan method’, beam emittances are routinely extrapolated from OTR beam profile measurements. As already pointed out in the ‘70s, much more information than the beam profiles can be extracted from the OTR emission [4]. The beam energy and divergence are accessible in the angular distribution of the OTR. In this case, the camera must be located in the focal plane of the optical system, which is focused at infinity. A lot of experiments have been done in this direction during the past years, demonstrating the strong potential of transition radiation for single shot emittance measurement [5] or beam energy and energy-spread determination [6]. OTR interferometry using a two-foil assembly has been also developed [7] and has shown its capability to enhance the performance of the OTR angular techniques.

In this paper, we report on the OTR study performed at the CLIC Test Facility 2 (CTF2) [8] using a 48MeV, 1nC electron bunch. Our effort has been concentrated on the angular distribution observation. Beam divergences were measured with a good accuracy and OTR based energy measurements have been compared with success to the classical energy measurements performed with a spectrometer line. We finally give some perspectives for its utilization in the CLIC context [9].

2 OTR FOR RELATIVISTIC PARTICLES

Let us consider the interface between vacuum and a material with a relative permittivity ε . Let us also assume that this interface is tilted with respect to the beam trajectory by an angle ψ , as shown in figure 1. Using the formalism developed in [4], the backward OTR spectral and angular distribution emitted with polarizations parallel and perpendicular to the observation plane can be expressed by:

$$\frac{\partial^2 I_{\parallel}}{\partial \omega \partial \Omega} = \frac{\alpha \cdot \hbar}{4\pi^2} \frac{\beta_z^2 \cos^2(\theta)}{\sin^2(\theta)} \left| \frac{(1-\varepsilon)(A \cdot \sin^2(\theta) - B)}{C \cdot D \cdot E} \right|^2$$

$$\frac{\partial^2 I_{\perp}}{\partial \omega \partial \Omega} = \frac{\alpha \cdot \hbar}{4\pi^2} \left(\beta_x^2 \beta_z^4 \sin^2(\phi) \cos^2(\theta) \right) \left| \frac{(1-\varepsilon)}{C \cdot D \cdot F} \right|^2$$

with $\beta_z = \beta \cos(\psi)$, $\beta_x = \beta \sin(\psi)$, α the fine structure constant, \hbar the reduced Planck constant and the following functions defined by:

$$A = 1 + \beta_z \sigma - \beta_z^2 - \beta_x \sin(\theta) \cos(\phi), \quad B = \beta_x \beta_z \sigma \sin(\theta) \cos(\phi)$$

$$C = (1 - \beta_x \sin(\theta) \cos(\phi))^2 - \beta_z^2 \cos^2(\theta), \quad D = 1 - \beta_x \sin(\theta) \cos(\phi) + \beta_z \sigma$$

$$E = \sigma + \varepsilon \cos(\theta), \quad F = \sigma + \cos(\theta), \quad \sigma = \sqrt{\varepsilon - \sin^2(\theta)}$$

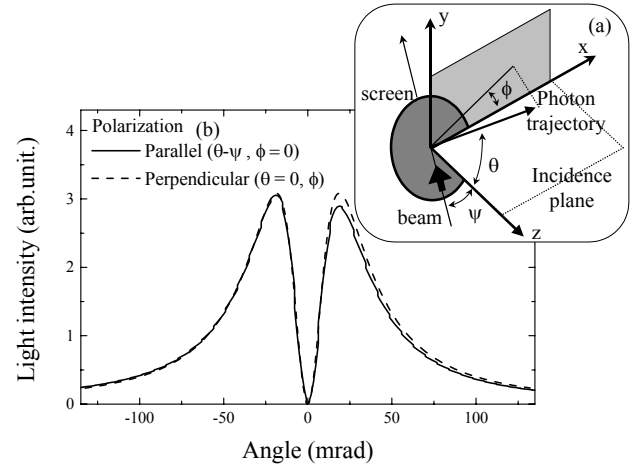


Figure 1: (a) Geometrical configuration: The incident plane contains both the normal to the screen and the beam velocity (b) OTR angular distribution, I_{\parallel} and I_{\perp} for a 50MeV electron. The tilt of the screen introduced an asymmetry of the lobes pattern, only visible in the I_{\parallel} signal. The relative position of the maximums with respect to the centre of the distribution gives a measurement of the beam energy ($=1/\gamma$).

Assuming that the electron beam has a Gaussian angular distribution defined as follow:

$$D_{\parallel,\perp}(s) = \frac{e^{-\frac{s^2}{2\sigma_{\parallel,\perp}^2}}}{\sqrt{2\pi} \cdot \sigma_{\parallel,\perp}}$$

The angular distribution of the OTR light is obtained by the convolution of $I_{\parallel,\perp}$ and $D_{\parallel,\perp}$. Some examples are given

in figure 2 assuming different beam divergences. In this calculation $\theta = \psi$, so that I_{\parallel} vanishes. Two important considerations result from this analysis: first there is a limitation in the minimum beam divergence measurable. For divergence lower than $1/10\gamma$, the divergence of the beam cannot be extracted from the OTR angular distribution. Secondly the angular distribution is diluted by the beam divergence so that for divergences above $1/\gamma$, the lobes pattern disappears making the beam energy measurement impossible.

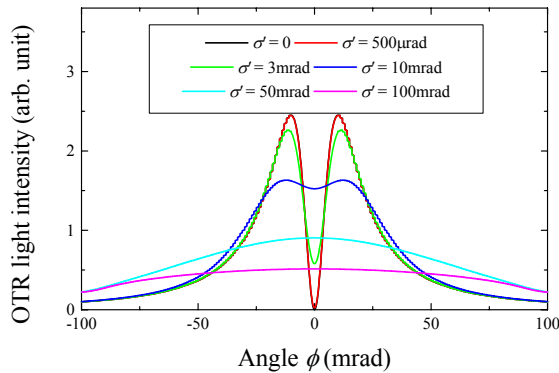


Figure 2: OTR angular pattern for different values of beam divergence

3 EXPERIMENTAL SET-UP

The layout of the CTF2 probe beam line is shown in figure 3.

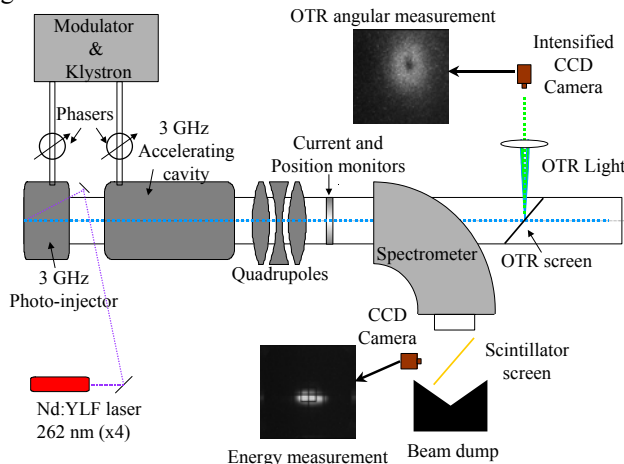


Figure 3: OTR test on the CTF2 probe beam line

A Nd:YLF laser 256nm (frequency quadrupled) is used to run a 3GHz radiofrequency photo-injector. Typically one InC electron bunch of 4ps FWHM length is produced and accelerated to a nominal energy of 48MeV in a normal conducting 3GHz accelerating structure. A spectrometer line, consisting of a bending magnet and a scintillating screen placed outside of the vacuum chamber, is used for the characterization of the beam energy and the tuning of the RF accelerating phase. An OTR screen has been inserted just downstream of this bending magnet. The target consists of a 100μm thick

aluminized Mylar foil, tilted by 45° with respect to the electrons trajectory. The optical system is composed of an achromat lens with a 80mm focal length and an intensified CCD camera located at the focal plane. The distance between the centre of the OTR screen and the lens is set to 75mm allowing an angular aperture of 130mrad (around $10/\gamma$).

4 OTR MEASUREMENTS

The image analysis is performed as follow; we first determine the centre of the OTR ‘doughnut’, around this position thin slices along the vertical and horizontal direction are selected and compared to our calculations. A minimization fit gives then the energy and the divergence of the beam.

2.1 Divergence measurements

The divergence of the beam on the OTR screen is adjusted by varying the current in the upstream quadrupoles. A set of 8 images is acquired for each current value in order to have sufficient statistics. The results are summarized in figure 4 with the OTR ‘Doughnut’ images and the corresponding projections (I_{\parallel}) superimposed with the theoretical fit calculations. The OTR ‘Doughnut’ is getting blurred when the divergence increases. Divergences from 2 to 6mrad were measured with an accuracy of a few percent, limited by the performance of the CCD (8bits coding) and the noise level (ambient light background and noise from the image intensifier).

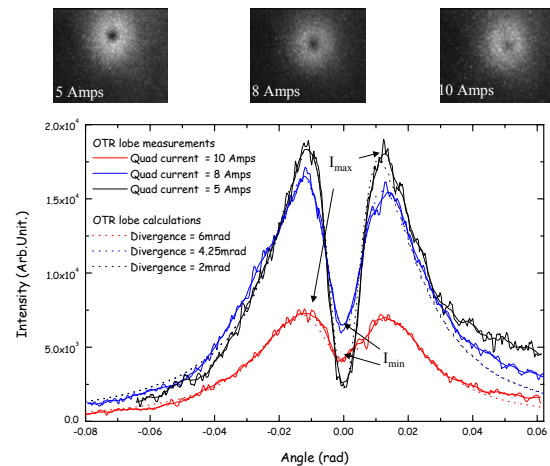


Figure 4: OTR angular distribution for three different beam divergences

2.2 Energy measurements

By changing the modulator voltage it is possible to control the beam energy. In figure 5 are shown the OTR angular distribution obtained for 4 different voltages. The RF phases of the gun and of the accelerating cavity are adjusted to obtain minimum energy dispersion. This was checked using the spectrometer line before each OTR measurement. Images, slices and fitted curves are displayed for each case. The performance of the energy measurement depends mainly on the optical system. The

distance between the screen and the lens fixed the range of measurable energy, and together with the size of our CCD pixels give the precision of the measurements. In our set-up this leads to an direct accuracy of 1MeV.

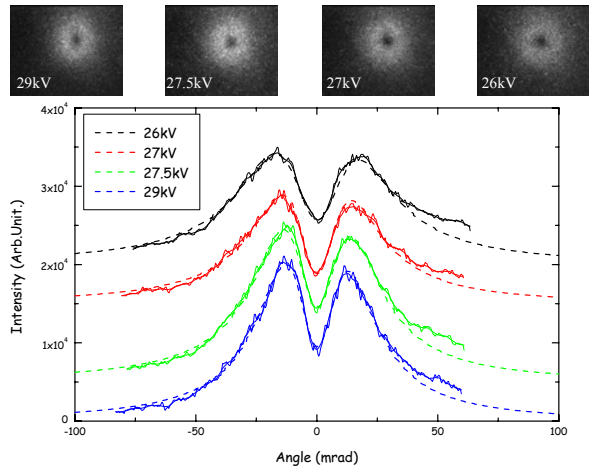


Figure 5: OTR angular distribution for different beam energy

The results, summarized in table 1, show that the agreement between spectrometer and OTR measurements is very good for the two first voltage values. A discrepancy of 10% is then observed, possibly due to aberrations in the optical system or a misalignment of the electron beam entering the spectrometer line, which is very sensitive for energy measurements.

Table 1: Energy variation measurements

Modulator voltage (kV)	29	27.5	27	26
Spectrometer line (MeV)	48	45	43.2	39.6
OTR images (MeV)	47.2	44.6	40.5	36.3

A second set of data has been acquired to try to measure the electron energy dispersion. Results for different tunes of the RF accelerating phase are given in figure 6.

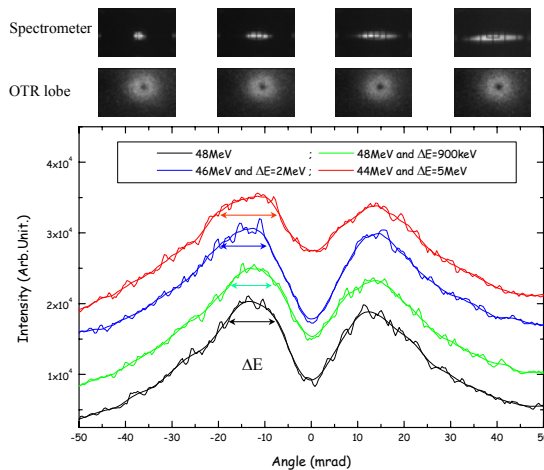


Figure 6: OTR angular distribution for different energy dispersion

To extract the energy dispersion from the OTR image, a more complex analysis is necessary. We measure the width (ΔE) of the OTR lobes at 90% intensity. The centre

of this ΔE gives the average energy. The beam divergence is calculated for this central energy by fitting the I_{\max} and I_{\min} values. The energy spread is then obtained by subtracting the calculated monochromatic width (ΔE_{mono}) from the measured ΔE . The results are reported in Table 2 and indicate that the energy spread is slightly overestimated compared to the spectrometer.

Table 2: Energy dispersion measurements in MeV

Spectrometer	48±0	48±0.9	46±2	44 ±5
OTR images	48.1±0	48.2±1.5	45.2±2.8	43.5±6.2

5 CONCLUSIONS

The observation of the OTR angular pattern can lead to the measurement of the beam energy and divergence. On the CTF2 machine, we have been measuring divergences of a few mrad with a good precision. Beam energy and energy dispersion measurements are compatible with the values obtained with the spectrometer line.

Using an appropriate optical set-up, single shot emittance measurement can be obtained. By using a pepperpot-like method on the OTR photon beam, the whole transverse phase space can be reconstructed [10].

For the CLIC beam, a rapid calculation indicates that in the main linac the beam emittance is 10^4 too small to allow an OTR-based divergence measurement. However energy or energy dispersion could be monitored along the linac where no spectrometer line could be envisaged.

Some investigations are specially needed to check what is the impact of the screen surface quality on this angular distribution. For a thermally resistant material like carbon, one could envisage a significant perturbation of the lobes.

6 ACKNOWLEDGMENT

The authors would like to express their gratitude to Dr. C. Vermare for helpful discussions, and Dr H.H. Braun and Dr. S. Doeber for their support during the measurements.

7 REFERENCES

- [1] I.M. Frank and V.I. Ginsburg, J. Phys. 9, 353, (1945).
- [2] D.W. Rule, Nucl. Inst. Meth. B 24/25, 901, (1987)
- [3] R.B. Fiorito and D.W. Rule, 1993 Faraday Cup Award, AIP Conf. Pro. 319, (1994).
- [4] E. Merle, Thesis, Bordeaux, (1994).
- [5] L. Wartski, Thesis, Orsay, (1976).
- [6] M. A. Tordeux and J. Papadacci, Proceeding of the European Particle Accelerator Conference, Vienna, 1818, (2000).
- [7] C. Vermare *et al*, Proceeding of the Linear Accelerator Conference, Monterey, 187, (2000).
- [8] M. Castellano *et al*, Proceeding of the Particle Accelerator Conference, New York, 2196, (1999).
- [9] L. Wartski *et al*, J. Appl. Phys. 46, 3644, (1975).
- [10] The CLIC study team, CLIC note 473, (2001).
- [11] The CLIC study team, CERN report 2000-08.
- [12] G.P. Le Sage *et al*, Phys. Rev. STAB 2, 122802, (1999).

OTR FROM NON-RELATIVISTIC ELECTRONS

C.Bal, E.Bravin, E. Chevallay, T. Lefèvre and G. Suberlucq, CERN, Geneva, Switzerland

Abstract

The CLIC Test Facility 3 (CTF3) injector will provide pulsed beams of high average current; 5A over 1.56μs at 140keV. For transverse beam sizes of the order of 1mm, as foreseen, this implies serious damage to the commonly used scintillating screens. Optical Transition Radiation from thermally resistant radiators represents a possible alternative. In this context, the backward OTR radiation emitted from an aluminium screen by a 80keV, 60nC, 4ns electron pulse has been investigated. The experimental results are in good agreement with the theoretical expectations, indicating a feeble light intensity distributed over a large solid angle. Our conclusions for the design of the CTF3 injector profile monitor are also given.

1 INTRODUCTION

The injector of the CTF3 facility in the nominal phase will produce intense beams [1]. The pulse will be 1.56μs long at a repetition rate of 50Hz, the nominal average current will be 5.4A, the electron energy 140keV and the beam size of the order of 1mm ($\sigma_{x,y}$). These values render the use of standard scintillating screens impossible since they will not stand the corresponding thermal load [2]. Reducing the beam current or the pulse length during the measurement can circumvent this problem. But for the optimum machine operation the observation of the beam profile in the transverse plane up to full intensity is required. For this reason alternative techniques must be developed. One solution consists of using Optical Transition Radiation (OTR) [3] with a graphite or carbide-based radiator. At the beginning of the '60s a lot of work was done on the OTR theory [4], together with experiments with electrons of energies between 1-100keV[5]. With the development of accelerators, OTR from relativistic particles [6] was studied and its application as a beam diagnostic tool has been widely developed. In the case of non-relativistic particles, OTR radiation, which is less efficient than scintillation in terms of light intensity, was never used, to our knowledge, for beam profile monitoring.

In order to investigate the feasibility of using an OTR screen for the CTF3 injector, we have been carried out some measurements on the 80keV electron beam available in the photocathode test stand at CERN [7]. Our paper is organised as follows. First, the OTR light characteristics are calculated for low energy electrons, in particular the angular distribution of the radiation. The beam line arrangement of the photocathode laboratory is described including the detection system added for this test. Experimental results are compared to our theoretical expectations and some perspectives for the CTF3 injector profile monitor are finally expressed.

2 OTR EMISSION FROM NON RELATIVISTIC ELECTRONS

We consider the transition between the vacuum and a material with a relative permittivity ϵ . The screen is tilted with respect to the beam trajectory (\vec{z}) by an angle ψ , as shown in figure 1. The OTR emission results from the contribution of the direct (\vec{n}), the reflected (\vec{n}') and the refracted (\vec{n}'') radiations emitted by the particle. Using the formalism developed by Wartski in [6], the backward OTR spectral and angular distribution emitted with polarizations parallel and perpendicular to the observation plane[†] can be expressed by:

$$\frac{\partial^2 I_{\parallel}}{\partial \omega \partial \Omega} = \frac{\alpha \cdot \hbar}{4\pi^2} \left| \frac{\vec{\beta}_{\parallel} \wedge \vec{n}}{1 + \vec{\beta} \cdot \vec{n}} + r_{\parallel} \frac{\vec{\beta}_{\parallel} \wedge \vec{n}'}{1 + \vec{\beta} \cdot \vec{n}'} - \frac{f_{\parallel}}{\epsilon} \frac{\vec{\beta}_{\parallel} \wedge \vec{n}''}{1 + \sqrt{\epsilon} \vec{\beta} \cdot \vec{n}''} \right|^2$$

$$\frac{\partial^2 I_{\perp}}{\partial \omega \partial \Omega} = \frac{\alpha \cdot \hbar}{4\pi^2} \left| \frac{\vec{\beta}_{\perp}}{1 + \vec{\beta} \cdot \vec{n}} + r_{\perp} \frac{\vec{\beta}_{\perp}}{1 + \vec{\beta} \cdot \vec{n}'} - \left(\frac{f_{\perp}}{\sqrt{\epsilon}} \right) \frac{1}{1 + \sqrt{\epsilon} \vec{\beta} \cdot \vec{n}''} \right|^2$$

with \hbar the reduced Planck constant, α the finite-structure constant ($=1/137$), $\vec{\beta}_{\parallel}$ and $\vec{\beta}_{\perp}$ the projection of electron velocity in the planes parallel and perpendicular to the observation plane and the corresponding Fresnel coefficients defined by:

$$f_{\parallel} = \frac{2\sqrt{\epsilon} \cos \theta}{\sqrt{\epsilon} \cos \theta + \sqrt{1 - \sqrt{\epsilon} - \sin^2 \theta}} \quad f_{\perp} = \frac{2\sqrt{\epsilon} \cos \theta}{\cos \theta + \sqrt{\epsilon - \sin^2 \theta}}$$

$$r_{\parallel} = f_{\parallel} - 1 \quad r_{\perp} = \sqrt{\frac{1}{\epsilon}} f_{\perp} - 1$$

and θ the angle between the normal of the screen and the direction of the OTR photons. The characteristic of the forward OTR emission can be obtained from the previous formula replacing β_z by $-\beta_z$ ($\beta_z = \beta \cos(\psi)$).

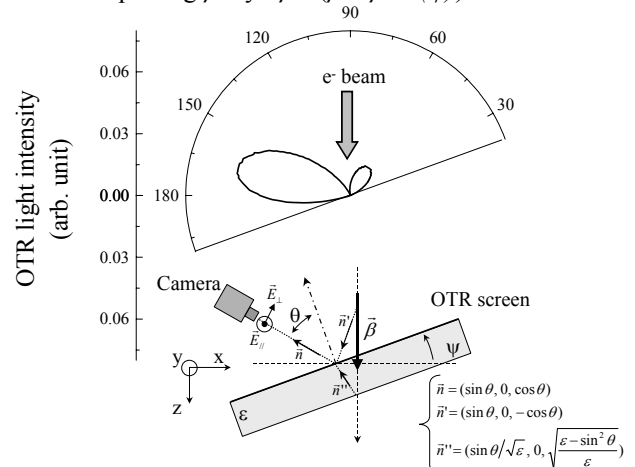


Figure 1: The angular distribution of the backward OTR emitted by 80keV electrons

[†] The observation plane is the plane that contains the photon's direction and the normal of the radiator

The normal of the screen is tilted with respect to the beam trajectory by 20° leading to a strong asymmetry of the OTR lobes. For the forward emission, the dominant term in the OTR formula is the first term, symbolizing the direct radiation of the particle. For the backward radiation, the second term, corresponding to the reflected radiation, is preponderant and the intensity of emission will depend on the material surface state. Thus using carbon-based radiators, which have low reflectivity coefficients, will reduce the intensity of OTR light emitted by the beam.

3 PHOTO-CATHODE LAB SET-UP

The photo-cathode laboratory, as depicted in figure 2, is equipped with a photo-injector capable of producing 4ns electron pulses with an energy of 80keV and a beam charge up to 60nC. This test stand is routinely used for the development and the fabrication of the CTF2 (CLIC) photo-cathodes [8].

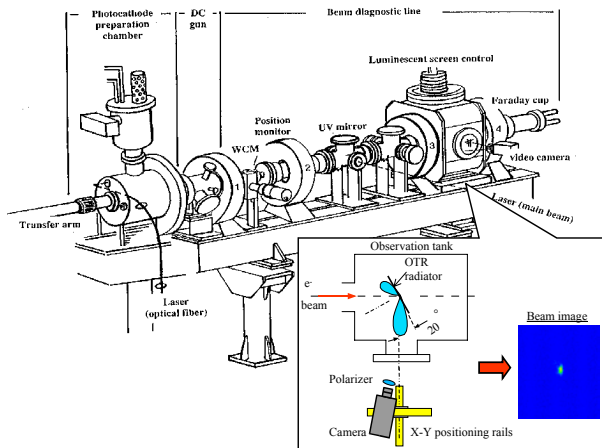


Figure 2: Layout of the electron beam line

UV pulses produced by a Q-switched Nd:YAG laser hit a Cs_2Te photo-cathode and liberate the electrons that are extracted by a DC potential of 80kV nominal. Four solenoids provide the required focusing down to the diagnostic tank installed at the end of the beam line, a couple of meters downstream.

For our test, the CsI(Tl) scintillating screen and the CCD camera normally used to observe the beam are replaced by a 1mm thick aluminium radiator and an intensified camera which can be gated to a few nanoseconds time interval. For the nominal set-up the camera is located at 50cm from the screen, providing a 20mrad detection angle. At low energies the OTR emission is getting very broad as you can see in figure 1. The screen is tilted by an angle of 20° with respect to the electron trajectory in order to send the OTR lobe in the direction of the camera.

By integrating the OTR formula over the visible range [400-700nm] and over our detection angle, the estimated number of photons per electron is $2 \cdot 10^{-6}$, giving a signal of $7.2 \cdot 10^5$ photons for the 60nC electron bunch. With this light intensity a normal CCD camera cannot be used, requiring at least 10 times more photons.

4 RESULTS

4.1 OTR identification

As the number of OTR photons is expected to be low, other sources of light in the machine can perturb our measurement. In our case, scintillation in the last laser mirror, the one used to deflect the laser beam onto the photo-cathode, was found to be the main source of background. This mirror, located close to the electron beam, can intercept the beam halo producing scintillation light. In order to identify the OTR emission we made two independent crosschecks, first looking at the polarisation of the light and secondly checking the emission duration. OTR can be considered as instantaneous compared to scintillation, which is governed by exponential decays ranging from tens of ns to ms. To disentangle the two light signals, our camera was gated down to 50ns, where the scintillation light intensity becomes very feeble. The gate duration cannot be shorter than that to take into account the intrinsic jitter of few tens of ns (typical for Q-switched laser). The transition radiation is measured and the beam profile can be obtained as shown in the picture in figure 2. One can also mention that the OTR light intensity varies from shot to shot, mainly due to fluctuations in the laser intensity (5%).

4.2 OTR emission versus beam charge

The OTR light is expected to be linear with the bunch intensity. By varying the laser pulse energy, the bunch charge can be adjusted from 20nC to 60nC. The corresponding results are given in Figure 3 by computing the total emission from the recorded images.

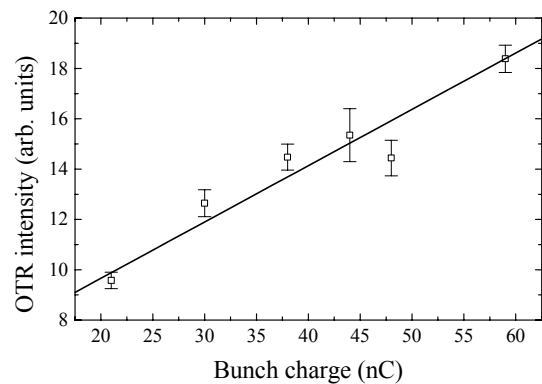


Figure 3: OTR light intensity versus the bunch charge.

The bunch charge dependence of the OTR light intensity is found to be linear with a relatively good precision. The offset due to the background is clearly seen on the fit curve. In addition to the other source of light present in the machine, noise due to the image intensifier contributes to the background level too. Error bars plotted in figure 3 are only calculated from a few shots.

4.3 OTR emission versus observation angle and distance

The camera, usually installed at 90° with respect to the beam trajectory, can be placed between 84° and 105°. Images are acquired for different observation angles and the results are displayed in figure 4 with the expected theoretical curve. A relatively good agreement is obtained, even if our experimental set-up does not permit to describe the whole OTR lobe. However it clearly indicates that 20° is not the best angle in terms of maximizing the light intensity sent to the camera (supposed to be at 90° to the beam trajectory).

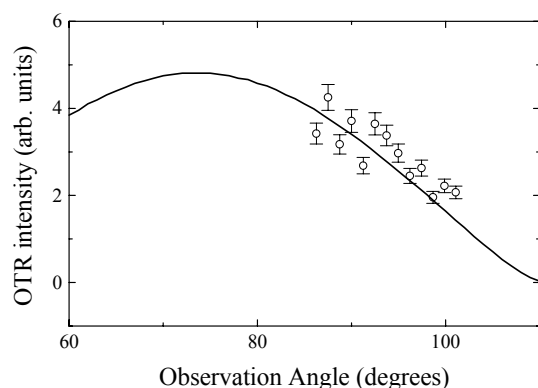


Figure 4: OTR intensity versus the observation angle.

The variation of the OTR light intensity with the observation distance has been also measured by displacing the camera over 20cm. Experimental data are shown in figure 5. The $1/d^2$ dependency is shown to illustrate the fact that the OTR emission cone for this electron energy is very large and behaves almost like an isotropic source.

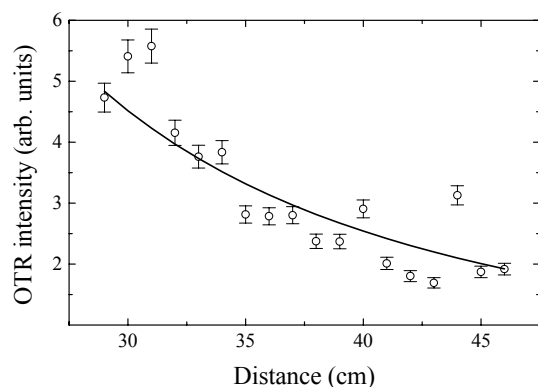


Figure 5: OTR intensity versus distance from the screen.

5 CONCLUSIONS AND PERSPECTIVES

Using the 80keV electron bunch available in the photocathode laboratory, backward OTR emission from an aluminium screen has been observed. Its characteristics, especially its angular pattern, are found to

be compatible with the theoretical expectations. The light intensity is feeble and the light is emitted over a broad angular distribution, 40° FWHM.

In the case of the CTF3 injector, a carbon screen must be envisaged to stand the thermal load induced by the beam. The total reflectivity (diffuse and specular) of our carbon sample has been measured using an integrating sphere reflectometer available at the EPFL in Lausanne. The carbon reflectivity in the visible region is 26% of the aluminium reflectivity, adding thus a limitation to the use of backward OTR. From this point of view, the forward OTR emission, which is not affected by the material reflectivity, could be an interesting option. In this case very thin foils must be used to make sure that multiple scatterings occurring in the screen are not affecting the beam size at the exit interface. Moreover, it is better not to degrade the beam energy since the OTR light yield behaves like β^2 [6] at low energy. The forward and backward OTR lobes are plotted in figure 7 for different tilt angles of the screen.

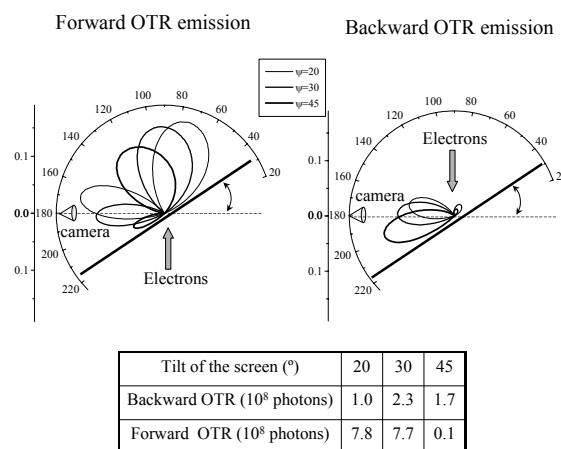


Figure 6: Forward and Backward OTR emission

The total number of photons available ([300-900nm]) for detection is also calculated assuming a detection angle of 20mrad. From the lobe configuration a compromise between the light intensity and the beam aspect ratio to the screen tilt can be found using forward OTR and a 30° angle. Backward OTR, less intense, would allow a better flexibility for the choice of the tilt angle.

6 REFERENCES

- [1] G. Geschonke et al, CERN/PS 2002-008, (2002)
- [2] E. Bravin,, CTF3 note 019, (2001).
- [3] I.M. Frank and V.I. Ginsburg, J. Phys. 9, 353, (1945).
- [4] R.H. Ritchie and H.B. Elridge, Phys. Rev. 126, 1935, (1962).
- [5] A.L. Frank, E.T. Arakawa and R.D. Birkhoff, Phys. Rev. 126, 1947, (1962). H. Boersch, C. Radeloff and G. Sauerbrey, Phys. Rev. Letters 7, 52, (1961).
- [6] L. Wartski, These de Doctorat, Universite de Paris-sud, Orsay, (1976).
- [7] E. Chevallay et al, CTF3 note 020, (2001).
- [8] H.H. Braun et al, CLIC note 487, (2001).

OPTICAL TRANSMISSION LINE FOR STREAK CAMERA MEASUREMENTS AT PITZ

J. Bähr, D. Lipka, H. Lüdecke, DESY Zeuthen, Zeuthen, Germany

Abstract

The photoinjector test facility at DESY Zeuthen (PITZ) produces electrons with a momentum of about 4–5 MeV/c. It is the aim to measure the temporal characteristics of the electron bunch train and single bunches with high accuracy of the order of 1 ps and better. Two types of streak cameras will be used in combination with different radiators which transform particle energy in light. The problem to be solved is the light transport over a distance of about 27 m. Basic demands to the optical system and design principles will be explained. The optical and technical solutions will be presented. The strategy of adjustment and commissioning of the optical system will be described. The system contains switchable optics for the use of different radiators (OTR, Cherenkov radiators). Diagnostic tools are foreseen at different positions along the optical axis. The results of different measurements in the laboratory will be presented. The problems on the minimalization of time dispersion in the system will be discussed.

INTRODUCTION

The photoinjector PITZ [1] at DESY Zeuthen is a dedicated facility for the investigation of rf-guns for future FELs and linear colliders. Different diagnostics methods are used to investigate the characteristics of the produced electron beam. One important goal is the measurement of the bunch length and longitudinal phase space [2] with a temporal resolution of 2ps and 0.2ps respectively limited by the streak camera to be used as basic tool.

A large fraction of the light created by the electron beam hitting or penetrating different radiators has to be transported by the optical transmission line onto the entrance slit of the streak camera. The light transport has to be performed creating minimum time dispersion and minimum light losses.

Radiators

Different radiators are foreseen to be applied basing on the effect of optical transition radiation (OTR) or the Cherenkov-effect. At a maximum beam momentum of currently about 4.7 MeV/c OTR results in a rather weak signal with a wide emission cone. Therefore the application of the Cherenkov effect will be the main method. A thin quartz plate and silica aerogel of a refractive index of $n = 1.03$ will be the first radiators to be investigated.

Streak Camera Data

Two types of streak cameras both from Hamamatsu are foreseen to be applied in the measurements.

The time resolution of the device C5680 is about 2 ps. The device is sensitive in the visible range and near UV and has a fiber-optical output by which the image is transmitted to the CCD. It has a synchroscan option and an internal gain of about $3 \cdot 10^3$.

The second streak camera available is FESCA-200 with a time resolution of 200 fs working in the single shot mode.

Principle of Optical Transmission line

The principle of the optical transmission line consists in an optical transport of a part of the light created in the radiators by imaging the created light distribution onto the entrance slit of the streak camera. The optical system consists mainly on a chain of telescopes.

Design Principles

A few basic design principles for the optical transmission line are listed below.

- Collect a maximum of created light (depending on the optical input scheme)
- Transmit the light over large distance (27 m) using telescopes
- Project the transported light onto the entrance slit of the streak camera
- Match between the collecting optics and the transmitting optics on one hand and between the transmitting optics and the demagnifying optics before the slit otherwise
- Make an aperture match between the optical sub-system before the entrance slit and the streak camera internal optics
- Minimize the number of optical elements, maximize transmission
- Optimize optical resolution
- Fix wavelength range
- Fix maximum object distribution

INPUT OPTICAL SCHEMES

Two different optical schemes are used to match different emission characteristics. A high aperture lens system is used to collect a moderate part of the emission cone of the OTR light and of the cone of low refracting silica aerogel (see Fig.1). Subsequent imaging by telescopes takes place.

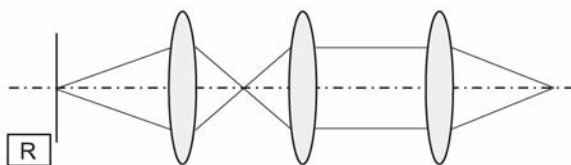


Fig.1: High aperture input scheme, (R: radiator)

For larger cones produced by Cherenkov radiators like quartz and higher refracting silica aerogel only a segment of the full cone is used and transmitted. A quasiparallel bundel is selected out of the cone and projected into the rear focal plane of the first lens. This light is then transmitted by a sequence of telescopes (see Fig.2).

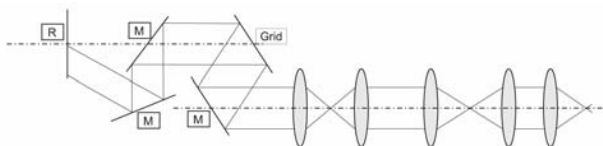


Fig.2: Scheme of cone sector imaging, (R: radiator, M: mirror)

The phase error caused by selecting a sector of the Cherenkov cone is foreseen to be compensated by use of a reflection grid [2] (principle see Fig.3).

SWITCHABLE OPTICS

A box containing three schemes of switchable optics is available and will be positioned just outside the vacuum window. One can switch between three branches of input optics:

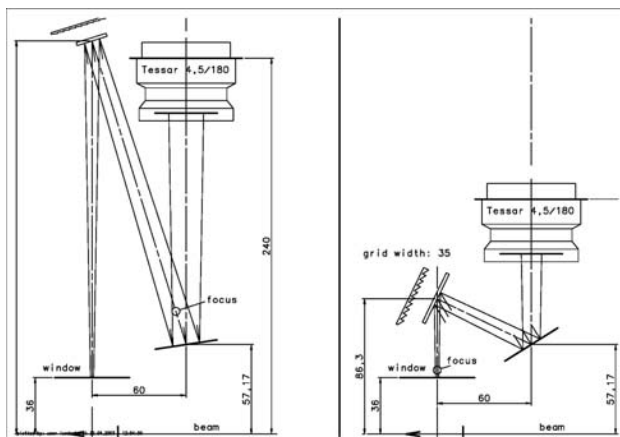


Fig. 3: Scheme using reflection grating

- A high aperture lens system 1.5/75mm for collecting part of the full cone of light emitted by OTR and the lowest refracting silica aerogel
- A scheme of reflection grating, mirror and first lens for a quartz plate radiator

- A system also consisting of a different reflection grating, mirror and first lens for higher refracting silica aerogel

The latter two systems are shown in Fig.3.

The movable optical elements are mounted on precise tables driven by air pressure.

The full scheme of the switchable optics is shown in Fig.4.

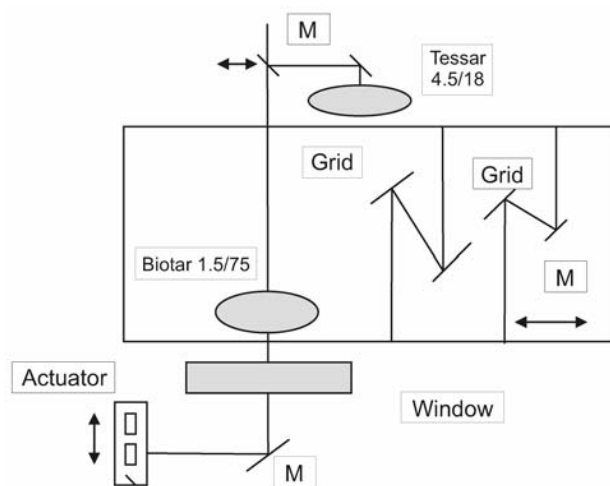


Fig.4: Scheme of switchable optics, (M:mirror), the actuator carries the radiators in vacuum

DESIGN RESULTS

As result of the designing activity the scheme shown in Fig. 5 was developed. It consists of the input optical scheme (switchable optics) and five telescopes. The basic values of the optical elements are shown in the table of Fig.5.

General Layout

	Radiator	T1	T2	T3	T4	T5
f	75 360	A	A	A	A	180 75 210 50
M	2	6.3	1	1	1	0.4 0.24
f(no)	1.5 4.5	16	16	16	16	4.5 4.5 4.5 1.8

A: Achromat f=2250mm, 140mm diameter
 f-number: f(no) = f/D, M: Magnification
 f: focal length D: lens diameter Ti: Telescope

Fig. 5: Scheme of the full optical transmission line

The full system will be closed by tubes to avoid straylight and background illumination. The optical transmission is restricted to the visible range to avoid the use of expensive UV optics. The object size is restricted to a diameter of 2 mm to avoid vignetting of the inclined bundels from off-axis points. The optical resolution is

aimed for at least 10 Lp/mm (corresponds to 100 microns).

OPTICAL RESOLUTION

The optical resolution of sub-systems of the optical transmission line was measured. The results are shown in Table 1. From these measurements an optical resolution of about 35 Lp/mm was estimated for the whole system which fulfills by far the design specifications.

Table 1: Optical resolution of sub-systems

L1	L2	L3	L4	L5	L6	L7	Magn.	Resol. Object Lp/mm	Resolut. Image Lp/mm
B1.5/75	T360	A					12.6	160	12.7
A	A						1	10	10
A	A	T180	T75	T210	P1.5/50		0.1	3.3	33
B	T360	A	T210	T70	T180	P	1.2	45	38
B1.5/75: Biotar 1.5/75							A: Achromat 2250		
T180: Tessar 4.5/180 (all tessars f-number 4.5)							P: Pancolar 1.5/50		

DISCUSSION OF TIME DISPERSION

One of the main goals of the design is a minimum contribution to time dispersion by the optical transmission line. Therefore mainly highly corrected systems are used as elements of the system, following the assumption that these elements having small transverse aberrations should have also small longitudinal aberrations. Time dispersion results immediately from longitudinal aberrations. It is foreseen to measure the contribution of the optical elements to the time dispersion in the optical system by using the PITZ laser beam coupling it into the optical system at different positions. In future a replacement of refracting elements by reflecting optics is an option of minimizing the time dispersion of the system.

ADJUSTMENT AND DIAGNOSTICS

High accuracy of alignment and diagnostics systems are preconditions for the proper quality of the optical system. The adjustment procedure is described in a separate manual which is too long to be described in this paper. Only general adjustment principles are explained below. The adjustment will be performed using different tools, like a laser, diaphragms and resolution charts in two cycles, first for the mirrors and after that for the lenses. Thereby the right position of the optical axis, the position of the optical elements, the proper focus and image position and the maximum of optical resolution are the adjustment goals. The test of the proper function of the optical transmission line can be realized by four kinds of diagnostics tools. They can be divided in two categories: transmitters and receivers. Light emitting diodes and back-illuminated resolution charts are used as transmitters, photomultipliers and TV-cameras are used as receivers. The four kinds of elements are mounted in diagnostics boxes, see Fig.6. There are four positions

along the optical axis where such diagnostics elements are positioned. The diagnostics boxes are integrated in the tube construction. The active elements can be inserted manually in the active position.

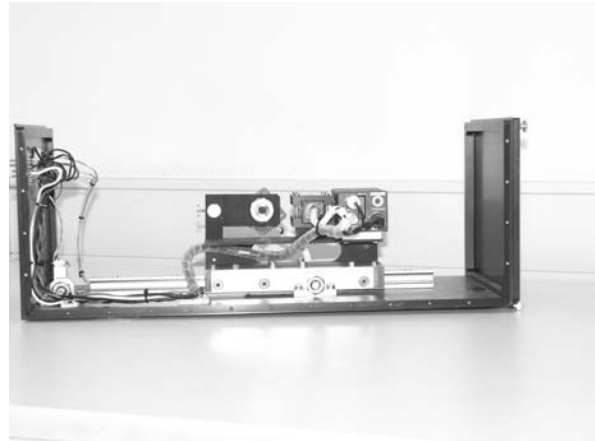


Fig.6: Diagnostics box

OUTLOOK

The commissioning of the optical transmission line is scheduled for end of May 2003. Practically all hardware elements are prepared. First measurements will start in June 2003. A similar read-out port will be realized in fall 2003 for the dispersive arm. For this port the task is to measure the full longitudinal phase space including the correlations therein. That means, not only the time characteristics have to be measured by streak camera but the momentum spectrum has to be projected onto the slit of the streak camera. This more complicated system is designed currently. The read-out will be performed by a special branch which is then matched to the main part of the optical transmission line described in this paper. In 2004 PITZ will be extended by a booster cavity. For this a complex diagnostics section is foreseen which contains several optical branches for streak camera readout of both types described. In future the application of reflective optics instead of lenses might be an option to minimize the time dispersion.

REFERENCES

- [1] F.Stephan, et al., Photo injector test facility under construction at DESY Zeuthen, FEL 2000, Durham.
- [2] D.Lipka et al., Longitudinal phase space measurements at PITZ, EPAC 2002, Paris.

AN IMPROVED PLL FOR TUNE MEASUREMENTS

O.Berrig

CERN AT/MTM, Geneva, Switzerland

Abstract

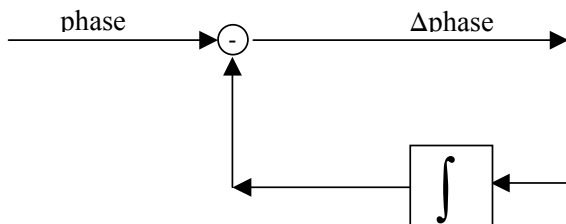
Phase locked loop (PLL) systems are being used on several machines for continuous tune measurements. All these implementations are based on a continuous sinusoidal beam excitation and a monitoring of the resulting beam oscillation.

The key element determining the dynamic performance of such a PLL is the phase detector between the beam oscillation and the internal oscillation. Most circuits use a quadrature phase detector, for which the high frequency carrier at twice the excitation frequency is attenuated by a low-pass circuit. The remaining ripple of this component contributes to the bandwidth/noise performance of the PLL.

In this paper we propose an alternative solution for the filter, notably an adaptive notch filter. We explain in detail design considerations and the resulting improvements in PLL bandwidth and/or noise figure.

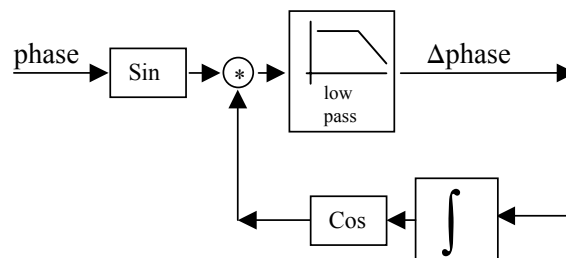
1 PLL BASICS

The following diagram shows the “raw” PLL:

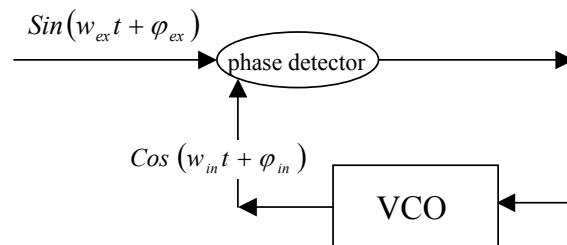


The definition of phase only has meaning when linked to a sine function. Since the sine function, which the PLL is locking on, is normally embedded within many other sine functions, only that phase should be extracted and the phases from the other sine function must be suppressed.

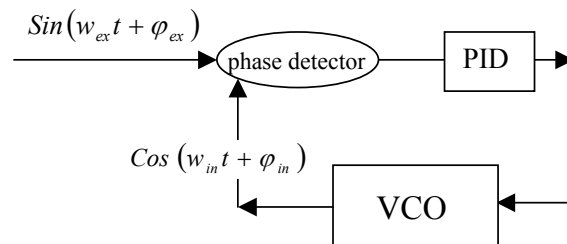
The phase difference could be extracted from the input sine function in a way similar to a Fourier integral, which is a very good filter. Assuming that the amplitude of the external sine has been normalized to 1 (e.g. by an amplitude regulation loop), the PLL becomes:



We can now introduce the concept of “phase detector” and VCO (Voltage controlled Oscillator):



Often a PID regulation is added (or in some cases, combined with the phase detector filter), which allows locking on widely varying input frequencies:



When the PLL is locked, the two inputs of the phase detector are 90 ° out of phase or “in quadrature”.

2 WHAT IS THE PROBLEM?

The output of a quadrature phase detector has a systematic noise, which limits the accuracy of the PLL. This error varies as $2w_{ex}t$, i.e. the double of the external frequency. The reason lies in the way the phase difference is calculated:

$$\Delta p = \text{LowPass}[2 \cdot \sin(wt + \varphi_{ex}) \cdot \cos(wt + \varphi_{in})]$$

$$\Delta p = \text{LowPass}[\sin(\varphi_{ex} - \varphi_{in}) + \sin(2wt + \varphi_{ex} + \varphi_{in})]$$

(The above equations assume that the PLL is locked and therefore $w \cong w_{ex} \cong w_{in}$)

The Low Pass filter is of course there to remove the term: $\sin(2wt + \varphi_{ex} + \varphi_{in})$. However, it is not perfect and a residue noise signal will be present at the output of the phase detector.

In order to enable the Low Pass filter to reject the $2wt$ noise signal better, one could of course use a higher order filter or lower its cut-off frequency, but both of these methods could have a negative impact on the locking ability of the PLL. E.g. the lowering of the filter cut-off frequency would either lower the bandwidth or lower the damping of the PLL.

The Low Pass filter has several functions:

- It removes the $2w$ noise term
- It removes the other frequency terms of the input signal (in fact it removes the products of these terms and the $\cos(wt + \varphi_{in})$ function)
- Together with the PID regulator, it determines locking capability of the PLL

Therefore, a better way to remove the systematic $2w$ frequency is to include a notch at $2w$ in the Low Pass filter. Since only one frequency is removed, there will be no impact on the other qualities of the PLL.

3 A PROPOSED SOLUTION

A simple way to remove the $2w$ noise is first to use a running average as a Low Pass filter. A running average has a frequency characteristic very similar to a first order filter with a cut-off frequency equal to:

$$w_{cut-off} = 2\pi / T$$

When using a running average as the Low Pass filter, the phase difference can then be recognized as a Fourier integral:

$$\Delta p = \frac{2}{T} \int_{t-T}^t \sin[w_{ex}t + \varphi_{ex}] * \cos[w_{in}t + \varphi_{in}] dt$$

This Fourier integral still has the $2w$ noise. The origin of the noise is a mismatch between the integration time and the frequency. If $T = 2\pi / w$ there would be no noise!

The proposed solution is to subtract the term $\sin(w_{in}t + \varphi_{in})$ from the input signal, and the $2w$ noise will be strongly rejected:

$$\Delta p = LP[2 \cdot \{\sin(wt + \varphi_{ex}) - \sin(wt - \varphi_{in})\} \cdot \cos(wt + \varphi_{in})]$$

$$\Delta p \approx \varphi_{ex} - \varphi_{in} \quad \text{where} \quad \varphi_{in} \cong \varphi_{ex} \wedge w_{in} \cong w_{ex}$$

The actual calculation is then:

$$\Delta p = \frac{2}{T} \int_{t-T}^t (V_{input} - \sin[w_{in}t + \varphi_{in}]) * \cos[w_{in}t + \varphi_{in}] dt$$

NB! w_{in} is kept constant during the integration, which gives a better noise reduction because it excludes any noise from the regulation loop.

The following example is a LEP type PLL, where a phase detector filter of the above type has been added. It is compared to the same PLL where the phase detector filter has been removed but instead a running average filter has been added to the output of the PLL. The two filters have the same integration time in order to have similar regulation characteristics:

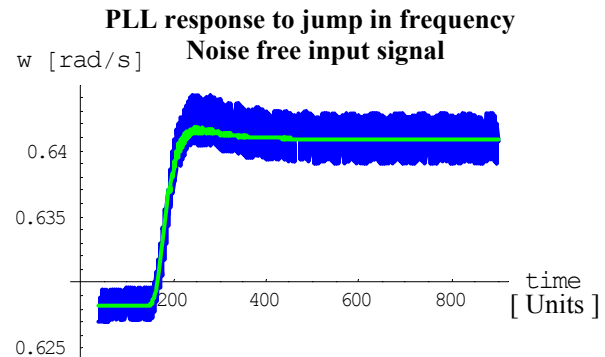


Fig 1. Blue curve: Filtered PLL output.
Green curve: Same PLL but with improved filter put onto the phase detector.

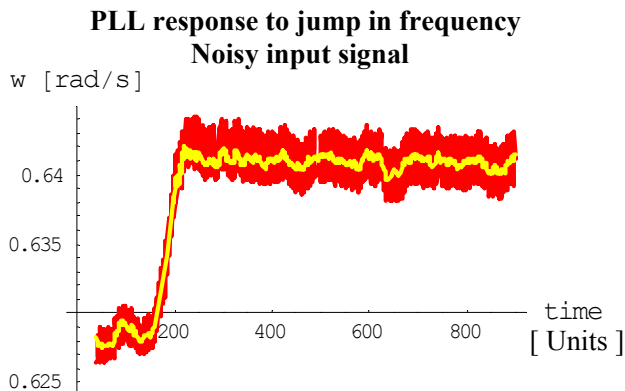


Fig 2. Red curve: Filtered PLL output.
Yellow curve: Same PLL but with improved filter put onto the phase detector.

In Fig.2 the ratio of the standard deviations for the red and yellow curves is ~ 5 i.e. in this example we get a factor 5 reduction in the noise. The less noise in the input signal, the more reduction we get in the 2ω noise signal.

In general one can say that a phase detector filter is better than a filter on the output of the PLL. The reason is that a phase detector filter removes the noise before it enters the regulation, so the noise does not stay in the loop but is removed at the entry.

In the following example, a neighboring frequency ω_n with factor 5 higher amplitude and 0.1 Hz away from the locking frequency is introduced:

PLL response to jump in frequency Noisy input signal and neighboring frequency

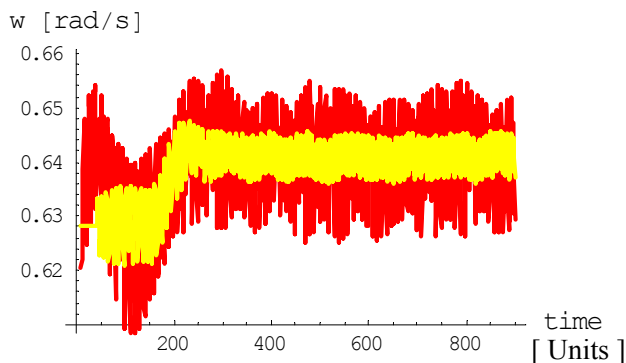


Fig 3. Red curve: Filtered PLL output.
Yellow curve: Same PLL but with improved filter put onto the phase detector.

Calculating the ratio of the standard deviations for the two curves, we get ~ 2.5 i.e. the PLL with the phase detector filter rejects the noise from the neighboring frequency 2.5 times better than the PLL with the filter on the output.

CONCLUSION

It is shown that a PLL with a quadrature phase detector is in the same family as a Fourier transformation.

The main point is to demonstrate that the 2ω noise that is inherent in quadrature phase detectors can be strongly rejected by an adaptive notch in the phase detector filter.

Further more it is shown that having the choice between a filter at the output of a PLL and a phase detector filter, it is better to use the phase detector filter because the noise of the input signal is then removed before it enters the regulation loop.

There is still scope for investigating the reduction of 2ω noise. How much can this noise be reduced as a function of the PLL regulation characteristics? And is it possible to integrate the phase detector filter with the PID regulation and still keep the notch filter?

ACKNOWLEDGEMENTS

I would like to thank A.Burns and H.Schmickler for their inspiration and ideas that helped me to investigate this subject.

REFERENCES

1. K.D. Lohmann, M.Placidi, H.Schmickler: "DESIGN AND FUNCTIONALITY OF THE LEP Q-METER", CERN/SL/90-32
2. O.Berrig: "Improvement of the PLL algorithm for the LEP Q-meter", SL-Note-98-024-BI

REAL TIME MANAGEMENT OF THE AD SCHOTTKY/BTF BEAM MEASUREMENT SYSTEM

M. Ludwig, M. E. Angoletta, CERN, Geneva, Switzerland

Abstract

The AD Schottky and BTF system relies on rapid acquisition and analysis of beam quantisation noise during the AD cycle which is based on an embedded receiver and digital signal processing board hosted in a VME system. The software running in the VME sets up the embedded system and amplifiers, interfaces to the RF and control system, manages the execution speed and sequence constraints with respect to the various operating modes, schedules measurements during the AD cycle and performs post processing taking into account the beam conditions in an autonomous way. The operating modes of the instrument dynamically depend on a detailed configuration, the beam parameters during the AD cycle and optional user interaction. Various subsets of the processed data are available on line and in quasi real time for beam intensity, momentum spread and several spectrum types, which form an important part of AD operation today.

INTRODUCTION AND OVERVIEW

Functional Overview

Beam diagnostics based on measurement of beam quantisation noise are principally nondestructive and therefore have always played an important role for antiproton machines at CERN. The Antiproton Decelerator's (AD) beam consists of a few 10^7 particles which have to be measured with sufficient precision at all frequencies on the flat tops and the ramps during an AD cycle (Fig. 1), with either bunched or randomly coasting beam.

The system hardware consists of longitudinal pick ups (measurement of beam intensity N and momentum spread dp/p), controllable signal amplifiers, an ADC and eight digital receivers controlled by a digital signal processing stage (DSP) hosted in a dedicated VME board (DRX) [1] and synchronised real-time software (RTT) running in the DSC (see [2] for in-depth description). For optional beam transfer function measurements (BTF) (measurement of transversal tune) which can be scheduled independently anywhere during an AD cycle a transversal Pick up and a controllable coloured noise generator for beam stimulation [3] are used. The RTT continuously

schedules measurements, sets up the system hardware, post-processes the data and communicates up-stream. The system is expected to always run, auto-adapt itself to the beam parameters and conditions, be highly configurable for machine development sessions and permanently produce on-line results which must be available for at least three AD cycles.

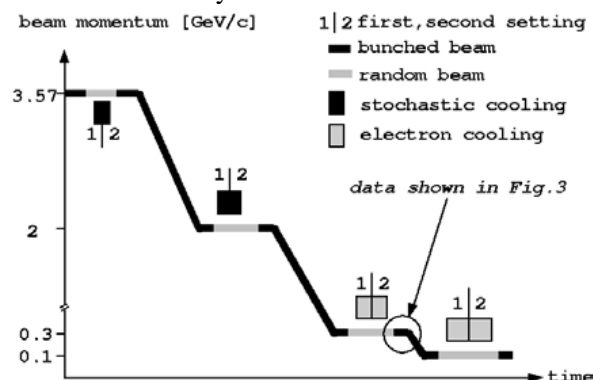


Fig.1: the beam momentum (black/grey trace) during an AD cycle, where the beam is bunched (black) or de-bunched (grey). Stochastic (black square) and electron cooling (grey square) on the flat tops all require different instrument settings. BTF measurements can be made on any ramp or flat top.

Structural Overview

The main logical components of the system with respect to the front-end software are shown in Fig. 2 together with directed and synchronised information flows. Analogue signals generated by three pick ups in each beam-plane enter the amplifier and signal mapping hardware. This hardware receives configuration for gain, filter, input and mapping of pick ups to amplifier channels organised in a table of settings which is stepped through depending on the revolution frequency (f tables, Fig. 2). It receives this configuration at times which are determined by the conditional clock and beam logic unit (CBL) as indicated by a many dimensional data flow arrow. The CBL is an eight-dimensional looping counter which steps down each 20ms clock tick (T_x , interrupts received from an external source) and is realized as software structure. It maps to the eight receivers and inhibits (according counter > 0) or releases (according counter $= 0$) the many

dimensional data flows. The CBL selects one process parameter set (PPA) for the DRX and one eight-dimensional counter setting for itself out of many configurations, and one setup for the amplifiers from the frequency table. This selection depends on the CBL counter values and on four external informations: T_x , f_{rev} , the beam bunched or de-bunched condition and the status of the stochastic and electron cooling systems (on or off).

The data from the set of receivers which participate in a particular measurement is read out, post-processed (see [2]) and the next measurement involving these receivers is started when the according data flows are released by the CBL. When the processing for any of the results is finished the timestamped values for N , dp/p , f_{rev} , schottky spectra and in the case of BTF measurements also correlation and noise stimulation data are released into the (circular) history buffer where they persist for at least three AD cycles. Control system standard communication software provides access to the history buffer for a graphical instrument interface in the control room offering views on selected data subsets and editing of instrument configurations.

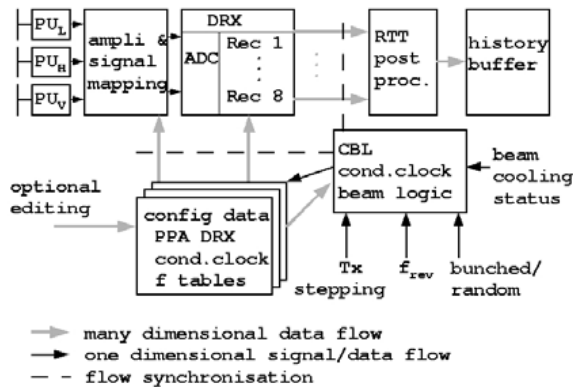


Fig. 2: system information flow overview showing the logical components in the front end software.

REQUIREMENTS, CONSTRAINTS AND CONTROLS

Repetition Rate

In order to study and survey the AD deceleration efficiency the repetition rate of the measurements has to be as high as possible. The time each single de-bunched beam measurement needs is determined by the settings of bandwidth, number of averages needed on an observation harmonic (where the pick ups and electronics have maximum performance for the given beam conditions) and the type of processing performed in the DRX, as shown in Table 1. For bunched beams the overall

execution time is kept below 20ms¹ by optimizing the ADC sampling clock for each measurement individually. Each row of Table 1 corresponds to a PPA for the beam condition and to a CBL setting, which determines the execution time for the receivers concerned by this measurement.

Table 1: settings used for different beam conditions, frequency spans wide sp1 (and additionally narrow for de-bunched beam sp2), observation harmonic n , number of averages (avg) for instrument setting 1 and 2 and their total execution time.

beam [GeV/c], condition	sp1 (sp2) [Hz], n [1]	avg [1]	execution time [ms]
3.57, bunched	14k, ~1	1	20
3.57, debunched	5000 (2000), 5	50	2200
2, bunched	14k, ~1	1	40
2, debunched	7000 (3500), 10	53	1460
0.3, bunched	14k, ~3	1	40
0.3, debunched	3600 (2500), 4	36	1920
0.1, bunched	14k, ~1	1	40
0.1, debunched	1500 (1000), 9	10	1400

Autonomous instrument

Taking into account the beam conditions which are likely to be encountered during an AD cycle sets of optimized settings can be found beforehand. Since the f_{rev} which is acquired from the RF system is not available during the flat tops it must be inferred from a look-up table. Furthermore the ADC sampling frequency must be kept proportional to f_{rev} and close as possible but below the maximum rate of 40MHz for each measurement on bunched beam, or kept fixed at 40MHz for de-bunched beam.

In the middle of any ramp the instrument configuration is switched from the previous flat top's bunched setting to the next flat-top's bunched settings with respect to the revolution frequency, with a relatively wide span. During the beam cooling on any flat top the initial wide span (sp1) is narrowed down (to sp2) when a certain percentage of the cooling time has passed (1st and 2nd settings in Fig.1).

Configurable instrument

The configuration data sets shown in Fig. 2 are activated following the inputs of the CBL and are subject to complex real-time constraints,

¹we often schedule with 40ms to decrease the amount of data

nevertheless they can be edited in order to adapt to changing requirements and to schedule single-shot BTF measurements at any time during the cycle. Any changes are read by the RTT once every few seconds and are activated in the system components when the according data flow gets released by the CBL, therefore the ongoing measurement and processing are not disrupted.

RESULTS

The data generated by the system for one AD cycle can reach many MBytes depending on the configuration but the control system should not have to sustain such a data rate for on-line visualisation, also the machine physicist is interested only in the subset of data related to the phenomenon under study. Therefore the non-synchronised standard communication software must rely on built-in knowledge about the measurement types and timestamps in order to select data subsets on request from the history buffer.

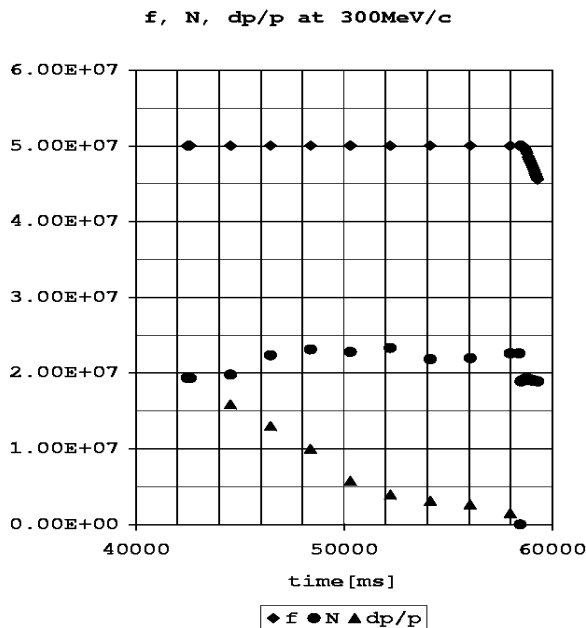


Fig.3a: data taken on 24 Sept 2002 at the end of flat top 300MeV/c: diamonds: f_{rev} [1/100 Hz]; circles: N [1]; triangles: dp/p [1e-10], injection $t=0$. The beam is bunched again at 58460ms.

The Fig. 3a shows the f_{rev} , N and dp/p at the end of the 300MeV/c flat top as indicated in Fig.1, with a measurement repetition rate of 1920ms (Table 1) for de-bunched beam and a high repetition rate of 40ms the beginning of the ramp. The dp/p , which is available only for de-bunched beam measurements, decreases during beam electron cooling on the flat top. Variations observed for N reflect uncertainties of 20% for de-bunched beam, the first

measurement on bunched beam is rejected (set to 0.0) due to strongly deformed bunches. The zoomed view on the same data (Fig. 3b) shows again a stable beam intensity around $1.9e7$ with better than 5% uncertainty for decreasing f_{rev} offering high temporal resolution.

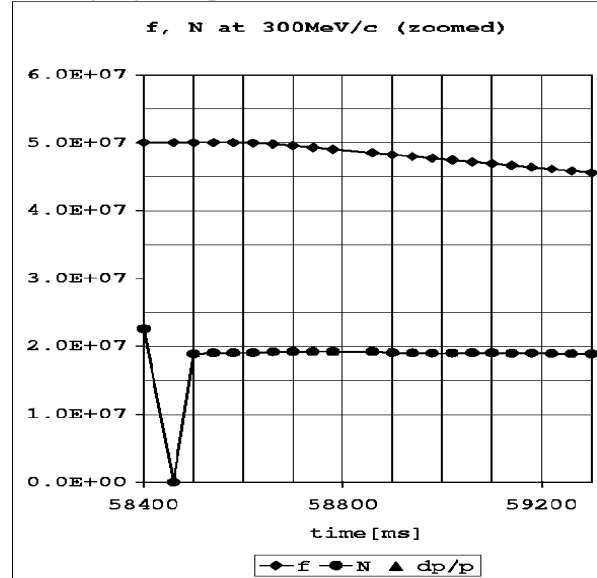


Fig. 3b: zoomed view on the data of Fig.3a (bunched beam) which shows the high temporal resolution for bunched beam measurements.

CONCLUSION

The dependency of the system settings on the beam conditions was translated, in the case of the AD, to a dependency on revolution frequency (and therefore time) and a few external conditions which drive a conditional beam logic unit. Both requirements of being highly configurable and completely autonomous are met, and a high temporal resolution is realized.

REFERENCES

- [1] M. E. Angoletta, V. Chohan, M. Ludwig, O. J. Marquersen, F. Pedersen, "The new digital-receiver-based system for antiproton beam diagnostics," PAC2001, Chicago Illinois, USA, 18-22 June 2001.
- [2] M. E. Angoletta, L. Bojtar, V. Chohan, A. Findlay, M. Ludwig, O. Marquersen, F. Pedersen, "Antiproton Beam Parameters Measurement by a new Digital-Receiver-Based System," CERN PS 2001/16, Geneva, Switzerland, 4. April 2002.
- [3] M. E. Angoletta, M. Ludwig, N. Madsen, O. Marquersen, F. Pedersen, "Real-Time Tune Measurements on the CERN Antiproton Decelerator," DIPAC 2001, Grenoble, Proceedings p.99.

RECENT ADVANCES IN THE MEASUREMENT OF CHROMATICITY VIA HEAD-TAIL PHASE SHIFT ANALYSIS

N. Catalan-Lasheras, S. Fartoukh, R. Jones[#], CERN, Geneva, Switzerland

Abstract

A so-called "Head-Tail" monitor has been operational in the CERN-SPS for a few years. The measurement of chromaticity using such a monitor relies on the periodic dephasing and rephasing that occurs between the head and tail of a single bunch for non-zero chromaticity. By measuring the turn-by-turn position data from two longitudinal positions in a bunch it is possible to extract the relative dephasing of the head and the tail, and so to determine the chromaticity. Until recently this technique had suffered from an unexplained "missing factor" when compared to conventional chromaticity measurements. This paper explains the source of this factor and also reports on the considerable experimental, simulation and analysis effort that has qualified the technique for use in the LHC.

INTRODUCTION

The determination of chromaticity by following the evolution of head-tail phase shifts after a transverse dipole excitation is a technique which does not rely on an accurate knowledge of the fractional part of the betatron tune and, for a machine operating well above transition, is virtually independent of beam energy.

Early experiments in the CERN-SPS [1] and at HERA-p (DESY) [2] have shown the feasibility of the technique for high-energy proton beams. More recent experiments [3] have highlighted several questions concerning the use of this technique for accurate chromaticity determination. The most important of these concerned a constant factor that appeared between the calculation of chromaticity via traditional techniques and that which was calculated from head-tail phase shift measurements. Here the source of this "missing factor" is explained and a method of correction is outlined. In addition this paper seeks to summarise the extensive theoretical work carried out on this technique [4] aimed at validating the robustness of the method for the LHC.

EXPLAINING THE "MISSING FACTOR"

A complete description of the detection and acquisition system can be found in [3]. A schematic of the layout can be seen in Fig. 1. All the results to date have shown discrepancies between the value of chromaticity measured via head-tail phase shifts and the traditional technique of tune tracking during energy modulation (referred to in the SPS as radial steering chromaticity measurements). A typical plot from such a comparison performed at the SPS is shown in Fig. 2. It can be seen that the head-tail results are consistently lower than the actual value, requiring a

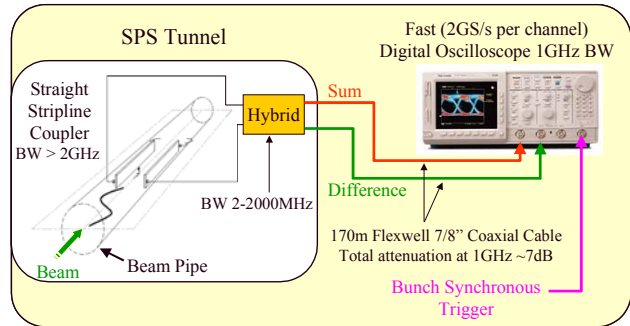


Figure 1. Schematic layout of the head-tail monitor in the CERN-SPS showing the various bandwidth limitations.

correction factor of 1.4, which remains essentially constant with chromaticity. The dotted line shows the trend of the head-tail measurements when corrected for this error, which is now seen to be in very good agreement with that measured using energy modulation.

In order to understand the origin of this correction factor, a more detailed study of both the underlying physics of the head-tail phase shift and the acquisition hardware associated with the head-tail monitor was initiated the results of which are presented in detail in [4].

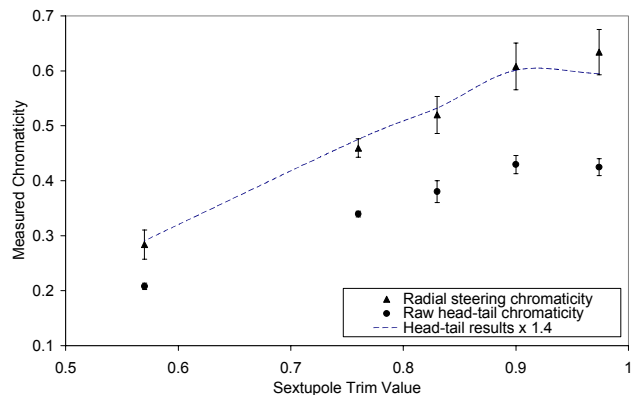


Figure 2. A comparison of head-tail and radial steering chromaticity, measured at 303GeV on the CERN-SPS.

These investigations showed that the source of the correction factor was the bandwidth limitations in the experimental set-up (indicated in Fig. 1). The main analogue contribution came from the 170m of cable connecting the hybrid in the SPS tunnel with the acquisition electronics. In addition, the 2 GS/s sampling rate of the oscilloscope reduces the upper frequencies that can be resolved without aliasing after digitisation to around 500 MHz. To see the effect that such bandwidth

[#]Rhodri.Jones@cern.ch

limitations have on the head-tail measurements, simulations were performed using PSpice with tracking data at input. The resulting chromaticity measurement was found to give a lower value than the original simulation, requiring a correction factor of ~ 1.3 . This was close to the factor of 1.4 found in the real SPS data, and pointed to the cable bandwidth limitation as the main reason for the “missing factor”. A simulated delta signal where the head and tail are oscillating out of phase is shown in Fig. 3(a). Also plotted is the resulting signal after having passed through the coupler and cable for both 2 GS/s and 8 GS/s digitisation rates. The effect of the limitations in the bandwidth is clearly shown as an elongation of the original signal (the second, inverted pulse comes from the reflection due to the coupler pick-up).

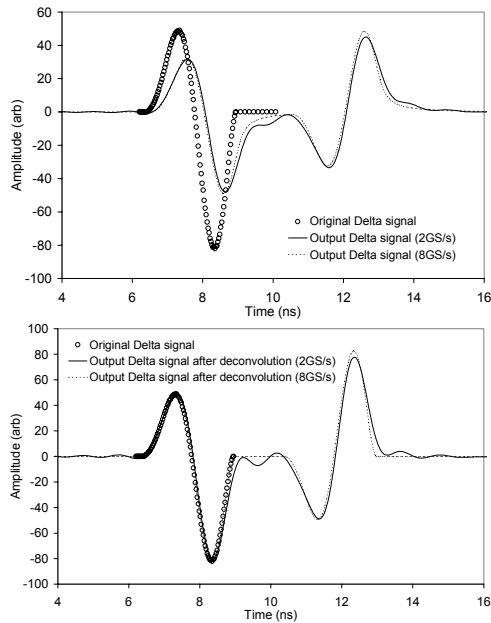


Figure 3. (a) The effect of cable bandwidth and sampling rate on an input delta signal. (b) The result of deconvolving the output signal with a known cable response for two different sampling rates.

On the basis of this evidence a deconvolution routine was added to the head-tail analysis program to take into account the attenuation and phase variations due to the cable. Fig. 3(b) shows the result of deconvolving the output signals shown in Fig. 3(a) with the known simulated cable response. For a sufficiently high sampling rate (8 GS/s in this case) it can be seen that the original signal is perfectly reproduced, as would be expected.

THE EFFECT OF ACCELERATION

Asymmetric Head-Tail Measurements on Accelerating Buckets

During acceleration, the deformation of the bunch alters the way in which the head and tail change phase.

Calculations using a simple two particle model have shown that the phase change at the head of the bunch is reduced, while that at the tail is increased. This can be expressed in terms of a scaling factor with respect to the expected maximum phase difference ($\Delta\psi_{\max,lin}$) obtained between any two slices in the bunch for a stationary bucket.

$$\Delta\psi_{\max}(\hat{\tau}) = S(\hat{\tau}) \Delta\psi_{\max,lin}(\hat{\tau}) \quad (1)$$

Fig. 4(a) shows the result of this for various synchronous phases of the RF when phase difference is calculated asymmetrically between the head and centre or centre and tail. It is clear from these results that an asymmetric measurement on an accelerating bucket can lead to large errors in the calculated chromaticity.

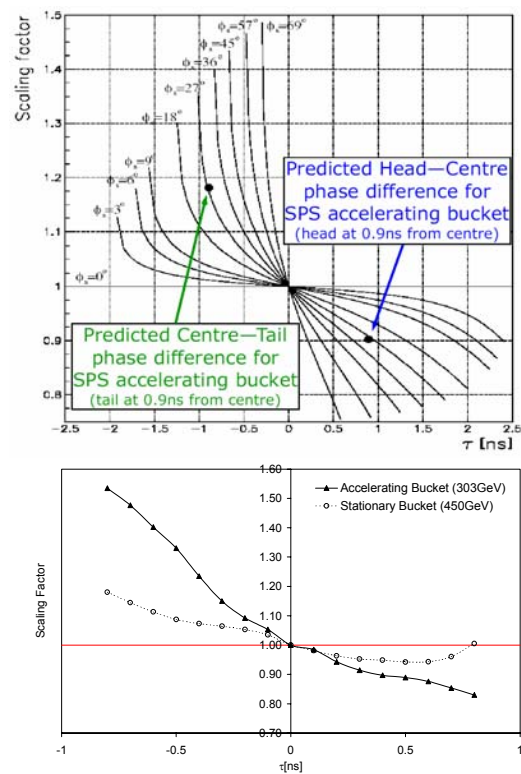


Figure 4. (a) Scaling factor $S(\tau)$ as defined in Eq. 1 for a 200 MHz RF system and different values of the synchronous phase. (b) Results from the SPS for an accelerating and stationary bucket.

The results of the simulations were compared to measurements taken at the SPS (Fig. 4(b)). In the case of the stationary bucket it can be seen that there is only a slight effect on the value of chromaticity even when the head or tail reach the extreme edges of the distribution, where the effects of non-linear synchrotron motion become important (which was not taken into account in the simulations). However, for the accelerating bucket there is a marked difference between measurements taken at the head of the bunch and those taken at the tail. A comparison with the simulations of Fig. 4(a) show a good agreement in the general trend of the scaling factor, with

the measured factor being somewhat larger than that predicted.

Symmetric Head-Tail Measurements on Accelerating Buckets

If one now considers symmetric head-tail measurements, i.e. calculating the phase difference between two positions located symmetrically about the bunch centre, then one obtains the results shown in Fig.5(a). Here the scaling factor $S_{\text{sym}}(\tau)$ is defined as:

$$S_{\text{sym}}(\tau) = [S(\tau) + S(-\tau)] / 2 \quad (2)$$

with $S(\tau)$ being the scaling factor defined in Eq 1. It can be seen that the error resulting from such symmetric measurements is very small for head/tail positions relatively close to the bunch centre.

The experimental results obtained from the SPS for a stationary and accelerating bucket are shown in Fig 5(b). For the stationary bucket there is no significant error up to head/tail positions of 0.6ns. After this the error increases, probably due to the residual imperfections and noise in the acquisition system. The general trend for the accelerating bucket is also in agreement with that obtained by calculation. However, for a reason which is not clearly understood, the overall scaling factor is found to be significantly larger than that predicted by the simulations.

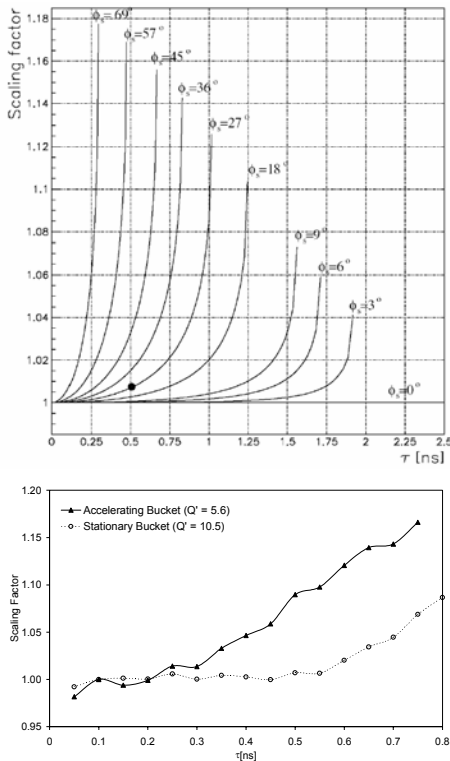


Figure 5. Scaling factor $S_{\text{sym}}(\tau)$ as defined in Eq. 2 for a 200 MHz RF system and different values of the synchronous phase.

CONCLUSIONS AND OUTLOOK FOR THE LHC

On the experimental side, both the method and acquired data is now much better understood. The addition of the deconvolution routine into the analysis algorithm to take account of cable attenuation has significantly reduced the “missing factor” between the head-tail and traditional chromaticity measurements.

In agreement with the simulations, it has been experimentally verified that the method is applicable both for stationary and accelerating buckets with the constraint that the measurement is performed close to and symmetrically about the bunch centre.

In addition, dedicated calculations have been performed for the LHC to take into account other possible causes of perturbation. Simulations of the effects of second and third order chromaticity show that even for the most pessimistic case the error introduced is less than 0.2 units of chromaticity. A 20% off momentum beta-beating and linear coupling (if arc-by-arc compensated as foreseen in the LHC) have also been shown to give very little perturbation to the measurement. Finally, an extrapolation of SPS data taken at 26 GeV seems to indicate that, at nominal current, the accuracy of the head-tail chromaticity technique should practically not be affected by the transverse impedance of the LHC ring.

For the future, a new system working with sampling rates of up to 10 GS/s will be installed in the SPS. It is hoped that this increase in the sampling rate along with the continued deconvolution of the cable response will completely eliminate the residual “missing factor”. In addition, closed orbit compensation electronics will be added to improve the sensitivity of the acquisition and allow the measurement to be made with much smaller excitation amplitudes.

REFERENCES

- [1] D. Cocq, O. R. Jones, H. Schmickler, “The Measurement of Chromaticity via a Head-Tail Phase Shift” presented at BIW’98, Stanford, CA, USA, May 1998.
- [2] A. Boudsko, O. R. Jones, H. Schmickler, M. Wendt, F. Willeke, “Chromaticity Measurements at Hera-p using the Head-Tail Technique with Chirp Excitation”, presented at DIPAC’99), Chester, UK, May 1999.
- [3] R. Jones, H. Schmickler, “The measurement of Q' and Q'' in the CERN-SPS by head-tail phase shift analysis” (CERN-SL-2001-020-BI), presented at PAC2001, Chicago, IL, USA, June 2001.
- [4] S. Fartoukh, R. Jones, “Determination of Chromaticity by the Measurement of Head-Tail Phase Shifts: simulations, results from the SPS and a robustness study for the LHC” (CERN-LHC Project Report 602).

DIAGNOSTICS FOR ELECTRON COOLED BEAMS

G. Tranquille, CERN, Geneva, Switzerland

Abstract

Nearly all modern storage rings use an electron cooling device to increase the phase space density of the circulating beam before its transfer to another accelerator or the experiments. For fast and efficient cooling, the properties of the electron and hadron beams need to be monitored before, during and after the cooling process.

In this paper we review the various techniques, both destructive and non-destructive, used to measure and optimise the different parameters that determine the quality of the cooling.

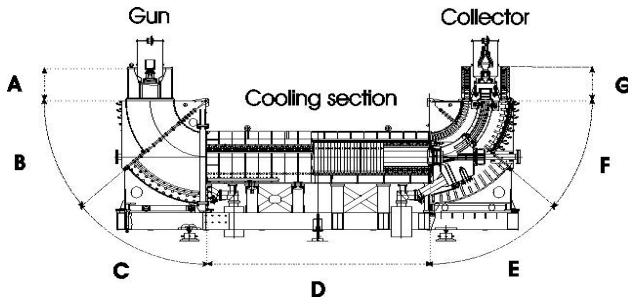


Figure 1: Electron cooler layout.

DIAGNOSTICS FOR THE ELECTRON BEAM

A typical electron cooling device (fig. 1) consists of three parts: i) the electron gun, where an intense and mono-energetic electron beam is generated, ii) the interaction region, where the cooling of the circulating beam takes place through Coulomb interaction between the electrons and the ions, and iii) the collector, where the electron beam is decelerated and the beam power recuperated. The whole system is immersed in a strong longitudinal magnetic field, which is needed to counteract the space-charge force of the electron beam [1].

The cooling time τ can be approximated by the following formula:

$$\tau = \frac{0.6\pi \cdot^2 A \beta^4 \gamma^5 \theta^3}{\eta I_e Z^2},$$

where η is the fraction of the ring occupied by the cooler, I_e the electron current, θ is the relative difference in angle between the electrons and ions ($\theta = \theta_i - \theta_e$, where θ_i is the ion beam angle, θ_e the electron beam transverse temperature $v_t/v_{||}$), A the atomic mass, Z the charge state of the ions and $\beta\gamma$ the relativistic factors. From the above formula the following parameters of the electron beam should be known: i) the electron current, ii) the beam position, iii) the velocity (both in magnitude and direction), iv) the longitudinal energy spread and v) the transverse energy. It is worthwhile to note that these parameters vary with radial position and also in the axial direction.

Beam destructive methods

Probes inserted into the electron beam will in most cases immediately melt or evaporate. The power-density load is such that the absolute limit in the energy of the electron beam is 20 keV when one considers such methods. In fact 10 keV seems more realistic unless the electron beam is pulsed.

Such devices also change the space-charge fields and self-fields of the electron beam resulting in measurements that may not necessarily reflect the real beam distribution. The current intersected by the probe is also an additional load on the high voltage power supply and hence can only be used at low electron beam currents.

Faraday cups, scintillation screens and pinhole collimators

The beam position and current density can be measured as a function of radial position and axial distance by the use of a water-cooled Faraday cup [2]. If a phosphor screen coupled to a camera is used, then one obtains a direct image of the current density distribution of the electron beam (fig. 2).

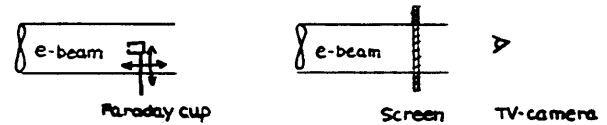


Figure 2: Electron beam measurement with a Faraday cup or scintillation screen.

By inserting a moveable pinhole collimator in the measurement system, a ‘pencil beam’ is generated and one obtains information on the divergence of the electron beam. This parameter is of the utmost importance for electron cooling as it gives a measure of the straightness of the guiding magnetic field.

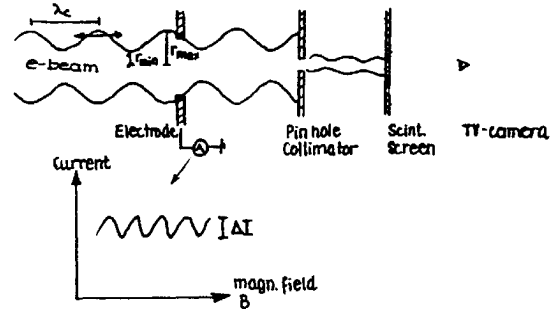


Figure 3: Measurement of the electron beam ripple.

Measurement of the beam ripple

The cyclotron motion of the electron is superimposed on a slow drift rotational motion caused by the crossed space-charge electric field and the longitudinal magnetic field. These two motions cause the electron beam radius

to oscillate in the axial direction with the Larmor wavelength. When changing the magnetic field, the change in beam radius can be measured as a current falling onto an iris shaped electrode (fig. 3). Since the variation in current is related to the Larmor radius, $r_L = \frac{1}{2}(r_{\max} - r_{\min}) = 2\Delta I/I$, it is possible to extract the transverse energy of the electron beam $E_t = \frac{1}{2}m(r_L\omega_c)^2$.

Cross wires

For low power density electron beams, cross wires [2] can be used to determine the beam position, size and density distribution. A thin tungsten wire that is made to intersect with the electron beam becomes incandescent and a camera can view the light given off. To measure the density distribution, the current on the wire can be recorded as a function of the radial position of the wire. This technique was used to validate the principle of a variable density electron gun for the IMP-Lanzhou electron cooling device (fig. 4).

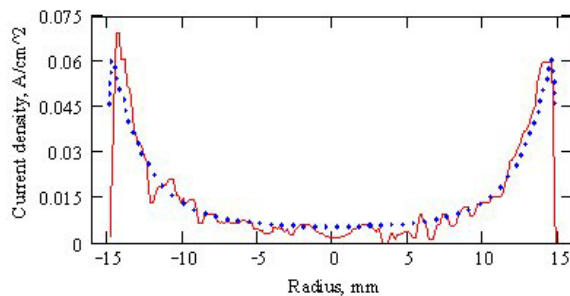


Figure 4: Electron beam density distribution measurement with a cross wire. The dots represent the calculated values and the solid line the measured distribution.

Non-destructive methods

A number of non-destructive methods for measuring the electron beam parameters exist and amongst the different methods the following have been tried on many cooler synchrotrons: i) electrostatic pick-up electrodes, ii) microwave radiation, and iii) laser beam diagnostics.

Pick-up electrodes

Cylindrical electrodes [2] situated inside the electron cooler vacuum chamber can be used to accurately determine the mean position of the electron beam. Electron beams used for cooling are DC, and thus have to be intensity modulated by applying a sinusoidal variation on the accelerating voltage for a signal to be measured on the pick-up. Gain switching of the head amplifiers enables the pick-up stations to also measure the position of the ion beam in the interaction region. In this way alignment of the two beams can be obtained relatively quickly and accurately. In addition to their function as beam position monitors, the electrodes can be used as clearing electrodes in space-charge neutralisation experiments [3].

Microwave radiation

Electrons spiralling around the magnetic field lines emit radiation with a total power proportional to the

transverse energy of the electrons [4]. This radiation can be detected with an antenna situated outside the beam anywhere along the trajectory. The power spectrum is centred at the cyclotron frequency, ω_c , but is Doppler-broadened with a width of $2\omega_c\beta$ (fig. 5). The power signal is very small, thus no absolute measure of the transverse energy is possible, but the main optical parameters such as the longitudinal magnetic field can be optimised with this method. Detection of microwave radiation is also only possible with intense electron beams.

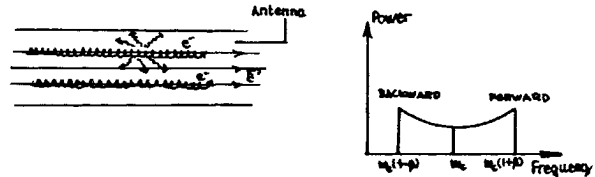


Figure 5: Electron beam microwave radiation.

Laser beam diagnostics

The principle [5] here is to measure the spectral density of Doppler-shifted backscattered light that is sent anti-parallel to the electron beam (fig. 6). The scattered laser light is blue-shifted with a reduction in wavelength by a factor 2-5. The analysis of this light is normally performed with a photomultiplier or a high-resolution Fabry-Perot spectrometer.

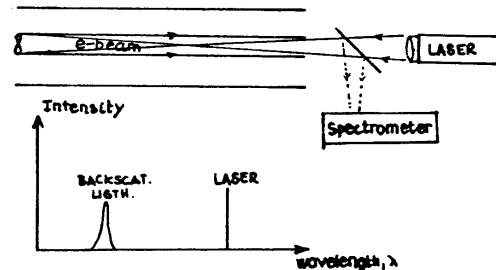


Figure 6: Principle of the laser beam diagnostics.

Laser beam diagnostics is a very powerful way of determining a number of very important characteristics of the electron beam. The velocity of the beam can be found from the Doppler shift in wavelength and the width of the backscattered spectrum gives the longitudinal energy spread. The electron beam current can even be estimated from the amplitude of the scattered light.

Scanning a thin laser beam across the electron beam makes it possible to measure current densities, velocity profiles and spreads as a function of radial position.

ION BEAM & COOLING DIAGNOSTICS

To measure the performance of the cooling process it is imperative to monitor a number of parameters of the circulating ion beam. The parameters of interest are i) the number of stored particles, ii) the particle momentum and momentum spread, iii) the ion beam position, and iv) the ion beam size. Furthermore the devices should be able to measure changes in these parameters with time constants smaller than the cooling times.

Schottky scans

A wealth of information on the beam can be obtained from the Schottky signals of the beam [6]. In the longitudinal plane the absolute momentum of the beam can be measured and the electron beam energy can be adjusted. The momentum spread of the beam at equilibrium as well as the intensity of the beam can also be obtained by analysing the frequency distribution. In the transverse plane the beam emittance and information concerning the ring optics (tune, chromaticity) can be extracted from the Schottky sidebands.

Schottky signals are observed on spectrum analysers and when used to observe the variation of the spectral density around a given frequency as a function of time (receiver mode), the longitudinal and transverse cooling times can be estimated. To follow the complete cooling process it is necessary to down mix the signals with the use of a single sideband mixer having a bandwidth of around 100 kHz followed by fast digitising and a Fourier transform. In this way a time resolution of a few milliseconds is obtainable with only a slight degradation in the signal to noise ratio. This technique was used quite extensively for the Pb ions cooling tests performed in 1997 on LEAR [7].

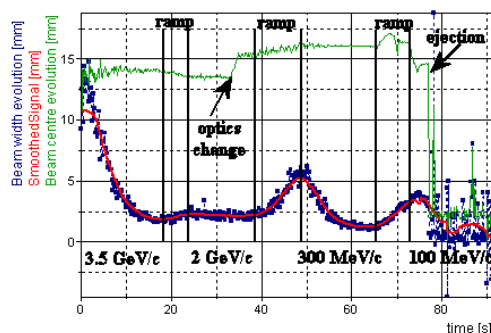


Figure 7: Antiproton vertical size & position during the AD deceleration measured by the IPM.

Ionisation profile monitors (IPM)

The principle is to measure the profiles of electrons (or ions) created in ionising collisions between the circulating ion beam and the rest gas molecules. By applying a transverse electric field the electrons are accelerated on to a detector, typically a multi channel plate (MCP) followed by a phosphor screen. Cooler rings typically operate in vacuums of the order of 10^{-11} torr and the ionisation rate is limited to some 10^4 s^{-1} . The MCP helps to amplify this number but in certain cases where the circulating beam intensity is low, additional systems, such as a gas injector, have to be envisaged. This is the case on the AD machine at CERN where the 10^7 antiprotons in the ring do not give a sufficient signal and a N_2 gas injector is needed to create a local pressure bump around the IPM [8].

IPMs are used to monitor the evolution of the beam size, the beam position in the IPM, and also the beam intensity at any given energy. An example of an IPM measurement is shown in fig. 7.

Neutral channel and recombination detectors

During the cooling process the centre of mass energy difference becomes very small and ions can capture an electron by radiative or di-electronic recombination. In the next bending magnet their trajectory becomes very different from that of the circulating ions. For proton beams, neutral hydrogen atoms are formed and travel straight towards a detector. For partially stripped ions, the down charged ions can be lost in the bending magnet. If the ring acceptance is large, then multiple charge states of the same ion can circulate in the machine.

The choice of detector depends on the required information. A scintillator coupled to a photomultiplier is used to measure the recombination rate from which the transverse energy of the electron beam can be evaluated. It is also a good means to correct any angular deviations between the electron and ion beams as the maximum signal is obtained when the beams are correctly aligned. Using a camera behind the scintillator, one can derive the profile and position of the ion beam from the profile and position of the recombined beam.

CONCLUSIONS

Many possibilities exist to measure both the electron and ion beam parameters in a cooler ring. For electron beams the least complicated systems are beam destructive and thus are only suitable for use on a test bench before installation in the ring. Non-destructive instrumentation used to determine the ion beam characteristics are also well suited for measuring the efficiency of the cooling process. Pick-ups can be used to accurately align the two beams whereas Schottky scans and ionisation profile monitors can record the complete cooling process in all three planes.

REFERENCES

- [1] J. Bosser, C. Dimopoulou, and G. Tranquille, LEIR E-cooler Conceptual Study, PS/BD/Note 2001-17.
- [2] H. Koziol, Beam Diagnostics for Accelerators, CAS, Oxford 1998.
- [3] J. Bosser, E. Holzer, V. Prieto, and G. Tranquille, Report on Electron Cooler Neutralisation Studies, PS/BD/Note 2002-140.
- [4] C. Rubbia, Microwave Radiation from the Transverse Temperature of an Intense Electron Beam, CERN EP-77-4, 1977.
- [5] W. Kells, Laser Diagnostics for Electron Cooling beam, Fermilab tech. Memo TM-771, 1978.
- [6] S. van der Meer, Diagnostics with Schottky Noise, Lecture Notes in Physics 343, pp. 423-433.
- [7] J. Bosser and 12 co-authors, Experimental Investigation of Electron Cooling and Stacking of Lead Ions in LEAR, Particle Accelerator, vol. 63, pp. 171-210.
- [8] G. Tranquille, Influence of the BIPM gas Injectors on AD Performance, PS/BD/Note 2002-15

CHARACTERISATION OF FAST FARADAY CUPS AT THE ELETTRA LINAC

M. Ferianis, S. Bassanese, G. D'Auria, Sincrotrone Trieste, I-34012 Trieste, Italy

C. Deibele, SNS, Oak Ridge, TN, USA

M. Poggi, INFN-LNL, I-35020 Legnaro (PD), Italy

Abstract

Since several years, the Diagnostic Group at Laboratori Nazionali di Legnaro (LNL) has been designing Fast Faraday Cups (FFC) to be used on their Heavy Ion Accelerators. Latest developments in this field include a Stripline FFC, jointly developed with the Spallation Neutron Source (SNS). A collaborative partnership has been set-up between LNL and the ELETTRA Laboratory to fully characterize new FFCs, using the 1GeV electron Linac in operation at the ELETTRA Synchrotron Light Source. Two FFCs, the stripline FFC, built at SNS, and a coaxial FFC, made at LNL, have been installed at ELETTRA who provided the wideband data acquisition and the remote control of the measurement. The first measurements, carried out using a 1GHz oscilloscope, have allowed the proper set-up of the instrument remote control as well as a low jitter triggering system, synchronous with the injected electrons. Wideband measurements were performed using oscilloscopes with bandwidths up to 20GHz, whereas the bandwidth of the Stripline FFC has been estimated to be roughly 20GHz.

A complete set of tests was carried out both on the coaxial FFC and on the stripline FFC. Moreover, thanks to the information provided by these wideband measurements, the Linac working point has been further optimized as well as the injection process into the ELETTRA Storage Ring.

INTRODUCTION

The ELETTRA Linac [1] is in operation since 1992 as injector of the ELETTRA Storage Ring, providing a 1.0GeV electron beam. Since 1996 [2] the Linac has also been used parasitically as a "test facility" both for material irradiation experiments and for testing diagnostic equipments [3]. The characterization of the new Fast Faraday Cups was carried out in the frame of this second activity.

The FFCs, designed to have information on beam temporal structure, have been developed at LNL for several years to measure the bunch length of ion beams. The experience gained in that field also yielded a collaboration with the SNS project at Oak Ridge, where a strip line FFC has been developed to measure the bunch length out of the low energy ($E=2.5\text{MeV}$ of H^-) section of the machine.

The ELETTRA Linac bunching structure

The bunching section of the ELETTRA Linac, shown in Fig. 1, includes:

- a 500MHz Sub Harmonic Chopper (TM_{110} deflecting cavity)
- a 500MHz Buncher (TM_{101} pill box cavity)
- 3GHz Pre-Buncher (TM_{101} pill box cavity)
- 3GHz Buncher (0.4m long $2/3\pi$ SW accelerating section)

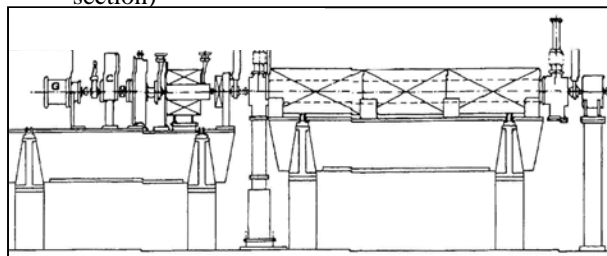


Figure 1: drawing of the ELETTRA Linac pre-injector: G=Gun, C=Chopper, PB5=Pre-buncher @500MHz, PB3=Pre-buncher @3GHz, B=Buncher @3GHz

With a proper setting of the parameters (amplitude and phase of the cavities) this configuration allows to select and fill a pure 500 MHz bucket of the Storage ring, in single bunch mode. This means that at the Linac exit all the charge is compressed in less than 1 nsec with a 3 GHz fine structure of the beam (2 or 3 S-Band micro-bunches, spaced by 330 ps). As we have observed with those measurements, changing the relative phases between the 500MHz cavities and the 3GHz ones, it is possible to change the number and the relative amplitude of the S-Band micro bunches.

THE FAST FARADAY CUPS

The FFC station, built at LNL and holding the two FFCs, has been installed on the Linac User port at 1GeV (fig. 2). An already available fluorescent screen located upstream the station has been used for alignment purposes and for checking the electron beam focusing.



Figure 2: view of the FFC station installed on the Linac User port at 1GeV. The cable of the coaxial FFC is visible in the foreground. On the right hand side, there is the linear translation stage of the Stripline FFC.

The Coaxial Fast Faraday Cup

The coaxial Fast Faraday Cup adopts a 50Ω SMA vacuum feed-through from Caburn MDC Company (ref. SMAD, part number 9251001), welded on a CF16 flange and put directly on beam axis on the user port at 1GeV: the central pin acts as a fixed “cup”. The CF16 flange is isolated from the beam pipe by a ceramic break; during the tests it has been shorted to ground the cup.

The Stripline Fast Faraday Cup

The stripline FFC (fig. 3) was designed by optimizing the electromagnetic-match of the beam-target to the connecting stripline circuit. This was performed iteratively using HFSS and showed a broadband match of -25 dB to over 50 GHz. The top and bottom grounds of stripline isolated the FFC signal from a noisy environment and consequently lowered the noise level.

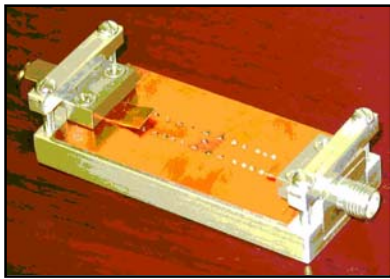


Figure 3: the stripline FFC developed at SNS: the output port is visible on the right, 50Ω termination on the left.

The grounds were stitched together in a random manner so that signal propagation resonances do not build up along the circuit card. The launch onto the circuit board from the coaxial cable was hand-matched using small tuning pieces of copper and measured using an Agilent 8722 operated in the time domain. The resulting launch and target have a reflection coefficient of better than -25dB to 40GHz. The overall thickness of the circuit board was set to 0.50mm and the length is about 50mm.

Signal generation process

The measurements presented in this paper have been obtained with 900MeV electrons: most of the electron energy [4] is lost via Bremsstrahlung (gamma rays + electron of lower energy), which we do not detect. Successively, lower energy electrons produce ions via electron-atom collisions. Missing valence electrons are supplied through the cable resulting in a positive pulse measurement. It is worthwhile noting that both central pin and surrounding “ground” are likely to be invested by the 900MeV beam. In fact, the diameter D of the SMA standard (IEC169-15, $D_{\text{jack-female}}=1.24$ to 1.29mm) is smaller than the beam diameter ($\pm 2\sigma=2$ to 3mm) which has been measured on the Fluorescent screen just in front of the FFC station. Therefore, as we are measuring the signal of the central pin relative to the “ground”, depending on the ratio of central pin signal to “ground” signal we observed both positive and negative pulses.

MEASUREMENT SET-UP

The driving criteria for the measurement set-up were to locate the oscilloscope as close as possible to the measurement point and to cure noise, both E.M. and from secondary radiation. After some preliminary tests, the final configuration included:

- the FFCs station located in the Linac Tunnel at $E=1\text{GeV}$ (see fig. 2)
- the Tunnel Station, close to measurement point, where the oscilloscopes have been placed
- the Remote Station, in the Linac Control Room

The Tunnel Station: oscilloscopes and triggers

The Tunnel Station is located close to the 1GeV point, to minimize cable effects on the measurement bandwidth, but outside the Tunnel, to avoid long-term radiation damage to the used instruments. The Remote Station is dedicated to the remote control of the oscilloscope and to data storage. The distance between these two stations is 150m and they are linked with a fibre optic Ethernet. The Linac Gun Trigger ($f=10\text{Hz}$), available in the Linac Control room, were delivered to the oscilloscopes using a coaxial cable driven by a fast pulse generator [5], acting also as a programmable delay unit.

Different oscilloscopes were used during the measurements, namely the Tektronix TDS5104 ($BW=1\text{GHz}$), the LeCroy8500-Wavemaster ($BW=5\text{GHz}$) and the Tektronix CSA803A ($BW\leq 50\text{GHz}$). The first two are real-time, fast sampling oscilloscopes (5GS/s and 20GS/s, respectively) whereas the last one is an ultra-wideband sampling scope, at 200KS/s.

The two real-time oscilloscopes can operate both in single-shot and in “equivalent sampling” mode, reconstructing the waveform over many subsequent trigger events. They can trigger either on external signal or on the signal itself. The CSA803A can trigger only on an external signal and requires an ultra low-jitter trigger typically at a frequency of 100KHz. As the repetition rate is 10Hz and the jitter of the external trigger was estimated to be $50\text{ps}_{\text{pk-pk}}$, it resulted critical in use.

Most of the fast acquisitions were made with the former two instruments, triggering on the signal itself and in “equivalent sampling” mode. Rather than relying on pulse-to-pulse time stability of the Linac with respect to the Gun Trigger, we profit by the stability of the 3GHz satellites inside each Linac macro pulse.

Time Domain Reflectometer characterization

A Time Domain Reflectometer (based on Tektronix Sampler 7S12 equipped with S-4 sampling head and S-52 Pulse generator on a 7603 scope) has been used to check the impedance of the acquisition structures. The coaxial FFC shows obviously an “open circuit” whereas the Stripline FFC is almost perfectly matched to 50Ω. By expanding the time axis and vertical deflection, we identified from impedance variations the different line components (FFC, connectors and in-vacuum cable).

MEASUREMENT RESULTS

During the early shifts, the Linac was operated in Multi Bunch (MB, a 70ns long macro pulse) to find the proper setting for the trigger-to-beam delay and to align the beam onto the coaxial FFC. After which, Single Bunch mode (SB, 2ns) was preferred as it allowed a clearer signal analysis, avoiding adjacent bunches to interfere with each other. Fig. 4 shows a MB acquisition on the coaxial FFC.

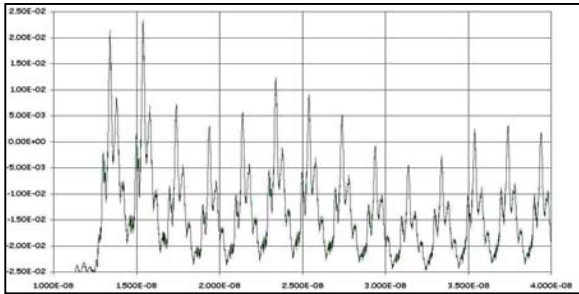


Fig. 4: Multi Bunch Linac macro pulse acquired with the coaxial FFC and the Tek 5104 1GHz oscilloscope. HOR: 5ns/div, VERT: 5mV/div. The 3GHz satellites are clearly visible on both sides of the main bunches.

A SB acquisition with the LeCroy8500 is shown in fig. 5: it is a RIS (Real-time Interleaved Sampling, the Le Croy acronym for “equivalent sampling”) acquisition. The t_{RISE} of the pulse is $95 \pm 3\text{ps}$, corresponding to a bandwidth of 3.66GHz, in agreement with scope data.

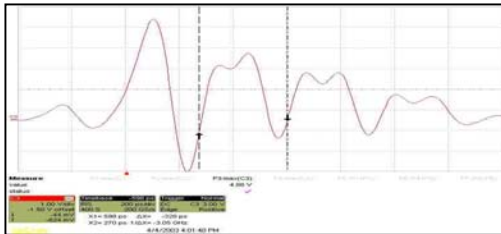


Fig. 5: Single Bunch acquisition, Coaxial FFC+Le Croy 8500 oscilloscope. HOR: RIS 200ps/div, VERT: 1V/div. At $V_{\text{phase}}=3\text{V}$, three 3GHz satellites can be observed.

Figure 6 shows a typical acquisition from the stripline FFC. Raw data is shown with no averaging. The jitter of the waveform can be estimated to be $<20\text{ps}_{\text{pk-pk}}$.

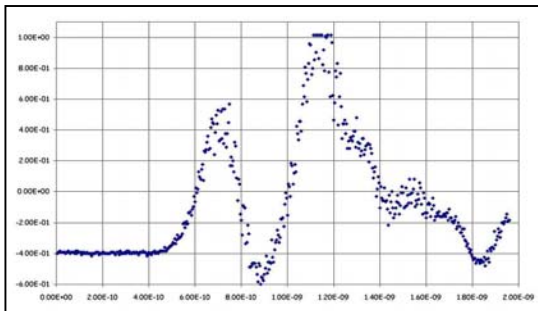


Figure 6: raw data from stripline FFC+Tek 5104. HOR: Eq. Time 200ps/div, VERT: 200mV/div. Two satellites are clearly visible. ΔT is $>330\text{ps}$ due to oscillatory pulse response.

Sub Harmonic Pre-Buncher phase variation.

A set of measurements has been carried out while changing the phase (V_{phase}) of the 500MHz SH-PB with respect to the 3GHz Buncher. The three satellite (at 0 and $\pm 330\text{ps}$) amplitudes changed by changing V_{phase} over a 2V interval, until a single satellite was measured.

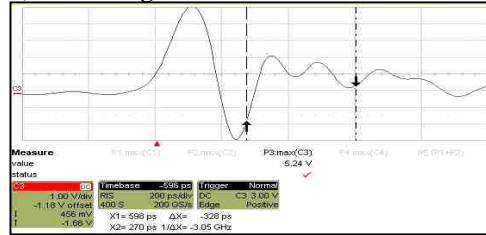


Fig. 7: Single Bunch: acquisition from Coaxial FFC+Le Croy 8500; HOR: RIS 200ps/div, VERT: 1V/div. At $V_{\text{phase}}=2.7\text{V}$, one main 3GHz satellite appears.

Data analysis tool

To analyse the waveforms obtained with different settings of the V_{phase} , a dedicated analysis tool was developed using NI LabView. After having loaded the “single satellite” waveform (fig. 7), individually scaled replicas are summed up, each shifted in time by 330ps. The “shift & sum” process is shown on fig. 8, left. The resulting waveform is shown on fig. 8, right, which is in good agreement with the acquisition of fig. 5.

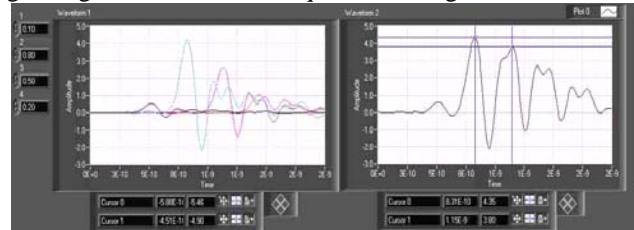


Fig. 8: reconstruction process with four satellites.

ACKNOWLEDGEMENTS

The Authors are grateful to the Linac and Machine operation staff for having operated the Linac; to G. Tromba for the enlightening conversation on electron-matter interactions; to R. Tommasini for having lent us the LeCroy 8500. Finally, we would like also to thank the radio protection unit for the patient work done prior to each access to the Linac tunnel.

REFERENCES

- [1] C. Bourat et al. “The 100MeV Pre-injector for the Trieste Synchrotron”, PAC 1989
- [2] M. Ferianis et al., “The OTR based Diagnostic System for the ELETTRA Linac: First Results and Future Upgrades”, Proceedings of Dipac 97, Frascati, 1997
- [3] M. Castellano et al. “Search for the prewave effect in transition radiation”, Phy. Rev. E67, 015501(R), 2003
- [4] G. Knoll “Radiation Detection and Measurement” 3rd edition, Wiley, 2000
- [5] DG535, Stanford Research Systems, CA 94089 USA

BEAM STUDIES MADE WITH THE SPS IONIZATION PROFILE MONITOR

G. Ferioli, C. Fischer, J. Koopman, F. Roncarolo
CERN, Geneva, Switzerland

Abstract

During the last two years of SPS operation, investigations were pursued on the ability of the SPS ionization profile monitor prototype to fulfill different tasks. It is now established that the instrument can be used for injection matching tuning, by turn to turn recording of the beam size after the injection. Other applications concern beam size measurements on beams ranging from an individual bunch to a nominal SPS batch foreseen for injection into the LHC (288 bunches). By continuously tracking throughout the SPS acceleration cycle from 26 GeV to 450 GeV the evolution of parameters associated to the beam size, it is possible to explain certain beam behaviour. Comparisons are also made at different beam currents and monitor gains with measurements made with the wire scanners. Data are presented and discussed, and the possible implementation of new features is suggested in order to further improve the consistency of the measurements.

1 INTRODUCTION

Data obtained with a gas ionisation beam profile (IPM) monitor under test in the SPS were already reported on several occasions, [1][2]. This type of monitor is one of the instruments considered to measure transverse beam distributions in the SPS and in the LHC. The device can be used in “high resolution mode”, using an optical detection bench with a CCD camera, and integrating the signal on several hundreds of beam passages (typically 20 milliseconds). For rms beam dimensions at the monitor much lower than 1 mm, a reproducibility better than 1% is possible, with a resolution lower than 0.1 mm. Moreover, data are in agreement within a few per cents with corresponding ones taken with wire scanners.

Tests were also performed in “high speed mode”, sampling the beam at the SPS revolution frequency. This is achieved by replacing the CCD camera by a Photo Multiplier Tube (PMT) associated to a high speed acquisition electronics. It was shown in [2] that using 16 anode strips and a resolution of 3mm per strip, was a bit marginal to detect turn to turn injection oscillations.

In the past two years new features occurred. Beams could be injected and accelerated to 450 GeV in the SPS with a structure fulfilling the nominal conditions required for injection into the LHC. The instrument was used to probe them in “high resolution mode”. Comparisons were made with the same data recorded with wire scanners.

Concerning the “high speed mode”, the spatial resolution was improved down to 1.2 mm per strip, by doubling the number of anode strips (32 instead of 16) and re-tuning the optics.

The paper analyses the results of measurements made under these new conditions.

2 TURN BY TURN MODE – INJECTION MATCHING STUDIES

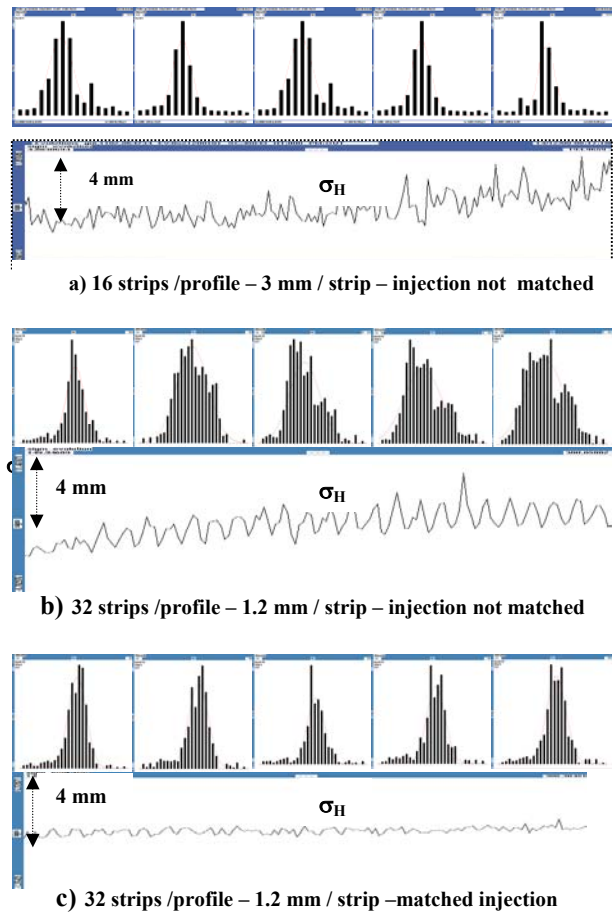


Figure 1: Beam profiles measured on one passage at injection into the SPS and associated evolution of the horizontal beam rms dimension on the first 200 turns when – a) and b): the injection conditions are not matched – and c): matching is tuned.

The results of investigations made with the IPM in fast acquisition mode using 32 anodes strips with a resolution of 1.2 mm per strip are displayed in Figure 1 case b) and c) when the injection conditions are respectively not matched and matched. Compared to the same data acquired under noisy conditions with a

resolution of 3 mm per strip and un-matched injection, case a), the oscillations of the rms value resulting from the mismatch are clearly detected, case b). A closer look would show up a periodicity of the oscillations of about six turns, related to the horizontal tune value. When matching conditions are better adjusted, case c), these oscillations are damped. The resolution on these oscillations of the rms value is in the order of 0.1 mm.

This test qualifies the IPM as a tool for injection tuning in a fully non-interacting way for the beam.

3 HIGH RESOLUTION MODE

In this mode, a CCD camera is used to acquire the beam profile, from a phosphorescent screen excited by the amplified electron signal. The resolution per pixel is 100 μm and each profile is integrated over 20 ms.

3.1 Single bunch profiles

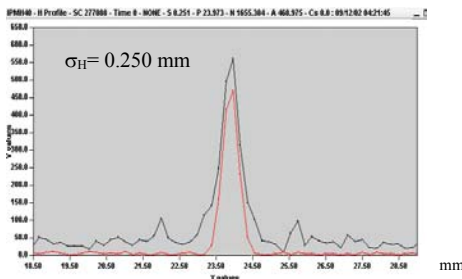


Figure 2: Profile of a bunch of $5 \cdot 10^{10}$ protons.

In Figure 2 a profile is presented, measured on a single bunch after acceleration to 450 GeV. The rms dimension resulting from the fit is 0.250 mm. This example illustrates again the sensitivity and resolution capability of the IPM. The vacuum was in the range of 10^{-8} hPa

3.2 SPS beams for injection into the LHC

The IPM was used during the 2002 run for the study of beams prepared in the SPS for the LHC. Nominal conditions in current foresee a beam made of four trains, (batches), each of 72 bunches, accelerated from 26 to 450 GeV. The bunch population is $1.1 \cdot 10^{11}$ protons.

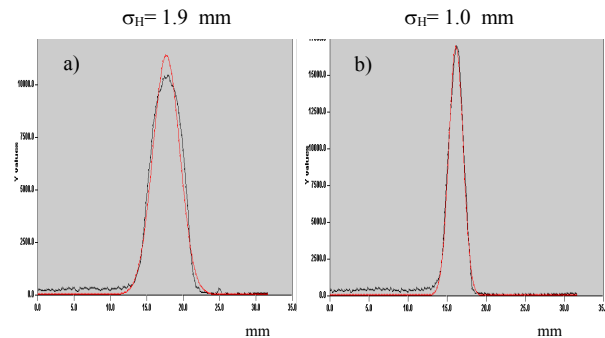


Figure 3: Profile of beam prepared for the LHC: 288 bunches of $1.1 \cdot 10^{11}$ protons: a) before (26 GeV) - b) at the end of acceleration (450 GeV).

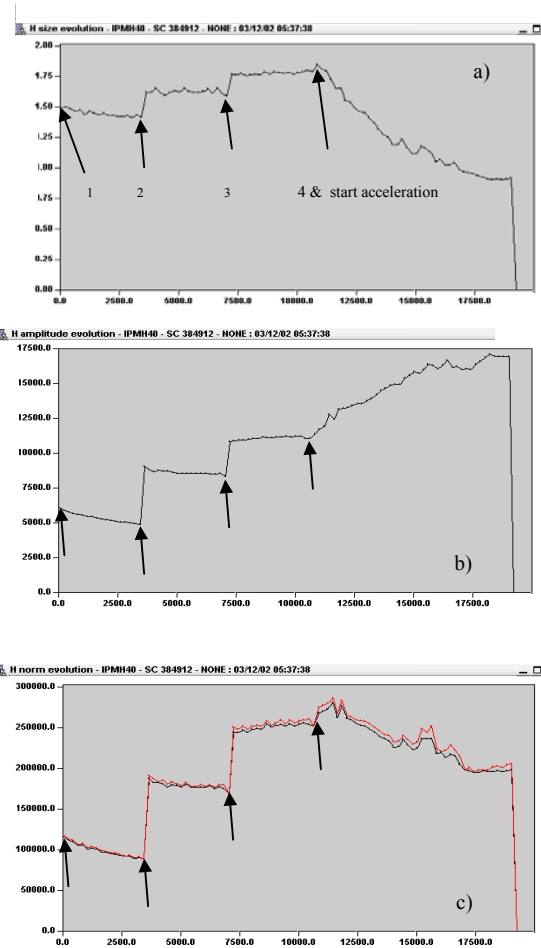


Figure 4: Evolution of: a) the horizontal beam rms, b) the amplitude and c) the integral of the IPM signal during injection then acceleration of 4 batches of 72 bunches of $1.1 \cdot 10^{11}$ protons.

Profiles of such a beam arranged in four trains are displayed in Figure 3, after injection of the fourth train at 26 GeV before acceleration starts (at 10.8 s within the cycle), and at the end of acceleration to 450 GeV just before beam dumping. The IPM allows continuous monitoring of the beam profile from injection of the first train (taken as the time origin) throughout the acceleration cycle. The evolution of a few related parameters is shown in Figure 4. The beam acceleration takes place between 10.8 s, after the fourth train is injected, and 19 s.

The variation of the beam horizontal rms value is represented in Figure 4 a). The beam widens by about 8% at injection of each train due to either a blow-up or to the fact that trains are not exactly on the same orbit. During acceleration, a global shrinking of 40% is apparent, which should actually be 10 times larger considering only the Lorentz factor from 26 to 450 GeV. Hence some blow-up occurs during acceleration; the final value got at 450 GeV is 1 mm (Figure 3 b) and should be twice smaller to meet the LHC emittance requirements.

Figures 4 b) and c) track the corresponding evolution of the profile amplitude and integral, the later being in principle directly related to the total circulating current. Steps are observed on the beam profile amplitude at injection of the second and third trains but with steadily decreasing magnitude, indicating that current loss or beam widening effects become more important at each injection. No step is seen at injection of the fourth train.

On the profile integral in Figure 4 c) the step amplitude is more balanced at the second and third injections, indicating that widening effects are better candidates than current losses. This is in agreement with the behaviour of the rms value (Figure 4 a)). Nearly no increase is observed on the profile integral at injection of the fourth train: the current brought by this train is balanced by losses occurring when the acceleration starts.

4 IPM AND WIRE SCANNERS

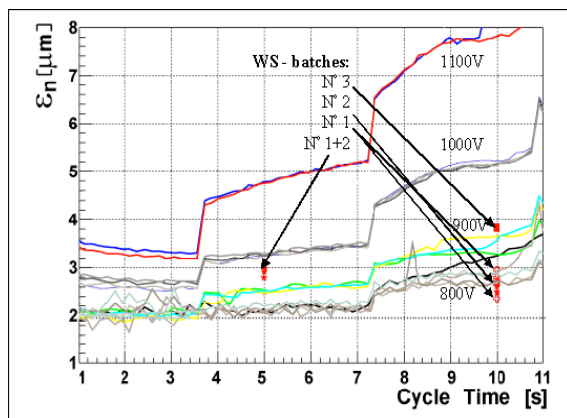


Figure 5: Evolution of the normalised horizontal beam emittance along the SPS cycle for different IPM gains

Data acquired with the IPM were compared with data taken in parallel with the wire scanners at given times of the SPS cycle. The results are illustrated in Figure 5 where the normalised horizontal emittance is processed from the recorded rms value. Different curves are for different IPM gain settings, adjusted by varying the voltage between the INPUT and OUTPUT ends of the micro channel plate between 800V and 1200V. Wire scanner data are given by the points at $t = 5s$ and $t = 10s$.

Good agreement between the two devices is observed within a given range of the IPM gain, (between 800 V and 900 V). For higher gains (1000 V and 1100 V) non-linearity and saturation effects show-up on the IPM, increasing the discrepancies between the data collected with the two devices. These effects are illustrated in Figure 6 where a discrepancy of 18 % on the rms value is observed between profiles of the same beam measured with the IPM at two different gains. To avoid this it would be necessary to control the gain during the cycle in order to stabilize the signal amplitude. This facility is foreseen.

However, there are sources of discrepancies when normalizing the data between the two devices. They are not at the same location and an error contribution of several per cents comes from the imperfect machine optics model. Another contribution is due to the different acquisition strategy. A wire scanner samples a beam portion at each passage and appreciates differences when its gating is adjusted on different beam trains having different distribution: the square dots are the results of scanning only the third train whereas the other points deal with the first two trains. For the IPM, each point is the result of integrating the whole beam over several hundreds of turns. Therefore, the two instruments appreciate in a different way a non-homogeneous beam structure and eventual instabilities.

Gain: 1050V- $\sigma_H=1.42$ mm Gain: 1150V- $\sigma_H=1.67$ mm

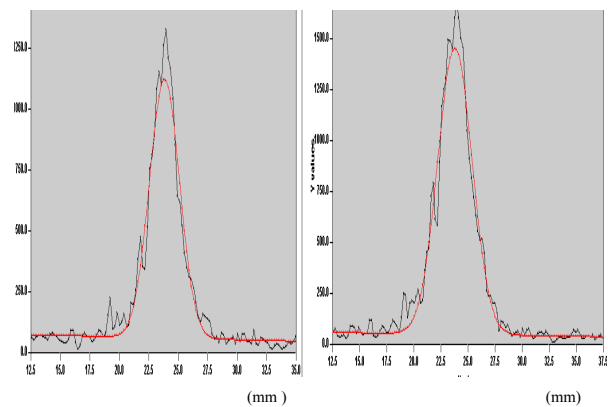


Figure 6: Profiles measured with the IPM at two different gains of the same coasting beam of $2 \cdot 10^{12}$ p.

5 SUMMARY

Using turn by turn acquisition, the IPM can be used for injection matching. In high resolution mode and continuous beam profile monitoring during an SPS cycle, the instrument is useful to observe phenomena and cure them to achieve the performance required for LHC. The same gain was used throughout one cycle. To cover the required dynamic and avoid saturation effects, the amplitude should be kept within a given range. Automatic gain control during the cycle is needed. A new IPM was installed last year in the SPS, with a design compatible for integration in the LHC where four devices are foreseen. Its behaviour with beams having the structure required for the LHC needs further investigations.

ACKNOWLEDGMENTS

It is a pleasure to acknowledge the support of R. Perret and M. Sillanoli.

REFERENCES

- [1] C. Fischer, J. Koopman, BIW2000, Cambridge, MA.
- [2] G. Ferioli et Al., DIPAC 2001, Grenoble, May 2001.

CAVITY MODE RELATED WIRE BREAKING OF THE SPS WIRE SCANNERS AND LOSS MEASUREMENTS OF WIRE MATERIALS

F. Caspers, B. Dehning, E. Jensen, J. Koopman, J.F. Malo, CERN, Geneva, Switzerland
F. Roncarolo, CERN/University of Lausanne, Switzerland

Abstract

During the SPS high intensity run 2002 with LHC type beam, the breaking of several of the carbon wires in the wire scanners has been observed in their parking position. The observation of large changes in the wire resistivity and thermionic electron emission clearly indicated strong RF heating that was depending on the bunch length. A subsequent analysis in the laboratory, simulating the beam by two probe antennas or by a powered stretched wire, showed two main problems:

- i) the housing of the wire scanner acts as a cavity with a mode spectrum starting around 350 MHz and high impedance values around 700 MHz;
- ii) the carbon wire used so far appears to be an excellent RF absorber and thus dissipates a significant part of the beam-induced power.

Different wire materials are compared with the classical cavity mode technique for the determination of the complex permittivity in the range of 2–4 GHz. As a resonator a rectangular TE_{01n} type device is utilized.

WIRES HEATING IN THE SPS TUNNEL

During the two last Machine Development periods in the SPS 2002 run, several wires were found broken. Such breaking can be typically related to the wire heating due to some energy deposition by the traversing protons on the wire. Dedicated electronics has been installed in order to have an indication of the wires heating during the LHC type beam injection and ramp in the SPS. In particular a constant current was supplied to the wire and the voltage drop across it was fed to a digital scope together with the difference between the input and output currents. The differential current ($I_{out} - I_{in}$) grow up is due to the wire heating and consequent emission of electrons for thermionic effect. Fig. 1 shows such voltage and differential current evolutions during the SPS cycle with LHC type beam. No scans were performed along this cycle. It is thus evident that the wire heating does not depend on the direct wire-beam interaction. In particular it is possible to relate the wire heating to the beam intensity (two batches of 72 bunches with $1.1 \cdot 10^{11}$ p/bunch injected in this case) and to the bunch length which is decreasing along the beam ramp to 450 GeV.

The measurements described in the previous section clearly revealed that the bunch length shortening causes a larger wire heating than the beam intensity. Such observations lead the study of possible RF coupling effects between the wire scanner wires and the proton beam travel-

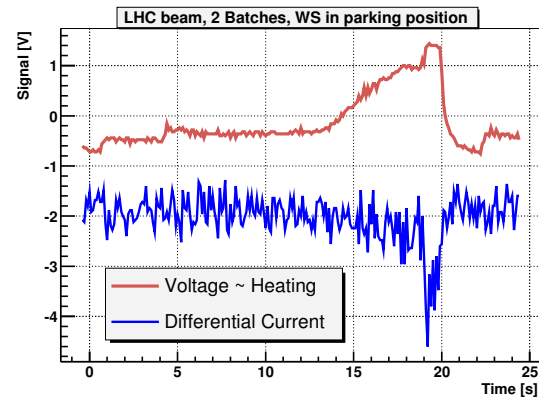


Figure 1: Wire heating due to the LHC beam injection in the SPS (No scan, wire in parking position). The beam energy ramp/bunch length decreasing begin $t=11$ s.

ling inside the wire scanner tank which is acting as a cavity.

The proton beam circulating in the ring has a frequency spectrum which mainly depends on the bunching structure (bunch length, bunch spacing). The build up of standing waves resonating inside the tank depends on the geometry and the tank materials. If one or more of the modes matches a beam spectral line, a rather large amount of RF power can be transmitted from the beam to the wires. These hypotheses have been investigated through dedicated laboratory measurements.

LABORATORY MEASUREMENTS

A spare SPS wire scanner tank has been equipped in the laboratory with two probe antennas connected to a Vector Network Analyzer (VNA) in order to simulate the RF modes in the beam spectrum frequency.

Beam-Wire coupling

Two connections to the ends of the wires of the wire scanner are used during normal operation to check the wire integrity (measuring the resistance) or to detect the secondary emission signal. In the laboratory they were applied to estimate the proton beam-wire coupling while simulating the beam with a stretched wire. A $0^\circ/180^\circ$ RF signal combiner circuit has been used to measure the differential signal at the wire ends. One port of the VNA has been connected to one end of the stretched wire, the other one at the combiner output giving the differential signal. Fig. 2 is well describing the effect. The plot gives the S_{21} signal together with the differential signal on the wire scanner wire. Where the frequency peak of the transmitted signal matches a peak of the differential signal, the power present

in the cavity can be absorbed by the wire. Different config-

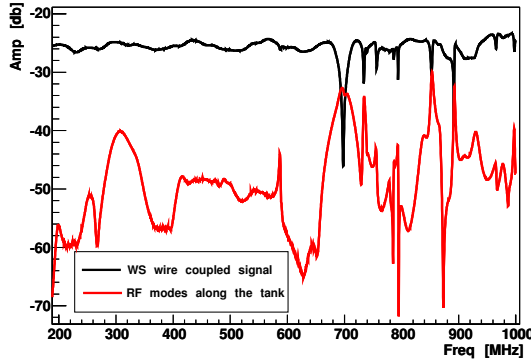


Figure 2: Beam-Wire Scanner coupling

urations have been set up in order to better understand the phenomenon:

1. none of the wires mounted on the forks, without ferrite tiles inserted,
2. one copper and one carbon wires mounted and kept in the parking position, without ferrite tiles,
3. two carbon wires mounted and kept in the parking position, without ferrite tiles,
4. two carbon wires mounted, the horizontal wire kept in the parking position and the vertical wire in proximity of the beam position, without ferrite tiles,
5. two carbon wires mounted, the horizontal wire kept in the proximity of the beam position and the vertical wire in the parking position, without ferrite tiles,
6. none of the wires mounted, nine ferrite tiles inserted in the tank,
7. one carbon wire mounted, nine ferrite tiles inserted in the tank,
8. two carbon wire mounted, nine ferrite tiles inserted in the tank.

For each measurement the Q factor has been evaluated by mean of the VNA, zooming in the resonance interval. For each resonance the antenna-probes position has been adjusted in order to reach the condition of weak coupling (S_{11} and S_{22} signals minimized to $< .5$ dB) thus allowing the evaluation of the unloaded Q . Fig. 3 shows two of the recorded signals, one with no wires mounted and no ferrite tiles inserted and one with no wires installed and nine ferrite tiles inserted. Fig. 4 summarizes all the quality factors as function of frequency, for all the measurement configurations. The RF modes damping by inserting the ferrite tiles is evident and suggested such configuration to reduce the power absorbed by the wire scanners wires. The ferrite type is TT2-111R (from Transtech, Maryland, USA) and its properties can be found in [2].

WIRE MATERIALS STUDIES

The classical cavity mode technique has been used for the determination of the complex permittivity of different wires in the range from 2–4 GHz. As a resonator a rectangular TE_{01n} type device is utilized. Different materials

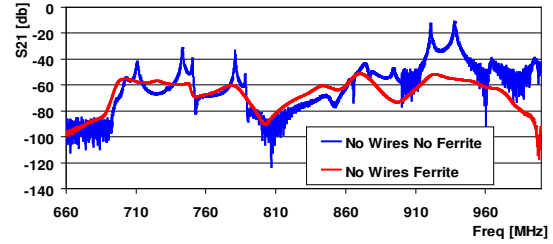


Figure 3: Transmitted signal from one end of the tank to the other using the antenna-probes method

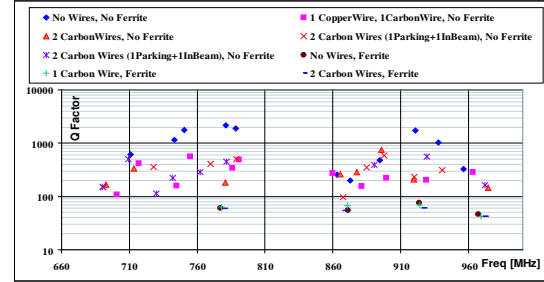


Figure 4: Unloaded Q factors for all the measurements setups as function of frequency

such as silicon carbide (SiC), carbon and quartz fibers were examined. SiC fibers are an interesting alternative to carbon fibers and their properties had to be investigated, since SiC bulk material is often used as a microwave absorber.

The complex permeability can be expressed as

$$\vec{\epsilon} = \epsilon_0 \vec{\epsilon}_r = \epsilon_0 (\epsilon'_r - j\epsilon''_r) \quad (1)$$

from where the loss factor can be defined:

$$\tan \delta_\epsilon = \frac{\epsilon''_r}{\epsilon'_r} \quad (2)$$

In the test cavity there are locations, in which either the electric or the magnetic field vanishes. If one puts a sufficiently small sample, which does not disturb the field, in these locations only the magnetic or electric properties of the cavity are influenced by the sample. In both cases the resonance frequency f_r and the quality factor Q are changed. ϵ''_r , ϵ'_r and $\tan \delta_\epsilon$ respectively can be found from these changes. [1] provides:

$$\frac{\Delta \vec{f}_r}{\vec{f}_r} = -\frac{\Delta \vec{W}}{\vec{W}} \quad (3)$$

The variables in this equation are complex. $\text{Im}(\vec{f}_r)$ and $\text{Im}(\vec{W})$ describe the losses in the empty cavity, and given the high Q they will be neglected in the following. If the sample is non-magnetic and positioned in a zero-magnetic-field region, then \vec{W} and $\Delta \vec{W}$ in Eq. (3) are only calculated from the electrical fields:

$$\begin{aligned} \frac{\Delta \vec{f}_r}{\vec{f}_r} &= \frac{\vec{f}_{rs} - \vec{f}_{re}}{\vec{f}_{re}} \\ &= \frac{-\epsilon_0 \int_{v_s} (\epsilon'_r - 1) E(x, y, z)_e E(x, y, z)_s * dV}{2\epsilon_0 \int_{v_r} E_e^2 dV} \end{aligned} \quad (4)$$

The subscripts e and s indicate the empty cavity and the cavity with sample, whilst V_s and V_r are the volumes of the sample and of the resonator. When the electric field is tangential to the surface of the sample and the sample ends on the resonator walls, then the internal field equals the external field:

$$E_e = E_s \quad (5)$$

Given a small volume of the sample:

$$\vec{E}_e(x, y, z) = \vec{E}_{e0} \quad (6)$$

and can be pulled out from the integrals of Eq. (4). The imaginary part of the resonant frequency shift is related to the change in quality factor:

$$\text{Im}(\Delta \vec{f}_r) = \Delta f_r'' = \frac{f_r}{2} \left[\frac{1}{Q_{L_s}} - \frac{1}{Q_{L_e}} \right] \quad (7)$$

Eq. (4) to Eq. (7) lead to the evaluation of the real and imaginary part of the dielectric constant:

$$\epsilon_r' = 1 - \frac{f_{r_s} - f_{r_e}}{f_{r_e}} \frac{V_r}{2V_s} \quad (8)$$

$$\epsilon_r'' = \left[\frac{Q_{L_e}}{Q_{L_s}} - 1 \right] \frac{1}{Q_{L_e}} \frac{V_r}{4V_s} \quad (9)$$

and therefore to the characteristic loss factor as defined in Eq. (2). ϵ_r'' can also be deduced from the material conductivity σ and the resonant frequency f according to:

$$\sigma = \omega \epsilon'' = 2\pi f \epsilon'' = 2\pi f \epsilon_0 \epsilon_r'' \quad (10)$$

Experimental Results

In the laboratory fibers of three different materials were considered: Carbon, Silicon Carbide and Quartz. Fig. 5 shows the measurements results as signal intensity versus frequency, around one of the resonating modes with maximum electric field at the sample location. The plot qualitatively proves the RF power absorption of Carbon, and the non-absorption of Silicon Carbide and Quartz. Fig. 5 also includes the results of a numeric simulation and measurement concerning the SiC material which is presently considered as a suitable RF absorber for the Compact Linear Collider (CLIC). A pyramid shaped piece of such material was inserted in the resonator at the same location where the wire scanner wires were placed. The fact that this material is absorbing RF power as shown by the simulation and by the measurements, proved that this is a SiC compound different from the one used for the wire scanners wires.

The insertion of one carbon fiber ($d=36 \mu\text{m}$) is reducing the signal amplitude to a level where the mode frequency is not well defined since the resonance curve is strongly asymmetric. Therefore, for this material, we could not apply Eq. (8). The imaginary part of the dielectric constant was evaluated both from Eq. (9) and Eq. (10). The insertion of 500 SiC fibers ($d=15 \mu\text{m}$) allowed the evaluation of both the real and imaginary part of the dielectric constant by mean of Eq. (8) and Eq. (9). The results for the

TE_{103} are summarized in the table below, together with the available data for the CLIC SiC bulk material [3]. Being Quartz a weakly absorbing material, in order to evaluate ϵ' and ϵ'' one should insert a large number of fibers as it has been done for SiC. However not enough Quartz material was available.

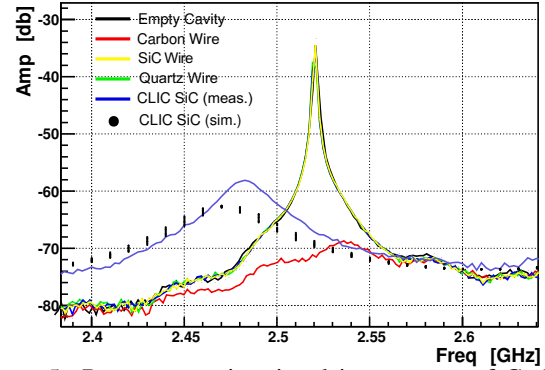


Figure 5: Resonant cavity signal in presence of Carbon, Silicon Carbide and Quartz

	ϵ_r'	ϵ_r''
C		$2.30 \pm 0.05 \cdot 10^5$
SiC	10.790 ± 0.016	2.158 ± 0.005
SiC (CLIC)	14.4	6.6

Table 1: Real and imaginary part of the dielectric constant for the TE_{103} mode, at 2.5 GHz.

CONCLUSIONS

The laboratory measurements investigated the RF coupling nature responsible for the wire breaking in the SPS wire scanners. The wire scanners tanks proved to act as resonant RF cavities in the beam spectrum frequency range. As a cure for the wire heating due to the beam-wire coupling, the SPS wire scanner tanks have been equipped with low outgassing ferrite tiles in order to damp the resonance modes. Carbon, used in the SPS until 2003, provided evidence of RF absorption properties. Therefore the wire material of few monitors were changed from carbon to silicon carbide, which has been characterized as a weakly absorbing material, and will be tested during the 2003 SPS run.

ACKNOWLEDGMENTS

We thank G. Burtin for the useful discussions.

REFERENCES

- [1] E.Nyfors, P.Vainikainen, *Industrial microwave sensors*, Artech House (1989)
- [2] E.Campisi, R.Doolittle, *Proceedings of the Workshop on Microwave-Absorbing Materials for Accelerators* (p.169), Newport News, Virginia, US (1993)
- [3] M.Luong, *Private communication*, CEA-CEN-Saclay, 91191 Gif sur Yvette, France

THE PS BOOSTER FAST WIRE SCANNER

S.Burger, C. Carli, M. Ludwig, K Priestnall, U. Raich, CERN, Geneva, Switzerland

Abstract

The very tight emittance budget for LHC type beams makes precise emittance measurements in the injector complex a necessity. The PS machine uses 2 fast wire scanners per transverse plane for emittance measurements of the circulating beams. In order to ease comparison the same type of wire scanners have been newly installed in the upstream machine, the PS Booster, where each of the 4 rings is equipped with 2 wire scanners measuring the horizontal and the vertical profiles.

The Booster wire scanners use new and more modern control and readout electronics featuring dedicated intelligent motor movement controllers, which relieve the system from the very stringent real time constraints imposed by the very high wire speed of up to 20m/s. In order to be able to measure beams at the very low injection energy of the PS Booster (50 MeV) secondary emission currents from the wire can be measured as well as secondary particle flows at higher primary particle energies during and after acceleration[1].

The solution adopted for the control of the devices as well as preliminary results obtained during measurements in 2002 are reported.

SYSTEM OVERVIEW

The new control of the PS Booster (PSB) fast wire scanner is subdivided into a data acquisition part controlled by the VME CPU and a motor control unit (MCU) provided by a VME slave processor board. The MCU is an independent embedded VME board featuring a 68332 CPU, an ADC, DAC and TTL

parallel I/O piggyback module. A complementary interface card is used for signal conditioning.

The acquisition part uses sampling ADCs for position and analogue signals measurements. The VME CPU communicates with the slave processor exclusively through parallel I/O signals making motor control entirely independent from the VME bus. Fig 1a) shows an overview of the complete system.

Due to the very high acceleration and speed needed, a 400W DC motor and an associated servo amplifier with velocity feedback are employed. The complex wire scanner mechanism is depicted in Fig 2.

MOVEMENT CONTROL

The software in the motor controller waits for triggers on its parallel input lines to power up the system and to step through speed tables defining the motor current function $V(t)$ through its DAC module. Currently 3 selectable wire speeds of 10m/s, 15ms, 20m/s are available. A resolver whose outputs are connected to the ADC determines the motor position. I/O channels see the end position switches (HOME and OUT). The speed tables are calculated by an offline program taking into account the geometry of the mechanism. They are linked to the embedded software, which is cross-compiled using gcc on a Linux workstation and downloaded into the MCU's flash memory.

The following constraints are taken into account:

1. The last crankshaft position $x(t_1)$ in [rad] given by the integration over the speed-table:

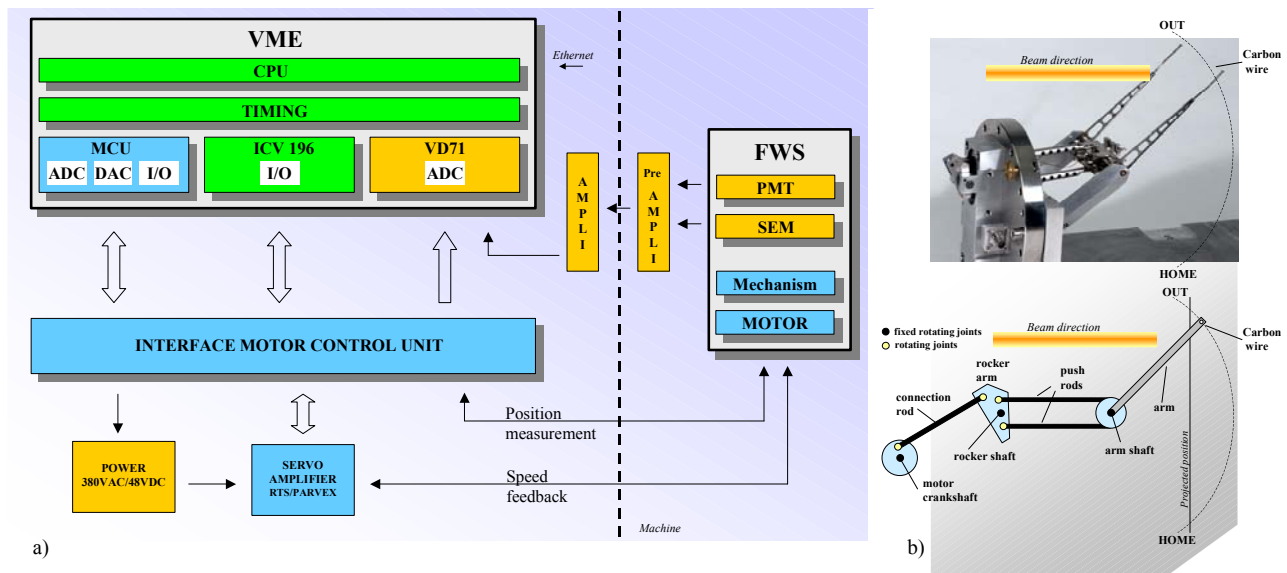


Figure 1: a) System overview of the fast wire scanner installed in the PS Booster. b) Picture and schematic of the mechanism of a fast wire scanner. Its complexity is due to stringent mechanical and physics constraints.

$$x = \frac{1}{T} \int_{t=0}^{t=t_1} V(t) dt \text{ must be OUT for a forward}$$

movement, with the tachymeter constant $T=32.8\text{mVs/rad}$ given by the motor electronics.

2. The projected speed of the wire during the acquisition phase should be constant.
 3. Acceleration peaks at the wire must be avoided in order to minimise mechanical stress.
- The peak acceleration for 20m/s is approximately 200g.

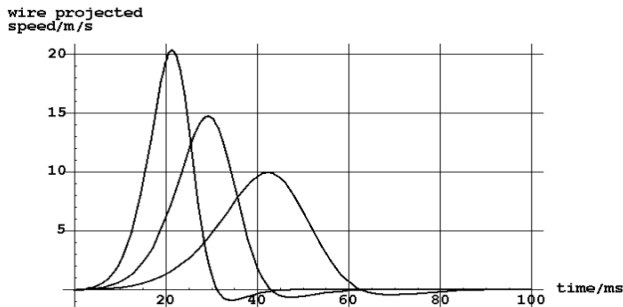


Figure 2: Wire projected speed curves versus time. During the interaction between the carbon wire and the beam (1 to 3 ms), the speed is the maximum of each speed curve followed by the wire.

BEAM PROFILE MEASUREMENTS ON PROTONS

In order to measure protons from their injection energy into the PSB at 50 MeV up to their ejection energy of 1.4 GeV we use 2 amplifier chains. One chain amplifies the secondary emission current (SEM) onto the wire while the second one treats signals from a scintillator/photomultiplier tube (PMT) installed outside the vacuum chamber.

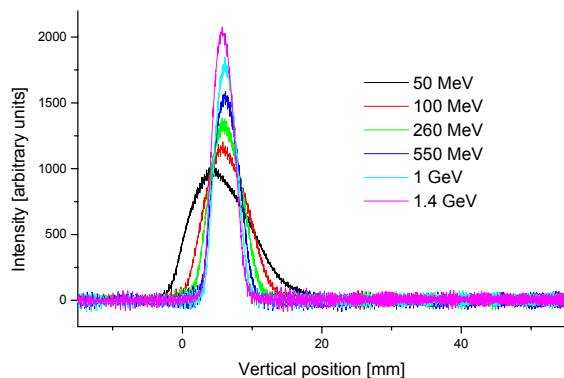


Figure 3: Evolution of the vertical beam profile along the PS Booster acceleration cycle, measured with the SEM detector. The amplitudes have been normalised taking into account the secondary emission efficiency for different kinetic energies and the revolution frequency.

The secondary emission channel is needed for primary particle energies below the pion production threshold. Fig. 3 shows raw data from secondary emission measurements along the acceleration cycle.

MEASUREMENTS ON PARTIALLY STRIPPED IONS

LHC will not only accelerate protons but also heavy ions (Pb^{82+}). During their acceleration in the PSB these ions are only partially stripped (charge state 53+) and the attempt of measuring their profile with the wire scanner will result in stripping and therefore in loss of the particles. However, the stripping effect can be used to measure amplitude distributions by slowing down the wire scanner to velocities slow enough so that it can be guaranteed that all ions will be lost.

In order to test this principle we used ions in the PSB produced for the SPS fixed target ion run in 2002. For the ion measurements a new speed table for 2 m/s has been defined.

Raw data containing the current measured with a DC beam current transformer (DCCT) as a function of time are plotted in Fig. 4. The last ions are lost, when the wire reaches the centre of the beam at a time t_0 . The point corresponding to the beam centre is determined by fitting a half-parabola through the raw data close to the point where the intensity vanishes as indicated in Fig. 4. The fact that only a small part of the data is fitted well by the parabola indicates that the phase space density is high in a small region at the centre and falls off quickly. This can be explained by the multi-turn injection of a beam with negligible direct space charge effects and is qualitatively confirmed by profile measurements of the extracted beam. Due to the low intensity of the ion beam, the raw intensity signal is rather noisy.

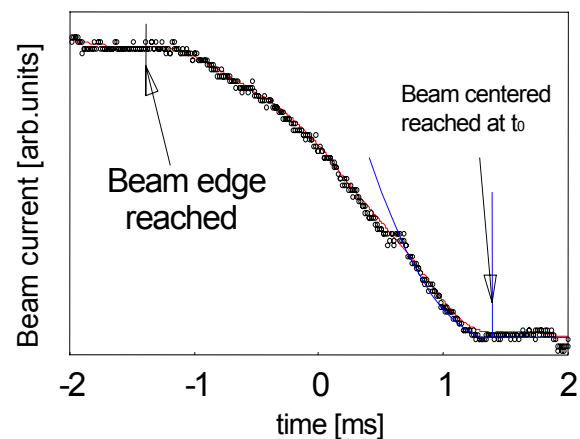


Figure 4: Raw intensity data recorded during scraping of the ion beam.

The oscillation amplitude A corresponding to the wire position at time t is given by $A=(t_0-t) v_{\text{wire}}$, where v_{wire} denotes the projected velocity of the wire. An amplitude density $\rho(A)$ can be derived from a normalized (varying from unity before the wire touches the beam to zero when the last ions are lost) current $I(A=(t_0-t) v_{\text{wire}})$ using $\rho(A) = dI/dA$.

In practice, it is difficult to apply above procedure due to the noisy signal. Figure 5 shows an amplitude density, which has been obtained by (i) smoothing the raw data using a Savitzky-Golay [2] smoothing filter, (ii) approximation of the smoothed data by a spline function (plotted in Fig. 4 in addition to the raw data) and, (iii) derivation of this interpolation.

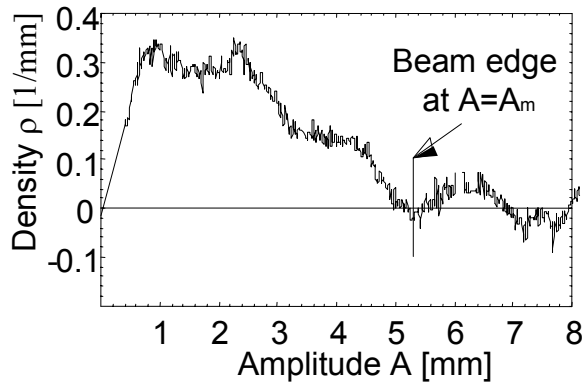


Figure 5: Amplitude density distribution

The rms transverse emittance of the beam is given by

$$\varepsilon = \langle A^2 \rangle / (2\beta), \text{ with } \langle A^2 \rangle = \int_0^{A_m} A^2 \rho(A) dA \text{ and } \beta = 3 \text{ m}$$

the betatron function at the location of the wire scanner. If the density plotted in Fig. 5 is inserted in above integral, one obtains a transverse rms emittance of $\varepsilon = 1.1 \mu\text{m}$. One notes that it is tricky to determine the beam edge, which strongly influences the final result.

Another method to evaluate the transverse emittance circumventing the difficulties in deriving a function describing the amplitude density from the measured data has been applied. The sum

$$S(A_n) = \sum_{A_i}^n \left(\frac{A_i + A_{i+1}}{2} \right)^2 (I_{i+1} - I_i) \text{ is introduced and}$$

plotted in Fig. 6. The emittance of the beam is given by $S(A_n \geq A_m) / (2\beta)$. With the help of the plot, one finds the emittance $\varepsilon = 1.15 \mu\text{m}$.

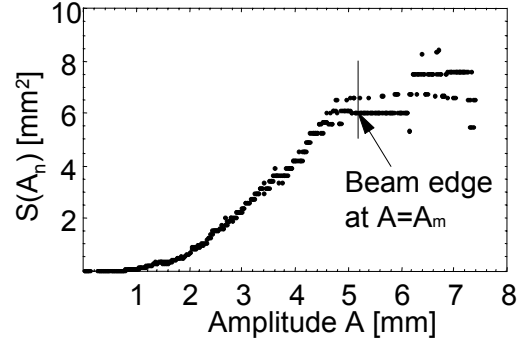


Figure 6: Approximation of the integral to determine emittance by a sum.

Comparative measurement have been done in a measurement line with the 3 profile method yielding rms emittances of $1.0 \mu\text{m}$ and $1.2 \mu\text{m}$ fitting the data with a Gaussian and, using spline fitting and integration afterwards, respectively. One concludes that, within the relative large uncertainties, the emittances measured by scraping the ion beam with the wire scanner agree with the reference measurement.

One should note that the measurements described above have been made for the vertical phase space and, thus, no contribution of the momentum spread via the dispersion had to be taken into account.

CONCLUSIONS

A series of 8 fast wire scanners has been installed in the PS Booster. These scanners are equipped with intelligent motor controllers capable of enforcing precise speed control avoiding acceleration peaks which would lead to high mechanical stress. The wire scanners can measure primary proton beams down to 50 MeV using secondary emission from the wire. For higher energies the flow of secondary particles, created through the interaction of the primary beam with the wire, is measured on a scintillator. Tests have been made on protons and on partially stripped ions where the scanners work like scrapers and beam loss is detected on a DCCT.

The wire scanners are now considered ready for routine operation.

REFERENCES

- [1] Wire Scanners in Low Energy Accelerators
I. Elmfors, A. Fasso, M. Huhtinen, M. Lindroos, U. Raich
- [2] W.H. Press, S.A. Teukolsky, S.A. Vetterling and B.P. Flannery, Numerical Recipes for Fortran 90
The Art of Scientific Programming, Cambridge University Press (1996)

UPGRADE OF THE ESRF FLUORESCENT SCREEN MONITORS

B.K.Scheidt, ESRF, Grenoble, France

e-mail: scheidt@esrf.fr

Abstract

The ESRF injector system contains 23 Fluorescent Screen monitors: 4 in the TL-1 transferline (200MeV), 8 in the Booster, and 11 in the TL-2 transferline (6GeV). They are based on Chromium doped Alumina screens that are pneumatically inserted in the beam path with an optical system collecting and focusing the emitted light onto a low-cost CCD camera with standard 75ohm video output. Serving mainly alignment purposes in the past 10 years, the upgrade now aims at a 200 μ m fwhm resolution for beam-size and profile measurements. This while preserving the main existing design components, notably the mechanics and the video & timing network.

The particularity of the Alumina screen not in vacuum but in atmosphere will be explained. Details of the mechanics, the optic system and the way of light flux adjustment will be given. An analysis of the factors determining the spatial resolution as well as the results obtained with different screen material will be presented.

BASIC PRINCIPLE

The fluorescent screen is mounted on a support that itself slides into a steel tube of 40mm inside diameter. With a simple steel finger this support is pushed against the very end of the tube, at the other end this finger is attached by a screw to a cf-63 flange. By means of a bellows and a pneumatic drive the assembly can be translated over 50mm at 90° angle to the electron beam path. When inserted the centre of the screen, at 45° angle to the beam path, is at the theoretical centre of the beam.

Light emitted from the screen surface is collected with an effective opening angle of only 1° determined by the lens opening of about 7mm at 400mm distance from the screen. A simple mirror deflects the light 90° at the tube's end towards the camera. The latter is so kept outside the direct view of the screen for better and long lasting protection against radiation damage. (see fig.1)

The camera and lens are housed in an immobile 2mm lead case with a lead-glass window. Only the mirror that is attached to assembly with tube and cf-63 flange moves when inserting & extracting the screen.

SCREEN OUTSIDE BEAM VACUUM

The screen is in ambient atmosphere and not in the UH Vacuum environment of the beam. The electron beam will first traverse the steel tube before hitting the screen surface about 20mm further down. At the beam energies of the ESRF of 200MeV and 6GeV the electrons will completely traverse the device and not cause any problem of excessive activation at this point. However, at 200MeV the scattering induced by the presently 0.5mm thick steel tube limits the spatial resolution, this is discussed further below. For practical reasons and limited costs of the upgrade, the old mechanics is maintained but may be

modified for a small number of TL-1 stations where the high resolution is essential.

A paper mask with 10lines/mm targets in the four corners is stuck directly to the screen, leaving a +/-10mm region free in the centre. It allows precise calibration and easy focussing adjustment at time of installation.

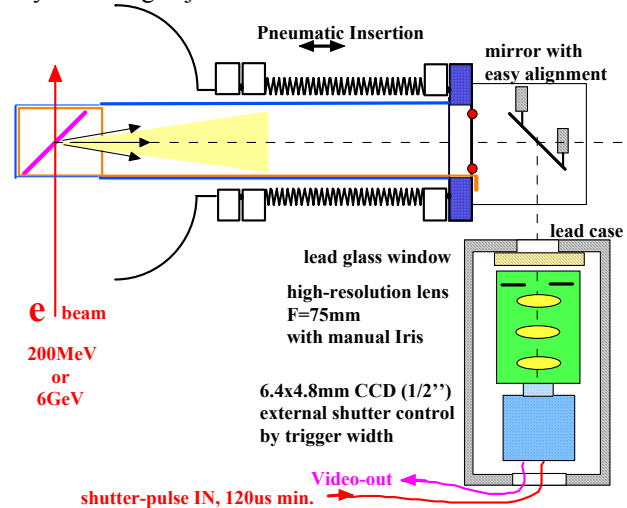


Fig. 1: Set-Up: screen in air and light collection optics.

CHOICE OF COMPONENTS

For the screen material a Chromium doped Alumina with reference AF-995R is used [1,2]. This product offers a strong resistance to radiation induced damage, was specifically developed for particle's viewing screen applications and is available at a price of 50Euros for a 50x50x1mm plate. This material has good luminosity properties and for our applications the amount of light flux is abundant and needs reduction. This is obtained with an electronic shutter in the Sony ST-50CE CCD [3]. With a few millisecc luminosity decay time of AF-995R and the shortest shutter time of 130us the right amount of beamspot intensity is obtained by adjustment of timing between the two as illustrated below in figure 2. The 75mm macro imaging lens offering >20lp/mm resolution in object space is from Edmund Optics [4].

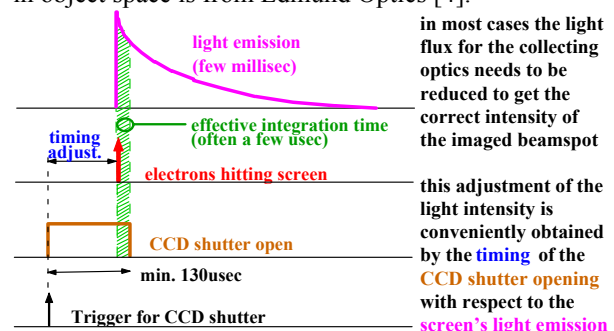


Fig.2: adjustment of light intensity with CCD shutter.

For the transport of the camera signal an extensive network of coaxial 75ohm cabling and video multiplexing was already in place since the original installation. The reuse of this determined the choice of a CCIR video standard for the cameras. A total of 23 signals are routed to one single National Instruments 1409 product for the image acquisition. The above-mentioned trigger for the camera's shutter is send over a separate cabling network with all cameras in series.

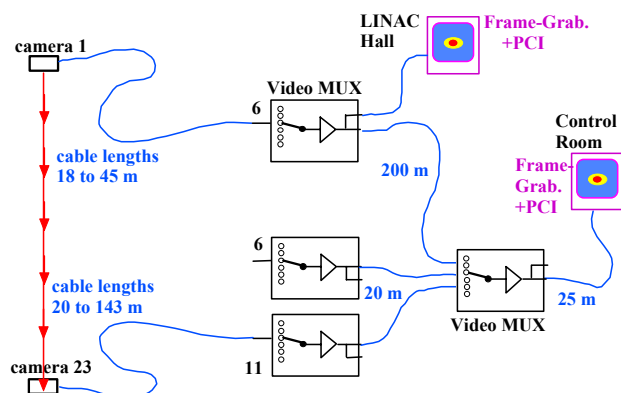


Fig.3: Video Network distribution for 23 stations.

SPATIAL RESOLUTION

Scattering in metal tube

For the 200MeV electrons the scattering caused by the present 0.5mm thick Steel wall is producing a limitation of nearly 600um. This effect, negligible at 6GeV, can be reduced by thinning the wall and/or using Aluminium.

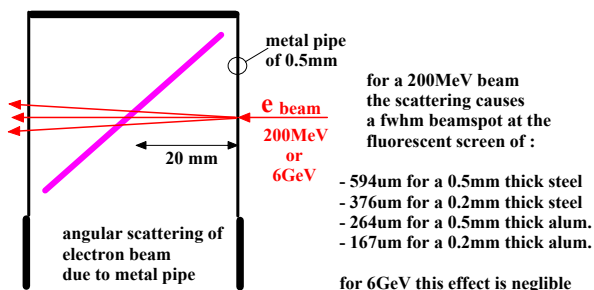


Fig.4: electron scattering limits spatial resolution.

Screen Characteristics

The screen itself limits the spatial resolution due to the combination of three characteristics : finite thickness of the screen, limited opacity of the screen material, and light scattering inside the screen. The electron beam creates a line of light emitters points inside the screen. The light coming from these points is not strongly attenuated, while it is scattered before it reaches the screen surface. The consequent blurring of the spot on the screen is simulated for a given light attenuation coefficient as in fig. 5 (top-left). For the same 1mm thickness but for opacity (or transparency) values a factor 10 and 100 stronger than AF-995R the fwhm beamspot blurring is a factor 0.67 and 0.5 smaller. The strong non-symmetry is explained by the 45° inclination angle. The

theoretical results are fully confirmed by measurements in which the AF-995R material was compared with Alumina screens of ~100 times stronger opacity. This was done in identical beam conditions in TL-2, at 6GeV so without suffering the resolution limitation due to the scattering effect. Both the factor 2 in spatial resolution improvement and the non-symmetric response are obtained.

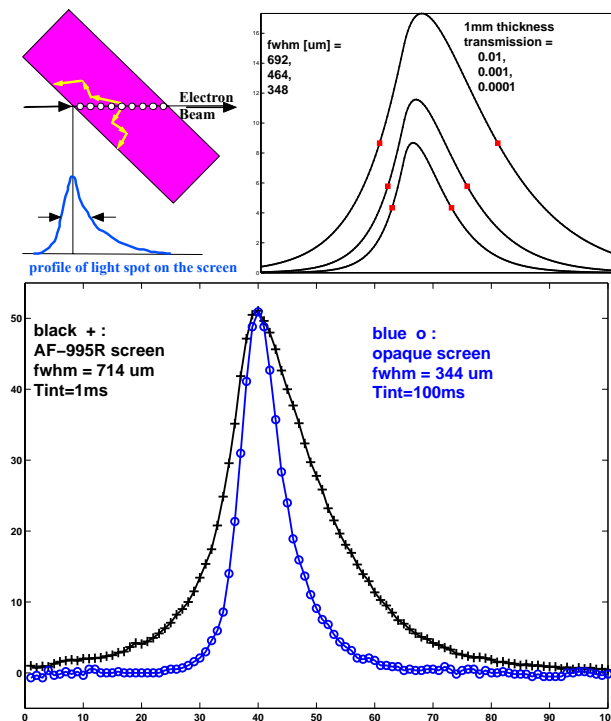


Fig.5: spatial resolution limit due to screen characteristics.

Optical Imaging System

Three factors determine the resolution of the optical system : diffraction ($\lambda=600\text{nm}$, $\alpha\sim 1^\circ$), depth-of-field (screen at 45°), and the system's pixel resolution. In electronic shutter mode the ST-50CE camera (due to CCIR interlaced standard) produces only 240 lines (i.e. a factor 2 less than normal) vertical resolution. Fig.6 shows the total resolution : even with only 240 lines the total resolution is less than 100um for 5-10mm diaphragm (at 400mm) at any part of the screen (range +/- 10mm).

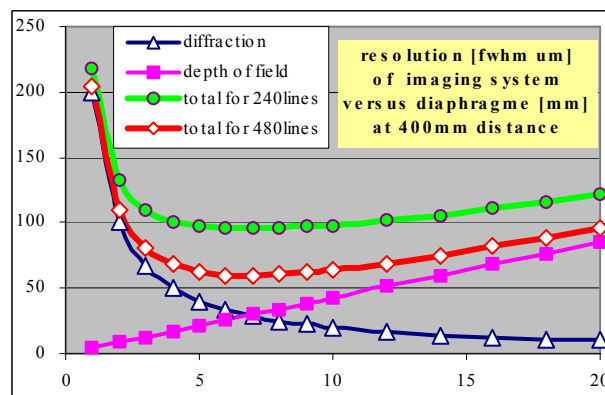


Fig.6: spatial resolution of optical imaging system.

RESULTS

The upgrade is so far installed in the 4 TL-1 screens and 2 screens in TL-2. The images acquired are first treated by Labview in which some symmetry operations are applied (rotation, left-right inversion) to correct effects introduced by mirrors and rotation of camera. After that the image matrix is treated by simple Matlab functions that determine the centre of gravity and the beamsizes of the spot at the maximum repetition rate of 10Hz.

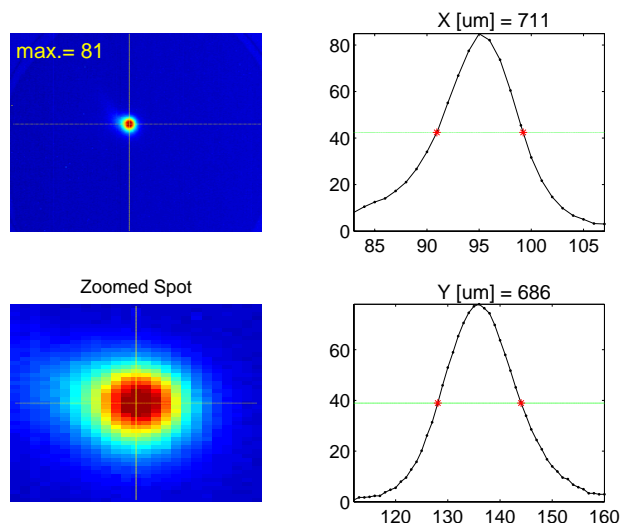


Fig.7: typical output result after Matlab treatment.

A series of measurements on the 2nd TL-1 screen were performed to determine the emittance. A preliminary result of 400nm.rad was obtained but needs a revision once the spatial resolution has been improved and the LINAC beam is better conditioned.

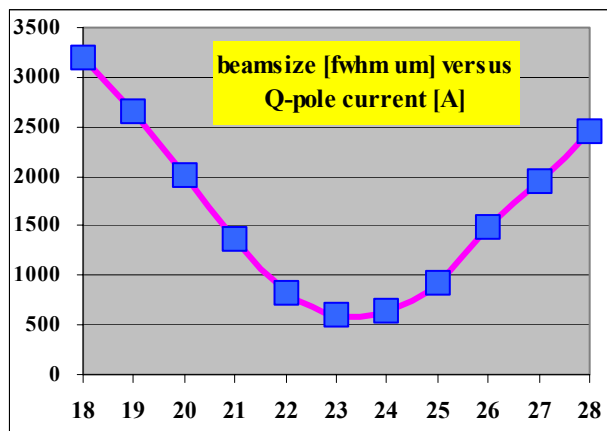


Fig.8: emittance measurements in TL-1.

CONCLUSION & FUTURE WORK

The upgrade of the screen monitors has been carried-out in a cost effective way while preserving a major part of the existing system. It can be summarised as follows :

- Optimised spatial resolution.
- Easier adjustment of light spot intensity.
- Easier and more precise focussing and calibration.
- Relieved motion mechanics.

- Higher quality screen material.
- Better protection against radiation damage for CCD.
- Availability of numeric results at 10Hz rate.

However, in today's configuration the aim of 200um fwhm spatial resolution is not yet achieved due to scattering produced by the system and certain screen characteristics. These limitations affect TL-1 and TL-2 to different extents, it can be stated that the spatial resolution today is in the 300 to 700um range.

While this is acceptable for the 8 stations in the Booster and for a number of other stations (see the nominal beamsizes at the TL-1 & TL-2 stations in fig.9), it would limit the precision of certain studies like the emittance measurement. In the near future the possibility to suppress or reduce the scattering effect will be considered by using a screen inside UHV or thinning the tube. Also, an improvement of the screen material characteristics is sought for which several possibilities will be examined soon : Thinning the AF-995R (230um has been achieved), using 'dark' (opaque) version Alumina, using thin Phosphor coatings [5] or thin YAG:CE scintillators [6].

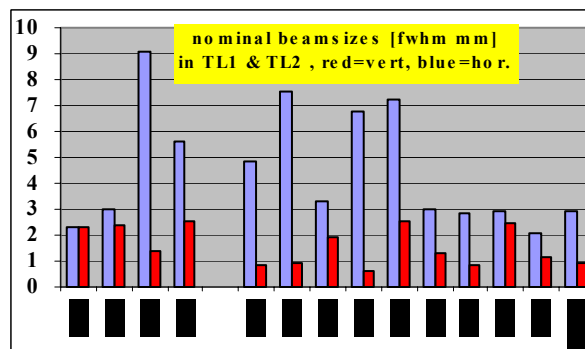


Fig.9: beamsizes in TL-1 and TL-2.

ACKNOWLEDGEMENTS

The author expresses thanks to P.Deschijnkel and M.Paulin for the preparation and installation of the system, to P.Pinel for the necessary help with the video and timing network, to F.Epauld for the video acquisition system, and to Th.Guenzel for the calculations of scattering effects.

REFERENCES

- [1] Saint-Gobain Céramiques Avancées Desmarquest 48 rue des Vignerons, F-94685 Vincennes Cedex, France, www.ndfc.saint-gobain.com
- [2] R.Jung, 'Single Pass Optical Profile Monitoring', this DIPAC-2003 proceedings
- [3] www.sony.net/Products/ISP/products/tv/
- [4] Edmund Industrial Optics, 101 East Gloucester Pike Barrington, NJ 08007, www.edmundoptics.com
- [5] Proxitronic, Robert-Bosch-Straße 34, D-64625 Bensheim, Germany, www.proxitronic.de
- [6] Crytur Ltd., Palackeho 175, 51101 Turnov, Czech Republic, www.crytur.com.

FIRST EXPERIMENTAL RESULTS AND IMPROVEMENTS ON PROFILE MEASUREMENTS WITH THE VIBRATING WIRE SCANNER

Arutunian[#] S.G., Bakshetyan K.H., Dobrovolski N.M., Mailian M.R., Soghoian H.E., Vasiniuk I.E.
Yerevan Physics Institute; K.Wittenburg, DESY

Abstract

The paper presents the first experimental results of transverse profile scans using a wire scanner based on a vibrating wire (vibrating wire scanner - VWS). The measurements were performed at the injector electron beam (10 nA) of the Yerevan synchrotron. The beam profile information is obtained by measuring the wire natural oscillations that depend on the wire temperature. This first experiments on weak electron beam proved this new method as a very sensitive tool, even suitable for very sensitive tail measurements.

Additional, improvements were tested to overcome problems connected with signal conditioning and signal transfer in the presence of electromagnetic noise. As a result the noises were clearly separated and reduced. A mathematical method for rejection of distorted data was developed. Experiments with the scanner at the PETRA accelerator at DESY are planned for measurements of beam tails.

INTRODUCTION

First experiment on scanning of weak electron beam of the injector of Yerevan synchrotron proved the possibility of beam profiling by the vibrating wire scanner (VWS) [1]. The profile of a low intensity electron beam (average current of the beam was few nA) was measured by using the vibrating wire scanner technique. The experimental results show that the sensitivity of vibrating wire scanners is optimal for extended measurements of beam tails.

The experiments have also shown, that the scanner was sensitive to external electromagnetic noise. It was observed that the level of distortion of frequency from the wire correlates with turn-on of high frequency accelerating klystrons independent of whether the electron beam fell on the wire. Analysing the noises allowed marking out the most sensitive parts of the readout system. The improvements were tested during the autumn 2002 experimental session. As a result the noises could be clearly separated and reduced. A mathematical method for rejection of distorted data was developed. Taking into account this experience a special board is developed for planned experiment with the scanner on the PETRA accelerator at DESY.

SCANNING EXPERIMENTS

The principle of operation of the vibrating wire scanner is based on the dependence of the wire natural frequency f_0 on the beam intensity at the given location. The energy deposition of the beam particles in the wire causes heating of the wire. Hence the stretched wire temperature can be

obtained by measuring its natural oscillations frequency by an autogenerator electronic circuit with a positive feedback loop.

Initial experiments on profiling were done using laser beams [2, 3]. The effective temperature precision was estimated to be about 10^{-4} degrees C (without noise).

In this experiment the profile of the low intensity (after collimation to about 10 nA) electron beam of the injector of the Yerevan synchrotron was scanned (bunches with RF of 2797.3 MHz with pulse duration of 2 μ s). The repetition rate of pulses was 50 Hz. A beryllium-bronze wire of 90 μ m diameter as vibrating wire was used. Fig. 1 represents the result of the reconstruction of the beam profile for the first scanning. Fig. 1 also presents the profile of the beam approximated by a normal distribution with $\sigma = 1.48$ mm and beam central position at 30.87 mm. The overall current of the beam was set to $I_0 \sim 10$ nA. Only half of the beam could be scanned because of the short throw of the scanner.

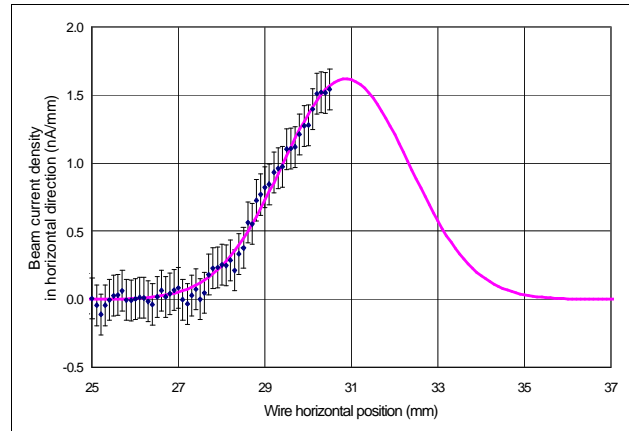


Fig. 1 Reconstructed horizontal profile of an electron beam with a current of about 10 nA. The reconstruction was done after a detailed noise analysis (see "noise studies").

Calculations of "tail sensitivity"

Let's estimate the sensitivity of VWS with respect to the lower limit of beam intensity. In this case radiational losses of wire temperature are negligible and the balance of temperature is determined by the thermal conduction along the wire. Let the temperature of the wire near its fixation points be T_0 and at the middle $T_0 + T_m$ (triangular profile of the temperature along the wire). Thermoconductive losses $P = 4\pi\lambda r_w^2 T_m / l$, where λ is the thermoconductivity of the wire with the radius r_w and length l . Total power deposited on the wire $Q = (\pi/2)^{0.5} (r_w^2 / \sigma_x) \exp(-x^2 / 2\sigma_x^2) (I_0 k d E / dy / e)$, where σ_x is the beam size, x is the wire location with respect to the

beam center, dE/dy are the ionization losses, k is coefficient transition ionization loss to heat of the wire. Usually k is approximately 0.3^* . From the thermal balance follows that:

$$T_m = (1/4(2\pi)^{0.5})(1/\sigma_x)\exp(-x^2/2\sigma_x^2) (I_0kdE/dy/e)/\lambda.$$

Note that there is no dependence of T_m on the wire radius.

For beryllium-bronze wire and 100 mA proton beam with $\sigma_x = 0.6$ cm (PETRA conditions) the value T_m of about 0.01 K (vibrating wire thermal sensitivity at presence of electromagnetic noises) is achieved at $x = 5.7 \sigma$.

The following estimation agrees well with this calculation: At the present experiment a significant increase of the temperature was achieved at about 2σ . At that wire position, the wire was hit by $1.8 \cdot 10^8$ e/s. For a 100 mA beam with a width of $\sigma = 0.6$ cm this amount is reached at about 6.1σ . Note that dE/dy for electrons and protons at ultra high energies is about identical.

NOISE STUDIES

Some problems connected with signal conditioning and transfer are discussed in the following. These problems were absent in test experiments in laboratory conditions and arise with RF power switch-on in the real experiments on accelerator beam scanning. The noise was caused by the klystron station of the Yerevan synchrotron injector.

Fig. 2 presents graphics of measured frequency signal before and after the klystrons turn-on in Injector (they were turned on approximately at 13:43).

A scheme of multiplying the vibrating wire frequency by factor 32 was used to increase the processing speed of the frequency measurements. The electronic multiplication of the wire oscillation results in a frequency of about 7963×32 Hz. It is transferred through a 50 Ohm coaxial line of length 70 m in form of a sequence of alternating-sign rectangular pulses with amplitude ± 10 V and with a recurrence rate of about 254.8 kHz. With the powered klystron, the signal became distorted (see Fig. 2)

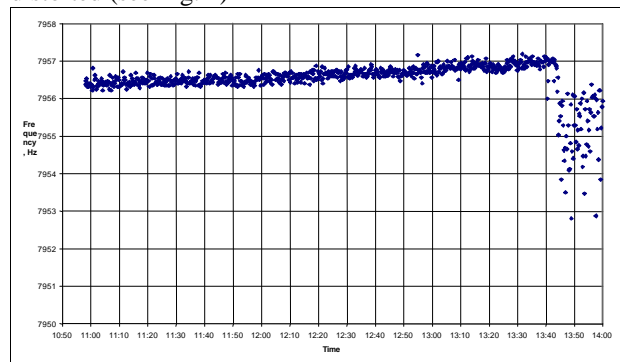


Fig. 2. Noise trace of the signal. At 13:43 the high frequency system was switched on and the noise appeared. Note that the beam was not present.

* about 70% of the energy disappears due to secondary particles emitted from the wire

The generation of various types of noise was studied in laboratory conditions afterwards. Voltages of different form (artificial noises, similar those observed during the experiments) were applied between the common point of the electronic circuit and metallic frame of the scanner to model the noise. Frequency registration was done by the same scheme as during the experiment

The most sensitive unit to electromagnetic noise was found to be the frequency multiplying circuit while the generator, the amplifier and the trigger circuits had no influence on the noise figure. Therefore a new method for frequency measurement was developed. The frequency measurement was carried out by gating the high frequency f_h pulses by one signal period. In the case frequency periods are applied during the time *gate* the relative accuracy of this method is described by the formula $f_0/f_0 = 1/(gate \cdot f_h)$. At f_h about 6 MHz the gain in the measurement accuracy becomes $f_h/(k \cdot f_0) = 30$. That means that the measurement accuracy is on the level of 0.03 Hz within the time interval of 30 ms. The two advantages of this method are i) the reduction of measurement time (therefore below we will name it as fast method); ii) the elimination of frequency multiplication block. This procedure will be done in the interface board inside the computer in the control panel far from noise source.

As a result of the new circuit, the frequency signal splits into several parallel traces (see Fig. 3a, in this example four traces) in the present of strong noise. The lowest trace is the non disturbed signal. As the trace level increases the number of points in it decreases, and there is only one point in the forth stripe. The distance between the traces is about 7.7 Hz at the main signal level of 7765 Hz, i.e. is equal to 1/1000 part of the main frequency. This shows that the noise affects the pulse counting by 1/1000 of the main frequency or 0.1 % only.

This measurement method in a real experiment was tested in autumn 2002 on the injector of the Yerevan synchrotron. A smooth trace with nearly no noise was registered when the klystron in the Injector were turned off. The picture changed when the klystrons turn on. As it was in laboratory experiment the main frequency trace is split into 4 levels (see fig. 3b): the main (lowest) trace contains over 90 % experimental data. About 7.3 % of all values are shifted by about 2.56 Hz and 3 % by 5.13 %. The frequency in the main trace is 2560 Hz, i.e. as in laboratory experiment the split is about 1/1000 of the main frequency. Actually the mentioned splitting allows rejecting the frequency spikes programmatically. This enables beam scanning experiments with a considerably signal-to-noise ratio.

PREPARATION FOR EXPERIMENTS AT PETRA

In 2003 it is planned to test the beam scanning system based on vibrating wire in the PETRA proton accelerator at DESY. Due to high sensitivity of vibrating wire scanners the interesting measurements of beam tails will

be performed [4, 5]. The electronic schemes were tested under laboratory conditions and are prepared for experiments at PETRA. The effect of the cables were tested for up to 100 m.

Thus, all the units of the PETRA beam scanning system by a vibrating wire are prepared for installation into the accelerator.

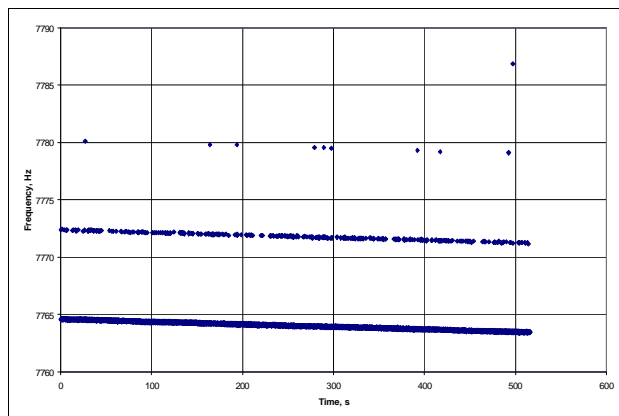


Fig. 3a Registration of frequency signals obtained by the fast measurement method under laboratory conditions in the presence of artificial noise.

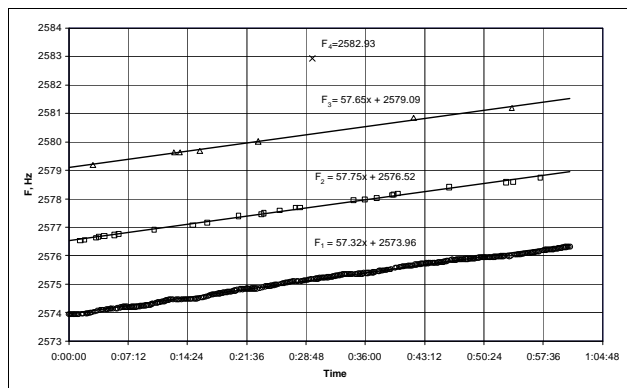


Fig. 3b Typical dependence of frequency on time, obtained by fast method in the presence of electromagnetic noises, associated with the RF klystron.

In the experiments the frequency measurements were done with a time gate of 1 s, i.e. averaging the time structure of the beam (bunches and pulses). In the case of low beam intensities this does not cause any problem. But for more intensity the problem of short-time heating of the wire can arise. The characteristic time of the wire heating in transverse cross-section is of order of $cr_w^2/\lambda \sim (2\div5)(r_w/m)^2$ s. Thus in case of $r_w > 10 \mu\text{m}$ one can neglect the bunch structure of the beam. However, the pulse duration is much more than the mentioned times, so the short time heating may reach the destruction limit. This problem is mentioned e.g. in [6, 7]. Note that the fast method of frequency measurement for VWS is sensitive to the pulse structure of the beam but not to the bunch structure.

SUMMARY

Experiments confirmed our expectation on the possibility of using a vibrating wire scanner (VWS) for charged particle beam transverse profile measurements. These measurements are particularly useful for low current beams. Specifically, it was confirmed that:

- Interaction of the beam with the wire does not quench the wire oscillations;
- The change in the natural oscillation frequency of the wire during interaction with the beam is a reliable method of measuring the transverse profile of extremely low intensity beams.
- The vibrating wire scanner can be a valuable tool for measuring low intensity beam profiles, and also for beam halo and beam tail measurements at several σ .

In these experiments the accelerator RF system induced noise in the measurement system. This problem was solved by standard engineering techniques.

REFERENCES

- [1] Arutunian S.G., Dobrovolski N.M., Mailian M.R., Vasiniuk I.E., Vibrating wire scanner: first experimental result on the injector beam of Yerevan Synchrotron. - Phys. Rev. Spec. Topics - Accel. and Beams, to be published.
- [2] Arutunian S.G., Dobrovolski N.M., Mailian M.R., Oganessian V.A., Vasiniuk I.E. Nonselective receiver of laser radiation on the basis of vibrating wire. - Proc. Conference Laser 2000 (November 2000, Ashtarak, Armenia).
- [3] Arutunian S.G., Dobrovolski N.M., Mailian M.R., Oganessian V.A., Vasiniuk I.E. Vibrating wires fence as a negligibly destructive beam profile and beam position monitor. - Proc. of the NATO Advanced Research Workshop on Electron-Photon Interaction in Dense Media, (25-29 June 2001, Nor Amberd, Armenia), NATO Science Series; II Mathematics, Physics and Chemistry, v. 49, pp. 303-308.
- [4] Wittenburg K. Beam tail measurements by wire scanners. - 11-th ICFA International Mini-Workshop on Diagnostics for High-Intensity Hadron Machines, October 21-23, 2002, ORNL Spallation Neutron Source, Oak Ridge, Tennessee, USA.
- [5] Arutunian S.G., Avetisyan A.E., Dobrovolski N.M., Mailian M.R., Vasiniuk I.E., Wittenburg K., Reetz R., Problems of installation of vibrating wire scanners into accelerator vacuum chamber. - Proc. 8-th Europ. Part. Accel. Conf., 3-7 June 2002, Paris.
- [6] Striganov S., Schmidt G., Wittenburg K., Estimation of the signal from the wire scanner in the TTF. - desyntwww.desy.de/mdi/downloads/WIRE_TTF.pdf
- [7] Hardekopf R., Meyer R., Sr., Plum M., Power J., Rose C., Sattler D., Shafer R., Wire-scanner design for the SNS superconducting-RF linac.- SNS01_PUB_0531.

Wire Scanner Beam Profile Measurement for ESRF

A. B. El-Sisi, Atomic Energy Authority, NRC, Plasma and Nuclear Fusion Dept.,
P.O.Box 13759, Cairo, Egypt

Abstract

The wire scanner is used in beam transfer lines of European Synchrotron Radiation Facility (ESRF) to provide data for beam profiles, which is being used in emittance measurements. The beam energy in the first transfer line is 200 MeV and the peak current is 25 mA. This work will discuss the operation of the wire scanner, and the first results of the scanner in ESRF. We get the emittance value for the vertical plane and the horizontal plane (1.5×10^{-6} m.rad, 2×10^{-7} mrad) respectively. When we used these values to simulate our result we find that, the simulation gives good fitting with real values.

1 INTRODUCTION

Method of beam transverse profile measurement in accelerators by wire scanner is wide spread in accelerator field [1,2,3]. The wire scanner beam profile measurement has been used extensively in the commissioning of many accelerators. It has been utilized to verify the focusing lattice, verify the functionality of the steering magnets, provide data for quad scan style emittance measurements, and helped to verify beam position diagnostics. The basic principle is based on secondary electrons generated by the interaction of the beam and the wire. The wire scanner in ESRF is controlled through TACO control system [4], accelerator control system. TACO is an object oriented control system developed at the European Synchrotron Radiation Facility.

2 EXPERIMENTAL FACILITY

ESRF is located at Grenoble – France. ESRF is essentially a complex of three accelerators, the preinjector, the booster synchrotron, and the storage ring. The later being equipped with insertion devices and beam-line front ends. The pre injector is 16-m long linear accelerator, which produce the electrons and accelerates them up to 200 MeV with peak current 25 mA in long pulse mode [5]. The booster is a 10 Hz cycling synchrotron 300 m in circumference, which increases the energy of the electrons up to 6 GeV before injection into the storage ring. Storage ring circumference is 844 m, 64 beam ports are spread around the storage ring to give access to beam lines on insertion device or alternatively on bending magnets. The beam of electrons is circulating at 6 GeV which make it capable for producing X-rays at each passage inside the bending magnets or insertion devices. Wire scanner is a diagnostic tool located in the transfer lines between the three accelerators TL1 and TL2, one for each line. The purpose of the wire scanner is

to provide horizontal and vertical beam profiles in transfer lines. The transverse beam emittance (ϵ) is deduced by the product of beam width (r) and beam divergence (\dot{r}) where $\epsilon = (r \dot{r})/\pi$. The wires are made from tungsten and gold (diameter is 40 μm) and are attached to an actuator driven by a stepping motor. The principle of providing profiles is based on the amount of secondary electrons generated by the interactions of the beam and the wire and measured in incremental steps. From these measurement steps the beam profile is constructed. This paper will discuss the operation of the scanner (Hardware and Software), testing the scanner during operation, obtain the profiles and finally calculating the emittance of beam in TL1. Figure (1) show a drawing of wire scanner, The basic parts of the hardware are the stepper motor and its controller, and the two ADC cards, one for each plane. The motion of wires must be continuous to avoid the wire vibration. The user of wire scanner has the ability to set the scanning parameters for profile (start position, number of measurements, and end position) using application program interface. Scanning is done under the angle 45° with the beam direction. Therefore, the position value obtained from the scanning is multiplied by $\cos 45^\circ$. Each step equals 0.1 mm in case the frequency equals 1 Hz. An external trigger must be adjusting to read the two ADC cards synchronized with the electron beam.

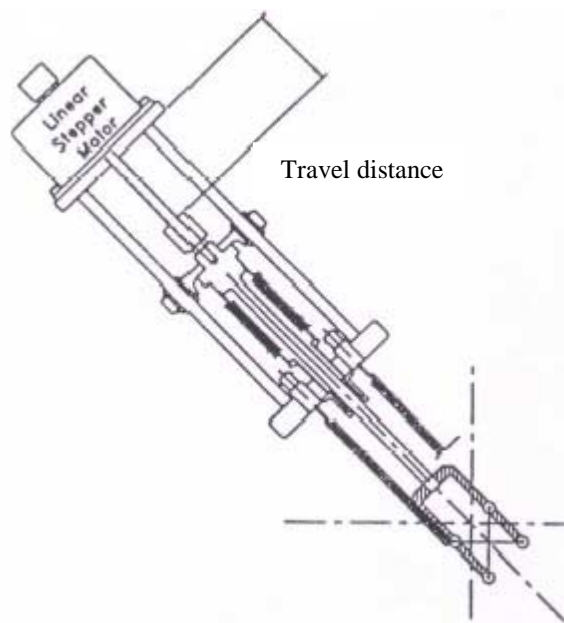


Figure (1) Schematic view of the wire scanner.

3 EXPERIMENTAL RESULTS

To get the profile of the beam, this required displacing the two wires inside the beam and measuring at each position the currents collected on the two wires. The wire scanner driver will have to drive the stepper motor (position, number of steps, speed) and drive the two ADC boards (setting the gains, reading the currents). Once the required number of measurement sequences has been completed, from the stored data of the complete cycle of measurement, we get the profile by using a special program in matlab. In order to minimize the overall measurement time, the sequence shall be synchronized on the beam pulse repetition frequency. The user of wire scanner can set it by the required frequency (1 Hz or 10 Hz). The profile data is stored in two different files. The first file contains the raw waveform data from the wire scanner for two plans (horizontal and vertical), the position data and the intensity of the beam at each point as well as the currents of the quadrupole's power supply during the cycle of measurement. Figure (2) shows the result of a typical profile measurement.

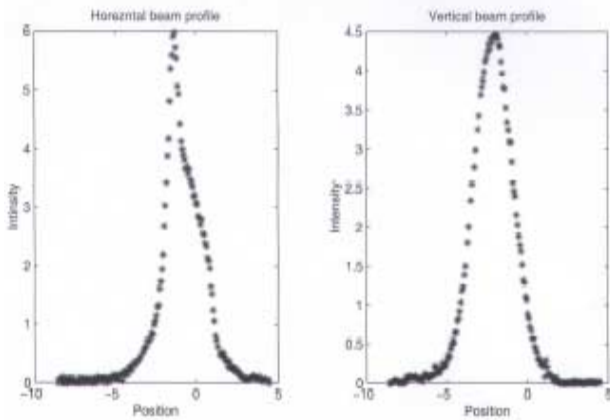


Figure (2) Typical profile measurement.

The second file contains just the processing operation to normalize the data, smoothing, calculated the width of the profiles, which will be used to calculate the emittance after that. Light beams are not straight lines in the mathematical sense [6]. They have a finite width and they are divergent, and such is also the electrons beam. The product of the initial divergence and the initial width of the electron beam is called the emittance. The smaller the emittance, the smaller the divergence and the width. The analogy between light beams and electron beam is quite strong. While the light is kept focussed by a set of glass lenses, the electron beam is being focussed by a set of magnetic lenses (quadrupoles). Quadrupole gives focusing in one plane and defocusing in the other plane. Alternating focusing and defocusing quadrupoles produce focusing in both planes. While the magnetic lenses can change the width or the divergence of the beam, they can never change the emittance according to Liouville's theorem. Therefore the emittance is a constant value

along the beam line. So we can define the emittance as the area in phase space occupied by the beam. Similarly, we define the acceptance as the area in phase space where a particle can have a stable motion. The acceptance may be limited either by the non-linearities (dynamic acceptance) or by the dimensions of the vacuum chamber (physical aperture). The acceptance plays a role in the design of the injection scheme and in the lifetime of the beam. We measured the emittance in a beam line consisting of three straight sections and two quadrupoles as shown in figure (3).

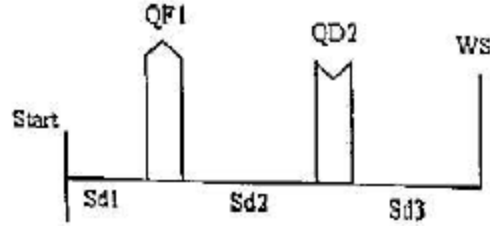


Figure (3) Beam line arrangement.

The motion of electrons in each plane can be described by the matrix expression:

$$X = T.X_o \quad (1)$$

Where X is the particle coordinate vector $X = \begin{pmatrix} x \\ x' \end{pmatrix}$

x is the position and x' is the divergence

and T transfer matrix, has the form $T = \begin{pmatrix} t_{11} & t_{12} \\ t_{21} & t_{22} \end{pmatrix}$

Starting from an arbitrary origin on the beam line, one can build the transfer matrix corresponding to the beam line by multiplying all the single element matrices:

$$T = T_n.T_{n-1}...T_2.T_1 \quad (2)$$

Then

$$X_n = (T_n.T_{n-1}...T_2.T_1).X_o \quad (3)$$

Due to Liouville's theorem, [7] all particles of the beam in phase space can be surrounded by an ellipse described by

$$\gamma x^2 + 2\alpha xx' + \beta x'^2 = \epsilon \quad (4)$$

Where (α, β, γ) describe the shape and orientation of the ellipse, and ϵ is the emittance. The surface area of the ellipse is equal $\pi\epsilon$. From equation (1) we can solve the equation (4) according to x_o and x_o' to obtain the coefficient (α, β, γ) which can be written as:

$$\begin{bmatrix} \beta \\ \alpha \\ \gamma \end{bmatrix} = \begin{bmatrix} T_{11}^2 & -2T_{12}T_{11} & T_{12}^2 \\ -T_{11}T_{21} & (T_{22}T_{11} + T_{12}T_{21}) & -T_{12}T_{22} \\ T_{21}^2 & -2T_{21}T_{22} & T_{22}^2 \end{bmatrix} \begin{bmatrix} \beta_o \\ \alpha_o \\ \gamma_o \end{bmatrix}$$

The beam matrix is defined as

$$\sigma = \begin{pmatrix} \sigma_{11} & \sigma_{12} \\ \sigma_{21} & \sigma_{22} \end{pmatrix} = \epsilon \begin{pmatrix} \beta & -\alpha \\ -\alpha & \gamma \end{pmatrix} \quad (5)$$

Based on the transfer matrix of the beam line we can calculate the new beam matrix at position P1.

$$\sigma_{11} = T \sigma_o T^T \quad (6)$$

So, we must know the beam matrix at a given point to know the emittance. The square half beam width is given by

$$w^2 = \sigma_{11}^2 = \sigma_{o11} T_{11}^2 + 2\sigma_{o12} T_{11} T_{12} + \sigma_{o22} T_{12}^2 \quad (7)$$

For complete set of tunings (at least three tunes) we can solve the equation (7) to get the new coefficient of sigma matrix at wire scanner position. The emittance measurement consists of measuring the width of the beam for different tunings of Quadrupole magnets. For each tune we calculated the half width of the beam at half maximum. After that we substitute in equation (9) for each tune to obtain the coefficients of sigma matrix ($\sigma_{0,11}$ $\sigma_{0,12}$ $\sigma_{0,22}$). By calculating the determinant of this sigma matrix we obtained the emittance value. By the same manner we can apply the same processing to calculate the emittance inside the transfer line between the booster synchrotron and the storage ring (TL2). By changing the current intensity of QF1 at (QD2 = 18 A) we get the emittance value for the vertical plane is 1.5×10^{-6} m.rad. Also by changing the current intensity of QD2 at (QF1 = 10.46 A) we get the emittance value for the horizontal plane is 2×10^{-7} m.rad. When we used these values to simulate our result we find that, the simulation gives good fitting with real values as shown in figure (9). Also by the same application program we can know the convergence of the beam or divergence from the shape of ellipse.

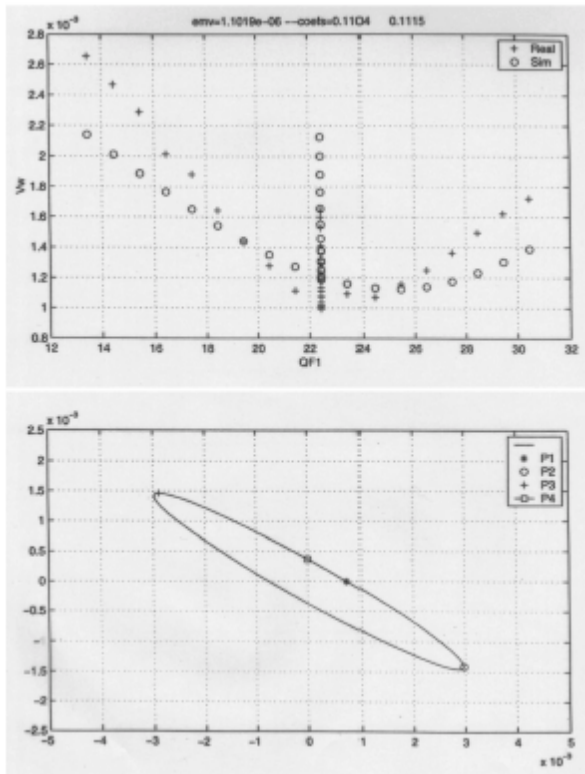


Figure (4) Width of vertical profile versus current of QF1 and simulation fitting, and the ellipsis correspond to the emittance

4 CONCLUSION

The wire scanner is used in transfer lines of ESRF to provide data for beam profiles, which is used in emittance measurements. The purpose of the scanner is to provide horizontal and vertical beam profiles. It has been utilized to verify the data for quad scan style emittance measurements. The result of a typical horizontal profile measurement shows a strange shape, this will lead to change the setting of LINAC to obtain the optimum case. By changing the current intensity of QF1 at (QD2 = 18 A) we get the emittance value for the vertical plane. The value is 1.5×10^{-6} m.rad. Also by changing the current intensity of QD2 at (QF1 = 10.46 A) we get the emittance value for the horizontal plane. The value is 2×10^{-7} m.rad. And we find that, the simulation gives good fitting with real values. There still remains some works to be done for the second transport line between the booster and the storage ring.

5 ACKNOWLEDGEMENT

I would like to thank ESRF that gave me chance to work as scientific collaboration for SESAME project. And also thank Dr. L. Farvacoue of ESRF, Theory Group for his advises concerning the equations of emittance calculation.

6 REFERENCES

- [1] Arutunian S.G. et al., Proceeding of PAC, New York, 2105, (1999).
- [2] J. F. O'Hara, et al., Beam Instrumentation Workshop, Cambridge, Massachusetts, 8-11 May, (2000).
- [3] Naoko Iida, et al., Proceeding of PAC, New York, 2108, (1999).
- [4] A.Götz, "TACO Manuel" European Synchrotron Radiation Facility, B.P. 220 – 38043 Grenoble cedex, France, Nov. (2000).
- [5] "ESRF Foundation Phase Report", European Synchrotron Radiation Facility, B.P. 220 – 38043 Grenoble cedex, France, Feb. (1987).
- [6] M. Pelsko, SESAME Workshop on Accelerator Science, Al Baqa Uni., Jordan, 9 Sep. (2000).
- [7] L. Farvacoue, Laboratory National Saturne, CEA, France, Mars (1980).

ADVANCED RESIDUAL GAS PROFILE MONITOR FOR HIGH CURRENT SYNCHROTRONS AND COOLER RINGS

P. Forck¹, T. Giacomini¹, A. Golubev², D. Liakin², V. Skachkov², A. Vetrov³

¹ Gesellschaft für Schwerionenforschung - GSI, Darmstadt

² Institute for Theoretical and Experimental Physics - ITEP, Moscow

³ Moscow State University - MSU, Moscow

Abstract

The modern ion accelerators and storage rings require faster beam profile measurement with higher resolution. We propose a new residual gas monitor, which will operate on secondary electrons whose trajectories are localized within \varnothing 0.1 mm filaments along uniform magnetic field lines excited by a permanent magnet. To adopt this resolution into the data acquisition system a CCD camera with upstream MCP-phosphor screen is used. To realize a fast turn-by-turn readout a photodiode array of 100-channel with amplifier and digitizer is foreseen.

DESIGN CRITERIA

Non-destructive profile measurement systems are needed to yield the beam emittance and it's evolution during the storage in a synchrotron. An advanced high performance residual gas monitor (RGM) system seen in Fig. 1 is under development. The main features are an applied magnetic field by permanent magnets and a fast turn-by-turn as well as a high-resolution read-out mode. It will be constructed to operate in numerous wide current and energy range synchrotrons as well as low current cold beams in cooling rings.

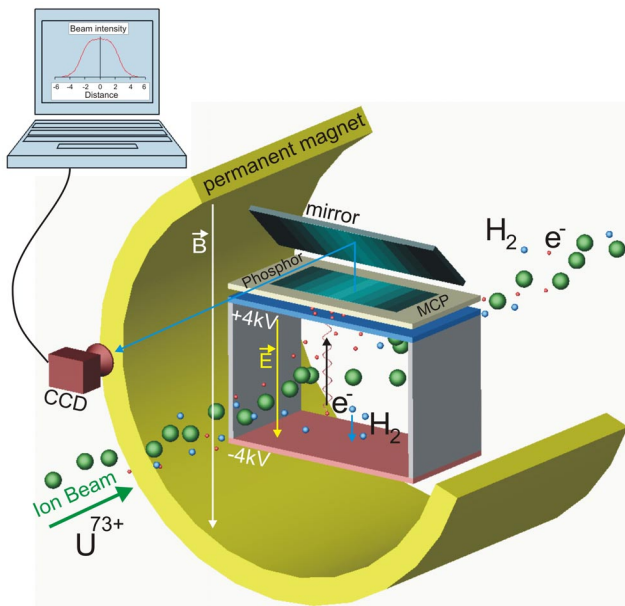


Figure 1: RGM operational principle.

It will serve as a prototype for the various existing and planned ring accelerators at the GSI facility [1].

In RGMs an electrostatic field accelerates the ionization products by the beam and residual gas towards a Micro Channel Plate (MCP). When these particles reach the MCP secondary electrons are produced and accelerated against a phosphor screen, where they produce light spots. These can be observed by a CCD camera or by a photo-diode array.

True beam profile: Beside the applied external electric field, the beam space charge field accelerates the ionized particles. To obtain an undistorted beam profile the particles are guided to the MCP surface by an external magnetic field parallel to the external electric field. Only when a magnetic field of about 0.1 T and an electric field of about 0.5 kV/cm are applied, the primary electrons are guided straightforward to the MCP as calculated for Fig. 2. The parameters are typical for a high current operation of the SIS synchrotron at GSI. To achieve 0.1 mm resolution limited by the MCP resolution, the applied magnetic field has to provide a cyclotron radius of the same size respective a field uniformity of 5% from starting point to the MCP. In general the cyclotron radius is given by the initial electron velocity after ionization.

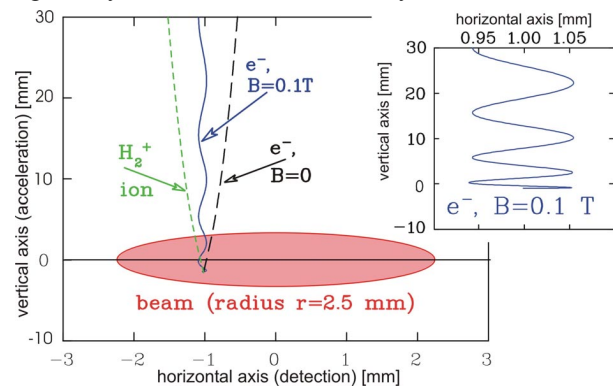


Figure 2: Trajectories of residual gas particles with and without magnetic field (10^9 U^{73+} per 10 m long bunch).

In different synchrotrons and storage rings various operating modes and different demands exist. We intend to provide a high-resolution (HRes) mode and a fast read-out mode (FRout).

HRes: For precise beam observations during the acceleration or cooling, a high spatial resolution down to

¹ Corresponding author: T.Giacomini@gsi.de

0.1 mm is needed. One time interval for profile measurement will cover the 0.1-100 ms range. In this case the beam image on the phosphor screen is observed with a digital CCD camera, providing the required exposure time 0.1-100 ms and a frame rate up to 100 fps (frames per second).

FRout: For high current synchrotrons, the beam profile evolution after injection - and therefore the transverse emittance - is of great importance to control the optimum matching conditions [2]. To evaluate the beam quadrupole moment and the resulting emittance blow-up it is sufficient to record the beam width of the first few hundred turns. A photo-diode array provides a turn-by-turn regime at ~ 1 mm resolution when a single beam profile is measured during ~ 1 μ s.

RGM MODULES

E-Field: Due to the need of a horizontal and a vertical profile measurement two monitors have to be installed. Considering the different field directions of both monitors special arrangements should be made for the shielding between them. A voltage of ± 4 kV is applied to the bottom and the top sheets establishing field strength of about 0.5 kV/cm.

REPM dipole: The split-pole [3,4] and quasi sheet multipole [5] rare earth permanent magnet (REPM) systems deliver the most compact design of a multipole. When longitudinal magnet size l , is several times greater than its bore radius R_1 , then magnetization spread and mechanical errors are the only sources of the field distortion. In practice ring type magnets [6] suffer higher deviations in magnetization while segmented multipoles are difficult to fabricate.

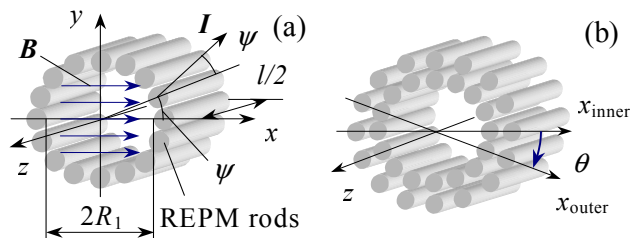


Figure 3: Rod type dipole – (a) and (b) – field compensation method in two-layer construction.

Unique advantage of rod type construction [7] provides arbitrary magnet assembly sizes due to the magnetic element unification. Since average magnetization is lower than in ideal magnet the field of a dipole with outer radius R_2 and rod magnetization I

$$B = c_f \mu_0 I \ln R_2 / R_1 \quad (1)$$

due to the space filling factor $c_f < 1$. The magnetic alloy of the REPM is Nd-Fe-B with remnant induction $B_r = 1.2$ T.

In short magnet $l \leq 2R_1$ seen in Fig. 3(a) the field becomes lower because of fringe fields and field

configuration differs from perfect uniform. In particular the rod dipole axis field, $B_0(z)$, given by

$$B_0(z) = \frac{c_f \mu_0 I}{4} \left[F\left(\frac{z-l/2}{R_2}\right) - F\left(\frac{z+l/2}{R_2}\right) - F\left(\frac{z-l/2}{R_1}\right) + F\left(\frac{z+l/2}{R_1}\right) \right], \quad (2)$$

where $F(\zeta) = \zeta(1+\zeta^2)^{-1/2} + 2 \ln(\sqrt{1+\zeta^2} + \zeta)$, is some lower than field eqn. (1) at the center $z=0$. Nevertheless the field integral is equal to the 'square wave field' eqn. (1) and the same length l .

For electron detection in RGM the 30 mm z -axis dimension of MCP defines the working region width $w_z < l$. Below $l=100$ mm the dipole outer radius shows a very rapid growth seen in diagram Fig. 4 calculated with eqn. (2) at $R_1=200$ mm while the REPM weight reaches minimum $W=64$ kg at $l=176$ mm (point S).

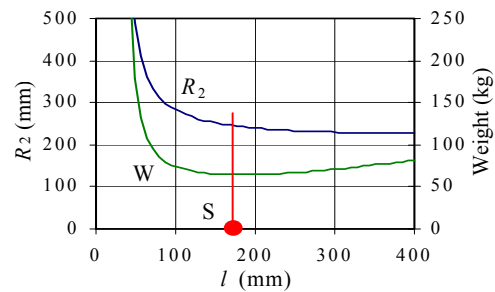


Figure 4: 0.1 T dipole outer radius and REPM weight dependencies.

The 5 % non-uniformity tolerance in the $210 \times 160 \times 40$ mm³ working region requires a single dipole length longer than 500 mm. Nevertheless a combination of several shorter dipole sections with different sizes reduces the full dipole length. Fig. 5(a) shows a 300 mm long Nd-Fe-B rod dipole with 200 mm long central section, having a total weight of 92 kg. Varying the central section bore radius the field curves seen in Fig. 5(b) corresponding to several y and z within working region can be fitted in 3 % accuracy range.

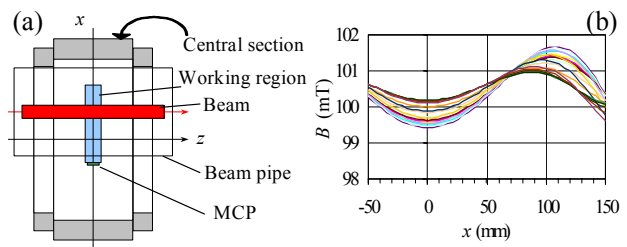


Figure 5: Three-section dipole – (a) and (b) – field.

During the vacuum bake-out the REPMs can be disassembled and removed from the beam pipe, because they cannot withstand temperature increasing up to 300°C. Due to high magnetic rigidity the dipole field is reversible so we divide the dipole into semi-cylinders.

The dipole will be made from relatively small magnetic elements assembled in two layers seen in Fig. 3(b). At a rotation angle of $\theta=180^\circ$ the center field can be reduced to nearly zero if the layer fields equal each other [8].

The monitor E - and B -fields result in a transverse kick up to several 10 mrad. They should be compensated by the same type of field configuration.

To minimize expenses of a new monitor development we foresee a monitor design, which covers the most possible variations of main vacuum, beam and accelerator parameters. Three-dimensional scaling the magnet sizes conserves both the magnetic field value and its configuration. The working region scaling should be also involved because the necessary magnetic field uniformity is extended on whole electron trajectories up to the MCP.

MCP and phosphor screen: For the large aperture applications it is planned to use MCPs of around $100 \times 30 \text{ mm}^2$ in Chevron configuration. The FRout mode makes it necessary to use a phosphor screen with a short decay time at least P47 type with a decay time of 70 ns. The amount of residual gas electrons has to be large enough for this application so a moderate pressure bump has to be applied.

Optical coupling: The specifics of this device are: low light intensity from the phosphor screen and very limited space due to the dipole volume. A movable mirror reflects the image from the phosphor screen to the CCD camera or to the photo-diodes seen in Fig. 6.

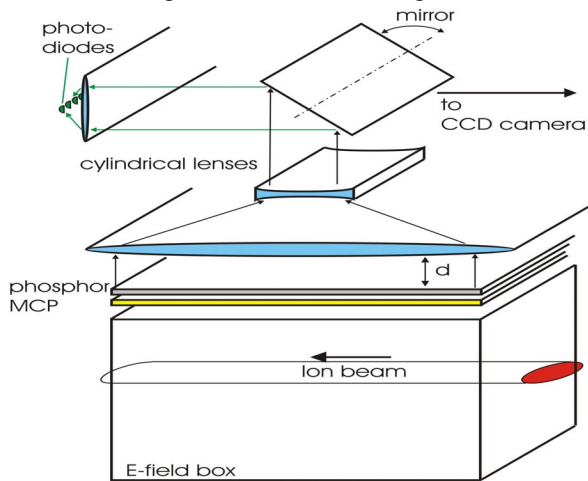


Figure 6: Basic optic scheme.

For the photo-diodes it is necessary to integrate the intensity of the light over the MCP length. This can be done by optical elements with cylindrical geometry, like parabolic mirror, cylindrical lenses, and Fresnel lens.

A special lens configuration improves the light transmission. A convex lens followed by a concave lens is mounted closer to the phosphor screen. This configuration collects a large light fraction fitting it to a smaller area. The light can be easily focused to the photo-diodes or observed by the CCD camera.

CCD camera and photo-diodes: CCD cameras are available as full-configured systems with high resolution, short exposure time and high frame rate. The fast turn-by-turn readout mode by the photo-diode array requires 0.1-1

μs sampling time and a data capacity for about 300 beam revolutions. Each photo-diode is equipped with an individual low-noise preamplifier and a variable gain amplifier to normalize the readout signal. Also a high performance digitalization system with peak performance of about 30 MSamples/s and a data storage capacity of about 20 kB/channel is needed.

CONCLUSIONS

The basic idea is the application of permanent magnets to create the required dipole field of the RGM. It offers a good homogeneity as well as a very compact design. With a proper mechanical design, i.e. a two-layer system, the magnetic field can be switched off. Two REPM dipoles can be fitted into 700 mm long free space and are removable for vacuum bake-out. We will integrate two modes of operation: a high spatial resolution mode by a CCD camera and a fast turn-by-turn mode by a photo-diode array. The monitor will be a very flexible and modular detection system, which covers a wide range of application.

REFERENCES

- [1] www.gsi.de and O. Boine-Frankenheim, "Accelerator Challenges of Proposed Radioactive Beam Facilities", Proc. EPAC-02, 2002, p. 99.
- [2] See e.g. M. Benedikt et al., "Injection Matching Studies Using Turn-by-turn Beam Profile Measurements in the CERN PS", Proc.-DIPAC-01, 2001, p. 189, and G. Ferioli, C. Fischer, I. Koopman, F. Roncarolo, "Beam Studies Made with the SPS Ionization Profile Monitor", These Proceedings.
- [3] K. Halbach, "Design of Permanent Multipole Magnets with Oriented Rare Earth Cobalt Material," Nucl. Instrum. Methods 169, 1980, p. 1.
- [4] N.V. Lazarev and V.S. Skachkov, "The Tipless Permanent Magnet Quadrupole Lenses," in Proc. 1979 Linear Acc. Conf., 1979, p. 380, and I.M. Kapchinskiy, N.V. Lazarev et al, "Permanent Magnet Small-size Quadrupole Lenses for Ion Linear Accelerators," MT-12, IEEE vol. 28-1, 1992, p. 531.
- [5] V.S. Skachkov, "Quasi-Sheet Multipole Permanent Magnets", Nucl. Instr. Meth. A, 500/1-3, 2003, p. 43.
- [6] V.S. Skachkov et al, "Circular Permanent Magnet Quadrupoles for Higher Frequency and Higher Shunt Impedance Linacs", Proc. EPAC-92, 1992, p. 1400.
- [7] V.S. Skachkov et al, "Drift Tubes for a Focusing Channel of Ion Linear Accelerator", in Proc. PAC-89, IEEE, v. 2, 1989, p. 1073.
- [8] V.S. Skachkov, "Split-Pole PM Dipoles and Quadrupoles with Variable Field", in Proc. EPAC-96, v. 3, 1996, p. 2190.

RESIDUAL GAS FLUORESCENCE FOR PROFILE MEASUREMENTS AT THE GSI UNILAC

A. Bank, P. Forck, GSI, Darmstadt, Germany, email: p.forck@gsi.de

Abstract

The high beam currents, delivered at the LINAC at GSI (UNILAC) can destroy intercepting diagnostics within one macro pulse. As an alternative for a non-destructive profile measurement the method for residual-gas-fluorescence is investigated. The fluorescence light emitted by the N_2 molecules of the residual gas at the blue wavelength range can be monitored with a modern CCD camera. The images are transferred via digital bus and after analysis of the images with a modern software the profiles are generated. Due to the short beam pulses the light intensities emitted by the residual gas are low and require a high amplification which is realized with an image intensifier with double MCP, connected with a fiber taper to the CCD-chip. The design and measurements are discussed.

Residual Gas Fluorescence

The profile of an ion beam can be determined by observing the fluorescence emitted by the residual gas molecules using a CCD camera. This method was previously applied e.g. at cw proton LINAC at Los Alamos [1] and the CERN SPS synchrotron [2]. The GSI UNILAC is a pulsed heavy ion LINAC with macro pulse lengths of several 100 μ s and is e.g. used to fill the proceeding synchrotron. The beam profile should be monitored within one macro pulse, therefore the use of a long integration time for an improved signal-to-noise ratio is impossible. Because of that short integration time and the pressure of the residual gas (typically: 10^{-7} – 10^{-8} mbar) the emitted light has to be amplified drastically, in this case by using a double MCP image intensifier.

Due to the large energy release in intersecting material (maximum of 1 MW beam power) at high current operation (up to 20 mA beam current) the traditional determination of transverse beam profile by using secondary emission grids (SEM-grids) can not be applied. To prevent melting, the macro pulse length has to be shortened. A non-intersecting residual gas monitor can be installed or the fluorescence of the residual gas can be used to detect the profiles in case of a full pulse length. The latter has the advantage that no mechanical parts have to be installed in the vacuum pipe, leading to a compact and cost-efficient design. In addition the spatial resolution of a SEM-grid is limited by the wire-spacing of about 1 mm. Using the fluorescence method up to 0.1 mm can be achieved. Another advantage is the compact commercial 'data acquisition system' incorporated in the CCD camera.

At GSI UNILAC the ions kinetic energy varies from 0.12 up to 15 MeV/u. Depending on ion type and charge

state this is close to the maximum of the electronic stopping power.

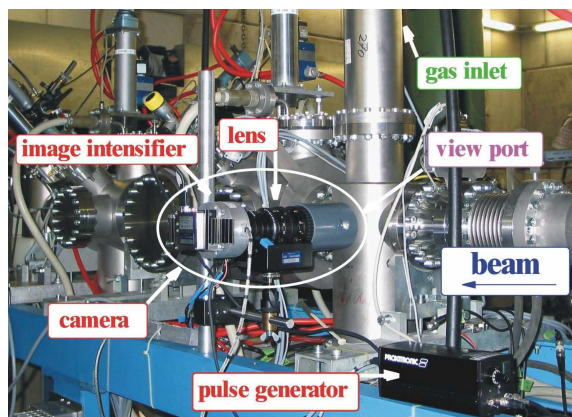


Fig.1: The installation of the intensified CCD-camera at the target location

The residual gas at the UNILAC contains mainly Nitrogen which has a large cross section for the excitation into the ionized N_2^+ molecular state, as measured in [3] by 200 keV proton collisions and at several GeV in [4]. The fluorescence light is emitted in the wave length range of 300 to 500 nm. A scaling proportional to the electronic stopping power of the beam ions is expected.

Components

Vacuum Chamber: The beam is viewed through a Suprasil window (wavelength transmission between 20 nm and 2 μ m) mounted on a \varnothing 35 mm flange. To suppress reflections, the tube is blackened by a vacuum suitable graphite lacquer (graphite grains solved in isopropanol).

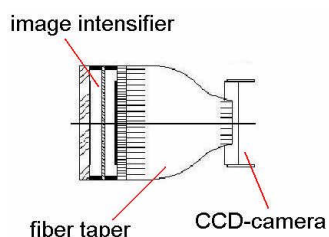
Zoom lens: A remote controlled c-mount zoom lens (Fujinon D14x7.5A-R11/12) with 7.5 – 105 mm focal length and a macro setting is installed. A short distance between the beam and the lens increases the yield of captured photons, but reduces the relative depths of focus. A small focal length increases the depth of focus (i.e. with the same relative iris setting a larger depth can be imaged) but reduces the spatial resolution. A suitable setting was found with a focal length of 15 mm, a distance between lens and center of beampipe of 39 cm resulting in an minimum F-number of 2 (~55 mm depth of focus needed) and an observation length of ~5 cm.

Image intensifier: The installed \varnothing 25 mm image intensifier has a double (chevron) MCP setting with a maximum gain of $\sim 10^6$. The captured photons are converted to electrons by a photo-cathode made of S20 UV-enhanced [5], having a quantum efficiency of 25-30

% at the interesting wavelength interval and a low dark current (~ 500 electrons / $s \cdot cm^2$). The voltage between the photo-cathode and the first MCP can be switched from transfer mode to a blocking mode within 100 ns, enabling an observation only during the beam delivery. This also gives the possibility to observe segments of the macro pulse (see Fig.6). On the P46 phosphor screen spots from single photons are visible. Due to the decay time of the phosphor of ~ 300 ns (90 to 10 %) fast changes of the beam parameters can be resolved. The resolution of $\sim 0,1$ mm on the MCP surface is sufficient for this application.

Taper coupling: To transmit the light from the image intensifier to the CCD a minifying taper coupling is used as shown in Fig.2. This taper is made of bundled glassfibers with shrinking diameter and a minification of 8/25 (ratio of CCD / MCP diameter). About 7 % of the light emitted in the half hemisphere is guided to the CCD which is approximately 5 times of the transmission using a relay optic.

Fig.2: Image intensifier coupled to CCD by reducing taper



CCD camera: A 8 bit Basler 302fs CCD camera with a maximum of 28 frames per second at 782×582 pixels was chosen. The CCD signals are directly digital-converted at the camera head and transferred using Firewire IEEE1394 [6] protocol. Compared to an analog video link, no degradation of the signal due to long cables occurs. At the moment the Firewire bus standard allows a maximum data rate of 400 Mb/s which equals to 100 frames per second at VGA resolution. The variable bus architecture with up to 63 nodes is well suited for the distributed diagnostic installations in the various beam lines. The maximum cable length for electrical transmission is 20 m. For the long distances between the diagnostics and the control room fiber optic cables driven by opto-couplers (NEC or Newnex Technology) are used.

Data analysis: After translation from optical to electrical signal, the data is transferred to a Windows PC via a cheap standard PCI interface. The software to analyse the data is written in Labview. It also allows to control the various camera functions, e.g. exposure time, electronic gain, trigger. The Firewire driver from the commercial package IMAQ is used to acquire the images and control the camera and the IMAQ Vision package for the image processing.

Test measurements

For the test measurements medium and high current Ar^{10+} and U^{28+} beams with energies of 4.7, 5.8 and 11.4 MeV/u are used. Typical currents were 0.5 to 2 mA

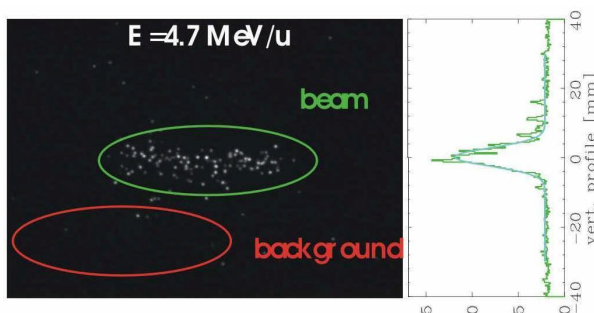


Fig.3: Image of a $200 \mu s$ U^{28+} beam with $I=700 \mu A$ recorded at the GSI LINAC with a vacuum pressure of about 10^{-5} mbar. The two dimensional image from the intensifier (left) and the projection for the vertical beam profile (right) is displayed.

and $200 \mu s$ macro pulse length. This corresponds to $\sim 10^8 \dots 10^9$ particles per macro pulse passing the viewport. In Fig. 2 an image of a single macro pulse U^{28+} is displayed. By using a regulated gas valve the pressure could be locally raised up to 10^{-4} mbar. Due to the high amplification of the double MCP, single photon events are visible. Projecting the light spots along the beam axis results in the vertical beam profile. The resolution of $300 \mu m/pixel$ is sufficient for these parameters. For images of less signal strength the data can be binned to improve the signal-to-noise ratio. Due to the statistical nature of the signal generation, the data quality can also be enhanced by data binning of the individual projections or by summing up several images.

The measurements show a low background, especially after blackening of the vacuum chamber. The uniformly distributed dots outside of the beam path seen in Fig.2 are caused by γ - or x-rays hitting the photo cathode generated by nuclear- or atomic inner shell excitations probably at the beam dump located 2 m apart. Their contribution is independent of the optical setting, and even visible if the iris is totally closed. The noise level increases occasionally for same beam settings, this seems to happen while the beam is hitting the aperture at a location near the image intensifier. Even in such case, the images can still be evaluated. Due to the statistical background distribution over the whole image and after projection, the noise level can be subtracted from the data. A assumed relation of the noise level and the beam energy could not be confirmed during the latest tests where a shielding was used to protect the image intensifier from the radiation.

The fluorescence data has been compared with the data of a residual gas monitor located 1m downstream in the beam line. As it can easily be seen in Fig.4 the correspondence is quiet well. In this beam setting the resolution of the fluorescence profile is particularly suitable whereas the residual gas monitor reaches it's border of resolution where only 5 to 7 points are distributed over the whole peak.

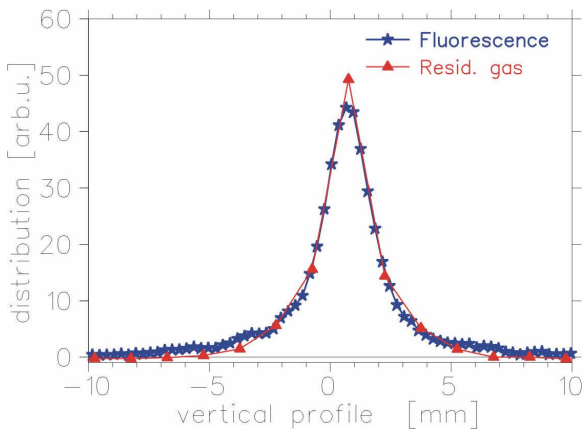


Fig.4: Comparison of the fluorescence profile with the data of a residual gas monitor measured at 11.4 MeV/u. The curves are normalized to the same integral.

A crucial point for the operation of the fluorescence monitor is a proper alignment of the optics. The depth of sharpness has to be defined well by choosing a proper focal length, object distance and iris [7]. A compromise between resolution and signal strength has to be found. It is advantageous to choose a moderate object distance, ~40 cm in our case. The loss of signal and resolution due to the larger distance to the beam is reobtained by the possibility of choosing a larger focal length and iris due to comparable larger depth of focus at that distance. In most cases the optical quality of a lens with small focal length is lower. An array of LED's opposite to the camera is used to match the depth of sharpness with the center of the beam pipe. It is also used as an on-line calibration for the reproduction scale.

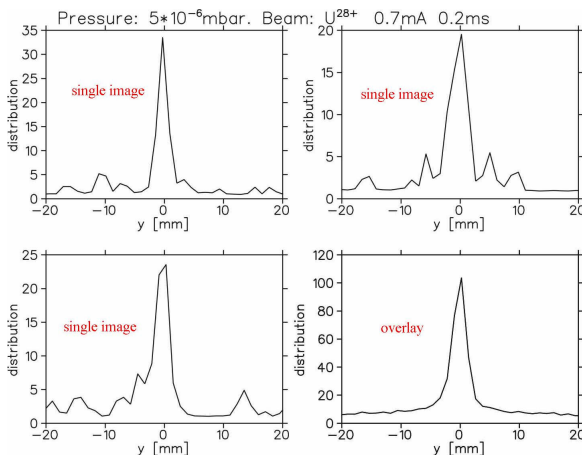


Fig.5: Three vertical projections of images of a single macro pulse and one projection (lower right corner) of an overlay of 32 images. All are made at $5 \cdot 10^{-6}$ mbar.

The lowest usable residual gas pressure for an optical setting (distance to beam center ~40 cm, focal length 15 mm, F-number 2.8) of the measurements with 700 μ A U^{28+} and 200 μ s pulse length was found at $5 \cdot 10^{-6}$ mbar. In Fig.5 3 projections of images of a single macro pulse as well as a projection of 32 consecutive images are shown. The averaging of

images of several macro pulses gives the possibility for further improvement of the signal-to-noise ratio.

An advanced application for the residual fluorescence measurement is the determination of the pulse width variation as shown in Fig.6. The fast switching of the voltage between the photocathode and the MCP can be used to restrict the exposure time. For a case of Fig. 6 one image of 40 μ s exposure time is recorded and the measurement is repeated with 8 different trigger delays. This type of measurement is not possible with an intersecting SEM-grid due to the risk of wire melting by the large beam power.

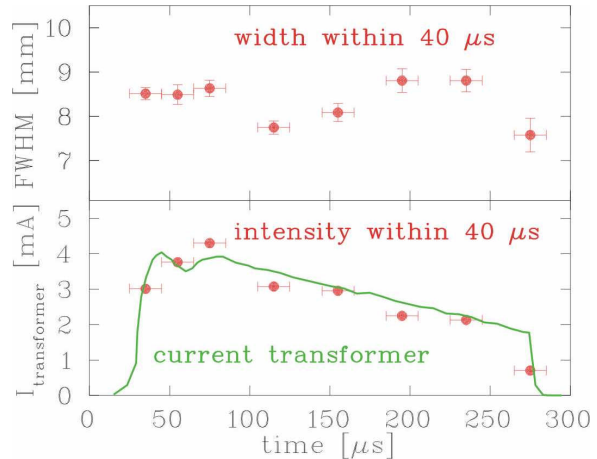


Fig.6: Measurement of the width structure of the macro pulse. In the lower graph the normalized image intensity to the measured beam current.

Conclusion

The described non-intersecting method for profile measurements can be applied for ion beams of high current at a pulsed LINAC. For a signal enhancement at lower currents, a moderate pressure bump can be applied easily. A direct image of the beam is generated without any installations inside the vacuum pipe. A resolution of up to 0.1 mm can be reached. More advanced detection schemes, e.g. like observation of a possible beam movement during one macro-pulse can be applied by using a short exposure time.

References

- [1] D.P.Sandoval et al., 5th beam Instrum. Workshop, Santa Fe, AIP Conf. Proc. 319, p. 273 (1993).
- [2] G.Burtin et al., Proc. 6th Euro. Part. Acc. Conf. EPAC, Vienna, p. 256 (2000).
- [3] R.H.Hughes et al., Phys. Rev. 123, 2048 (1961).
- [4] M.A.Plum et al.Nucl. Instr. And Meth. In Phys. Research A 492 p.74-90 (2002).
- [5] www.proxitronic.de
- [6] D. Anderson, FireWire architecture: 1394a www.mindsharing.com, Addison-Wesley (1999).
- [7] P.Forck, A.Bank, Euro. Part. Acc. Conf. EPAC Paris, p.1885 (2002).

IONISATION BEAM PROFILE MONITOR AT THE COOLER SYNCHROTRON COSY-JÜLICH

V. Kamerzhiev, J. Dietrich, Forschungszentrum Jülich GmbH, Germany

Abstract

For beam profile measurements, a residual-gas ionisation beam profile monitor using a position sensitive micro channel plate (MCP) detector was developed and installed at the cooler synchrotron and storage ring COSY.

Since COSY operates with beam intensities up to 10^{11} protons/deuterons and a vacuum of 10^{-11} - 10^{-9} mbar, there is a high risk of detector damage. The aging of the channel plates was investigated by means of scanning electron microscope and energy dispersive x-ray microanalysis. Different implemented detector protection mechanisms are discussed. Profile measurements with electron cooled beams are reported.

INTRODUCTION

To optimise the performance of an accelerator precise measurements of many beam parameters are required. To determine the actual charge distribution inside the beam and to find the value of beam emittance non destructive beam profile measurements are needed. One of the known techniques [1] relies on the ionisation of residual gas by the beam particles. A device utilising this principle was installed in the COSY ring [2,3].

DESIGN

Between two electrodes a parallel ion drift field is maintained. Residual gas ions are drifted onto MCP chevron assembly that provides an electron multiplication factor up to 10^7 [4]. The secondary charge produced from each ion is collected by a wedge and strip anode (see Fig. 1) [5].

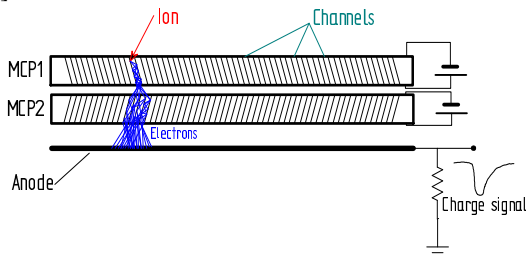


Figure 1: Position sensitive detector.

The charge signals from each electrode are first converted into time signals which are then digitised. A PC running CoboldPC software [6] is used for data readout, analysis and visualisation. The detector and the readout method used allow the measurement of position of separate residual gas ions and are especially suitable for low and medium intensity beams. The images of higher contrast compared to the phosphor screen approach are achievable [6].

Position sensitive anode

A position sensitive wedge-and-strip anode is placed on a 2 mm thick ceramic substrate of 65 mm outer diameter with germanium layer on the opposite side (see Fig. 2). The anode consists of three electrodes called by their geometry wedge, strip and meander.

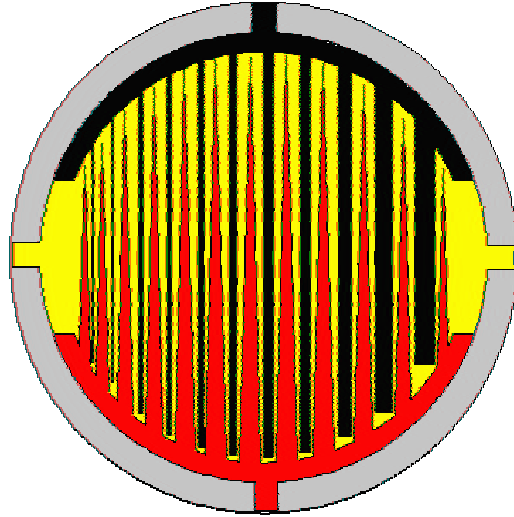


Figure 2: Wedge-and-Strip Anode.

Since this is a charge coupled device, secondary electrons leaving the MCP assembly hit the germanium layer and induce a signal on the anode structure (see Fig. 1) [7]. The charge of secondary electron cloud is distributed over all electrodes. To determine the position of cloud's centre of mass i.e. the residual gas ion coordinates one should measure the charge on each electrode independently and compute x and y values using the formulae:

$$x = \frac{Q_s}{Q_s + Q_w + Q_m};$$

$$y = \frac{Q_w}{Q_s + Q_w + Q_m}$$

where Q_s , Q_w and Q_m are measured charges on strip, wedge and meander respectively. As one can see in Fig. 2 the equations are derived just from the geometry of the anode structure.

Electronics

The charge-to-time converter is based on the LeCroy's MQT 300AL chip [3,8] which utilises a Wilkinson dual slope converter. The time signals are transported to control room where a time-to-digital converter (TDC)

and a PC are installed. The TDC is connected to the computer via internal ISA card [6,9].

Software

As mentioned above CoboldPC program [6] is used for data acquisition, analysis and visualisation. The program has a modular structure and can be easily adopted for different hardware and data analysis algorithms i.e. other detector types.

RESULTS

Vertical profiles of electron-cooled and uncooled proton beam have been measured (see Fig. 3). At the moment of data acquisition there were about $1.3 \cdot 10^9$ protons at 45 MeV in the ring. Residual gas pressure was measured to be 10^{-9} mbar.

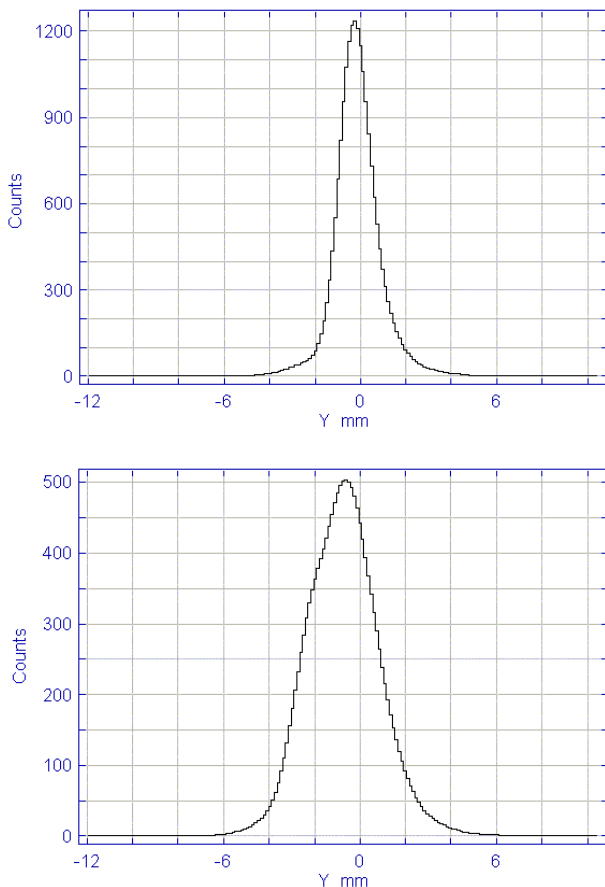


Figure 3: Profile of a cooled (upper trace) and an uncooled (lower trace) proton beam.

As one can see the density of the electron cooled beam is higher compared with the uncooled one (see fig. 4). The profile of the cooled beam meets the expectation and corresponds good to the H^0 profile measured simultaneously. However the width of the uncooled beam seems to be too small. Unexpected aperture limitations could be the reason for this discrepancy [10].

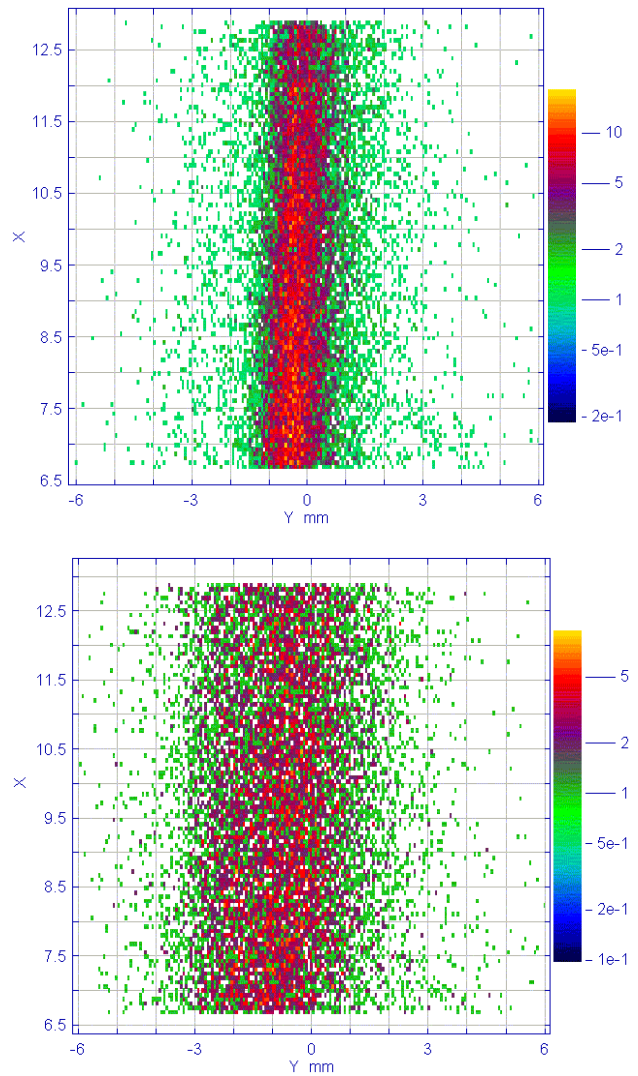


Figure 4: 2D image of a cooled (upper image) and an uncooled (lower image) proton beam.

EXPERIENCE

The lifetime of micro channel plates and the ionisation event rate are crucial issues for the profile measurement of intense proton beams. Regular monitoring of MCP condition, e.g. gain distribution and detection efficiency is necessary to provide reliable beam profile measurements. Despite we used Long-LifeTM MCPs aging effects such as an inhomogeneous distribution of the gain over the surface have been observed. For monitoring and online calibration purposes an α -source has been fixed on the flange opposite to the one the detector is mounted on. So the detector can be illuminated with α -particles. Different detector protection mechanisms such as moveable (pneumatic driven) protection screen and MCP high voltage triggering were implemented to improve detector lifetime and performance. MCPs with inhomogeneous gain distribution have been investigated by means of scanning electron microscopy and energy dispersive x-ray microanalysis (EDX) [11].

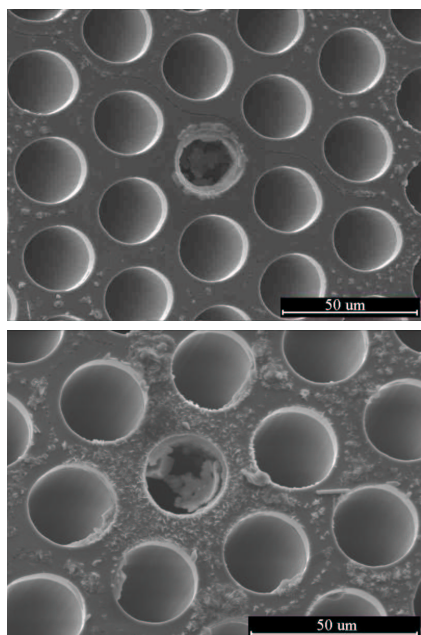


Figure 5: MCP surface seen by scanning electron microscope.

Small damaged regions on the MCP surface faced to the anode were found. Elementary composition on this regions was determined using EDX.

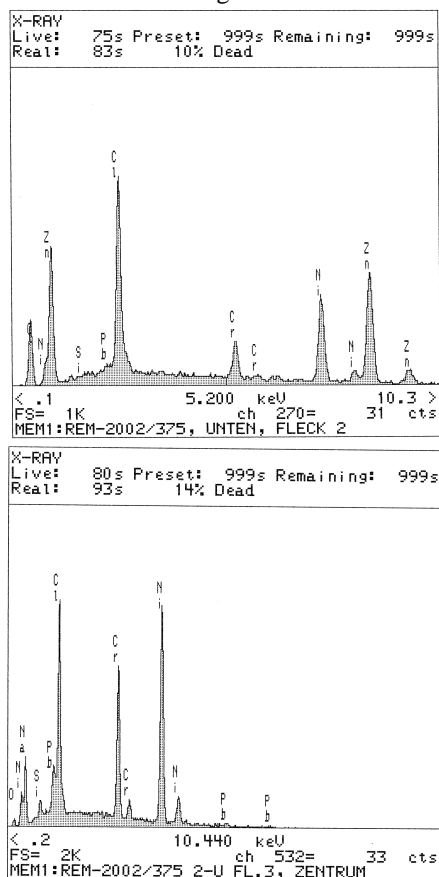


Figure 6: Energy dispersive x-ray microanalysis of the MCP surface.

We still do not properly understand the interrelation between the inhomogeneous gain distribution and damaged regions also the origin of *Cl* on the surface.

ACKNOWLEDGEMENTS

The authors would like to thank O. Jagutzki and K. Ullmann-Pfleger from the University of Frankfurt am Main and COSY team for useful discussions and support.

REFERENCES

- [1] K. Wittenburg, Strahlprofilmonitore für den HERA-Protonenring, DESY HERA 1986-06.
- [2] M. Schulz-Rojahn, Messung von Strahlprofilen am internen COSY-Protonenstrahl mittels Restgasionisation, Doctor's thesis, Bonn, 1998.
- [3] V. Kamerzhiev, Diploma thesis, FZ Jülich, 2000.
- [4] J.L. Wiza, Microchannel Plate Detectors, Nucl. Instr. and Meth. 162 (1979) 587-601.
- [5] O. Jagutzki, J.S. Lapington, L.B.C. Worth, U. Spillmann, V. Mergel, H. Schmidt-Böcking, Position sensitive anodes for MCP read-out using induced charge measurement Nucl. Instr. and Meth. A 477 (2002) 256-261.
- [6] <http://www.roentdek.com/>.
- [7] J.S. Lapington et al., Spatial resolution limitations of microchannel plate/conductive charge division readout devices, Nucl. Instr. and Meth. A 273 (1988) 663-666.
- [8] LeCroy MQT 300A datasheet.
- [9] <http://www.acam.de/>.
- [10] H.J. Stein, private communication.
- [11] R. Schneider, Prüfbericht Institut Fresenius, Dresden, 2002.

RECENT DEVELOPMENTS OF THE EXCYT RADIOACTIVE BEAM DIAGNOSTICS

L.Cosentino, P.Finocchiario

INFN-LNS, via S.Sofia 44, 95125 Catania, Italy

Abstract

The EXCYT radioactive beam facility at LNS, based on the ISOL technique, will start producing its first radioactive beams during 2004. We have set up a suitable high sensitivity diagnostics, in order to guarantee a real time monitoring of the beam parameters (transversal profiles, ion composition and current), also for very low intensity values (well below 10^5 particles per second). By making use of a simple technique based on a thin CsI(Tl), we can also efficiently image beams of very low kinetic energy (50 keV).

1 INTRODUCTION

At INFN-LNS Catania the EXotics with CYclotron and Tandem (EXCYT) facility, based on the Isotope Separator On-Line (ISOL) technique, is going to start the production of radioactive ion beams. The beam energy will range from 0.2 MeV up to 8 MeV/A, its emittance is expected below 1π mm-mrad, with an energy spread of 10^{-4} [1]. The ISOL technique consists of stopping a stable primary beam, in our case $A < 48$ $E < 80$ MeV/A produced by a superconducting cyclotron, inside a thick target. There nuclear reactions give rise to a wide variety of radioactive species, which are extracted and transported to a high resolution magnetic isobaric separator, in order to pick out the ions of interest. The EXCYT isobaric separator consists of two main stages, each one composed of two magnetic dipoles. The first stage is placed on a 250 kV platform, while the second is grounded. The beam is finally accelerated by means of a Tandem accelerator ($V \leq 15$ MV). The typical particle rate will fall in the range between 10^3 and 10^8 pps, depending on the intensity of the primary beam (< 1 pA), on the production cross section in the target and on the overall efficiency from the ion source to the experimental area.

The beam diagnostics is an important issue of the facility, since it allows to check on-line the beam properties along the transport line, in order to perform the tuning operations. To this purpose we have developed suitable easy-to-use devices, capable of fulfilling the requirements of sensitivity and reliability [2, 3].

LEBI (Low Energy Beam Imager/Identifier) is a compact device used for stable and radioactive low energy beams (50 – 300 KeV), capable of beam imaging, particle rate measurement and identification of nuclei.

GFIBBS is a scintillating-fibre based system, operating with both stable and unstable beams, which can reconstruct with remarkable sensitivity the transverse X and Y profiles after the final acceleration. The identification of the accelerated nuclear species is performed by means of a high resolution silicon telescope.

2 PREACCELERATION, BEAM IMAGING AND IDENTIFICATION

2.1 The LEBI device

LEBI exploits the radioactivity of the beam particles, which are implanted onto a thin Mylar tape placed in contact with a CsI(Tl) plate [4]. The emitted radiation (mainly β and γ rays) crosses the plate, thus producing a light spot representing the transverse profile of the beam, that is watched by a high sensitivity CCD camera ($\sim 10^{-4}$ lux). LEBI can also be employed with stable beams, in order to set up the transport elements along the beam line (quadrupoles, magnetic dipoles of the isobaric separator, etc). In this latter case LEBI is positioned a little bit lower, in order to allow the beam to hit directly the scintillating plate (Fig. 1).

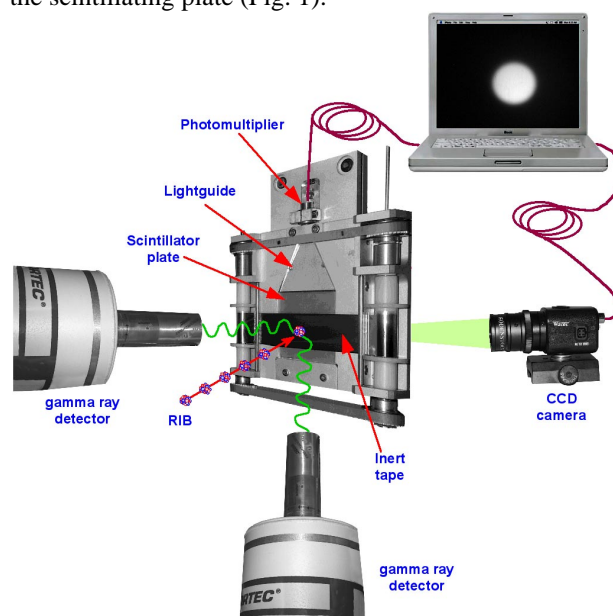


Figure 1: Sketch of the LEBI device for low energy beam imaging and identification.

The plate is enveloped into a grid made of thin metallic wires connected to ground potential; this prevents the plate charge-up, which would deflect the incoming low energy ions thus producing image distortions or no image at all.

For decays in which the daughter nuclei emit gamma rays, a couple of high purity germanium detectors, installed close to the plate, allow a suitable identification of the radioisotopes. Since the gamma ray spectrum is a fingerprint of the emitting nucleus, the recognition of well defined peaks by means of gamma spectroscopy, allows to tag the nuclear species present in the beam. These detectors are positioned close to the Mylar tape, at a relative angle of 90° . They should collect events with at least two gamma rays emitted in coincidence, so that the background can be strongly reduced, highlighting the gamma cascades bound to the selected gammas. In such a way, it is possible to perform a strong selection of the nuclear species, provided that it has at least a couple of gammas in cascade.

By replacing the CsI(Tl) plate with a $5 \times 5 \times 5 \text{ cm}^3$ plastic scintillator, beta counting and spectroscopy can be performed. These measurements allow to identify the implanted radioactive nuclei, by means of the spectrum shape and of the decay constant λ . The wound used tape is well shielded by means of small plastic slabs, in order to prevent residual beta rays of previous implantations from reaching the scintillator. Further anticoincidence detectors, made of CsI(Tl) plates coupled with photodiodes and encapsulating the plastic scintillator, will be exploited to reduce the background radiation.

2.2 Off line testing and simulation

The spatial resolution of LEBI is mainly affected by the isotropical emission of the radiation from the implanted nuclei. If we imagine to use a point-like source placed on the plate, the radiation will cross it in all directions (in such a case the plate covers a solid angle of $2\pi \text{ sr}$), thus producing a light spot with a halo around it. The expected FWHM of the spot is of the order of the plate thickness.



Figure 2: Picture of a beta-electrons beam, produced by means of a collimated ^{90}Sr hitting the LEBI scintillating plate.

An experimental test, in which a pencil-like β beam was exploited, has been performed by using a 1 mm collimated ^{90}Sr source, with intensity below 10^3 pps . It was placed in front of a CsI plate 2 mm thick. The profile of the observed light spot shows a $\text{FWHM} \approx 1.7 \text{ mm}$ (Fig. 2). By means of a simple quadratic subtraction, we can evaluate a spatial resolution of about 1.5 mm.

We have also developed a Monte Carlo simulation code, based on the energy loss of beta rays inside the CsI(Tl) crystal, which is capable of reproducing the shape of the light spot created when the plate is crossed by the radiation. As an example where a realistic beam is simulated, we assumed to produce a ^{18}F beam that contains ^{18}N as a contaminant, see Fig. 3. The predominance of the contribution due to ^{18}N ions depends on the value of its decay constant ($\lambda_{^{18}\text{N}} = 1.11 \cdot \text{sec}^{-1}$), much larger than ^{18}F ($\lambda_{^{18}\text{F}} = 1.05 \cdot 10^{-4} \text{ sec}^{-1}$).

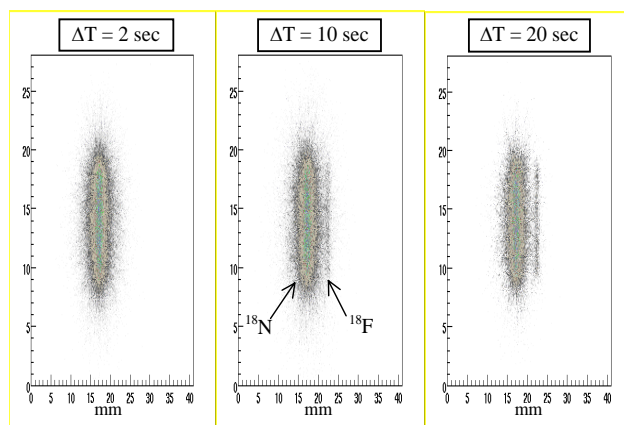


Figure 3: Simulated response of LEBI, placed after the 2nd stage of the mass separator, to a ^{18}F beam and its contaminant ^{18}N . ΔT is calculated starting from the beam implantation.

A simple test of radioactive isotope recognition by means of a couple of germanium detectors, was performed with a ^{60}Co source. We observed that a strong background suppression is achieved when both detectors are used, showing, if needed, that the technique is reliable.

2.3 Imaging of stable beams

In order to test the effectiveness of LEBI to operate with very low energy beams, we produced several different beams of energy down to 50 keV, spanning from hydrogen to silver [5]. For this purpose we employed the ion source of our Tandem accelerator. The measured sensitivity, in terms of beam current, is typically less than 1 pA, and for the lightest elements we were able to display beams with intensities of tens of fA. In Fig. 4 we show a spot corresponding to a ^{109}Ag beam, at 170 keV energy and 4 pA intensity.

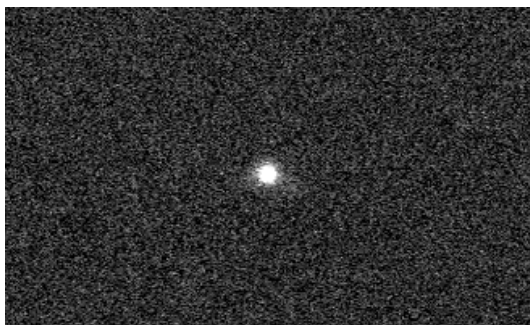


Figure 4: On-line picture of a 4 pA ^{109}Ag beam at 170 keV. The spot size is about 1 mm.

3 POST-ACCELERATION

3.1 Beam profiling

The Glass Fibre Based Beam Sensor (GFIBBS) represents our general solution for beam profiling, since we proved it is reliable, cheap and simple. It is based on a pair of glass or plastic scintillating fibres scanning the beam. The two fibres are mutually perpendicular and are readout by means of a single compact PMT, Fig. 5. It allows to reconstruct the X and Y beam profiles in a single scan with high efficiency. Since plastic fibres are not radiation hard, they are mainly used at low particle rates, when single particle counting can also be performed. Several tests with glass fibres, carried out by exploiting different beams [6], have shown a beam current sensitivity typically well below 10^5 pps.

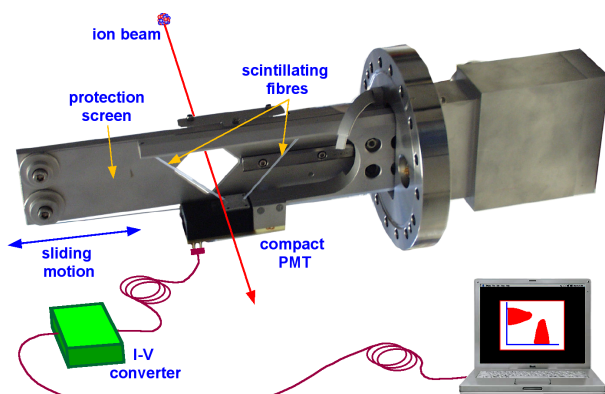


Figure 5: Sketch of the GFIBBS device, for beam profiling after the acceleration.

3.2 Beam identification

The identification of the accelerated ions is performed by means of a silicon telescope. The capability of such a detector to efficiently identify in Z the nuclei, combined with the strong selection in A operated upstream by the mass separator, allows to uniquely determine the nuclear composition of the beam. The silicon telescope can be accurately positioned around a target (typically gold), placed along the beam line, in order to intercept the scattered ions. The angle where the telescope must be

placed is chosen as a function of the expected intensity and energy, in order to have a detected intensity not larger than 10^4 particles per second on the telescope. This prevents a quick detector damage. In order to estimate the discrimination efficiency between the ions of interest and the isobaric contaminant species, a test was done by exploiting elastic scattering from the reaction $^{16}\text{O} + ^{196}\text{Au}$. At the same time a three-peaks alpha source, placed close to the telescope, was used to perform the energy calibration. This data allowed to measure the experimental error, useful for extrapolating the expected errors when detecting other ion species foreseen with EXCYT. As an example we took into consideration three elements: ^{11}Be , ^{17}F and ^{18}F . Based on the measured data with the oxygen beam, for each species and their isobaric contaminants we estimated the energy loss in the ΔE detector; then we built the related ΔE -E scatter-plot with the realistic error bands. In Fig. 6 we show the resulting plot for the ^{11}Be case. These plots allowed to calculate the probability of misidentification, that between contiguous elements stays below 10^{-10} .

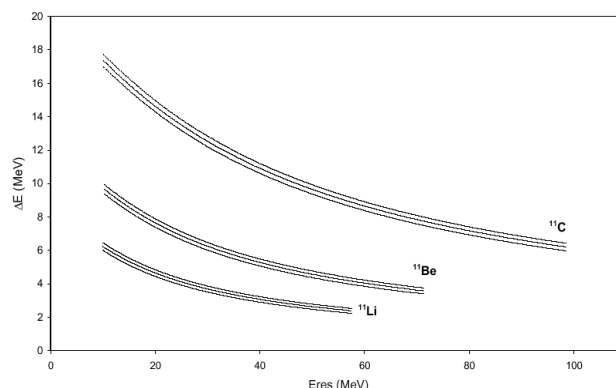


Figure 6: Discrimination plot ($\pm\sigma$) for ^{11}Be . The two main contaminants, ^{11}Li and ^{11}C , are shown.

REFERENCES

- [1] G. Ciavola et al., Nucl. Instr. and Meth. B126 (1997) 258-261.
- [2] P. Finocchiaro, DIPAC 97, 3rd European Workshop on Beam Diagnostic and Instr. for Particle Accel., Lab. Naz: Frascati, October 14th, 1997.
- [3] P. Finocchiaro, CAARI 98, 15th Internat. Conf. on the Appl. of Accel. In Research and Industry, Univ. of North Texas Denton, November 4-7, 1998.
- [4] S. Cappello et al, Nucl. Instr. and Meth. A 479 (2002) 243.
- [5] P. Finocchiaro, L. Cosentino, submitted for publication to Nucl. Instr. and Meth. B.
- [6] P. Finocchiaro et al., Nucl. Instr. and Meth. A419 (1998) 83-90.

NETWORK ATTACHED DEVICES AT SNS*

W. Blokland and T. Shea, ORNL, Oak Ridge, TN, USA
M. Stettler, LANL, Los Alamos, NM, USA

Abstract

The Spallation Neutron Source (SNS) diagnostic instruments at Oak Ridge National Laboratory are based on the Network Attached Device (NAD) concept. Each pickup or sensor has its own resources, such as networking, timing, data acquisition, and processing. NADs function independently thus reducing the brittleness inherent in tightly coupled systems.

This paper describes our implementation of the nearly 400 NADs to be deployed. The hardware consists of rack-mounted PCs with standard motherboards and PCI data-acquisition boards. The software suite is based on LabVIEW and EPICS, communicating through a shared memory interface. LabVIEW supports the agile development demanded by modern diagnostic systems. EPICS is the control system standard for the entire SNS facility. Program templates and documentation tools are available to the programmer. SNS diagnostics are developed by a multi-laboratory partnership, including ORNL, BNL, LANL, and LBNL. The NAD concept proved successful during the commissioning of the SNS front-end both at LBNL and ORNL.

INTRODUCTION

The basic idea behind a Network Attached Device is to implement an instrument as a single networked device with its own resources [1].

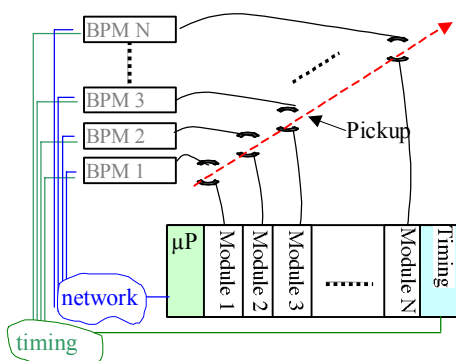


Figure 1. The NAD versus VME configuration.

For example, a typical VME implementation of a Beam Position Monitor (BPM) handles many pickups per crate, while the NAD implementation assigns each pickup its

own resources such as a processor, a timing decoder, and a network interface, to make one independent device, see Figure 1. To create a set of BPMs, the NAD implementation makes copies of a single device. This leads to simpler software and reduces failure interaction. The VME implementation has to deal with managing shared resources among the multiple BPMs. If a system is expanded, a separate integration test is needed to check the interaction of the larger set of modules with each other and the shared resources. The NAD devices don't interact and no new testing is needed when adding NADs. A failure or required maintenance in one component of a VME implementation would most likely bring down all BPMs within the crate. In the NAD implementation each device is independent and any failure in or maintenance to a component would only affect that one device, thus limiting the scope of the outage. In most cases that means that the accelerator can continue to operate.

IMPLEMENTATION

The NAD can be implemented in many ways. In its ultimate form it would likely resemble a system-on-a-chip with a sensor. However, to make use of the wide variety of development and management software and low cost computer and data-acquisition hardware, we have chosen to base the NAD on a PC-based system. The PC-based systems consist of standard motherboards, rack-mounted for easy installation in the field, see Figure 2.



Figure 2. A rack mount PC.

LabVIEW is chosen as the main software development environment operating under Windows 2000 or XP. LabVIEW has a very well integrated visual development environment for data-acquisition and signal processing. Many vendors supply LabVIEW drivers with their hardware. Combined with the SNS software suite, described below, the SNS collaboration can efficiently implement the NADs.

* The Spallation Neutron Source (SNS) project is a partnership of six U.S. Department of Energy Laboratories: Argonne National Laboratory, Brookhaven National Laboratory, Thomas Jefferson National Accelerator Facility, Los Alamos National Laboratory, Lawrence Berkeley National Laboratory, and Oak Ridge National Laboratory. SNS is managed by UT-Battelle, LLC, under contract DE-AC05-00OR22725 for the U.S. Department of Energy.

SOFTWARE SUITE

Especially because the software development is a multi-laboratory effort, it is important that all software is similarly structured. This will enable the small Diagnostics Group at SNS to maintain and upgrade software from the other labs and also efficiently write software for the locally implemented projects, such as the Laserwire. A software suite provides that common structure. The software suite supports the instantiating of the software for a NAD to easily create a set of NADs. Each item of the software suite is discussed in the following sections.

EPICS IOC and Shared Memory Interface

The SNS control system uses EPICS. The NADs' first version of the EPICS interface was based on the ActiveX Channel Access Server interface by LANL [2]. The NADs switched to the full IOC when this became available for Windows. The IOC has a more mature and well supported code base. While early LabVIEW code had a shared memory interface to the ActiveX interface, the new shared memory interface connects LabVIEW directly to the IOC. The shared memory interface and IOC combination increased performance and reliability over the ActiveX interface. On the LabVIEW side, a call to write a 100 doubles to the shared memory interface, including buffering, takes about 0.03 milliseconds on an 800Mhz P3, about 7 times faster. 100 floats generated and communicated to a remote Channel Access client at 1000Hz take less than 5% time of the same CPU. More performance data will be presented in [3].

The shared memory interface implements functions to

- create, find and destroy variables,
- read from and write to variables,
- set and receive events, and
- retrieve information about variables.

All these functions can be called from LabVIEW. The events are associated with EPICS interrupts. For example, if the LabVIEW program needs to know whether an output PV has been set, an associated interrupt awakens a LabVIEW task. This task then queues a message to any other task to schedule any action that needs to be taken. This method avoids the inefficiency of the polling. The IOC initializes the Shared Memory Interface using the EPICS database (.db) syntax. After LabVIEW has started the IOC, the IOC reads in a .db file and, while creating the PVs, also creates the shared memory variables. A LabVIEW routine then obtains a reference for each variable to use with the shared memory functions. This same routine is used to automatically generate the .db file. This way the programmer does not need detailed knowledge about EPICS database syntax. The utility also generates the command file to start EPICS and a table for documentation purposes, see Figure 3. The macro substitution feature of the database files is exploited to keep the PV names the same in each NADs LabVIEW program but different in each NAD's IOC.

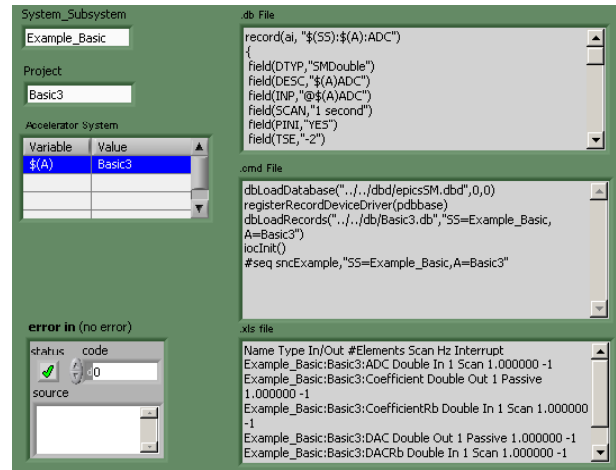


Figure 3. The utility that generates a .db file.

Programming Template

The template concept implements the common software structure for all NADs. Not only will the common structure ease the maintenance, it also gives the programmer a head start. A typical template implements

- multiple tasks,
- queues to synchronize and communicate between tasks,
- state machines to organize program execution.
- a LabVIEW task to process shared memory interface events,
- PV referencing to automatically generate db files,
- error handling,
- configuration file setup, and
- user interface using the event structure.

The front-panel of a template example with a continuous cycling task is shown in Figure 4.

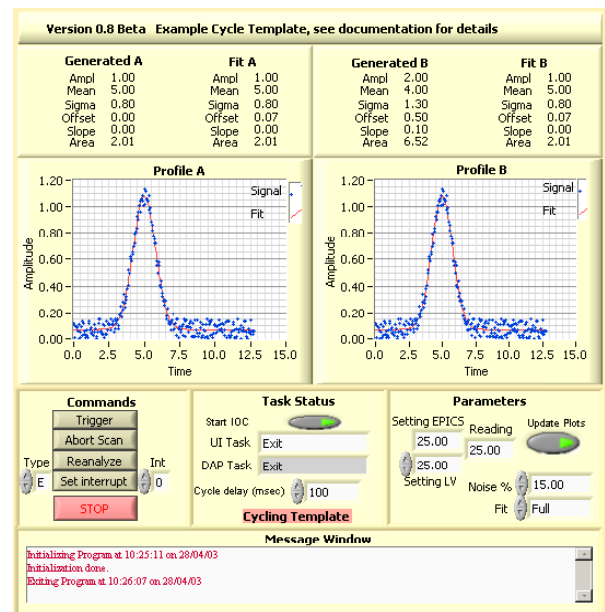


Figure 4. Front panel of the Cycle Template VI.

Various programs using the template structure have been made and are available as examples. A tutorial helps the programmer understand the features of the template. The tutorial consists of a series of programs that start out very basic but successively add features to arrive at the program structure of the template.

Documentation and Development Tool

Each item of the software suite is described in the Style Guide, and this is the place for the programmer to start. The Style Guide includes guidelines for commenting the LabVIEW program using the built-in description fields. The documentation and development tool VHIerarchy, written by the author at Fermilab, uses these comments to create a framed HTML document of the whole hierarchy of the program, see Figure 5. VHIerarchy also provides tools to clean up VI libraries or directories.

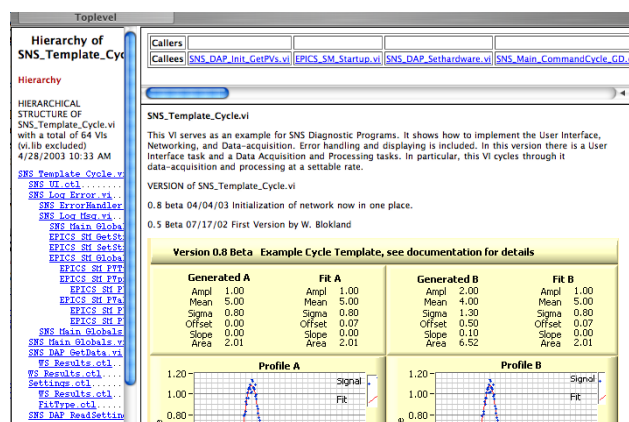


Figure 5. HTML page generated by VHIerarchy

Testing of NAD

The LabVIEW version of the ActiveX Channel Access client enables the testing of the control logic of the NADS by reading and setting the EPICS PVs on the development computer. Clients have been implemented and are part of the tutorial and template.

EXPERIENCE

Early versions of NADs have been implemented by LANL and BNL in the form of Wire Scanners, Beam Position Monitors, and Beam Current Monitors [4]. The NADs functioned well during commissioning of the MEBT at Berkeley and ORNL. Some downtime occurred due to a problem with the shared timing system. The PCI timing card was not ready yet and triggers for all BPMs were taken from one VME crate. When this crate was reset, because another device within the crate had to be reset, the timers were not restored. All BPMs then failed to trigger at the right time and did not give correct positions. If the BPM had been fully NAD compliant and had its own timing card, this failure mode would have been avoided.

NADs based on the template have been running without problems. One NAD is in use by the Accelerator Physics group to test the speed of the Java console applications. Others have been created for new MEBT diagnostics and future installations, such as the D-Plate.

FUTURE

To manage the hundreds of NADs with a small diagnostics group we are in the process of selecting a PC management package, such as SMS or Altiris. Our strategy is to use the Oracle database as the one depository for all files to be installed on a NAD and to use the PC management package to set up and maintain our NADs. The management package will also do remote monitoring to diagnose a NAD and perform inventory tracking. Replacing or building the software on a NAD is to become a push button operation.

At this point, we have used Windows 2000 or XP and not XP embedded with a real-time extension. XP embedded would give a smaller OS but would require the effort of customization. We have not yet needed the smaller OS size or the real-time attributes.

A new Channel Access Client for LabVIEW is under development to be portable among the EPICS and LabVIEW supported operating systems.

SUMMARY

This paper presented the implementation of Network Attached Devices at SNS. The hardware is based on rack mounted PC (x86) motherboards. The software is based on LabVIEW, EPICS IOC, and Windows 2000 or XP. A software suite has been created to interface LabVIEW to EPICS, to provide a common program structure, to help document, and to assist development of NADs by several laboratories. The NAD concept of using a set of independent devices to implement an instrument system proved itself during the commissioning of the MEBT. Over 10 NADs have been commissioned and 30 more are being installed for commissioning this summer.

REFERENCES

- [1] T. J. Shea et al, "SNS Accelerator Diagnostics: Progress and Challenges," pp 512-16 PAC 2001, Chicago, IL, USA, June 18-22, 2001.
- [2] K.U. Kasemir, "ActiveX: CA client and server for Active-X programs," at <http://www.aps.anl.gov/epic/extensions/index.php>.
- [3] D. Thompson and W. Blokland, "A Shared Memory Interface between LabVIEW and EPICS," to be published at ICALEPCS 2003, Gyeongju, Korea, October 13-17, 2003.
- [4] Mike Plum, "Diagnostic challenges at SNS," this conference, Mainz, Germany, 5-7 May 2003.

PARASITIC BUNCH MEASUREMENT IN e^+/e^- STORAGE RINGS

H. Franz (HASYLAB*), M. Seebach (MDI[#]), A. Ehnes (HASYLAB), M. Werner (MDI)

Deutsches Elektronen-Synchrotron DESY, Hamburg, Germany

e-mail: hermann.franz@desy.de michael.seebach@desy.de

ABSTRACT

The lepton storage rings DORIS and PETRA at DESY are used as sources for synchrotron radiation experiments. In normal operation the distance between bunches should be 96 ns in PETRA and in DORIS. The adjacent buckets must not have any stored particles or, in reality, as few as possible. This is particularly important for time-triggered photon measuring experiments. The principle of the 'parasitic bunch' measurement down to a fraction of 10^{-6} of the main bunch within 20 seconds is described. Additionally, the sources of the 'parasitic bunches' and the actions to minimize them are discussed.

INTRODUCTION

Fast time resolved X-ray measurements make use of the inherent time structure of a storage ring (SR). Depending on the size of the ring and the filling pattern (the distance between bunches) the active time window may be in the range of few ns to few μ s. This allows studying kinetics in pump-probe experiments or dynamics using resonant scattering processes [1]. In particular the latter is very sensitive to spurious charge in the machine, which is usually accumulated in buckets adjacent to the intentionally filled bunch. For this reason most SRs used to produce synchrotron radiation have installed a system to detect the time structure of the machine with high sensitivity [2, 3]. In the following we describe a system, which has been installed at PETRA allowing us to detect spurious charge already during the injection process.

SOURCES OF PARASITIC BUNCHES - THE IDEAL MACHINE

All lepton SRs at DESY (DORIS, PETRA and HERA) have a 500 MHz RF-system, i.e. buckets are separated by 2 ns. All storage rings and the pre-accelerators are synchronized via a common bunch-marker system. However, not all buckets are filled with e^+/e^- . The normal bunch distance in PETRA is an integer multiple of 48 buckets (96ns). This means a maximum of 80 bunches may be injected. However, also other patterns are possible. The situation at DORIS is similar. In an ideal storage-ring only the addressed buckets contain e^+/e^- . All other buckets must not have any stored particles. In any real machine some particles are stored in other buckets, in particular in the adjacent buckets, the so-called 'parasitic bunches'.

THE 'PARASITIC BUNCH' SITUATION

In principle any SR with non-uniform filling patterns should have parasitic bunches. This is due to the fact that in the initial stages of the pre-accelerator system

bunches are rather elongated. In particular at DESY the situation is as follows [4, 5]:

Right after the electron gun and a focusing lens the 'ante-linac-chopper' (a vertical electrostatic kicker combined with an upstream collimator) leads to a first bunching of the beam. This results in 10 to 60 ns long pulses at a repetition rate of 20 ms (50 Hz). In order to use the linac (running at 3 GHz) most efficiently those pulses are too long. Thus after further lenses and collimators the 3 GHz-prebuncher (a cavity with 20 kV gap-amplitude and a power of 1.5 kW) concentrates most particles in 50 ps long bunches. After being accelerated to 450 MeV in 12 linac modules particles are accumulated in PIA, a 28.9 m ring running at constant beam energy with a 10.4 MHz HF-system. In PIA several shots from the electron gun are accumulated in one bunch, which may then be several ns long. To reduce the bunch length further the accumulated beam is shortened in the last 40 ms before ejection to DESY-2 by a 125 MHz-system. This treatment reduces the bunch length to a rms value below 0.2 ns at a bunch distance of 8 ns. On the way to DESY-2 the beam extracted from PIA is again filtered by a 'post-linac-chopper' to suppress 8 ns-parasitic bunches. However, during the transfer from the 125 MHz-system at PIA to the 500 MHz-system DESY-2 2 ns parasitic bunches are created by any non-ideal behaviour in the transfer. This may be for example a deviation from the optimum setting of the DESY-2 injection energy due to jitter in the magnet currents or a wrong setting of the DESY-2 injection phase. The latter must be optimized for minimal longitudinal oscillations during injection. The same holds for the transfer from DESY-2 to PETRA and DORIS, respectively.

Further on we have learnt from first measurements that high PIA current causes post-bunches up to 6 ns. The reason for this behaviour is not clear yet, but it could be a longitudinal instability at high bunch charge.

THE PRINCIPLE OF THE 'PARASITIC BUNCH' MEASUREMENT

The parasitic bunch measurement is achieved by an avalanche-photo diode (APD) (EG&G, C30703F) [6] detecting scattered X-rays from a 1 mm thick graphite foil. It is located in the PETRA undulator beamline 31.3 m downstream of the dipole separating the lepton from the undulator beam. This dipole is used as source for the parasitic bunch measurements. The detector signals are amplified close to the diode by a fast three-stage amplifier. The overall time resolution is approximately 0.8 ns. The amplified signal is analyzed using a time-to-digital-converter (TDC) and a multi-channel-analyzer (MCA). To reduce the influence of the so-called "walk" and to reduce the background due

to electronic noise the amplified detector signal is filtered by a constant-fraction-discriminator (CFD) (Fig. 1).

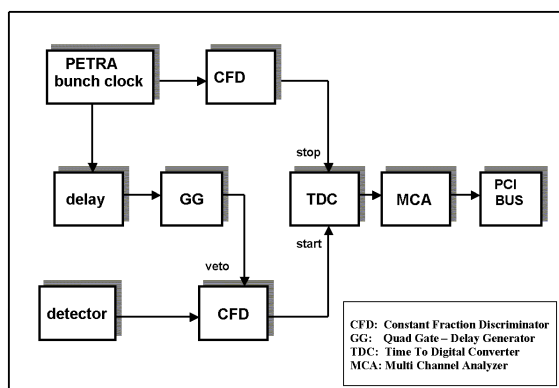


Fig. 1: Standard signal processing of the 'parasitic bunch' measurement (schematically).

The CFDs, used also in the synchronizing bunch-clock branch, are fast NIM-modules. Thus the start- and stop-signals are short 5 ns pulses triggering the TDC. The TDC digitizes the time lag between start (detector) and stop (bunch-clock) pulse and stores the event in the MCA.

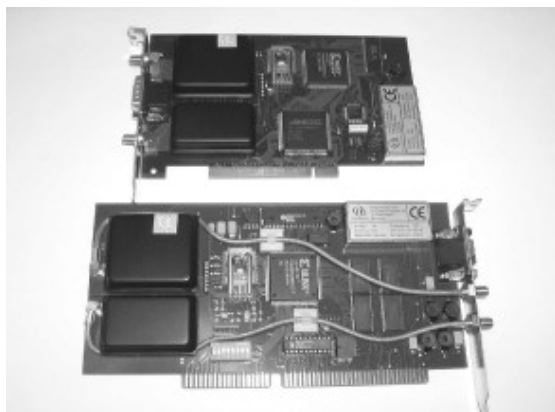


Fig. 2: Pictures of the TDC-boards 'TimeHarp' (PicoQuant) for PCI- and ISA-bus. CFDs and MCAs are included.

The TDC-board [7] (Fig. 2) offers 4096 channels with minimum width below 40 ps and can work at count rates up to 3 MHz (300 ns recovery time).

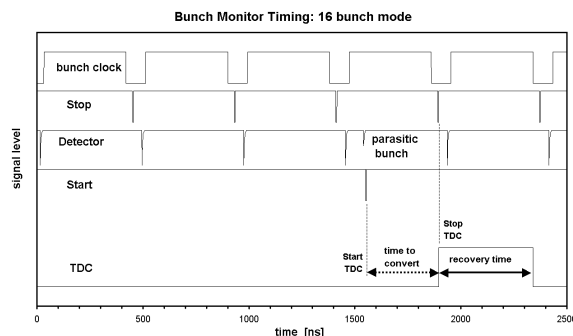


Fig. 3: Schematic pulse sequence for PETRA 16 bunch mode. Near 1500 ns an event due to a parasitic bunch is plotted.

A second mode uses a TAC (time-to-amplitude-converter) converting the time delay to uni-polar pulses digitized in turn by an ADC in 'peak height analysis mode'. The timing-diagram in Fig. 3 shows schematically the pulse sequence. A gate blocks start events generated by main bunch signals. To measure a histogram not affected by recovery-time and pile-up effects, the detector count rate should be limited to below 1.5% of the sync rate. In addition the detector must be carefully shielded (see Fig. 4) against stray light, which similar to light from parasitic bunches, reaches the detector with a time delay.

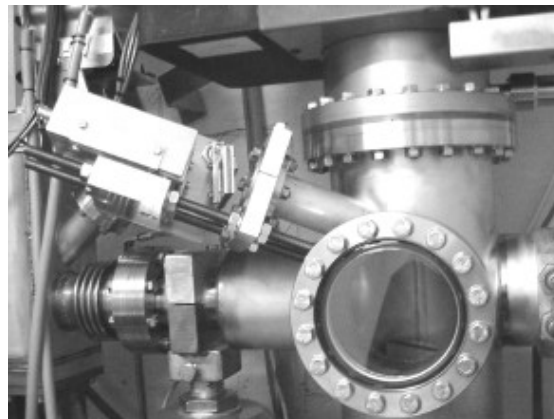


Fig. 4: Parasitic bunch monitor in PETRA. Left: APD-detector, with lead shielding, electric connections and slit. On the right edge of the picture the holder for the graphite foil is seen.

For the machine operation a Server and Client was developed in VisualBasic-6 under Windows NT4. LabVIEW, C++, Delphi and Visual Basic are supported as well. Driver Libraries for Linux are available.

EXAMPLES OF MEASUREMENTS, IMPROVEMENT OF THE SITUATION

To test the performance of the timing system an ex-situ histogram was taken with signals 2 ns apart supplied by a waveform generator (Fig. 5, note that all measurements are displayed on logarithmic scale).

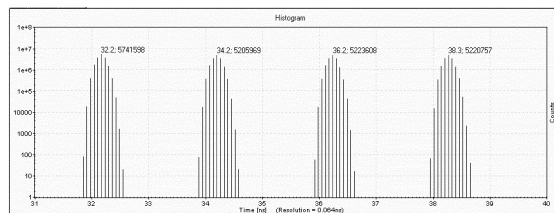


Fig. 5: Histogram of pulses from a STANFORD wave generator with roughly 2 ns distance (FWHM = 160ps).

Figures 6 and 7 show examples of a decent and a bad filling in PETRA. The situation for optimum settings of the pre-accelerators is depicted in Fig. 6. Besides the main bunch at 525.5 ns two pre-bunches with 10^{-3} at 2 ns and 10^{-5} at 4 ns normalized to the main bunch are visible.

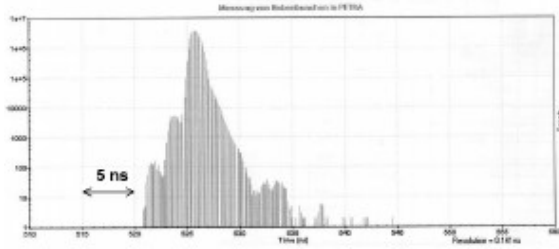


Fig. 6: Main bunch and parasitic bunches from 4 ns ‘before’ to some 10 ns ‘after’ the main bunch. This plot represents a reasonably clean pattern.

“Behind” the main bunch the measured intensity decays to a level of 10^{-6} within 8 ns. The parasitic post bunches are not resolved as clearly as the pre-bunches as the detector response is asymmetric with a broader tail on the falling edge [6] and stray light may contribute to the detected signal. Even after 8 ns some intensity is visible detecting few 100 spurious positrons circulating several meters behind the main bunch.

Fig. 7 shows a measurement during an injection with wrong setting of the DESY-2 injection energy. Strong pre and after bunches are visible in a range of 30 ns.

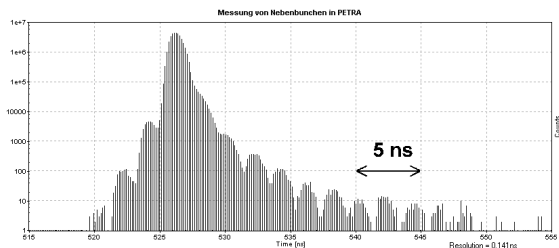


Fig. 7: Main bunch and parasitic bunches from 6 ns ‘before’ to some 20 ns ‘after’ the main bunch. These data were taken at reduced DESY-2 injection energy (450 MeV).

A systematic study of the influence of several machine parameters in the pre-accelerator chain has resulted in the following conclusions:

The most sensitive parameter is the DESY-2 injection energy; if this value is too low parasitic bunches up to 20 ns are injected into PETRA. Parasitic bunches in the region up to 6 ns are created if the current in PIA exceeds 40 mA. Further on the 500MHz-DESY-2-RF-phase must be adjusted properly otherwise 2 ns parasitic bunches are injected to DORIS or PETRA. The same holds for the timing (time zero of the deflection electric field) and collimator position of the ‘post linac chopper’.

As a tool to avoid parasitic bunches the control software of DESY-2 knows the so-called ‘ejection-veto’. When enabled, the software checks the setting of the injection energy and blocks ejection if the difference is outside the defined tolerance.

POSSIBLE IMPROVEMENTS OF THE ‘PARASITIC BUNCH’ MEASUREMENT

The main point for improvements concerns the comfort of using the control software i.e.:

- automatic detection of the position of the main bunch relative to the bunch marker

- evaluating the intensity in all buckets and reporting the relative population of parasitic bunches for operators
- ‘Fit to PETRA buckets’, i.e. display the histogram in a 2 ns pattern
- display several histograms simultaneously to detect changes quantitatively
- creating a file-system for histograms
- using the veto in the detector branch to gate out the main bunch. This reduces the counting time as higher flux may be used without running into recovery time problems.

Concerning the hardware the HV setting should be remote controlled. To increase the resolution a smaller and faster APD now available commercially could be installed. In addition a remote controlled filter will increase the flexibility concerning counting time and injected current.

CONCLUSION

We have reported a system to detect parasitic bunches in the e+/e- machine PETRA at DESY. The monitor detects X-rays scattered by a graphite foil 1 mm thick with an APD detector and fast electronics. The control software allows to routinely detect the filling pattern during the injection process. In case of unacceptably high parasitic bunch intensity the injection may be interrupted and continued with optimized pre-accelerator parameters.

For the upgraded machine PETRA-III, a third generation X-ray source at extremely low emittance (1 nmrad), we plan to install a similar system. This will allow optimizing the injection process in particular in top-up mode operation. One can think of either running in a ‘single trigger mode’ evaluating the filling of every bunch in the machine on a level of nA between two injections (roughly one minute apart). On the other hand by triggering the system after every bunch the purity of the bunch filling may be checked and optimized.

REFERENCES

- 1: H. Franz, T. Asthalter, M. Dommach, A. Ehnes, K. Messel, I. Sergueev, *Hyperfine Inter.* **141/142**, 131 (2002)
- 2: D. P. Siddons, R. J. Nawrocky, and U. Bergmann, in *Proceedings of the 1993 Particle Accelerator Conference*, Washington, DC (IEEE, Piscataway, NJ, 1993).
- 3: G. Mülhaupt, R. Ruffer, *Hyperfine Inter.* **123/124**, 13 (1999)
- 4: J. Hameister, K. Balewski, K. Wittenburg, O. Kaul, M. Nagl (DESY), private communication
- 5: BKR-Dokumentation, DESY, available from the authors
- 6: A.Q.R. Baron, *Hyperfine Inter.* **125**, 29 (2000)
- 7: www.picoquant.com
- *: Hamburger Synchrotronstrahlungs-Labor
- #: Machine Diagnostics and Instrumentation

DIAGNOSTICS OF THE PROSCAN PROTON-THERAPY BEAM LINES

R. Dölling, PSI, Villigen, Switzerland

Abstract

PROSCAN, an extended medical facility using proton beams for the treatment of deep seated tumours and eye melanoma, is in preparation at PSI [1]. An overview is given on the beam line diagnostics now under development, with emphasis on beam profile measurement.

INTRODUCTION

In the PROSCAN facility (Fig. 1) a 250 MeV proton beam of 1 to 500 nA will be extracted from the COMET cyclotron. After degradation to the range of 230 to 70 MeV it can be delivered (at a maximum current of 10 nA) into one of four areas: Two gantries, an eye treatment room and a material irradiation area. Fast changes of beam energy are foreseen for the spot-scanning treatment of deep-seated tumours in the new gantry 2. Several diagnostics will be used to control the beam parameters in different modes of operation. At present most of the components are under development and prototypes will be tested in the next half year.

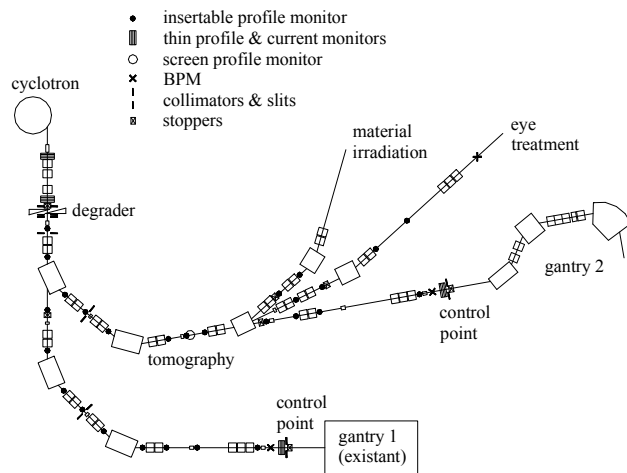


Figure 1: Overview of beam lines.

INSERTABLE PROFILE MONITORS

Insertable monitors, successively introduced into the beam, yield the input information for the calculation of a beam envelope with the "Transport" code [2]. Each single monitor allows the measurement of the temporal development of a beam profile. Since these monitors are not thin, only a measurement at one location at a time is possible.

Multi-strip ionisation chambers (MSIC) are used to obtain enough signal from the small beam current (0.1 to 40 nA). All ionisation chambers are filled with ambient air. Metallized ceramic 0.63 mm thick boards separated by 4 mm wide air gaps provide the strip pattern and high-voltage electrodes in order to measure (the projections of)

the vertical and horizontal beam profiles (Fig. 2). The pitch of the metallized strips varies from 0.5 to 1 and 2 mm (plus one broader strip at each side). 2x 68 strips are fed to the outside by flexible-printed-circuit cables.

With two exchangeable printed circuit boards placed in an electrically shielded box at the top of the profile-monitor feed-through the signals are routed to the 2x 16 channels of the electronics. With this arrangement, a strip pitch of 0.5, 1, 1.5, 2, 3 or 4 mm can be chosen for a "1 broader + 14 regular + 1 broader"-strip arrangement in each plane. This variability allows for the adaptation of the strip pitch to the expected range of beam profile width. This is required due to the limited number of only 16 channels per plane that is foreseen for most of the monitors. Simulations [3] indicate that for 16 channels beam position and width can be measured accurately if the FWHM beam width is in the range 1x to 10x strip pitch and the profile is of conventional shape. A pattern with varying strip pitch can also be chosen to further enlarge the range of possible beam profile width of a fixed configuration.

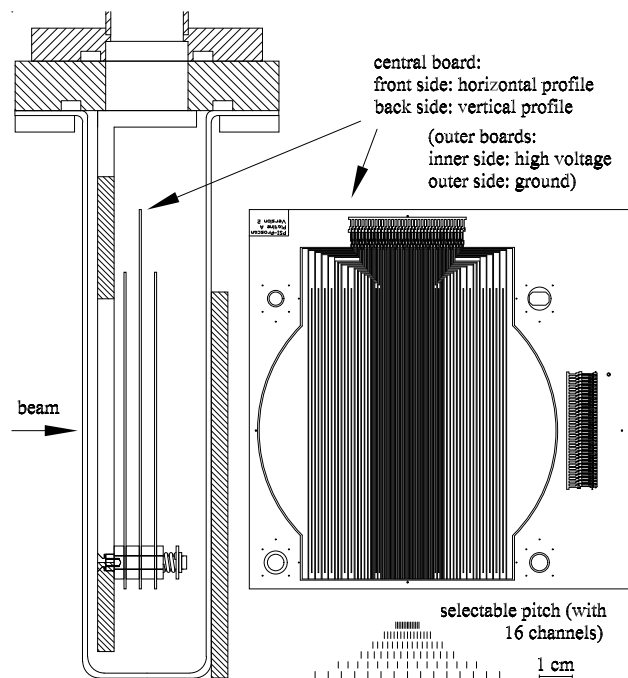


Figure 2: Insertable profile monitor.

At three successive locations, a higher resolution is foreseen for beam tomography. A "1 broader + 30 regular + 1 broader"-strip arrangement in each plane will be realised by doubling the number of cables and electronic modules. At these locations, the available strip pitch is 0.5, 1 or 2 mm. For the tomography measurements also an additional insertable screen monitor is also foreseen. It

will be observed via a mirror using a concrete shielded CCD-camera.

A shielded 40-wire twisted-pair cable is used to transport the signals to the electronics located some 40 meters away outside of the concrete shielding.

+0.6 kV power supplies with low ripple feed the HV-electrodes via an RC-filter. With one exception, the electric field is sufficient to suppress the effect of recombination (calculated according to [4]) on the measured currents to below 10 % at the expected beam current densities and beam energies.

The MSIC is placed in a box filled with ambient air and moved into the beam by a pressured-air actuator. No attempt has been made to make the monitor thin. (Thinner ceramic board is available, but usually less flat.) On the contrary the wall thickness of the box (2x 1 mm) is enlarged by an attached square of aluminium of 5 mm thickness in order to further degrade the beam and prevent its transportation through the gantry. This eliminates the possibility of patient irradiation with a disturbed beam in the case of a profile monitor placed erroneously in the beam.

The strip pattern will be adjusted in the directions transversal to the beam to the requested accuracy of 0.1 mm to the reference given by the flange of the vacuum box.

THIN PROFILE MONITORS AND CURRENT MONITORS

In front of the degrader and at the "control point" in front of the gantries, MSICs are inserted permanently in the beam. These must be very thin to prevent excessive scattering of the beam. Titanium foils of 6 μm thickness are used for the strip-planes and HV-planes. Two ionisation chambers (IC) for the redundant measurement of the integral current are formed by additional foils (2 HV and 2 measurement). The ratio of the currents at both locations is rapidly monitored as a safety measure.

A "1 broader + 30 regular + 1 broader"-strip pattern with 1 mm pitch is used. The alternating measurement and HV-planes are separated by a gap of only 2 mm. A bias of +2 kV is applied. The high electric field counteracts the non-linearity due to recombination and reduces the charge collection time ($\sim 15 \mu\text{s}$). For the expected beam parameters under standard operation, recombination effects should be below 5 %. Nevertheless, with smaller beam diameters, recombination effects are dominant at higher beam currents.

The pre-tensioned foils (full or with the etched strip pattern) will be mounted on the supporting frames made from thick-film plated ceramic board (Fig. 3). This is done using non-conducting glue while electrical connection to the printed circuit pattern is done with small strings of conducting glue. As an alternative, soldering will be tested, which requires a thin sputtered silver coating of the outer parts of the foil. A flexible-printed-circuit cable is used for the connection to the outside terminal.

The integrity of the strips can be checked by capacitively coupling a voltage pulse or AC-signal to the strip ends opposed to the read-out.

The measurement head is separated from the vacuum by a box with thin (35 μm) titanium windows, which are clamped between flanges [5]. A similar but insertable monitor of this type is used shortly after the cyclotron.

In order to get signals not compromised by recombination at higher beam currents, the same devices are placed in vacuum and used as multi-strip secondary emission monitors (MSSEM) and current monitors (SEM) at the locations near the cyclotron and in front of the degrader. (Nevertheless, at low beam current the signal is too low for the electronics used.) Titanium is known for the stability of its secondary emission coefficient against ageing [6].

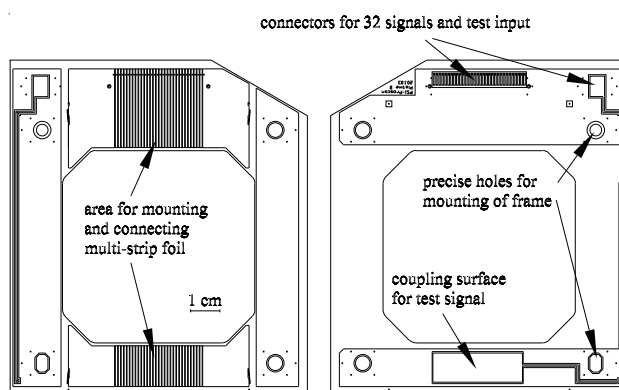


Figure 3: Supporting frame for multi-strip foil.

HALO MONITORS AND IONISATION CHAMBERS

Standard external ionisation chambers are located behind the dipoles close to the beam pipe. Only losses close to an air-filled chamber generate enough signal for the electronics used. More sensitive "halo-monitors" are placed around modified bellows adjacent to the quadrupole doublets and triplets (Fig. 4). These 4-segment ionisation chambers, which protrude circumferentially 5 mm into the beam pipe of 90 mm diameter, give enough signal to detect traversing beam current fractions of below 1 pA. This should also give an online control of the stability of the beam settings.

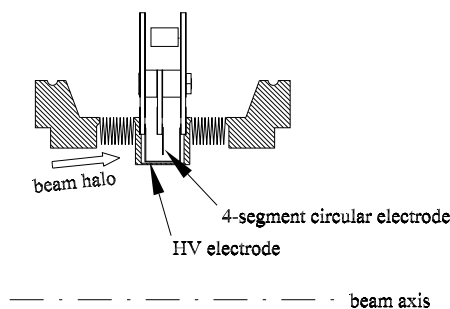


Figure 4: Halo monitor.

BPMS

Stripline-BPMs with a Q of ~ 180 are planned as an online control of the beam angle upstream of the "control point" in front of the gantries and the eye treatment room [7]. At the "control point", the beam passes through an air gap of ~ 20 cm where the above mentioned thin MSIC and IC, a collimator with ~ 0.8 cm diameter, and a fast stopper are located. We are also considering placing a thin 4-segment ionisation chamber for a fast control of the beam position at this location.

ELECTRONICS AND SHIELDING

All currents from MSIC, MSSEM, IC, SEM, halo monitors, external ionisation chambers, stoppers and slits are measured with multi-channel logarithmic-amplifier modules. In the first phase, a 16-channel CAMAC-module will be used with a current range of 10 pA to >200 μ A. It allows single channel readout as well as the measurement of up to 4096 profiles with a minimum time step of 1 ms. Algorithms for data evaluation and the generation of interlocks can be implemented. A trigger input allows the observation of time dependent machine behaviour by simultaneous operation of several modules [8]. In the later phases, this will be replaced by 32-channel and 4x4-channel (4 separate isolated grounds) VME-modules, which are under development. The high voltage for MSIC, MSSEM, IC, SEM, halo monitors, external ionisation chambers and suppressor electrodes of faraday cups will be delivered by VME-modules also under development.

The very low signal levels require the omission of ground loops. Therefore, the internal shield and "ground" of the analogue amplifier electronics is only grounded via the internal shield of the measurement-cable (and in the case of the 40-wire cable by 8 wires), which is grounded at the diagnostic head at the beam line. The ground of the digital electronics refers to the CAMAC- or VME-crate ground. The ground transition for the signals is provided by a differential amplifier. This is the standard technique used at our lab and applies as well to the HV-modules. Additional shielding is provided by enclosing measurement- and HV-cables from one diagnostic head together in a second shield (copper braid) which is grounded at many locations along the way. The diagnostic cables are placed on its own support, separate from magnet cables and water pipes in order to reduce electromagnetic and microphonic noise.

VACUUM BOXES

The vacuum boxes for profile monitors, stoppers, moving slits, etc. are individually adjustable on a (already nearly accurately placed) girder of several meters length (Fig. 5). The box design allows an inexpensive production using water cutting, brazing and only minimal machining of the stainless steel parts [9]. The main flange of the box includes 4 "ears" with precision holes. Its adjustment can be surveyed with or without the diagnostic head installed.

The head with drive is pre-adjusted on a corresponding gauge.

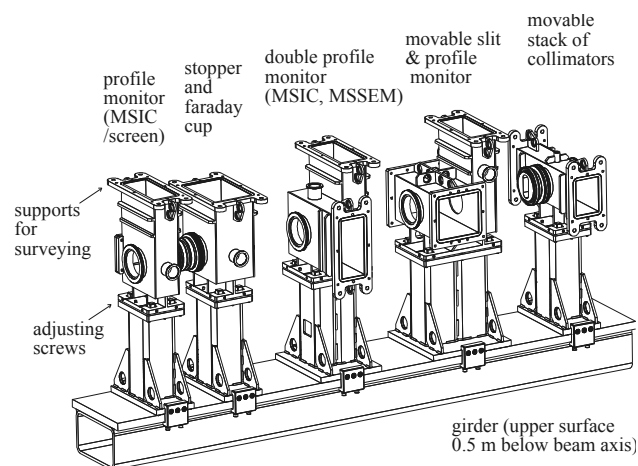


Figure 5: Vacuum boxes with support.

REFERENCES

- [1] PSI Annual Report 2002, vol. VI, p. 51-73.
- [2] http://people.web.psi.ch/rohrer_u/trans.htm.
- [3] R. Dölling, Auswertung von MSIC-Messungen und Einfluss der Streifenzahl auf die Genauigkeit von Profilschwerpunkt und -breite, PROSCAN-document P24-DR84-305.
- [4] G. Mie, Der elektrische Strom in ionisierter Luft in einem ebenen Kondensator, Ann. Phys. (Leipzig) 13 (1904) 857.
See also: H. Attix, Introduction to radiological physics and radiation dosimetry, Wiley, 1986, p. 334
- [5] Standard technique used by PSI vacuum group.
- [6] G. Ferioli, R. Jung, Evolution of the secondary emission efficiencies of various materials measured in the CERN SPS secondary beam lines, DIPAC'97, p. 168.
- [7] Work of M. Dehler, PSI.
- [8] Work of L. Rezzonico, P.-A. Duperrex, U. Frei, G. Gamma, PSI. See also: R. Dölling, L. Rezzonico, U. Frei, S. Benz, P.-A. Duperrex, M. Humbel, Profile Measurement of Scanning Proton Beam for LiSoR Using Carbon Fibre Harps, BIW'02, AIP Conf. Proc. 648 (2002) 361.
- [9] Design by M. Graf, PSI.

This article is PROSCAN-document P24-DR84-310.
The original poster is PROSCAN-docum. P24-DR84-309.

A SYSTEM FOR BEAM DIAGNOSTICS IN THE EXTERNAL BEAM TRANSPORTATION LINES OF THE DC-72 CYCLOTRON

G.G. Gulbekian, B.N. Gikal, I.V. Kalagin, V.I. Kazacha, FLNR JINR, Dubna, Russia
A. Gall, DNPT FEI STU, Bratislava, Slovakia, e-mail: gall@nrsun.jinr.ru

Abstract

The isochronous four-sector Cyclotron DC-72 will be the basic facility of the Cyclotron Center of the Slovak Republic in Bratislava. It will be used for accelerating ion beams with mass-to-charge ratio A/Z from 1 (H^+) to 7.2 ($^{129}Xe^{18+}$) with energy from 2.7 MeV/amu ($A/Z=7.2$) to 72 MeV ($A/Z=1$).

In the paper a system for external beam diagnostics is presented. It is intended for on-line data acquisition of the accelerated beam main parameters (current, position, profile, emittance and energy of the ion beams). The system allows one to provide effective tuning the acceleration regime as well as adjusting the ion beam transport lines with the ion optical systems to effective transportation the ions from the cyclotron exit to physical targets and set-ups.

INTRODUCTION

Cyclotron DC-72 represents an isochronous four-sector cyclotron. The ion beam extraction from the cyclotron will be made by means of electron stripping on a graphite foil. The ions will be extracted in two directions: A and B. Main parameters of the DC-72 cyclotron are given in Table 1, and the design parameters of ion beams are given in Table 2.

Table 1: Main parameters of the DC-72 cyclotron [1]

Pole diameter	2.6 m
Extraction radius	1.118 m
$B_{average}$ at extraction radius	1.12 – 1.51 T
Number of sectors	4
Sector angle	45°
Number of Dees	2
Dee angle	42°
Frequency range	18.5÷32 MHz
Harmonic numbers	2, 3, 4, 5, 6
Ion source for H^+ , D^+ , $^2H^{1+}$	Multicusp
Ion source for heavy ions	ECR
Extraction	stripping foil
Emittance on the target	$< 20 \pi$ mm-mrad

The main areas of using DC-72 cyclotron ion beams will be the following [1]:

- Nuclear medicine and oncology;
- Production of radioisotopes for oncology (^{123}I , ^{81}Rb , ^{81m}Kr , ^{67}Ga , ^{111}In , ^{201}Tl);
- Production of very short living radioisotopes for positron emission tomography (^{11}C , ^{13}N , ^{15}O , ^{18}F);
- Proton therapy of eye;

- Fast neutron therapy (FNT) and boron neutron capture therapy (BNCT);
- Metrology of ionizing radiation;
- Fundamental research;
- Applied research and development programs, surface treatment of metallic and other materials;
- Nuclear physics and techniques;
- Nuclear structure and reaction kinematics studies;
- Educational programs for students of nuclear physics and related fields.

Table 2: The design parameters of DC-72 ion beams [1]

Ch.	Technology and set-ups	Ion beam	Energy [MeV/u]	Intensity [$e\mu A$]
1	^{123}I production	p	30	50
2	^{87}Rb production	p	30	30
3	^{67}Ga , ^{201}Tl , ^{111}In prod.	p	30	100
4	Proton therapy	p	72	0.05
5	Fast neutron therapy	p	66–72	30–35
6	Applied research	Li–Xe	2.8–2.7	5–1
7	Mass-spectrometry	C–Kr	8.6–2.8	20–2
8	Physical research	Li–Xe	2.8–2.7	5–1

EXTERNAL BEAMS DIAGNOSTICS

Beam intensity measurement

The ion beam intensities at the cyclotron extraction region and in the beam transportation lines are the main parameters. The beam current measurements will be realized by special Faraday Cups (FC) (20 pieces). The sketch of FC is shown in Fig.1. At the FC design, we paid special attention to problem of FC cup radioactive activation and choice of the appropriate material. Also, we spent some time to calculate the 3D temperature distribution in the cup. From the point of view of minimal activation, the cup of FC will be made of aluminum. To satisfy the temperature condition the cup has a water-cooling system [2]. The accelerated particles are absorbed in the cup and the integrated electrical charge creates an electrical current that is measured by a current-to-voltage converter (LOG104) and than converted to a digital signal by the A/D converter (MCP3201). After all, the current value will be shown at the console in the cyclotron control room.

To eliminate the influence of secondary electrons emission on the current measurement accuracy we use a transversal magnetic field created by CoSm permanent magnets that surround the cup. The calculation results of the magnetic field distribution are presented in [2].

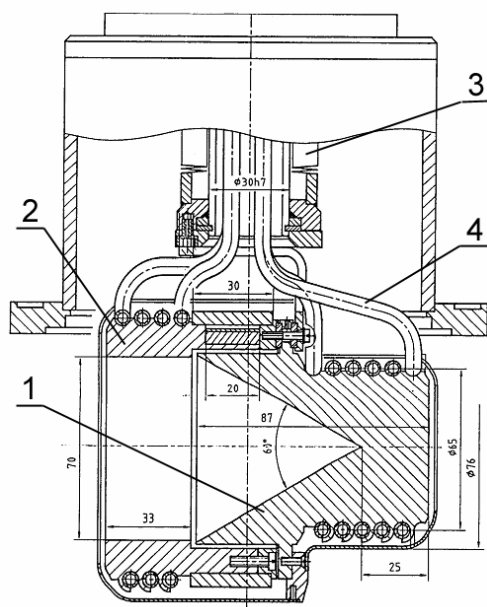


Figure 1: The sketch of the Faraday Cup, where:
1- aluminum cup, 2- aluminum diaphragm, 3- pneumatic drive, 4- cooling pipe

Beam profile and transverse position measurements

To determinate the ion beams transverse position, horizontal and vertical profile and dimensions, a rotating wire scanner will be used [3]. The scanner consists of a spiral rotating Tungsten wire, bended as a helical spiral under 45° . The rotation moment is transferred to the scanner wire from the electromotor (SD-54) through magnetic coupling that provides a large number of measurement cycles. The vacuum zone is separated from the atmosphere by a motionless metal membrane. The wire position is controlled by the system from a disk with a slit and OPIC photo-interrupter (GP1A10). The scanner will be installed in the ion beam transportation lines under 45° in relation to transversal axes of quadrupole lenses. The wire crosses the ion beam in two planes (horizontal and vertical) for one turn (Fig. 2).

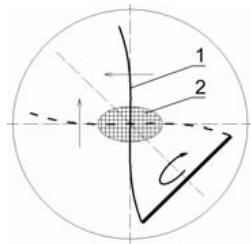


Figure 2: The scheme of the beam intersection by the scanner wire at rotating, where:
1- Tungsten wire, 2- beam cross section

The accelerated particles are absorbed in the wire and the integrated electrical charge creates an electrical current that flows through four sliding contacts, and then by LOG104 and MCP3201. Finally, the received signal is processed and the ion beam transverse position, horizontal and vertical profile in 2D pictures and beam RMS dimensions will be shown at the console in the cyclotron control room.

The basic parameters of the rotating wire scanner

- Wire diameter 1.5 mm;
- Rotation radius of a wire 45 mm;
- Revolution frequency 38.4 rpm;
- Signal processing range $0.01 \div 100 \mu\text{A}$;
- Accuracy of profile measurements $< 5 \%$
- Maximum beam diameter 70 mm

17 pieces of the rotating wire scanner will be placed in the external beam transportation lines. The sketch of the scanner is shown in Fig.3.

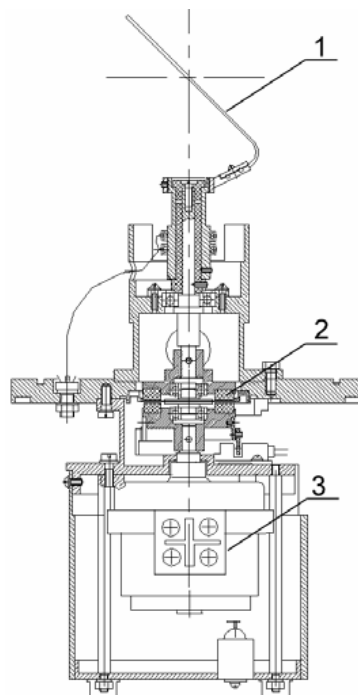


Figure 3: The sketch of the rotating wire scanner, where:
1- Tungsten wire, 2- magnetic coupling, 3- electromotor

Beam profile, transverse position and beam intensity measurements at the extraction

For measurements of ion beams transverse position, horizontal and vertical profile and dimensions at the extraction region the profile grids will be used. Profile grid consists of 30 vertical lamellas installed with the step of 11 mm, and 30 lamellas installed under 45° to the horizontal plane with the step of 12 mm. The aperture of the grid itself is $350 \times 60 \text{ mm}^2$, lamellas are copper plates with cross-section of $1 \times 10 \text{ mm}^2$, the length of each one depends on the location. Lamellas are insulated one from another with ceramic, fixed to the water-cooled base frame.

The accelerated particles are absorbed in lamellas and the integrated electrical charge creates an electrical current. After the received signal from each lamella is processed, the ion beam transverse position, horizontal and vertical profiles, and beam RMS dimensions will be shown at the cyclotron control console.

Profile grid is combined with the rectangular Faraday Cup ($370 \times 80 \times 50 \text{ mm}^3$) for simultaneous measurement of

ion beam intensity. The cup will be made of aluminum, and has water-cooling through embedded copper pipe.

This device will be installed in the extracting region of the cyclotron, over the radius of $R \sim 2.2$ m, where there is sufficient magnetic field to eliminate the influence of secondary electrons emission on the ion beam current measurement accuracy. For moving the device to the measuring position a pneumatic drive will be used.

Beam energy measurement

The system is intended for obtaining the on-line information about ion beam energy.

The principle of energy determination is based on the measuring the ion beam bunch time-of-flight between two points (two capacitive electrodes) placed at the well-known distance to each other (TOF-method) [4]. The two pickup electrodes will be placed in the direct part of the ion beam transportation lines. The distance between pickups is 4.462 m in A direction, and 4.362 m in B one. These distances have been chosen from the point of view of tuning simplicity and possibility to make the beam energy measurement without additional commutation and tuning of channels in both directions. The today accuracy of energy measurement satisfies to the existing requirements.

In the case of necessity to develop the system and to increase the accuracy in energy determination, there are some possibilities to increase the distances up to 7.456 m, 10.124 m, 11.918 m and 14.586 m in A direction, and up to 8.576 m in B one.

In the case of the distance between two pickups is bigger than the geometrical distance between bunches, it is necessary to know the quantity of bunches between the electrodes. For this purpose it is possible to take approximate value of extracted ion beam energy. This rough estimation of beam energy can be made knowing the beam extraction radius of the accelerator and RF frequency of the accelerating field, that's why there is not necessary to use the third electrode.

The precision of the beam energy measurement depends on the error in the determination of the distance between electrodes, and on the accuracy of time-of-flight measurement.

Table 3: The energy resolution $\Delta W/W$ for TOF at the pickup distance of 4.362 m. The accuracy in the distance measurements is 1 mm, and the accuracy of time-of-flight measurements is 0.1 ns.

Particle	p	p	^{129}Xe	^{12}C
W [MeV/u]	30	72	2.7	8.6
$\beta=v/c$	0.248	0.372	0.076	0.135
f_{RF} [MHz]	22.22	31.63	19.36	22.96
Total TOF [ns]	58.70	39.12	191.5	107.8
Bunch spacing [m]	3.344	3.525	1.176	1.762
$\Delta W/W$ [%]	0.34	0.51	0.11	0.2

The electrical signals from the pickup electrodes are amplified by the high-frequency amplifiers with amplification factor of ~ 150 at 1GHz bandwidth. The amplified signals are given out to the TEKTRONIX TDS-5054 oscilloscope located in the cyclotron control room. The amplified signals will be processed, and the calculated energy will be shown at the cyclotron control console. The typical energy resolutions $\Delta W/W$ of the system are given in Table 3.

Transverse emittance measurements

The transverse emittance is one of the main parameters of charged particles ion beams. For transverse emittance measurement a gradient variation method will be used [4]. The procedure of transverse emittance measurement is based on the measurement of the beam profile width as a function of the quadrupole lens gradient. This transverse emittance measurement is possible in several places of the ion beam transportation lines by using the rotating wire scanners located at the well-known distance from the quadrupole lens. The accuracy of the transverse emittance measurements will be about 25 % that satisfies to the existing requirements. In the case of necessity to develop the system there is a possibility to use the three profiles method with rotating wire scanners without the necessity of quadrupole variation.

Aperture diaphragm

The aperture diaphragms will be used for beam size limitation, for rough estimation of the beam position in the transportation lines and for protection of the transportation line components against damage at incorrect beam adjustment.

14 aperture diaphragms will be placed in the ion beam transportation lines after the correction magnets at extraction zone, before entrances into bending magnets and in front of the last diagnostic blocks of every channel. The aperture diaphragm is a ring-shape with the inner diameter of 80 mm and thickness of 25 mm. It is made of aluminum and not water-cooled. Every diaphragm will be established in the transportation lines on isolators, and the signal from each ones will be given out at the cyclotron control console.

REFERENCES

- [1] Conception of DC-72 Cyclotron, Technical report FLNR JINR, Dubna, 1998.
- [2] G.G. Gulbekian, B.N. Gikal, A. Gall, I.V. Kalagin, G.N. Timoshenko, Ch.K. Pachadziev, "The Device to Measure Currents in External Beam Transportation Lines of the DC-72 Cyclotron", Preprint JINR P9-2002-164, Dubna, 2002.
- [3] G.G. Gulbekian et al., Proc. of International Conference on Cyclotrons and their Applications, Bechyne, CSSR, 1985, p. 269-274.
- [4] B. Wolf, "Handbook of Ion Sources", CRC Press, 1995.

MULTIFUNCTION TEST-BENCH FOR HEAVY ION SOURCES

S.Barabin, V.Batalin, A.Kozlov, T.Kulevoy, R.Kuybida, D.Liakin[#], A.Orlov, V.Pershin, S.Petrenko, D.Seleznirov, Yu.Stasevich.

Institute for Theoretical and Experimental Physics, Moscow, Russia

Abstract

The new test-bench for heavy ion sources has been created in ITEP. It is planned to equip test-bench with a set of measurement devices to cover wide range of beam widths, divergences, durations, currents etc. It will provide measurements of different heavy ion beams parameters, particularly, emittance and charge state distribution. The last parameter may be measured both by the time-of-flight method and with the magnet analyzer. Two emittance measurement devices will be installed. It will be possible to use both slit/grid and CCD based “pepperpot” methods, which will give advantages of combination of classical emittance measurements with performance of the CCD based devices. The detailed description of test-bench and its equipment is presented. The first results at MEVVA ion source and beam investigations are discussed.

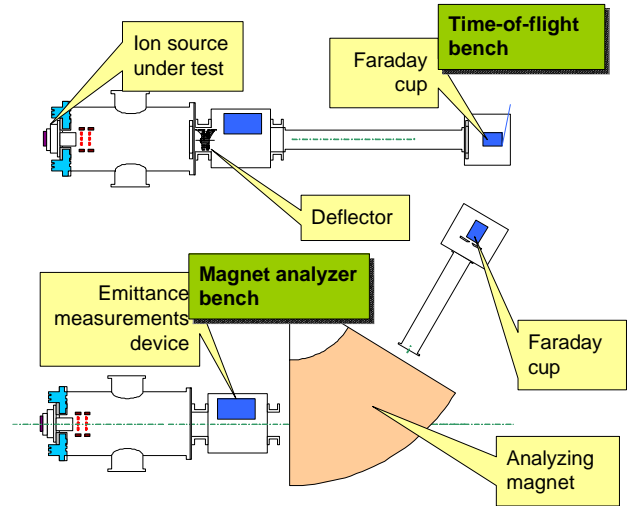


Fig. 1. Structure of the test-bench.

TEST-BENCH STRUCTURE

The structure of heavy ion sources test-bench is shown on fig. 1. Two independent vacuum tanks are available for time-of-flight and magnet analyzer ion beam spectrum measurements. A 100 mA 20-80 kV high voltage source is shared between those chambers.

TOF ANALYZER

Time-of-flight (TOF) method allows measuring the charge state distribution (CSD) evolution during the ion beam pulse that can be used for investigation of process into ion source plasma [1].

The ITEP test-bench for TOF measurements includes: cylindrical deflector, drift channel and current detector

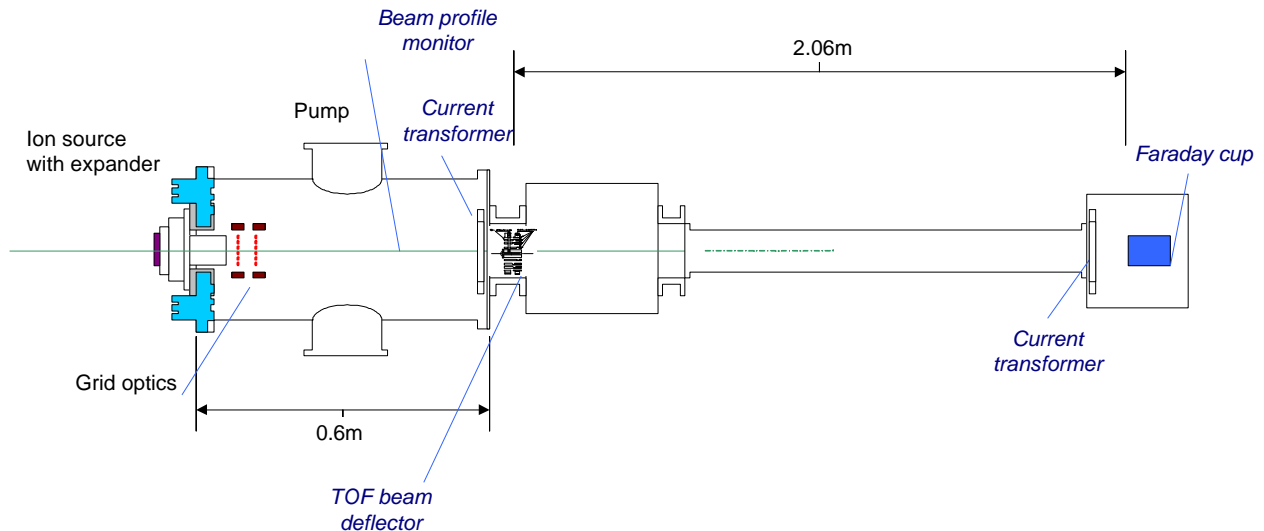


Fig. 2 Layout of TOF test-bench.

[#]Liakin@vitep1.itep.ru

(see Fig. 2). The deflecting voltage pulse has variable amplitude of 0 – 1.5 kV and duration of about 100 ns (Fig. 3). Distance between deflector and detector is 2.06 m length.

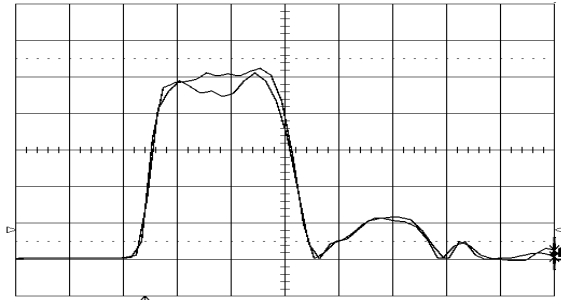


Fig.3. Gate pulse created by LC forming line with $\rho=50\Omega$ and thyatron switching unit. Sweep speed is -50 ns/division.

Cylindrical deflector is shown in the Fig. 2. There are two kinds of ring electrodes – grounded and potential. The length of all ground electrodes is 3cm. Deflector has 4 driving gaps with follows parameters:

N	h, mm	L, mm
1	4.4	5
2	7.3	11.4
3	4.3	10
4	4.6	13.6

where h is a gap width, L is a length of potential electrodes. These parameters were calculated for accelerating beam voltage $U_{beam}=30$ kV and deflection voltage $U_{defl}=1$ kV. First test showed that accelerating beam voltage $U_{beam}=24$ kV and deflection voltage $U_{defl}=1$ kV are optimal. Additional round plate is placed on the central ground electrode. It has diameter 25mm and in shadow of this plate the detector is placed.

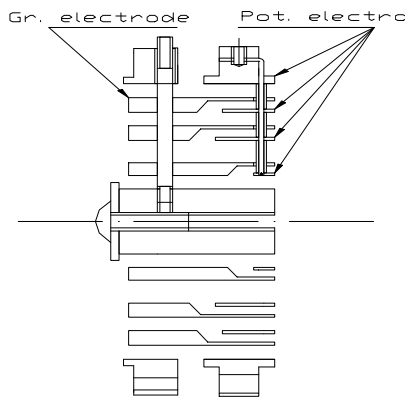


Fig.4. Construction of cylindrical deflector.

First measurements by TOF method at the ITEP test-bench were carried out with copper beam generated by MEVVA ion source. Total current of investigated beam was 25 mA. The typical measured CSD is shown in Fig.5

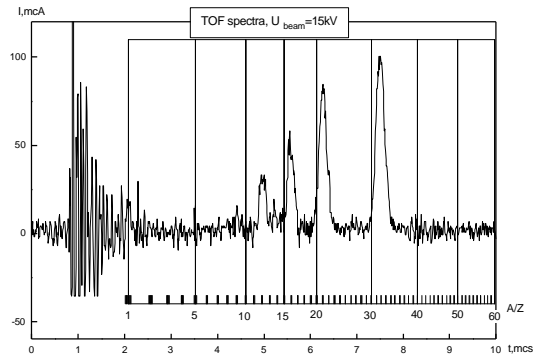


Fig.5. Copper ion beam time-of-flight spectrum measured at ITEP test-bench.

EMITTANCE MEASUREMENTS

Two emittance measurement devices are planned to be installed on this test bench. The classical slit-grid method will be equipped with single platform carrying both slit and grid frames. It allows to reduce number of mechanical feedthroughs, diminish the requirements to the platform positioning accuracy and allows to produce compact design of slit-grid assembly. Quite simple configuration is supposed to be used at the beginning. To meet the requirements of wide range ion beams measurements it is planned to update this configuration up to 48 fine spaced commutated wires to increase the gauge performance. The advantages of the direct current measurements with harp detector led used this device for calibration purposes, for radioactive beam parameters measurements and for special measurements with high dynamic range requirements. For routine emittance measurements the ion current-to-image intensity conversion method will be used. This method already has been approved for commissioning measurements of few heavy ion sources in ITEP.

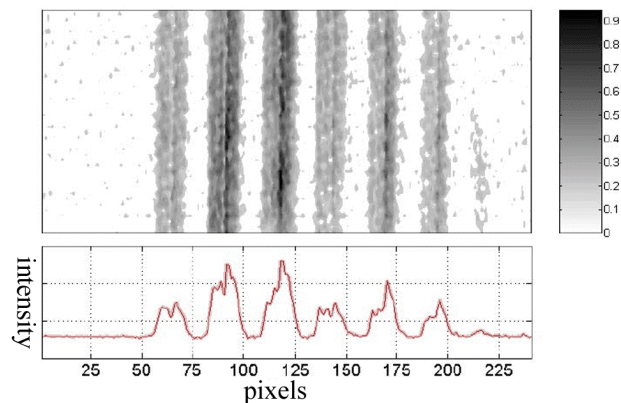


Fig.6. Image obtained in multislit-phosphor screen emittance measurement and integrated intensity values is used for beam emittance evaluation.

Similar device equipped with pepper-pot mask is used widely in ITEP for low energy proton beam diagnostic. On Fig. 6 the CCD image and integrated intensity value along vertical dimension are shown. In this case just

simple phosphor screen has been used as ion density detector due to relatively high input ion beam current.

Wide parameters spectrum ion sources are foreseen to be tested on this equipment. A low current and short pulses devices are not excluded. To gain ability to cover parameters of such devices we envisage to use MCP assembly to intensify ion density distribution image.

	dimensions	resolution	Additional parameters
MCP	50x50 mm	0.05mm	Single stage with phosphor screen.
CCD	60x50 mm	0.05mm	Digital interface, 10 bit resolution

Using devices with parameters shown in Table 1 allows maximum six simultaneously operated slits used with phosphor screen with or without MCP to obtain compatible with harp method divergence resolution. Depending of the beam transversal dimension this number may be reduced down to 3 or 2 so few additional slit stepping possibility in transversal direction very desirable. Another configuration with increased slits number by cost of divergence resolution also will be used to provide 'single shot' measurement features.

REMOTE CONTROL AND AUTOMATION EQUIPMENTS

To be able to provide a series of measurements with good performance and high accuracy the automatic system status logging as well as remote device control are important. We consider the distribute chain of embedded front end microcontrollers as a basic configuration for our control system. Most of the needs of test-bench will be covered with set of 8 and 32 bit microcontrollers developed in ITEP and approved in different scientific and industrial applications. CAN bus is chosen as operating network to join microcontrollers and to connect them to the operators terminal. Due to high responsibility level of embedded devices there are no special requirements to the OS stability or hardware reliability of the terminal computer. A desktop PC and Windows OS were selected as basis for operators terminal.

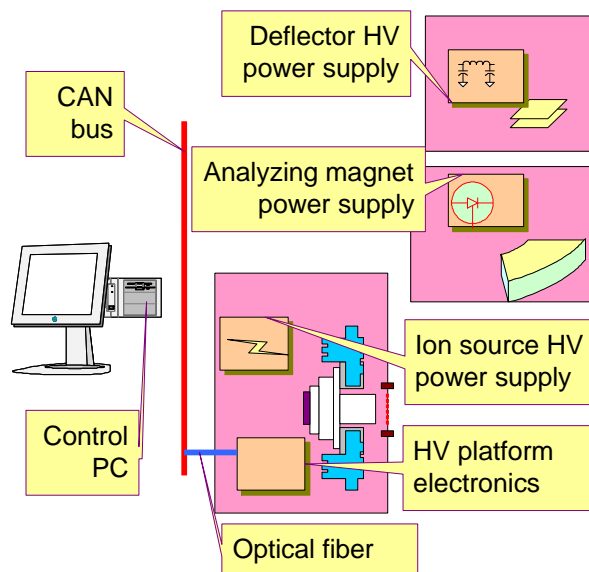


Fig.7. A block-scheme of controlled equipment.

CONCLUSIONS

Described test equipment is being constructing to meet the growing demands of the ion sources developers. Time-of-flight method is currently available. Next stage by stage commissioning stipulates that the possibilities of this test-bench will extends in time depending on number of participants and economical reasonability.

REFERENCE

- [1] I.G. Brown, J.E. Galvin, R.A. MacGill, and R.T. Wright. Improved time-of-flight ion charge state diagnostic. RSI 58 (9), 1987, pp.1589 – 1592.

APPLICATION OF BEAM DIAGNOSTICS FOR INTENSE HEAVY ION BEAMS AT THE GSI UNILAC

W. Barth, L. Dahl, J. Glatz, L. Groening, S. Richter, S. Yaramishev
Gesellschaft für Schwerionenforschung, D-64291 Darmstadt, Germany

Abstract

With the new High Current Injector (HSI) of the GSI UNILAC the beam pulse intensity had been increased by approximately two orders of magnitudes. The HSI was mounted and commissioned in 1999; since this time the UNILAC serves as an injector for high uranium intensities for the synchrotron SIS. Considering the high beam power of up to 1250 kW and the short stopping range for the UNILAC beam energies (< 12 MeV/u), accelerator components could be destroyed, even during a single beam pulse. All diagnostic elements had to be replaced preferably by non-destructive devices. Beam transformers instead of Faraday cups mainly measure the beam current, beam positions are measured with segmented capacitive pick-ups and residual gas monitors instead of profile harps. The 24 installed phase probes are also used to measure widths and phase of the bunches, as well as beam energies by evaluating pick-ups at different positions. The residual gas ionisation monitors allow for on-line measurements of beam profiles. The knowledge of the real phase space distribution at certain position along the linac is necessary for optimising the machine tuning, for the improvement of the matching to the synchrotron, and for a better understanding of beam dynamic issues under space charge conditions. The paper reports the application of different beam diagnostic devices for the measurement of transverse beam emittances at different UNILAC beam energies and at different beam intensities. Additionally, measurements of the bunch structure after the HSI and the design of a new device for the measurement of the longitudinal emittance at the end of the UNILAC are included.

INTRODUCTION

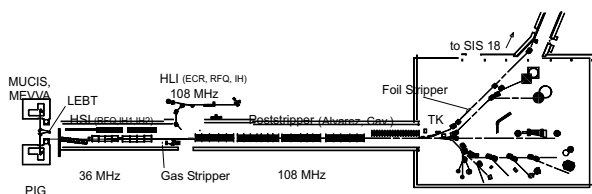


Fig. 1: Schematic overview of the GSI UNILAC.

The GSI-UNILAC is specified to deliver up to $4 \cdot 10^{10}$ U^{73+} particles to the heavy ion synchrotron (SIS) during 100 μ s, whereby the HSI accelerates 15 emA $^{238}U^{4+}$. The required beam parameters (for the uranium case) are summarized in Table 1. In 1999 the UNILAC (see Figure 1) underwent a renewal of its prestripper section to increase the ion beam current to $I = 0.25$ A/q (emA) for mass over charge ratios of up to 65. The high

Table 1: Specified beam parameters along the UNILAC.

	HSI entrance	HSI exit	Alvarez entrance	SIS injection
Ion species	$^{238}U^{4+}$	$^{238}U^{4+}$	$^{238}U^{28+}$	$^{238}U^{73+}$
El. Current [mA]	16.5	15	12.5	4.6
Part. per 100 μ s pulse	$2.6 \cdot 10^{12}$	$2.3 \cdot 10^{12}$	$2.8 \cdot 10^{11}$	$4.2 \cdot 10^{10}$
Energy [MeV/u]	0.0022	1.4	1.4	11.4
$\Delta W/W$	-	$4 \cdot 10^{-3}$	$\pm 1 \cdot 10^{-2}$	$\pm 2 \cdot 10^{-3}$
$\epsilon_{n,x}$ [mmrad]	0.3	0.5	0.75	0.8
$\epsilon_{n,y}$ [mmrad]	0.3	0.5	0.75	2.5

current injector HSI consists of ion sources of MEVVA-, MUCIS- or Penning-type, a mass spectrometer, and a low energy beam transport system (LEBT). The 36 MHz RFQ accelerates the ion beam from 2.2 keV/u to 120 keV/u. The matching to the following IH-DTL is done with a short 11 cell adapter RFQ (Super Lens). The IH-DTL consists of two separate tanks accelerating the beam to the full HSI-energy of 1.4 MeV/u [1]. Before injection into the Alvarez accelerator the HSI-beam is stripped (gas stripper) - charge analysis is indispensable. A five stage accelerator provides seven discrete beam energies in the range of 3.6 to 11.4 MeV/u, the following 10 single gap resonators allow any energy up to 13 MeV/u. In the transfer line to the synchrotron at 11.4 MeV/u a foil stripper and another charge state separator system is in use.

OPERATING BEAM DIAGNOSTICS

Table 2: Number of beam diagnosis devices in the UNILAC.

Element	Number	Resolution
Faraday Cups	73	100 nA (high power capable)
Current Transformers	45	100 nA (100 kHz)
Profile Grids	103	≥ 1 mm
Capacitive Pickups (to determine positions)	34	$\Delta W/W = 0.1$ %
Emittance Meas. Device	8	variable
Bunch Shape Monitors	2	25 ps (0.3 °)

The wide spread of beam intensities – from pA up to mA demands for a very versatile set of different beam diagnostics elements. To measure the different beam properties such as position, profile, intensity, energy, transverse emittance and, bunch shape various beam diagnostic elements (listed in Table 2) are employed.

The Faraday cups serve primarily as beam stoppers, and secondarily as diagnostics devices. Current transformers and profile grids are used for beam set-up and tuning. The capacitive pick-ups measure the beam energy by a time-of-flight technique; the sampled signal of up to two pick-ups can be displayed on a video screen.

Using this visualization it is possible to evaluate the shape and stability of the macro-pulse.

The measurement of the transverse beam emittances is either used during machine development.

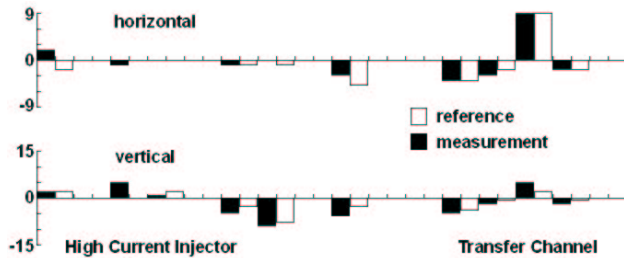


Fig. 2: Online monitoring of beam position with the rf-bunch pick-ups at the HSI and transfer channel; the measured positions and stored reference are represented.

BEAM DIAGNOSTICS FOR HIGH CURRENT OPERATION

If the HSI delivers highly intense uranium beams, the power stored in one pulse (100 μ s) can easily destroy any conventional beam destructive diagnostics element. So either the beam intensity has to be reduced to perform the measurements, or dedicated non-destructive measurements have to be used [2]. At the UNILAC both paths are followed: non-destructive devices such as the current transformers as well as residual gas monitors are installed. An online surveillance system automatically reduces the frequency and the length of the beam pulses. This keeps the deposited power well below any destruction threshold.

The outmost number of rf-bunch pick-ups are 4-segmented probes, which allow to derive the beam position by digitizing the power of the 6th harmonic of the rf-frequency. Next to this function the current transformers are also the basis of the online transmission surveillance system. This surveillance system is directly linked to the control system and can monitor each of possible different ion beams independently. If a significant beam loss is detected, an interlock signal is generated that cuts off the beam pulse within less than 10 μ s.

EMITTANCE MEASUREMENTS

Measurements of transverse emittances for the several energy steps of the HSI (and at 1.4 MeV/u) were done exclusively with a slit-grid device for short pulses. The emittances were measured in the LEBT-section, for 120 keV/u, 750 keV/u and 1.4 MeV/u the beam was transported to a measurement device in the gas stripper region; another device is placed after the Alvarez. Fig. 3 summarises the measured emittance data for an Ar^{1+} beam with 10 mA at RFQ injection and 6.5 mA at the HSI exit. The Ar^{10+} current (after stripping and charge state analysis) came up to 7 mA by gas stripper density

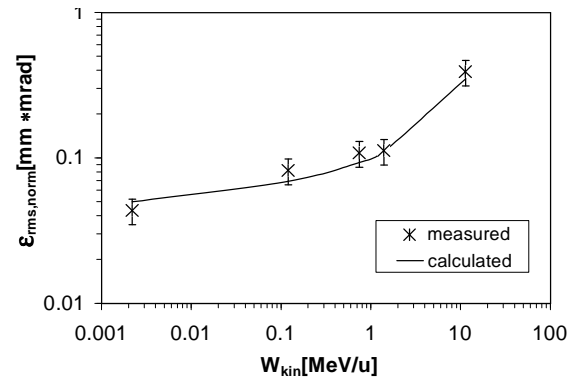


Fig. 3: Measurement of the emittance along the UNILAC.

variation. The measurements agreed to the calculation, if a measuring error of about $\pm 15\%$ is taken into account.

For high current operation a pepper-pots system capable to measure the transversal emittance within one macro-pulse was used, for more details see [2].

As an example Fig. 4 represents the variation of the beam emittance influenced by space charge forces due to an intensity increase of an Ar^{10+} -beam. The intensity variation is done in the LEBT section. Whereas the beam divergence measured after the prestripper does not change, a significant dependence of the beam distribution after stripping and transport to the poststripper takes place. Thus intensity depending matching to the Alvarez accelerator is inevitable.

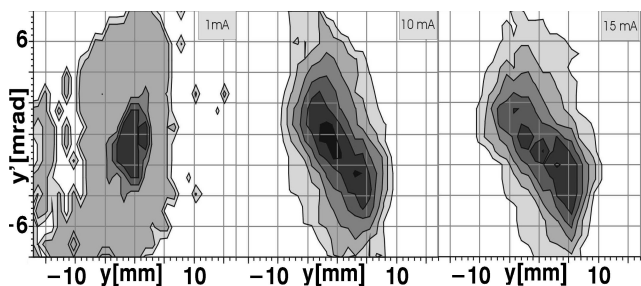


Fig. 4: Measured emittance as a function of Ar^{10+} -intensity.

BUNCH SHAPE MEASUREMENT

Bunch shape measurements were done using diamond detectors, whereas the ion beam (here Ar^{1+}) passes a thin Au-foil – the “Rutherford”-scattered particles hit the detector below a small angle. The bunch shape is obtained by measuring the arrival time of the particles against a reference [1]. It was even possible to observe the typical “zero current” phase space distribution in longitudinal plane, leading to intensity peaks at the centre and at the beginning (resp. at the end) of the measured bunch shape.

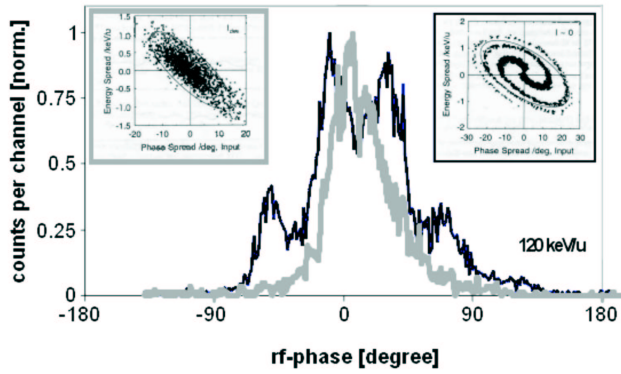


Fig. 5: Bunch shape measurement for high and low currents; additionally the corresponding calculated longitudinal beam emittances are represented.

ONLINE MEASUREMENT OF THE LONGITUDINAL EMITTANCE

At the injection to the SIS the total momentum spread must be lower than 0.1%. The efficiency in setting the longitudinal beam focusing is considerably increased if an image of the longitudinal phase space distribution is available during the setting procedure. The proposed set-up [4] for such an online measurement comprises an iris, magnetic bends, a vertical rf-chopper at 108 MHz, and a beam profile screen (Fig. 6). The method is based on the transformation of the longitudinal particle coordinates into transverse coordinates. With the dispersion D_x after bending magnets the particles energy deviation dp/p_i is transformed at first order into the horizontal position

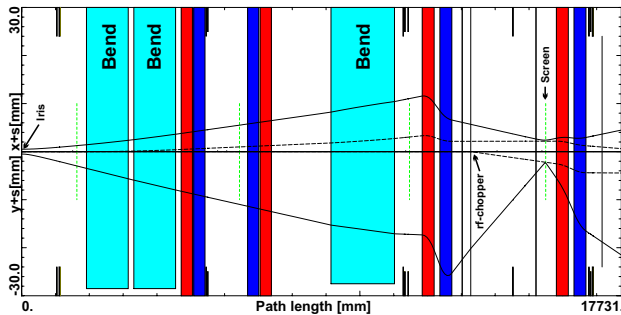


Fig. 6: Set-up for measurement of the longitudinal phase space distribution with horizontal (upper) and vertical (lower) beam envelopes (solid) and design orbits (dotted)

$$x_i = D_x \cdot dp/p_i + O[(\epsilon_{x,i} \beta_x)^{1/2}].$$

If the bunch passes a vertical rf-chopper the particles longitudinal phase $\phi_{l,i}$ is transformed into a vertical kick, being a vertical offset y_i after a subsequent drift L .

$$y_i = L[\text{const.} U_{\text{gap}} \cdot \sin(\phi_{l,i})] + O[(\epsilon_{y,i} \beta_y)^{1/2}],$$

where U_{gap} is the peak voltage in the chopper, $\epsilon_{x,y,i}$ is the single particle emittance, $\beta_{x,y}$ is the β -function at the screen, and O indicates terms that scale with the expression within the brackets. The constant includes the beam parameters and the geometry of the chopper. To obtain simple linear transformations, the transverse beam emittances are limited by an iris before the first bend. Additionally, a small beam spot, i.e. $\beta_{x,y}$, must be set at the screen while the chopper is not active (Fig. 6, left). The energy spread dominates the minimized spot size. Afterwards the vertical rf-chopper is activated (Fig. 7, right) in order to fully image the longitudinal phase space distribution at the position of the chopper. The obtained resolution is given by the opening of the iris, by the dispersion, and by the resolution and size of the beam profile screen. Using an iris of 1 mm and an inter-wire distance at the screen of 1 mm, we expect for an energy of 11.4 MeV/u a resolution of 10 keV/u and 3° (108 MHz) in energy spread and in phase spread, respectively. The set-up for the longitudinal emittance measurement will be installed and commissioned in June 2003.

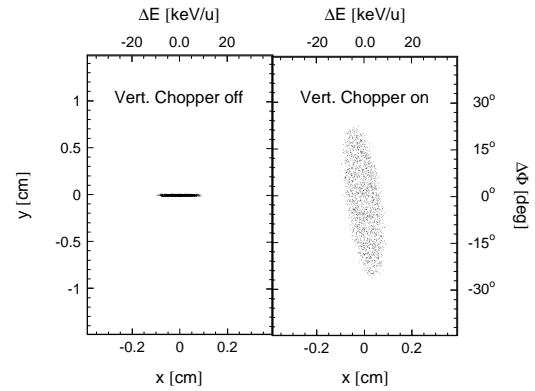


Fig. 7: Simulated beam spot image at the screen for a minimized beam size while the vertical rf-chopper is not active (left) and while it is active (right). The horizontal axis corresponds to the energy spread and the vertical axis corresponds to the phase spread (108 MHz).

REFERENCES

- [1] W. Barth, *Commissioning of the 1.4 MeV/u High Current Heavy Ion Linac at GSI*, Proc. of LINAC2000, Monterey, USA, (2000).
- [2] P. Forck, et al., *Measurement of the six dimensional Phase Space at the New GSI High Current Linac*, Proc. of LINAC2000, Monterey, USA, (2000).
- [3] T. Hofmann et al., AIP proceedings of the Beam Instrumentation Workshop, Boston (2000).
- [4] J. Glatz, GSI Darmstadt, private communication.

A MODULAR VME DATA ACQUISITION SYSTEM FOR COUNTER APPLICATIONS AT THE GSI SYNCHROTRON

D. A. Liakin*, T. Hoffmann, P. Forck

Ges. f. Schwerionenforschung, 64291 Darmstadt, Germany

*ITEP, Moscow

e-mail: D.Liakin@gsi.de

Abstract

Particle counters perform the control of beam loss and slowly extracted currents at the heavy ion synchrotron (SIS) at GSI. A new VME/Lynx – PC/Linux based data acquisition system has been developed to combine the operating purposes beam loss measurement, spill analysis, spill structure measurement and matrix switching functionality in one single assembly. A detailed PC-side software description is presented in this paper. The software has been divided into time critical networking and data deploying threads and low or normal priority interface tasks to achieve best system stability. Some new abilities in the fields of data computation and presentation are described. First experiences gained while the commissioning of the system are discussed.

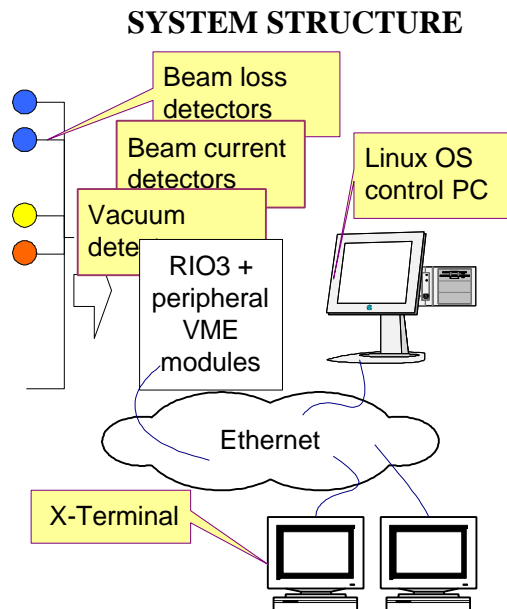


Fig. 1 Scheme of the system structure.

The structure of the new system is shown in Fig. 1. The VME data acquisition modules are controlled by a CES RIO3 processor with an installed Lynx as a real time operating system. The set of acquired data is transferred via 100MBit Ethernet connection to the control PC for being processed by different applications. Detailed description of the used hardware and LynxOS software can be found in [1].

PRINCIPLE OF OPERATION AND DATA STRUCTURE.

All detectors which are used in this system are operating in a pulse counting mode. Even if some detectors initially deal with continuous signals like currents and voltages, finally current-to-frequency or voltage-to-frequency converters are used. A high dynamic range and linearity are advantages of using modern VME counters[2] compared to other methods of data acquisition. At the same time, high timing resolution can be obtained with matched signals, therefore a fine time structure of investigated processes is also available.

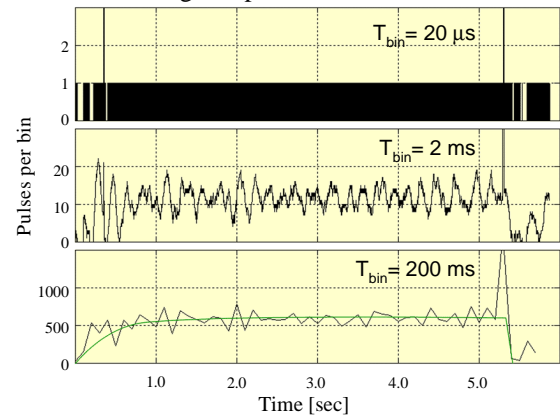


Fig. 2. The beam current in amount of pulses is shown as a function of time. The time unit is 20μs at the top, 2ms in the middle and 200ms at the bottom.

The sampling frequency may be changed according to the aims of different applications. As an example the beam current transformer signal is shown in Fig. 2. At the top one can see the full bandwidth case. In this situation the sampling frequency of 50 kHz is higher than the incoming pulse rate and only one pulse may be acquired within this 20μs interval. At the bottom the low bandwidth case is shown. Low bandwidth is acceptable for the most applications except those where special analysis is required. Spectral parameter of the Fig. 2 top signal are shown in Fig.3. A Fourier spectrum and a spectrogram[3] were prepared to investigate the fine structure of this signal. The Fourier spectrum shows a presence of a number of harmonics of a 1kHz internally generated frequency. In contrast to a simple spectrum the spectrogram illustrates the possibility to detect a more complex non-periodic system behaviour. A current-to-frequency converter is used to convert measured current

values to the pulse sequence shown in Fig.2. This 'floating' pulse frequency cannot be detected just by Fourier spectrum observation. In addition the spectrogram gives information about the signal nature – the 'floating' frequency signal is clear visible in Fig. 3.

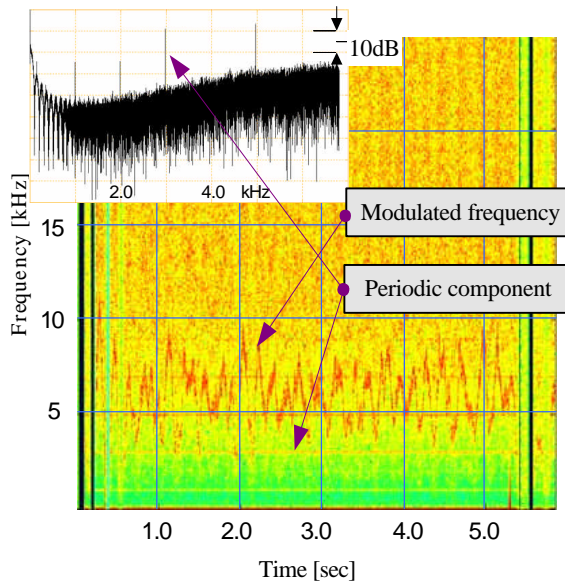


Fig. 3. The spectrum (on left top corner) and a spectrogram of signal shown in Fig. 2.

In this case the detected 'details' do not belong to the input signal, but to the internal transformer frequency. They reflect features of the used electronic devices. The incoming signal has a spectrum limited with a frequency about 100 Hz, so the original data is easily filtered from the complex mixture of frequencies shown in Fig. 3.

DATA DISTRIBUTION AND PROCESS SYNCHRONIZATION

An extendable set of applications may be used for online data acquisition control and evaluation on the Linux PC. A special data redistribution and process synchronization mechanism has been developed to provide the possibility to use the same data within different applications simultaneously. Due to the large data amounts which have to be transmitted and due to all applications which are running on the same PC, it is not reasonable to transfer the data to each application separately and to use multiple sockets for the data reception. Instead of this, the experimental data is routed to a single task which is not equipped with complex visualisation possibilities or high quality data evaluation algorithms. It provides a high reliable input data stream processing and an initial data manipulation. This hidden task consists of a high priority thread which is working in very close interaction with the Linux operation system. Fig. 4. shows the main structure of the data distribution. Incoming data passes through numerous network layers provided by the network equipment and OS software to the preliminary data stream interpreter. A high priority interpreter thread analyses incoming data and interprets

the type and amount of data. If this data is suitable for evaluation, analysis or presentation it is then accommodated in a dedicated shared memory segment. Corresponding event and semaphore mechanisms are used to grant and synchronize the access to the stored data from other applications. The allowed access time is limited due to reliability requirements. Thus the performance of the applications using shared objects are protected for being slowed down. Usually only the required part of the data set is copied to their internal memory for future evaluation.

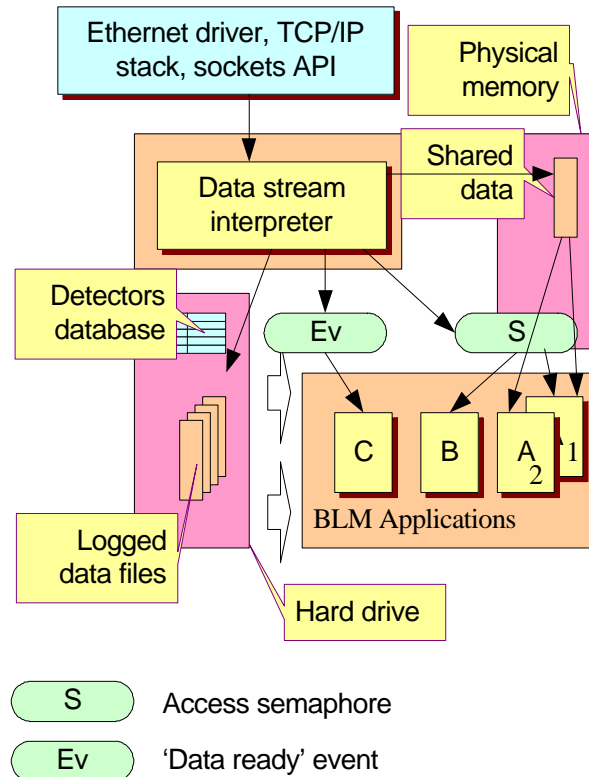


Fig. 4. A special task is used to accept and interpret the input data stream to redistribute data between different applications.

DATA TRANSMISSION

The hardware is divided into the VME front-end and the PC back-end. Currently the remote VME processor has a direct 100Mbit connection to the control PC. It includes the risk of losing a part of the data due to the public character of this network media. Priority was put on safe program operation instead of an absolute errorless data transfer. The transceiver does not verify the correct data transmission - if the network is busy and the internal buffer is full the next set of data will not be sent and data will be lost. The advantage of this situation is that limited front-end processor resources will never be locked by incoming data. From the other side, the receiver has no mechanism to force the transmitter to repeat the last transfer, so only local error handling operations on the control PC are possible and are required to handle data transport problems.

DATA PRESENTATION

Several types of presentation tools are implemented at the moment. A table form data presentation has been realised to display the counter end values after each cycle. This kind of visualisation (Fig. 5a) has proved its value and is compatible with the GSI crossbar system. Data logging graphs of selected detectors are suitable for an all area cycle by cycle beam loss and current monitoring (Fig. 5b). A highly resolved spill structure analysis tool delivers detailed information (Fig. 5c) within a single cycle. This type of data acquisition may be used in offline and online mode and is successfully used with e.g. beam loss observation.

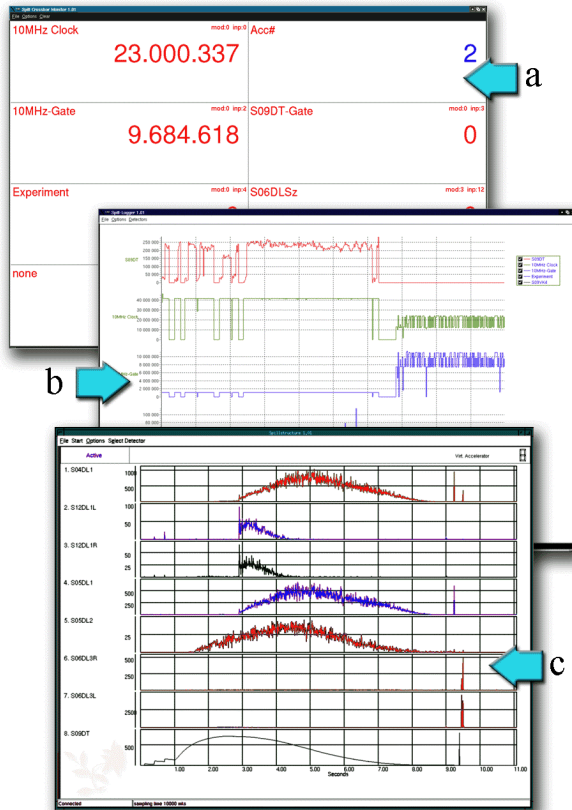


Fig. 5. Examples of application layouts. The crossbar application (a), the history logging and detailed process structure presentation (c) are shown.

SYSTEM PERFORMANCE

Currently four VME multi-channel scaler modules SIS3801, 32 channels each, are used. Every scaler input can be enabled or disabled independently. As default a sampling rate of 1 kHz is used with all 128 channels enabled. For high resolution measurements sampling rates of up to 500 kHz may be set. For this case the amount of active channels has to be reduced. A slow VME bus read/write cycle (1 μ s for a single 32 bit data read operation) of the CES RIO3 processor is limiting the performance.

MEMORY LEAK PROBLEM

Due to the permanent operation the undesirable memory leak problem gains in importance. Special attention has been paid to detect its presence and then to investigate sources and methods to avoid it. As a first step all applications and subroutines were checked for memory leaks. It turned out that it is difficult to observe the memory distribution in multitasking multithread systems like Linux or Window. The special Borland Kylix[4] memory reallocation mechanism also makes this task uncomfortable.

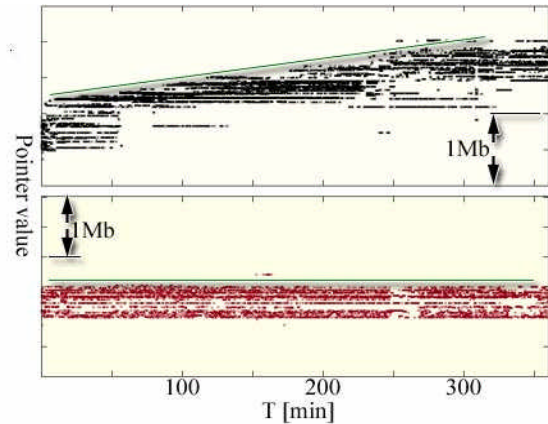


Fig. 6. The probe variable allocation pointer value behavior before (on top) and after optimization.

A simple dynamic variable pointer value was recorded over a long time period to check memory usage in our case. The result is shown in Fig. 6. Though the source of this memory leakage was still undefined after this operation while at the same time the leak itself was obvious. Advanced investigations showed that a huge amount of memory was occupied by processes of allocating and de-allocating memory space somewhere inside of a graphical library. Some leaks were found after detailed observation of the library source code. Others disappeared after changing the state of some objects from dynamic to static. As a result of all leakage corrections the pointer value seems to be stable (Fig. 6, bottom). We have found no reasons to build special tools to control precisely the memory allocation. Instead of this, the probe variable is being observed for restarting the program by itself in case of a significant process memory growth.

REFERENCES

- [1] T. Hoffmann, D. A. Liakin and P. Forck "A Fast VME Data Acquisition System for Spill Analysis and Beam Loss Measurement," 10th BEAM INSTRUMENTATION WORKSHOP 2002, Upton, N.Y. (USA), 2002, pp. 329-336.
- [2] <http://www.struck.de/>
- [3] Oppenheim, A.V., and R.W. Schaffer, "Discrete-Time Signal Processing", Prentice-Hall, Englewood Cliffs, N.J., 1989, pp. 713-718.
- [4] <http://www.borland.com/>

POSTERS TUESDAY

BEAM POSITION AND PHASE MEASUREMENTS USING A FPGA FOR THE PROCESSING OF THE PICK-UPS SIGNALS

G. Naylor, E. Plouviez, G. F. Penacoba

European Synchrotron Radiation Facility (ESRF), Grenoble, France

Abstract

We have implemented the signal processing needed to derive the transverse beam position and the beam phase from the signals of a four electrode BPM block on a FPGA (field programmable gate array). The high processing rate of a FPGA allows taking the full benefit of the high data acquisition rate of the more recent ADC. In addition, it is possible to implement on a FPGA a processing algorithm exactly tailored to the measurement of the beam parameters. The efficiency of the signal processing has also been improved by a careful choice of the frequencies of the sampling clock and of the RF front-end local oscillator, which are derived from the storage ring RF frequency. This paper describes the BPM, the RF front-end electronics and the FPGA algorithm. It presents some of the applications of this BPM at the ESRF and gives measurement results.

INTRODUCTION

ADC with resolution and sampling rate adequate for the acquisition of storage ring beam signals have been available for several years. The sampling rate of these ADCs is in the 20MSPs to 100MSPs. Such a high data rate cannot be efficiently processed by a regular DSP. A solution to this problem is to pre process the data in order to decimate the data flow using a specialized circuit called a Digital Down Converter (DDC)[1]. This solution gives good results but does not take full advantage of the periodicity of a beam signal. Therefore, a FPGA was used with a processing algorithm tailored to the time structure of our SR beam. The main features of this processing are:

- Synchronous I/Q demodulation

- Computation of the amplitude and phase modulation

The useful frequency range of the BPM pick-up signals usually starts well above the maximum frequency that an ADC can handle. In our case we selected a 10 MHz bandwidth around 352.2 MHz in the pick-up signals, and the maximum input frequency of the ADC that we use (AD9225) is only 100 MHz. So a RF front-end circuit must be implemented to down convert the frequency of the pick up signals in the input frequency range of the ADC. The efficiency of the digital signal processing will depend on the wise choice of the frequency shift applied to the pick-up signals. In our case, we wanted to be able to measure the bunches position and phase in case of so-called time structure mode filling of the storage ring: The ring is then filled with 1 or 16 high intensity bunches equally spaced. So we needed a sampling frequency

equal to one quarter of the bunch spacing in the 16 bunch filling mode.

RF FREQUENCY DOWN CONVERSION

General Layout

The layout of the RF front-end is shown in figure 1.

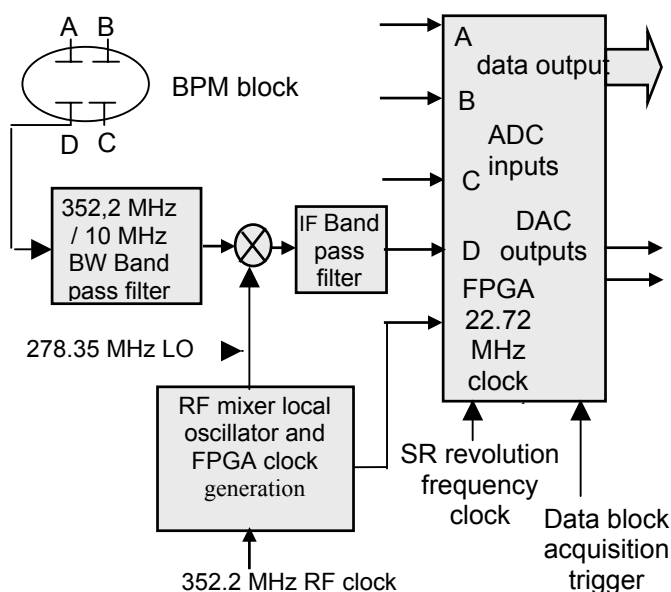


Figure 1: Layout of the BPM

The ESRF RF frequency is 352.2 MHz, the ring harmonic number is $992=32 \times 31$ and the revolution frequency is $f_{rev}=355\text{KHz}$. The choice of the clock and local oscillator frequency has been done following this line

ADC sampling clock frequency

The maximum sampling frequency of the 12-bit ADC AD9225 is 40MHz (definitely not the ultimate fast ADC available today...). The T delay between 2 bunches with a 16 bunch filling pattern of our storage ring is 88.018 ns; $1/T = 352.2\text{MHz} / 62 = 5.68\text{MHz}$. We have chosen 22.72 MHz for the ADC sampling clock frequency f_s , $2 \times 352.2\text{MHz} / 31$. Using such a clock, a synchronous in phase and in quadrature acquisition (I/Q) of all the harmonics of f_{rev} up to 11.36 MHz can be performed

Local oscillator frequency

The intermediate frequency IF can be higher than $f_s/2$ providing the IF signal bandwidth is lower than $f_s/2$

(under sampling); but the intermediate frequency IF must be such that the phase of the IF signal shifts by $\pi/4$ over one period of the f_s signal in order to produce an I/Q detection. We have chosen $IF=13*f_s/4$ ie $IF=73.848\text{MHz}$; therefore the local oscillator frequency f_{LO} is $f_{RF}=f_{IF}=278.352\text{ MHz}$. These frequencies have been synthesized using oscillators synchronized by PLLs on the right harmonics of f_{rev} .

Selectivity of the RF and IF filters

The digital filtering of the ADC data will give correct results on condition that the image frequency signals in the RF spectrum and in the IF spectrum have been removed by analog filters. In the case of a beam signal, with a periodic spectrum of $N \times f_{rev}$ lines with symmetrical sidebands created by the transverse and longitudinal oscillations, this aliasing is not harmful provided the sampling is synchronous with the beam revolution. So the requirement for the RF and IF band pass selectivity is much less stringent than with a non-synchronous scheme for the RF frequency down conversion and ADC sampling.

DIGITAL SIGNAL PROCESSING

FPGA compact PCI board

A compact PCI general-purpose mother board has been developed at the ESRF in the Digital Electronics Group, to offer a quick answer to internal developments requiring fast and reasonably complex processing with a flexible I/O interface. Application specific mezzanines are added to this board. The FPGA circuit used on this board is a *Xilinx VIRTEX 600E*.

ADC/DAC mezzanine

The input signals of the board are converted at a rate of 22.72 MHz by four AD9225 12 bits AD converters housed on a mezzanine. This mezzanine is also used to input the sampling clock signal as well as other synchronisation signals (storage ring revolution frequency and injection timing). In addition two 12 bits DAC have been implemented on the mezzanine to output the results of the processing.

ALGORITHM PROGRAMMING ENVIRONMENT

The VHDL language used for the programming of the *Xilinx* FPGA cannot be really mastered by occasional users. However, high-level programming tools are available to write down and test signal-processing algorithms, which can be compiled in VHDL afterwards. We have used such a tool: *System Generator*, available from *Xilinx*. *System Generator* compiles in VHDL a processing model described by a *Simulink* block diagram [2]. So the only VHDL programming needed then is the allocation of the input/output resources.

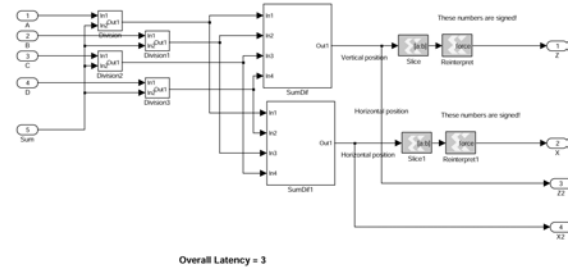


Figure 2: Part of the graphical *Simulink* algorithm layout

PROCESSING ALGORITHM

Beam position

The FPGA uses the A_n, B_n, C_n, D_n and $A_{n+1}, B_{n+1}, C_{n+1}, D_{n+1}$ IF signals coming from the 4 pick-ups of the BPM and sampled by the four ADCs over successive clock periods; it computes the following values:

- $A=(A_n^2 + A_{n+1}^2)^{1/2}$, B, C and D
- $\Sigma=A+B+C+D$
- $\Delta z=((A+B)-(C+D)) / \Sigma$ vertical position signal
- $\Delta x=((A+D)-(B+C)) / \Sigma$ horizontal position signal

It averages $\Sigma, \Delta x, \Delta z$, over one revolution period to generate a turn-by-turn position measurement.

It calculates the beam position:

$$x = f_x(\Delta x, \Delta z) \text{ and } z = f_z(\Delta x, \Delta z)$$

$f_x(\Delta x, \Delta z)$ and $z = f_z(\Delta x, \Delta z)$ are look-up tables representing the non-linear field law in the cross section of the BPM pick-up.

Beam phase

The FPGA computes the following values

- $I=(A_n + B_n + C_n + D_n)$, in phase signal
- $Q=(A_{n+1} + B_{n+1} + C_{n+1} + D_{n+1})$, quadrature signal

(phase and quadrature with respect to a $f_{clock}/4$ reference signal).

- $\Sigma=(I^2+Q^2)^{1/2}$: amplitude signal

It output ϕ , phase signal, with $\cos \phi = I / \Sigma$ and $\sin \phi = Q / \Sigma$

Averaging and filtering

A signal synchronous with the revolution frequency allows the selective acquisition and processing of data over a fraction of the revolution period as shown on figure 1; the position and phase signals can also be averaged inside a revolution period or over several turns in order to ease the detection of the various signals observed on a SR beam: synchrotron and betatron oscillations, low frequency beam motion due to the ground vibrations, etc. Space is still available on the FPGA for further processing like FIR filtering or digital frequency down conversion.

STATUS AND TEST RESULTS

System tested

A test system is working. A device server allows it to transmit four blocks of 2048 processed data on the compact PCI bus. The acquisition of the data blocks is triggered using the storage ring revolution frequency signal and a low repetition rate data block acquisition trigger as shown on figure 1.

Resolution of the pic- up signal detection

For a beam signal with an amplitude half of the full ADC input range (± 1024 LSB) and a uniform storage ring bunch filling (22Mps flow of valid data), the following signal to noise ratio would be expected, providing the front end electronics noise is negligible:

A,B,C,D signals: 130dBc/Hz

Σ signals: 136dBc/Hz

I/ Σ and I/ Σ signals: 130dBc/Hz

This would result in a phase resolution of 3.10^{-7} rd/(Hz) $^{1/2}$ and a position resolution of $2.5\text{nm}/(\text{Hz})^{1/2}$ or $1\mu\text{m}$ turn-by-turn for our 35 mm gap vacuum chamber.

Resolution of the pick-up signal detection

However it is not realistic to neglect the noise contribution of the RF front end, especially for the phase detection. For the phase detection, the frequency range of interest is around the synchrotron frequency f_s ; On the ESRF storage ring, f_s about 1.5 KHz. A 278.35MHz local oscillator to be used in our RF front-end would have to exhibit a phase noise of less than 130dBc/Hz at 1.5 KHz from the carrier to have a negligible effect on the resolution of our system. On our prototype system, the phase resolution at 1.5KHz was limited to $6.10^{-3}\text{rd}/(\text{Hz})^{1/2}$ as shown on figure 3 since our prototype local oscillator uses a 20% tuning span VCO.

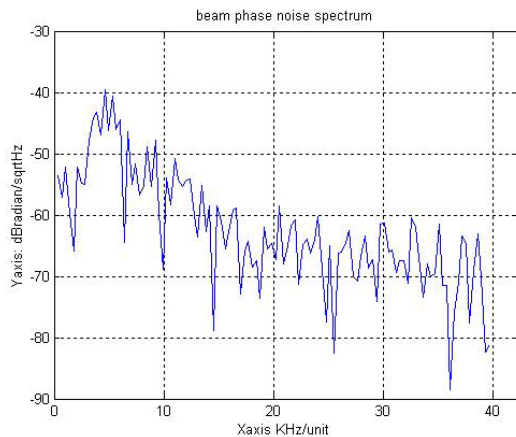


Figure 3: Plot of the spectrum of the phase signal, showing the detrimental effect of the local oscillator phase noise on the resolution.

On the final design, using a custom-made VCXO with a $-97\text{dBc}/\text{Hz}$ phase noise at 1.5KHz from the carrier, we expect a $2.10^{-5}\text{rd}/(\text{Hz})^{1/2}$ resolution, which is about the resolution required to monitor the random phase jitter of our beam at the synchrotron frequency.

Resolution of the beam position detection

The beam position detection relies on an amplitude detection of the IF signals coming from the RF front-end. The amplitude detection should be almost insensitive to the local oscillator phase noise. We actually found a position detection resolution of $10\text{nm}/(\text{Hz})^{1/2}$, or $4\mu\text{m}$ turn-by-turn.

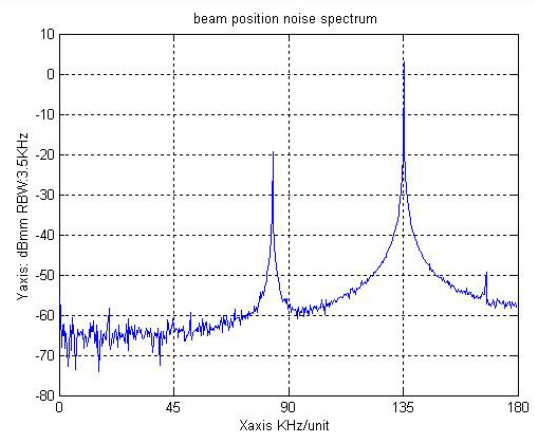


Figure 4: Plot of the spectrum of the position signal (oscillation amplitude: 2mm/ vertical scale: dBmm)

CONCLUSION

The use of a FPGA board together with a high level algorithm development environment allowed the design of a relatively sophisticated BPM/beam phase monitor using mostly standard components. However, the clocks and the oscillator of the RF front-end must be designed carefully in order to avoid spoiling the potential performance of such a design.

ACKNOWLEDGMENT

This work is based on the "CUB" FPGA board and ADC mezzanine developed by J. Cerrai and G. Goujon from the Digital Electronics Group of the ESRF. The RF front-end circuits and the RF synchronous clocks were developed by P. Arnoux of the Diagnostics Group.

REFERENCE

- [1] R. Ursic, "Digital receivers offer new solutions for beam instrumentation," PAC'99, New York, April 1999.
- [2] http://www.xilinx.com/products/software/sysgen/product_details.htm

Pill-box Cavity BPM for TESLA Cryomodule

V. Sargsyan, DESY-Zeuthen and TU-Berlin, Germany

Abstract

A new cavity BPM with $10\mu\text{m}$ resolution is designed and built to perform single bunch measurements at the TESLA linear collider. In order to have a low energy dissipation in the cryogenic supermodule, the inner surface of the cavity is copperplated. Cross-talk is minimized by a special polarisation design. The electronics, at 1.5 GHz, is a homodyne receiver normalized to the bunch charge. Its LO signal for down-conversion is taken from the same cavity.

THE PICK-UP STATION

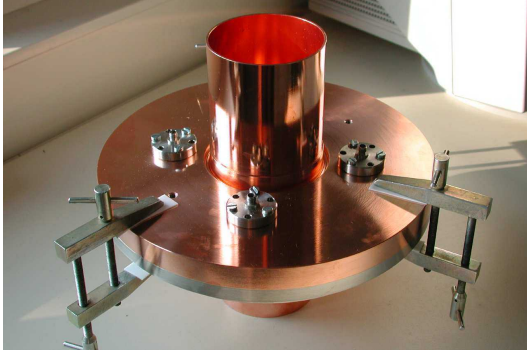


Figure 1: The pick-up station with four feed-troughs

A cylindrical pill-box cavity has been constructed as seen in figure 1. The pick-up station is fabricated from stainless steel. Dimensions and material properties of the structure are listed on table 1.

Table 1: Cavity dimensions and material parameters

type of stainless steel		1.4429
shrinkage from 293K to 2K [%]		0.3
conductivity (293K)	$[\Omega^{-1}\text{m}^{-1}]$	$1.33 \cdot 10^6$
cond. (2K)	$[\Omega^{-1}\text{m}^{-1}]$	$1.88 \cdot 10^6$
Room Resistivity Ratio (copper)		6.9
conductivity (293K)	$[\Omega^{-1}\text{m}^{-1}]$	$3.569 \cdot 10^6$
cond. (2K)	$[\Omega^{-1}\text{m}^{-1}]$	$24.84 \cdot 10^6$
Cavity diameter	[mm]	222 (221.3 at 2K)
Beam-pipe diameter	[mm]	78 (77.8 at 2K)
Cavity length	[mm]	18 (17.9 at 2K)
Coupling antenna depth	[mm]	7.6

In order to decrease energy dissipations on the walls the cavity was copper plated.

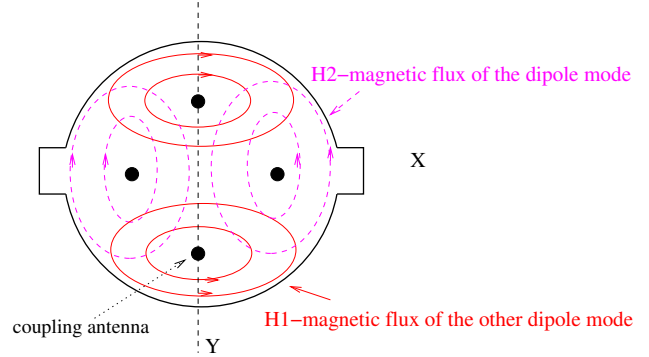


Figure 2: Cut of the cavity with two rectangular recesses

Two rectangular recesses were symmetrically eroded inside the cavity, in x-direction, see figure 2. It is done to get minimal cross-talk [2].

Fabrication tolerances result to changes in the anticipated TM_{110} -dipole mode frequency, see the following table. This results in a total error of

Table 2: Mechanical parameters sensitivity

dimension	target [mm]	sensitivity $\pm 100\mu\text{m}$	tolerances [μm]	shrinkage [μm]
cavity radius	111	$\mp 1.247\text{ MHz}$	± 10	-433
cavity length	18	$\pm 0.158\text{ MHz}$	± 100	-203
pipe radius	39	$\mp 0.305\text{ MHz}$	± 50	-146

$$\Delta f = \sqrt{\Delta f(\delta R_{\text{res}})^2 + \Delta f(\delta l)^2 + \Delta f(\delta r)^2} \approx 252\text{ kHz} \quad (1)$$

For simulations of the structure and resonant mode parameter computations the computer code GdfidL was used [1]. The signal which an antenna couples from the cavity on 1.512 GHz dipole mode frequency is

$$V^{\text{out}}(1.512\text{ GHz}) = V_{110}^{\text{out}} + V_{010}^{\text{out}} + V_{020}^{\text{out}} + V_N \quad (2)$$

Where

- V_{110}^{out} is the coupled voltage of the dipole mode,
- V_{010}^{out} is the coupled voltage of the common mode on 1.512 GHz-dipole mode frequency,
- V_{020}^{out} is the coupled voltage of the second monopole mode on 1.512 GHz-dipole mode frequency, and
- V_N is the noise level, which is approximately -70 dBm (0.07 mV).

These values are computed theoretically, and for TESLA with a bunch charge of 3.2 nC and 10 μ m beam-offset they are summarized in table 3.

Table 3: Voltages on 1.512 GHz frequency

signal	voltage
V_{110}^{out}	4.41 mV
V_{010}^{out}	2.77 mV
V_{020}^{out}	14.78 mV
V_N	0.07 mV

Frequency scan of the cavity

A frequency scan of the cavity by means of a Network Analyser results to S_{21} measurements, see figure 3.

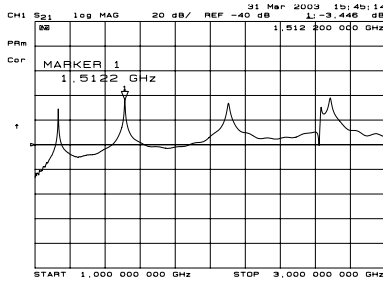


Figure 3: S_{21} against the frequency

The results are summarized in the following table:

Table 4: Data of frequency scan

	measured (warm)	computed
Q_L^{110}	700	822
f_{110}^x	1.512 GHz	1.51 GHz
Q_L^{110}	760	839
f_{110}^y	1.522 GHz	1.522 GHz
Q_L^{010}	1133	1700
f_{010}	1.131 GHz	1.133 GHz

Cross-talk measurement

Cross-talk isolation measurements were performed as indicated in figure 4. At first, we generated and coupled the signal through the antennas in the same direction, as in figure 4a. The two remaining coupling ports were loaded by 50 Ω . Left plot in figure 5 shows the result of this measurement. Here signal level is obtained as a function of frequency. A maximum at 1.522 GHz with a level of -1.8 dB is observed.

Next, we repeated the measurement using antennas in perpendicular to each other directions (figure 4b) and obtained the second plot in figure 5. Here two maxima are

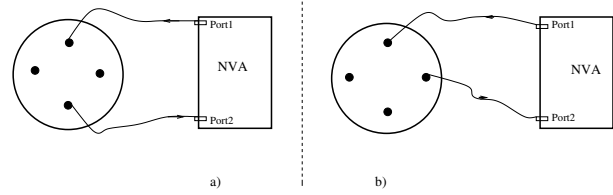


Figure 4: Layout of the cross-talk measurement

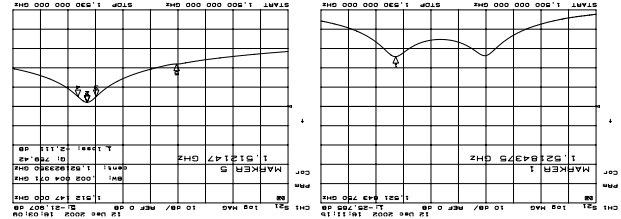


Figure 5: Signal level in [dB] against frequency. The signal level is graded by 10 dB. The reference 0 dB-line is the middle one

visible. The corresponding signal at the second maximum with the same frequency has a level of -25.8 dB. The first maximum on 1.512 GHz refers to the second dipole mode in the perpendicular plane.

The cross-talk isolation value is the 24 dB signal level difference between left and right plots in figure 5 on the same 1.522 GHz frequency. The cross-talk between the other ports was about the same.

ELECTRONICS

The parameters of the signals which should be handled by the electronics are:

Table 5: Signals from the pick-up station

bunch distance	337 ns (2.96 MHz)	
TM ₁₁₀ GHz	1.5 GHz	
TM ₀₁₀ GHz	1.14 GHz	
TM ₀₂₀ GHz	2.64 GHz	
Charge	3.2 nC	1.0 nC
V_{110}^{out} ($\delta x = 10 \mu\text{m}$)	-34.1 dBm	-44.2 dBm
V_{010}^{out} (10 μm)	-38.1 dBm	
V_{020}^{out} (10 μm)	-23.6 dBm	
V_{110}^{out} ($\delta x = 2.5 \text{ mm}$)	13.8 dBm	

Comparing parameters such as *dynamic range*, *signal to noise ratio*, *amount of electrical components* (less components means cheaper electronics system) we have chosen a *homodyne* system of signal detection [3], which is shown in figure 6.

The electronics, at 1.5 GHz, is a homodyne receiver, which provides bunch charge normalized signals. It has 5 output channels: two for x-position detection; two for

y-position detection, and one for charge detection (see figure 6). The LO signal is taken from the cavity itself. The IF

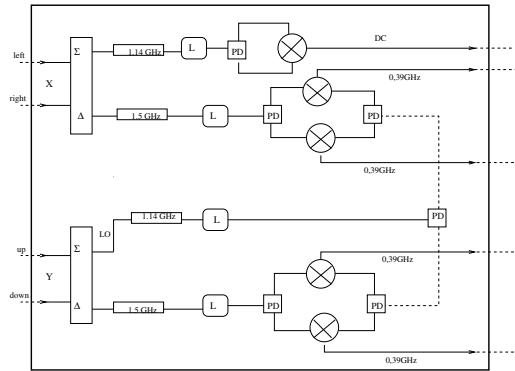


Figure 6: Electronics box

signal has a 0.4 GHz frequency. Before the signal digitizing we apply a Sample-Hold system, which selects the part of the IF signal of 2.9 GHz, the TESLA bunch repetition frequency.

RESOLUTION MEASUREMENTS

The test-measurements are performed at the DESY-Zeuthen laboratory. The generator-antenna was moved with a 10 μm step-size in x-direction (y-direction) over a range of ±1 mm. With the detected I_x and Q_x values we computed the V_x

$$V_x = \sqrt{I_x^2 + Q_x^2}. \quad (3)$$

Figure 7 illustrates the sensitivity of the BPM. The bigger slope means higher sensitivity. To valuate the resolution we

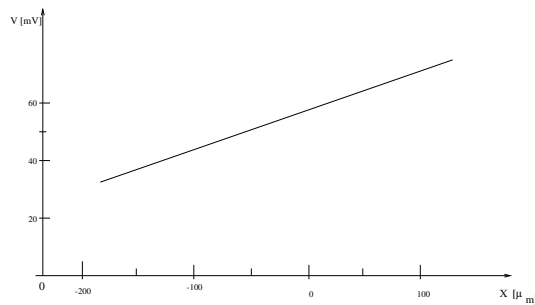


Figure 7: BPM sensitivity plot

compare the measured position with the real antenna positions, see figure 8.

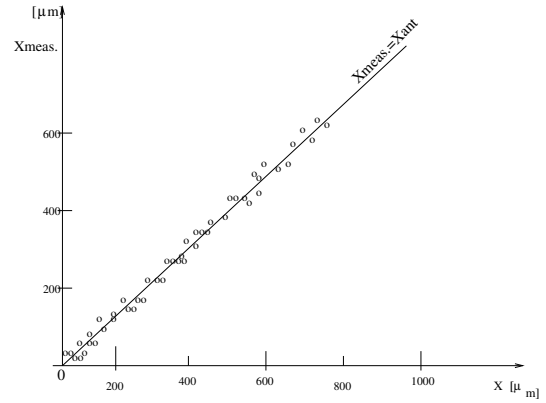


Figure 8: BPM resolution plot

The TESLA-bunch excites the cavity 10 times stronger than it was in laboratory conditions. Hence, we aspect 8 μm resolution performance.

REFERENCES

- [1] W. Bruns,
<http://www.gdfidl.de>
- [2] V. Sargsyan,
Cross-Talk Problem in Pill-Box Cavity,
TESLA 2003-01, DESY, January 2003
- [3] A. Liapine, V. Sargsyan.
Survey of RF Receiving Techniques,
TET-Note, TU-Berlin, February 2002

ADVANTAGES OF IMPLEMENTING DIGITAL RECEIVERS IN FIELD PROGRAMMABLE GATE ARRAYS (FPGA)

Saša Bremec, Rok Uršič, Uroš Mavrič
Instrumentation Technologies, Solkan, Slovenia

Abstract

Today's state-of-the-art FPGA technology allows designers to satisfy almost any demand for high-speed data processing that is needed in digital signal processing (DSP) applications and fast data transfers. Dedicated FPGA resources are used in DSP applications to perform down conversion, filtering, and data formatting. New trends in system architecture favor serial data rather than parallel data transfer by using FPGA's internal resources, BlockRAMs (BRAMs), high-speed serial input/outputs (IO), and hard core processors.

1 INTRODUCTION

The latest trends show that the FPGA technology is gaining its share and becoming implementation technology of choice among digital receivers designers. This trend also reflects mature state of FPGA devices. An other appealing characteristic of FPGAs is their ability to integrate multiple functions or a complete system on a single chip. This is a generic trend in today's integrated circuit design and is referred to as system-on-chip (SoC) concept. Other features of today's high end FPGAs include embedded processors (PowerPC, ARM), which can run a variety of real time operating systems (RTOS) and powerful serial links, which support implementation of a multitude of open-standards protocols like Gigabit Ethernet, Fibre Channel, RapidIO, Infiniband and similar.

2 DIGITAL DOWN CONVERTER

The main advantage of implementing digital receivers on FPGAs in beam position monitors (BPM) or other similar beam instrumentation applications is that designers can tailor and optimize their designs to the

requirements of the specific applications. ASIC devices, on the other hand, where all the functional building blocks are embedded only allow the designer to change different parameters.

As an example we present a specific configuration of a digital receiver that was optimized for one of our applications. The requirement was to provide a simultaneous stream of wide-band and narrow-band measurements. Figure 1 shows the corresponding functional block diagram.

Fast analog to digital converter supplies a constant stream of data from a directly sampled IF or RF signal. The data stream is then split into two chains, which are multiplied by a stream of sine and cosine samples respectively, generated by a numerically controlled oscillator (NCO). If the frequency of the NCO corresponds to that of the input sampled frequency, then two signals following the multiplier contain the base-band component and the component at twice the NCO frequency. The cascaded integrator comb (CIC) filter followed by the finite impulse response (FIR) filter eliminate the second harmonic component and provide the required spectral shaping. The CORDIC building block calculates amplitude of the signal from the stream of I and Q samples. The data stream then splits into two branches. The top one provides additional filtering for low-bandwidth application, while the bottom one is used for wideband applications.

Another advantage of using FPGAs in digital receivers is that they allow implementing a variety of analog to digital converter configurations and architectures. Using advanced technique sampling rates up to 300 Msamples/s can be obtained, something currently not achievable with standard ASICs.

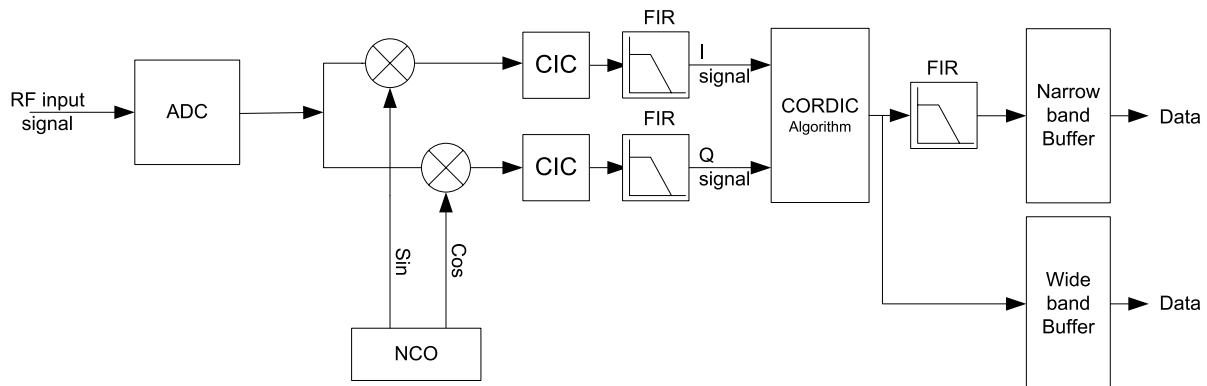


Figure 1 A specific configuration of a digital receiver that was optimized for one of our applications. The requirement was to provide a simultaneous stream of wide-band and narrow-band measurements..

3 SYSTEM-ON-CHIP (SoC) CONCEPT

Every new FPGA generation integrates more and more discrete components that are required to create a working system and making your printed circuit boards simpler and less expensive. This is a move towards a system-on-chip design. The goal is to make the IO structure so extensive that designers will never have to use the glue logic to understand the intricacies of each new standard. For example, by integrating a variety of different memory

interfaces into FPGA, the designer can easily connect any known memory device without having to create its own custom interface designs. IT is expected that this trend will continue in the future.

There are two other powerful functional features added to the latest high end FPGAs and will greatly contribute to the proliferation of the SoC concept: the addition of the soft and hard-core embedded processors an powerful, multi Gbit/s serial interfaces. They are discussed below.

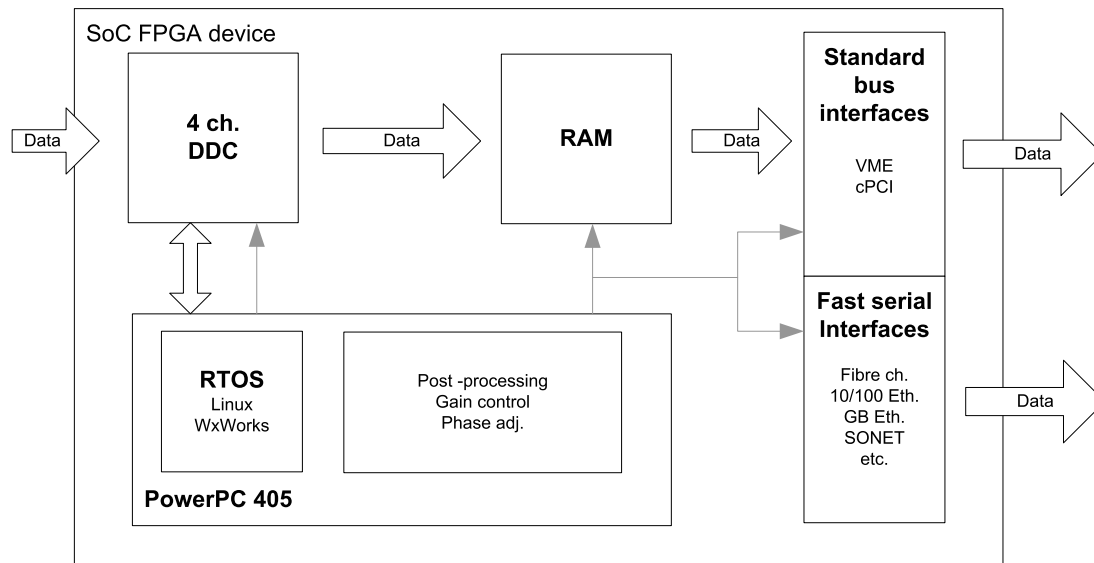


Figure 2 An example of SoC concept implementation of a Digital Receivers.

4 SOFT AND HARD PROCESSOR CORES

Soft Cores

Main advantage taken from these soft embedded processors is that designers can select the peripherals features they want to, and as many as the design needs. This allows to implement the fully customized processor and to optimize it to specific tasks. These cores are not affecting of the obsolescence problem, so typically for stand-alone processors devices.

Hard Cores

When the designs need more MIPS power the right choice is to use the embedded hard-core processor. These processors are more complex to program, but the reliable running of RTOS allows designers to implement specific task, which can be written in standard programming

languages. As an example let's take the Virtex-II Pro™ FPGA family from Xilinx. They implement PowerPC hard core, which was developed in partnership with IBM. It gives you a well-known, very high performance architecture. The processor is embedded with-in the programmable logic fabric, so all of the processor IO pins are available to the internal programmable logic for maximum flexibility. Plus, the processor IO pins do not take up valuable FPGA IO resources, unless you need them. This allows to move data much faster.

5 IO INTERFACES

FPGA is a solution that supports various system interfaces and thus offers designers a great flexibility. As an example let's again take the Virtex-II Pro™ FPGA family. The SystemIO solution offers exactly this: support for physical interfaces as well as cores that support the network protocols for all the common and emerging system IO interfaces. These FPGAs enable high performance interfaces to memories from Cypress, IDT, Micron, SiberCore, GSI Technology and others, as well as interfaces to networking On the other hand Application

Specific Standard Parts (ASSP) from vendors such as AMCC, PMC Sierra, and Vitesse.

The demands of high speed networking and other high performance systems, requires the use of gigabit-per-second serial IO capability for interconnecting devices, backplanes, and systems. In addition, some of the new communications standards and backplane standards are based on these high speed serial IO capabilities, including POS-PHY4, FlexBus4, HyperTransport™, InfiniBand™, Fibre Channel, Gigabit Ethernet, and so on. With the Virtex-II IO capability one can connect directly to a backplane without external components.

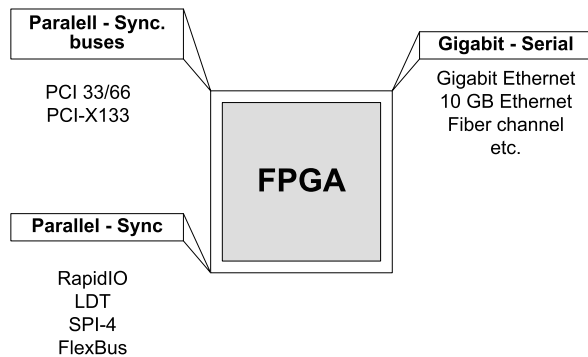


Figure 3 One of the main advantages of modern FPGAs is a variety of supported IO standards.

6 IMPLEMENTATION RESULTS

An important parameter when designing digital receiver on FPGAs is how many channels one can squeeze on a single chip. There are many parameters that influence

number of logic cells needed to implement a digital receiver. The extent of such discussion is well beyond the scope of this paper. However, as a rule of thumb one can look at table 1, which shows how many digital receiver channels, which architecture is shown in figure 1, fit onto a particular FPGA integrated circuit from Xilinx.

FPGA Device	Slice n°	DDC ch./ FPGA
XC2VP30	14.720	7
XC2V1000	5.120	2
XCV1000E	12.288	4

Table 1 FPGA usage vs. digital receiver channels

7 CONCLUSION

Advanced process technology has enabled to develop high-density FPGA devices that are extremely well suited to the needs of high-performance real-time signal processing. With the addition of embedded processor cores and powerful IO options they provide a valuable combination of high performance and configurability – both required for high performance digital receiver applications.

REFERENCES

- [1] U. Mavrič, R. Uršič and S. Bremec, “Experience with sampling of 500MHz RF signal for digital receiver applications”, this conference
- [2] J. Mitola, Software Radio Architecture: Object-Oriented Approaches to Wireless Systems Engineering, John Wiley & Sons, 2000
- [3] Jeffrey H. Reed, Software Radio: A Modern Approach to Radio Engineering, Prentice Hall, 2002

EXPERIENCE WITH SAMPLING OF 500MHz RF SIGNAL FOR DIGITAL RECEIVER APPLICATIONS

Uroš Mavrič, Saša Bremec, Rok Uršič
Instrumentation Technologies, Solkan, Slovenia

Abstract

This article presents test results of the prototype system that was built to evaluate feasibility of direct sampling of 500 MHz RF signal for use in digital receiver applications. The system consists of variable gain RF front-end, fast analog to digital converter (ADC) and field programmable gate array (FPGA), which provides the glue-logic between the ADC and a PC computer.

1 INTRODUCTION

The new trend in RF front-end design is to minimize the RF front-end complexity and to digitalize the signals as close as possible to the antenna. As a result, down-conversion can be omitted and the RF signal can be directly sampled using under-sampling technique.

The prototype was designed and constructed to investigate and evaluate the most important parameters that influence the performances of such a system.

2 PROTOTYPE

The prototype consists of RF amplification and filtering chain, fast analog to digital converter, and FPGA to control the outgoing data from the ADC and direct them to a serial port of the computer (PC).

2.1 RF amplification and filtering chain

Figure 1 shows the RF processing chain that consists of a few amplifiers (MMIC), filters, and variable attenuators. The cumulative amplification of a series of amplifiers boosts the incoming RF signal to cover the required dynamic range. Furthermore, the analog input of the ADC is set to +10dBm (full-scale) in order to give the best linear performances. Two variable attenuators provide a mechanism for keeping the output signal power constant whatever the input signal within the dynamic range is.

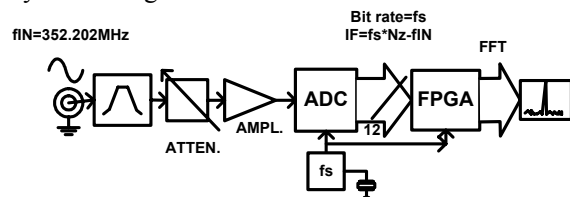


Figure 1: Prototype for direct RF sampling. It consists of amplification and filtering chain, fast analog to digital converter, FPGA, and personal computer for additional processing (FFT) and data visualization.

Relative position of variable attenuators in the RF processing chain and the switching scheme determine SNR and SFDR performance. In addition, the RF processing chain can be optimized for minimum noise figure or maximum third order intercept point, yielding high linearity. Figure 2 shows how SNR for these two cases varies with respect to the input signal. It is worth to mention that only the switching scheme changed.

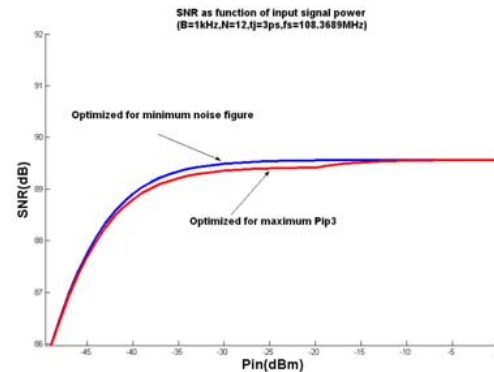


Figure 2: SNR as a function of the RF input signal. The upper curve is the SNR when attenuators are switched to keep the noise figure at its minimum. The lower curve is the SNR when attenuators are switched to give maximum P_{IP3} .

The input band-pass filter acts as an anti-aliasing filter and it covers only one Nyquist zone (Figure 4). If the input signal is a pulse and the pulse repetition frequency is much lower than the input band-pass filter bandwidth, the input signal doesn't anymore have a CW shape but the shape of the signal, which is shown in the Figure 3. It is important that pulse width is long enough to ensure enough samples to be taken by the analog to digital converter. A rule of thumb is 10 samples per pulse. At the same time we have to be aware of its amplitude, which should be well below the 1 dB compression point of the first amplifier after the band-pass filter. The pulse shown in Figure 3 gives a satisfying peak-to-average characteristic for a typical synchrotron light source operated in the single bunch mode.

2.2 ADC (analog to digital converter)

We use AD9433, which permits sampling of RF signals up to 750MHz with a sampling rate of maximum 125MSPS. In order to fulfill the Nyquist criteria it is necessary to use the previously mentioned under-sampling technique (Figure 4).

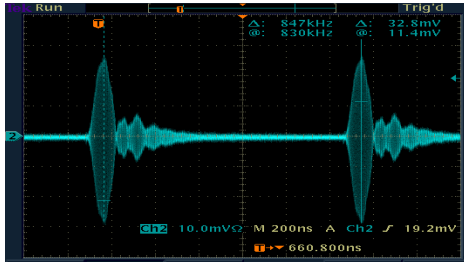


Figure 3: Pulse response of the band-pass filter measured in a single bunch mode. The pulse is wide enough to ensure enough samples to be collected.

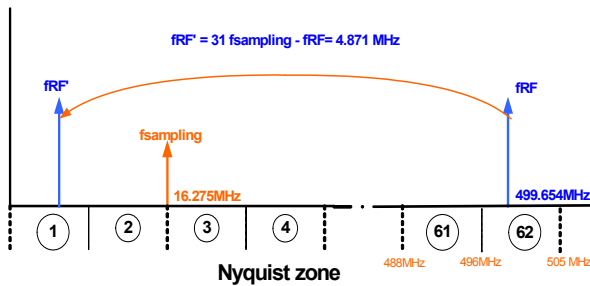


Figure 4: Under-sampling technique used to get intermediate frequency (IF).

3 CRITICAL PARAMETERS

There are several critical parameters that should be taken into account when designing a digital receiver RF front-end. These are gain, attenuation, sampling frequency, jitter of the sampling clock, anti-aliasing filter bandwidth, and sharpness. Although there are many degrees of freedom, the most important requirements we need to satisfy are good SNR, low SFDR, and good linearity of the whole system.

3.1 SNR (signal-to-noise-ratio)

The following sources of noise affect our prototype signal to noise ratio: thermal noise produced in the RF processing chain, quantization noise in the ADC, and clock jitter.

A mathematical model of all three sources of noise was estimated. The results are shown in the Figure 3.

3.2 Linearity

Linearity of the system is determined by the RF front-end as well as by the analog to digital converter. In the RF front-end all the amplifiers should work under $P_{0.1dB}$ compression point, which should be considered a linear region of the characteristics. The input signal power in the analog to digital converter should be set in a determined region (close to full-scale) in order to minimize the effect of differential and integral non-linearities.

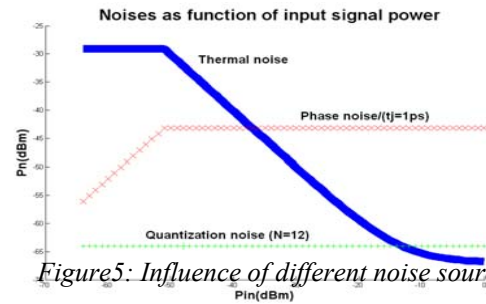


Figure 5: Influence of different noise sources.

4 DISCUSSION OF CRITICAL PARAMETERS

Noise sources and linearity directly affect the performance of the whole system. If the output sample stream from the analog to digital converter is used to determine beam position we have degradation in measurement accuracy and resolution due to nonlinear characteristics of the RF processing chain and different noise sources.

At lower input signals the SNR is determined by thermal noise in the RF processing chain. As the input signal increases, its rate of increase is much steeper than the decrease of the noise figure of the system yielding better signal to noise ratio at the output. The second noise source is the quantization noise, which is caused by the finite granularity of the analog to digital converter. The quantization noise level is independent from the input signal power. But at certain input power thermal and quantization noise equal and from that point on it would be worthless to further amplify the input signal. From that point on the noise level is determined exclusively by the quantization noise. Last but not least the Figure shows that the main noise source is the phase noise of the crystal oscillator, which determines the SNR limit at the upper input signals. Its time domain representation is expressed as the RMS value of jitter of the clock signal. In Figure 3 a 3ps jitter was assumed. Phase noise levels that can be achieved depend on the analog frequency we want to sample and on the sampling frequency stability.

We have also developed a mathematical equation to investigate the linearity problem. It describes loss in resolution by introducing non-linearity in the prototype. In the equation (1) ξ is the relative deviation from voltage V' at the output of the RF processing chain.

$$\Delta G = -20 \cdot \log\left(1 + \frac{\xi}{V'}\right) \quad (1)$$

5 RESULTS

On the data from the AD converter FFT was applied. The result for a maximum input signal (minimum gain) is shown in Figure 6.

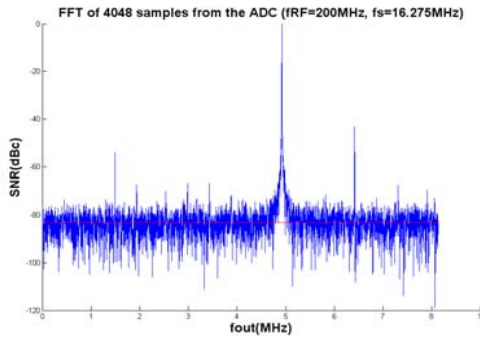


Figure 6: FFT of 4048 samples from ADC. Data rate was 16.275MSPS and the analog frequency was 200 MHz. Many spurs can be measured but they are in the expected range.

5.1 Parameters measured

The first parameter we measured was resolution, which is limited by the output signal to noise ration.

$$SNR_{Nyquist} = SNR_{Measured} - 10 \cdot \log_{10} \left(\frac{N}{2} \right) \quad (2)$$

$$SNR_{1kHz} = SNR_{Nyquist} + 10 \cdot \log_{10} \left(\frac{\frac{f_s}{2}}{1kHz} \right) \quad (3)$$

For representative results we use conditions mentioned in Figure 6 (i.e. $f_s=16.275\text{MHz}$, number of samples $N=4048$, measured $SNR_{1kHz}=83.22\text{dB}$ and input RF signal $f_{RF}=200.000\text{MHz}$). Considering the non-coherent nature of noise and supposing that beam's actual position is in the center the following equation applies:

$$dx = \frac{K}{2 \cdot \sqrt{SNR}} \quad (4)$$

The calculated value for resolution is $0.207\mu\text{m}$. Figure 7 shows measured SNR as a function of input signal. The solid line is the expected SNR at the same conditions.

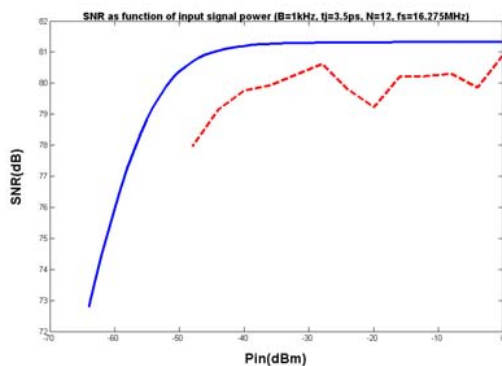


Figure 7: Measured and expected SNR function of input signal power. The dotted line is the measured SNR at the output of the ADC. The solid line represents the calculated SNR where $t_j=3.5\text{ps}$, a 12bit ADC, and

$f_s=16.275\text{MHz}$ were used. Note that the sampling frequency differs from that in Figure 2, which gives lower process gain and SNR respectively.

The second parameter we measured is the system nonlinearity. As it can be seen in the Figure 7 the measured SFDR is -40dBc . By using equation described in chapter 4 and assuming that $5\mu\text{m}$ of error is permitted we can calculate that no more than 0.01dB of gain drop should be achieved. Intermodulation products and the SFDR parameter were estimated by calculating the common P_{IP3} . Two signals, which differ 1kHz in frequency and 10dB in amplitude, would give -40dBc of SFDR.

6 CONCLUSIONS

In this article we examined the requirements, critical parameters, and measurements for direct RF sampling. The RF front-end mainly determines signal to noise ration and linearity. Consequently we should make efforts on this part of the digital receiver. The results show that direct RF sampling offers good performance from the signal to noise and from the SFDR point of view. We can conclude that carefully designed direct RF sampling receiver would yield sub-micrometer resolution of a few kHz bandwidth.

REFERENCES

- [1] U. Mavrič, "An Interface For Direct RF sampling", Thesis At Faculty For Electrical Engineering in Ljubljana, 2002
- [2] S. Bremec, DIPAC2003, Mainz, May 2003
- [3] www.i-tech.si

Dynamic X-Y Crosstalk / Aliasing Errors of Multiplexing BPMs

Till Straumann, SLAC, Menlo Park, CA 94025, USA

Abstract

Multiplexing Beam Position Monitors are widely used for their simplicity and inherent drift cancellation property. These systems successively feed the signals of (typically four) RF pickups through one single detector channel. The beam position is calculated from the demultiplexed base band signal. However, as shown below, transverse beam motion results in positional aliasing errors due to the finite multiplexing frequency. Fast vertical motion, for example, can alias into an apparent, slow horizontal position change.

INTRODUCTION

Fig. 1 shows a typical arrangement of four BPM pickup electrodes or “buttons” in the cross section of a vacuum chamber. A bunched beam of charged particles travels in z -direction, inducing RF signals to the pickups. A multiplexing BPM processing system (fig. 2) sequentially samples the buttons $A..D$ using a single receiver channel. Since only amplitude ratios are needed to determine the beam position, this approach features good drift rejection.

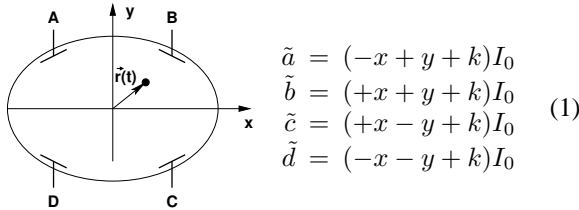


Figure 1: BPM Geometry and linear model equations

LINEAR MODEL

To the first order, the amplitudes of the pickup signals induced by a particle beam at position (x, y) can be approximated by eqns. 1 where x and y are assumed to be properly scaled according to the beam pipe geometry, and deviations from symmetry are neglected. k is a constant offset and I_0 denotes the beam current.

Note that $\tilde{a}.. \tilde{d}$ actually refer to RF signal amplitudes. However, for the purpose of this analysis, we neglect the fact that a practical system (fig. 2) multiplexes RF signals into a single receiver/detector. We simply assume the presence of four identical detectors upstream of the multiplexer such that the entire analysis can be performed in base-band.

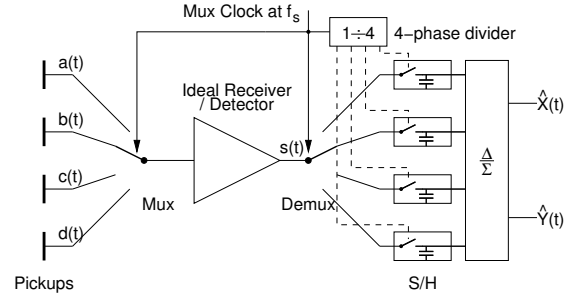


Figure 2: Multiplexing BPM system block diagram. All signals are in baseband, normalized to the beam current.

The beam position can be determined from the normalized button signals $a..d = \tilde{a}/I_0.. \tilde{d}/I_0$:

$$\begin{aligned} \tilde{I}_0 &= (+\tilde{a} + \tilde{b} + \tilde{c} + \tilde{d})/4 \\ \hat{x} &= (-a + b + c - d)/4 \\ \hat{y} &= (+a + b - c - d)/4 \end{aligned}$$

We use a “^” accent to distinguish the system response from the “true” beam position.

DYNAMIC SYSTEM BEHAVIOR

Let’s now investigate the dynamic behavior of the multiplexed BPM system running at a multiplexing clock frequency of f_s , i.e. each button gets measured at a rate of $f_s/4$. Beam motion can be described by a time dependent vector in the x, y plane.

$$\vec{r}(t) = \{x(t), y(t)\}$$

For further analysis, we assume the motion to be band-limited to $\pm f_s/2$.

Multiplexer Analysis

The time-multiplexed signal $s(t)$ consists of a stream of “excerpts” of the individual pickup signals $a(t)..d(t)$. We introduce the abbreviated notion:

$$s^\square(t) = \{a, b, c, d\} = \begin{cases} a(t) & 0 \leq t < T_s \\ b(t) & T_s \leq t < 2T_s \\ c(t) & 2T_s \leq t < 3T_s \\ d(t) & 3T_s \leq t < 4T_s \end{cases}$$

Besides sampling the pickups in a “(counter) clockwise” (a, b, c, d) fashion, there exists the possibility of scanning them in the “butterfly” sequence $s^\bowtie(t) = \{a, c, b, d\}$. (Due

to symmetry, all other possible schemes are equivalent with either of the two basic ones.)

Introducing our linear model (eqns. 1)¹, we obtain

$$\begin{aligned} s^\square(t) &= \begin{Bmatrix} -x & +x & +x & -x \\ +y & +y & -y & -y \\ +k & +k & +k & +k \end{Bmatrix} \\ &= \begin{matrix} x(t) \{-1, +1, +1, -1\} \\ + y(t) \{+1, +1, -1, -1\} \\ + k \{+1, +1, +1, +1\} \end{matrix} \end{aligned} \quad (2)$$

By rearranging the piecewise continuous function $s^\square(t)$ we could decompose it into three terms, each a product of a continuous, position/time dependent function with a simple discontinuous “rectangular wave” function. In the same way, $s^\boxtimes(t)$ can be stated:

$$\begin{aligned} s^\boxtimes(t) &= \begin{matrix} x(t) \{-1, +1, +1, -1\} \\ + y(t) \{+1, -1, +1, -1\} \\ + k \{+1, +1, +1, +1\} \end{matrix} \end{aligned} \quad (3)$$

The multiplexer can be seen as a *modulator*: x and y are modulated onto two (“rectangular wave”) quadrature carriers at $f_s/4$ (“clockwise” multiplexing). The constant offset (“ k ”) term remains at base-band. The “butterfly” multiplexer modulates x and y onto two carriers at $f_s/4$ and $f_s/2$, respectively. Introducing the “carrier sequences”

$$\begin{aligned} c_0(t) &= \{+1, +1, +1, +1\} \quad \text{“base band”} \\ c_1^i(t) &= \{-1, +1, +1, -1\} \quad f_s/4; \text{“I phase”} \\ c_1^q(t) &= \{+1, +1, -1, -1\} \quad f_s/4; \text{“Q phase”} \\ c_2(t) &= \{+1, -1, +1, -1\} \quad f_s/2 \end{aligned} \quad (4)$$

we rewrite eqns. 2 and 3:

$$s^\square(n) = x(t) c_1^i(t) + y(t) c_1^q(t) + k \quad (5)$$

$$s^\boxtimes(n) = x(t) c_1^i(t) + y(t) c_2(t) + k \quad (6)$$

The “carriers” defined by eqns. 4 have the properties

$$\begin{aligned} c_i(t) * c_i(t) &= c_0(t) & c_1^i(t) * c_1^q(t) &= -c_2(t) \\ c_0(t) * c_i(t) &= c_i(t) & c_1^i(t) * c_2(t) &= -c_1^q(t) \\ & & c_1^q(t) * c_2(t) &= -c_1^i(t) \end{aligned} \quad (7)$$

Frequency Domain To facilitate analysis in frequency domain, we already account for the downstream sample and hold processing and calculate the z -transform of $s^\square(nT_s)$ sampled at integer multiples of the multiplexer clock period:

$$\begin{aligned} s^\square(nT_s) &= x(nT_s) (\sin(n\frac{\pi}{2}) - \cos(n\frac{\pi}{2})) \\ &+ y(nT_s) (\sin(n\frac{\pi}{2}) + \cos(n\frac{\pi}{2})) \\ &+ k \end{aligned} \quad (8)$$

For the sequences $c_1^i(nT_s)$ and $c_1^q(nT_s)$, adequate representations involving trigonometric functions were chosen:

$$\begin{aligned} c_1^i(nT_s) &= \sin(n\frac{\pi}{2}) - \cos(n\frac{\pi}{2}) = -\sqrt{\frac{j}{2}} j^n + \sqrt{\frac{-j}{2}} j^{-n} \\ c_1^q(nT_s) &= \sin(n\frac{\pi}{2}) + \cos(n\frac{\pi}{2}) = -\sqrt{\frac{-j}{2}} j^n + \sqrt{\frac{j}{2}} j^{-n} \\ c_2(nT_s) &= \cos(n\pi) = (-1)^n \end{aligned} \quad (9)$$

¹The respective sums are written vertically into four columns corresponding to the four “time slots”

Using the correspondences [1]

$$\begin{aligned} f(nT_s) &\Leftrightarrow F(z) \\ f(nT_s) q^n &\Leftrightarrow F(z/q) \end{aligned} \quad (10)$$

the z -transform of eq. 8 becomes (we use lower case symbols for time domain and upper case symbols for z or frequency domain dependent variables)

$$\begin{aligned} S^\square(z) &= -\sqrt{\frac{j}{2}} X(z e^{-j\frac{\pi}{2}}) + \sqrt{\frac{-j}{2}} X(z e^{j\frac{\pi}{2}}) \\ &- \sqrt{\frac{-j}{2}} Y(z e^{-j\frac{\pi}{2}}) + \sqrt{\frac{j}{2}} Y(z e^{j\frac{\pi}{2}}) + \frac{k}{1-z^{-1}} \end{aligned}$$

In frequency domain, the spectra $X(f)$ and $Y(f)$ (which, according to our assumption are band limited to $\pm f_s/2$), appear shifted by an amount of $\pm f_s/4$ since

$$z e^{\mp j\frac{\pi}{2}} \Big|_f = e^{j\frac{2\pi}{T_s} f} e^{\mp j\frac{\pi}{2}} = e^{j\frac{2\pi}{T_s} (f \mp \frac{f_s}{4})} = z \Big|_{f \mp \frac{f_s}{4}}$$

Again, the “mixing” behavior of the multiplexer becomes apparent: The time multiplexed signal $s(t)$ can be seen as a *frequency multiplexed* representation of the position information $\{x, y\}$ where $X(f)$ and $Y(f)$ occupy different “slots” in frequency domain. In case of the “clockwise” sampling scheme, X and Y are in fact centered around the same frequency, $\pm f_s/4$, but the complex spectra are in quadrature. The Y contribution to the “butterfly” signal $S^\boxtimes(f)$ appears shifted by $f_s/2$ as can easily be seen by performing the z -transform with the representation $c_2(nT_s) = \cos(n\pi)$ according to eq. 9.

Fig. 3 sketches the X and Y spectral contributions to the multiplexed signal for “clockwise” (left) and “butterfly” (right) sampling. In the former case, X and Y appear both centered around $\pm \frac{f_s}{4}$ but with different symmetry properties with respect to the origin²; in the latter case, Y is shifted by $\pm \frac{f_s}{2}$ and its spectral density is doubled due to overlapping. The singular contribution of the constant term k is not shown.

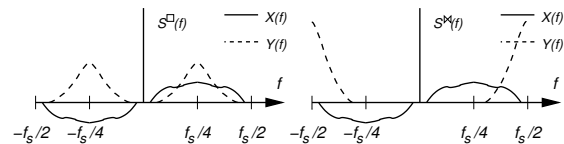


Figure 3: Multiplexed signal spectra (limited to the first Nyquist zone); “clockwise” (left) and “butterfly” (right) schemes.

Demultiplexer

The demux subsystem of fig. 2 shall be transformed into an equivalent structure which is easier to understand. Fig. 4 shows the demultiplexer and the difference network for the x channel. We begin with moving the negative coefficients

²In reality, the spectra are of course *complex* and the schematical “even”/“odd” symmetries merely should symbolize the fact that the carrier phase affects the shifted spectra’s phase response such that the “composite” spectrum S still can be decomposed into X and Y contributions.

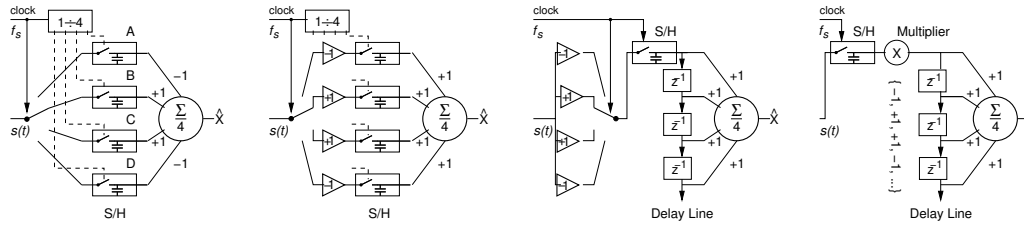


Figure 4: Transformation of the demultiplexer into an equivalent structure

upstream of the S/H circuits. This eliminates the need for “remembering” if a given S/H output has to be fed into a – or + input because the sign has already been accounted for. The “old” samples can then simply be passed along a delay line which is fed by a single S/H running at the full multiplexer frequency f_s . Finally, – as we already know, – the multiplexer tapping off the weighted input signal can be replaced by a modulator.

Hence, the demultiplexer in combination with the difference network works as a *demodulator* translating the desired component of the composite signal $s(t)$ back to base-band. The demodulator output signals (for the moment, we neglect the averaging effect due to the delay line which is discussed below) of a “clockwise” and “butterfly” BPM are (multiplying eqns. 5 and 6 by the appropriate “carrier” and using eq. 7)

$$\begin{aligned} \hat{x}^\square &= c_1^i (x c_1^i + y c_1^q + k) = x - y c_2 + k c_1^i \\ \hat{y}^\square &= c_1^q (x c_1^i + y c_1^q + k) = y - x c_2 + k c_1^q \\ \hat{x}^\bowtie &= c_1^i (x c_1^i + y c_2 + k) = x - y c_1^q + k c_1^i \\ \hat{y}^\bowtie &= c_2 (x c_1^i + y c_2 + k) = y - x c_1^q + k c_2 \end{aligned} \quad (11)$$

The fact that the difference network actually accumulates a “history” of four samples also becomes obvious in the transformed structure. The averaged delay line shows the typical fourth order CIC behavior ($\frac{1-z^{-4}}{1-z^{-1}}$) [2].

DISCUSSION

Eqns. 11 can be transformed to z -domain yielding e.g. for the first line (including the delay line filtering effect):

$$\begin{aligned} \hat{X}^\square(z) &= (X(z) + X_Y^\square(z) + k C_1^i(z)) H(z) \\ X_Y^\square(z) &= -Y(z e^{j\pi}) = -Y(-z) \\ C_1^i(z) &= (1 + j z^{-1}) / (1 + z^{-2}) \\ H(z) &= (1 - z^{-4}) / (1 - z^{-1}) \end{aligned} \quad (12)$$

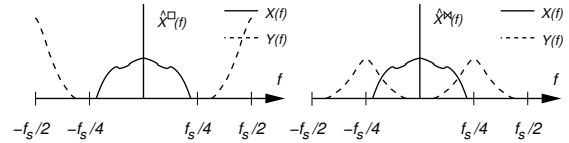
In addition to the desired “ X ” position information, the system response contains a “crosstalk” or “alias” contribution X_Y . The constant offset k introduces a “carrier feedthrough” (as can be seen from eqns. 11 – $C_1^i(z)$ does not converge for $|z| = 1$). The “filter” response, $H(z)$, a consequence of the delay line, features zeroes at $\frac{f_s}{4}$ and $\frac{f_s}{2}$ thus effectively notching the k contribution.

Evaluating z at real frequencies, the crosstalk term becomes

$$X_Y^\square(f) = -Y(e^{j2\pi f T_s} e^{-j2\pi \frac{f_s}{2} T_s}) = -Y(f - f_s/2)$$

i.e. the Y channel feeds into \hat{X}^\square but shifted by $\frac{f_s}{2}$. This means that e.g. a purely sinusoidal vertical beam motion $y(t) = y_0 \sin(\frac{\omega_s}{2} t)$ appears at the output \hat{x} as a steady state error $\hat{x}(t) = y_0$. The analogous crosstalk contributions to \hat{Y}^\square , \hat{X}^\bowtie and \hat{Y}^\bowtie are

$$\begin{aligned} Y_X^\square(f) &= -X(f - \frac{f_s}{2}) \\ X_Y^\bowtie(f) &= \sqrt{\frac{-j}{2}} Y(f - \frac{f_s}{4}) - \sqrt{\frac{j}{2}} Y(f + \frac{f_s}{4}) \\ Y_X^\bowtie(f) &= \sqrt{\frac{-j}{2}} X(f - \frac{f_s}{4}) - \sqrt{\frac{j}{2}} X(f + \frac{f_s}{4}) \end{aligned}$$


 Figure 5: System frequency response (limited to the first Nyquist zone) showing y - x crosstalk for the “clockwise” (left) and “butterfly” (right) schemes.

Note that although from looking at fig. 3 the “butterfly” multiplexing scheme might seem favorable because the X and Y contributions are farther separated in S^\bowtie than they are in S^\square , the opposite is actually true: as illustrated by fig. 5, the demultiplexing process shifts the spectral contributions X and Y in different directions and whereas X_Y^\square ends up centered around $\frac{f_s}{2}$, X_Y^\bowtie is only separated by $\frac{f_s}{4}$ from the desired X at base band, effectively reducing the useful system bandwidth by a factor of two.

CONCLUSION

Multiplexing BPM processors suffer from x - y crosstalk in addition to “normal” aliasing³ as a consequence of a finite multiplexing rate. The crosstalk signal is shifted in frequency by an amount determined by the clock rate, the pickup geometry and scanning sequence.

REFERENCES

- [1] R. Unbehauen, “Systemtheorie”, Oldenbourg, Wien, 1993.
- [2] W. Hess, “Digitale Filter”, B.G. Teubner, Stuttgart, 1989.

³Although we assumed the motion to be band limited, in a real system the necessary filtering upstream of the RF detector is unrealizable. The multiplexed signal s^\square could be filtered with a *band pass* around $\frac{f_s}{4}$ to eliminate crosstalk errors. Aliases from spectral components beyond the first Nyquist zone still constitute a problem, however.

CAVITY BEAM POSITION MONITOR FOR THE TESLA ENERGY SPECTROMETER

A.Liapine, TU-Berlin, Germany

Abstract

In order to measure the beam position with a precision of better than $1\mu\text{m}$ in the TESLA energy spectrometer a cavity beam position monitor is proposed. A slotted cavity with a waveguide coupling is used to achieve a good common mode rejection and therefore a better precision. The paper gives a short overview of the monitor functionality and describes resolution measurements which were made on a 1.5GHz cavity prototype with homodyne electronics. The estimation based on this measurements shows about 100nm of spatial resolution.

INTRODUCTION

A magnetic chicane spectrometer is foreseen for the beam energy measurements in TESLA (TeV Energy Superconducting Linear Collider) (Fig.1) [1]. This type of spectrometer realizes a simple principle - the beam is deflected from its original direction by a magnet and the deflection angle is determined measuring the beam position in a few points after the magnet. Mapping the magnetic field with high accuracy one can obtain the average beam energy as:

$$E_{beam} = \frac{ec \int B dl}{\theta} \quad (1)$$

The problem is that the beam energy at the end of the linac is so high that the deflection angle is small and can not be increased because the synchrotron radiation rises drastically. Therefore the beam position has to be measured with a very high precision, a few 100nm , in order to get the demanded accuracy of a few 10^{-5} .

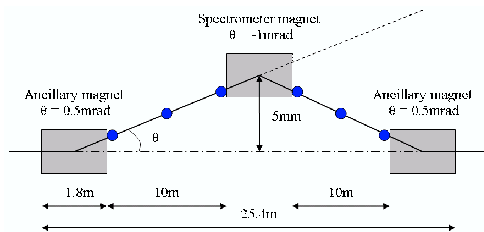


Figure 1: The foreseen spectrometer layout

SLOTTED CAVITY BPM

A slotted cavity beam position monitor (BPM) was proposed for the application in the spectrometer [2]. The goal of the slotted cavity structure (Fig.2,4) is a strong rejection of the first monopole modes [3], which deliver strong noise signals at the frequencies close to the frequency of the dipole mode of the cavity (Fig.3).

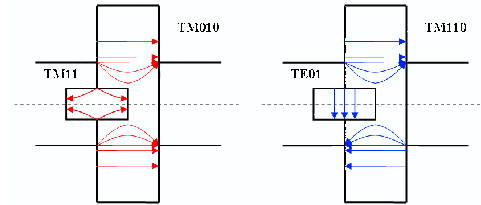


Figure 2: Mode selection in a slotted cavity

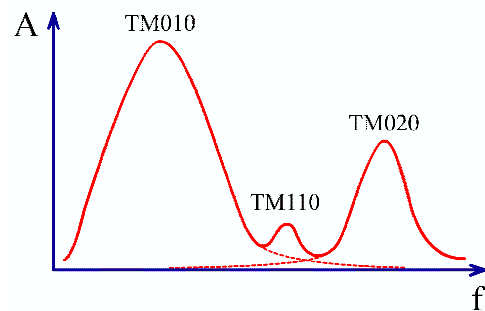


Figure 3: The influence of the monopole modes

A prototype of the slotted cavity for the laboratory measurements was designed and built for the frequency of 1.5GHz (Fig.4, 5). Results of the estimations and simulations done for the prototype are listed in the Table 1.



Figure 4: Cavity prototype inside

The resonance frequency of the common mode is 1.0GHz . The common mode is practically uncoupled that is why the cavity was made from stainless steel in order to make the quality factor of the common mode smaller.

The common mode voltage V_{in} excited in the cavity is about 130dB higher as the voltage of the dipole mode. At the cavity output this difference is already at 45dB because

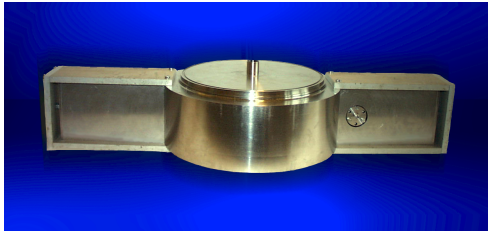


Figure 5: Cavity prototype with coupling waveguides

Table 1: Parameters of the prototype

Parameter	TM010	TM110
f, MHz	1010	1518
Q_0	2110	1680
Q_{ext}	$\rightarrow \infty$	820
$\frac{R}{Q}, Ohm$	144	$2 \cdot 10^{-5}/100nm$
BW, MHz	0.5	2.8
Decay time, ns	662	115
$V_{in}, V/3.2nC$	1450	$4 \cdot 10^{-4}/100nm$
$V_{out}, mV/3.2nC$	9.3/100 μm of slot shift (5 μV at f_{110})	0.056/100nm of beam offset
V_{angle}/V_{offset}	—	34
$V_{noise}, \mu V$	—	1.6

of the mode selective coupling. The part of the common mode which lies at the frequency of the dipole mode resonance is than 10 times weaker as the dipole mode signal of 100nm offset because of the frequency discrimination. The rest of the common mode signal is suppressed in the output waveguides with a higher cutoff frequency and filtered out in the electronics, so that it does not affect the measurement. The same happens with the second monopole mode except the suppression in the waveguides, but it is weaker excited.

SIGNAL PROCESSING

Signal processing electronics is based on the homodyne principle. The dipole mode signal is mixed down using a reference signal with nearly the same frequency coming from an additional reference cavity (Fig.6). This signal is also used for the charge measurement which is needed in order to exclude the charge dependence of the dipole mode signal.

The advantage of the homodyne principle (also called direct conversion) is simplification of the electronics because it contains only one conversion stage and the output signal frequency is very low, so that no expensive analog-to-digital converters (ADCs) are needed. Another point - this electronics consists of only a few components. This means that a low self-noise of the electronics is achievable.

A prototype electronics was constructed and tested (Fig.7). The tests show the upper limit of the input signal

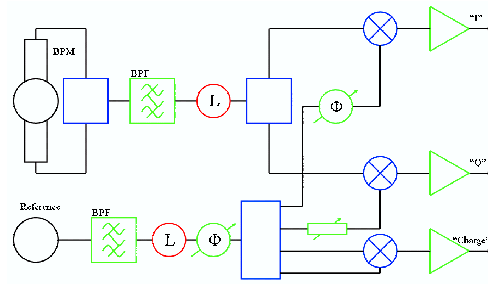


Figure 6: Electronics scheme

to be 0dB. This limit is extendable to at least 15dB by a modification of amplifiers. This gives together with a noise floor of about 80dB a very wide dynamic range, which is enough to cover the the range of -1..+1mm of the offset.

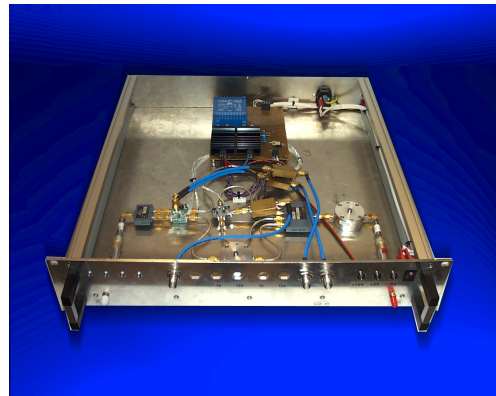


Figure 7: Prototype electronics

This type of the electronics can be also used for the suppression of the angle-dependent component of the dipole mode. The angle-dependent component is excited if a bunch passes through the cavity with some slope to the z-axis (Fig.8) and can essentially reduce the resolution. Provided the frequency of the reference signal and of the monitor are exactly the same it is possible to split angle- and position-dependent components with I/Q-mixer because of their 90° difference in phase. Unfortunately up to now it is not clear how to make a stable reference signal with exactly the same frequency. Therefore a simple tilt of the cavity is preserved as a solution of this problem.

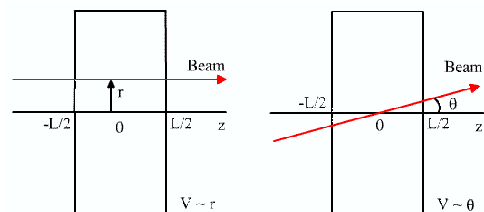


Figure 8: Dipole mode excitation

MEASUREMENTS

Cavity and electronics tests were made with a measurement setup consisting of a voltage controlled oscillator, an antenna for the cavity excitation, precision movers, a powermeter, ADCs and a control software written with LabVIEW. The cavity is excited with the antenna driven by the voltage controlled oscillator. The frequency of the excited signal and the antenna position are controlled by software.

The cavity response at the dipole mode frequency is measured with the powermeter while the antenna is moved. The response characteristic was at first measured without electronics in the range from -1mm to $+1\text{mm}$ in order to check the resolution of the monitor itself (Fig.9). A linear fit was applied in order to find the r.m.s resolution. The measured value scaled to the nominal bunch charge is $\sigma = 400\text{nm}$. But it includes the curvature of the measured characteristic around zero which causes an additional non-linearity (Fig.10). The nature of this feature is not completely clear. It can be caused by self-noise of the powermeter but it can also be caused by a dipole mode resonance slide while the antenna is moving.

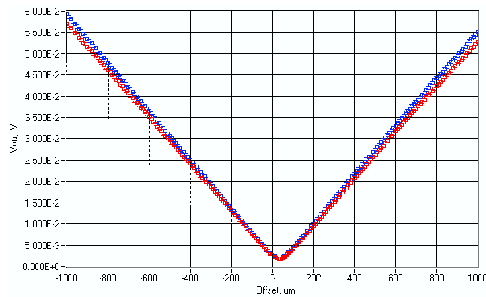


Figure 9: Cavity response for the two outputs. R.m.s resolution is $\sigma = 400\text{nm}$

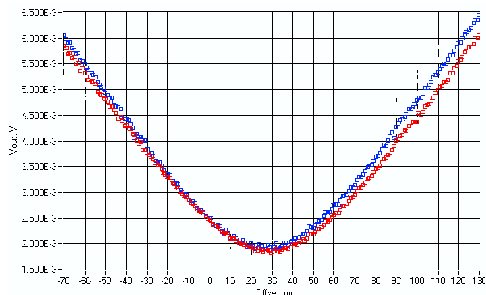


Figure 10: Cavity response around zero offset. R.m.s. resolution is $\sigma = 60\text{nm}$

Tests with the signal processing electronics show better results. The r.m.s. of the fit is still about 400nm (Fig.11) but the signal is linear around zero and the r.m.s. resolution around zero (Fig.12) is around 40nm .

The measured common mode rejection well coincides the estimation and is about 100dB .

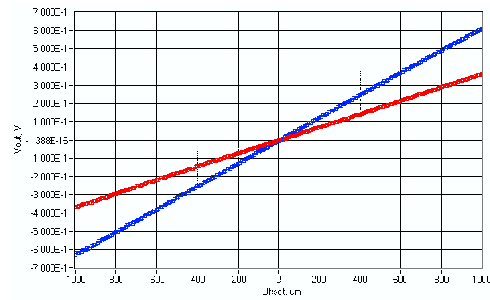


Figure 11: Cavity response measured with electronics. Resolution $\sigma = 400\text{nm}$. Red curve represents the "I"-channel and the blue one the "Q"-channel

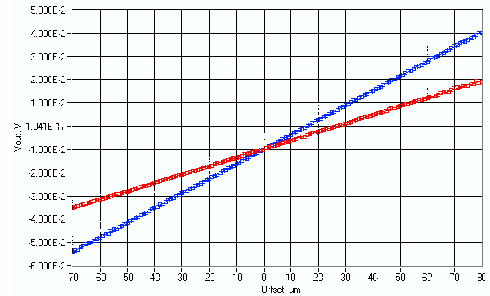


Figure 12: Cavity response measured with electronics around zero. Resolution $\sigma = 40\text{nm}$

CONCLUSION

A prototype of the high precision slotted cavity beam position monitor for the TESLA energy spectrometer was designed, tested and precision measurements were made with the prototype and a homodyne type down-conversion electronics. Precision measurements show a resolution about 100nm . Further work will be concentrated on a smaller 5.5GHz prototype which should have a lower angle-dependent component excitation.

ACKNOWLEDGEMENTS

The author would like to thank H.Henke, H.J.Schreiber and V.Sargsyan for helpful advices and precise questions and H.Thom and J.Krueger for helping to construct the prototype.

REFERENCES

- [1] TESLA Technical Design Report Part IV pp. 143-144, DESY, March 2001.
- [2] A. Liapine, "Beam Position Monitor for the TESLA Energy Spectrometer", EPAC2002, Paris, June 2002.
- [3] W.Schnell, "Common-mode rejection in resonant microwave position monitors for linear colliders", CERN-LEP-RF/88-41 CLIC Note 70, 1988.

THE LHC ORBIT AND TRAJECTORY SYSTEM

E. Calvo*, C. Boccard, D. Cocq, L. Jensen, R. Jones, J.J. Savioz, CERN, Geneva, Switzerland
D. Bishop, G. Waters, TRIUMF, Vancouver, Canada

Abstract

This paper describes the definitive acquisition system selected for the measurement of the closed orbit and trajectory in the CERN-LHC and its transfer lines. The system is based on a Wide Band Time Normaliser (WBTN) followed by a 10-bit ADC and a Digital Acquisition Board (DAB), the latter developed by TRIUMF, Canada. The complete chain works at 40MHz, so allowing the position of each bunch to be measured individually. In order to avoid radiation problems with the electronics in the LHC tunnel, all the digital systems will be kept on the surface and linked to the analogue front-ends via a single mode fibre-optic connection. Slow control via a WorldFIP field bus will be used in the tunnel for setting the various operational modes of the system and will also be used to check power supply statuses. As well as describing the hardware involved, some results will be shown from a complete prototype system installed on four pick-ups in the CERN-SPS using the full LHC topology.

INTRODUCTION

The installation of the cabling structure and magnets in the LHC tunnel and its transfer lines started a few months ago in order to be ready for the commissioning in 2007. The complete Orbit and Trajectory system design is already definitive. The BPM sensors and electronics have been tested on the SPS, and the series production has started or will start by the end of the year for most equipment. This paper will review the chain of equipment involved in this system: from the beam sensors to the acquisition and processing units. The results of the tests in the SPS during 2002 will be also presented.

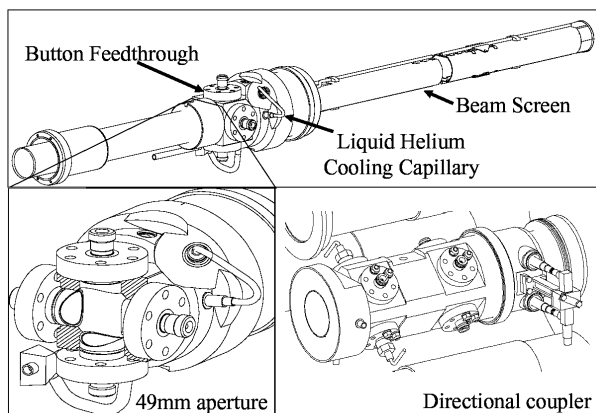


Figure 1. a) BPM body used in the LHC arcs. b) Zoom of the electrodes. c) Directional coupler used near the interaction points.

* eva.calvo.giraldo@cern.ch

COMPLETE SYSTEM LAYOUT

In the short straight sections of the LHC ring there is one BPM monitors per ring, per quadrupole. They are connected through a cryogenic coaxial cable to the outside of the cryostat and then to an electronic chassis, placed on the floor under the quadrupole. Each chassis contains a power supply card, 4 Wide Band Time Normaliser (WBTN) cards, an intensity measurement card and a control-communication card. The different working modes of the chassis are set and monitored through the control card, which receives and sends information via a WorldFIP field bus. The measured position (or the intensity) of the beam is sent to the surface through a single mode optical fibre at 1310 nm. At each of the 8 access points, there are two racks, one per half octant. Inside each, there are 4 VME chassis, with a CPU, a TTC timing receiver card, and up to 18 Digital Acquisition Boards (DAB). Each DAB is able to handle the data from two measured planes. The calculated orbits are sent at 10 Hz through an Ethernet link up to a central processor, which calculates and sends any corrections to the orbit correctors and to the control room. Figure 2 shows the explained scheme.

BEAM SENSORS

The sensors used to measure the position of the beam in the LHC are going to consist mainly of a BPM body with 4 button electrodes (about 1008) placed at one end of each quadrupole, as shown in Fig.1a) and b). However, near the interaction points the two beams are going to share the same vacuum pipe, making it necessary to use directional couplers (about 24 in total) in order to discriminate with the desired resolution the position of each beam. The length of the strip-line coupler has been designed in order to provide the same shape of signal as that from the button electrodes. This is a critical requirement given the "timing working mode" of the front-end electronics. The induced signals will be transmitted to the outside of the cryostat through eight semi-rigid cryogenic 50Ω coaxial cables. All this equipment will be installed inside the cryostat (in a secondary vacuum environment) at 5-25 K, with very high radiation dose levels (up to about 1000Gy/y). Moreover, through out the lifetime of the LHC, they have to withstand being cooled down and warmed up from 5K to 300K (and vice versa) tens of times without damage or deterioration to the seals or the electrical connections, since they will be extremely difficult to access after installation. As a consequence, hard requirements on the thermal conductivity, vacuum, impedance, electrical length and radiation tolerance are imposed which make their manufacturing and testing a challenge.

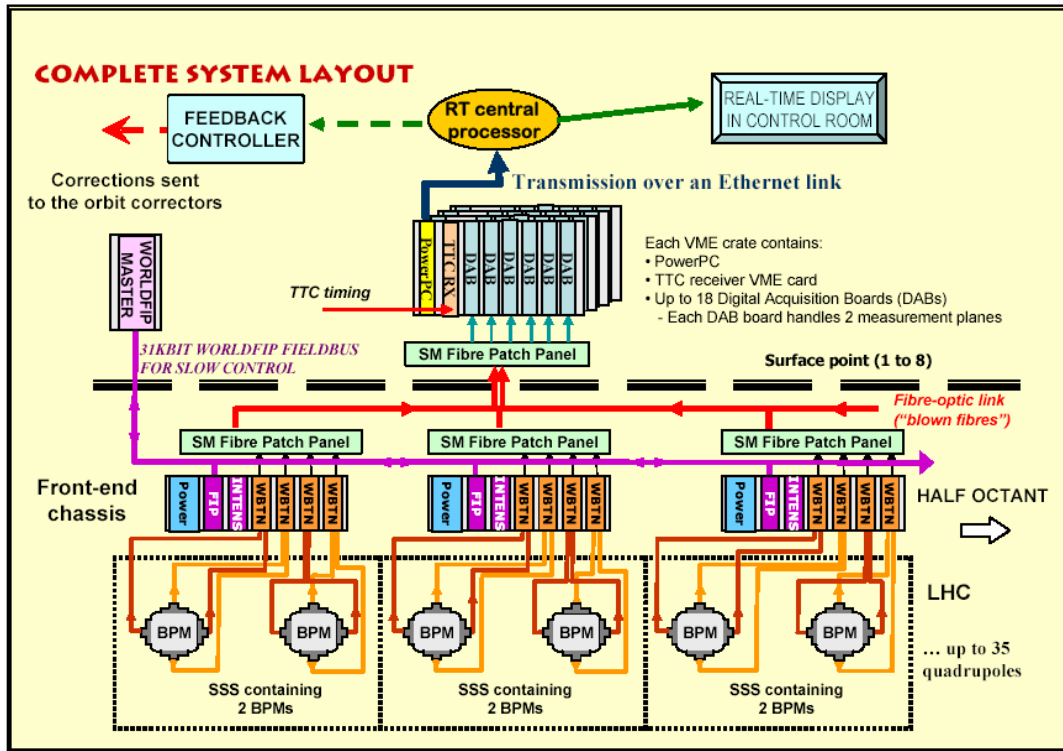


Figure 2. Layout of the LHC orbit and trajectory system.

TUNNEL ELECTRONICS

One of the main issues to take into account from the design stage of the electronics that will be placed in the LHC tunnel is the radiation tolerance they have to withstand. Doses up to 10G/y in the arc areas and up to 20G/y near the dispersion suppressor are expected [1]. Conventional electronics do not resist these levels. Because of that, the decision was taken to place all digital systems in surface buildings. Only the front-end electronics (called Wide Band Time Normaliser - WBTN) will remain under the quadrupoles, using specially designed rad-hard power supplies, a control-communication card and a fibre optic link to the surface. A beam intensity measurement card based on the same technology is also foreseen.

Front-end electronics

The WBTN uses an original method of normalizing the beam position with respect to the beam intensity. The method consists of measuring the time interval between the zero crossings of two signals which are the result of recombining the direct and delayed signals coming from opposite electrodes [2]. This method results in a system with a wide bandwidth up to about 70 MHz (able to measure the position of individual bunches) and a wide dynamic range of about 50 dB (from $1 \cdot 10^9$ to $2 \cdot 10^{11}$ p per bunch). In order to be radiation tolerant, it has been based on ECL high-frequency components which tolerate up to $5 \cdot 10^4$ Gy. Figure 3 shows the measured linearity as a function of the bunch charge.

This card also provides a sum signal which is foreseen to be used in an intensity measurement.

The power supplies are simple linear power supplies with specially designed rad-hard voltage regulators. These can be remotely monitored, and switched on/off.

Control electronics

The remote control of the chassis status is performed with a dedicated digital module. This monitors and sets the configuration of the chassis through a rad-hard anti-fuse FPGA (used extensively in space applications) and reads and sends the information through a WorldFip fieldbus at 31.25kbps. The WorldFip components have been successfully tested in radiation environments [3].

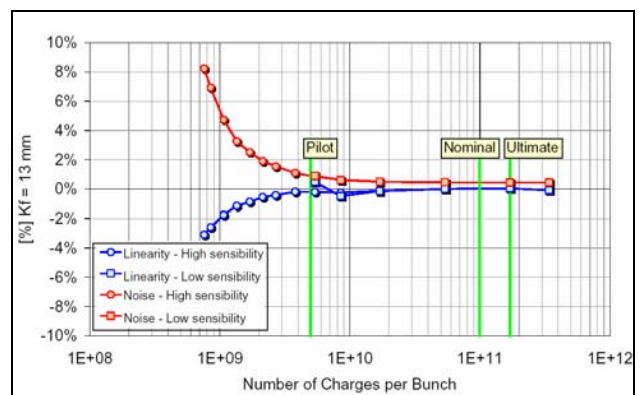


Figure 3. Linearity of the WBTN (LHC beam position front-end electronics card). Measured with a centered bunch of variable intensity.

Transmission systems

The position or intensity measurement (depending on the user request) is sent to the digital acquisition system on surface through a 1310 nm single mode optical fibre that will be blown through about 2 km of optical ducts. In both cases, the analogue data is coded in the time interval between the rising edges of two consecutive pulses (between 8.3 ns and 11.7 ns). This coding method has several advantages. The calibration of each segment in order to compensate for different lengths is not needed. Additionally the system will be less sensitive to the pulse degradation (in amplitude or rise time) due to ageing or radiation damage. A Fabry-Perot laser diode of 2 mW power and 1 GHz bandwidth will be used as the transmitter. This is the power required in order to have a jitter on reception smaller than 8 ps ($\sim 0.2\%$ of resolution), considering that the ageing and radiation will increase the fibre attenuation and decrease the power efficiency of the laser diode. The expected attenuation (based on tests) of this fibre with the radiation is smaller than 3 dB/km after 500 Gy. The decrease in power efficiency of the lasers after being irradiated has been considered negligible, smaller than a 5%.

ACQUISITION ELECTRONICS

The acquisition electronics is split in two parts:

- i) First a mezzanine card that receives the optical signal and makes the AD conversion of the position of each bunch (40MHz) at 10bits.
- ii) Secondly a Digital Board Acquisition (DAB) which takes care of the selection, sorting, pre-processing and validation of the data. The DAB has been developed by TRIUMF, in Canada. Each DAB is able to process the data from two planes of measurement (i.e. it has two mezzanines cards). It is capable of functioning in three parallel modes [4]:
 - The *Orbit Mode*: calculates the accumulated position of all bunches, of each batch (up to 12), and of 16 selectable bunches over 224 turns (~ 20 ms).
 - The *Capture Mode*: In this mode, the user can obtain the turn by turn position information of selected bunches, or the sum of the positions in a given batch or the average position of all bunches over a large number of turns.
 - The *Post Mortem Mode*: Records the last movements of the beam prior to total beam loss or a beam dump. It includes two cyclic buffers which contain the average of all bunches for the last 1000 turns and the last 1000 global orbit acquisitions.

There is also an extra working mode, called *Calibration Mode*, where the DAB is not synchronised to the 40 MHz bunch clock or to the 11 kHz revolution frequency. Instead, it uses the ADC strobe signal to trigger the acquisitions, allowing it to work independently of any machine timing. It is this mode which is used to calibrate the system using the pulses generated by a local 40 MHz oscillator on the low-level digital control card.

FUNCTIONAL TEST ON THE SPS

The LHC orbit system will be used as part of a real-time control system to stabilise both the global orbit and the local orbit at various positions in the rings. In order to explore the challenges of real-time control, it was decided to test a local orbit feedback system on the CERN-SPS. During 2002 this set-up involved equipping 4 horizontal pick-ups with the full chain of LHC acquisition electronics. Orbit measurements were performed every 100 ms, with the results transmitted to the control room, where they were displayed in real-time. The aim in 2003 will be to close the loop using a second real-time link connection to the existing orbit correctors. Figure 4 shows the display of the 4 pick-up positions throughout a complete SPS cycle, which is comprised of a 10 second injection plateau followed by acceleration from 26GeV to 450GeV. The resolution of the system was measured to be around $5\mu\text{m}$ with a reproducibility including shot to shot beam jitter of better than $20\mu\text{m}$. The linearity of the system was also tested using local orbit bumps and found to be within the estimated 5% accuracy of the position as calculated from the orbit corrector settings.



Figure 4. Control room display of the trajectory and orbit system during the 2002 tests on the SPS.

REFERENCES

- [1] C. Fynbo and G.R. Stevenson, "Compendium of annual doses on the LHC arcs", LHC Project Note 251, CERN, 2001.
- [2] D. Cocq, "The wide band normaliser – a new circuit to measure transverse bunch position in accelerators and colliders", Nuclear Instruments and Methods in Physics Research A 416 (1998) p.1-8.
- [3] J. Casas-Cubillos, et al., "SEU tests performed on the digital communication system for LHC cryogenic instrumentation", Nuclear Instruments and Methods in Physics Research A 485 (2002), p.439-443.
- [4] R. Jones, "Digital Acquisition Board for the LHC Trajectory and closed orbit system." Functional Specification. LHC-BI-ES.

CAVITY-TYPE BPMs FOR THE TESLA TEST FACILITY FREE ELECTRON LASER

H. Waldmann*, H. J. Schreiber, DESY Zeuthen, D-15738 Zeuthen, Germany

Abstract

For measurements of the beam position at the undulator section of the TESLA Test Facility (TTF) at DESY cavity-type beam position monitors were developed, installed and brought into operation. Apart from some theoretical aspects results of in-beam measurements at the TTF are presented and the pros and cons of this monitor concept are discussed.

INTRODUCTION

For a successful operation of a Free Electron Laser (FEL) [1] working in a self-amplified spontaneous emission mode an overlap between the electron beam and the photon beam over the entire length of the undulator is required. Therefore a "beam based alignment" is fundamental. This requires beam position monitors (BPMs) with a resolution of a few μm . To meet these requirements the TTF-FEL with three undulators was equipped with high-precision BPMs [2] and correction coils within the undulators. Additionally, diagnostic stations containing a cavity-type BPM and a wirescanner at the entrance, the exit and between two adjacent undulator modules [3 - 5] were installed.

PRINCIPLE

Because [6] gives a detailed theoretical background on cavity-type BPMs only a few relevant aspects are summarized as follows. A charged particle passing a cavity generates a superposition of an infinite sum of rf modes. In a circular cavity predominantly the common modes TM_{010} and TM_{020} and the less distinct dipole mode TM_{110} are excited. Fig. 1a shows a sketch of the field lines of the electrical field of the TM_{010} and TM_{110} modes, Fig. 1b the corresponding amplitudes as a function of the frequency.

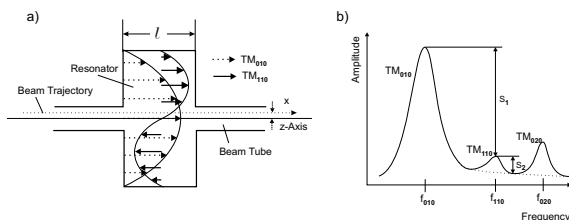


Figure 1: a) Excitation of the TM_{010} and TM_{110} -modes, b) Amplitudes of the TM_{010} , TM_{110} and TM_{020} modes as a function of frequency

Transversal beam displacement is measured using the

* waldmann@ifh.de

detection of the TM_{110} (12.025 GHz) mode. The amplitude of this mode scales with the bunch charge and the beam offset, i.e. it disappears for a centered beam. The common mode TM_{010} can be used for measuring the bunch charge. For small displacements its amplitude is nearly independent of the position.

EXPERIMENTAL SETUP

The cavity-type BPM consists of a cupreous cavity body integrated into the diagnostic station, pickup antennae, cables for the output signals and electronics for signal processing.

For the horizontal and vertical beam displacements two separate circular cavities were used. "Nose cones" close to the beam pipe were integrated to reduce interferences. Each cavity was connected to the beam pipe. In order to define horizontal and vertical directions waveguides were arranged radially in opposite directions (see Fig. 2). The microwave signals are transmitted via antennae into coaxial cables. The signals from two opposite antennae were

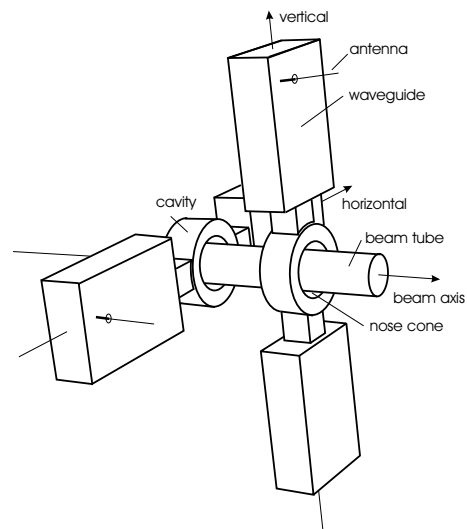


Figure 2: Sketch of the cavity BPM consisting of the beam tube, cavities with nose cones, waveguides and feedthroughs with antennae

combined in a 180° hybrid circuit. The resulting difference signal was mixed by an I-Q-mixer with a reference signal of 12.025 GHz. The resulting I (in-phase) and Q (in quadrature) were finally converted by a fast 14-bit ADC at a preselected sample time. The beam displacement can be detected using $S = \sqrt{I^2 + Q^2}$, the left-right ambiguity is resolved by the phase information $\phi = \arctan \frac{Q}{I}$.

For the beam charge measurement the sum signal, representing the common mode with a frequency of 7.5 GHz, is splitted by a direction coupler and mixed by an I-Q mixer in the same way.

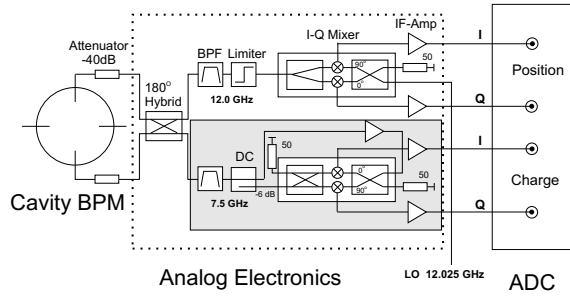


Figure 3: Layout of the electronics with the band pass filter (BPF), the direction coupler (DC), the amplifier (IF Amp), the analog-to-digital converter (ADC) and the terminal resistance (50Ω). Marked in gray is the part optionally used for charge measurements

RESULTS

Before upgrading the TTF-linac to TTF Phase II in-beam tests of the BPMs were performed. For the measurements two BPMs (before and after the first undulator) were selected (in the following denoted as 0UND1 and 0UND2).

The data taken can be divided into two types:

1. Measurements of the bunch charge detecting the TM_{010} mode at a fixed position.
2. Measurements of x- and y beam displacements for a given bunch charge.

In all measurements, the correction coil settings used for SASE operation defined the 'ideal' beam orbit. The corresponding beam position was denoted as $x=y=0$. Based on these settings beam steering was done symmetrically in horizontal and vertical directions. The data were taken in a single-bunch regime of 1 MHz. Each point represents an average of 20 bunches.

In Fig. 4 the signal representing the common mode as a function of the bunch charge for the SASE correction coil settings of monitor 0UND1 is shown. Linearity between -94 dBm until -10 dBm can be observed. These boundaries are limited by the noise power and the 1 dB-compression point, resp.

Fig. 5 shows the signals representing the dipole mode of the monitors as a function of the beam displacement of both x or y directions for both monitors and a bunch charge of 1 nC. A fairly good linearity can be derived. From these measurements the sensitivity and the resolution of the BPMs can be deduced. Table 1 summarizes the slopes of the signal voltages $dS/dx|dy$ of Fig. 5 (denoted also as sensitivity) and the deduced resolutions σ for horizontal and vertical directions.

If a beam passes the center of a cavity, the amplitude of the dipole mode will go through zero and the phase will

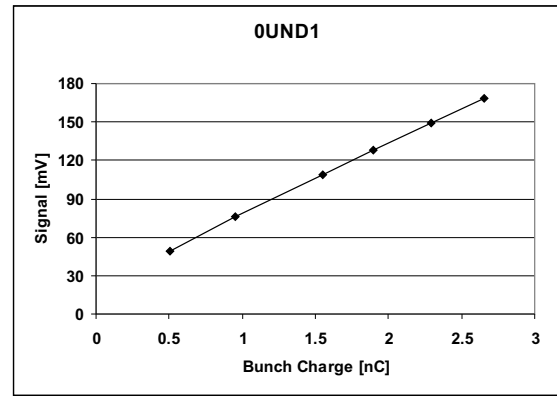


Figure 4: Signal from the Σ -port against the bunch charge. The bunch charge was measured by a toroid monitor.

shift by 180° , i.e. the measured signal will change its sign. As can be seen in Fig. 5c, just in one case (0UND2/horiz.) such a phase shift could be observed. Monitor responses at $x \approx 600$ and $800\mu m$ in Fig. 5c were reflected at the zero line. One might deduce that either the SASE setting parameters provide a significant beam off-set in the monitors or the BPMs have an a priori off-centered position due to installation misalignments. Also, residual common mode leakage of the TM_{010} mode through the band pass filter might cause an electrical zero-point shift. We expect that all effects contribute and cause substantial off-sets between the ideal beam orbit and the center of the BPMs.

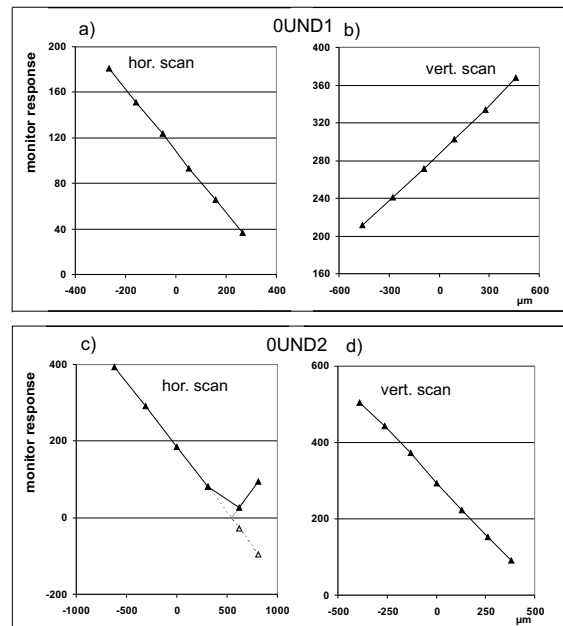


Figure 5: Horizontal and vertical scans of BPMs 0UND1 and 0UND2 for 1 nC bunch charge

	0UND1			0UND2		
	$dS/dx dy$ [mV/ μ m]	σ [μ m]	V_n [mV]	$dS/dx dy$ [mV/ μ m]	σ [μ m]	V_n [mV]
x	-0.27	3.3	0.88	-0.34	2.0	0.68
y	0.169	5.2	0.88	-0.55	1.3	0.72

Table 1: The slopes, the resolutions σ and the 1-standard deviation noise signals V_n of the monitors 0UND1 and 0UND2.

COMPARISON BETWEEN LO AND TM₁₁₀ FREQUENCY

Inevitable inaccuracies during the fabrication of the monitors cause differences of the TM₁₁₀ mode frequency between individual BPMs. We have studied consequences of this problem by calculating the behaviour of the I and Q signals in the time domain, including an I-Q mixer with an LO frequency of 12.025 GHz and, for simplicity, a zero-degree phase difference. Fig. 6 shows the calculated I and Q values as a function of time for four dipole frequencies with differences of $\Delta f = 0, 6, 12$ and 18 MHz relative to the LO frequency. We note that within the simulation the cavity response function $S(t) = \sqrt{I^2(t) + Q^2(t)}$ which involves the beam displacement (solid line) is independent on Δf and (not visible in fig. 6) on the phase difference assumed. In order to determine the maximum of Δf allowed for e.g. a resolution of 5 μ m, we rely on the I and Q time-behaviour in fig. 6 and derive $\Delta f = 6.5$ MHz for the worst case. Deviations of the design cavity radius result to TM₁₁₀ frequencies which can easily exceed this boundary. MAFIA simulations have shown that an alteration of the cavity radius of 10 μ m causes a frequency shift of 6 MHz. Consequently, fabrication of the cavity has to be done very carefully.

CONCLUSION

In order to realize the severe requirements of a "beam based alignment" in the TTF-FEL it was decided to use cavity-type BPMs within the diagnostic stations before, behind and in between the undulator modules.

Arguments in favour of this choice were

- large signals for off-centered beams enabling high position resolution,
- simple fabrication with high precision due to cylindrical geometry,
- simultaneous beam charge measurement through the common mode TM₀₁₀ signal allowing for charge-independent beam position measurements,
- strong (x,y) cross talk suppression since the two cavities are well separated in longitudinal beam direction.

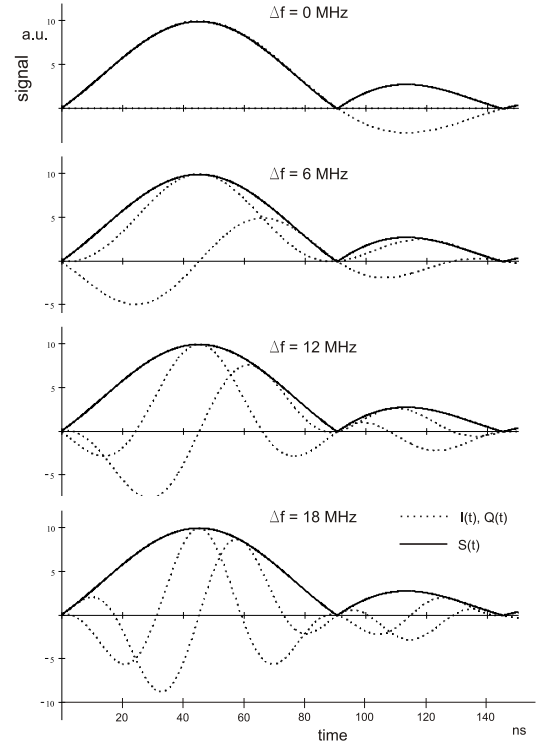


Figure 6: Simulated time variations of S, I and Q for various frequency differences between LO and the resonance frequency

Also, some disadvantages can be listed:

- a lot of care has to be taken over the fabrication of the cavities,
- for a centered beam the dipole mode, i.e. the beam displacement signal, disappears.

REFERENCES

- [1] TESLA FEL, TESLA-FEL Report 95-03, June 95
- [2] R Lorenz, T Kamps, M Wendt, DIPAC97, Frascati, Italy (1997)
- [3] R Lorenz, H Henke, T Kamps, U Hahn, M Wendt, DIPAC97, Frascati, Italy (1997)
- [4] U Hahn, J Pflüger, G Schmidt, Nucl. Instr. and Meth. A 429 (1999) 276
- [5] G Schmidt, U Hahn, M Meschkat, F Ridoutt, Nucl. Instr. and Meth. A 475 (2001) 545
- [6] R Lorenz, Cavity Beam Position Monitors, Proc. 8th Beam Instrumentation Workshop, SLAC (1998) 53

BEAM PHASE MEASUREMENT IN THE AGOR CYCLOTRON

S. Brandenburg, T.W. Nijboer, W.K. van Asselt
Kernfysisch Versneller Instituut (KVI), 9747 AA Groningen, the Netherlands

Abstract

Beam phase measurement to optimize the isochronism is an essential part of the diagnostics in multi-particle, variable energy cyclotrons. In the AGOR cyclotron an array of 13 non-intercepting beam phase pick-ups is installed. To reduce the large disturbances from the RF system the measurements are traditionally performed at the 2nd harmonic of the RF frequency. To further improve the sensitivity intensity modulation of the beam has been introduced. Measurements with the different methods are presented, demonstrating that the intensity modulation strongly improves the sensitivity of the measurement. Useful beam phase measurements can now be made for beam intensities down to 10 nA.

The AGOR facility

The AGOR cyclotron has been designed to accelerate all elements, explicitly including protons. The maximum energy per nucleon for ions is $600(Q/A)^2$ MeV, while protons can be accelerated to a maximum energy of 200 MeV. The magnetic field is produced by two sets of superconducting coils and can vary from 1.7 to 4 T. Fifteen sets of correction windings are mounted on the

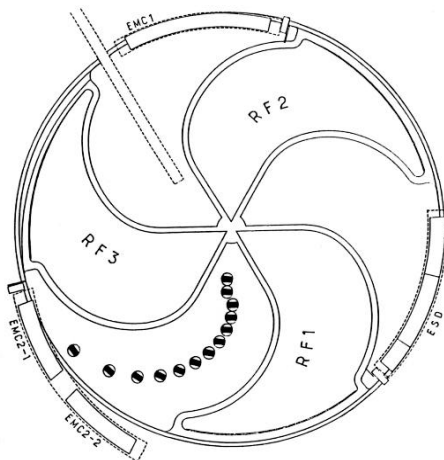


Figure 1. Cross-section through the median plane

three-fold symmetric iron hill sectors, which are located between the three RF cavities as shown in figure 1. These cavities provide the accelerating voltage for the beam and operate in the frequency range of 24 to 64 MHz, at harmonic mode 2, 3 or 4.

Extraction of the beam from the cyclotron is accomplished by successively an electrostatic channel, a room temperature electromagnetic channel, a superconducting electromagnetic channel and finally a superconducting quadrupole doublet.

Motivation for beam phase measurements

Cyclotrons operate without longitudinal phase stability, and therefore there is no automatic feedback from the RF system on the beam, like in synchrotrons. The magnetic field and thus the beam phase is affected by different mechanisms:

- Accuracy of calculated settings for different beams. For most beams the magnetic field values have to be obtained from interpolation in field maps. These are available at 20 points in the operating diagram for the main coils. This leads to inaccuracies of the reference for the magnetic field of $3\text{--}5 \cdot 10^{-4}$.
- There are tight tolerances on the isochronism of the magnetic field. For protons ($h = 2$) a maximum field error of $\Delta B/B \sim 1.5 \cdot 10^{-4}$ results in a phase slip of 90° , when acceleration stops.
- The reproducibility of the magnetic field is adversely affected by long term variations of the temperature of the magnet iron, causing changes of the saturation magnetization of 0.2 mT/K [1].
- Accumulation of phase slip can also increase vertical beam blow-up in regions with weak vertical focusing because of the increased time spent in the region.
- The precessional extraction process is very sensitive for amplitude and phase of field perturbations. This sensitivity is strongly enhanced by large phase errors. As in the non-isochronous fringe field the phase slip rapidly builds up even with optimal tuning, reproducibility of the extraction strongly depends on control of the isochronism.

Inaccuracies in the magnetic field thus directly influence the acceleration and extraction process. Therefore precise and reproducible tuning of the magnetic field is essential. Measurement of the beam phase is the tool to achieve this. The ultimate goal for such a phase measurement system is a push-button operation with only minor impact on routine operation.

Experimental hardware

In the AGOR cyclotron an array of 13 non-destructive beam phase pick-ups has been installed, see figure 1 for their location. Each probe consists of two electrodes placed symmetrically with respect to the median plane. The probes are connected to multiplexers mounted on the top and bottom of the cyclotron yoke as close as possible to the probes, while maintaining serviceability. The outputs of the multiplexers are connected to the input of the phase measurement system, outside the cyclotron vault, by means of double-shielded coaxial cables. These cables are carefully matched in length to keep phase errors to a minimum. See figure 2 for a schematic of the system. Besides beam induced signal there is also signal induced by the RF cavities. Due to the coupling of the magnetic and electric fields the signals from the RF system on the two electrodes of a probe are 180 degrees

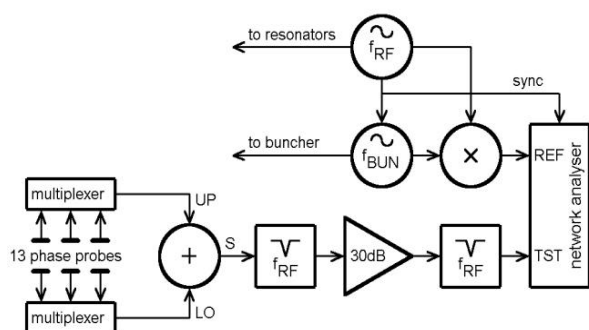


Figure 2. Schematic of phase measurement system

out of phase, while the beam signals of both electrodes are in phase. For this reason one of the first components in the phase measurement system is a power combiner, which reduces the RF components and its harmonics, while the beam induced signals are added. An attenuation of at least 20 dB on the fundamental RF frequency is obtained in this way. A further reduction of the first harmonic perturbation is still necessary in order to avoid saturation in the next components. Additional attenuation of about 30 dB is obtained with coaxial stub filters. The final stage is a wideband amplifier to better match the signal to the dynamic range of the network analyzer.

Signal processing and experimental results

In this section the different methods, which have been used to measure the beam phase, are described. In all cases the resolution bandwidth of the network analyzer is set to 300 Hz and the maximum acquisition memory (400

measurements) of the instrument is used to improve the signal-to-noise ratio further. Under these conditions a measurement takes about 15 seconds per probe, which is considered acceptable for the planned routine measurements.

Second harmonic measurement

Traditionally phase measurements are performed on the second harmonic of the RF frequency [2,3,4]. This is because the ratio of beam induced over RF induced voltages is more favourable. Because at the second harmonic still unambiguous phase can be obtained [2], measurements at even higher harmonics have not been attempted. The measurements show that in the absence of beam, there still exists a second harmonic component on the signals of the probes. This signal grows strongly with increasing frequency and limits the operational frequency range of this method[4]. The nature of this growth is not understood. Because of this perturbing signal the measurements, if at all possible, have to be done with and without beam and the beam phase is extracted by

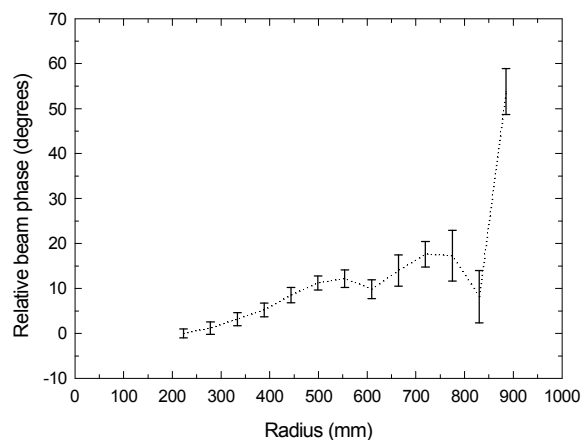


Figure 3. Phase measurement at the second harmonic of the RF frequency

vectorial subtraction. Figure 3 shows the result of such a measurement. The reference signal for the network analyzer is obtained from a frequency doubler. The data are corrected for the different azimuthal positions of the inner two probes. The cyclotron was tuned for an 8 MeV/A C^{2+} ion beam and there was significant intensity loss during the acceleration cycle because of charge exchange between the beam and the residual gas. Nevertheless, at the low RF frequency used for this beam, clean results are obtained even at outer radii where the intensity was approximately 10 nA.

Intensity modulation of the beam

By modulating the beam with a frequency slightly different from the RF frequency, beam phase information will appear in the Fourier spectra at multiples of that modulation frequency. Figure 4 shows frequency spectra obtained this way. The figure shows very strong beam induced spectral lines at multiples of the modulation frequency.

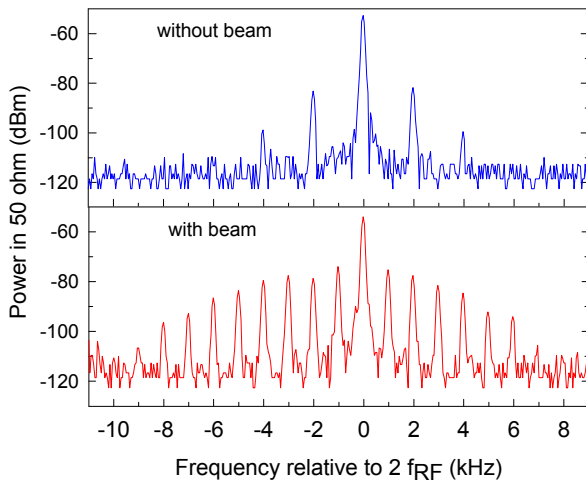


Figure 4. Probe signals with and without beam

Figure 5 shows results of measurements for two different modulation frequencies. The measured phase profiles show an additional phase slip proportional to the modulation frequency. The actual phase profile can be calculated from a set of measurements at two modulation frequencies. This result is also shown in figure 5. It shows that at the modulation frequency of 1 kHz the differences between measured and calculated profiles are rather small. The figure suggests to use even lower modulation frequencies. The resolution bandwidth of the network analyser and the measurement time limit the minimum value for the modulation frequency to about 1 kHz. By modulating the intensity with the buncher at the orbital frequency, the phase slip of the modulation changes in multiples of 2π . In this way direct phase measurements are possible. This method requires exact phase locking of the signal generators for the RF and the buncher. The frequency range of the buncher limits the applicability of this method.

Discussion

We have demonstrated that with low frequency modulation of the beam and the appropriate signal processing phase measurements over the whole frequency range of the RF system can be obtained. The method is also sensitive enough that it can be used for beam

intensities down to 10 nA. The use of a network analyzer as central part of the signal processing electronics has proven to be very advantageous for the low intensity beams.

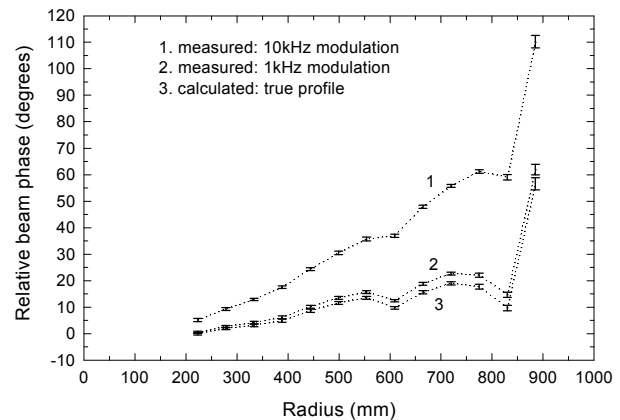


Figure 5. Phase measurements by low-frequency modulation

The status of the beam phase measurement system is that we have to implement automatic and remote control of the different components. Further we have to feedback the results of phase measurements for calculating optimal correction coil settings.

Acknowledgements

This work has been supported by the Rijks Universiteit Groningen (RuG) and by the European Union through the Large-scale Facility program LIFE under contract number ERBFMGE-CT98-0125.

It has been performed as part of the research program of the 'Stichting voor Fundamenteel Onderzoek der Materie' (FOM), with support of the Nederlandse organisatie voor Wetenschappelijk Onderzoek' (NOW).

References

- [1] L.P. Roobol et al., Proc. 15th ICCA(1998)221
- [2] W. Brautigam et al., IEEE Trans.NS.26(1979)2375
- [3] B. Launé et al., Proc.13th ICCA(1992)487
- [4] S. Brandenburg et al., Proc. 15th ICCA (1998)183

AN X-BAND CAVITY FOR A HIGH PRECISION BEAM POSITION MONITOR*

Ronald Johnson, Zenghai Li, Takashi Naito[#], Jeffrey Rifkin[†], Stephen Smith, and Vernon Smith
Stanford Linear Accelerator Center, Menlo Park, CA, USA

Abstract

The next generation of accelerators will require increasingly precise control of beam position. For example designs for the next linear collider require beam-position monitors (BPMs) with 300 nm resolution. The accelerator designs also place difficult requirements on accuracy and stability. To meet these requirements a cavity BPM operating at 11.424 GHz was designed. The BPM consists of two cavities: an xy-cavity tuned to the dipole mode and a phase cavity tuned to the monopole mode. The xy-cavity uses a novel-coupling scheme that (in principal) has zero coupling to the monopole mode. This report will present the mechanical design, simulations, and test results of a prototype BPM. In addition BPM designs with even higher precision will be discussed

INTRODUCTION

Designs for the next generation of accelerators place stringent requirements on Beam Position Monitor (BPM) systems. These requirements are driven by the need to establish and maintain precise optics to prevent emittance growth. Requirements include measurement of beam position with high precision, good accuracy, and good stability. For example the Next Linear Collider (NLC) [1] will require BPMs to have precision of 300 nm, accuracy of 200 μm , and stability of 1 μm (over 24 hours).

A preliminary design of the NLC uses over 1900 BPMs placed at each quadrupole along the (X-band) main linacs. Each of these QBPMs is rigidly attached to the quadrupole and the whole assembly is mounted on precision movers. Beam based alignment will be used to determine and adjust the centers of the magnets. But this is an invasive procedure that is not compatible with production operation. Accelerator components must remain stable over long periods.

The two usual choices for BPM pickups are striplines or cavities. The mechanical complications of striplines makes insuring good stability a problem, especially when the beam tube has an internal diameter of only about 12 mm. In addition the position signal for striplines is the difference of two large numbers. This difference must be obtained with precision analog electronics or with digital electronics with a large number of effective bits.

On the other hand cavity BPMs can be machined out of a single block of metal with tolerances of about 0.5 μm . Simple pillbox cavities can be fiducialized to the outside with errors of this order. Also when the beam is centered in the cavity the position signal is zero and signal is generated only as the beam moves off axis.

For these reasons a research project on development of a cavity BPM that could meet the NLC requirements was started. This report presents results on the prototype BPM that was designed and fabricated. An initial report [2] on this prototype has been published but construction of the BPM is now complete.

DESIGN AND FABRICATION

The main linacs of the NLC operate at X-band (11.424 GHz). Although other frequencies could be selected, the cavity BPM was designed at this frequency for two reasons. First, the QBPMs are to provide a phase reference for the low-level rf control. Second, this frequency is consistent with a compact design and well established machining techniques.

A simple cylindrical cavity was designed with a thickness that would not add significant impedance to the beam. The BPM does feature a novel design for coupling the signals out [3,4]. A rectangular waveguide at right angles to the cavity intercepts the cavity only at the corner; coupling is through the magnetic field. Only the TM_{11} mode couples to the waveguide and the monopole mode (TM_{01}) does not couple. This is illustrated in Figure 1.

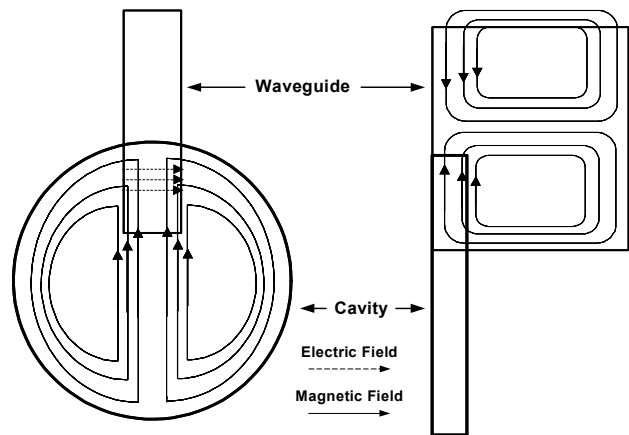


Figure 1: Coupling scheme for the cavity BPM.

Four waveguides intercept the cavity symmetrically horizontally and vertically. Signals from the vertical waveguides provide x-offsets and signals from the horizontal waveguides provide y-offsets. Extensive MAFIA simulations were performed in perfecting the design.

*Work supported by Dept. of Energy Contract DE-AC03-76F00515

[#]Permanent address: KEK, 1-1Oho, Tsukuba, Ibaraki 305-0801, JAPAN

[†]Present address: Lyncean Technologies, Inc., Palo Alto, CA, USA

Dimensions of the cavity are 29.426 mm in diameter and 3.0 mm thick. The waveguides are 18.0 mm by 3.0 mm by 30.0 mm. In addition to the xy-cavity a phase cavity was designed where the monopole mode resonates at 11.424 GHz. The cavity dimensions are 24.711 mm in diameter and 2.0 mm thick.

The body of the device is machined out of a single block of copper (OFE Class II) 43.0 mm in length, 34.0 mm in diameter, and with a 12.0 mm diameter beam tube on the axis. Copper end caps 5.0 mm thick were machined to complete the cavities. Short (16.25 mm) stainless steel beam pipes were brazed to each end of the BPM. A 3-D view of the cavity BPM without the beam pipe extensions is shown in Figure 2.

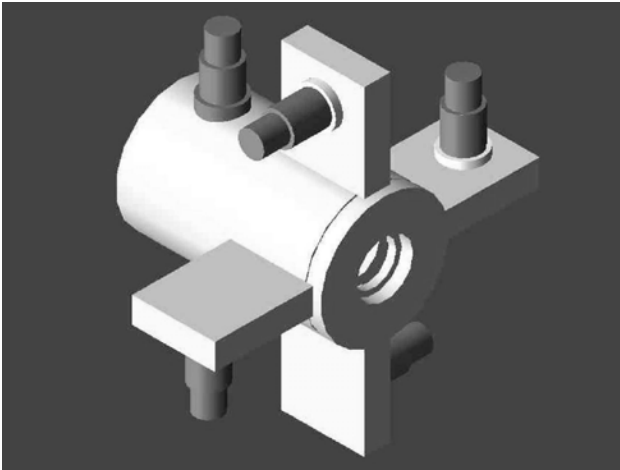


Figure 2: A 3-D view of the cavity BPM.

Waveguides are formed from two pieces of copper brazed together and brazed to the body. Electrical feedthroughs couple signals out of the waveguides serving as both a vacuum break and as pickups for converting waveguide fields to coaxial cable signals.

Tolerances for the critical dimensions of the cavity and waveguides were specified to be 1.0 μm . However the actual parts produced did not meet these tolerances. For example the diameters of the xy-cavity and phase cavity are +8 and -2 μm off their specified values. The tolerances specified are achievable and the actual parts were not bad considering that it was the first attempt.

Another problem in the construction was that following welding all the feedthroughs had vacuum leaks. It is expected that the welding heated the ceramic seals excessively. Although this BPM will not be used in a beam line, the issue must be addressed.

TEST RESULTS

In order to excite the cavity BPM a stub antenna was built. It is a small length (quarter wavelength) of the center conductor of a RG141 hard line coaxial cable. The antenna was mounted on an xy-stage. The x-stage was moved by a precision micrometer (minimum division 0.5 μm). The y-stage had much less precision (minimum division 25 μm). Measurements were made using a 20 GHz vector network analyzer.

The test setup is shown in Figure 3. The cavity BPM was mounted on a low precision xyz-stage to facilitate initial alignment.

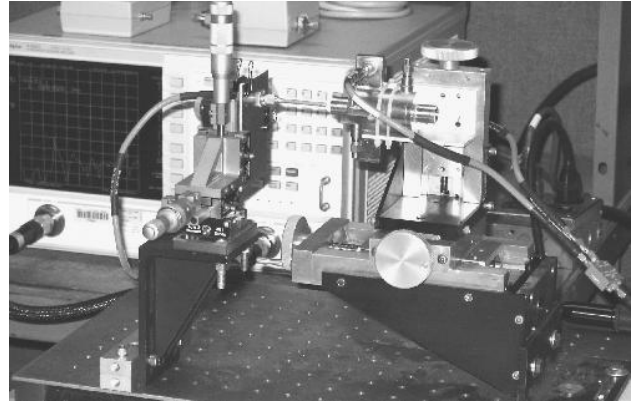


Figure 3: Cavity BPM test setup.

The frequency response (i.e. S_{21} measurements using the VNA) of the xy-cavity (top) and the phase cavity (bottom) are shown in Figure 4.

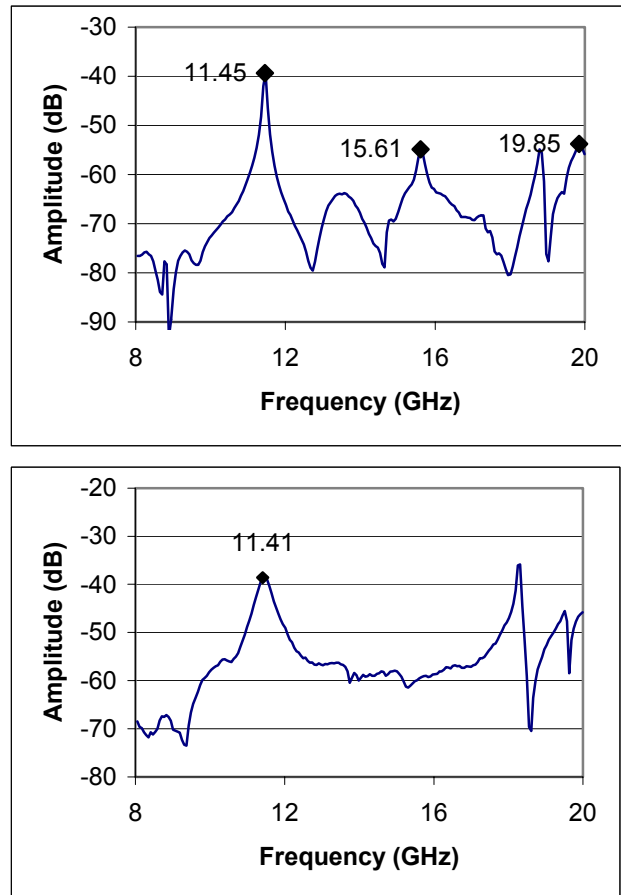


Figure 4: Frequency response of the cavity BPM.

The TM_{11} mode is at 11.45 GHz (+26 MHz off the design value). This error is not due to the error in cavity diameter. It is more likely due to lack of precision in the MAFIA calculations of the frequency shift due to the waveguides. Resonances at 15.61 GHz and 19.85 GHz are identified as the TM_{21} and TM_{31} modes. The monopole

mode for the cavity is at 8.72 GHz which is below the cutoff for the waveguides, but it was previously measured using WR75 waveguide couplers. For the phase cavity the TM_{01} mode is at 11.41 GHz (-13 MHz off the design value). Coupling from port to port was also measured using the VNA. These data are summarized in Table 1.

Table 1. Cavity BPM resonant structure.

	MAFIA	Measured			
Mode	Freq. (GHz)	Freq. (GHz)	Q	Coupling X-X (dB)	Coupling X-Y (dB)
XY Cavity					
TM_{01}	8.72	8.55	200	-66	-60
TM_{11}	11.43	11.45	590	-6.8	-25.5
TM_{21}	15.92	15.61	~90	-13.8	-13.2
TM_{31}	20.2	19.85	~80	-8.2	-29.6
Phase Cavity					
TM_{01}	11.43	11.41	~30	NA	NA

The electrical center of the cavity BPM was compared to the mechanical center by moving the antenna from one edge of the beam tube to the other. An average of the micrometer readings at the two edges determines the mechanical center. The electrical center was determined by finding the minimum of the dipole resonance. The centers differ by about 20 μm in x and in y by less than 25 μm . The y difference is an upper limit because the y micrometer has less precision.

Measurements of resolution were made only for the x motion because of the higher precision for this motion. Initial measurements using the minimum of the dipole resonance locate the center to a few microns. As the antenna passes through zero the phase also goes through zero; however, there is an arbitrary phase in the system. This can be offset by setting the phase of the VNA. Doing so puts all the position signal in the imaginary channel of the VNA. After setting the phase offset, scans of $\pm 50 \mu\text{m}$ were made. The average rms deviation from a straight line for four scans was 200 nm. It is clear that a large part of the deviation was due to the micrometer runout. Over a restricted scan of $\pm 10 \mu\text{m}$ the runout was much smaller. Four scans over this range produce an average rms resolution of 100 nm. In Figure 5 plots of the response verses position are illustrated.

CONCLUSIONS

A research program to investigate cavity BPMs has led to the successful construction of a prototype of such a BPM that would be suitable for the QBPMs of NLC. The BPM was designed for operation at 11.424 GHz and features a novel-coupling scheme that suppresses the monopole mode.

The results of tests show good suppression of the monopole mode so that there is no significant interference

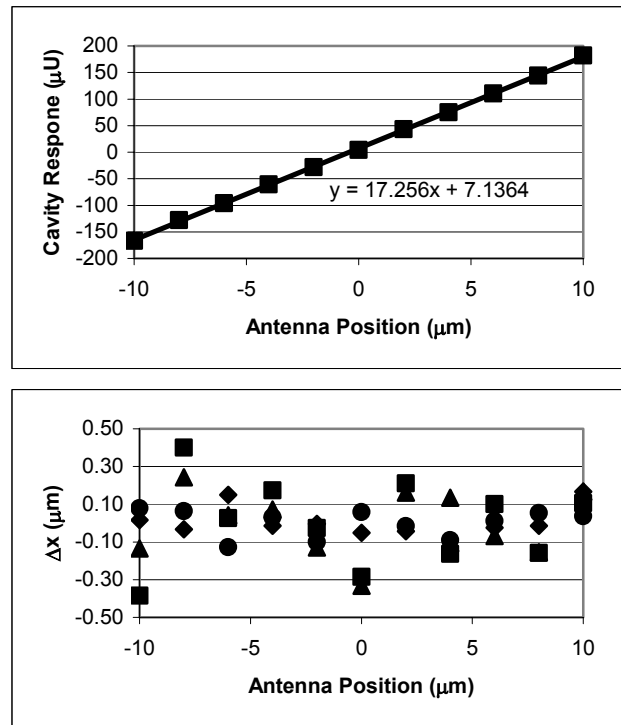


Figure 5: Top - Response of cavity BPM vs antenna position. Bottom – Difference between the calculated position and the antenna position.

with measurements of the dipole mode. The most important conclusion is that the resolution has been measured to be about 100 nm. This resolution meets the NLC requirements for the QBPMs. Of course these measurements are CW not pulsed.

Plans are being made to construct additional BPMs of this type and test them in an accelerator. The resolution that can be obtained under actual beam conditions will direct the future development of these BPMs. There is interest in producing BPMs with resolution of a few nm. For cavities of this design the signal strength can be increased by simply using a larger cavity.

REFERENCES

- [1] The NLC Design Group, T. Raubenheimer, ed., "Zeroth-Order Design Report for the Next Linear Collider," LBNL-PUB-5454, SLAC Report 474, UCRL-ID-124161, 1996.
- [2] R. Johnson, *et al.*, "Cavity BPMs for the NLC," *Proc. of the Beam Instrumentation Workshop 2002*, ed. G. Smith and T. Russo, Upton, NY, 2002, pp. 321-328.
- [3] T. Slaton, *et al.*, "Development of Nanometer Resolution C-Band Radio Frequency Beam Position Monitors in the Final Focus Test Beam," *Proc. Of the XIX International Linac Conference*, Chicago, 1998, pp. 911-913.
- [4] V. Balakin, *et al.*, "Experimental Results from a Microwave Cavity Beam Position Monitor," *Proc. Of the 1999 Particle Accelerator Conference*, New York, 1999, pp. 461-464.

DESIGN OF BPM PU FOR LOW-BETA PROTON BEAM USING MAGIC CODE

S. J. Park, J. H. Park, Y. S. Bae, W. H. Hwang, J. Y. Huang, and S. H. Nam,
Pohang Accelerator Laboratory, POSTECH, Pohang, Korea
and

Y. S. Cho, J. M. Han, S. H. Han, B. H. Choi
Proton Engineering Frontier Project, KAERI

Abstract

We have designed the BPM PU based on capacitive buttons for use in the KOMAC (Korea Multi-purpose Accelerator Complex), the high-intensity proton linac that are under development at the KAERI (Korea Atomic Research Institute), Korea. The KOMAC is aiming to produce CW 20-mA beam current at the 100-MeV energy. We have chosen the button-type PU since it is easier to fabricate than other type PUs including the stripline, and it could provide enough signal power because of the high beam current. The PU sensitivity was calculated by the MAGIC that is a kind of the Particle-In-Cell code that originates from the plasma science community. The utilization of the MAGIC code is especially useful for BPM PUs in the low-beta sections of the accelerator, because it is difficult to obtain the PU sensitivity experimentally due to the difficulties in simulating the low-beta beams by the electromagnetic waves in a test bench. In this presentation, we report on the design of the BPM PU based on the MAGIC calculation.

1 INTRODUCTION

Front-ends of modern HPPAs (High-Power Proton Accelerators), such as RFQs and DTLs are generally complex and have tight installation spaces. This is especially true for diagnostic devices, and their design and installation often become designer's "nightmare." Meanwhile, diagnostics including BPMs and CTs are very important for successful commissioning and operation of the accelerators. Hence, their implementation should be considered from the early stage of the accelerator design. Successful compromise between the two conflicting side is possible when the diagnostic devices can be made compact without sacrificing their performances. Compact devices are easy to handle, economical, and generally have better high-frequency characteristics. Modern beam diagnostic devices are far more compact than their ancestors. For example, some CTs from the Bergoz Instrumentations are now integrated with CF flanges and their total length (axial) can be made as small as 30 mm. Majority of BPM PUs (Pick-Ups) for proton accelerators are still striplines that yield well defined response even for low-intensity beams. But their sizes are still too big to be installed in the narrow front-ends the accelerator. For example, the axial length of the striplines for the SNS

(Spallation Neutron Source, USA) linac exceeds 100 mm, even if they are installed in the vacuum. Button-type capacitive PUs have been simple and reliable, but their application to the proton machines has been limited because of their insufficient response to low-intensity beams. Modern HPPAs (High-Power Proton Accelerators) such as the KOMAC are designed to have very high beam intensities, so that even the buttons could generate enough signals for precision beam position measurements. Refer to Table 1 for the major beam parameters of the KOMAC accelerator.

Table 1: Beam parameters of KOMAC accelerator

	Operation Mode		note
	CW	Pulse	
Beam Energy	3 - 20 - 100 MeV		BPM operation region
β	0.08 - 0.20 - 0.43		
V	1.003 - 1.021 - 1.107		
Average Beam Current (Iav)	Max 20 mA	Peak 20 mA	
Pulse Width	-	Few ms	
Bunch Length	160ps		PARMILA simulation result
Bunching Frequency	350 MHz		

In this context, we have chosen the button-type PU for use in the KOMAC accelerator. One of the disadvantages of the buttons is that, it is difficult to predict the PU sensitivity using analytic formulas. In fact, the PU sensitivity for low-beta beams can not be practically determined even by experimental methods, due to the difficulty of simulating electromagnetic fields from the low-beta beams. In this regard, we have decided to utilize the computer code for determining the sensitivity of the button-type PU. We have chosen the MAGIC code which is a kind of the PIC (Particle-In-Cell) code and can treat the particle and electromagnetic system in the full three dimensional manner.

2 THEORETICAL CONSIDERATIONS

The theoretical estimation of the sensitivity of stripline PU was established by R. E. Shafer.^[1] He found the sensitivity of the stripline PU as the dB ratio of the wall currents induced at two opposite electrodes that are parts of a cylindrical beam pipe and extend infinitely in the axial direction. Here we only quote the result. The dB ratio is given by,

$$\left(\frac{I_{WR}}{I_{WL}} \right)_{dB} = \frac{160}{Ln(10)} (1 + G) \frac{\sin(\phi/2) x}{\phi b} + O(x^2) \quad (1)$$

where, the G is approximately,

$$G = 0.319 \left(\frac{\omega b}{\beta \gamma c} \right)^2 - 0.0145 \left(\frac{\omega b}{\beta \gamma c} \right)^3 \quad (2)$$

and, ϕ = electrode width,
 b = radius of beam pipe,
 x = beam position,
 ω = angular frequency,
 β = particle velocity (v/c),
 γ = the beam energy,
 c = velocity of light.

Note that for highly relativistic beams, $G = 0$, and the PU sensitivity depend only on the PU geometry. One of the main features of Eq. (1) and (2) is that the PU sensitivity depends on the beam energy and the processing frequency.

Shafer's theory is useful for estimating the PU sensitivity as the function of the beam energy, the frequency, and other parameters. One of major limitations of the theory is that it can not be applicable to general three dimensional geometries, such as the button-type PU. There are commercial electromagnetic codes that can simulate 3D geometries, including the MAFIA T3. The MAFIA T3 can handle only ultra-relativistic particles and can not be applied to low-beta beams. (The port boundary of the MAFIA T3 can accept only TEM mode whose phase velocity is equal to that of the light. And low-beta beams generate fields that are not in the simple TEM mode.)

3 MAGIC SIMULATIONS

The limitations of the Shafer's theory and the MAFIA code have led us to consider on using the MAGIC code. It is versatile and can handle arbitrary combinations of particle beams and electromagnetic structures. Like the MAFIA T3, the MAGIC also can not match the wide-band beam fields to its port boundaries. Without the proper matching of the wave fields at the port boundaries, we get many oscillations in the simulation output that will deteriorate the reliability of the simulation results. In order to circumvent this difficulty, we have utilized lossy medium placed close to the ports that absorbs incident waves. The position of the lossy objects and the ports can

be made far from the region of major interests in the simulation without distorting the physical reality.

Fig. 1 shows the 3D model of the button PU for the MAGIC simulation and its cross-sectional view in the transverse plane. In the left figure of Fig. 1, proton bunches travel left-to-right direction. Beam signals are coupled to the four buttons that are installed around the circumference of the beam pipe. Buttons are connected to 50-ohm coaxial lines whose dimensions are different from those of usual fabrication. This simplified the simulation geometry without sacrificing reliability of the simulation.

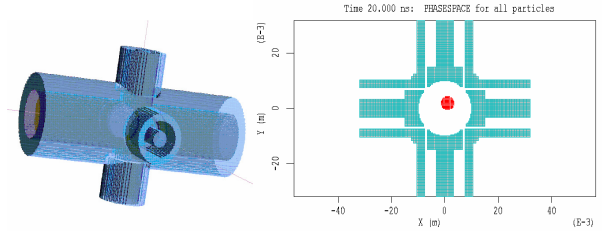


Figure 1: Modelling of button-type PU for MAGIC simulation. Left figure: 3D model, Right figure: Cross-sectional view. Dot inside beam pipe in right figure indicates proton beam. Diameter of beam pipe is 20 mm.

Default beam parameters used in the simulation are shown in Table 2. The left figure of Fig. 2 is the voltage waveform developed between the inner and outer conductors of the coaxial line. As expected, they are considerably longer than the beam bunch length, which is due to the axial extension of fields from the low-beta beams. ($\beta = 0.08$ for $E = 3$ MeV) With increasing the beam energy, beam fields concentrate in the transverse plane, and the pulse widths of signals coupled to buttons are shortened approaching that of charge distribution in the beam. This is shown in Fig. 4 which is the signal waveform for the beam energy of 100 MeV. Compare this with Fig 2.

Table 2: Default beam parameters used in MAGIC simulation.

Beam Energy	3 MeV
Average (Peak) Beam Current	20 (570) mA
Bunching Frequency	350 MHz
Bunch Length	43 ps rms

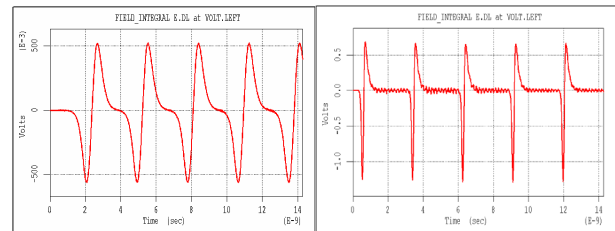


Figure 2: Waveforms of voltage signal developed at the end of one of coaxial lines for beam energies of 3 MeV (left) and 100 MeV (right).

The contour plot of longitudinal electric field (E_z) and the vector plot of (E_x, E_z) are shown in Fig. 3. They clearly show the longitudinal extension of the field due to the low-beta beam.

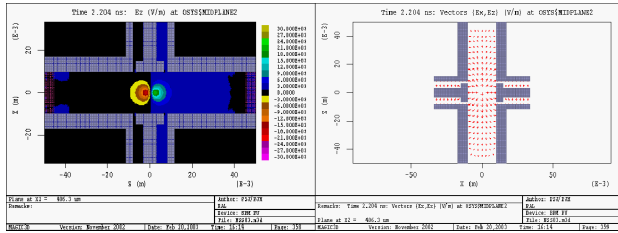


Figure 3: Contour (left) and vector (right) plots of electric fields showing their longitudinal extension. Right figure is rotated by 90 degrees with respect to left one.

The dependence of the PU sensitivity on the beam energy was simulated with result shown in Fig. 4. As expected from the Shafer's theory, the sensitivity increases dramatically with decreasing the beam energy. It also increases with increasing frequency at low energies but converge to the same value at high energies.

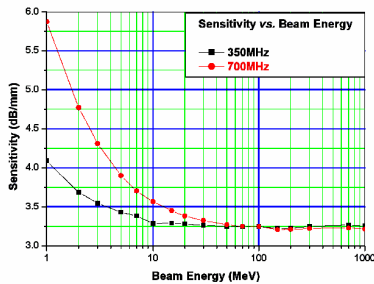


Figure 4: Dependence of PU sensitivity on beam energy.

Sensitivity of the PU to beam position change was simulated by moving the beam in the transverse plane in the step of 1 mm. The sensitivity map was obtained by plotting the delta-over-sum values of band-pass filtered voltage signals appearing at the ends of the coaxial lines. The center frequencies and bandwidth of the band-pass filter were 350 or 700 MHz and 20 MHz respectively. See Fig. 5 for the sensitivity maps for the frequencies of 350 and 700 MHz.

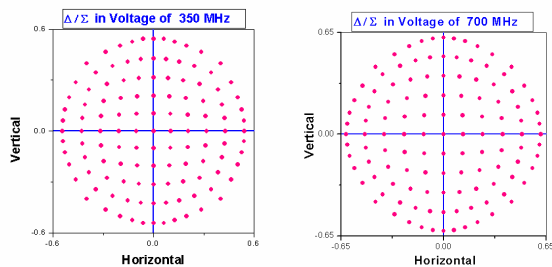


Figure 5: Sensitivity map of button PU at the frequencies of 350 and 700 MHz. Beam pipe diameter

= 20 mm. Button diameter = 12 mm. Beam energy and beta are 3 MeV and 0.08 respectively.

Note that the sensitivity for 700 MHz was about 7.5% larger than that of the 350 MHz.

In order to confirm the validity of the MAGIC simulation, we have simulated the BPM PU of the PLS (Pohang Light Source). The PU consists of four buttons with 9.5-mm diameter installed in vacuum chamber that has diamond-like cross section. Table 3 compares some of simulation results with experimental measurements. Beam parameters used in the simulation are; Beam energy = 2.5 GeV, Average (Peak) current = 200 (1600) mA, Bunching frequency = 500 MHz, Bunch length = 26 ps. The measured signal amplitude may contain substantial errors due to our rough estimation of the cable attenuation for the wide-band pulses. Simulated sensitivity values needs further refinement with finer meshes.

Table 3: Comparison between MAGIC simulation and experimental measurement results of PLS BPM PU.

		Simulation	Measurement
Signal Amplitude (V)		5.5	3
On-center Sensitivity (%/mm)	X	6.6	6.15
	Y	7.7	6.13

4 CONCLUSION

We conclude this article with the following summarizing remarks:

1. A button-type PU for use in the KOMAC (Korea Multi-purpose Accelerator Complex) accelerator was designed.
2. Electrical performance of the PU was simulated by the MAGIC code.
3. Dependence of the PU sensitivity on the beam energy and the frequency well corresponded to the theoretical predictions.
4. Simulation results of the PLS (Pohang Light Source) electron BPM PU reasonably agreed to the experimental measurements.
5. The MAGIC code is versatile and useful for designing and simulating delicate aspects of BPM PUs.

6 REFERENCES

- [1] R. E. Shafer, "Sensitivity of PUs for low beta beams," Proc. of the BIW93.

PERFORMANCE OF THE ELBE BPM ELECTRONICS*

P. Evtushenko, R. Schurig, Forschungszentrum Rossendorf, Dresden, Germany

Abstract

The radiation source ELBE is based on a superconducting LINAC. Initially it was designed to operate in CW mode with repetition rates either 13 MHz either 260 MHz. Later it was decided to operate the accelerator with reduced repetition rates for diagnostic reasons and for certain users. Now it is possible to operate with bunch frequency $13/n$ MHz, where n can be 2,4,8,16,32,64 and 128. It is required that the BPM system supports any of these operation modes. A core element of the BPM electronics is a logarithmic detector AD8313 made by Analog Devices Inc. The logarithmic detector is a direct RF to DC converter rated up to 2.5 GHz. Initial design of the BPM electronic was sophisticated only for CW operation with repetition rate more than 10 MHz, since bandwidth of the AD8313 is about of 10 MHz. Additionally a sample and hold amplifier is built in to provide enough time for an ADC to make measurements. The sample and hold amplifier is synchronized with a bunch frequency. In the paper we present results of the modified BPM electronics test.

THE BPM ELECTRONIC

The BPM electronics is based on the logarithmic detector AD8313 from Analog Devices [1], which is a direct RF to DC converter rated up to 2.5 GHz. Thus the BPM electronic is built without mixing down the RF signal of the BPM. The electronics operate at the fundamental frequency of the accelerator, which is 1.3 GHz. The electronics is placed in two different 19" chassis around accelerator outside the accelerator cave. An HELIAX® type RF cables connect BPMs to the RF front end. The cables have attenuation in a range 5÷6 dB at 1.3 GHz. The BPM signal goes through the bandpass filter with 3 dB bandwidth of 8 MHz. Then it is amplified with constant RF gain of about 25 dB to be matched to the linear range of the AD8313. The range goes from -65 dBm up to -5 dBm. The output of the logarithmic amplifier is matched to the ADC working range with the trim gain. The trim gain consists of adjustable gain and adjustable offset. So that four channels on one board are adjusted with difference typically 5%. Later the difference is taken in to account by software. One digit of the ADC corresponds to 8 μ m beam displacement. Principal scheme of the BPM electronics is depicted on Fig. 1.

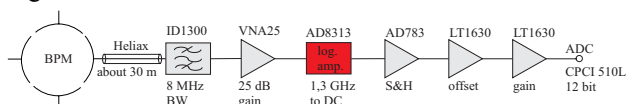


Figure 1: The electronics scheme.

Main characteristic of the BPM electronics is shown on Fig. 2, where the electronics output is plotted as a function of the RF input. We decided to put four channels on a board, since the cross talk from channel to channel was measured to be less than -20 dB, which is low enough.

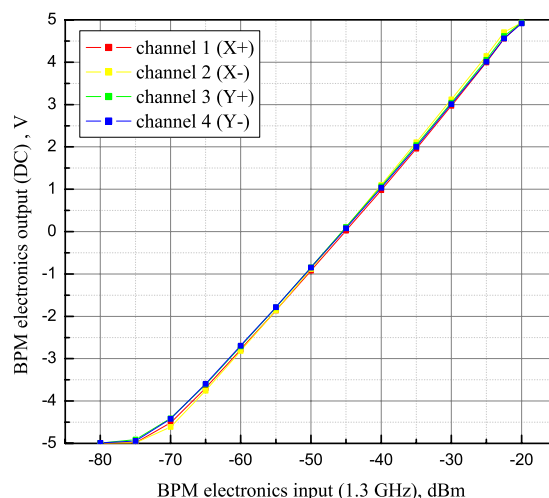


Figure 2: The electronics response curve.

THE LOW REPETITION RATE PROBLEM

The logarithmic detector has output bandwidth of about 10 MHz. With a bunch repetition rate of 13 MHz the AD8313 provides a DC output, which can be simply amplified and sampled by an ADC. When the bunch repetition rate becomes less than certain the logarithmic detector output shows the pulsed structure as well. Such a situation is demonstrated on Fig. 3. A short pulse generator drives the logarithmic detector. The generator was connected to channel 1 of the oscilloscope. Output of the AD8313 evaluation board is on channel 2. On the upper oscillogram the generator frequency is high enough to make the AD8313 output just a DC signal. On the lower oscillogram the generator frequency is reduced in factor four and is less than the logarithmic detector bandwidth. As one can see in this case every pulse of the generator is transformed by AD8313 into another more broad pulse but not into a DC signal. In a case with an electron beam and real signal from the BPM the width of the logarithmic detector pulsed output is defined by the bypass filter bandwidth or in other words by its quality factor. The real signal has 100 ns flat top. The ADC used for the data acquisition has a sampling time of 400 ns. Obviously even with proper timing the ADC does not have enough time to measure

* P.Evtushenko@fz-rossendorf.de

the signal correctly. For that reason a sample and hold (S&H) amplifier is built in between the logarithmic detector and the trim gain operational amplifier. There is a logical trigger, which is derived from the bunch frequency and the macropulse signal, to control the S&H. Every BPM board has a delay line to compensate for a different arriving time of an electron bunch to different BPMs. The accurate S&H timing allows holding maximum of the AD8313 signal providing enough time for the ADC sampling. Certainly the ADC uses external clock linked to the bunch frequency.

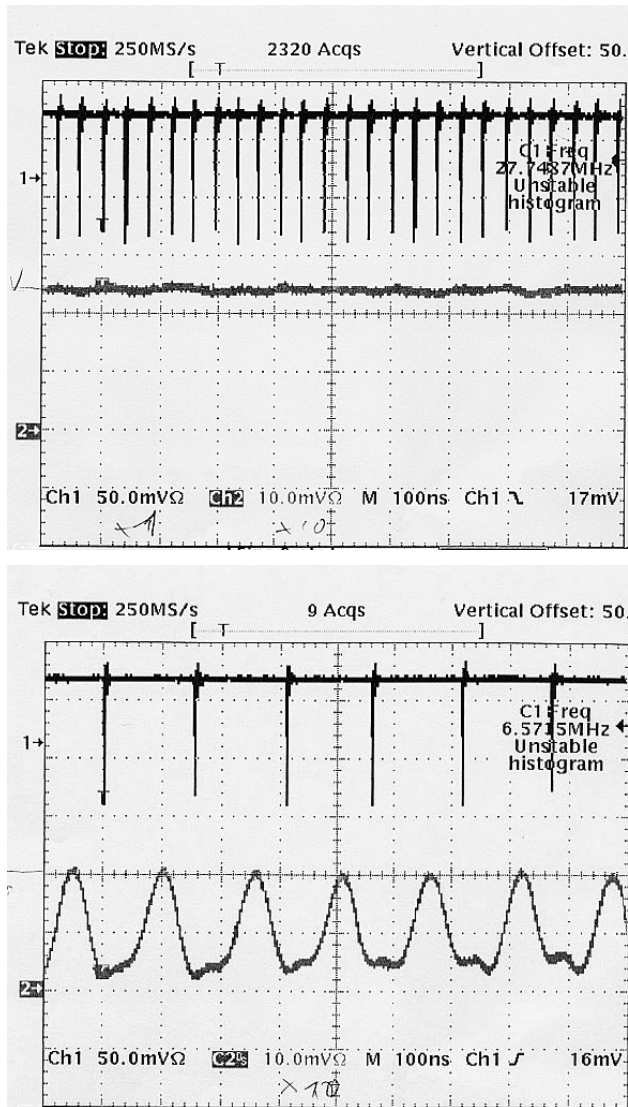


Figure 3: The AD8313 response at the different bunch frequency.

The sampling frequency of the ADC is constant and equals 101.5625 kHz, which is 13/128 MHz; this is the lowest possible bunch frequency. Changes in the board layout can introduce some extra noise and affect the beam position measurements. Because of this the modified BPM electronics were tested again, main criteria of the test is the BPM accuracy and its resolution.

ACCURACY OF THE POSITION MEASUREMENTS

To measure the beam position monitor accuracy one have to supply an “ideal beam”, in other words the beam used for such measurements have to have stability degree much better than the assumed accuracy. Otherwise one could not distinguish between the beam motion and the electronics noise. All BPM electronics prototypes have demonstrated the accuracy in the range between 10 μm and 30 μm . Since it is not easy to make a beam stable better than 10 μm we have measured the BPM accuracy with the help of stable RF generator. For these measurements the generator via one-to-two splitter was connected to the RF cables, which normally connect two opposite BPM channels (X+ and X-) to the RF frond end. Because of the bandpass filter the frond end sees only one 1.3 GHz component of the broadband BPM signal. Thus the generator operating at 1.3 GHz was representing the ideal beam. Dependence of the 1.3 GHz component power of the BPM signal from the average beam current is known very well. Thus adjusting the generator power level we could simulate different current of the beam. The BPM DAQ system was used in the measurements as well. There is a LabVIEW application, which uses data from the DAQ and calculates position of the electron beam as a function of time within the macropulse. These are real time measurements of the beam position with the sampling rate of 101.5625 kHz. The noise in the position signal is caused by the electronics noise only. Thus we know to which beam displacement corresponds the electronics noise. The position signal was measured for several milliseconds at different RF power level of the generator. For every measurement standard deviation from the mean value was calculated. The standard deviation is the accuracy of a single position measurement. Results of the measurements are shown on the Fig. 4.

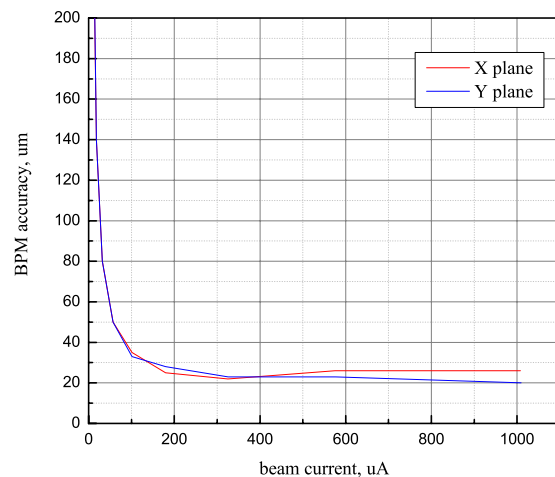


Figure 4: BPM accuracy.

The accuracy is better than 100 μm when the average beam current exceeds 25 μA . We would like to note here that the resolution of 100 μm was required and generally resolution is better than accuracy. Another important point is that we are interesting first in a stable accelerator operation and second we are measuring average position of a macropule, then the accuracy and the resolution are better in factor $N^{-1/2}$, where N is the number of measurements within the macropulse.

OFFSET MEASUREMENTS

Tolerances of the BPM manufacturing cause the electrical centre of the BPM to be different from the mechanical one. Electrical chains of the electronics working on the opposite electrodes of an BPM are also slightly different. These are the reasons for the offset in the beam position measurements and their current defence. The BPM was designed so that we can measure both this effects and take them in to account. The procedure was already described in [2] and is similar to the one used at CEBAF, JLab. One of the Y plane electrodes is driven by RF generator and signal from X plane electrodes are measured and equivalent X position is calculated. Results of such measurement for one BPM are shown on Fig. 5. If the BPM were a perfectly symmetric and the different chains of the electronics were identical we would not measure any “beam” displacement. The offset is measured for both planes for every BPM and is later taking in to account for position calculation by the BPM software.

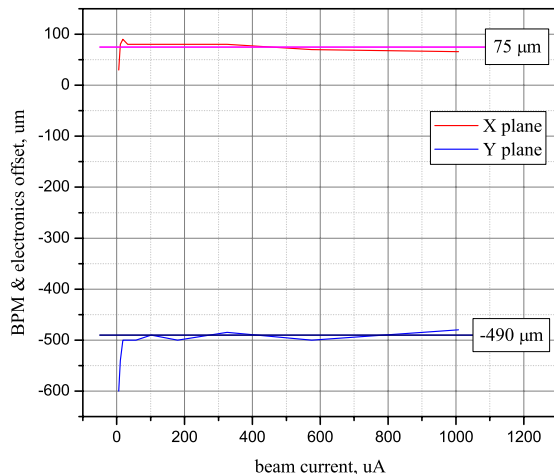


Figure 5: Measured BPM offset.

LONG-TERM STABILITY

Reproducibility of any accelerator is an important issue. Certainly have optimised the accelerator for a some application and having the optimal beam trajectory one want to be sure that next time running the machine for the same application one has the same optimal trajectory. Besides during a run it is important to see if there is a drift

of the accelerator components. Thus if an operator see a beam displacement during a run or after loading accelerator settings he want to be sure that the beam displacement is the real one and is not just the BPM electronics drift. To understand the long-term stability degree of the electronics the technique described in the section about accuracy was used. This time the generator output power was constant and the equivalent beam position was measured for several hours. Results of the measurements are shown on Fig. 6.

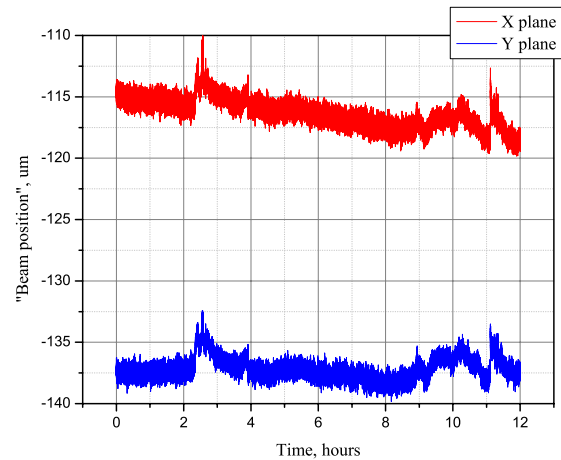


Figure 6: Long-term stability of the BPM.

The BPM electronics drift corresponds to a beam displacement of about 5 μm was measured within 12 hours measurements period.

ACKNOWLEDGMENTS

We would like to thank all colleges for useful discussions and for running accelerator during the measurements.

REFERENCES

- [1] www.analog.com
- [2] P. Evtushenko et al., Proceedings of DIPAC 2001 Grenoble, 2001

A HIGH DYNAMIC RANGE BEAM POSITION MEASUREMENT SYSTEM FOR ELSA-2

Ph.Guimbal*, P.Balleyguier, D. Deslandes, CEA/DPTA Bruyères-le-Châtel, France
H. Borron, Electrical and Electronic Engineering Dept., University College, London

Abstract

New beam lines are presently under construction for ELSA, a 18 MeV electron linac located at Bruyères-Le-Châtel. These lines need a beam position measurement system filling the following requirements : small space occupancy, good sensitivity, wide dynamic range (more than 90 dB), high noise immunity, single-bunch/multi-bunch capability. We designed a compact 4-stripline sensor, and an electronic treatment chain based on log-amplifiers. This paper presents the design, cold and hot test results.

INTRODUCTION

The ELSA facility [1] was designed in the late 80's as a test bench for high-power FEL physics and technology. It is now mainly used as a versatile 1-18 MeV electron source or as a picosecond hard X-ray source. In response to this shift in the user's needs, dedicated beamlines are under construction in a new experimental area [2].

In 1988, during design stage, two types of diagnostics were chosen for transverse beam monitoring :

- thin OTR screens (300 nm Al on 8 μ m kapton film)
- button-type or stripline (depending on available space) BPMs

Subsequent ELSA operation showed the limits of these diagnostics :

- OTR screens allow precise measurement of the transverse profile, but are not very sensitive. They were replaced by two-screen systems (like the one described below on fig. 1) with an OTR screen and a scintillator screen (Cr:Al₂O₃ deposited on a thin film).
- the button BPMs (10 mm in diameter capacitive pickups) are not sensitive enough
- the BPM electronic treatment chain is not reliable enough and was specifically designed for FEL operation. Therefore, it can be used only for 14.44 MHz (and 14.44 MHz/n) rep-rate train of bunches.

THE ELSA-2 COMBINED STATION

For these reasons, it was decided to design a new diagnostic station (fig. 1 et 2) with the following constraints:

- all-in-one OTR/scintillator/BPM station to save space and allow easy comparison of OTR and BPM data
- simple design
- high sensitivity BPM

- high dynamic range electronics, compatible with every macropulse structure of the beam, which means any sub-pattern extracted from a 144 MHz train.
- a length equal to a standart 6-way tee (164 mm)

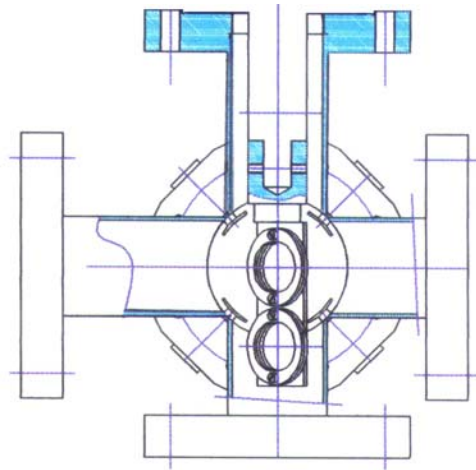


Fig. 1. Schematic drawing of the new diagnostic station combining two screens (OTR and scintillator) and a 4-stripline BPM : transverse view, showing the screens.

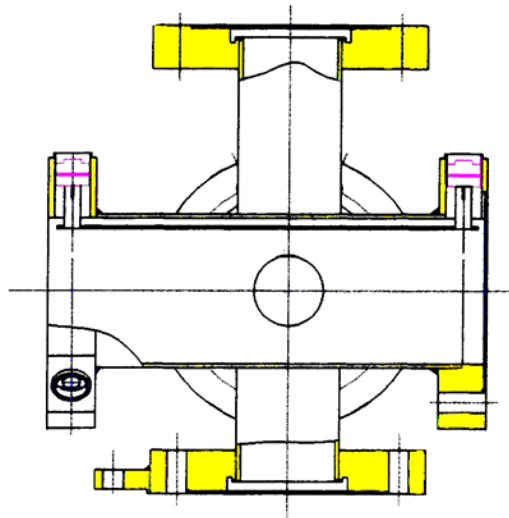


Fig. 2. Longitudinal view, showing the stripline ports.

For the BPM electronics (see details below), we chose a central frequency of 288.89 MHz. The corresponding wavelength (about 1 meter) is much longer than the stripline. In this case, the sensitivity grows with the

*email : philippe.guimbal@cea.fr

stripline length. For that reason, we chose to house the SMA sockets in the flanges. This symmetrical design also offers the opportunity to get a good impedance matching (see figure 3) by putting an external $50\ \Omega$ load at the downstream port.

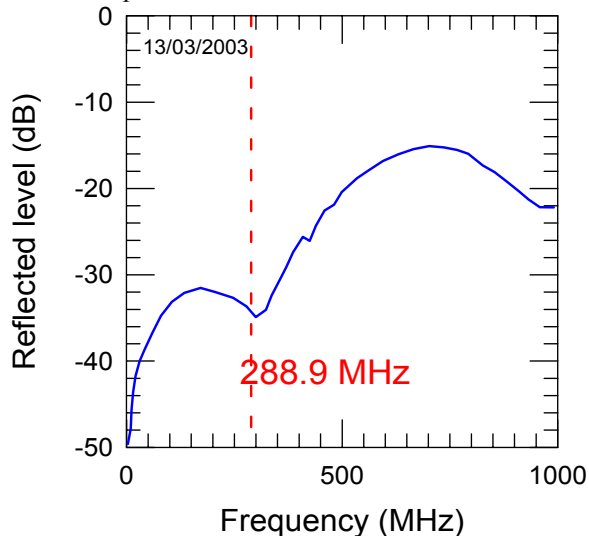


Fig. 3. Measurements show a good impedance matching of the BPM at the working frequency (better than 30 dB return loss).

Compatibility between the screen holder movement and the strips limits the subtended angle of the strips to slightly less than 45° , and imposes their locations at 45° of the horizontal and vertical axis. Numerization and post-processing of the position data will translate these data in the X et Y axis, in accordance with the implementation of the ELSA steerers and quadrupoles.

BPM ELECTRONICS

Because of the wide variety of beam energy, current and transverse dimension and the wide variety of requirements for the realtime bandwidth, numerous schemes have been proposed for BPM electronics in the last decades [3].

Early stage design was strongly influenced by the arrival on market of inexpensive high performance log amplifiers, offering 100 dB dynamic range and 500 MHz input bandwidth.

Our requirements were :

- a macropulse current between 1 and 100 mA
- a position sensitivity of 100 μm (stripline radius $R=27\text{ mm}$)
- no calibration required after an initial check
- very simple design.

These requirements already imply a dynamic range of more than 80 dB :

- 40 dB for the current range
- 40 dB for the 0.1 mm resolution (to first order : $\Delta/\Sigma=2 \Delta x/R$)

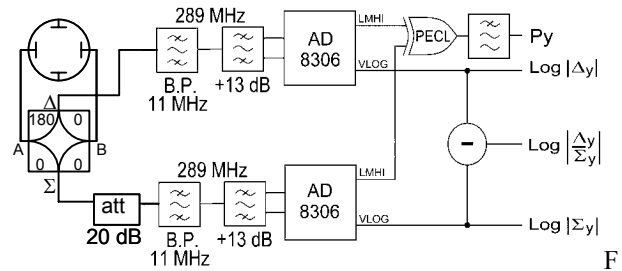


Fig. 4. Scheme of the electronics of one of the two channels of an ELSA-2 BPM.

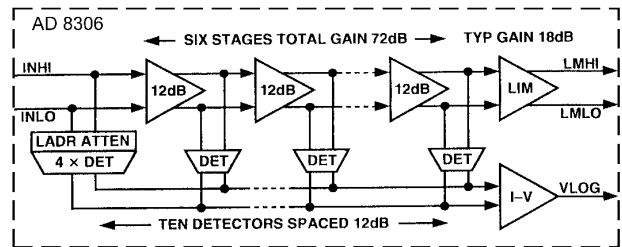


Fig. 5. Functional block diagram of the AD8306 log amplifier (source Analog Devices).

As seen on figure 4, the actual scheme is very simple :

- signals issued from two opposite striplines are carried along two equal-length semi-rigid short cables
- a hybrid Σ/Δ circuit creates the sum and difference, followed by a 20 dB attenuator on Σ channel
- a narrow-band filter at 289 ± 5 MHz samples a single harmonic of the signal.
- it is followed by a resonant impedance matching filter for adaptation of the 50Ω line to the 1 k Ω input of the log amplifier (giving an extra +13 dB gain)
- an AD8306 limiting-logarithmic amplifier (fig. 5) gives two outputs : the logarithm of the envelope with a slope of 20 mV/dB (video bandwidth of 5 MHz) and a limiter output
- $\log(\Delta)$ and $\log(\Sigma)$ signals are treated analogically to extract current and position informations
- limiter outputs of the Δ and Σ channels are phase-compared to tell on which side of the center the beam actually is.

The 4 channels of a BPM are packed on a 70x100 mm² electronic board (cf. figure 6) whose design must be **very** careful from a EMC point of view, not to reduce the dynamic range and log conformance (cross-talk between channels put less constraint than these two points). A box in the accelerator room includes two such circuits (one for each transverse direction). The box is close to the strip line in order to avoid degrading the signal to noise ratio of the Δ/Σ signals.

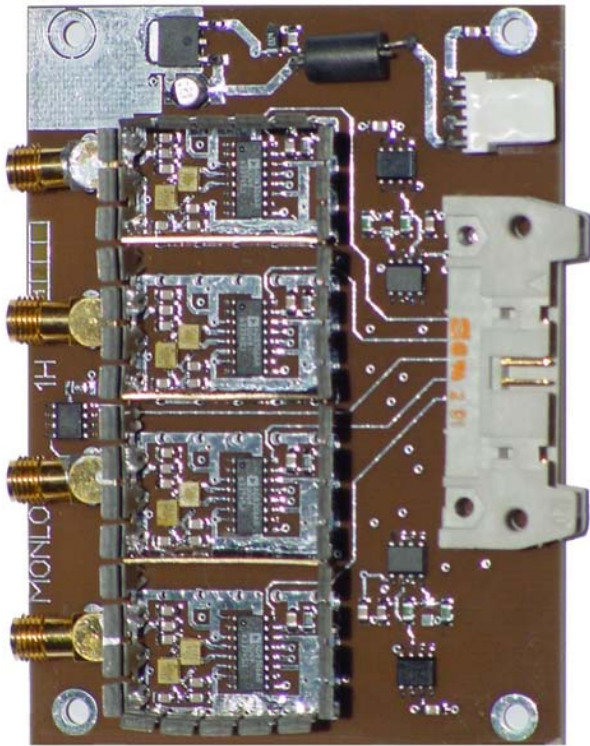


Fig. 6. Top view of the main circuit board

BPM TESTS

Electronic board tests on bench

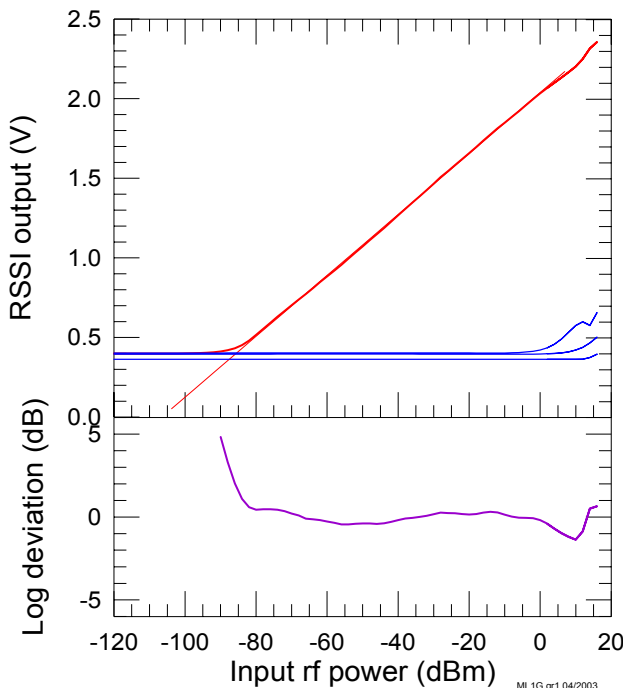


Fig. 7. Log response of the main board.
The slope is 20 dB/m

Measurement of the log output is very close to the AD8306 datasheet. The useful dynamic is more than 95 dB and the log conformance (lower part of fig. 7) shows a

peak-peak deviation slightly above 1 dB on a 80 dB range. Such a performance requires a very high attention paid on the printed circuit layout.

BPM tests on ELSA

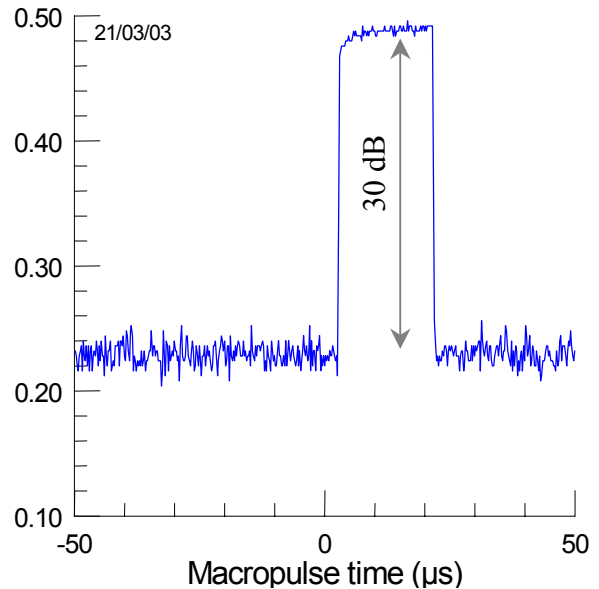


Fig. 8. Response of a Σ channel, on ELSA. The macropulse is 20 μ s long. Vertical scale is in Volts, 10 mV/dB (half the value of the AD8306 slope, because of the 50 Ω termination on scope).

First tests on ELSA (cf. figure 8) showed a BPM sensitivity more than 10 dB above the 1990 stripline design and a minimum current around 0.5 mA for the desired position precision of 0.1 mm, with a real-time bandwidth of 3 MHz.

ACKNOWLEDGMENTS

The authors wish to thank the ELSA team (A. Bayle, A. Binet, A. Bloquet, J.-L. Flament, V. le Flanchec, A. Godefroy and G. Vallart) for their helpful assistance and especially J. Raimbourg, for his contribution to the early design of the system.

REFERENCES

- [1] J.-G. Marmouget, A. Binet, Ph. Guimbal, J.-L. Coacolo, "Present performance of the low emittance high bunch charge ELSA photoinjected linac", EPAC'2002, Paris, June 2002, p. 1795.
- [2] Ph. Guimbal et al., "Status of the ELSA-2 project", EPAC'2002, Paris, June 2002, p. xxxx.
- [3] R.E. Shafer, "Diagnostics for high-brightness beams", Linac'90 proceedings, p. 797

Impedance-Matching-Transformer for Capacitive Pick-Ups

W. Kaufmann, J. Schölles, GSI, Darmstadt, Germany

Abstract

The transfer lines from GSI's heavy ion synchrotron (SIS) to the experimental set ups are equipped with segmented capacitive pick-ups for beam position measurement. This beam position measurement will be designed for single-bunch evaluation. Best choice for taking measurements with maximum sensitivity is a high-impedance tap at the pick-up referring to the bunch length of 50...500 ns. Therefore the feeding of 50 Ω coaxial cables will be realized by an impedance-matching transformer located close to the pick-up. It should have an impedance > 10 k Ω on the primary side and 50 Ω matching on the secondary side with a foreseen bandwidth of 200 MHz. So it is possible to use low noise amplifiers with 50 Ω input in a radiation save environment without loading the pick-up with 50 Ω .

INTRODUCTION

Many capacitive pick-ups at the GSI's synchrotron are used as position and phase pick-ups. Normally, high impedance head-amplifiers with an input impedance of 1 M Ω amplifies the plate signals close to the vacuum feed trough. Looking at the equivalent circuit of pick-up and amplifier explains why a high impedance signal tap is useful. This configuration behaves as a high pass filter as specified in [1]. Three different cases have to be taken into account as shown in figure 2.

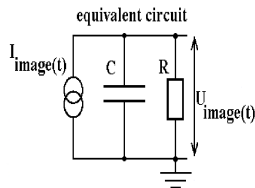


Figure 1: Equivalent circuit of one pick-up plate and amplifier

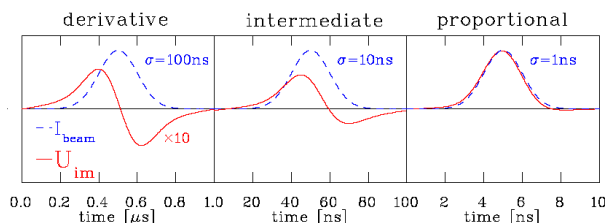


Figure 2: Theoretical bunch shaping

$$U_{\text{image}} = \frac{A}{\beta\pi\epsilon_0 C} \cdot \frac{j\omega RC}{(1 + j\omega RC)} I_{\text{beam}}(\omega) \quad (1)$$

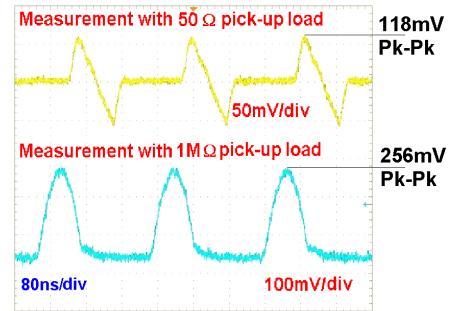


Figure 3: Measured bunch signals

Highest gain can be achieved in the proportional case. Measurements have approved the theoretical predictions (3). Figure 4 gives an information about the voltage gain of an 1 M Ω amplifier compared to a 50 Ω configuration.

It shows the calculated absolute value of the longitudinal transfer impedances ratio of a 1 M Ω and a 50 Ω amplifier.

In the range up to 1 GHz a 1 M Ω amplifier provides a higher gain. In practice, reflections will be generated due to the discontinuity of pick-up capacitance and amplifier input. But in the case of the used head amplifiers with its short cable length of a few centimeters this effect is negligible.

For beam position monitoring, at the high energy transfer lines from the SIS to the experimental area, it is necessary to use high impedance amplifiers to get a gain in position signals and a higher sensitivity. With a look to the future project of the GSI and its higher intensities it is important to make the maintenance at the beam diagnostics easier and saver. This means to get away from the beam tube into a radiation poor region of the plant.

$$U_{\text{image}} = 20000 \frac{\sqrt{1 + \omega^2 \cdot (50\Omega \cdot C_{\text{pickup}})^2}}{\sqrt{1 + \omega^2 \cdot (1M\Omega \cdot C_{\text{pickup}})^2}} \quad (2)$$

Furthermore some cryogenic regions at the new accelerator parts are provided. In this parts it is absolutely fatal to use head amplifiers with any power dissipation.

To work with 50 Ω coaxial cables is the best way to get away from the beam tube in an adequate manner. But

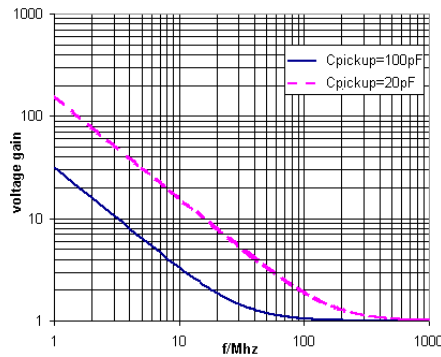


Figure 4: Calculated voltage gain (equation 2)

this causes reflections due to the mismatch to pick-ups high impedance to the 50 Ω coaxial cable. So the need of a broadband matching transformer is given. In consequence of its transforming properties the transformer can realize a high impedance at the primary side and a low at its secondary.

REALIZATION

It was necessary to accomplish preliminary inspections at air chokes, double hole-core inductors and toroids for an appropriate choice of the transformer configuration.

The choice of an air choke is the most invitingly transformer structure, because the medium air is everywhere available and has no saturation effects. Variations in temperature are not critical. But measurements showed, that it is not possible to reach a good coupling coefficient in due to leakage inductances. A loss in signal amplitudes is the result.

Particularly high coupling coefficients are reachable with ferrite double hole-cores and ferrite toroids. An accomplished power sweep up to +30 dBm shows no saturation effects.

The coupling coefficient for the used toroid sample is $\kappa = 0.995$. The dimensions of the core are 5.8 mm outside diameter, 3 mm inner diameter, a core thickness of 3 mm and an AL-value of 500 nH. The transformer windings are evenly distributed over the toroid core and the used Cu-wire has a diameter of 0.1 mm. With 45 windings on primary and 3 windings on the secondary side, its theoretical transformation ratio is $N = 15$. This means that the input impedance of the primary side with its 45 windings should have a value of

$$Z_{in} = 15^2 \cdot 50 \Omega = 11.25 \text{ k}\Omega \quad (3)$$

That is in the range of the desired 10 k Ω . But the measurements in figure 5 with a Z_{in} of only 5.8 k Ω do not approve this input impedance value.

The transfer function and the time domain signal shows, that the theoretical transformation ratio is not reached (fig. 5). The reason is the non-ideal behavior

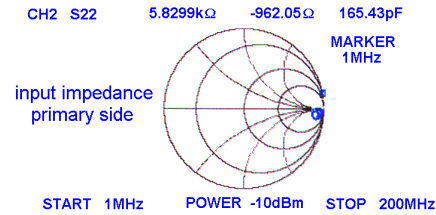


Figure 5: Smith diagram of the input impedance at the primary side with 45 windings

of the transformer in the rf-case, the measured transformation ratio is not equal to the theoretical. For a real transformer the following equivalent circuit and calculations are obtained. The calculations are based on measured data.

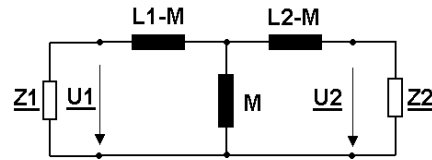


Figure 6: Equivalent circuit of the real transformer [3]

CALCULATIONS

The following calculations refer to the sample in test. The scattering factor is calculated by

$$\sigma = \frac{L_1(L_2 = \text{shorted})}{L_1(L_2 = \text{opened})} \quad (4)$$

and evaluates to

$$\sigma = \frac{9.5 \mu\text{H}}{1 \text{ mH}} = 0.0095$$

The coupling factor

$$\kappa = \sqrt{1 - \sigma} \quad (5)$$

evaluates to $\kappa = 0.995$.

The mutual inductance

$$M = \kappa \sqrt{L_1 L_2} \quad (6)$$

evaluates to $M = 98.5 \mu\text{H}$.

The transformation ratio

$$\frac{U_1}{U_2} = \frac{L_1}{M} + j\omega \frac{M\sigma}{\kappa^2 Z_2} \quad (7)$$

evaluates to

$$\frac{U_1}{U_2} = 10.1$$

The frequency depending term of equation 7 is negligible. This calculated transformation ratio is equal to the

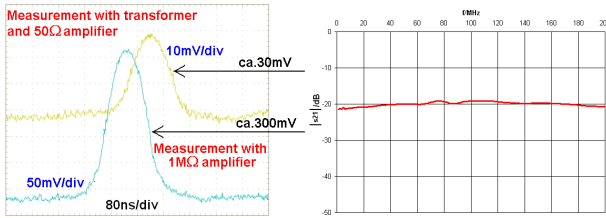


Figure 7: Measured bunch signals and transfer function of the transformer sample

observed ratio of the measurements (fig. 7) and also corresponds to the impedance value measured in fig. 5.

The fact, that the signal voltage is transformed down causes not automatically a loss in sensitivity, because the noise voltage is also transformed down. The use of 50 Ω amplifiers reduces the influences of the amplifier noise voltage in comparison to the 1 M Ω amplifier. So the dominant factor for the sensitivity is only the signal to noise ratio. The combination transformer and 50 Ω amplifier brings actually a gain up to 15 MHz. Figure 9 bases on the same calculation as figure 4. Only $R = 10\text{k}\Omega$ and the result is divided to the transformation ratio of 10. Furthermore galvanic isolation of the primary

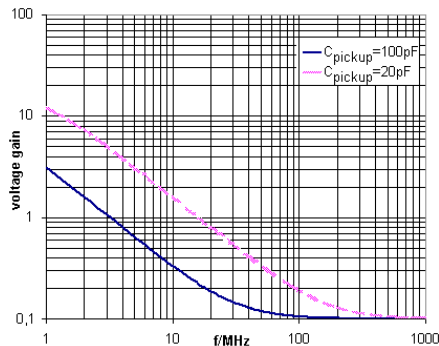


Figure 8: Calculated voltage gain with transformer

and secondary transformer sides reduces ground couplings and rejects disturbances. As the measurements of the secondary transformer side shows, there is a mismatching between transformer and 50 Ω . To avoid reflections at this discontinuity an additional passive matching network is necessary. The following matching network bases on a so called Zobel-network. The circuit was simulated and optimized with the rf simulation tool APLAC. Since a basic demand of circuitry is to make circuits as

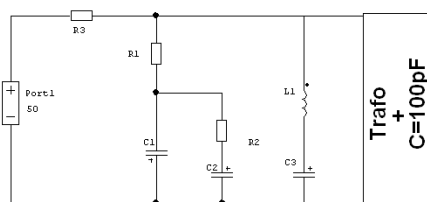


Figure 9: Zobel matching network the transformer sample

easy as possible another solution will be discussed in the optimization part.

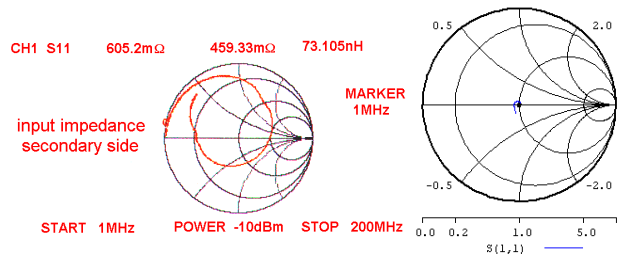


Figure 10: Smith diagram of the input impedance at the secondary side with 3 windings and matched transformer

OPTIMIZATION

In spite of the non-ideal transformation ratio of 10:1 the signal has an acceptable quality. There is no need to come up to the proposed transformation ratio of 15:1. So the prior aim of optimization should be the matching of the transformer secondary side to 50 Ω . Besides the described additional matching network the choice of a right ferrite core is another possibility to achieve a good matching to 50 Ω .

One of the ferrite material properties are a decreasing of permeability versus an increasing of the frequency. For a fixed output impedance the permeability of the core has to be proportional to $1/f$, but such a behavior is not available. Due to parasitic effects, it is necessary to get a low total number of windings. So a high permeability at low frequencies is required. This is very important, because at low frequencies the highest voltage gain is to anticipate (fig. 4, 9).

A test series with toroids from "Amidon" showed that not any of the materials type 43, 61, and 77 fitted these rules. But an approximation can be done by the combination of different ferrite materials. As a result, a stack of toroid slices from different ferrite materials will be given.

REFERENCES

- [1] P. Forck, "Lecture Notes on Beam Instrumentation and Diagnostics", JUAS 2003, p. 77
- [2] J. von Parpart, „Breitbandige Ferrit-Hochfrequenztransformatoren“, Hüthig Verlag, 1997
- [3] H. Freitag, „Einführung in die Vierpoltheorie“, Teubner Studienskripte, 1975

DEVELOPMENT OF A BUNCH FREQUENCY MONITOR FOR THE PRELIMINARY PHASE OF THE CLIC TEST FACILITY CTF3

A. Ferrari*, A. Rydberg, Uppsala University, Sweden
 F. Caspers, R. Corsini, L. Rinolfi, F. Tecker, CERN, Geneva, Switzerland
 P. Royer, Université de Lausanne, Switzerland

Abstract

In the framework of the CLIC RF power source studies, the feasibility of the electron bunch train combination by injection with RF deflectors into an isochronous ring has been successfully demonstrated in the preliminary phase of CTF3. A new method, based on beam frequency spectrum analysis, was experimented to monitor this scheme. A coaxial pick-up and its read-out electronics were designed and mounted in the CTF3 ring to allow comparison of the amplitudes of five harmonics of the fundamental beam frequency (3 GHz) while combining the bunch trains. The commissioning of the monitor was a successful proof of principle for this new method, despite the short length of the bunch trains and the presence of parasitic signals associated to high-order waveguide modes propagating with the beam inside the pipe.

INTRODUCTION

The Compact Linear Collider (CLIC) RF power source is based on a new scheme of bunch frequency multiplication: a 30 GHz drive beam is obtained by combining electron bunch trains in isochronous rings, using RF deflectors [1]. The preliminary phase of the CLIC Test Facility CTF3 [2] successfully demonstrated the feasibility of such a scheme at low charge [3]. A train of five pulses, produced by the source at the front-end and accelerated in a linac, was injected into an isochronous ring, using RF deflectors that create a time-dependent closed bump of the reference orbit and thereby allow the interleaving of the pulses at the injection. In this paper, we present a new method to monitor the bunch train combination, based on frequency spectrum analysis. When the first pulse is injected into the isochronous ring, the distance between two consecutive bunches is 10 cm, i.e. 333 ps. Therefore, all harmonics of 3 GHz can be found in the beam power spectrum. At the end of the bunch train combination, the distance between two consecutive bunches is reduced by a factor five. As a result, only the harmonics of 15 GHz should be found in the beam power spectrum (see Fig. 1). A coaxial pick-up and its read-out electronics were developed in order to extract the information contained in the beam. The bunch frequency monitor was installed and commissioned at CERN

during the last operating period of the CTF3 preliminary phase in 2002 [4]: a description of the measurements that were performed, as well as an analysis of the results that were obtained, are summarized in this paper.

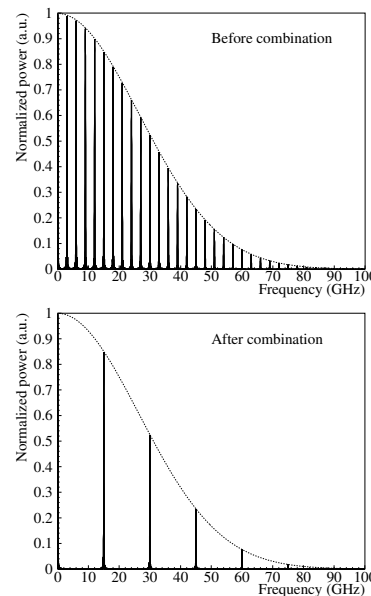


Figure 1: Calculated normalized power spectra for a train of gaussian bunches with a fwhm length of 10 ps before and after the bunch train combination with a factor five.

DESIGN OF THE PICK-UP AND ITS READ-OUT ELECTRONICS

Description of the coaxial RF pick-up

The geometry of the extraction coaxial pick-up was chosen in order to include a miniature ultrahigh vacuum feedthrough [5] while meeting various technical constraints (see Fig. 2). This feedthrough can be considered as a two dielectric coaxial line, with a constant inner diameter of 0.4 mm. On the vacuum side, the inner conductor is maintained in its central position by a small ceramic ring. A hole of 1.5 mm diameter was drilled in the beam pipe wall for the extraction of the signal. On the other side, the feedthrough is terminated by a K connector. The geometry of the pick-up was included in MAFIA simulations [6] and its transfer impedance was derived for the five frequencies of interest (9, 12, 15, 18 and 21 GHz).

* The research of A. Ferrari was supported by a Marie Curie Fellowship of the European Community Programme "Improving Human Research Potentiel and the Socio-economic Knowledge Base" under contract number HPMF-CT-2000-00865.

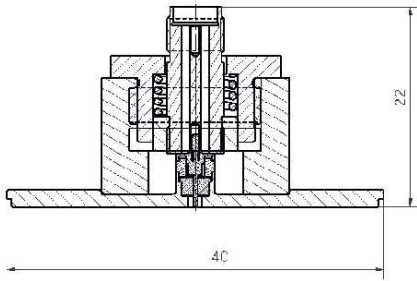


Figure 2: Technical drawing of the pick-up (the dimensions are in mm). The vacuum side is at the bottom of the figure.

Description of the read-out electronics

The signal coming from the pick-up is transported to the read-out electronics through a 50 Ω low loss SMA cable, on which a 6 dB attenuator is mounted in order to damp the possible multiple reflections between the pick-up and the input of the read-out electronics. The signal then goes through a wideband amplifier, a 10 dB attenuator, and a second low loss SMA cable. Afterwards, it is divided into five channels using two power splitters. Each channel consists of a bandpass filter to select the harmonic of interest, of a low noise amplifier, and of a diode used in the square law region to produce the envelope of the RF signal. After their extraction through SMA-BNC connectors, the signals are transferred to an oscilloscope for further analysis. The layout of the read-out electronics is shown in Fig. 3.

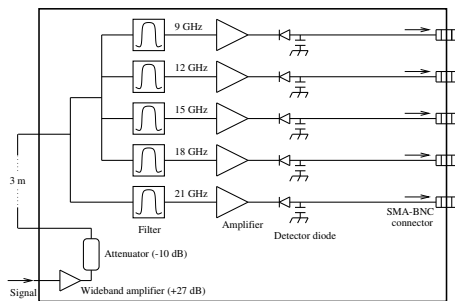


Figure 3: Schematic layout of the read-out electronics.

Before making measurements with beam, a calibration was performed to check the frequency response of the read-out electronics and to measure its amplitude response at each frequency of interest. When doing this, we noticed that the amplitude of the output signal on the oscilloscope was strongly dependent on the length of the RF pulse at the input of the read-out electronics. In particular, if the length of the input RF pulse is of the order of a few ns (which is the length of a bunch train in the CTF3 preliminary phase), the read-out electronics does not reach a steady state and the peak amplitude of the output signal is thus smaller than in the case of a long input RF pulse. An accurate calibration of the read-out electronics was therefore difficult, because of the uncertainties on the shape and the length of the bunch trains in the ring.

COMMISSIONING WITH BEAM

Time domain measurements

To visualize directly the time structure of the bunch trains in the ring, the pick-up signal was read directly on a 20 GHz sequential sampling oscilloscope. A high-quality trigger was given to this oscilloscope, which was running at a few Hz. Fig. 4 shows the waveforms measured just upstream of the wideband amplifier, before and after the bunch train combination with a factor five.

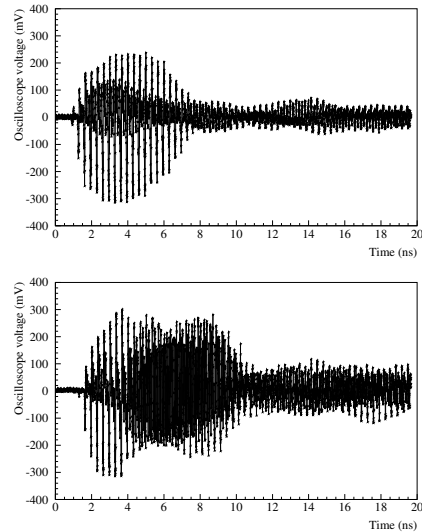


Figure 4: Time structure of the signal induced in the pick-up by the passage of a bunch train in the CTF3 ring, before (top) and after (bottom) combination.

Not only the signal produced by the 6-7 ns long bunch train is detected. Some reflections may occur in the pick-up itself but, most likely, some waveguide modes may be excited along the beam path and propagate together with the bunch train. Since these modes can be produced at many locations in the ring and since they have different velocities, some are detected at the same time as the bunch train, while others arrive up to tens of ns later. A Fourier Transform analysis of the time signal was performed at each step of the bunch train combination. As expected, only the harmonics of 3 GHz are found in the frequency spectrum and the power associated to 15 GHz increases while the bunch trains are combined. However, the repartition of the power between the various harmonics is not uniform along the bunch train. In particular, after the bunch train combination, only the core of the pulse has an almost pure 15 GHz structure, while all harmonics of 3 GHz can still be found at the edges of the pulse. The fact that the bunch trains do not perfectly overlap is the main reason for this effect. Finally, by treating separately the pulse and the tail, we noticed that the power spectrum of the signal induced by the wakefields contains the same harmonics as the signal induced by the bunches themselves, although not with the same amplitudes. For all harmonics, the power found in the

first 8 ns of the waveform is about one order of magnitude larger than the power found in the tail.

Frequency domain measurements

To study the evolution of the beam frequency spectrum during the bunch train combination, the pick-up signal was filtered in the read-out electronics before analysis with a digital oscilloscope. When doing these measurements, the charge per bunch was found to be about 0.06 nC and the bunch length was measured between 7 and 12 ps fwhm. The beam transverse position at the location of the monitor was derived from measurements upstream and downstream of the pick-up: we found respectively -1.0 ± 1.0 mm and -1.6 ± 0.8 mm in the horizontal and vertical directions. MAFIA simulations were performed to estimate the power level induced by a 6.6 ns long RF pulse at the pick-up output in these experimental conditions, for each harmonic of interest and at each stage of the bunch train combination. An RF synthesizer driven by a DC pulse generator was used in order to inject 6.6 ns long RF signals in the read-out electronics, at each frequency of interest and with the power levels estimated with MAFIA. The output waveforms were then compared with the signals coming directly from the pick-up at each step of the bunch train combination, see Fig. 5. The distance between the pulses is 420 ns, which corresponds to the combiner ring circumference. At 15 GHz, the signal amplitude clearly increases each time a new bunch train is injected and, at the end of the bunch frequency multiplication, most of the power is found in the 15 GHz harmonic. However, other channels also receive some signal and there are a few discrepancies between the expected and measured signal amplitudes. This is probably due to the fact that the longitudinal overlap between the five bunch trains is not perfect (the bunch frequency multiplication mainly occurs in the core of the final pulse). Indeed, the signal pattern is not consistent with a systematic phase error at injection. Another reason may be the presence of wakeguide modes between the bunches: depending on their phase, they can induce either an increase or a decrease of the output signal amplitude.

CONCLUSION

We have reported on the successful commissioning of a new instrument aimed at monitoring the combination of electron bunch trains in the combiner ring of the CTF3 preliminary phase, however with two limitations: the first one is the fact that the time extension of the bunch trains is smaller than the rise time of the read-out electronics, which makes it difficult to measure accurately the absolute power level contained in each harmonic (in the next stages of CTF3, the length of the bunch trains will be 130 ns). The second limitation is the presence of waveguide modes propagating in the beam pipe, in the wake of the electron bunches, and leading to a distortion of the signal coming from the monitor.

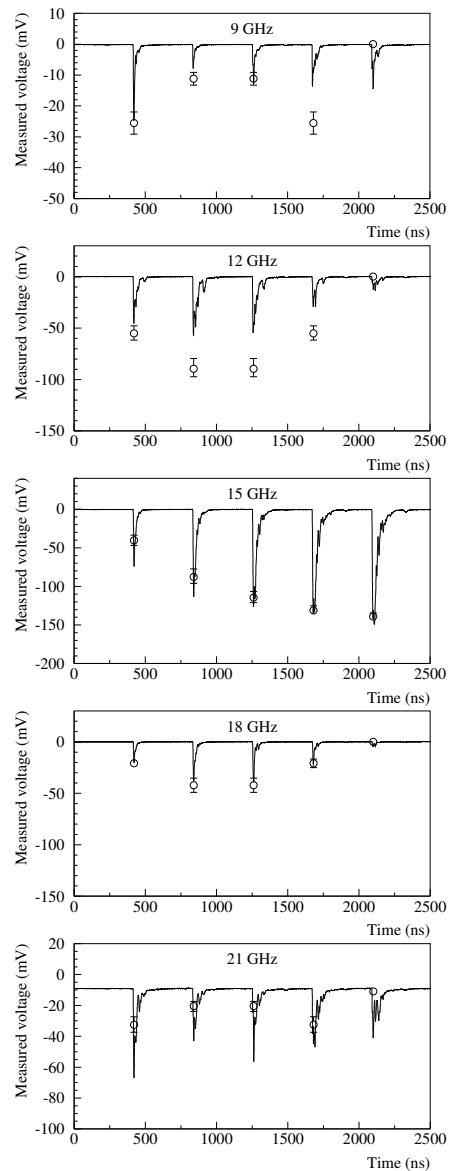


Figure 5: Bunch frequency monitor signals, while a bunch train combination with a factor five occurs: the open circles show the expected amplitude when combining trains of 20 bunches in the measured experimental conditions.

REFERENCES

- [1] R. Corsini (Ed.) et al., CERN-99-06 (1999).
- [2] G. Geschonke (Ed.) et al., CERN/PS 2001-072.
- [3] C. Biscari, R. Corsini, A. Ferrari, A. Gallo, A. Ghigo, L. Rinolfi, P. Royer, F. Tecker, CTF3 note 054, CERN-AB note 2003-023.
- [4] F. Caspers, R. Corsini, A. Ferrari, L. Rinolfi, P. Royer, A. Rydberg, F. Tecker, CLIC note 557.
- [5] J. Durand, T. Tardy, R. Trabelsi, CERN-PS/LP/96-09 (tech), CERN-EST/96-03.
- [6] CST (Computer Simulation Technology), "Mafia Release 4.106", CST Darmstadt, Germany.

TRANSVERSE FEEDBACK SYSTEM FOR THE COOLER SYNCHROTRON COSY-JÜLICH – FIRST RESULTS

V. Kamerdzhev, J. Dietrich, I. Mohos, Forschungszentrum Jülich GmbH, Germany

Abstract

The intensity of an electron cooled beam at COSY is limited by transverse instabilities. The major losses are due to the vertical coherent beam oscillations. To damp these instabilities a transverse feedback system is under construction. First results with a simple feedback are presented. Due to operation of the system the intensity and lifetime of an electron cooled proton beam at injection energy could be significantly increased. Measurements in frequency and time domains illustrate the performance of the system.

INTRODUCTION

The cooler synchrotron COSY delivers unpolarized and polarized protons and deuterons in the momentum range 300 MeV/c up to 3.65 GeV/c. Electron cooling at injection level and stochastic cooling covering the range from 1.5 GeV/c up to maximum momentum are available to prepare high precision beams for internal as well as for external experiments in hadron physics. Electron cooled beam at injection energy can become unstable [1,2]. Major current losses result from the vertical coherent oscillations of the dense electron cooled beam. One of possible cures of this problem is an active feedback system which damps the instabilities [3].

DOES COSY NEED A FEEDBACK SYSTEM

Let us look at the behaviour of an electron cooled intense proton beam at injection energy. To do this standard diagnostic equipment such as beam current transformer (BCT) and beam position monitor (BPM) have been used. BPM difference (Δ) signals in time and frequency domains have been simultaneously analysed.

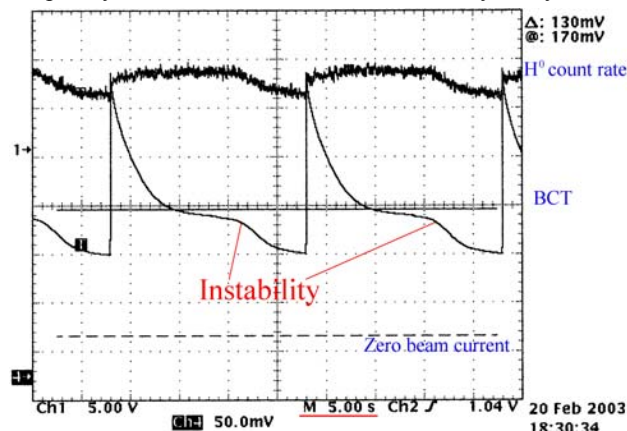


Figure 1: BCT (100 mV are equal to 1 mA beam current) and H^0 count rate signals.

On Fig. 1 the beam losses due to the instability are shown. The proton beam was cooled by 170 mA electron current. Vertical and horizontal BPM difference signals together with BCT signal are demonstrated on Fig. 2. Since the vertical aperture of the vacuum chamber in the arcs is more than two times smaller than the horizontal one

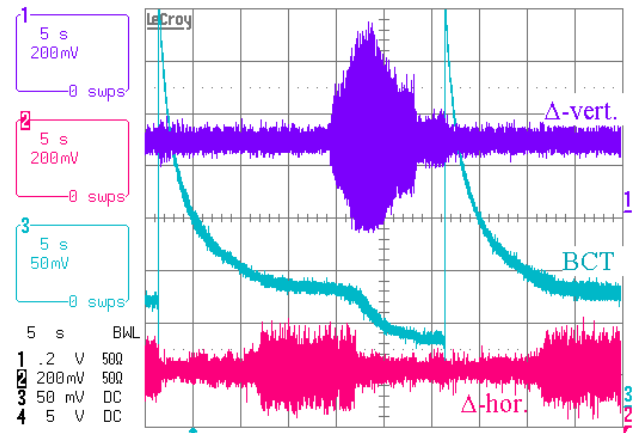


Figure 2: Vertical/horizontal BPM Δ -signals and BCT.

the beam oscillations in vertical plane are more dangerous and result in significant losses (see Fig. 2). Due to these reasons there is a necessity of the vertical damping.

SIMPLE FEEDBACK SYSTEM

The goal is to damp coherent vertical oscillations of the coasting proton beam at injection energy [4]. If the cavity gap is properly short-circuited the frequency spectrum of the vertical Δ -signal contains only vertical betatron sidebands (see Fig. 3).

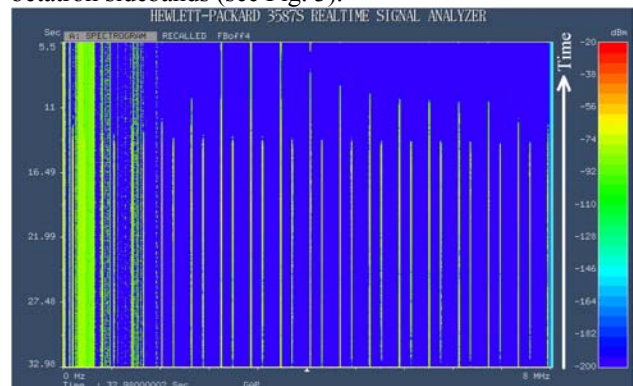


Figure 3: Frequency spectrum of the vertical Δ -signal.

In such a case the feedback system consists of a pick-up with a hybrid, preamplifier, delay, 180°-splitter, power amplifier and a kicker. No additional signal processing is necessary.

Hardware

One of the beam position monitors (electrostatic, diagonally cut) with high impedance preamplifiers and analog electronics with 70 MHz bandwidth was used to measure the beam position deviation (see Fig. 2) [5]. This signal was delayed by means of a very well shielded coaxial cable and fed into a 180° splitter. Two power amplifiers drive the stripline kicker wired in differential mode. Each of the downstream ports of the kicker was terminated with 50 Ω . The betatron phase advance from the pick-up to the kicker by typical tunes was about 97°.

RESULTS AND SYSTEM PERFORMANCE

Through the operation of the feedback system major beam losses could be prevented (see Fig. 4).

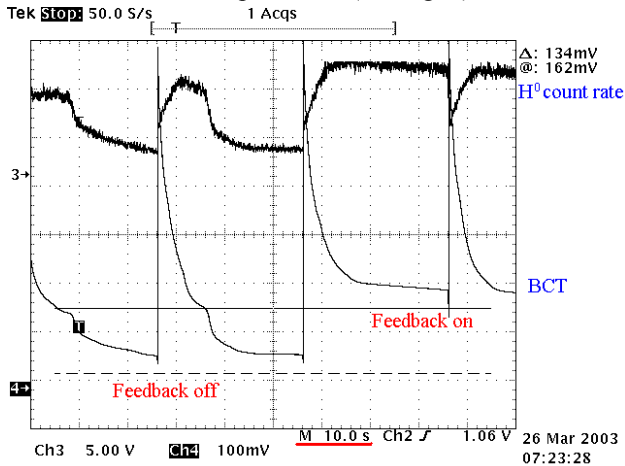


Figure 4: BCT and H^0 count rate signals with feedback on and off.

Measurements in time and frequency domains show that the coherent beam oscillations are effectively damped. Even in presence of external interference up to 1.5 MHz no beam disturbing could be detected (see Fig. 3,5).

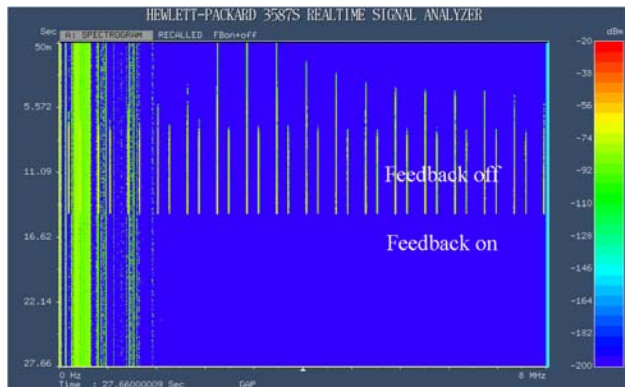


Figure 5: Frequency spectrum of the vertical Δ -signal with feedback on and off.

One of the interesting applications of the system is stacking of proton and deuteron beams. Stacking of electron cooled proton beam during several minutes has been observed. About 160 injections were stacked and accelerated (see Fig. 6). This improvement is especially

important for internal experiments which run with polarized protons and long cycle times. In this case stacking of many injections would not change the machine duty cycle significantly but the luminosity would be remarkably increased [6].

OUTLOOK

The next step in the development of the feedback system will be the improvement of signal to noise ratio. We expect this will bring more stacked beam intensity and quality. It is also planned to extend the system in horizontal plane. It seems to be necessary because the amplitude of horizontal oscillations has become bigger due to the intensity increase.

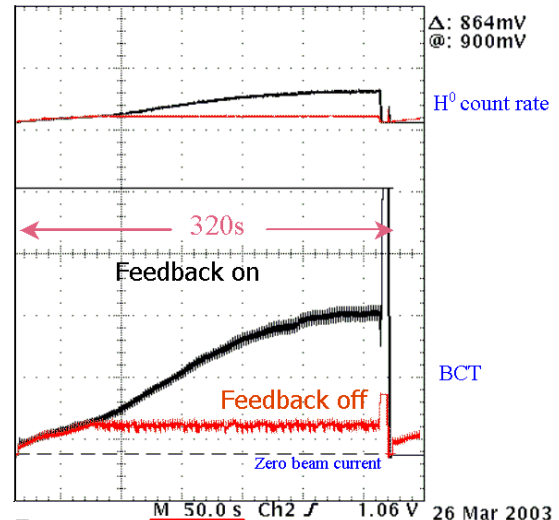


Figure 6: Stacking process with feedback on and off.

However some additional signal processing such as beam offset suppressing (BOS) and filtering will become necessary [7]. The first prototype of the BOS circuit will be tested during next weeks.

ACKNOWLEDGEMENTS

The authors are very grateful to H.J. Stein, D. Prasuhn and COSY team for useful discussions and support.

REFERENCES

- [1] H.J. Stein et al., Present performance of electron cooling at COSY-Jülich, submitted to RUPAC-2002.
- [2] I.N. Meshkov et al., Observation of instabilities of electron cooled proton beams, IKP annual report 2001.
- [3] D. Boussard, Cures of Instabilities, CERN 95-06, 22 Nov. 1995, Vol. I.
- [4] L. Vos, Damping of coherent oscillations, Nucl. Instr. Meth. A 391 (1997) 56-63.
- [5] F. Pedersen, Feedback Systems, CERN-PS-90-49.
- [6] D. Prasuhn private communication.
- [7] L. Søby private communication.

A NEW WIDE BAND WALL CURRENT MONITOR

P.Odier CERN, Geneva, Switzerland

Abstract

Wall current monitors (WCM) are commonly used to observe the time profile of particle beams. In CTF3, a test facility for the CERN Linear Collider study CLIC, high current electron beams of $1.5 \mu\text{s}$ pulse length are bunched at 3 GHz and accelerated in a Linac working in fully loaded mode, for which a detailed knowledge of the time structure along the pulse is mandatory. The WCM design is based on an earlier version developed for CTF2, a previous phase of the test facility, in which the beam duration was only 16 ns. Due to the longer pulse width the low frequency cut-off must be lowered to 10 KHz while the high frequency cut-off must remain at 10 GHz. The new WCM therefore has two outputs: a direct one for which an increase of the inductance results in a 10 GHz to 250 kHz bandwidth while the second one, using an active integrator compensating the residual droop, provides a 10 kHz to 300 MHz bandwidth. The new WCM has been installed in CTF2 late 2002 in order to test its high frequency capabilities prior to its use in CTF3. Design considerations and first results are presented.

1 INTRODUCTION

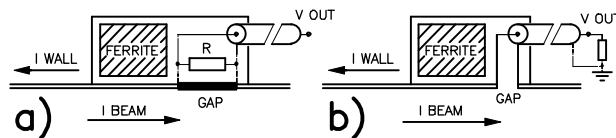
In CTF3, the test facility for the CERN Linear Collider study, high current electron beams of $1.5 \mu\text{s}$ pulse length are bunched at 3 GHz and accelerated in a Linac working in fully loaded mode, for which a detailed knowledge of the time structure along the pulse is mandatory. The new WCM design is based on an earlier version developed for CTF2 a previous phase of the test facility[1,2], in which the beam duration was only 16 ns.

The $1.5 \mu\text{s}$ pulse duration in CTF3, much larger than in CTF2, requires a significant decrease of the WCM low frequency cut-off, down to 10 kHz in order to limit the signal droop along the pulse. The high frequency cut-off should remain 10 GHz since the bunch repetition frequency will be 3 GHz. Owing to limited space availability, the overall length of the WCM should not exceed 260 mm. The monitor sensitivity is not a critical parameter in CTF3 since the mean beam current during the pulse is high enough, 1.5 A to 35 A.

2 DESCRIPTION OF THE NEW WCM

2.1 Principle of WCM

The general principle of resistive wall current monitor is very simple. A resistor is connected, either directly (Fig.1a) or through a vacuum feedthrough and a cable (Fig.1b) across a gap made in the wall of the vacuum pipe.



Figures 1a and 1b: principle of WCM

The image current, which accompanies the beam along the inside of the vacuum pipe develops a voltage across the resistor. A screening box filled with magnetic material, usually ferrite, is electrically connected on the two sides to force the image current to pass through the resistor. The equivalent circuit of such an arrangement is shown in Fig.2.

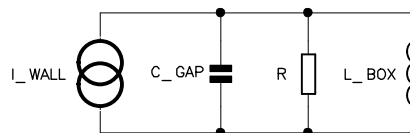


Figure 2: equivalent circuit

The dependence of the observed signal to beam radial position is minimised by collecting and summing the image current in 8 places around the gap circumference using 8 feedthroughs and an external combiner.

2.2 Bandwidth limitations

The high frequency cut-off depends on C_{gap} and on R . The standard connectors and coaxial cables being 50Ω and the number of outputs being limited to 8 by the physical size of the monitor, the value of R is $50 \Omega / 8 = 6.3 \Omega$. For a given vacuum pipe diameter, the value of C_{gap} depends on the length of the gap and on the permittivity of the insulator. In principle the gap length should be smaller than the beam length, which is 1.5 mm rms in CTF3. For practical reason the gap length has been fixed to 2 mm. It is made of a simple cut in the vacuum pipe; the capacitance of a ceramic gap would have been too high for the expected frequency bandwidth. For this reason the connections as in Fig. 1b have been chosen.

The low frequency cut-off depends on R , already mentioned, and on L the inductance of the screening box, which should be increased for CTF3 purpose.

2.3 Vacuum issues

The pressure required in the linac is in the region of 10^{-7} mbar and lower than 10^{-8} mbar in the combiner ring. With no ceramic gap in the WCM the interior of the screening box is under vacuum. This imposes a 150 °C bake-out process and determines the type of ferrite to be used. In order to avoid virtual leakages, particular care has been taken with respect to welding from inside as

well as the introduction of space between the ferrite rings to increase the vacuum conductivity.

2.4 Ferrite and Inductance issues

One of the important purposes of the ferrite is to absorb the $\lambda/4$ resonances created inside the screening box. The other purpose is to have a high permittivity to help in producing the high inductance needed to decrease the low frequency cut-off. Thus, the elements determining the choice of the ferrite are:

- Microwave absorption on a wide frequency spectrum in the GHz range
- Tolerate up to 150 °C
- Desorption as low as possible
- Permeability μ as high as possible

Nowadays the choice of ferrite fulfilling these requirements is quite small. The quality used for the CTF2 WCM being no longer available, the quality #61 from Fair-Rite® has been used. Unfortunately it has a permeability 3 times lower than the one used in the CTF2 WCM which does not allow the expected inductance increase by enlarging the ferrite volume.

The circular shape ferrites needed to fill the screening box have been difficult to machine from tiles and some were destroyed during the production.

2.5 Feedthrough

For the WCM high frequency behaviour, the vacuum feedthrough should behave as a 50 Ω transmission line on a very wide frequency bandwidth; furthermore it should accept the 150 °C bake-out. The same type as for CTF2 has been adopted [3].

2.6 Mechanics

The cross-section of the WCM on Fig.3 shows the 2 mm width gap, the feedthroughs and the stack of ferrites in the screening box.

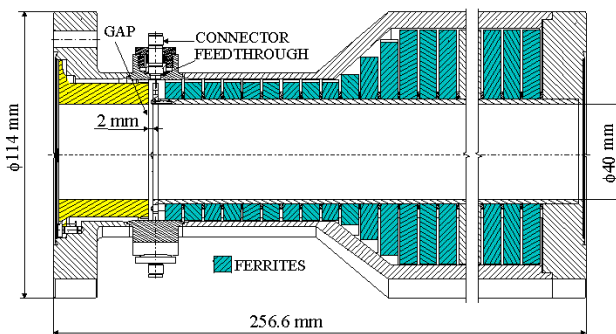


Figure 3: WCM general cross-section

2.7 External combiner and Integrator

The 8 outputs of the WCM are binary combined [4] using 50 Ω semi-rigid cables and combiners. They are carefully adjusted to provide an output sum signal independent of the beam position in the WCM and with

minimum time dispersion. On a second output an active integrator compensating the residual droop provides a 10 kHz to 300 MHz bandwidth.

In Fig.4 we see the 8 outputs of the WCM connected through the combiner to the direct output and to the integrator.

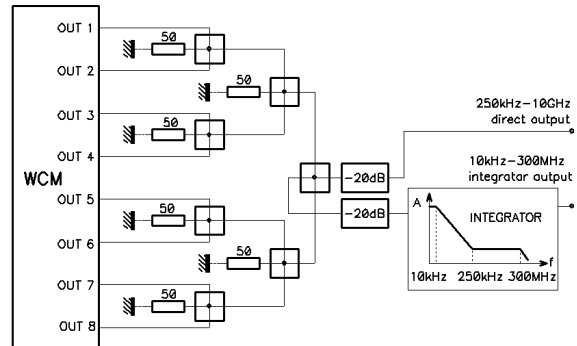


Figure 4: WCM general layout

Table 1 summarises the WCM specifications:

Table 1: WCM Specifications

Impedance	4 Ω
Low-frequency cut-off, direct output	10 kHz
Low-frequency cut-off, integrator output	250 kHz
High-frequency cut-off	10 GHz
Number of feedthroughs	8
Gap length	2 mm
Beam aperture diameter	40 mm
Length	256 mm
Flange type	DN63CF
Max temperature for bake-out	150 °C

3 RESULTS

3.1 Laboratory test results

The WCM has been tested in laboratory on 2 different test-benches [5]:

1. A time-gated test-bench for high frequencies where very short pulses are applied to a non terminated thin wire passing through the WCM. The WCM pulse response is then observed during the short time before the reflections occur.

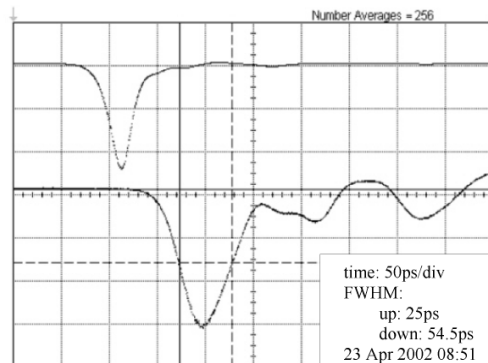


Figure 5: Pulse response of the prototype

In Fig.5, the upper trace is the pulse at the input of the test-set (FWHM=25 ps) and the lower trace is the WCM response measured on a 20 GHz scope after a 1 meter long cable (FWHM=55 ps, thus the WCM equivalent high frequency cut-off is 7.7 GHz).

2. A coaxial test-bench for middle and low frequencies where a step function is applied to a 50 Ω coaxial structure mounted upstream and downstream the WCM being tested. The low frequency cut-off is calculated from the measurement of the exponential decay.

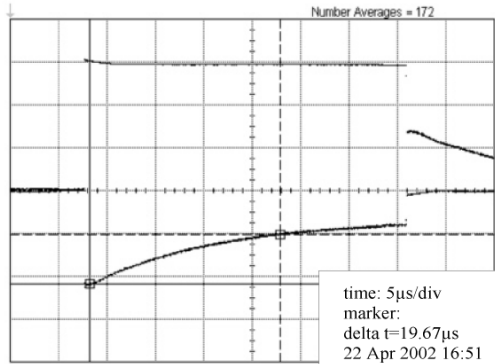


Figure 6: Step response of prototype + integrator

In Fig.6, the upper trace is the 33 μ s pulse at the input of the test-set and the lower trace is the WCM response seen after the integrator ($\tau=19.7 \mu$ s, thus the low frequency cut-off is 8kHz).

3.2 Results obtained with beam

Since CTF3 will start only in May 2003, the new WCM has been installed in CTF2 in November 2002 (Fig.7) in order to test its high frequency capabilities under real beam conditions.

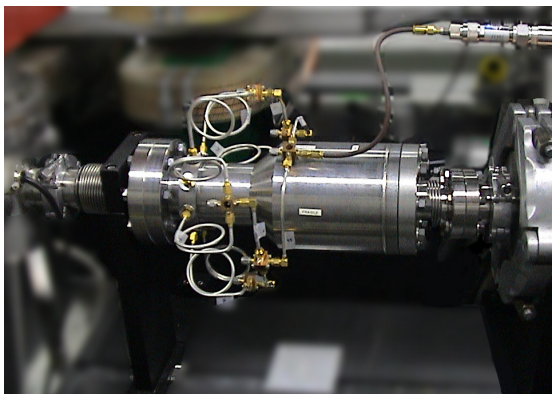


Figure 7: WCM in CTF2

The measurement made after 17 meters of low loss coaxial cable on a 20 GHz sampling scope is shown on Fig.8. (beam conditions: 1 bunch, charge=0.8 nC, FWHM=15 ps). The pulse response is close to the one obtained on the time-gated bench-test in the laboratory but degraded by the cable. A ringing after the pulse indicates a likely resonance in the screening box or in the

feedthrough. Nevertheless, the 97 ps FWHM shows the very fast time response of the WCM.

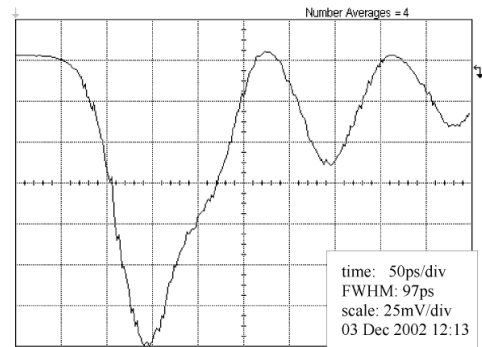


Figure 8: WCM signal on CTF2 beam

4 CONCLUSIONS AND OUTLOOK

The test performed on CTF2 has been successfully accomplished and proved that the design modifications to lower the WCM low frequency cut-off do not affect its high frequency behaviour. Some improvement remains to be made to reduce the 6 GHz resonance.

Two WCMs will be installed in CTF3 in July 2003. A series of 14 units will be prepared for installation in the future CTF3 stages. A new process of machining the extremely hard ferrite tiles (high pressure water jet) will be tested to reduce the tiles breakage.

5 ACKNOWLEDGMENTS

I would like to thank Jacques Durand for having passed on a technically sound and interesting project and for having been so patient in explaining the numerous details of this monitor. Jean-Pierre Potier is acknowledged for his encouragements for writing this paper. Elie Chazarenc and Luigi Leggiero are thanked respectively for the mechanical study and for the very accurate Electron-Beam Weldings.

6 REFERENCES

- [1] J. Durand, H. Braun, "Wall Current Monitors for CTF3", CERN CTF3-Note-014, 2000
- [2] J. Durand, T. Tardy, M. Wurgel, "A 10 GHz Wall Current Monitor", CERN PS/LP/Note 95-09, 1995
- [3] J. Durand, T. Tardy, R. Trabelsi, "A miniature ultrahigh vacuum feedthrough usable from DC to 20 GHz", CERN PS/LP/Note 96-09, 1996
- [4] J. Durand, "Combining Wideband Signals from a Wall Current Monitor", CERN PS/LP/Note 94-14, 1994
- [5] J. Durand, "Prototype "froid" WCM CTF3: quelques résultats", CERN CTF3_note_041, 2002

Microwave measurement of intra bunch charge distributions

M. Dehler,

Paul Scherrer Institut, CH-5232 Villigen PSI, Switzerland

e-mail: Micha.Dehler@psi.ch

Abstract

A direct way of obtaining intra bunch charge distributions is to measure the amplitude roll off as well as the phase behavior of the spectrum of the single bunch self field. To that effect, a microwave pickup together with a microwave front end has been installed in the storage ring of the Swiss Light Source (SLS). As pickup, button type bpms are used, which have been designed for a broad band behavior in the excess of 30 GHz. Three bpms together with their individual front ends are used in order to sample the beam spectrum at frequencies of 6, 12 and 18 GHz, which compares to the standard spectrum of a 1 mA single bunch extending to approximately 12 GHz (13 ps rms bunch length). The signals are mixed to base band in loco using the multiplied RF frequency as a LO. By shifting the LO phase, simultaneously the amplitude roll off as well as the complex phase of the beam spectrum can be obtained. Where using a resonator as a pickup would smear out the response over several bunches, allowing only the determination of average values, the current setup has a band width of approximately 2 GHz, so that individual bunches in the 500 MHz bunch train can easily be resolved.

INTRODUCTION

Intra bunch properties like the bunch length or the intra bunch charge distribution is reflected in the spectral composition of the self field of the bunches.

Measuring the bunch length makes use of the following property of Fourier transforms. With $h(t)$ as an arbitrary distribution and $H(j\omega)$ its Fourier transform, the following holds for the relation between its n -th order moment m_n and the Fourier transform [1]:

$$(-j)^n m_n = \frac{\partial^n H(j\omega)}{\partial \omega^n} \Big|_{\omega=0}$$

An alternative representation uses cumulants, $H(j\omega)$ is expressed via its cumulants k_n

$$H(j\omega) = \exp(j\omega k_1 - \frac{\omega^2}{2} k_2 - j \frac{\omega^3}{6} k_3 \dots)$$

With $\log(H(j\omega)) = a(\omega) + j\phi(\omega)$, odd cumulants are solely determined from the phase

$$k_{2n+1} = (-1)^n \frac{\partial^{2n+1} \phi}{\partial \omega^{2n+1}}$$

and even cumulants from:

$$k_{2n} = -(-1)^n \frac{\partial^{2n} a}{\partial \omega^{2n}}$$

Relating these to the properties of the beam, k_1 is the center of gravity of the bunch, k_2 its variance aka square of the rms length, k_3 the unnormalized skewness and k_4 the unnormalized excess of the charge distribution in the bunch.

In comparison to other alternatives, this approach for the measurement makes the minimum amount of assumptions about the bunch, be it the shape of its distribution, be it the presence of single or multi bunch instabilities.

With an theoretical bunch length of 13 ps at a nominal single bunch current of 1 mA, the roll-off of the bunch spectrum happens at around 12 GHz, so that measurements should go up to at least 18 GHz. One cannot hope to have an integral view of the bunch spectrum from DC-18 GHz, so the interesting question is the number of frequencies, one needs to sample in order to be sure to see any feature in the bunch charge distribution. This is given by maximum bunch length, which we estimated to be 36 psec. Due to this length even a pure sinusoidal modulation of the density will give a bump in the bunch spectrum with a width of 4.5 GHz to both sides of the modulation frequency. So including some security factors it was decided to setup measurements at 6, 12 and 18 GHz.

HARDWARE

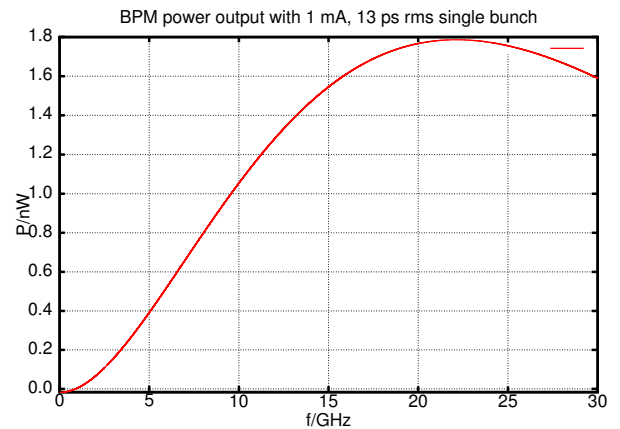


Figure 1: Power spectrum at the output of the two-button BPM assuming a 1 mA single bunch with the theoretical value for the SLS of 13 ps rms.

The hardware setup consists of three separate channels for processing the signals at the dedicated frequencies. As a signal pickups three special BPMS with two buttons sitting in the 28 mm high chamber of the SLS injection straight are used. For an optimum high frequency response, the BPM

electrodes consist just of a 50 Ohms line with an inner conductor of 1 mm diameter leading to the vacuum chamber. Since no traditional button shape is used, the stray capacitance of the electrode of 0.02 pF is negligible and the high frequency behavior purely determined by the geometrical dimensions.

Taking not into account the behavior of the ceramic feed through used, which is only specified up to 18 GHz, the power spectrum as seen in figure 1 shows a strong high pass behavior. Including the Gaussian roll off of a 13 ps bunch length into the calculation gives maximum power at around 23 GHz – with zero bunch length, the peak would sit at around 80 GHz. Interesting values for the use of wide band electronics are the peak powers emitted by the electrodes. With the worst case assumption of no bunch lengthening, a 10 mA/13 ps rms single bunch produces a peak of 4 dBm or 2.2 mW.

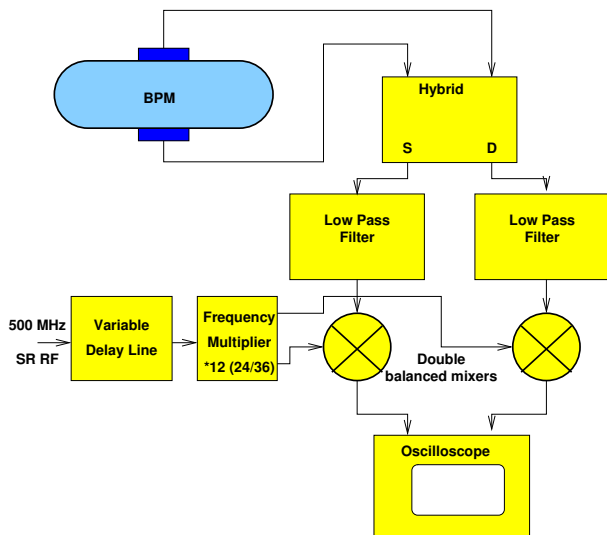


Figure 2: Layout of the electronics front end for one of the channels.

As seen in figure 2 the BPM signals pass low pass filters and are fed into hybrids giving sum and difference signals. Subsequent double balanced mixers convert these to base-band with an overall bandwidth at the IF outputs of DC - 2 GHz. In order to be able also to extract the phase informations, the LO signal is obtained by multiplying the storage ring RF of approximately 500 MHz. Thus being phase locked, the LO phase can be shifted via a variable delay line, the DC offset of the IF output as a function of the delay time will give amplitudes as well as phases of the BPM signal. An advantage of this approach compared to e.g. I/Q demodulation is, is that the effects of asymmetries in the mixers as well as cross modulation can be detected and corrected during the measurement.

BEAM MEASUREMENTS

As yet only the sum signals were used for longitudinal phase space measurements. Figure 3 gives an impression of

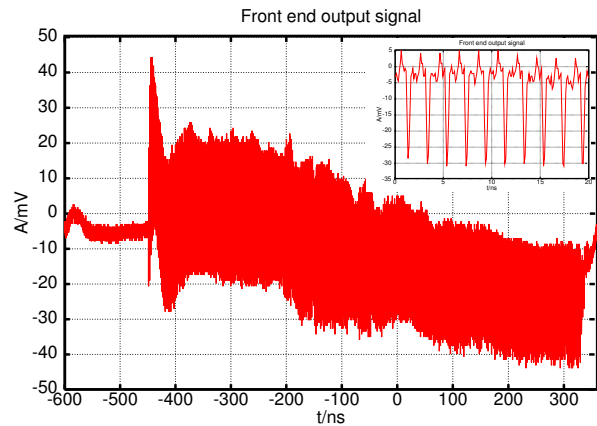


Figure 3: Signal of the 6 GHz channel with a multi bunch (400 out of 480 buckets filled, total current 200 mA)

a typical output signal obtained with a partial filling. The overall slope of the amplitude over the train shows clearly the phase slip caused by beam loading effects. The insert gives the fine detail of the signal allowing a good identification of individual bunches.

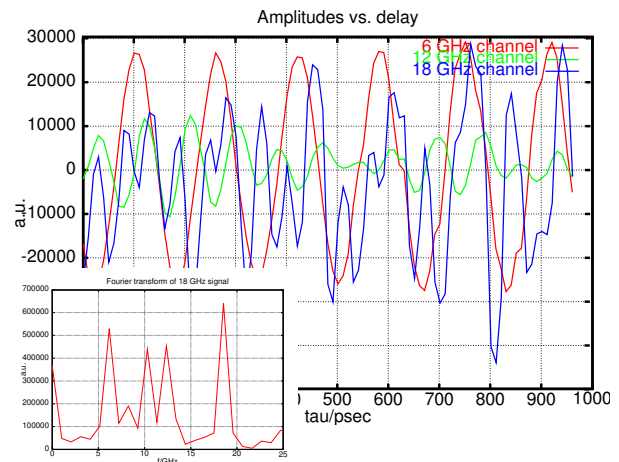


Figure 4: Amplitudes versus delay setting (Bunch current 0.2 mA). In the insert Fourier transform of the 18 GHz output.

While in the long term, a read out of individual bunch signals within the train is planned using a dedicated fast ADC ([3]), these measurements were done in single bunch mode using a GPIB controlled scope for readout. For various delay setting, the signal average in the vicinity of the bunch position was taken, as in figure 4. Two measurement problems can be seen here, the first being irregularities in the setting of the delay line leading to jumps in the 6 GHz output. The second is most pronounced in the 18 GHz output and is caused by harmonics in the frequency multiplier, which lead to spurious effects in the mixers and can be avoided by introducing additional filtering in the multiplier. Nonetheless, doing a Fourier transform of the signal versus delay will identify the correct amplitudes and phases.

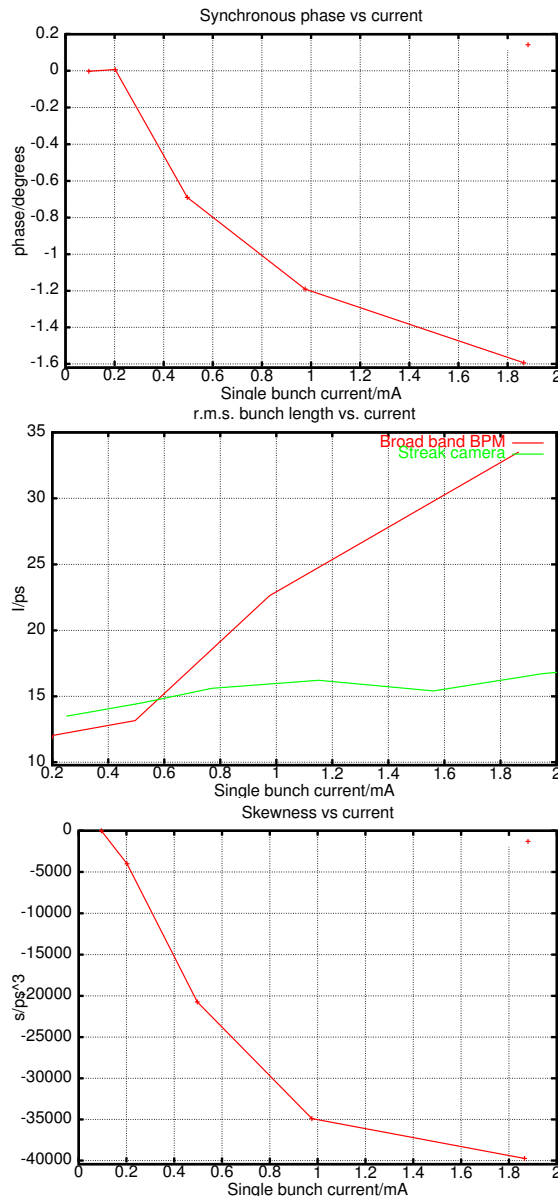


Figure 5: Synchronous phase, bunch length and unnormalized skewness versus bunch current. Bunch length compared to streak camera measurement is showing effect of synchrotron motion.

With the results obtained, a fit to the higher order moments was done. In order to calibrate the front end for its transmission characteristics, the results for a 0.1 mA bunch current were assumed to be a Dirac type distribution, and subsequent measurements calibrated to that. The fit showed up to be good for the first three moments, the signal distortions discussed above proved to be too strong to allow a reliable estimate of the fourth order moment (figure 5).

Despite a resolution of the delay line setting of 10 psec and some precision quirks in setting it, a sub picosecond precision corresponding to 0.2 degrees phase in the synchronous phase can be obtained. For the bunch length, the

results are distorted due to the multi turn averaging done by the read out scope. As it happens for higher currents, synchrotron oscillations will give an increased value for the averaged bunch length signal. When comparing results to streak camera measurements [2], the otherwise comparable results diverged from 1 mA one, where also synchrotron oscillations were observed with a magnitude explaining the difference. A multiturn signal using the the ADC boards mentioned below should also allow the measurement of synchrotron motion and eliminate this problem. Interesting is also the third order moment describing the symmetry of the space charge distribution, the negative sign indicating an asymmetry in the distribution with a extended bunch tail and a compact bunch head, which can be explained by the asymmetry of the longitudinal wake forces.

OUTLOOK

The near future will bring further optimization in order to improve the signal integrity of the front end, allow reliable estimates of higher order moments. A promising approach is going to be to take multi bunch data using the ADC boards currently in development at SLS, which allows to obtain intra bunch parameters for the individual bunch in the filling. As yet to be explored are the use of the difference outputs yielding vertical position information, eventually in combination with the side bands of the microwave channels.

REFERENCES

- [1] A. Papoulis, "Signal Analysis", McGraw-Hill, 1977.
- [2] V. Schlott, personal communication.
- [3] M. Dehler et al, "Capabilities of the SLS Multi Bunch Feedback Electronics", this conference.

Measurement of the longitudinal phase space at the Photo Injector Test Facility at DESY Zeuthen

J. Bähr, I. Bohnet, J. H. Han, M. Krasilnikov, D. Lipka*, V. Miltchev, A. Oppelt,
F. Stephan, DESY Zeuthen, Zeuthen, Germany,
K. Flöttmann, DESY Hamburg, Hamburg, Germany

Abstract

A setup for the measurement of the longitudinal phase space at the photo injector test facility at DESY Zeuthen is described. The measurements of the momentum distribution, the length of an electron bunch and of their correlation are discussed. The results of the momentum distribution measurement are shown, a maximum mean momentum of 4.7 MeV/c and a RMS momentum spread of 14 keV/c is observed. The setup for the measurement of the bunch length includes a Cherenkov radiator which is used to convert the electron beam into a photon beam with a wavelength in the visible range. The Cherenkov radiation mechanism is chosen in order to measure the bunch length with good time resolution. A silica aerogel radiator with low refractive index will be used. Geant 4 simulations show that a resolution of 0.12 ps can be reached. The time dependent behaviour and the position of the photon bunch will be measured by a streak camera system. A simultaneous measurement of the bunch length and the momentum spread will provide the full information about the longitudinal phase space. The design considerations of the radiators and their properties are discussed.

INTRODUCTION

The photo injector test facility at DESY Zeuthen (PITZ) has been developed with the aim to deliver low emittance electron beams and study their characteristics for future applications at free electron lasers and linear accelerators. The energy of the electron beam varies in the range between 4 and 5 MeV. A description of PITZ can be found in [1].

Successful optimisation and improvement of the PITZ performance requires good beam diagnostics for investigating the electron bunch properties. This paper is focused on longitudinal emittance measurements.

A spectrometer dipole and a YAG screen are used for the measurement of the momentum distribution of the electron bunch. The bunch length can be measured by using a radiation process, where a photon bunch is produced with the same time properties as the electron bunch has. The photon bunch is transported by an optical transmission line [2] to a streak camera, where the bunch length will be measured. At the electron energies available at PITZ a large amount of photons can be produced in the Cherenkov radiation process. To be able to transport the photon bunch to the streak camera small output angles from the radiator are requested.

Therefore, Cherenkov radiation in silica aerogel (SiO_2) is suggested for the photon production mechanism.

For the measurement of the full longitudinal phase space of the electron bunch a dipole, a Cherenkov radiator in the dispersive arm and a streak camera will be used. The produced photon bunch provides the information about the time properties and the momentum spread of the electron bunch. The simultaneous measurement of the bunch length and momentum spread allows to investigate the correlation between these characteristics.

MOMENTUM DISTRIBUTION

The mean momentum of the electron bunch as a function of the set point phase compared to a simulation with ASTRA [3] is shown in Fig. 1. In a large phase range the mean momentum is consistent with the simulation, where an appropriate phase shift is chosen. Up to now, the highest measured mean momentum at PITZ is 4.7 MeV/c, which corresponds to a gun gradient of 41.5 MV/m and a RF power of 3.15 MW.

Fig. 2 compares a measured momentum distribution with the simulation. The experimental data are obtained by using the projected image from the YAG screen in the dispersive arm, the space coordinates are recalculated into values of momentum. The simulation was done from the gun cathode to the middle of the dipole, it was not tracked through the full dipole, while the data are taken on the

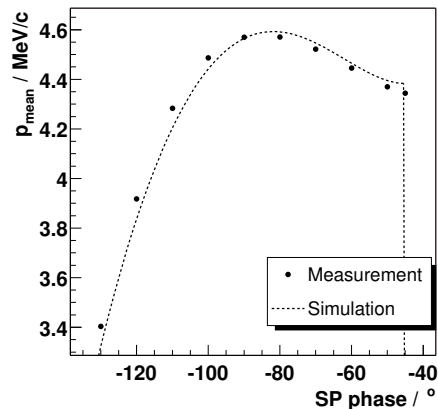


Figure 1: Mean momentum of the electron bunch as a function of set point phase for a gradient of 40.5 MV/m compared to the simulation. The errors of the measurements are of the order of 50 keV/c.

* dlipka@ifh.de

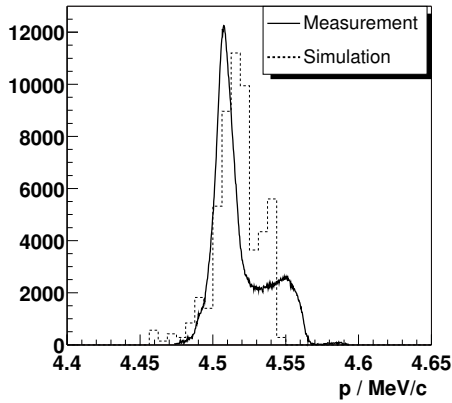


Figure 2: Momentum distribution compared to the simulation at a set point (SP) phase of -70° , gradient 40.5 MV/m and electron bunch charge 1.1 nC.

screen of the dispersive arm. This explains the disagreement between the measurement and the simulation. The resolution limit due to the finite beam size and the divergence of the spectrometer system is about 5 keV/c. A higher intensity for lower momenta and lower intensity for higher momenta are observed which results from strong longitudinal space charge of a short bunch due to a short laser pulse of 7 ps FWHM at the first half cell of the gun.

The RMS momentum spread as a function of the set point phase is compared with the simulation as shown in Fig. 3, the same phase shift as in Fig. 1 is used in the simulation. A smallest momentum spread of 15 keV/c for 1 nC is measured at a set point phase of about -60° . The measurement of the momentum spread and the simulation are consistent. For each phase a different electron bunch charge is measured (see Fig. 4) because of the short laser

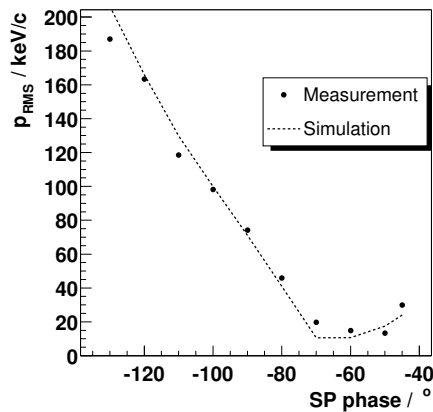


Figure 3: RMS momentum spread of the electron bunch as a function of set point phase for a gradient of 40.5 MV/m compared to the simulation. At small RMS momentum spread the errors are of the order of 5 keV/c.

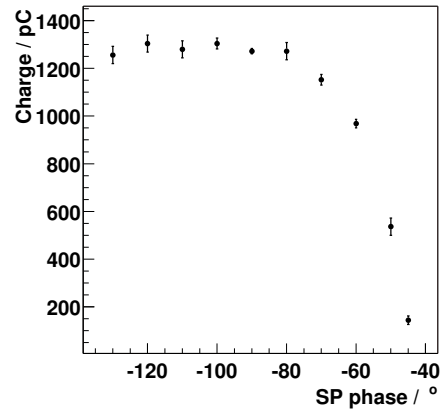


Figure 4: Measured electron bunch charge as a function of set point phase.

pulse and apertures in the system. Therefore the set point phase with highest mean momentum (see Fig. 1) is not equally to the phase with smallest RMS momentum spread (see Fig. 3).

BUNCH LENGTH

The photon bunch length will be measured using a Cherenkov radiator, an optical transmission line [2] and a streak camera. A large amount of Cherenkov photons is required in conjunction with a small output angle with respect to the optical axis of the transmission line. A time resolution of the whole system smaller than 1 ps is necessary. In order to obtain the adequate photon yields [4] silica aerogel will be used.

For the calculation of the time resolution for different aerogels Geant 4 simulation with a point-like electron source as input have been performed. The acceptance of the optical transmission line is estimated with an acceptance angle of 20° and a maximum object size of 5 mm. In the Geant 4 simulation the Cherenkov effect, Rayleigh scattering, ionization and multiple scattering are considered. In addition an Aluminium window of a thickness of 20 μm is placed in front of the aerogel to prevent the gun cathode from outgassing molecules into the vacuum chamber. The simulated time resolution of the different radiators is presented in table 1. Aerogel with a refractive index of 1.03 will be used instead of 1.05 because of the large Cherenkov

n	thickness / mm	σ_t / ps
1.01	20	0.51
1.03	2	0.12
1.05	1	0.11

Table 1: Time resolution of the different aerogels and Aluminium window; the thickness of the aerogel is chosen to obtain the same number of photons for all samples.

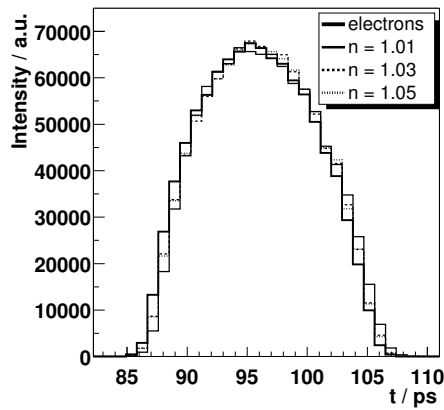


Figure 5: Simulated distributions of an electron bunch and Cherenkov photon bunches, produced in aerogel of different refractive indices and thicknesses (see table 1). The distributions are normalized to their area.

angle of 16.6° of the latter which does not match to the acceptance angle of about 14° of the realized optical system.

For a consistency check a typical electron bunch distribution simulated with ASTRA [3] is used as an input for the Geant 4 simulation. Fig. 5 shows the time structure of the electron bunch and the Cherenkov photon bunch for the considered aerogels. As expected, the photon distribution repeats that of the electron bunch. The time resolution of the transmission line is estimated to be of the order of 0.3 ps, whereas the streak camera has a time resolution of 0.2 ps.

LONGITUDINAL PHASE SPACE

A schematic view of the experimental setup planned to be used for the measurement of the longitudinal phase space is shown in Fig. 6. Measurements of the electron positions at different y -coordinates provides the information about their momenta, while the length in z corresponds to the bunch length.

The photon bunch, produced in the Cherenkov radiator, is transported to the streak camera, where its length and y -position can be measured simultaneously.

The opening angle of the Cherenkov light cone is too big for the optical transmission line, and hence only a fraction of the Cherenkov cone can be used. By using a fraction of the cone fused quartz can be used as radiator, too. The time resolutions for the different radiators are given in table 2. The best resolution is obtained for aerogel with the refractive index of 1.05, but fused quartz will be used as well because of its vacuum stability.

OUTLOOK

Momentum distribution measurements will be extended for different gun parameters (charge, gradient, focusing

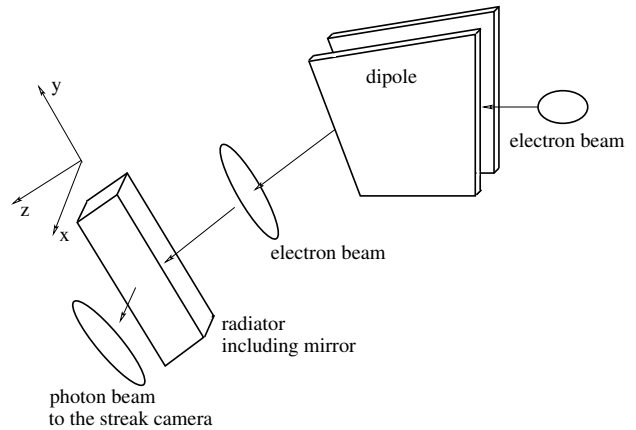


Figure 6: Setup for the measurement of the longitudinal phase space.

n	thickness / mm	σ_t / ps
1.01	20	3.98
1.03	2	0.43
1.05	1	0.35
1.46	0.1	0.41

Table 2: Time resolution of different radiator candidates, the thickness is chosen to obtain the same number of the photons.

solenoid, gun phase) and compared to the simulation including the aperture of the beam line.

The commissioning of the bunch length measurement setup is scheduled for end of May 2003. First measurements will start in June 2003. The parts of the setup for the measurement of the whole longitudinal phase space are in the production phase, the expected date of its integration in the facility is fall 2003.

In 2004 the photo injector will be extended by a booster cavity. The energy of the electrons after the booster will go up to about 30 MeV. At this energy optical transition radiation can be used in order to transform the electron bunch into a photon bunch, which provides an even better time resolution than the Cherenkov radiation mechanism.

REFERENCES

- [1] F. Stephan et al., Photo Injector Test Facility under Construction at DESY, FEL 2000, Durham, book edition of the proceedings, ISBN 0-444-50939-9
- [2] J. Bähr et al., Optical transmission line for streak camera measurement at PITZ, Dipac 2003, Mainz.
- [3] K. Flöttmann, A Space Charge Tracking Algorithm (ASTRA), <http://www.desy.de/~mpyflo/>, 2003
- [4] Q. Zhao et al., Design of the Bunch Length Measurement for the Photo Injector Test Facility at DESY Zeuthen, PAC 2001, Chicago.

TRANSVERSE EMITTANCE MEASUREMENTS AT THE PHOTO INJECTOR TEST FACILITY AT DESY ZEUTHEN (PITZ)

K. Abrahamyan, J. Bähr, I. Bohnet, M. Krassilnikov, D. Lipka, V. Miltchev*, A. Oppelt, F. Stephan,
 DESY Zeuthen, Zeuthen, Germany,
 K. Flöttmann, DESY Hamburg, Hamburg, Germany,
 Iv. Tsakov, INRNE Sofia, Sofia, Bulgaria

Abstract

The components and functionality of the emittance measurement system at PITZ are introduced. In brief some design considerations are reviewed as well. The influence of the noise due to dark current and electronic noise in beam size measurements is discussed and estimated. Results from recent transverse emittance measurements are presented and compared with simulations. Examples of a strongly distorted trace space are also considered where the application of a single slit scanning technique is a successful alternative of the multi-slit method.

INTRODUCTION

The main research goal of the Photo Injector Test Facility at DESY Zeuthen (PITZ) is the development of electron sources with minimized transverse emittance like they are required for the successful operation of Free Electron Lasers and future linear colliders [1]. The process of electron beam optimization requires characterization of the transverse emittance at a wide range of operation parameters. A slit/pepper-pot emittance diagnostic is designed and commissioned in order to characterize the trace space of the space charge dominated electron beam produced by PITZ.

EMITTANCE MEASUREMENT SYSTEM (EMSY)

EMSY (Figure 1) consists of two sets of masks for sampling the trace space distribution in both transverse directions. Each set is mounted on a separate carrier (actuator). In general EMSY has four degrees of freedom: rectilinear vertical and horizontal motion and rotation around both transverse axes. All motions are remote controllable. The masks are made out of 1-mm thick tungsten* plates. The slits have an opening of 50 μm , the diameter of the pepper pot mask holes is of the same size. There are two variations of multi slit masks installed in EMSY: with 1mm and 0.5 mm slit to slit separation. The design of the masks meets some general requirements introduced in [2], [3]:

-The beamlets produced by a slit mask must be emittance dominated

-The distance between the slits is a compromise between obtaining a good representation of the phase space and avoiding overlapping of the beamlets

-The contribution of the initial beamlet size to the beamlet size at the observation screen should be as small as possible

-The thickness of the mask is a compromise between the need to scatter electrons to form a uniform background and the desire to minimize the slit-edge scattering.

The masks are installed on the two actuators in the following arrangement: on the vertical actuator a multi-slit mask, a pepper-pot mask and a single slit mask are mounted. On the horizontal one: multi-slit mask, single-slit mask and YAG screen for direct observation of the electron beam.

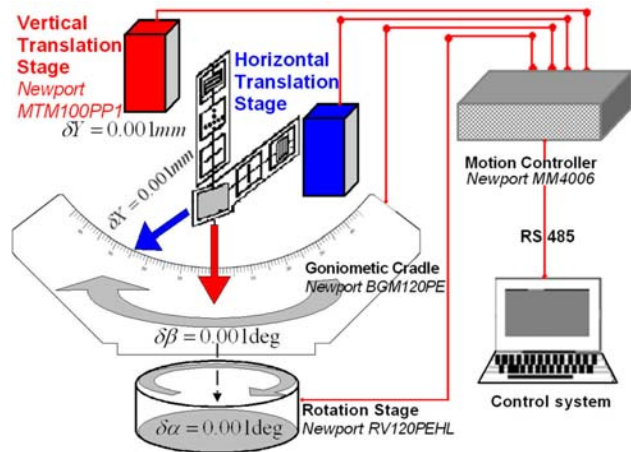


Figure 1: The emittance measurement system.

BEAM SIZE AND TRANSVERSE EMITTANCE MEASUREMENTS

The beam position and RMS size measurements are performed by calculating first and second central moments of intensity distributions of images obtained by CCD cameras:

* miltchev@ifh.de

$$\bar{x} = S \cdot \frac{\sum_{i,j} i \cdot C(i,j)}{\sum_{i,j} C(i,j)}$$

$$\sigma^2 = \frac{\sum_{i,j} (S \cdot i - \bar{x})^2 \cdot C(i,j)}{\sum_{i,j} C(i,j)}$$

Where the summation is over the rows and columns of the image matrix C and S is a scaling factor. In order to minimize the influence of the noise due to dark current and electronic noise a background subtraction is applied prior to the calculation of beam positions and RMS sizes. Since the background subtraction is never perfect the remaining noise still contributes significantly to the RMS size. An estimation $\delta\sigma$ of this influence could be given by comparison between the RMS-size results σ_{avr} and σ_{env} obtained after subtracting an average and an envelope background image respectively:

$$\delta\sigma = \frac{\sigma_{avr} - \sigma_{env}}{2}$$

Here the average background is determined by averaging the dark current profiles over a given number of RF pulses. The envelope background is determined by taking always the peak camera pixel values for a given number of dark current images. Since the envelope background subtraction cuts more of the tails of the intensity distribution one obtains $\sigma_{avr} \geq \sigma_{env}$. On the other hand the subtraction of an average background tends to underestimate the influence of the noise. Therefore one could evaluate the size σ as:

$$\sigma = \frac{\sigma_{avr} + \sigma_{env}}{2} \pm \delta\sigma \quad (1)$$

In this paper (1) is used for evaluating the beam size.

The goal of our emittance measurements is to obtain a value for the normalized RMS emittance defined as:

$$\epsilon_x = \beta\gamma \left[\langle x^2 \rangle \langle x'^2 \rangle - \langle xx' \rangle^2 \right]^{\frac{1}{2}}$$

For practical use it is more convenient to apply an equivalent definition as derived in [4]:

$$\epsilon_x = \beta\gamma \sqrt{\langle x^2 \rangle \langle \tilde{x}'^2 \rangle}, \text{ where } \tilde{x}' \text{ is the uncorrelated}$$

divergence. The RMS size $\langle x^2 \rangle$ is measured directly at

the position of the slit masks. $\langle \tilde{x}'^2 \rangle = \sum_i w_i \cdot \left(\frac{\sigma_i}{L} \right)^2$ is

deduced by analyzing the beamlet profiles observed on a YAG screen downstream of EMSY (Figure 2), here σ_i denote the transverse size of the beamlets and w_i are the corresponding weights, which depend on their intensity. L

is the distance between the slits and the screen of observation.

Often when measuring with a multi-slit mask the beamlet profiles partially overlap on the screen. In such cases the projected intensity is fitted to a sum of gaussian functions in order to estimate the size of the beamlets and their contribution to the overall intensity distribution. The applicability of this method is limited to the cases when the overlapping is not too strong and fits well to the above-mentioned assumption. The scanning with a single slit gives the possibility to analyze each profile separately without any assumption of the beam shape. This method was mainly used in the measurements presented below.

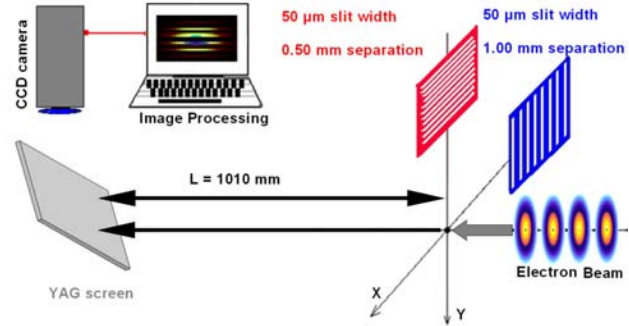


Figure 2: Measuring beam divergence

RESULTS

One example of scanning with a single slit through the horizontal cross section of the beam is shown in Figure 3. The scanning step is 0.300 mm the bunch charge is 0.66 nC. The mean momentum was measured to be 4.57 MeV/c. The current in the main solenoid was $I_{main}=290$ A. This current corresponds to a beam waist at the position of the slit. The X-RMS size of the beam at the position of the slit (1.62 m after photocathode) was measured directly to be 0.38 ± 0.01 mm. The measured normalized X-RMS emittance is equal to 5.3 ± 0.7 mm.mrad.

Analog an Y-RMS emittance of 4.7 ± 0.5 mm.mrad is obtained

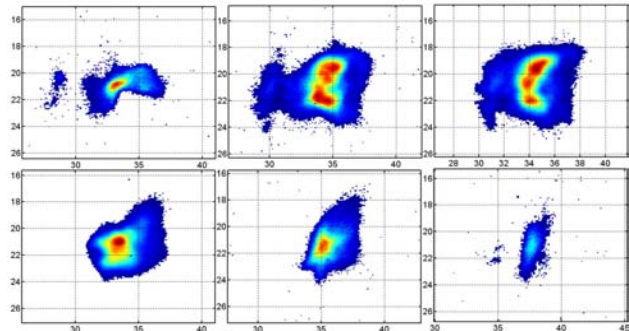


Figure 3: Single slit measurement in X-direction

The simulation results show values $\epsilon_x = 5.6$ mm.mrad, $\epsilon_y = 4.5$ mm.mrad. Figure 4 shows the simulated phase space, corresponding to the measurements shown in Figure 3. The phase space distribution shown on this figure is typical for the case when the beam is focussed on

the position of the emittance measurement system, which leads to extreme increase of the space charge forces acting on the beam particles.

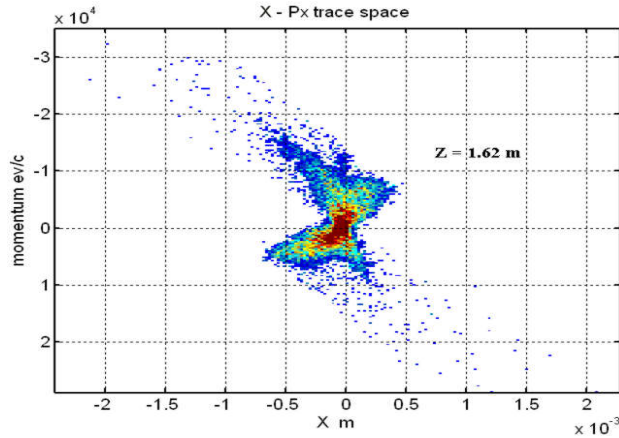


Figure 4: Simulated phase space

The transverse emittance was measured as a function of the current of the main solenoid (Figure 5). The measurements were done at the following conditions: Gun gradient = 40.0 MV/m, bunch charge = 0.66 nC, Mean momentum = 4.58 MeV/c.

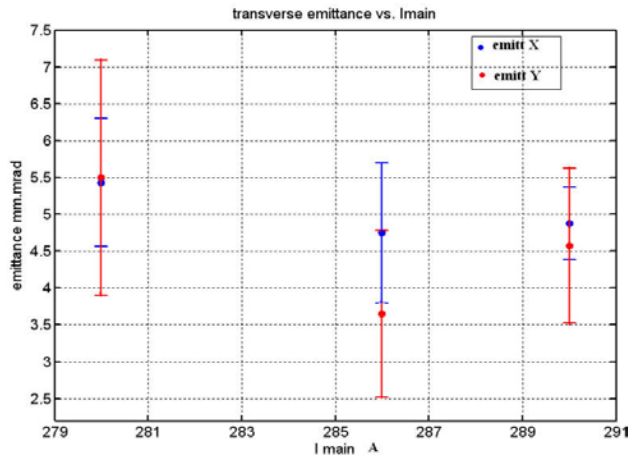


Figure 5: Transverse emittance vs. solenoid current

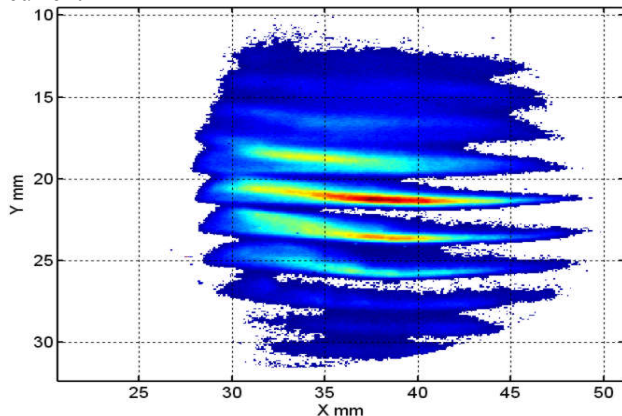


Figure 6: Beamlet profiles measured by the vertical multi-slit mask

Emittance $\epsilon_y = 5.8 \pm 0.6$ mm.mrad was measured with the vertical multi-slit mask as shown in Figure 6 at the following conditions: gun gradient = 40.5 MV/m, $I_{\text{main}} = 300$ A, charge = 0.49 nC, $P_{\text{mean}} = 4.56$ MeV/c, Beam rms size at slits = 1.05 mm.

CONCLUSIONS AND OUTLOOK

The emittance measurement system at PITZ is fully commissioned. Measurements of the transverse beam emittance were done in a wide range of machine parameters. The transverse emittance numbers presented in this paper are not the optimum values that are possible with the RF gun at PITZ. The main reason for this is that the current laser system produces very short pulses of 7 ps FWHM, which lead to strong space charge forces at the cathode. The short laser pulse profile is done in preparation of installing a flat top longitudinal laser profile in 2 months. Also the current longitudinal position of the main solenoid is optimised for the future flat top laser shape. All this means that better experimental results are expected in near future

REFERENCES

- [1] F. Stephan et. al. Photo injector test facility under construction at DESY Zeuthen, FEL 2000 Durham
- [2] K. Flöttmann, Pepper pot Design for Space Charge Dominated High Brightness Beams, TESLA- FEL 96-09, DESY, 1996.
- [3] P. Piot, Zeroth-order considerations for a single slit- based Emittance Diagnostics at the PITZ facility
- [4] K. Flöttmann, Some basic features of the beam emittance, Phys. Rev. ST Accel. Beams 6,

Development of a Bunch-Length Monitor with Sub-Picosecond Time Resolution and Single-Shot Capability*

Daniel Sütterlin¹, Volker Schlott¹, Hans Sigg¹, Heinz Jäckel²

¹ Paul Scherrer Institute, CH-5232 Villigen, Switzerland

² Institute of Electronics, ETHZ, CH-8092 Zürich, Switzerland

Abstract

A bunch-length monitor with single-shot capability is under development at the 100 MeV pre-injector LINAC of the Swiss Light Source (SLS). It is based on the electro-optical (EO) effect in a ZnTe crystal induced by coherent transition radiation (CTR). A spatial auto-correlation of the CTR in the EO-crystal rotates the polarisation of a mode-locked Nd:YAG laser to produce an image on an array detector representing the Fourier components of the CTR spectrum. Up to now a theoretical model for the emission of transition radiation has been developed in order to design optics allowing efficient transport of the CTR onto the EO-crystal. The frequency dependency of the CTR due to the finite size of the target screen has been measured in the sub-THz regime at the SLS LINAC. The results strongly support the theoretical descriptions of the radiation source. By expanding the intensity pattern in higher-order Laguerre-Gaussian modes, the transmission through the optical transfer system is calculated.

EO AUTO-CORRELATION

The electro-optical effect provides the potential to measure electron bunch lengths with sub-ps time resolution. A number of experiments have already been performed using the coincidence of fs-laser pulses with coherent radiation emitted from short electron bunches [1]. At the SLS, a novel bunch length monitor is under development, which uses an actively mode-locked Nd:YAG laser to analyse the spatial auto-correlation of CTR in an EO-crystal. A schematic set-up of the monitor is shown in fig. 1.

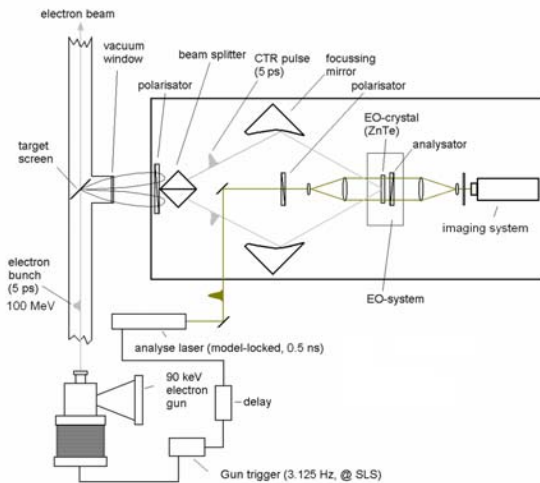


Figure 1: Schematic setup for EO-auto-correlation.

In this experiment, the synchronization of the laser with the CTR from the electron beam is not considered as critical due to the relatively long pulses of the Nd:YAG laser (< 500 ps), however the signal to noise ratio needs to be addressed more carefully.

The interference pattern produced by the auto-correlation of CTR in the EO-crystal can be expressed as:

$$I(\vec{r}, \omega) = 2I(\omega) \left[1 + \cos \left[2 \sin(\theta) \frac{\omega}{c} r_1 \right] \right] \quad (1),$$

where θ is the incident angle between the wave vector k and the normal vector n on the EO-crystal.

The power of the analyse laser is therefore modulated by the EO-crystal according to

$$I^{out} \approx I_{Laser} \left(\frac{\pi d}{V_{\lambda/2}} \right)^2 E_{CTR}^2. \quad (2)$$

$V_{\lambda/2}$ is the so-called half wave voltage necessary to rotate the laser polarisation by $\pi/2$:

$$V_{\lambda/2} = \frac{\lambda}{2n^3 r_{41}}. \quad (3)$$

For ZnTe the half wave voltage is 3.8 kV. Assuming a thickness of the electro-optical crystal of 0.5 mm the laser power modulated by a field of 1 kV/cm is $2 \cdot 10^{-3} I_{Laser}$.

Background intensity $B_{Background}$ and noise contributions have to be considered as well. According to eq. (1), the incoherent background is in the same order of magnitude as the signal itself. The most dominant noise sources, which contribute during the entire duration of the laser pulse (≈ 500 ps), are: the stray light scattered into the detector due to the limited extinction of the polarizer, the limited polarisation state of the laser beam and the strain induced birefringence of the electro-optical crystal. The weighted contributions are given by $\epsilon_{Polariser}$, ϵ_{Laser} and ϵ_{Strain} . Although polarisers with $\epsilon_{Polariser} < 10^{-5}$ are available, the experimentally achievable total extinction $\epsilon_{Total} = \epsilon_{Polariser} + \epsilon_{Laser} + \epsilon_{Strain}$ may thus not be better than 10^{-4} .

The resulting signal dynamic is given by

$$d_s = 10 \log_{10} \left(\frac{I_{Signal}}{I_{Signal} + B_{Background} + \epsilon_{Total}} \right) \quad (4).$$

With an assumed bunch length of 5 ps (at the SLS pre-injector LINAC) the signal dynamic is -8 dB. Assuming a detection system with a dynamic range d_N of about 30 dB (commercial CCD-camera) a signal to noise ratio defined as $d_{S/N} = d_N + d_s$ of > 20 dB is achievable for electric field strengths of more than 1 kV/cm.

EMISSION CHARACTERISTIC OF CTR

Although EO auto-correlation can be performed with different kind of coherent radiation sources, we are intending to use transition radiation (TR) in our experiments, since TR diagnostics ports, which are commonly used for the measurement of transverse beam parameters, are widely available in linear accelerators.

In general, TR is emitted when, uniformly moving charged particles cross the boundary between two media with different electric properties (dielectric constants). For the transition from vacuum ($\epsilon = 1$) to metal the TR intensity for a single electron is given by:

$$\frac{d^2 I}{d\omega d\Omega} = \frac{e^2 \beta^2}{4\pi^3 \epsilon_0 c} \frac{\sin^2(\theta)}{(1 - \beta^2 \cos^2(\theta))^2}. \quad (5)$$

The well known formula above has been derived by Ginzburg and Frank [2] and is valid for OTR only, as the target screen is assumed to be large compared to the wavelength of the emitted radiation. The CTR spectrum for electron bunches in the SLS pre-injector LINAC is settled in the frequency range below 1 THz. Therefore, the description of Ginzburg and Frank may prove to be insufficient. Hence, we apply a model for the emission characteristics of transition radiation, taking the finite target screen into account. For a relativistic electron travelling along the z-axis we define the longitudinal fourier transform by:

$$\hat{A}(\omega) := \int_{-\infty}^{\infty} A(\eta) e^{-i\eta\omega} d\eta = e^{-i\frac{z}{\beta c}\omega} \int_{-\infty}^{\infty} A(t) e^{-it\omega} dt \quad (6)$$

where $\eta := t - \frac{z}{v} = t - \frac{z}{\beta c}$.

The fourier components of the magnetic field [3] are proportional to $\hat{B}_0(r, \omega) \propto \frac{\omega}{c\gamma} K_1\left(\frac{\omega}{\beta c\gamma} r\right)$. (7)

The magnetic field is inducing currents j in the metallic target screen: $\hat{j}(r, k) = \vec{n} \times \hat{B}_0$ where \vec{n} is the normal vector on the target screen. These currents are acting as elementary electrical dipoles, which generate a vector potential calculated by the following expression

$$d\hat{A} = \frac{1}{4\pi} \hat{I} d\vec{r} \frac{e^{ikR(r, \varphi)}}{R(r, \varphi)}, \text{ where } \hat{I} = d\varphi \cdot \vec{r} \cdot \hat{j}. \quad (8)$$

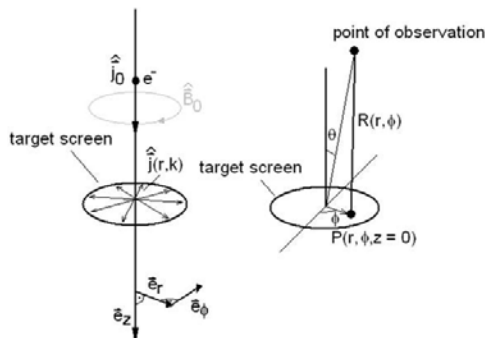


Figure 2: Left side: the magnetic field inducing currents. Right side: observation of radiation in the farfield.

For a single electron with normal incidence on a circular target screen the resulting intensity in the farfield is proportional to

$$\frac{d^2 I}{d\omega d\Omega} \propto \left| \frac{\omega^2}{c^2 \gamma} \int_0^{\text{Radius}} r K_1\left(\frac{\omega}{\beta c \gamma} r\right) J_1\left(\frac{\omega}{c} \sin(\theta) r\right) dr \right|^2 \quad (9)$$

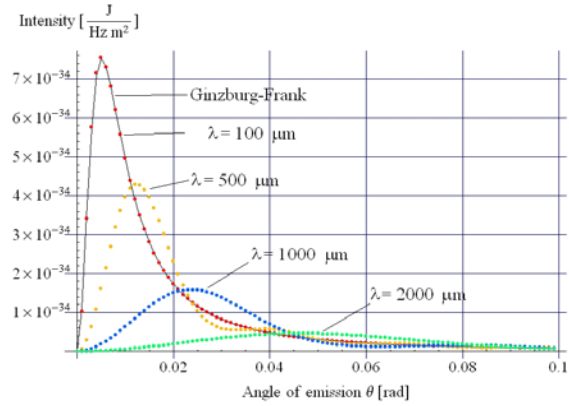


Figure 3: Emission characteristic of CTR for a single electron with normal incidence on a circular target screen of radius 19 mm. For wavelengths of $< 100 \mu\text{m}$ the characteristic agrees well with the expression (5) given by Ginzburg and Frank.

It can be seen, that the emission angle of TR increases drastically at longer wavelengths, where the coherent part of the emission spectrum from a short electron bunch is to be expected. This effect has to be considered for the design of a preferably efficient transport system to the EO auto-correlation experiment.

EXPERIMENTAL CHARACTERISATION

The emission characteristic of CTR was experimentally investigated at the diagnostic station ALIDI-SM-5 behind the 100 MeV SLS pre-injector LINAC. The transverse intensity distribution was mapped using polarizer grids and a PYE UNICAM golay cell detector, measured to be sensitive up to wavelengths of 1 cm.

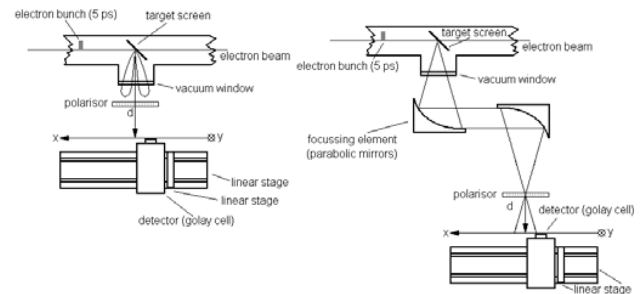


Figure 4: Set-up A (left): Mapping of the CTR farfield at a distance d of 250 mm from the source. Set-up B (right): Two parabolic mirrors with focal lengths of 200 mm and 60 mm diameter were used to produce an image of the source. The CTR intensity distribution was then measured at a distance of 70 mm from the focal plane.

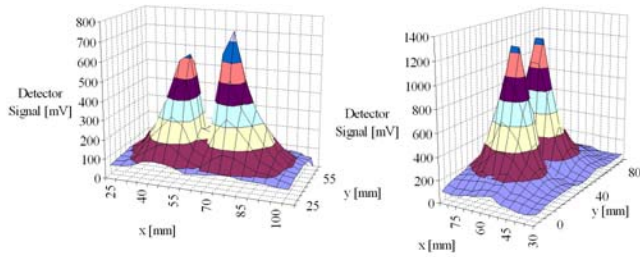


Figure 5: Intensity distribution of the horizontal (left) and vertical (right) polarization of CTR, measured at the SLS LINAC (set-up A). The asymmetry in the horizontal scan is predicted by the model when considering the target screen to be rotated by 45 degree into the electron beam.

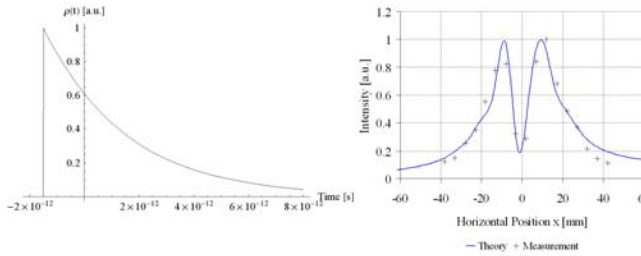


Figure 6: Cut through the horizontally polarized CTR intensity distribution (left side of fig. 5) compared with the theoretical curve for an electron distribution ρ as shown on the left side (3 ps).

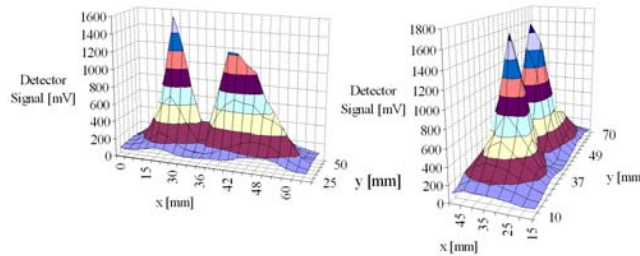


Figure 7: Scans of horizontal respectively vertical polarisation after passing the imaging optics of set-up B. The radial polarisation of CTR is conserved.

The emission angles of CTR as shown in figure 5 are 100 mrad and therefore considerably larger than the 10 mrad predicted by Ginzburg and Frank for an electron beam energy of 100 MeV. According to our theoretical description of CTR emission, the spectrum is dominated by frequencies above 100 GHz. The good agreement of our CTR emission model with the experimental data allows the expansion of the transverse CTR intensity distribution in higher-order Laguerre-Gaussian modes. Subsequent propagation of CTR through an optical system can thus be described as a superposition of higher-order modes of a Gaussian beam. In this description an optical element with a certain aperture is acting like a high-pass filter cutting off the disperse intensity at low frequencies. Hence, the transmission function of an optical system can be calculated accordingly.

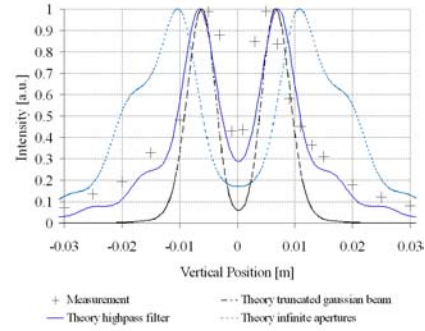


Figure 8: Calculated transmission through set-up B for the superposition of (only) 10 Laguerre-Gaussian modes (same electron distribution as assumed for fig. 6). Pointed line: Infinite apertures. Point-dashed line: Truncated due to mirror apertures. Full-line: The two parabolic mirrors treated as high-pass filters with $\nu_{\text{cutoff}} = 300$ GHz.

The peak field strength of CTR achievable at the SLS pre-injector LINAC was measured in order to estimate the CTR intensity distribution in the EO-crystal.

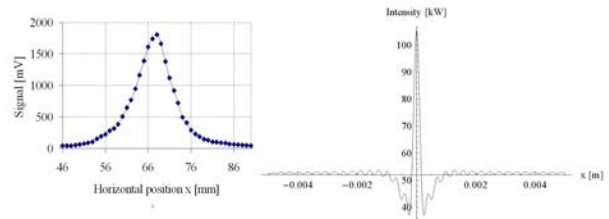


Figure 9: Left side: Horizontal scan of CTR in the focal plane of set-up B. The peak field strength exceeds 3 kV/cm. Right side: Simulated intensity pattern on the EO-crystal (acc. to eq. 1), assuming 3 optical elements with $\nu_{\text{cutoff}} = 300$ GHz and the same electron distribution as assumed for fig. 6 with 0.5 nC.

SUMMARY

A theoretical model for the CTR emission has been presented and confirmed by experimental data. Expansion of the CTR intensity distribution in higher-order modes of a Gaussian beam allows the determination of the transfer function of an optical system. CTR intensities were calculated based on the SLS pre-injector LINAC parameters, exceeding the peak electric field strengths of 1 kV/m, required for the proposed EO auto-correlation experiment.

REFERENCES

- [1] X. Yan et al., Subpicosecond EO-Measurement of Relativistic Electron Pulses. PRL, Vol. 85,16 (2000).
- [2] V.L. Ginzburg, I. Frank, J. Phys. USSR 9, 353(1945).
- [3] N.F. Shul'ga et al., Theory of Relativistic-Electron TR in a Thin Metal Target, Atoms, Spectra, Radiation Vol. 90,4 (2000).

*Funding: SNF (Schweizer National Fonds)

FAST TUNE MEASUREMENT SYSTEM FOR THE ELETTRA BOOSTER

S. Bassanese, M. Ferianis, F. Iazzourene Sincrotrone Trieste, S.S. 14 Km163.5, 34012 Trieste, ITALY

Abstract

A major upgrade of the ELETTRA injector is currently on going: the 1GeV Linac will be replaced with a 100MeV Linac and a 2.5GeV Booster Synchrotron, cycling at 3Hz. A new set of diagnostics is under development for these two new machines. The new Fast Tune measurement system for the Booster represents a significant improvement as compared to the present Tune measurement system.

To completely characterise the dynamics of the Booster during the energy ramp, whose duration is 160ms, a set of 25 tune values is required, corresponding to a 6.4ms interval between successive measurements. The accuracy of this measurement is $<10^{-3}$. Such frequency spans are achievable using a Real Time Spectrum Analyser (RTSA) from Tektronix, which is a fast sampling instrument with built-in FFT algorithm and data presentation.

In this paper, after describing the system specifications and architecture, we present the results of the preliminary tests, which have been carried out both in the laboratory and on the Storage Ring.

INTRODUCTION

The new injector, which will replace the 1GeV Linac, is a new 100MeV Linac and a 2.5GeV Booster synchrotron. Full energy injection and top-up operation of the Storage Ring are the driving forces for this major machine upgrade. This new operating condition (constant current and energy) will greatly improve the stability of the ELETTRA light source as both the Storage Ring and the Beam lines will work under stationary conditions.

The development of the new diagnostics has started and it includes a new fast tune measurement system for the Booster synchrotron. Compared to the present Tune System [1], the performance up-grade mainly concerns the tune measurement rate, which will be shifted from the present 0.5Hz to 200Hz.

Actually for sake of reliability there will be two systems measuring the Booster Tunes, independently: the one described in this paper, based on the RTSA, and a second system, based on the Digital BPM Detector, already in use at ELETTRA [2]. The first one is believed to be useful especially during Booster commissioning, due to the convenient data presentation provided by the RTSA [3] as spectrograms. The second one will be installed as an Automatic Tune Measurement system, continuously checking the mean tunes.

In this paper we present the design of the fast tune measurement system based on the RTSA and the tests, performed on the Storage Ring, with the prototype of the new system. Full advantage has been taken from recently available new instruments, called Real Time Spectrum

Analyzers. The tests carried out confirmed our expectations on performance improvement.

SYSTEM DESCRIPTION

The specifications for the fast tune measurement system require the real time measurement of horizontal and vertical tune and chromaticity during the energy ramp.

The time variation of the bending magnetic field during the ramping cycle of the Booster produces an eddy current in the metallic vacuum chamber of the bending magnet [4]: the main effect is an induced time-varying sextupolar component. To fully characterize the chromaticity variation and to keep it at the desired values [5], a minimum of 25 measurements per ramp is required, with a frequency resolution of 10^{-3} . The nominal duration of a ramp is 160ms, but it will go up to 1s during the commissioning phase of the Booster, which calls also for the system to be flexible.

Tune excitation and detection

A block diagram of the system is shown in fig. 1. A white noise excitation scheme has been adopted which is band-limited around the expected tune frequencies. The limited bandwidth of the excitation signal allows a more efficient use of the power amplifier.

The output of a white noise generator is band-pass filtered and amplified by a wide-band power amplifier. During preliminary tests, carried out on the ELETTRA Storage Ring at 2GeV, 50W (in a 100 kHz bandwidth) of diagonal excitation produced tune peaks of -71dBm over a noise floor of -95dBm . Therefore, the Amplifier Research model 150A100B, a 150W amplifier with a bandwidth 10KHz-100MHz, has been selected for beam excitation. A strip-line kicker, equipped with four 50 Ω electrodes, will be used for both single plane (Horizontal or Vertical) and Diagonal excitation.

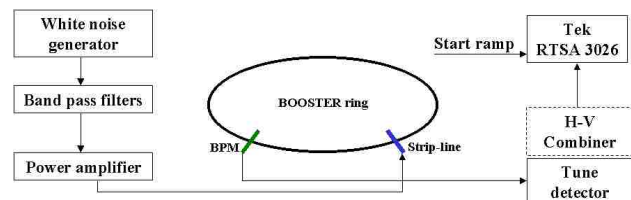


Figure 1: Fast Tune measurement system block Diagram

The transverse beam oscillations will be picked-up by a dedicated Beam Position Monitor placed at a high beta (β_v, β_h) location; the 500MHz signals from the BPM will be down converted by the ELETTRA Tune Detector [1].

The two outputs of the Detector provide the horizontal and vertical components of the betatron oscillations in base band. These signals will be summed up and delivered to the RTSA 3026 from Tektronix.

Final Integration of the System

The fast tune measurement system will be integrated in the new injector control system by means of client/server architecture (see fig.2). Nevertheless, as the presentation of the measurement data by means of spectrograms is convenient for the machine operators, the RTSA monitor will be made available in the Control Room, through a VGA fibre optic extender.

The RTSA functions will be accessed through macro-tasks, eliminating the need for the end user to be aware of all the settings and commands of the instrument itself.

A Motorola MVME 5100 VME CPU, running Linux [6], will control the fast tune measurement and interface it to the control system through the main Ethernet port. A GPIB [7] card from National Instrument (directly plugged into the PMC port of the CPU) will control both the RTSA and the power amplifier: a dedicated software driver is currently under development. The second Ethernet port, linked to the RTSA Ethernet port, will allow the direct download of the saved data without accessing the LAN. A digital I/O port will control the switch box for the selected excitation scheme (single plane or diagonal). The measurement macro-tasks will run on the low level CPU as requested by the operator.

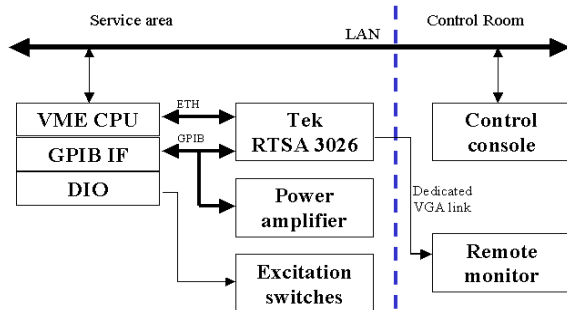


Figure 2: Integration of the system in the control system

THE RT SPECTRUM ANALYZER

The RTSA performs a real time frequency analysis of the input signal from its time samples, taken at 25.6 MS/s; the results are displayed on a spectrogram which is a 2D colour plot showing subsequent spectra vs. time, in much same way as on the Tektronix 3052 [8]. On each line of the spectrogram, a spectrum is represented; the amplitudes of the frequency components of each line are represented with colour grading. The measurement results can be stored on a local disk. Two operating modes are available: in Roll mode the instrument continuously acquires, computes and presents the data at a low refresh rate. In Block mode the RTSA, after having acquired all the necessary data to build the spectrogram over whole time interval, performs the calculations. By doing so the Block mode assures the maximum time resolution of the spectrogram where subsequent spectra are taken at fixed time intervals. With a 1024 point FFT a new 200 KHz spectrum is obtained every 400µs. Furthermore, in Block mode the acquisitions can be triggered by an external signal

Description of the Block Mode

In Block mode each measurement session is made up of a predefined number of blocks (fig. 3), each block starting with the predefined trigger event. In a similar way, each block is made up of a predefined number of frames, each frame holding one spectrum. The time resolution of the spectrogram is the time distance between each frame.

At the end of each acquisition the RTSA computes the spectrum of each frame and presents the data.

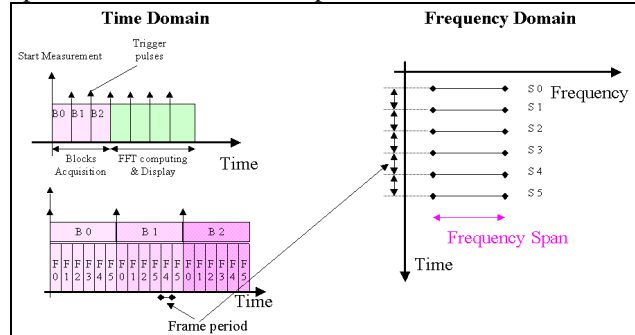


Figure 3: block mode acquisition

According to the FFT algorithm, once the number of points of the spectrum (N) has been fixed, they are obtained from twice as much samples (2N). Therefore, the narrower the spectrum span, the longer the frame duration according to the relation

$$\Delta T = \frac{1}{\Delta f} = \frac{1}{Span/N} = \frac{N}{Span}$$

where N is the number of the spectrum points (fixed by the manufacturer, N=640), ΔT is the frame length and Δf is the spectrum resolution.

Therefore, the higher the frequency resolution is, the longer the frame duration. Successive frames can be either adjacent or separated in time. The time between two successive frames is the frame period.

RTSA SET UP FOR THE BOOSTER

Single or multiple ramp block mode acquisitions have been foreseen for the Booster tune measurement, each block triggered by a "Start Ramp" pulse. With the following frequency spans (200, 100 and 50 KHz) a minimum frame period of 400µs is achievable. With the 20 KHz span this minimum frame period is 4ms: up to 40 spectra per ramp can be acquired for a maximum number of 25 consecutive ramps.

Development set-up

The RTSA is a field test instrument dedicated to cellular phone systems with some features not directly linked to our application that may render it not of immediate use. Furthermore, we decided to thoroughly test the RTSA and its command set before its final use.

Therefore, a Man-Machine Interface (MMI) has been developed as a NI LabVIEW application and some post processing tools have been implemented to check data transfer from the instrument (i.e. Tune frequencies vs. time). This system will be installed on the ELETTRA

storage ring for a complete test before its final implementation on the Booster.

MEASUREMENT RESULTS

First a complete characterization has been carried out in the laboratory (fig. 4) to test the different operation modes of the RTSA, its sensitivity both in time and frequency.

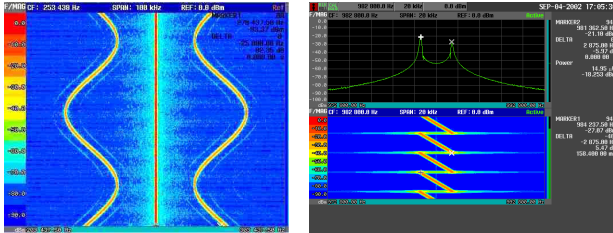


Figure 4 LEFT: spectrogram obtained in the laboratory showing a 250 KHz carrier, amplitude modulated ($F_{mod}=25\text{ KHz}\pm 10\text{ KHz}$). RIGHT: laboratory spectrogram of a frequency swept carrier ($f_c=982.8\text{ KHz}$) with a 160ms ramp ($\Delta f=\pm 1.5\text{ KHz}$).

Then, a series of measurements have been carried out on the Storage Ring to fully characterize the excitation schemes including the Power amplifier. Finally, real beam measurements have been performed to define the RTSA final configuration.

In figure 5, the effect on the vertical tune due to a periodic perturbation of a vertical corrector is shown. In figure 6, a dynamic measurement of the vertical (left) and horizontal (right) tune is shown during an energy ramp of the Storage Ring: a strong deviation of the horizontal tune is visible which led to a partial beam loss.

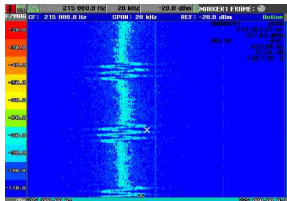


Figure 5 Measurement of the Vertical Tune: a variation was induced in the beam using a vertical corrector; 3 cycles of sine burst were applied at 20Hz. $\Delta f_{pk-pk}=2770\text{Hz}$

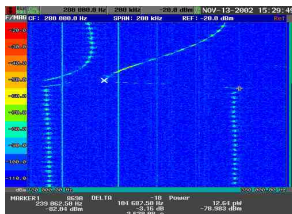


Figure 6: Dynamic measurement of both tunes during an energy ramp, horizontal tune is on the right. The cursor is located after the resonance, which can be easily recognized after amplitude increase (-59dBm). The dotted traces are due to the 1Hz switching of the excitation plane, used on the Storage Ring.

Dynamic Measurement of the Chromaticity

To further analyse the capabilities of the new system, in particular the dynamic ones, a preliminary dynamic measurement of the chromaticity has been performed on the Storage Ring. By applying an external modulating signal ($f=3\text{ to }5\text{ Hz}$) to the Master Generator of the Storage Ring Radio frequency system, with a peak to peak RF frequency change of 4kHz. The SR chromaticity was set to +2.2 in both planes. Measurement results are shown in figure 7 for the vertical plane.

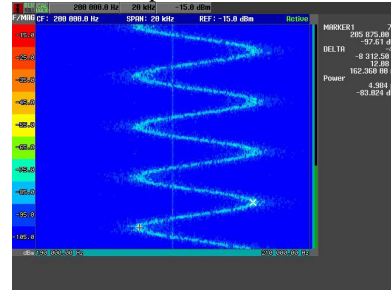


Figure 7: Chromaticity Measurement Vertical plane

The peak-to-peak changes of the tune have been compared to the values measured with standard tune measurement system (static measurement). The dynamic measurement showed a smaller tune variation, by 30%. Further measurements are foreseen to complete our experiment.

CONCLUSIONS

The Real Time Spectrum Analyzer 3026 proves to be adequate for the fast tune measurement of the ELETTRA Booster. Its frequency analysis characteristics and its data presentation in form of spectrograms have allowed rapid development of the prototype system. Integration in the final control system will start as soon as the on-field use phase will be completed.

REFERENCES

- [1] A.Carniel, R. De Monte, L.Tosi "Tune Feedback System at ELETTRA" EPAC'94, London, June 1994.
- [2] M. Ferianis, R. De Monte, "The Low Gap BPM System at ELETTRA: Commissioning results" Dipac 2001, Grenoble
- [3] 3026, 3GHz RTSA; Sony-Tektronix Corp. Tokyo.
- [4] G. Emmie, J. Rossbach, "Eddy Current Effects in the DESY-II Dipole vacuum chamber" DESY M-84-05, April 1984
- [5] F.Iazzourene, "Chromaticity and Dynamic aperture simulations for the ELETTRA Booster Synchrotron". To be published
- [6] Yellow Dog Linux (www.yellowdoglinux.com)
- [7] PMC-GPIB, NI488DDK, National Instruments product catalogue
- [8] Tektronix 3052, Digital Spectrum Analyzer, Data Sheet 1989.

CRYOGENIC CURRENT COMPARATOR FOR ABSOLUTE MEASUREMENTS OF THE DARK CURRENT OF SUPERCONDUCTING CAVITIES FOR TESLA

K. Knaack, M. Wendt, K. Wittenburg, DESY Hamburg
R. Neubert, S. Nietzsche, W. Vodel, Friedrich Schiller Universität Jena
A. Peters, GSI Darmstadt

Abstract

A measurement system for detecting dark currents, generated by the TESLA cavities, is proposed. It is based on the cryogenic current comparator principle and senses dark currents down to the nA range. Design issues and the application for the CHECHIA cavity test stand are discussed.

1. INTRODUCTION

The 2x250 GeV/c TESLA linear collider project, currently under study at DESY [1], is based on the technology of superconducting L-band (1.3 GHz) cavities. The two 10.9 km long main linacs are equipped with a total of 21024 cavities. A gradient of 23.4 MV/m is required for a so-called superstructure arrangement of couples of 9-cell cavities. To meet the 2x400 GeV/c energy upgrade specifications, higher gradients of 35 MV/m are mandatory.

Dark current, due to emission of electrons in these high gradient fields, is an unwanted particle source. Two issues are of main concern, thermal load and propagating dark current [2].

Recent studies [3] show, that the second case seems to be the more critical one. It limits the acceptable dark current on the beam pipe "exit" of a TESLA 9-cell cavity to approximately 50 nA. Therefore the mass-production of high-gradient cavities with minimum field emission requires a precise, reliable measurement of the dark current in absolute values. The presented apparatus senses dark currents in the nA range. It is based on the cryogenic current comparator (CCC) principle, which includes a superconducting field sensor (SQUID). The setup contains a faraday cup and will be housed in the cryostat of the CHECHIA cavity test stand.

2. REQUIREMENTS OF THE DARK CURRENT INSTRUMENT

Electrons can leave the niobium cavity material, if the force of an applied external electric field is higher than the bounding forces inside the crystal structure. The highest field gradients occur at corners, spikes or other discontinuities, due to imperfections of the cavity shape. Another potential field emitter is due to any kind of imperfection on the crystal matter, like grain boundaries, inclusion of "foreign" contaminants (microparticles of e.g.

In, Fe, Cr, Si, Cu) and other material inhomogeneous. At these imperfections the bounding forces are reduced and electrons are emitted under the applied high electromagnetic fields [4]. With a series of special treatments the inner surface of the TESLA cavities are processed to minimize these effects. A reliable, absolute measurement of the dark current allows the comparison of different processing methods and a quality control in the future mass-production.

TESLA will be operated in a pulse mode with 5 Hz repetition rate. The 1.3 GHz rf pulse duration is 950 μ s. During this time the dark current is present and has to be measured. Therefore a bandwidth of 1 kHz of the dark current instrument is sufficient. As field emission is a statistical process, the electrons leave the cavity on both ends of the beam pipe. Thus, half of the dark current exits at each side, and has to be measure on one side only. With the 1.3 GHz rf applied, we expect that the dark current has a strong amplitude modulation at this frequency. This frequency has to be rejected from the instrument electronics to insure its proper operation. The dark current limits and the related energy range of the electrons are shown in Table 1.

Parameters	9-cell test cavity in CHECHIA	TESLA cavity modules (12x9-cell cavity)
Energy of dark current electrons	up to 25....40 MeV	up to 350....560 MeV
dark current limits	< 50 nA	< 1 μ A

Table 1: Expected dark current parameters

The use of a faraday cup as dark current detector for the TESLA cavity string will suffer from the high electron energies and low currents. The capture of all secondary electrons in the stopper are challenging. The use of a cryogenic current comparator as dark current sensor has some advantages:

- measurement of the absolute value of the dark current,
- independence of the electron trajectories,
- simple calibration with a wire loop,
- high resolution,
- the electron energies are of no concern.

The required liquid He temperature for the CCC and the cryogenic infrastructure for the whole apparatus will be provided by the CHECHIA test stand. An effective shielding to external magnetic fields has to be considered,

because the CCC detector measures the magnetic field of the dark current. At GSI Darmstadt a CCC detector system has demonstrated its excellent capabilities to measure ion currents in the extraction beam line of the heavy ion synchrotron [5].

3. PRINCIPLE OF THE CRYOGENIC CURRENT COMPARATOR (CCC)

A CCC is mainly composed of a superconducting pickup coil, a highly effective superconducting shield, and a high performance SQUID measurement system (Fig. 1):

In principle, the CCC, first developed by Harvey in 1972, is a non-destructive method to compare two currents I_1 and I_2 (see Fig. 1) with the high precision of a SQUID. For that reason, the two currents are fed into a superconducting tube with a special pick-up coil as antenna. Using a meander-shaped flux transducer only the azimuthal magnetic field components which are proportional to the currents in the wires will be sensed by the SQUID. All other field components are strongly suppressed. A more detailed description can be found in [5].

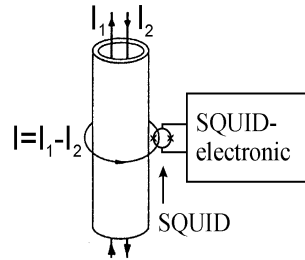


Fig.1: Principle of the Cryogenic Current Comparator

4. THE CHECHIA CCC DESIGN

The dark current CCC design is realized as co-operation of DESY, FSU and GSI. The instrument will be placed in the CHECHIA cavity test stand and operates at 4.2 K.

4.1 Pickup Coil

A single turn pickup coil is formed as superconducting niobium toroid with a slot around the circumference. It contains a VITROVAC 6025-F core (Vacuumschmelze GmbH, Hanau, Germany) providing high permeability and low noise even at liquid helium temperatures. The material inhomogeneities of the core are averaged by complete encapsulation of a toroidal niobium coil.

4.2 Shielding Aspects

The resolution of the CCC is reduced if the toroidal pickup coil operates in presence of external magnetic fields. As external fields are in practice unavoidable, an effective shielding has to be applied. A circular meander-shaped shielding structure ("ring cavities", Fig. 2) is able to pass the azimuthal magnetic fields of the dark current, while strongly attenuating non-azimuthal field components. Using a superconductive shielding material like niobium leads to an ideal diamagnetic conductor, which implies the vanishing of all normal components of the magnetic fields at the superconductive surface. The attenuation characteristics of CCC shieldings were analyzed analytic

in great detail [6-8]. Applied to the shielding of the proposed TESLA CCC with a inner radius of 69.0 mm, an outer radius of 112 mm, 14 "ring cavities" and a meander slot width of 0.5 mm an attenuation factor of approximately 120 dB for transverse, non-azimuthal magnetic field components is estimated. This result is based on the superposition of the analytic results for the different shielding substructures, here: coaxial cylinders and "ring cavities" (shown in [9]).

A numerical analysis was set up for verification. To compare with the analytic computations, first the numerical approach on the coaxial cylinders was tested. A pill box cavity was used to apply external fields of first order (magnetic dipole). In this way it was possible to use the MAFIA eigenmodesolver E in simple 2D r_z -coordinates, analyzing the dipole modes. For a ratio $r_a/r_i = 1.1$ the analytic result of [6] could be verified to a few percent (radial components of the magnetic fields of the first eigenmode). Applying this numerical method to the actual shielding structure gives a minimum attenuation of 94 dB, which seems to be more realistic.

The same numerical method was used to study the shielding efficiency at rf. Now TM monopole modes are excited, which apply the same azimuthal fields as the dark current. The attenuation through the shielding structure at frequencies > 900 MHz is very high. It is in the negligible range of 200 dB. This gives confidence, that the strong 1.3 GHz component will be suppressed sufficiently.

4.3 SQUID Measurement System

The key component of the CCC is a high performance SQUID system developed and manufactured at the FSU Jena. A detailed description of the functional principle of the SQUID measurement system is given in [5].

In a DC coupled feedback loop, the field of the dark current to be measured is compensated at the SQUID by an external magnetic field provided from the SQUID electronics (Fig. 3). Both the SQUID input coil and the pickup coil form a closed superconducting loop so that the CCC is able to detect DC currents. Using a modulation frequency of 307.2 kHz results in a bandwidth of about 70 kHz. Thus, it will be possible to characterize the pulse shape of the dark current beam (950 μ s pulse length, 5 Hz repetition rate) which is overlaid by the RF structure applied to the cavities. Currently the SQUID measurement system is ready for use. The first measurements with all special cabling and feedthroughs were successfully done and a current system sensitivity of $167 \text{ nA}/\Phi_0$

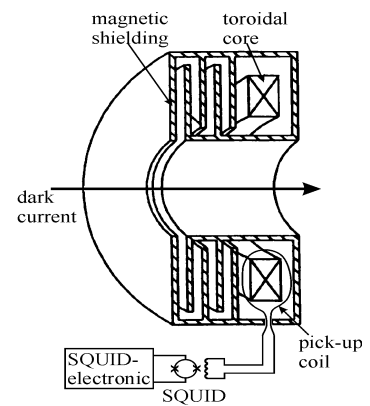


Figure 2: Schematic view of magnetic shielding, pickup coil and SQUID system

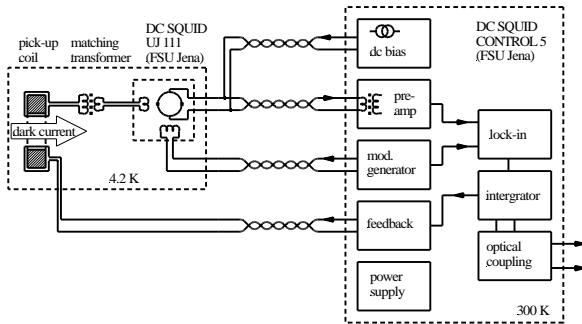


Figure 3: Simplified electrical scheme of the CCC

was achieved using a special pick-up coil to emulate the real pick-up coil under fabrication. The flux noise of the whole system was measured to be as low as $8 \times 10^{-5} \Phi_0/\sqrt{\text{Hz}}$ in the white noise region (see Fig. 5). These values correspond to a noise limited current resolution of the CCC as low as 13 pA/ $\sqrt{\text{Hz}}$. According to our experience, in the final system the resolution will be decreased by at least one order of magnitude because of the additional noise contribution of the VITROVAC core of the pick-up coil.

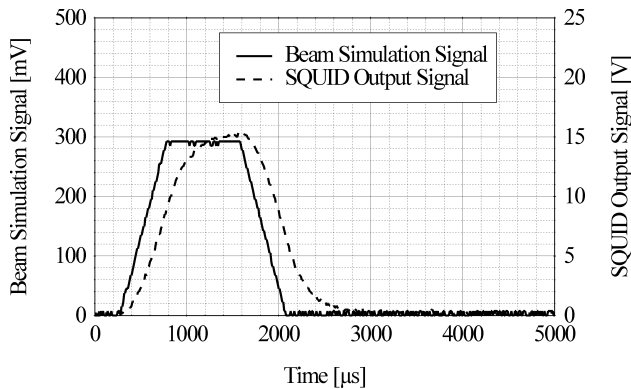


Figure 4: SQUID response and test signal

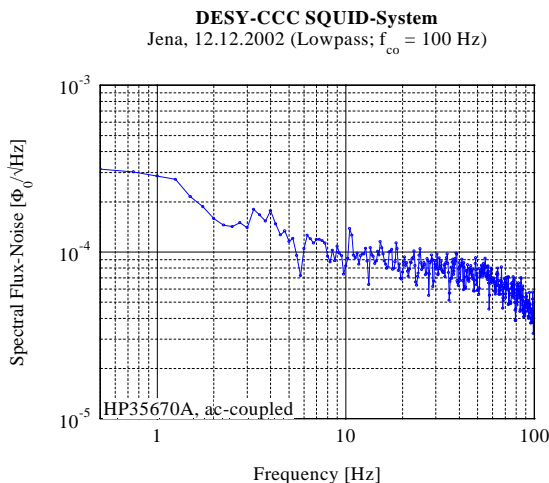


Figure 5: Spectral noise density

4.4 Faraday Cup

This design for the CHECHIA test stand includes a faraday cup in order to compare the CCC dark current measurements. Otherwise, the energy of the dark current electrons is so small that they will be stopped completely in a small faraday cup (Fig. 6). The current to ground will be measured by an electronics. A HV-screen will collect the secondaries from the stopper electrode.

In the TESLA cavity-module test stand the energy of the dark current electrons will reach much higher energies (Table 1). In this case the measurement with a faraday-cup is not possible. The size of the Faraday-cup will become very large and the HV-screen will not collect all of the electrons.

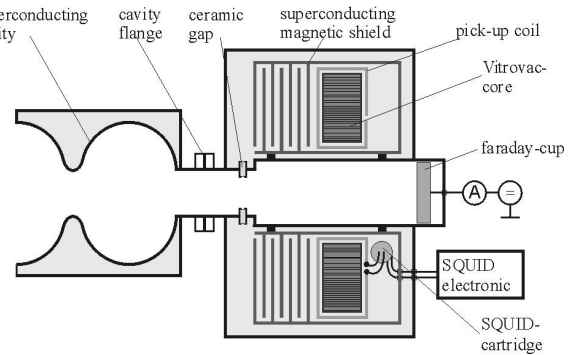


Figure 6: Schematic Design of the CHECHIA CCC

5. OUTLOOK

The mechanical construction of the CHECHIA CCC is completed and the fabrication started with the magnetic shielding and the pick-up coil, which are the most sophisticated mechanical parts.

The results of the next test-setup, consisting of the SQUID electronics and the completed superconducting shielding including the pick-up coil, will be shown at the EUCAS conference in autumn of this year.

6. REFERENCES

- [1] R. Brinkmann, et. al.; TESLA Technical Design Report
- [2] C. Stolzenburg, Untersuchungen zur Entstehung von Dunkelströmen in supraleitenden Beschleunigungsstrukturen, Ph. D. Thesis, Hamburg University 1996
- [3] R. Brinkmann; Dark Current Issues; TESLA Collab. Meeting - CEA Saclay 4/2002
- [4] G. R. Werner, et. al.; Proc. of the Part. Acc. Conf. PAC 01, pp.1071-73
- [5] A. Peters, W. Vodel, H. Koch, R. Neubert, C.H. Schroeder; Proc. of 8th BIW, Stanford, 1998, AIP Conf. Proc. 451
- [6] K. Grohmann, et. al.; CRYOGENICS, July 1976, pp.423-429
- [7] K. Grohmann, et. al.; CRYOGENICS, October 1976, pp.601-605
- [8] K. Grohmann and D. Hechtfischer; CRYOGENICS, October 1977, pp.579-581
- [9] P. Gutmann and H. Bachmair; in V. Kose, Superconducting Quantum Electronics, 1989, pp.255-259

A 40MHZ BUNCH BY BUNCH INTENSITY MEASUREMENT FOR THE CERN SPS AND LHC.

H. Jakob, L. Jensen, R. Jones[#], J.J. Savioz, CERN, Geneva, Switzerland

Abstract

A new acquisition system has been developed to allow the measurement of the individual intensity of each bunch in a 40MHz bunch train. Such a system will be used for the measurement of LHC type beams after extraction from the CERN-PS right through to the dump lines of the CERN-LHC. The method is based on integrating the analogue signal supplied by a Fast Beam Current Transformer at a frequency of 40MHz. This has been made possible with the use of a fast integration ASIC developed by the University of Clermont-Ferrand, France, for the LHC-b pre-shower detector. The output of the integrator is digitised using a 12-bit ADC and fed into a Digital Acquisition Board (DAB) that was originally developed by TRIUMF, Canada, for use in the LHC orbit system. A full system set-up was commissioned during 2002 in the CERN-SPS, and following its success will now be extended in 2003 to cover the PS to SPS transfer lines and the new TT40 LHC extraction channel.

INTRODUCTION

In order to be able to evaluate the quality of the LHC beam before its extraction from the CERN-SPS it was necessary to develop a beam intensity measurement capable of distinguishing between the individual LHC bunches spaced by 25ns. This system was also foreseen for beam optimisation, allowing the operators to see the intensity structure of the beam throughout the SPS cycle, providing information on where in the batch losses are occurring and at what time. Since the same system was to be installed in the PS to SPS transfer lines it was important that the same electronics was capable of measuring standard, 200MHz structure SPS fixed target beams. To this end a new beam current transformer (BCT) system has been developed and installed in the SPS and its transfer lines. This is comprised of a commercial fast BCT, a specially adapted housing, a calibration unit, an integrator card containing a fast 40MHz integrator ASIC and a digital acquisition readout. There are currently 4 such systems installed in the SPS, one at each end of the PS to SPS transfer lines, one in the SPS ring itself, and one in the TT40 extraction channel towards the LHC and CNGS. A further 4 systems will be installed over the coming years: 3 completing the layout for the LHC transfer lines and one in front of the CNGS target station.

THE SPS FAST BCT SYSTEM

The Fast Beam Current Transformer

The new fast beam current measurement in the SPS makes use of commercially available Bergoz low-droop,

passive, fast beam current transformer (FBCT) as the detection device. The 40 winding core used has a frequency response up to ~400MHz and a droop of less than 0.1% per microsecond. This low droop is important if difficult baseline correction is to be avoided during the passage of the beam. The FBCT is installed in a specially designed housing aimed at maintaining a clean signal response (see Fig. 1). An 80nm titanium coating is applied to the vacuum side of the ceramic gap, giving a series resistance of ~20Ω and effectively damping any cavity resonances.

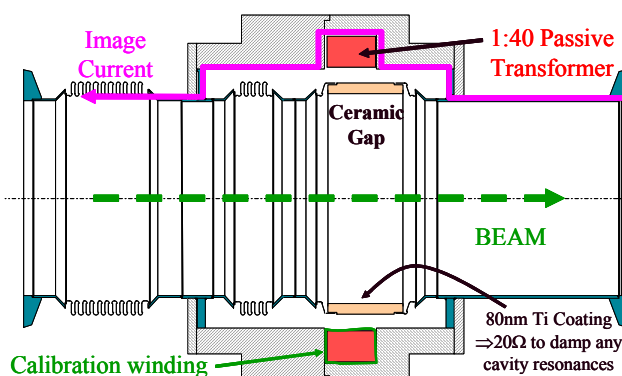


Figure 1. Schematic of the SPS Fast BCT

A calibration winding has been added to the transformer core to allow the injection of a 5μs, 128mA calibration pulse generated on demand by a switchable current source. This provides the absolute calibration for the system and corresponds to 2×10^{10} charges in 25ns.

Fig.2 shows the typical response of the FBCT to LHC type beam. Each of the 4 batches visible contain 72 bunches separated by 25ns.

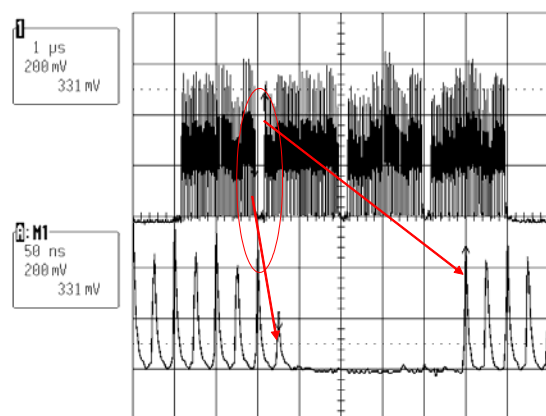


Figure 2. SPS Fast BCT response to LHC type beam.

[#]Rhodri.Jones@cern.ch

The 40MHz Integration Card

The output of the FBCT is fed into a 40MHz integration card which performs both the integration and the AD conversion. The card is based around a 40MHz integration ASIC developed by the Laboratoire de Physique Corpusculaire, Université Blaise Pascal, Clermont-Ferrand for use in the LHC-b preshower detector [1]. The ASIC has 8 individual channels capable of integrating at up to 40MHz. Each channel consists of 2 separate integrators followed by track & hold circuitry working at 20MHz. While one integrator integrates, the other discharges, with the track and hold outputs multiplexed to give an effective integration frequency of 40MHz (see Fig 3).

A 50Ω input of $\pm 3\text{nV}$ s, equivalent to $\pm 120\text{mV}$ for 25ns, gives $\pm 1\text{V}$ at the output. In practice only one channel is used for the FBCT application, with the output digitised by a 40MHz, 12-bit ADC. In order to be able to take into account the DC offset introduced into the system by a circulating beam the ADC is configured to be bipolar. This means that a single measurement effective uses only 11 bits. The FBCT input signal is attenuated to give a full scale ADC output corresponding to 2×10^{11} charges in 25ns, allowing it to handle the ultimate LHC bunch intensity of 1.7×10^{11} charges.

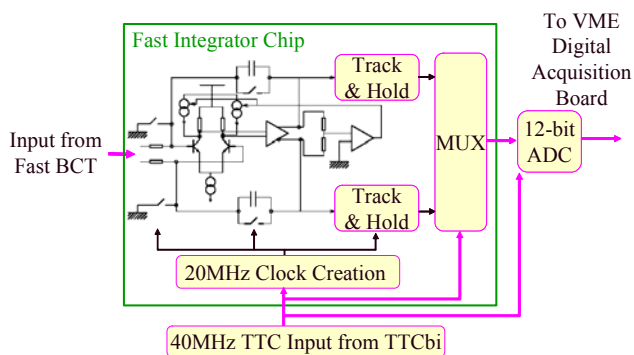


Figure 3. Schematic of the FBCT 40MHz integrator mezzanine card

Fig. 4 shows the measured response of the 2 individual integrators within a selected channel to a DC input voltage. As can be seen the individual integrators are highly linear but have slightly different gains. The reason for this difference is twofold: the simple gain difference between integrators and a difference in the effective integration time of the two integrators. The latter is clearly visible if the DC results are compared to the response to a pulsed signal ($\ll 25\text{ns}$) of the same effective charge per 25ns period. The simple gain difference of the two integrators can be calculated directly from the difference in the pulsed response (in this case negligible), while the effective integration time can be inferred from the difference between the DC and pulsed values. Each integrator typically integrates for between 20ns and 23ns of each 25ns clock period.

The integration and ADC clocks are derived from the SPS 40MHz bunch synchronous timing, distributed using the Timing, Trigger and Control (TTC) system developed for the LHC [2]. A reset of the integrators is performed on each turn clock to ensure that the same integrator is always used for a given 25ns acquisition window.

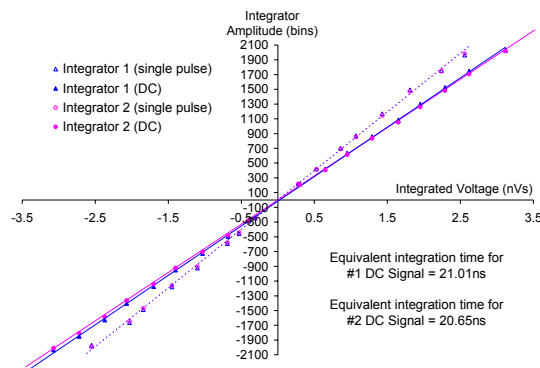


Figure 3. Comparison of the DC and pulsed response of both integrators for a single channel

Data Treatment and Display

The 40MHz integration card has been developed as a mezzanine card to the Digital Acquisition Board (DAB), a VME board developed by TRIUMF, Canada for the LHC orbit and trajectory acquisition system [3]. A single DAB is capable of handling two 12-bit 40MHz input streams, and is quickly becoming the standard data treatment board for all 40MHz LHC related beam instrumentation applications.

For the FBCT application, the DAB is used in its so-called “capture” mode, a single shot acquisition of a user specified number of bunches and turns. For the transfer line FBCTs an acquisition is performed at every injection, while for the SPS ring FBCT, data is acquired at 100ms intervals throughout the SPS cycle. On completion of an acquisition the DAB generates an interrupt for the local controller, a PowerPC running Lynx-OS. This PowerPC is responsible for reading the acquired data and applying the calibration procedure.

The calibration procedure differs depending on whether the FBCT measures DC or pulsed beams. Here DC is taken to mean any beam for which the 25ns integration effectively filters the bunch to bunch response, e.g. for standard SPS 200MHz fixed target beams. In both pulsed and DC cases the turn preceding the injection, or for the circulating beam the beam dump gap, is used to calculate the average offset for each integrator. This can then be subtracted from the data of interest.

In DC mode integrator number 2 is simply gain corrected with respect to integrator number 1 using the values measured in the laboratory. The final value for each integrator is then converted to charges per 25ns by comparing the result with that obtained for a calibration pulse equivalent to 2×10^{10} charges in 25ns.

In pulsed mode, i.e. for bunches spaced by 25ns or more, the value obtained for each integrator is first adjusted using the known individual integration times to obtain the equivalent DC value. The calibration then proceeds as described for the DC case.

A graphical user interface allows the operator to select the bunches of interest and to compare the evolution of these bunches throughout the SPS cycle.

SPS RESULTS IN 2002 & 2003

Use of the FBCT for Beam Optimisation

The first tests of the new fast BCT system were performed in 2002 using the monitor located in the SPS ring. All acquisitions were taken using LHC type beam, with up to 4 batches of 72 bunches separated by 25ns. Fig. 4 shows an example of the type of information available from such a system. In this case there was a poor RF capture of the first batch after injection. The uncaptured beam can clearly be seen to drift away from the batch, slowly dispersing itself around the SPS ring.

Other studies which will benefit from this system are the investigation of instabilities such as the electron cloud phenomenon in the SPS, where losses tend to occur towards the tail of each batch. The system is also intended to be used as part of the beam quality interlock for all beams destined for the LHC.

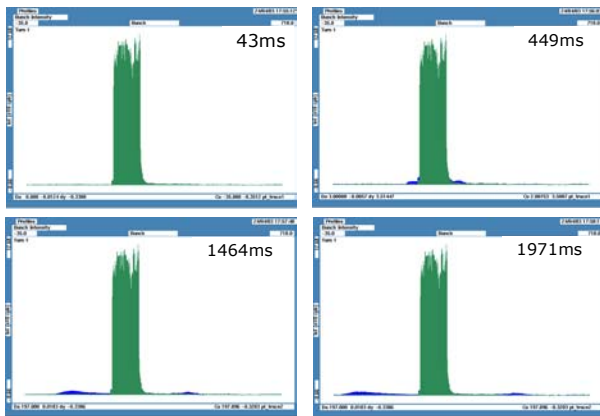


Figure 4. Evolution of one LHC batch in the SPS for 2276ms after injection with poor RF capture.

Use of the FBCT with 200MHz Beams

In order to investigate the suitability of the new FBCT system for the measurement of standard SPS 200MHz fixed target beams, and to qualify the calibration procedure, the data from the SPS ring monitor was compared to the DCCT data throughout the SPS cycle. In this case only the total batch intensity was required from the FBCT, since no bunch to bunch information was available, each integration being the sum of some 5 bunches. The result from such a comparison is shown in Fig. 5. The DCCT data is an average taken over 1ms, while that for the FBCT is based on a single-shot, single turn measurement. The band around the DCCT measurement has been added to indicate a $\pm 2\%$ window.

The agreement in the absolute calibration value obtained from the two different systems is very good, especially considering that no averaging was performed on the FBCT data. This therefore validates both the use for the system with 200MHz beams and the calibration procedure.

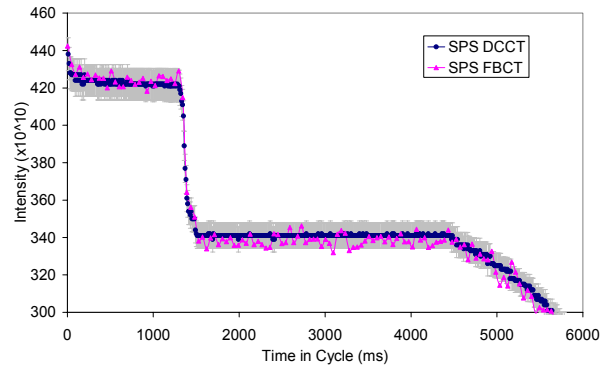


Figure 5. Comparison of the DCCT and FBCT intensity values for a 200MHz fixed target beam throughout its cycle in the SPS.

CONCLUSIONS AND OUTLOOK

The new fast BCT systems for the SPS and its transfer lines have been commissioned successfully. The initial results show that the absolute calibration is accurate to better than 2% for 200MHz fixed target beams. It remains to be seen what accuracy can be achieved for the bunch to bunch measurements, which unlike the 200MHz beam, will suffer from any transient signals generated by previous bunches.

One of the main uses of this system in the future will be as part of the beam quality interlock for the LHC. For LHC luminosity runs it has been specified that the bunch to bunch intensity variations of the injected batches should be less than 10%. It will be the fast BCT's job to measure this bunch distribution just before extraction and lift the extraction veto only if this is the case.

In the future all the SPS, LHC and CNGS transfer line fast BCTs will use the same fast BCT acquisition system measuring both 40MHz LHC beams and 200MHz fixed target beams. The LHC fast BCTs themselves will also probably be based on the same acquisition system, although the transformers will differ due to the much reduced vacuum chamber dimensions.

REFERENCES

- [1] G. Bohner et al., "Very front-end electronics for the LHCb preshower", LHCb-2000-047, CERN, 2000.
- [2] B.G. Taylor, "TTC Distribution for LHC Detectors", IEEE Trans. Nuclear Science, Vol. 45, No. 3, pp. 821-828, 1998.
- [3] E. Calvo et al., "The LHC orbit and trajectory system", presented at DIPAC2003, Mainz, Germany.

CURRENT MEASUREMENTS OF LOW-INTENSITY BEAMS AT CRYRING

A. Paal, A. Simonsson, A. Källberg, Manne Siegbahn Laboratory of Physics, Stockholm, Sweden

J. Dietrich, I. Mohos, Institut für Kernphysik, Jülich, Germany

Abstract

The demand for new ions species leads to an increasing number of cases in which the ions can only be produced in small quantities. thus weak ion currents below 1 nA quite often have to be handled and measured in low energy ion storage rings, like CRYRING.

INTRODUCTION

Various detector systems have been developed to measure such low intensity bunched and coasting beams by using the overlapping ranges of those systems (Fig.1).

Bunched beam measurements

Bunched beam parameters:

Frequency range: 40 kHz-1.5 MHz

Duty cycle: 10%-50%

Pulse width: 60 ns-13 μ s

A Bergoz Beam Charge Monitor with Continuous Averaging (BCM-CA) and an Integrating Current Transformer (ICT) was installed 1997 to measure the bunched beam intensity with 200 A full scale range and 20 nA RMS resolution.

Modifications:

-We have built a new amplifier with 86 dB gain and $0.6 \text{ nV}/(\text{Hz})^{1/2}$ RMS input noise.

-It was moved close to the ICT.

In the Bunch Signal Processor the gain by 20 dB has been decreased to get lower slow offset.

-A low pass filter has been added (10 Hz, 100 Hz).

Result: The 200 μ A full scale range have been extended down to 5 μ A with 1 nA RMS resolution.

A bunched beam current measurement is shown in Fig.2.

The amplified sum signal of the capacitive pick up closest to the ICT can be used to set up the measuring windows for the BCM and for the second Gated Integrator. The RMS resolution is about 100 pA. The PU Amplifier [1] has $1.2 \text{ nV}/(\text{Hz})^{1/2}$ RMS noise.

Coasting beam measurements

To measure the coasting beam intensity, neutral particle detectors have been built [2, 3]. At high particle energies the RGBPMs are used [4]. Their fast Micro channel plate detectors can handle 1 Mcps count rate.

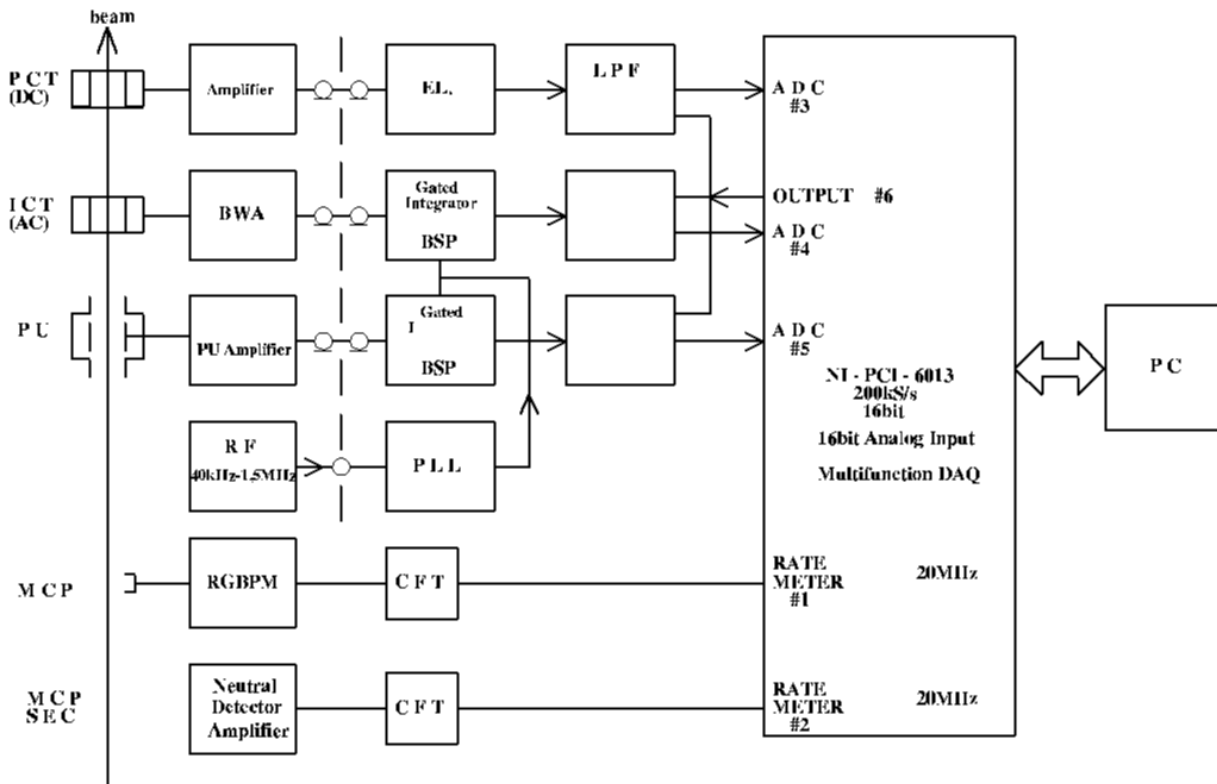


Figure 1: Beam Current Monitoring system of CRYRING

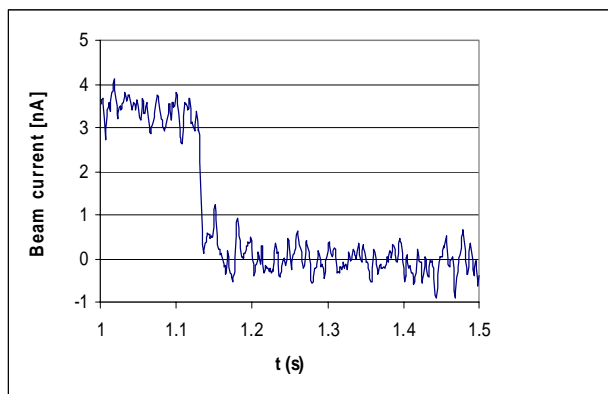


Figure 2: DN_2O^+ beam. After 1.12 s the RF is turned off.

Presently a 50 Mcps Secondary Electron Multiplier is under construction. The ETP Pty. Ltd Active Film Multiplier, type 14850H TOF with a conversion dynode, is planned to use. Its max dark count rate is 0.05 cps.

On the magnetic flat-top, 100 ms is available to calibrate the count rate of the neutral particle detectors, the residual -gas ionization beam profile monitor, and the segmented capacitive pick up signal.

References

- [1] Bojowald J. et al., 'DIPAC 93 proceedings, p. 171
- [2] A. Källberg, et al., DIPAC 97 proceedings, p. 150
- [3] D. Hanstorp, Meas. Sci. Technol. **3** (1992) 523
- [4] A. Kerek et al., EPAC 98 proceedings, p. 1577

DARK CURRENT MEASUREMENTS AT THE PITZ RF GUN

I. Bohnet, J. H. Han*, M. Krasilnikov, F. Stephan, DESY Zeuthen, 15738 Zeuthen, Germany
K. Flöttmann, DESY Hamburg, 22603 Hamburg, Germany

Abstract

For photocathode rf guns with electric fields of more than 40 MV/m at the photocathode and with an rf pulse length of 100 μ s or more, the amount of dark current might be comparable with the photoelectron beam. At the photoinjector test facility at DESY Zeuthen (PITZ) the dark current was measured with a Faraday cup for various settings of the solenoid fields at the rf gun. We discuss the dark current behavior for different photocathodes. Experimental results are compared with simulations.

INTRODUCTION

The photoinjector test facility at DESY Zeuthen (PITZ) has been developed with the aim to achieve high quality electron beams and study their characteristics for future applications at free electron lasers and linear colliders. At PITZ, the photocathode rf gun is operated with a rf frequency of 1.3 GHz, a maximum electric field of 41 MV/m at the photocathode, a maximum rf pulse length of 900 μ s, and a maximum repetition rate of 10 Hz.

Due to the high electric field and the long field emission time, the amount of dark current might be comparable to the photoelectron beam. Such a strong dark current degrades the electron beam quality and impairs emittance and energy spread measurements. More seriously, a large dark current is a severe hazard for a superconducting linac as it may produce X-rays, cryogenic losses, and radioactive activation. In the following paper, the generation of dark current and its properties are studied with measurements and simulation.

FIELD EMISSION AT THE RF GUN

The field emission of electrons is the main source of dark current. The field emission current at the rf gun can be parameterized in terms of the modified Fowler-Nordheim equation [1]

$$I_F = \frac{1.54 \times 10^{-6} \times 10^{4.52\phi^{-0.5}} A_e (\beta E)^2}{\phi} \times \exp\left(-\frac{6.53 \times 10^9 \phi^{1.5}}{\beta E}\right), \quad (1)$$

where E is the surface electric field in V/m, ϕ is the work function of the emitting material in eV, β is a field enhancement factor, and A_e is the effective emitting area.

* jhhan@ifh.de

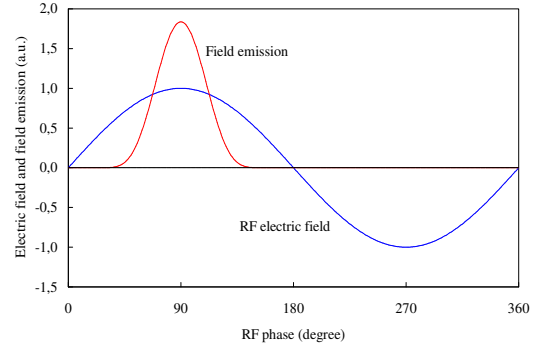


Figure 1: Intensity distribution of the field emission and the strength of the rf electric field for an rf cycle. The field emission curve was computed from the modified Fowler-Nordheim equation (Eq. 1) with an sinusoidal rf field and the typical β and ϕ values of 200 and 4.5 eV, respectively.

Figure 1 shows that the field emission is concentrated on the maximum electric field region of an rf cycle. Therefore, the field emitted electrons produced on the cathode are preferably accelerated in forward direction by the rf electric field.

At the rf gun, the field emitted electrons from other sources, like the iris or the entrance to the coupler, cannot follow the downstream component of the accelerating field, because these electrons are not synchronized to the accelerating rf electric field. However, they are able to heat up the cavity surface and may create secondary electrons.

The average field emission current during one rf cycle is described as [1]

$$\bar{I}_F = \frac{5.7 \times 10^{-12} \times 10^{4.52\phi^{-0.5}} A_e (\beta E_0)^{2.5}}{\phi^{1.75}} \times \exp\left(-\frac{6.53 \times 10^9 \phi^{1.5}}{\beta E_0}\right), \quad (2)$$

where E_0 is the amplitude of the sinusoidal macroscopic surface field in V/m.

MEASUREMENTS

The experimental setup is shown in Fig. 2. A molybdenum (Mo) cathode is a circle with a radius of 8 mm and a cesium telluride (Cs_2Te) cathode is a circle with a radius of 4 mm on a Mo substrate which has the same geometry as the Mo cathode except for the Cs_2Te coating. The

Mo cathode is used for conditioning of the rf gun and the Cs₂Te cathode is used to produce the photoelectron beam in normal operation. A main solenoid is located at 28 cm downstream of the cathode. The rf frequency is 1.3 GHz and the rf power is transferred into the gun cavity through a coaxial coupler. A laser with a wavelength of 262 nm produces the electron beam with a pulse length of 8 ps. The bunch repetition rate of the laser pulse train is 1 MHz.

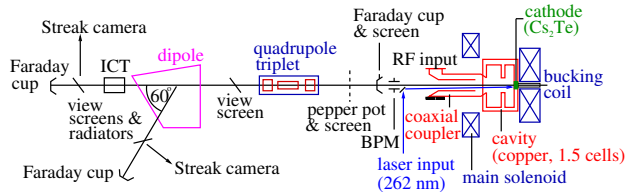


Figure 2: Schematic view of the gun and diagnostic sections.

Dark current signals were obtained with a removable Faraday cup which is located about 76 cm downstream of the cathode. The average dark current during an rf cycle was measured at the end of the rf pulse. Using the spectrometer dipole it was determined that the dark current has nearly the same momentum as the electron beam, which means the major part of the dark current is generated near the photocathode.

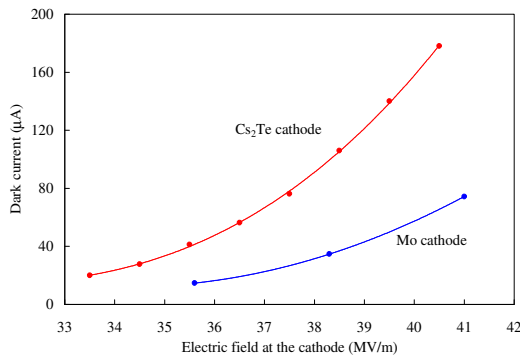


Figure 3: Maximum dark current measured as a function of the electric field at the cathode.

The dark current is higher for the Cs₂Te cathode than for the Mo cathode (Fig. 3) and the magnetic field dependencies are different for the Cs₂Te and Mo cathodes (Fig. 4, 5).

The amount of dark current reaching the Faraday cup depends on the strength of the magnetic field of the main solenoid. This is related to the current by B_0 [mT] = $0.6 \times I_{Main}$ [A]. The iris in the gun, the beam tube, the entrance to the coupler, and the mirror reflecting the laser beam onto the photocathode play a role as apertures for the dark current beam. A guiding force provided by the main solenoid field and the rf field guides the dark current through these apertures. The focusing behavior (see Fig. 4 and 5) of the dark current shows that the dark current has an energy comparable to the electron beam and starts near the

cathode because the best focusing condition on the Faraday cup of the electron beam with low charge is about 250 A at 40 MV/m accelerating electric field.

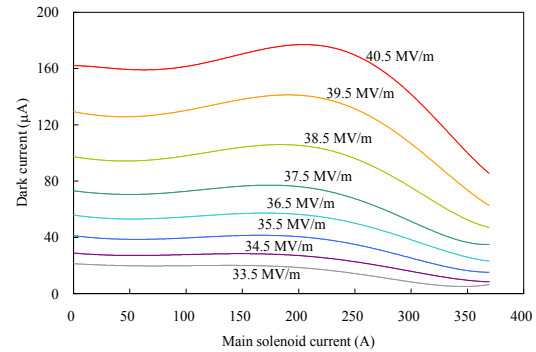


Figure 4: Dark current as a function of the main solenoid field for a Cs₂Te cathode at different rf fields.

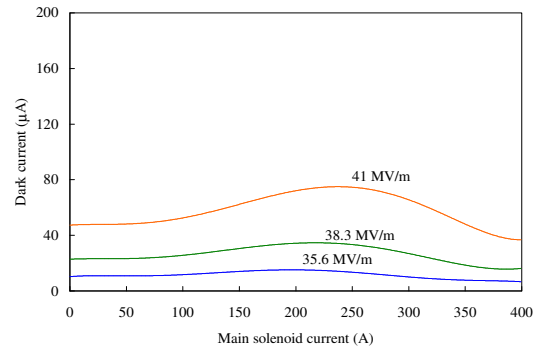


Figure 5: Dark current as a function of the main solenoid field for a Mo cathode at different rf fields.

With an rf electric field of 40.5 MV/m and a main solenoid current of 200 A, the dark current for a Cs₂Te cathode is about 180 μA. According to simulation results, about 50 % of the field emitted electrons from a 4 mm rms area at the cathode reach the Faraday cup. This means the amount of dark current generated near the Cs₂Te cathode is comparable to the electron beam in normal operation.

The field enhancement factor β was found from the Eq. 2 [1]

$$\frac{d(\log_{10} I_F / E^{2.5})}{d(1/E)} = -\frac{2.84 \times 10^9 \phi^{1.5}}{\beta}. \quad (3)$$

In this calculation, the work function ϕ was assumed to be 4.75 eV [2] for the Cs₂Te cathode and 4.2 eV for Mo cathode. The calculated field enhancement factors for the Cs₂Te and Mo cathodes are 220 and 164, respectively. The effective emitting areas were calculated to be $1.1 \times 10^{-15} \text{ m}^2$ and $1.2 \times 10^{-15} \text{ m}^2$ for the Cs₂Te and Mo cathodes, respectively.

In normal operation, the bucking solenoid is used to compensate the longitudinal magnetic field produced by

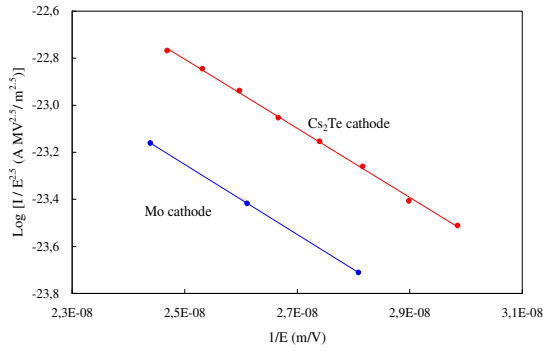


Figure 6: Fowler-Nordheim plots to find enhancement factors and effective field emission areas for each cathodes.

the main solenoid at the cathode. But Fig. 7 shows that the bucking solenoid can also affect the dark current behavior for the Cs₂Te cathode. Such a bucking solenoid dependency of the dark current was not found for the Mo cathode. The relation between the main and the bucking solenoid currents to compensate the magnetic field at the cathode is $I_{Bucking} [A] = 0.0846 \times I_{Main} [A]$ for the present experimental setup. The magnetic field at the cathode has no influence on electron field emission (see Eq. 1). The magnetic field dependence of the dark current is possibly caused by secondary electron emission.

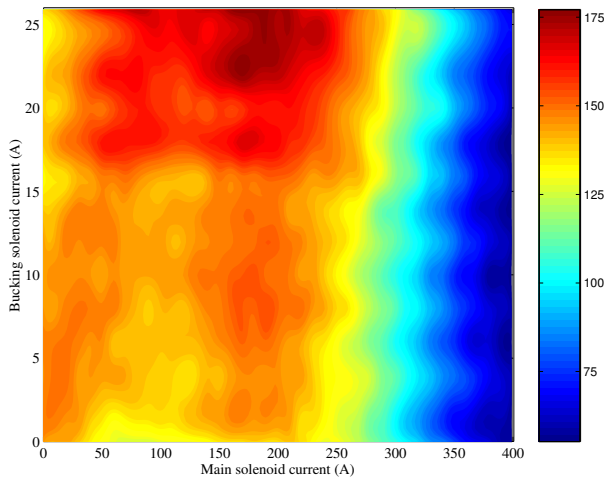


Figure 7: Contour plot of the dark current at 40 MV/m for the Cs₂Te cathode with the combination of the main solenoid and the bucking solenoid currents.

A particle tracking code (ASTRA) [3] was used to simulate the dark current. In this simulation, the dark current source was assumed to be the cathode itself and the surrounding area, a Gaussian distribution with $\sigma = 4$ mm was taken. The time structure of the field emission current has been derived from Fig. 1. A Gaussian distribution in the rf phase was assumed with a center value of 90° and a variance of 20° . The simulation result using ASTRA without secondary electron emission is similar to the dark current

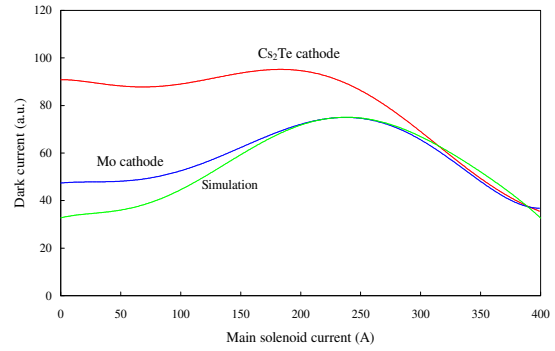


Figure 8: Comparison of dark current measurements for the Cs₂Te and Mo cathodes with the ASTRA simulation. Measurements are normalized at the high magnetic field region.

behavior for the Mo cathode (see Fig. 8). The study on the dark current behavior for the Cs₂Te cathode is ongoing considering secondary electron emission.

SUMMARY

The main source of the dark current at the rf gun is found experimentally and in simulations to be the cathode and the surrounding area. The magnetic field dependence of the dark current is quite different for the Cs₂Te and Mo cathodes. The simulation using ASTRA without secondary electron emission is similar to the dark current behavior for the Mo cathode. The dark current behavior for the Cs₂Te cathode is possibly caused by secondary electron emissions, which will be studied in future.

REFERENCES

- [1] J. W. Wang and G. A. Loew, "Field emission and rf breakdown in high-gradient room-temperature linac structures," SLAC-PUB-7684, 1997.
- [2] S. H. Kong, et. al., "Cesium telluride photocathodes," J. Appl. Phys. **77**, 6031 (1995).
- [3] K. Flöttmann, A Space Charge Tracking Algorithm (ASTRA), <http://www.desy.de/~mpyflo/>.

IONISATION CHAMBERS FOR THE LHC BEAM LOSS DETECTION

E. Gschwendtner, R. Assmann, B. Dehning, G. Ferioli, V. Kain
CERN, Geneva, Switzerland

Abstract

At the Large Hadron Collider (LHC) a beam loss system will be used to prevent and protect superconducting magnets against coil quenches and coil damages. Ionisation chambers will be mounted outside the cryostat to measure the secondary shower particles caused by lost beam particles.

Since the stored particle beam intensity is eight orders of magnitude larger than the lowest quench level and the losses should be detected with a relative error of two, the design and the location of the detectors have to be optimised. For that purpose a two-fold simulation was carried out: The longitudinal loss locations of the tertiary halo is investigated by tracking the halo through several magnet elements. These loss distributions are combined with simulations of the particle fluence outside the cryostat, which is induced by lost protons at the vacuum pipe.

The base-line ionisation chamber has been tested at the PS Booster in order to determine the detector response at the high end of the dynamic range.

INTRODUCTION

The magnet coil quench and damage levels are time and energy dependent. This results in a large range of loss rate variations requiring observations of ionisation chamber currents between 10^{-12} and 10^{-3} A [1]. The required time resolution for the arc monitors is 2.5 ms and for all other detectors it is 89 μ s (i.e. 1 LHC turn).

These requirements show already that the demands on the design of a reliable beam loss detection system are extremely high. Here are three different design aspects of the loss system are investigated:

- The longitudinal beam loss distribution of the tertiary halo along the magnets. It is emitted by the secondary collimators and will be lost at aperture limits.
- Calculations of the particle fluences outside the cryostat, which is induced by lost protons. This defines the most suitable positions, the needed number and the impact on the dynamic range of the detectors.
- The signal response of the ionisation chamber in a high rate environment similar to the LHC.

First results are shown.

TERTIARY HALO LOSS DISTRIBUTION STUDIES FOR 450 GeV

The longitudinal beam loss distribution was obtained by tracking particles populating the tertiary halo at 450 GeV through parts of the LHC. The tertiary halo particles stem from the collimation insertion IR7 escaping

the secondary collimators. The halo particles were tracked with SIXTRACK and the scattering routine K2. The left plot in Fig. 1 shows the (X,Y)-distribution of the halo after the collimators. MAD-X in the ‘one-pass’ mode was applied to track the particles from the collimation insertion IR7 to the chain of the LHC magnet elements we investigate. Finally the linear tracking program SLICETRACK was used to slice the elements and calculate the longitudinal beam loss distribution.

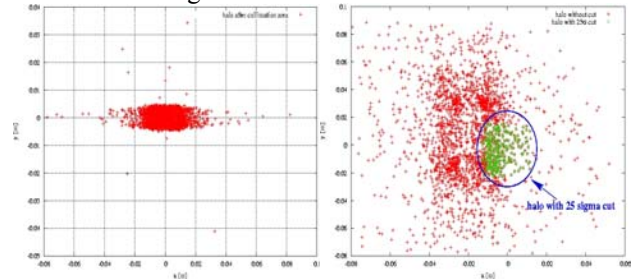


Figure 1: Left: Tertiary halo distribution after the collimation section IR7. Right: Halo tracked with MAD-X to the dispersion suppressor in IR1. Particles with amplitudes larger than 25σ are cut.

The MAD-X tracking was based on the sequence V6.4.aperture containing information on apertures in the LHC. So particles exceeding these apertures get already lost during the transfer from the collimation section to the sliced chain of elements (e.g. tracking with MAD-X until IP5 results in the loss of all halo particles). But for the time being the LHC sequence does not contain all apertures and the particles can still reach unrealistic amplitudes in the tracking process. Thus we were forced to apply a cut in particle amplitudes before tracking through the sliced elements. Out of a geometrical argument we discarded particles with amplitudes exceeding 25σ that is still quite large (see right plot in Fig. 1).

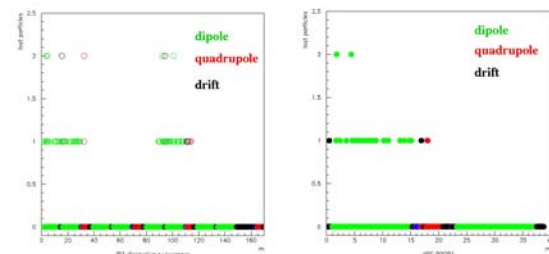


Figure 2: Loss distributions along the dispersion suppressor (left) and an arc short section (right) right of IP1. No beam excursions and misalignments are introduced.

We have investigated two cases: the loss distribution along the dispersion suppressor and along an arc short section, both right of IP1 for LHC beam1. SLICETRACK

can be used with quadrupole, dipole magnets and drifts. Different beam pipes can be simulated and several kinds of misalignment can be taken into account. It tracks the particles through these elements and compares the amplitudes with the aperture restriction after every slice of the element. No scattering is included. Aperture restrictions are treated as black absorbers.

Fig. 2 shows the loss distributions for the dispersion suppressor and the arc short section when no misalignment has been applied. Since most of the particles are off-momentum, we see that the losses happen along the bending magnets.

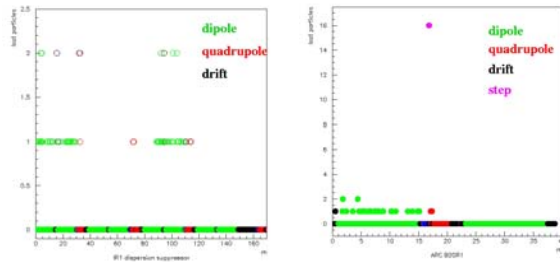


Figure 3: Left: loss distribution in the dispersion suppressor with a 4mm global beam orbit shift. Right: Losses along the arc short section when a misalignment error of 2mm in Y has been introduced.

The left plot in Fig. 3 shows the loss distribution in the dispersion suppressor when a 4mm global orbit shift has been introduced. More losses happen now in the quadrupoles. In the right plot we see that many particles in the arc short section are lost at the point where a step of 2mm in Y has been brought in.

Since the tertiary halo consists of mainly off-momentum particles, the halo is basically lost at the bending magnets and at mechanically aperture limitations. It can be assumed that the primary and secondary halo losses occur mainly at positions where the beta-functions are highest (quadrupole magnets).

EXPECTED DETECTOR SIGNALS AND POSITIONS

At the positions, where most of the beam losses occur, simulations of the particle fluences outside the cryostat and induced by lost protons at the aperture have been performed with the Monte Carlo Code Geant 3.21.

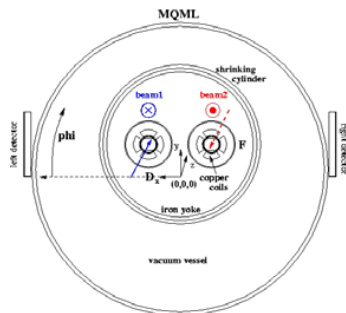


Figure 4: Cross-section of the MQML quadrupole in Q10.

The geometry used in these simulations corresponds to the dispersion suppressor layout. The arrangement consists of four quadrupole elements (Q8-Q11) separated by two dipoles (MBA, MBB), respectively. We assume that lost beam particles hit the beam screen under an angle of typically 0.25mrad in the horizontal (vertical) plane when the magnet is focusing (defocusing) in X. The simulated shower particles produced by lost protons are counted in two detector-elements placed left and right outside the cryostat (see Fig. 4).

We have already shown in Ref. [2] that the shower maximum is about 1m after the beam loss location. The shower width is 0.5m. For one proton with 7TeV lost in the middle of the magnets we observe $1 \cdot 10^{-2}$ charged particles/p/cm² in the detector. Several following (smaller) shower peaks are due to the gap between the magnets.

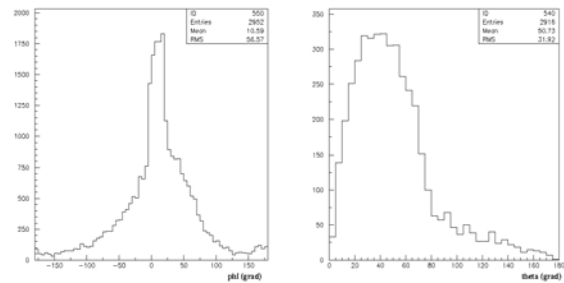


Figure 5: Left: Phi-distribution of particles escaping the cryostat. Right: Theta-distribution of particles escaping the cryostat.

The left plot in Fig. 5 shows the phi-distribution of the particles around the cryostat. Most of the particles escape the vacuum vessel in the plane of the beam-tube which corresponds to an angle of $\phi = 9-12$ degree. In the right plot the theta-distribution (angle between the particle momentum and the X-axis) of the particles are shown. The average is $\theta = 50$ degree.

In addition the energy deposition in the detector elements (filled with air) is calculated. With a beam energy of 7TeV (450GeV) the energy deposition is ~ 4.3 keV/cm (3.8 keV/cm).

A summary of the signal rates for the different energies and loss distributions is given in Ref. [2] and [3].

TESTS OF THE IONISATION CHAMBER IN THE PS BOOSTER

The ionisation chamber has been tested in the PS Booster at different beam intensities in terms of signal shape, linearity response and electron and ion induced signal.

A photo of the detector is shown in Fig. 6. The baseline layout is a N₂ filled cylinder with a surface of 80cm², a radius of 4.75cm, consisting of 30 gaps separated by 1mm thick Aluminium discs and a gap-width of 0.55cm. A typical bias voltage is 1500V.

The detector was placed in the beam-line in front of the beam-dump. The energy of the protons in the beam and passing through the detector was $E_{\text{kin}}=1.4\text{GeV}$, the duration of a spill was 50ns. The beam intensity varied between $5 \cdot 10^8$ to $1 \cdot 10^{10}$ protons/spill. The size of the beam at the detector has been estimated to be $\sigma_{\text{horiz.}} = 3.5\text{mm}$ and $\sigma_{\text{vert.}} = 3.5\text{mm}$ and 1.7mm .



Figure 6: Photo of an ionisation chamber.

The number of electron/ion pairs N created along the detector per 1 proton can be calculated with

$$N = \text{cluster/cm} \cdot \text{electron/cluster} \cdot \text{gap-width} \cdot \text{nr-of-gap}.$$

With $\text{cluster/cm}=23$, $\text{electrons/cluster}=1.89$, $\text{gap-width}=0.55\text{cm}$ and $\text{number-of-gaps}=30$ we get $N=717\text{electron/ion pairs per 1 proton}$. From the ionisation chamber signal we can now recalculate the number of protons MP that passed through the detector with

$$MP = \int V(t)dt / (N \cdot R \cdot e)$$

with e , the elementary charge, $N=717\text{el/ion pairs per 1 proton}$, $R=50\Omega$ and $\int V(t)dt$, the measured voltage signal integrated over $300\mu\text{s}$ ($89\mu\text{s}$) that is induced by both the electrons and the ions (see Fig. 7).

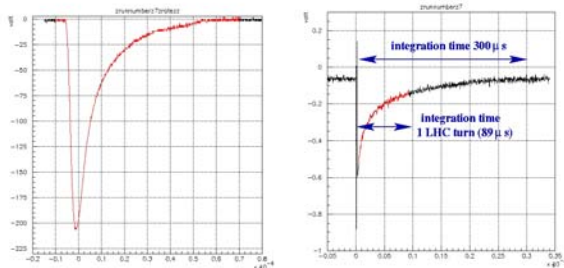


Figure 7: Electron (left plot) and ion (right plot) induced signal in the ionisation chamber from a PS Booster intensity of $9 \cdot 10^9$ protons/spill.

The left plot in Fig. 8 compares the measured proton intensity integrated over $300\mu\text{s}$ and $89\mu\text{s}$, respectively, versus the PS Booster intensity. We see at higher

intensities ($1 \cdot 10^{10}$ protons/spill) a non-linear response of the ionisation chamber. However, the right plot of Fig. 8 shows that the ratio of the measured intensity for $89\mu\text{s}$ and $300\mu\text{s}$ integration times does not depend on the beam intensity.

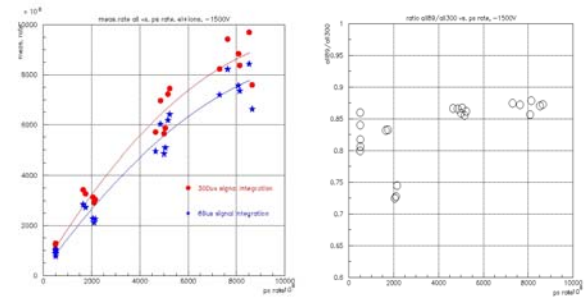


Figure 8: Left: Measured proton intensity vs. PS Booster^F intensity. Right: Ratio of measured intensity for $89\mu\text{s}$ and $300\mu\text{s}$ integration times vs. PS Booster intensity.

SUMMARY

The loss distribution calculations of the tertiary halo show that losses concentrate around the bending magnets due to the non nominal momentum of the majority of protons and also around positions where mechanical limitations of the aperture can be assumed.

The shower simulations show that the phi-distribution of the shower particles is independent of the loss locationⁿ both in the beam tube and along the magnets.

Tests of the ionisation chamber in the PS Booster show that the electrons and ions are collected in less thanⁿ $300\mu\text{s}$. At high intensities ($1 \cdot 10^{10}$ protons) a non-linear^r response of the ionisation chamber is observed. The error^r does not depend on the beam intensity when integrating^g the signal every LHC turn ($89\mu\text{s}$).

REFERENCES

- [1] B. Dehning, CERN-AB-2003-008 ADM, Proceedings^S of the Workshop on LHC Performance, Chamoni^X XII, France (2003).
- [2] E. Gschwendtner et al., 8th European Particle Accelerator Conference, La Vilette, Paris, France^r (2002).
- [3] A. Arauzo-Garcia et al., CERN-SL-2001-027-BI, CERN, (2001).

OPTICAL FIBRE DOSIMETER FOR SASE FEL UNDULATORS

H. Henschel, J. Kuhnenn, Fraunhofer-INT, Euskirchen, Germany

M. Körfer*, DESY, Hamburg, Germany

F. Wulf, HMI, Berlin, Germany

ABSTRACT

Single pass Free Electron Lasers (FELs) based on self-amplified spontaneous-emission (SASE) are developed for high-brightness and short wavelength user applications. These light sources are related to short undulator periods which can be realized with permanent magnet designs. Unfortunately, the material is radiation sensitive and the undulators require a protection system. To monitor particle losses directly inside the undulator gap and to guarantee full magnetic performance for a long time, an optical fiber dosimeter has been developed and operated at the TESLA Test Facility (TTF). The dosimeter system allows online dose monitoring and beam particle loss optimisation.

INTRODUCTION

High gain single pass SASE FELs require high peak current (kA), ultra-short (100 μm) and low emittance (few mm mrad normalized) electron bunches. The TTF achieved long bunch trains with 1800 bunches per second, a bunch charge of 4 nC and a bunch spacing down to 444 ns. The average beam power was 1.8 kW. To realize safe beam operation a machine protection system was necessary. Due to the radiation sensitive permanent magnet material a protection of the undulator with an upstream collimator system was installed. The necessarily tight tolerance of the magnetic field integrals is $\leq 10 \text{ T mm}^2$ (rms). Therefore, local particle losses and resulting doses inside the radiation sensitive permanent magnet undulator were recorded with an online dosimeter system. The fibre sensor should be as close as possible to the magnet surface inside the undulator gap. Since the gap between magnetic yoke and the flat vacuum chamber is less than 1 mm conventional online dosimeters do not fit in such a geometry. Moreover, the strong magnetic field environment is not compatible with electrical sensor cabling. The TESLA collaboration developed an optical fibre dosimeter for SASE FEL undulators. At TTF, the fibre optical power-meter system and an Optical Time Domain Reflectometer (OTDR) system [1] has been successfully operated, which allows one to obtain the accumulated dose continuously.

OPTICAL FIBRE DOSIMETER

The most obvious effect of ionising radiation in optical fibres is an increase of light attenuation. The radiation penetrates the fibre and creates additional colour-centres which cause a wavelength-dependent attenuation that can be measured with a power-meter (Fig.1).

Radiation Effect on Optical Fibre

The high purity of the modern fibre raw materials has reduced their radiation sensitivity. However, if the core material of Germanium (Ge)-doped Multi-Mode Gradient Index (MM-GI) fibres is co-doped with Phosphorus (P), their radiation-induced attenuation increases significantly so that these fibres are suitable for dosimeter purposes. A dedicated optical fibre for dosimeters shows (wavelength-dependent) a nearly linear increase of attenuation after irradiation. For the optical fibre used the calibration of dose D versus light attenuation A is valid up to 1000 Gy and independent of the dose-rate and source type. No systematic influence on the dose rate was observed between about 0.006 and 70 Gy/min.

General Layout

A LED is connected with an optical fibre (Fig. 1). Light passing through the fibre will be continuously measured with the power-meter. Due to the irradiated fibre part, the light intensity suffers absorption leading to an attenuation step. The trace of attenuation increase versus time can be displayed at the accelerator control desk.

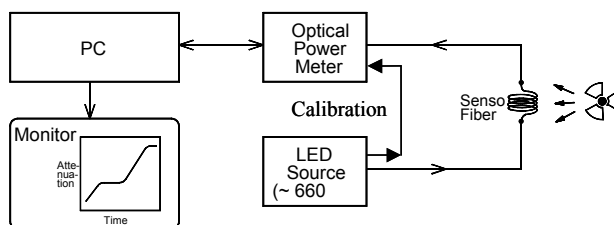


Figure 1: Scheme of an optical fibre dosimeter. The radiation produces absorbing "colour centres" in the sensor fibre. The light attenuation has been measured with an optical power-meter and allows one to determine the radiation dose.

* corresponding author: markus.koerfer@desy.de

The light attenuation at the exit of the fibre depends on the total fibre length. For precise calculations of dose the exact length of the exposed fibre part is relevant. To ensure, that the forerun-fibres upstream and downstream deliver no parasitic radiation induced attenuation the fibre material was radiation hard and the cables are laid in shielded regions.

Irradiated Optical Fibre Part

The electron beam passing the undulator was in a vacuum chamber with an outer height of 12 mm and inner height of 9.5 mm. The dose profile generated around the chamber and directly at the permanent magnet surface was measured. Perpendicular to the beam propagation a sequence of Thermo Luminescence Dosimeters (TLDs) were installed in a line. The doses of each TLD set were measured several times. A representative measurement of dose versus TLD number is shown in Figure 2.

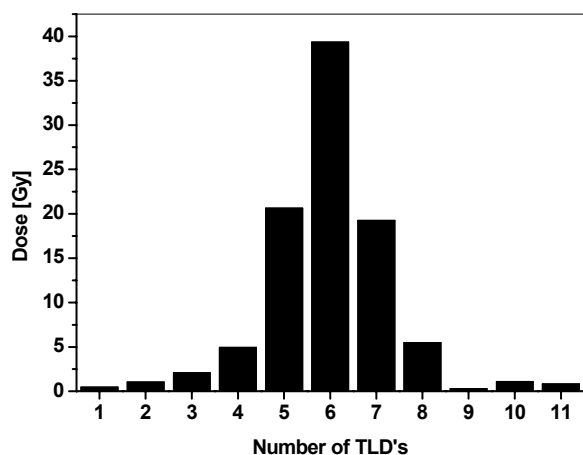


Figure 2: Cross profile of particle losses in the undulator. A sequence of 11 TLD's above the vacuum chamber, located perpendicular to the beam direction. Each TLD sensor with 6 mm length had a gap of 1 mm to the next one.

The TLD sensors were 6 mm long and 1 mm apart. The resulting dose distribution was very narrow and can be approximated by a rectangle of the half height and equivalent area with a width of about 24 mm. Using this simplified assumption all irradiated fibre parts on top and bottom of the chamber were in addition assumed to be the same. Note, that the profile measurement could include different accelerator set ups, i.e. a combination of different profiles. The accuracy of this simple method was sufficient for our application. However, more precise dose calculations require measurements at each sensor position at all times.

DOSIMETER OPERATION AT TTF 1

The system allows a sensitive dose measurement along the undulator. Figure 3 shows a diagram of the layout. Three undulators at TTF 1 were equipped with several turns of the sensor fibre around the beam pipe at different positions in the narrow gap. Due to the expected exponential dose distribution along the undulators the sensor positions were provided with different numbers of fibre turns.

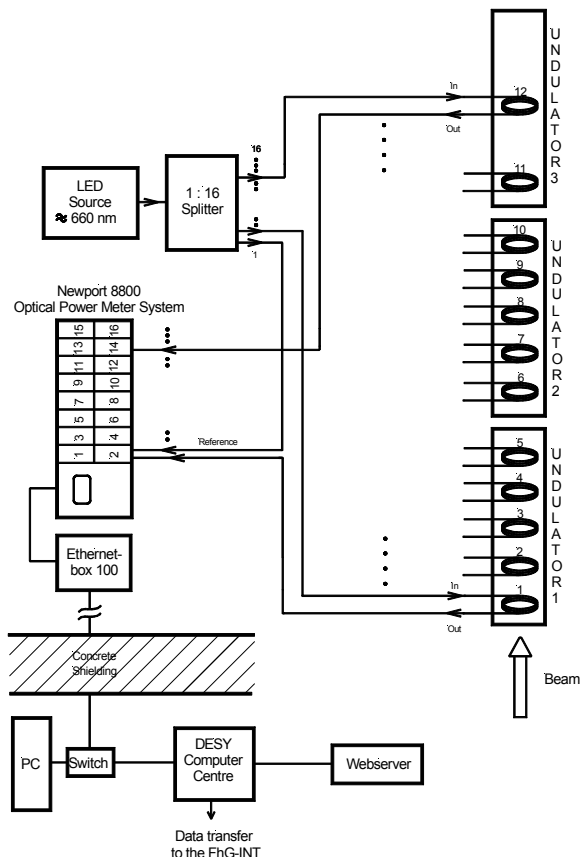


Figure 3: Scheme of the fibre optical dosimeter arrangement at TTF1. LED light was subdivided onto different fibre sensors in the undulators. One splitter output was used as reference, for correcting drifts of the LED source.

At the entrance of the undulator section 5 windings per sensor were chosen while at the end the sensors had 20 windings. The light of the LED was guided to a 1:16 splitter made of 50/125 μm GI fibre. One splitter output was used as a reference for corrections of the LED intensity drifts. Finally 12 residual outputs were connected to radiation sensitive sensors. Noise reduction was realized by an internal averaging routine of the power-meter as well as by the data evaluation program. The stability of the system was < 0.001 dB within a few hours. Such a high stability and accuracy can only be obtained with LED sources. The dynamic range was about 50 dB and covered the linear range of the dose

calibration mentioned above. The resolution of the system was about 60 mGy (for 10 windings @ 660 nm).

MEASUREMENT

Data were accumulated over a time period of six months. The dosimeter system behaved properly. The fibre sensors were replaced every two month before the accumulated dose had reached 1 kGy. As an example, ten days of the second measurement period from the end of January 2002 to March 2002 are shown in Figure 4. The accumulated dose at the five positions in the first undulator were selected. During accelerator shutdowns the fibre attenuation slightly annealed. To take this into account, only dose values corresponding to attenuation increases were summed up. This allows the determination of the accumulated dose independent of annealing.

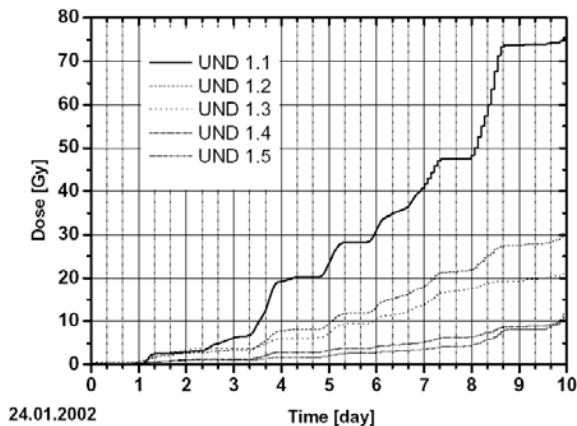


Figure 4: Representative plot of the accumulated dose at five positions in the first undulator. The distance between sensor positions is about 80 cm. The beam operation set-ups are strongly related to the accumulated dose.

In the beginning, three days were set aside for accelerator access and beam operation for high order mode investigations in the super-conducting cavities. The first strong dose increase is related to the optimisation of SASE gain by tuning the optic twiss parameter in front of the undulator (i.e. transversal collimator). Continued optic studies for the beam transport through the collimator were completed in roughly 16 hours (two shifts). The procedure included the emittance measurements with quad scans at the collimator. The next step in the dose trace is probably due to beam energy jitter and resulting beta-function beat. Afterwards, between days six and nine two dose accumulations appear. These are related to Coherent Synchrotron Radiation (CSR) studies in the injector (i.e. bunch compressor BC2) and bunch length measurements with a streak camera downstream of the undulator. The first step is generated by changing beam parameters while the second one is caused by changing the phase of the acceleration module in front of BC2. The major slope

(Figure 4) implies a higher dose rate and higher particle losses versus time. The total accumulated dose at each sensor position in a time period of 2 months is shown in Figure 5.

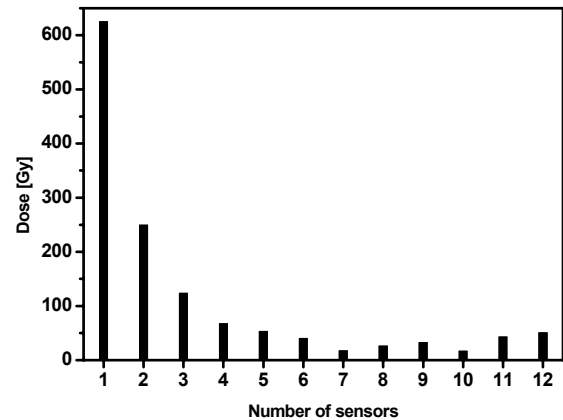


Figure 5: Accumulated dose along the undulator at each sensor position. The number of sensors corresponds to the sensor location inside the undulators in Figure 3.

Note, the fibre sensor has integrated the dose for different accelerator operation modes, such as SASE operation and CSR studies. Nevertheless, the expected exponential decrease of dose along the undulator generated by low energy photons escaping the absorber system of the collimator is included [2].

CONCLUSIONS

A new online sensing system that measures the local origin of dose in SASE undulators was developed and operated during the TTF1 run. The advantages of an optical fibre power-meter dosimeter are:

- It enables the operator to control radiation emission in very lengthy objects.
- The dosimeter sensitivity can be adjusted to the dose by selection of fibre type, LED wavelength and spool windings.
- The dose can be measured in narrow slits, which are inaccessible for conventional online dosimeter systems. Bare (i.e. uncabled) fibres usually have a diameter of only 250 μm .
- Both radiation and beam loss in undulators can be tuned by an operator continuously.

REFERENCES

- [1] H. Henschel, M. Körfer, F. Wulf, Fibre Optical Radiation Sensing System for TESLA, DIPAC 2001
- [2] H. Schlarb, Design and Performance of the TESLA Test Facility Collimator System, EPAC 2002

BEAM LOSS DIAGNOSTICS BASED ON PRESSURE MEASUREMENTS

E.Badura, B.Franczak, W.Kaufmann, P.Horn, H.Reeg, H.Reich-Sprenger, P.Schütt, P.Spiller, K.Welzel, U.Weinrich, Gesellschaft für Schwerionenforschung mbH, Darmstadt, Germany

Abstract

The GSI is operating a heavy ion synchrotron, which is currently undergoing an upgrade towards higher beam intensities. It was discovered that beam losses induce a significant pressure increase in the vacuum system. This effect can be used as beam loss diagnostics. In addition fast total pressure measurements were put into operation in order to detect the time constants of the pressure increase and decrease.

1 Measurement Principle

The energy loss per unit length of ions in matter depends on the kind, energy and charge state of the ions as well as on the target material. For heavy ions this energy deposition might be so high that effects like sputtering, melting, crack formation, etc. might occur. During such impacts a lot of gas molecules are released. The desorption yield, i.e. the number of gas molecules released per impact ion has been reported to be in the range from 10^3 to 10^5 . This effect has been studied at CERN [1] and is object to further investigations at GSI [2]. The typical value measured for the stainless steel vacuum chamber of the GSI heavy ion synchrotron SIS is 10^4 .

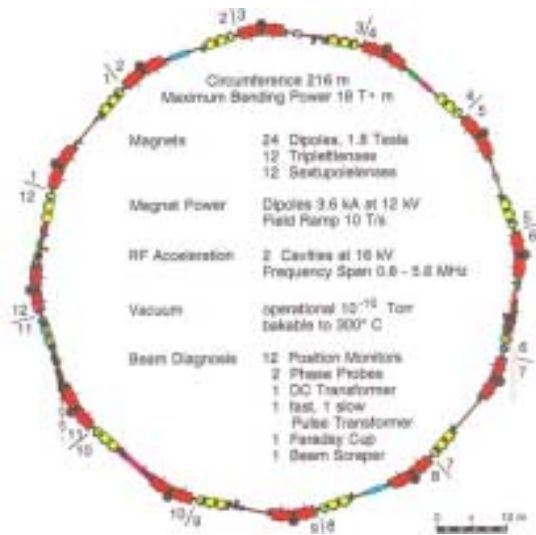


Fig. 1: The GSI heavy synchrotron SIS

The release of gas molecules increases the pressure in the vacuum system of the accelerator. The measurement of the pressure rise with pressure gauges contains the information about the amount of the lost ions as well as their impact point on the vacuum chamber. In the SIS the total pressure measurement is done with 12 IE514 extractor gauges from

Leybold equally distributed around the ring. These gauges can reliably measure down to a few 10^{-12} mbar. The distance between two gauges is 18 m.

The pressure rise due to ion losses is immediate. There is also a typical pumping down time, which depends on the kind of gas molecules and the pumping system. In the SIS this pumping down time is the range from 10 ms to 10 s.

It is important to mention two cases: a constant loss rate and single loss events. One can consider a constant loss rate when the rate at which the losses take place is shorter than the pumping down time. In this case the pressure will increase to a kind of dynamic equilibrium. In the SIS this is the case for chemically inert gases in combination with short cycle times of the synchrotron. For the case of long cycling times and/or chemically active gases the released gas molecules are pumped away before the next significant ion loss appears.

2 Average total pressure and lifetime

Heavy ion circular accelerators operate at low pressure. The base pressure for the SIS for example is around $2 \cdot 10^{-11}$ mbar. This corresponds to about a total of $2 \cdot 10^{12}$ free gas molecules in the vacuum system. With the above mentioned desorption coefficient the amount of ions necessary to create a total pressure rise equivalent to the base pressure of the SIS can be estimated to about $2 \cdot 10^8$. If this amount of ions is lost in a short time the lifetime decreases by a factor of two. This is therefore about the detection limit for beam losses just from total average pressure or lifetime. The value of $2 \cdot 10^8$ ions accelerated is close to the operation value for U^{28+} . Measurements of the total pressure and beam lifetime as function of the loss rate were done and are summarised in the following tables:

Beam type	Loss rate [10^7 ions/s]	Pressure [10^{-11} mbar]	Lifetime [s]
no beam		1.96	
U^{28+}	1.2	2.13	5.0
U^{28+}	11.4	2.62	3.6
U^{73+}	0.88	1.99	14.4
U^{73+}	1.6	2.03	12.4
U^{73+}	2.2	2.22	12.3

Tab. 1: total pressure and lifetime as function of loss rate

Ion species	U^{28+}	U^{73+}
Pressure increase [mbar/ions/s]	$9.9 \cdot 10^{-20} \pm 41\%$	$7.2 \cdot 10^{-20} \pm 63\%$
Pressure · lifetime [s · mbar]	$1.0 \cdot 10^{-10} \pm 6\%$	$2.7 \cdot 10^{-10} \pm 6\%$

Tab. 2: lifetime as function of pressure and pressure increase as function of loss rate

There is a program to further increase the intensity for uranium operation by about three orders of magnitude up to $2 \cdot 10^{11}$ ions per cycle. The beam loss induced pressure rise has therefore to be drastically reduced by means of total beam loss reduction, reduced desorption coefficient and increased pumping speed.

In order to reach this goal the detection of beam losses, partial and total pressure is currently improved in order to provide efficient diagnostic for machine optimisation.

3 Localised losses

Losses are in general not equally distributed around the ring. If for example the losses are localised to a single point in the vacuum system, the pressure rise also occurs locally. In this case the detection of the local pressure rise is possible even without a significant impact on the lifetime. During different measurements it was found that a local pressure rise is reduced by about one order of magnitude over the length of one sector, i.e. about 18 m. This is due to the limited conductance of the vacuum chamber in combination with the pumping stations in the sector. As the SIS contains 12 sectors one can say that a local pressure rise extends over 1/12 of the ring. The detection limit for local losses from the pressure rise is therefore about one order of magnitude lower than for the average pressure. This means that already losses of a few 10^7 ions can be detected. This was indeed proven by measurements. It has to be mentioned here that the distribution of the base pressure around the ring is far from being uniform. Consequently the detection limit for local losses also varies from extractor gauge to extractor gauge.

With a detection limit of a few 10^7 lost ions it is possible to follow up the operation settings for high intensity heavy ion operation and to optimise the settings with it.

4 Time dependence of pressure

In the 10^{-11} mbar pressure range the collected ion current on the extractor gauges is very low. The standard treatment with the IM520 control unit is too slow to provide sufficient time resolution for the follow up of the pressure increase and decrease after an ion impact. Therefore a fast current to frequency converter was used to measure this dynamic. The basic parameters of this electronic are:

- Sensitivity of 1pC/pulse
- Pulse width of 50ns
- A dynamic range of 7 decades

- A maximum output frequency of 10 MHz
- Linearity of 0.1% below 1 MHz and 3% between 1 MHz and 10 MHz
- TTL 50 Ohm output

In figure 2 the electronic layout is shown.

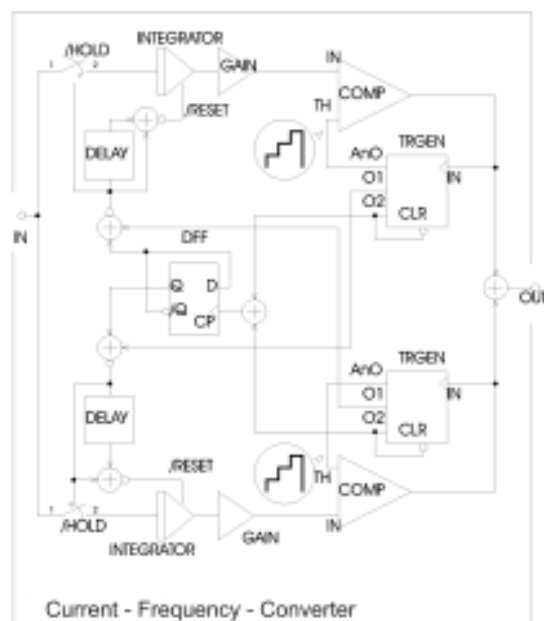


Fig. 2: Electronic for the fast pressure measurement

In figure 3 the electronic output is shown for three extractor gauges during a slow beam loss induced pressure increase. The total time scale is 100 s.

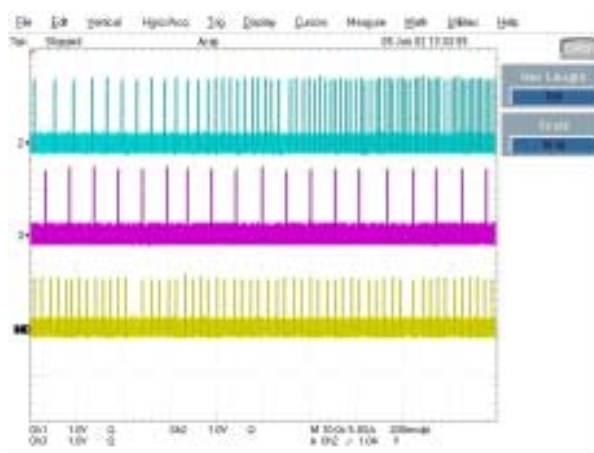


Fig. 3: Output of the fast pressure measurement during a pressure increase.

The time resolution of the measurement is given by the time that the extractor gauges need to accumulate 1pC ion current. At 10^{-11} mbar this time is about one second. It is therefore possible to follow up a dynamic pressure increase for pumping down times in the range for 10 seconds even down to the 10^{-12} mbar range. In order to measure in the 100 ms range, on the other hand, a pressure increase of at

least 10^{-10} mbar is required. In this respect it has to be mentioned that seven fast residual gas analysers are installed around the ring. In principle they yield the potential to follow up the evolution of a specific gas molecule with a time resolution better than one second. This potential will be exploited in the near future.

5 Potential of the method and outlook

At the GSI pressure measurements provide beam loss diagnostics for some important operation modes.

As the vacuum system is closed all released gas molecules stay within the detection volume. This eases the positioning of this diagnostics.

Another advantage is that for vacuum reasons this diagnostic is anyhow installed. Therefore the investment and operation costs remain low.

As the beam loss induced desorption is a major issue for the operation of high intensity heavy ion accelerators this diagnostic is ideal to overcome this obstacle.

The main disadvantage of this method is that it can only be used at high intensity heavy ion accelerators.

At GSI this diagnostic was made operational mainly for vacuum reasons. The task of full integration into the machine control system has still to be provided to be fully operational as optimisation tool. The next step will be the exploitation of the residual gas analyser network. With this system it is possible to follow up the evolution of different gas species. There is a hope to identify a gas species which is strongly released from the chamber wall but not so present in the base pressure. This will provide an improved signal to noise ratio. If one only sticks to one mass the time resolution of the RGAs is in the subsecond range so that also the dynamics of the pressure can be studied.

References

- [1] Ion-stimulated gas desorption yields and their dependence on the surface preparation of stainless steel, E.Mahner, J.Hansen, D.Küchler, M.Malabaila, M.Taborelli, EPAC2002, Paris
- [2] Measurement and Calculation of U28+ beam lifetime in SIS18, A.Krämer, O.Boine-Frankenheim, E.Mustafin, H.Reich-Sprenger, P.Spiller, EPAC2002, Paris

DAFNE BEAM LOSS MONITOR SYSTEM

G. Di Pirro, A. Drago, F. Sannibale, Laboratori Nazionali di Frascati INFN (LNF-INFN), Via E. Fermi 40, 00044 Frascati (RM), Italy

Abstract

At the DAFNE collider a beam loss monitor system has been installed to continuously monitor the particle losses. The acquisition is based on 32 Bergoz beam loss monitors, of the Wittenburg type, installed close to the main rings vacuum chamber, buffer and monitoring circuitry and a scaler (SIS 3801) as acquisition board. We developed a front-end software that allows acquiring the integrated value of the BLM counts and a stream of 1000 point for each monitor, to cover a history of 3000 s. The operator program allows displaying the instantaneous BLM values over the machine together with a representation of the past history.

1 INTRODUCTION

DAFNE [1] is an electron/positron collider, composed by two rings and with two interaction regions. More than 1 A has been stored in collision. With beams at high current any beam loss along the machine pipe becomes a source of high background. To understand if we have anomalous beam losses we installed a beam loss monitor system on the machine pipe. The small size of the accelerator allows us to try a first installation with a low monitor number. A requirement to the installation is to allow upgrading the system in the future without any change in the software environment.

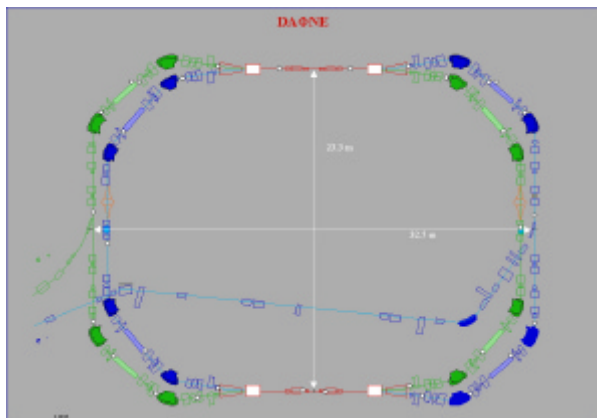


Fig.1 Dafne BLMs positions

We installed 31 monitors in total: 13 on the electron ring, 14 on the positron and 4 near the interaction region. The position has been chosen downstream already existing beam scrapers on the machine. Other monitors are placed at the point where the pipe is narrow near the splitter. Some other are near the dipoles and the wiggler. The BLMs are placed in equivalent positions in both rings. There are some monitors near the two experiments as well.

2 HARDWARE

The high density of elements installed on the DAFNE accelerator requires a compact beam loss monitor; moreover the monitor must be easy to install on the vacuum pipe. We chose the Beam Loss Monitor by Bergoz [3] for his compact size ($33.5 \times 68.5 \text{ mm}^2$) and performances, a VME counter/scaler by Struck SIS 3801 [5] as acquisition board with an in house developed fan out. The acquisition board and the fan out are put inside a VME control system crate.

Fig 2 illustrates BLM operation. The BLM produces voltage pulses when the active area of a PIN photo-diode is struck by minimum ionizing particles (MIP), usually created by high energy particles striking residual gas molecules or a beam pipe obstruction. Presumably a MIP produces current flow in both detectors while a photon does not.

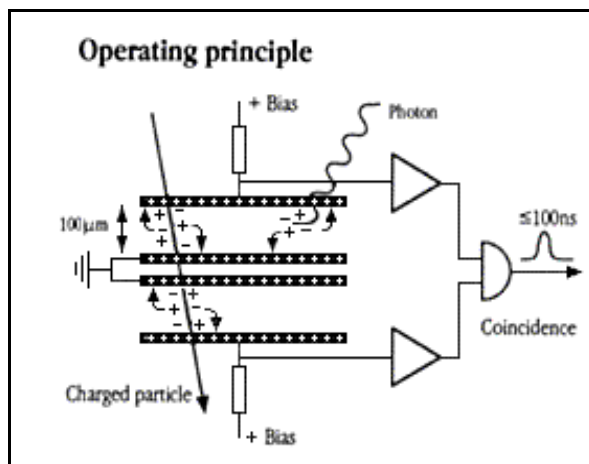


Fig 2 Operating principle (courtesy of Bergoz)

The acquisition board (SIS 3801) is a 100 MHz 32-channel scaler/counter. To synchronize the acquisition we use the 25 MHz internal clock which can be read on the first channel of the board. To the other 31 channels we connect the BLMs. A fan out board has been developed to interface the monitor with the acquisition board.

The beam loss monitor fan out is a VME module designed by the DAFNE electronics laboratory with the aim to interface mechanically and electrically the commercial parts and simplifies the test of the system. The fan out module is made of terminals to interface 32 Bergoz input sensors, 32 channel TTL buffers, 2 channel outputs with BNC connectors for diagnostics purpose, two manual knobs to select the channels to be monitored, and terminals to connect easily the SIS3800 counter. The diagnostics interface allows checking each input channel

using an oscilloscope, looking at the pulses in time domain and correlates these data with the counter outputs.

3 SOFTWARE

The DAFNE control system [2] is based on distributed CPUs with a memory resident database to exchange information with the consoles in the accelerator control room. The DAFNE control system allows separating the acquisition program from the human interface on the control room console. The acquisition program runs on the CPU that has in charge the beam loss monitor while the display program runs on one of the consoles.

The exchange of data between the front-end and the console is based on a real time database. The descriptive record in the real time database contains all the information needed to manage the acquisition board and to exchange data with the consoles (fig 3). The real time record is divided in two parts. The static record contains all the information needed to manage the VME board, the SIS381 board address, the beam loss monitor name and the address of the history storage area. The dynamic record contains all variables acquired by the VME board. In detail, the record contains the counting data in two different formats, the total counts and the counts per second.

Fig 3 Real Time Data Base records

The acquisition program continuously runs on the beam loss monitor acquisition CPU.

The program is integrated in the standard control system acquisition program. When the clock register reaches the integration time the program puts the data in the real time database and in the history memory.

The history memory is 1000 points deep for each channel. In the default case the time window for each point is 3 seconds that gives us 3000 seconds of acquired memory. The history memory is a circular memory that is continuously written. The dynamic record contains all information about the current position of the last written data.

The console level program allows the display of the data in different ways to give better understanding of the behavior of the particle losses. The program displays in real time all BLMs divided in the positron and electron area. In each part we can display the instantaneous data, the intensity chart of 200 points and with a cursor we can read a single BLM value and his position on the schematic machine layout. We can also display cumulative data such as the sum of all BLMs and the ratio between the counts and the beam current. We can also take a reference data and display the ratio between these data and the acquired ones.



Fig 4 Console display

The console program allows selecting the beam loss monitor to display on the window. With this program the history data can also be displayed, showing the evolution of each monitor in the last 3000 s (fig 5).

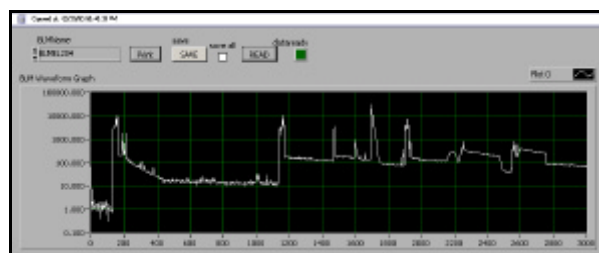


Fig 5 History Display

This tool allows us also to save the history data in tab-formatted file for an offline analysis.

4 CONCLUSIONS AND FUTURE DEVELOPMENTS

The BLM monitoring system demonstrated its potentiality to understand the sources of background. From the data analysis there isn't any evidence of beam scraping the vacuum pipe. We started a study to use the beam loss monitor as a general tool to setup other system

installed in the machine. The scraper setup can be optimized by monitoring the beam losses as a function of the scraper position.

The system can be easily upgraded to increase its performance just adding monitors and acquisition boards.

We will start with a systematic measurement in different operating conditions of the accelerator to possibly find a cleaner use of the machine. To make this measurement easier we beam loss monitors are included on the automatic data logging system of the DAFNE control system [6]

5 ACKNOWLEDGEMENTS

We want to thank O. Coiro, O. Giacinti and D. Pellegrini for their support in the hardware installation and setup.

We are also grateful to all the Accelerator Division staff for their continuous suggestions and encouragement to make a good and useful job.

REFERENCES

- [1] G. Vignola and DAFNE Project Team, DAFNE, “The First γ -Factory, EPAC'96”, Sitges, June 1996, p. 22.
- [2] G. Di Pirro et al. “DANTE: Control System for DAFNE based on Macintosh and LabView”, Nuclear Instrument and Methods in Physics Research A 352 (1994) 455-475.
- [3] BERGOZ Precision Beam Instrumentation 01170 Crozet, France (<http://www.bergoz.com>)
- [4] W. Bialowons, K. Wittenburg, Ridoutt, “Electron Beam Loss Monitors for HERA”, EPAC 1994, LONDON
- [5] SIS GmbH, Moorhod 2d, 22399 Haburg, Germany (<http://www.struck.de>)
- [6] G. Mazzitelli et al., The KLOE/DAPHNE Status Logging, Analysis and Database System, ICALEPCS 2001, San Jose California, November 2001, WEDT002
(<http://www.slac.stanford.edu/econf/C011127/proceedings.html>)

DISCUSSION SESSION

Discussion-Session
Session 1: Wednesday (11:15–13:00 Hrs)

Machine Protection And Interlock Systems

K. Wittenburg, DESY, Deutsches Elektronen Synchrotron, Hamburg, Germany
e-mail: `kay.wittenburg@desy.de`
K. Scheid, ESRF, European Synchrotron Radiation Facility, Grenoble, France
e-mail: `scheidt@esrf.fr`

The purpose of a MPS is to protect the equipment against abnormal beam behaviour. High intense and high brilliant particle, photon and X-ray beams are capable of causing significant damage to components in a fraction of a second, i.e. too fast for any human reaction.

The aim of this session is to discuss existing and planned MPS with both their specific and their general requirements. Among points to be reviewed in the need for the MPS to be fail-proof are:

- the choice of sensors and components,
- the logic,
- the strategy, etc.

Some typical questions that will be raised are:

- What are the criteria for determining that an alarm situation has been reached?
- What is the subsequent action of the system?

Very often the MPS may allow different beam modes, depending on beam permit inputs:

- Which kind of beam modes exist?
- Which are the input signals?
- How are these systems integrated with the accelerator controls?
- What is the impact on their operation?

This session will include a few very brief presentations of existing and planned MPS' from different machines to illustrate the above questions and to stimulate the subsequent discussion.

Discussion-Session
Session 2: Wednesday (11:15–13:00 Hrs)

Global Accelerator Network, Control Systems And Beam Diagnostics

U. Raich, CERN, Geneva, Switzerland

e-mail: Ulrich.Raich@cern.ch

H. Schmickler, CERN, Geneva, Switzerland

e-mail: Hermann.Schmickler@cern.ch

Falling funds force all accelerator centers to look for new sources of financing and for the most efficient way of implementing new projects. This very often leads to collaborations between institutes scattered around the globe, a problem well known to big high energy physics experiments. The collaborations working on big detectors e.g. for LHC started thinking about detector acquisition and control systems which can be remotely used from their respective home institutes with minimal support on the spot.

This idea was taken up by A. Wagner from DESY for the TESLA machine, who proposed the Global Accelerator Network (GAN) enabling users from around the world to run an accelerator remotely.

Questions around this subject that immediately come to mind

- Is the GAN only relevant to big labs? Or is it reasonable e.g. for operators or engineers in charge to do certain manipulations from home?
- Are our instruments ready for the GAN?
- Does the fact of being GAN ready increase the cost of the instruments?
- What are the advantages and disadvantages?
- Do we want these features? Or do inconveniences prime over advantages?
- Do any of the labs already have experience with GAN or any system going into this direction?
- What does GAN mean for the relationship between controls and beam diagnostics (a sometimes difficult chapter)?
- Can measurement systems be put onto the WEB and if yes, which ones?
- Where are the limitations?
- Can the scope of GAN be expanded to remote diagnostics and active maintenance of equipment, i.e. collaborating partners maintain their product in service after commissioning?
- What about common machine experiments with people sitting in different control rooms?
- What communication systems have to be put in place for this?
- Are there security issues and how do we deal with them?

Discussion-Session
Session 3: Wednesday (11:15–13:00 Hrs)

Beam Synchronous Timing Systems

A. Peters, GSI, Gesellschaft für Schwerionenforschung, Darmstadt, Germany
e-mail: A.Peters@gsi.de
M. Ferianis, ELETTRA, Sincrotrone Trieste, Trieste, Italy
e-mail: mario.ferianis@elettra.trieste.it

For many beam diagnostics purposes beam synchronous timing systems are needed in addition to the timing systems supplied by the control systems of the different accelerators. The demands and techniques of different accelerator facilities will be discussed along the following aspects:

- Bunch and macro pulse synchronous timing systems
 - Solutions for different time scales from ps to ms
 - Coupling to the RF and control systems of the different accelerators
 - Electronics for the beam synchronous timing systems:
 - parameters,
 - techniques,
 - controlling.
- Use of industrial products for bunch synchronous timing systems, e.g. function generators
 - Distribution of the timing signals:
 - electronically via cables,
 - optically via fibres or
 - wireless
 - Coupling to and use of timing standards:
 - IRIG-B,
 - GPS,
 - ...

The participants should present and describe solutions from their facilities with some transparencies as a starting point for the discussion.

APPENDICES

- **Authors**
- **Institutes**
- **Participants**
- **Vendors**

List of Authors

Bold papercodes indicate primary authors

Abrahamyan, K.	PT23	Di Pirro, G.	PT34
Angoletta, M.E.	IT07 , PM07	Dietrich, J.	PM19 , PT19 , PT28
Arutunian, S.G.	PM15	Dobrovolski, N.M.	PM15
Assadi, S.	IT08	Dölling, R.	PM25
Assmann, R.	PT30	Doolittle, L.	IT08
Baboi, N.	CT11	Drago, A.	PT34
Backe, H.	IT09	Dykes, M.	IT02
Badano, L.	CT09	Ehnes, A.	PM24
Badura, E.	PT32	El-Sisi, A.B.	PM16
Bae, Y.S.	PT14	Evtushenko, P.	PT15
Bähr, J.	PM05 , PT22 , PT23	Fartoukh, S.	PM08
Bakshetyan, K.H.	PM15	Ferianis, M.	PM10 , PT25 , DW03
Bal, C.	PM04	Feroli, G.	IT03 , PM11 , PT30
Balleyguier, P.	PT16	Ferrando, O.	CT09
Bank, A.	PM18	Ferrari, A.	PT18
Barabin, S.	PM27	Finocchiaro, P.	PM21
Barth, W.	CT02 , PM28	Fiorito, R.B.	PM01
Bassanese, S.	PM10 , PT25	Fischer, C.	PM11
Batalin, V.	PM27	Flöttmann, K.	PT22 , PT23 , PT29
Berden, G.	IT05	Forck, P.	PM17 , PM18 , PM29
Berrig, O.	PM06	Franczak, B.	PT32
Bishop, D.	PT08	Franz, H.	PM24
Blokland, W.	PM23	Gall, A.	PM26
Boccard, C.	PT08	Gasior, M.	CT01
Bohnet, I.	PT22 , PT23 , PT29	Giacomini, T.	PM17
Borrion, H.	PT16	Gikal, B.N.	PM26
Brandenburg, S.	CT10 , PT12	Gillespie, W.A.	IT05
Bravin, E.	PM03 , PM04	Glatz, J.	PM28
Bremec, S.	PT04 , PT05	Gobulev, A.	PM17
Bulfone, D.	CT08	Gössel, A.	CT11
Burger, S.	PM13	Göttlicher, P.	CT04
Calvo-Giraldo, E.	PT08	Groening, L.	CT02 , PM28
Cameron, P.	IT08	Gschwendtner, E.	PT30
Carli, C.	PM13	Guimbal, Ph.	PT16
Caspers, F.	PM12 , PT18	Gulbekian, G.G.	PM26
Cassinari, L.	IT02	Hamdi, A.	CT04
Catalan-Lasheras, N.	PM08	Han, J.H.	PT22 , PT29
Chevallay, E.	PM04	Han, J.M.	PT14
Cho, Y.S.	PT14	Han, S.H.	PT14
Choi, B.H.	PT14	Henning, W.F.	IT01
Cocq, D.	PT08	Henschel, H.	PT31
Connolly, R.	IT08	Hoffmann, T.	PM29
Corsini, R.	PT18	Horn, P.	PT32
Cosentino, L.	PM21	Huang, J.Y.	PT14
Dahl, L.	PM28	Hüning, M.	CT11
D'Auria, G.	PM10	Hutchins, S.	IT03
Dehler, M.	CT08 , PT21	Hwang, W.H.	PT14
Dehning, B.	PM12 , PT30	Iazzourene, F.	PT25
Deibele, C.	PM10	Jablonka, M.	CT04 , CT11
Denard, J.-C.	IT02	Jackel, H.	PT24
Deslandes, D.	PT16	Jakob, H.	PT27
Desmons, M.	CT04	Jamison, S.P.	IT05
Devanz, G.	CT11	Jensen, E.	PM12

Jensen, L.	PT08, PT27	Oppelt, A.	PT22, PT23
Johnson, R.	PT13	Orlov, A.	PM27
Jones, R.	PM08, PT08, PT27	Paal, A.	PT28
Jung, R.	IT03	Park, J.H.	PT14
Källberg, A.	PT28	Park, S.J.	PT14
Kain, V.	PT30	Penacoba, G.F.	PT01
Kalagin, I.V.	PM26	Pershin, V.	PM27
Kamerdzhev, V.	PM19, PT19	Peters, A.	PT26, DW03
Kaufmann, W.	PT17, PT32	Petrenko, S.	PM27
Kazacha, V.I.	PM26	Pezzetta, M.	CT09
Knaack, K.	PT26	Plouviez, E.	PT01
Knippels, G.M.H.	IT05	Plum, M.A.	IT08
Körfer, M.	PT31	Poggi, M.	PM10
Koopman, J.	PM11, PM12	Pollet, P.	CT08
Koutchouk, J.-P.	IT10	Post, H.	CT10
Kozlov, A.	PM27	Priestnall, K.	PM13
Kramert, R.	CT08	Privitera, P.	CT03
Krasilnikov, M.	PT22, PT23, PT29	Pugachov, D.	CT04
Krejčík, P.	IT06	Raich, U.	PM13, DW02
Kube, G.	IT09	Reeg, H.	PT32
Kuhnhenh, J.	PT31	Reich-Sprenger, H.	PT32
Kulevoy, T.	PM27	Richter, S.	PM28
Kuybida, R.	PM27	Rifkin, J.	PT13
Langenhagen, H.	CT05	Rinolfi, L.	PT18
Launé, B.	CT10	Roncarolo, F.	PM11, PM12
Lauth, W.	IT09	Royer, P.	PT18
Lefèvre, T.	PM03, PM04	Rydberg, A.	PT18
Li, Z.	PT13	Sannibale, F.	CT03, PT34
Liakin, D.A.	CT02, PM17, PM27, PM29	Sargsyan, V.	PT02
Liapine, A.	PT07	Savioz, J.J.	PT08, PT27
Lipka, D.	PM05, PT22, PT23	Scheidt, K.	PM14, DW01
Lonza, M.	CT08	Schlarb, H.	CT04
Loung, M.	CT04	Schlott, V.	PT24
Ludwig, M.	PM07	Schmickler, H.	DW02
Lüdecke, H.	PM05	Schölles, J.	PT17
MacLeod, A.M.	IT05	Schöpe, H.	IT09
Magne, C.	CT11	Schreiber, H.J.	PT09
Mailian, M.R.	PM15	Schreiber, S.	CT11
Malo, J.F.	PM12	Schreuder, H.W.	CT10
Mavrič, U.	PT04, PT05	Schütt, P.	PT32
Mazzitelli, G.	CT03	Schurig, R.	CT05, PT15
Michel, P.	CT05	Seebach, M.	PM24
Miltchev, V.	PT22, PT23	Seleznirov, D.	PM27
Mohos, I.	PT19, PT28	Shea, T.J.	IT08, PM23
Molinari, G.	CT09	Shen, J.L.	IT05
Naito, T.	PT13	Shkvarunets, A.G.	PM01
Nam, S.H.	PT14	Sigg, H.	PT24
Napoly, O.	CT11	Simonsson, A.	PT28
Naylor, G.A.	CT07, PT01	Skachkov, V.	PM17
Neubert, R.	PT26	Smith, R.	IT02
Neumann, R.	CT04	Smith, St.	PT13
Nietzsche, S.	PT26	Smith, V.	PT13
Nijboer, H.W.	PT12	Soghoyan, H.E.	PM15
Nölle, D.	CT04	Spiller, P.	PT32
Odier, P.	PT20	Staack, M.	CT04
Oepts, D.	IT05	Stasevich, Yu.	PM27

Proceedings DIPAC 2003 – Mainz, Germany

Stephan, F.	PT22, PT23, PT29	Vetrov, A.	PM17
Stettler, M.	PM23	Vodel, W.	PT26
Straumann, T.	PT06	Waldmann, H.	PT09
Suberlucq, G.	PM04	Waters, G.	PT08
Sütterlin, D.	PT24	Weinrich, U.	PT32
Tecker, F.	PT18	Welzel, K.	PT32
Teichert, J.	CT05	Wendt, M.	CT04, CT11, PT26
Tranquille, G.	PM09	Wenninger, J.	IT04
Tsakov, I.	PT23	Werner, M.	CT04, CT06, PM24
Uršič, R.	PT04, PT05	Wilke, I.	IT05
Valente, P.	CT03	Wittenburg, K.	CT04, PM15, PT26, DW01
van Asselt, W.K.	CT10, PT12	Wulf, F.	PT31
van der Meer, A.F.G.	IT05	Yan, X.	IT05
Vasiniuk, I.E.	PM15	Yaramishev, S.	PM28
Verzi, V.	CT03		
Vescovi, M.	CT03		

Institutes List

ASTec

Daresbury Laboratory, Daresbury, UK

- Dykes, M.
- Smith, R.

Abertay

University of Abertay Dundee, Dundee, UK

- Gillespie, W.A.
- Jamison, S.P.
- MacLeod, A.M.
- Yan, X.

BNL

Brookhaven National Laboratory, Upton, NY, USA

- Cameron, P.
- Connolly, R.

CEA

Commissariat à l'Energie Atomique, Saclay, France

- Desmons, M.
- Devanz, G.
- Hamdi, A.
- Jablonka, M.
- Loung, M.
- Magne, C.
- Napoly, O.

CEA-DPTA

Commissariat à l'Energie Atomique, Bruyères-le-Châtel, France

- Balleyguier, P.
- Deslandes, D.
- Guimbal, Ph.

CERN

Geneva, Switzerland

- Angoletta, M.E.
- Assmann, R.
- Bal, C.
- Berrig, O.
- Boccard, C.
- Bravin, E.
- Burger, S.
- Calvo-Giraldo, E.
- Carli, C.
- Caspers, F.
- Catalan-Lasheras, N.
- Chevallay, E.
- Cocq, D.
- Corsini, R.
- Dehning, B.
- Fartoukh, S.
- Ferioli, G.
- Fischer, C.
- Gasior, M.

- Gschwendtner, E.
- Hutchins, S.
- Jakob, H.
- Jensen, E.
- Jensen, L.
- Jones, R.
- Jung, R.
- Kain, V.
- Koopman, J.
- Koutchouk, J.-P.
- Lefèvre, T.
- Ludwig, M.
- Malo, J.F.
- Molinari, G.
- Odier, P.
- Priestnall, K.
- Raich, U.
- Rinolfi, L.
- Roncarolo, F.
- Savioz, J.J.
- Schmickler, H.
- Suberlucq, G.
- Tecker, F.
- Tranquille, G.
- Wenninger, J.

CNU

Capital Normal University, Beijing, China

- Shen, J.L.

DESY

Deutsches Elektronen-Synchrotron, Hamburg, Germany

- Flöttmann, K.
- Gössel, A.
- Göttlicher, P.
- Knaack, K.
- Kube, G.
- Körfer, M.
- Neumann, R.
- Nölle, D.
- Pugachov, D.
- Schlarb, H.
- Schreiber, S.
- Seebach, M.
- Staack, M.
- Wendt, M.
- Werner, M.
- Wittenburg, K.

DESY-HASYLAB

Deutsches Elektronen-Synchrotron, Hamburg, Germany

- Ehnes, A.
- Franz, H.

DESY-Zeuthen

Deutsches Elektronen-Synchrotron, Zeuthen, Germany

- Abrahamyan, K.
- Bohnet, I.
- Bähr, J.
- Han, J.H.
- Krasilnikov, M.
- Lipka, D.
- Lüdecke, H.
- Miltchev, V.
- Oppelt, A.
- Schreiber, H.J.
- Stephan, F.
- Waldmann, H.

DNPT

FEI STU Bratislava, Slovakia

- Gall, A.

EE-UCL

Electrical and Electronic Engineering Dept., University College, London, UK

- Borrion, H.

ELETTRA

Sincrotrone Trieste, Trieste, Italy

- Bassanese, S.
- D'Auria, G.
- Ferianis, M.
- Iazzourene, F.

ESRF

European Synchrotron Radiation Facility, Grenoble, France

- Naylor, G.A.
- Penacoba, G.F.
- Plouviez, E.
- Scheidt, K.

ETHZ

Institute of Electronics, Zürich, Switzerland

- Jackel, H.

FNAL

Fermi National Accelerator Laboratory, Batavia, IL, USA

- Hüning, M.

FOM

Institute for Plasma Physics 'Rijnhuizen', Nieuwegein, The Netherlands

- Berden, G.
- Knippels, G.M.H.
- Oepts, D.
- van der Meer, A.F.G.

FSU Jena

Friedrich-Schiller Universität, Jena, Germany

- Neubert, R.

- Nietzsche, S.
- Vodel, W.

FZR

Forschungszentrum Rossendorf, Dresden, Germany

- Evtushenko, P.
- Langenhagen, H.
- Michel, P.
- Schurig, R.
- Teichert, J.

Fraunhofer-INT

Fraunhofer-INT, Euskirchen, Germany

- Henschel, H.
- Kuhnhenh, J.

GSI

Gesellschaft für Schwerionenforschung, Darmstadt, Germany

- Badura, E.
- Bank, A.
- Barth, W.
- Dahl, L.
- Forck, P.
- Franczak, B.
- Giacomini, T.
- Glatz, J.
- Groening, L.
- Henning, W.F.
- Hoffmann, T.
- Horn, P.
- Kaufmann, W.
- Peters, A.
- Reeg, H.
- Reich-Sprenger, H.
- Richter, S.
- Schölles, J.
- Schütt, P.
- Spiller, P.
- Weinrich, U.
- Welzel, K.
- Yaramishev, S.

HMI

Hahn-Meitner Institut, Berlin, Germany

- Wulf, F.

I-Tech

Instrumentation Technologies, Solkan, Slovenia

- Bremec, S.
- Mavrič, U.
- Uršič, R.

IKP

Forschungszentrum Jülich GmbH, Jülich, Germany

- Dietrich, J.
- Kamedzhiev, V.

- Mohos, I.
- Dietrich, J.
- Kamerdzhev, V.
- Backe, H.
- Lauth, W.
- Schöpe, H.

INFN-LNF

Laboratori Nazionali di Frascati dell'INFN, Frascati, Italy

- Di Pirro, G.
- Drago, A.
- Mazzitelli, G.
- Sannibale, F.
- Valente, P.
- Vescovi, M.

INFN-LNL

Laboratori Nazionali di Legnaro, Legnaro, Italy

- Poggi, M.

INFN-LNS

Laboratori Nazionali del Sud, Catania, Italy

- Cosentino, L.
- Finocchiaro, P.

INFN-Roma

Istituto Nazionale di Fisica Nucleare, Sez. di Roma, Roma, Italy

- Privitera, P.
- Verzi, V.

IPN

Institut de Physique Nucléaire, Orsay, France

- Launé, B.

IREAP

Institute for Research in Electronics and Applied Physics, University of Maryland, College Park, MD, USA

- Fiorito, R.B.
- Shkvarunets, A.G.

ITEP

Institute for Theoretical and Experimental Physics, Moscow, Russia

- Barabin, S.
- Batalin, V.
- Gobulev, A.
- Kozlov, A.
- Kulevoy, T.
- Kuybida, R.
- Liakin, D.A.
- Orlov, A.
- Pershin, V.
- Petrenko, S.
- Seleznirov, D.
- Skachkov, V.
- Stasevich, Yu.

JINR

FLNR JINR Dubna, Russia

- Gikal, B.N.
- Gulbekian, G.G.
- Kalagin, I.V.
- Kazacha, V.I.

KAERI

Proton Engineering Frontier Project, Korea

- Cho, Y.S.
- Choi, B.H.
- Han, J.M.
- Han, S.H.

KEK

High Energy Accelerator Research Organization, Ibaraki, Japan

- Naito, T.

KVI

Kernfysisch Versneller Instituut, Groningen, The Netherlands

- Brandenburg, S.
- Nijboer, H.W.
- Post, H.
- Schreuder, H.W.
- van Asselt, W.K.

LANL

Los Alamos National Laboratory, Los Alamos, NM, USA

- Plum, M.A.
- Stettler, M.

LBNL

Lawrence Berkeley National Laboratory, Berkeley, CA, USA

- Doolittle, L.

LTI

Lyncean Technologies, Inc., Palo Alto, CA, USA

- Rifkin, J.

MSI

Manne Siegbahn Laboratory of Physics, Stockholm, Sweden

- Källberg, A.
- Paal, A.
- Simonsson, A.

MSU

Moscow State University, MSU, Moscow, Russia

- Vetrov, A.

NRC

Atomic Energy Authority, NRC, Plasma and Nuclear Fusion
Dept., Cairo, Egypt

- El-Sisi, A.B.

NRNE

Institute for Nuclear Research and Nuclear Energy of the
Bulgarian Academy of Science, Sofia, Bulgaria

- Tsakov, I.

ORNL

Oak Ridge National Laboratory, Oak Ridge, TN, USA

- Assadi, S.
- Blokland, W.
- Shea, T.J.

POSTECH

Pohang Accelerator Laboratory, Pohang, Korea

- Bae, Y.S.
- Huang, J.Y.
- Hwang, W.H.
- Nam, S.H.
- Park, J.H.
- Park, S.J.

PSI

Paul Scherrer Institut, Villigen, Switzerland

- Bulfone, D.
- Dehler, M.
- Dölling, R.
- Kramert, R.
- Lonza, M.
- Pollet, P.
- Schlott, V.
- Sigg, H.
- Sütterlin, D.

RPI

Rensselaer Polytechnic Institute, Troy, NY, USA

- Wilke, I.

SLAC

Stanford Linear Accelerator, Stanford, CA, USA

- Baboi, N.
- Johnson, R.
- Krejcik, P.
- Li, Z.
- Smith, St.
- Smith, V.
- Straumann, T.

SNS

Spallation Neutron Source, Oak Ridge, TN, USA

- Deibele, C.

SOLEIL

Société Synchrotron Soleil, Saint-Aubin, France

- Cassinari, L.
- Denard, J.-C.

TERA

Fondazione TERA, Università degli Studi Milano, Milano, Italy

- Badano, L.
- Ferrando, O.
- Pezzetta, M.

TRIUMF

Vancouver, Canada

- Bishop, D.
- Waters, G.

TU-Berlin

Technische Universität, Berlin, Germany

- Liapine, A.
- Sargsyan, V.

UNIL

Université de Lausanne, Switzerland

- Royer, P.

UUS

Uppsala University, Sweden

- Ferrari, A.
- Rydberg, A.

YPI

Yerevan Physics Institute, Armenia

- Arutunian, S.G.
- Bakshetyan, K.H.
- Dobrovolski, N.M.
- Mailian, M.R.
- Soghoyan, H.E.
- Vasiniuk, I.E.

Participants List

— A —

Finn **Abildskov** (IFA)
fa@phys.au.dk
 Department of Physics and Astronomy
 University of Aarhus, Ny Munkegade,
 bygn. 520
 DK-8000 Aarhus, Denmark
 ☎ +45-89-42-37-76
 ☎ +45-86-12-07-40

Maria Elena **Angoletta** (CERN)
Maria.Elena.Angoletta@cern.ch
 CERN Laboratory
 AB Division
 CH-1211 Geneva 23, Switzerland
 ☎ +41-22-76-72605
 ☎ +41-22-76-77740

— B —

Laura **Badano** (TERA)
laura.badano@tera.it
 Fondazione per Adroterapia
 Oncologica
 c/o Università Bicocca - Dipartimento
 Scienze dei Materiali
 I-20126 Milano, Italy
 ☎ +39-2-64485418
 ☎ +39-2-64485417

Jean-Louis **Baelde** (GANIL)
baelde@ganil.fr
 Grand Accélérateur National d'Ions
 Lourds
 Boulevard Henri Becquerel
 F-14076 Caen Cedex 5, France
 ☎ +33-2-31-45-47-75
 ☎ +33-2-31-45-47-28

Jürgen **Bähr** (DESY Zeuthen)
baehr@ifh.de
 Deutsches Elektronen-Synchrotron
 Zeuthen
 Platanenallee 6
 D-15738 Zeuthen, Germany
 ☎ +49-33762-77235
 ☎ +49-33762-77330

Pascal **Balleyguier** (CEA)
pascal.balleyguier@cea.fr
 Commissariat à l'Energie Atomique
 BP12
 F-91680 Bruyères le Chatel, France
 ☎ +33-1-69-26-60-61
 ☎ +33-1-69-26-70-24

Alexander **Bank** (GSI)
a.bank@gsi.de
 Gesellschaft für
 Schwerionenforschung
 Planckstraße 1
 D-64291 Darmstadt, Germany
 ☎ +49-6159-712228
 ☎ +49-6159-712104

Silvano **Bassanese** (ELETTRA)
silvano.bassanese@elettra.trieste.it
 Sincrotrone Trieste S.C.p.A.
 Area Science Park S.S. 14 km 163.5
 I-34012 Trieste, Italy
 ☎ +39-40-37581
 ☎ +39-40-9380902

Winfried **Barth** (GSI)
W.Barth@gsi.de
 Gesellschaft für
 Schwerionenforschung
 Planckstraße 1
 D-64291 Darmstadt, Germany
 ☎ +49-6159-712170
 ☎ +49-6159-712987

David **Belohrad** (CERN)
David.Belohrad@cern.ch
 CERN Laboratory
 CH-1211 Geneva 23, Switzerland
 ☎ +41-22-76-76318
 ☎ +41-22-76-77740

Giel **Berden** (FOM / FELIX)
berden@rijnh.nl
 FOM Institute 'Rijnhuizen' / FELIX
 Edisonbaan 14
 NL-3439 MN Nieuwegein, The
 Netherlands
 ☎ +31-30-609-6895
 ☎ +31-30-603-1204

Julien **Bergoz** (BERGOZ)
bergoz@bergoz.com
 Bergoz Instrumentation
 Espace Allondon Ouest
 F-01630 Saint Genis Pouilly, France
 ☎ +33-4-50-42-66-42

Olav **Berrig** (CERN)
Olav.Ejner.Berrig@cern.ch
 CERN Laboratory
 Geneva 23
 CH-1211 Geneva, Switzerland
 ☎ +41-22-76-75134

Klaus **Blasche** (GSI)
k.blasche@gsi.de
 Gesellschaft für
 Schwerionenforschung
 Planckstraße 1
 D-64291 Darmstadt, Germany
 ☎ +49-6159-712383
 ☎ +49-6159-712039

Willem **Blokland** (SNS)
blokland@sns.gov
 Spallation Neutron Source
 701 Scarboro Rd
 37830 Oak Ridge, USA
 ☎ +1-865-574-6583
 ☎ +1-865-574-6617

Sytze **Brandenburg** (KVI)
brandenburg@kvi.nl
 Kernfysisch Versneller Instituut
 Zernikelaan 25
 NL-9747 AA Groningen, The
 Netherlands
 ☎ +31-50-363-3600
 ☎ +31-50-363-4003

Enrico **Bravin** (CERN)
Enrico.Bravin@cern.ch
 CERN Laboratory
 CH-1211 Geneva 23, Switzerland
 ☎ +41-22-76-71885
 ☎ +41-22-76-77740

Sasa **Bremec** (I-Tech)
sasa@i-tech.si
 Instrumentation Technologies
 Srebrničev trg 4a
 SI-5250 Solkan, Slovenia
 ☎ +386-5-3332300
 ☎ +386-5-3332305

Stephen **Buckley** (DL)
s.r.buckley@dl.ac.uk
 Daresbury Laboratory
 Keckwick Lane
 WA4 4AD Warrington, United Kingdom
 ☎ +44-1925-603981
 ☎ +44-1925-603124

Stephane **Burger** (CERN)
Stephane.Burger@cern.ch
 CERN Laboratory
 CH-1211 Geneva 23, Switzerland
 ☎ +41-22-76-71933
 ☎ +41-22-76-77740

— C —

Eva **Calvo Giraldo** (CERN)
Eva.Calvo.Giraldo@cern.ch
 CERN Laboratory
 CH-1211 Geneva 23, Switzerland
 ☎ +41-22-76-75969
 ☎ +41-22-76-77740

Lodovico **Cassinari** (SOLEIL)
Lodovico.Cassinari@synchrotron-soleil.fr
 Soci   Synchrotron SOLEIL
 L'Orme des Merisiers
 F-91192 Gif sur Yvette Cedex, France
 ☎ +33-1-69-35-98-21
 ☎ +33-1-69-35-94-54

Madeleine **Catin** (CERN)
madeleine.catin@cern.ch
 CERN Laboratory
 CH-1211 Geneva 23, Switzerland
 ☎ +41-22-76-74619
 ☎ +41-22-76-77740

Luigi **Cosentino** (LNS-INFN)
cosentino@lns.infn.it
 Laboratori Nazionali del Sud - INFN
 Via S. Sofia, 44
 I-95123 Catania, Italy
 ☎ +39-95-542353

— D —

Micha **Dehler** (PSI)
micha.dehler@psi.ch
 Paul Scherrer Institut
 WSLA/006
 CH-5232 Villigen PSI, Switzerland
 ☎ +41-56-310-4572
 ☎ +41-56-310-3383

Bernd **Dehning** (CERN)
Bernd.Dehning@cern.ch
 CERN Laboratory
 CH-1211 Geneva 23, Switzerland
 ☎ +41-22-76-75541
 ☎ +41-22-76-77740

Jean-Claude **Denard** (SOLEIL)
jean-claude.denard@synchrotron-soleil.fr
 Soci   Synchrotron SOLEIL
 L'Orme des Merisiers
 F-91192 Gif sur Yvette Cedex, France
 ☎ +33-1-69-35-98-14

Giampiero **Di Pirro** (LNF-INFN)
giampiero.dipirro@lnf.infn.it
 Laboratori Nazionali di Frascati - INFN
 Via Enrico Fermi 40
 I-00044 Frascati (RM), Italy
 ☎ +39-69-4032269
 ☎ +39-69-4032256

Erika **Ditter** (GSI)
e.ditter@gsi.de
 Gesellschaft f  r
 Schwerionenforschung
 Planckstra   1
 D-64291 Darmstadt, Germany
 ☎ +49-6159-712160
 ☎ +49-6159-712935

Rudolf **D  lling** (PSI)
rudolf.doelling@psi.ch
 Paul Scherrer Institut
 WBGA C14
 CH-5232 Villigen PSI, Switzerland
 ☎ +41-56-310-3405
 ☎ +41-56-310-3383

Christoph **Dorn** (GSI)
C.Dorn@gsi.de
 Gesellschaft f  r
 Schwerionenforschung
 Planckstra   1
 D-64291 Darmstadt, Germany
 ☎ +49-6159-712318
 ☎ +49-6159-712104

Michael **Dufau** (ASTeC)
m.j.dufau@dl.ac.uk
 Daresbury Laboratory
 Keckwick Lane
 WA4 4AD Warrington, United Kingdom
 ☎ +44-1925-603270
 ☎ +44-1925-603124

Pierre-Andre **Duperrex** (PSI)
pierre-andre.duperrex@psi.ch
 Paul Scherrer Institut
 WBGA C14
 CH-5232 Villigen PSI, Switzerland
 ☎ +41-56-310-4775
 ☎ +41-56-310-3383

Douglas Michael **Dykes** (ASTeC)
d.m.dykes@dl.ac.uk
 Daresbury Laboratory
 Daresbury
 WA4 4AD Cheshire, United Kingdom
 ☎ +44-1925-603142
 ☎ +44-1925-603192

— E —

Ashraf **El-Sisi** (AEA-NRC)
ashrafelsisi@hotmail.com
 Bergoz & GSI
 Atomic Energy Authority, Nuclear
 Research Center,
 Cairo, Inshass, Egypt
 ☎ +20-2-2876031
 ☎ +20-2-4691749

Pavel **Evtushenko** (ELBE)
P.Evtushenko@fz-rossendorf.de
 ELBE at Forschungszentrum
 Rossendorf e.V.
 Postfach 510119
 D-01314 Dresden, Germany
 ☎ +49-351-260-3376
 ☎ +49-351-260-3690

— F —

Mario **Ferianis** (ELETTRA)
mario.ferianis@elettra.trieste.it
 Sincrotrone Trieste
 Area Science Park S.S. 14 km 163.5
 I-34012 Trieste, Italy
 ☎ +39-40-3758545
 ☎ +39-40-9380902

Arnaud **Ferrari** (ISV)
ferrari@tsl.uu.se
 Department of Radiation Sciences,
 Uppsala University
 Box 535
 S-75121 Uppsala, Sweden
 ☎ +46-18-471-58-27
 ☎ +46-18-471-35-13

Ralph **Fiorito** (IREAP-UMD)
rfiorito@umd.edu
 Institute for Research in Electronics
 and Applied Physics, University of
 Maryland
 University of Maryland
 20742 College Park, USA
 ☎ +1-301-405-8484
 ☎ +1-301-314-9437

Peter **Forck** (GSI)
p.forck@gsi.de
 Gesellschaft f  r
 Schwerionenforschung
 Planckstra   1
 D-64291 Darmstadt, Germany
 ☎ +49-6159-712311
 ☎ +49-6159-712104

— G —

Adrian **Gall** (JINR)
gall@nrmail.jinr.ru
 Joint Institute for Nuclear Research
 Joliot-Curie 6
 141980 Dubna, Russia
 ☎ +7-096-216-4364
 ☎ +7-096-216-5083

Marek **Gasior** (CERN)
Marek.Gasior@cern.ch
 CERN Laboratory
 CH-1211 Geneva 23, Switzerland
 ☎ +41-22-76-72530
 ☎ +41-22-76-77740

Tino **Giacomini** (GSI)
T.Giacomini@gsi.de
 Gesellschaft für
 Schwerionenforschung
 Planckstraße 1
 D-64291 Darmstadt, Germany
 ☎ +49-6159-712048
 ☎ +49-6159-712104

Kondo **Gnanvo** (CERN)
Kondo.Gnanvo@cern.ch
 CERN Laboratory
 CH-1211 Geneva 23, Switzerland
 ☎ +41-22-76-76069
 ☎ +41-22-76-77740

Lars **Groening** (GSI)
la.groening@gsi.de
 Gesellschaft für
 Schwerionenforschung
 Planckstraße 1
 D-64291 Darmstadt, Germany
 ☎ +49-6159-712344
 ☎ +49-6159-712987

Ursula **Grundinger** (GSI)
u.grundinger@gsi.de
 Gesellschaft für
 Schwerionenforschung
 Planckstraße 1
 D-64291 Darmstadt, Germany
 ☎ +49-6159-712610
 ☎ +49-6159-713049

Philippe **Guimbal** (CEA)
philippe.guimbal@cea.fr
 Commissariat à l'Energie Atomique
 Service DPTA/SP2A
 F-91680 Bruyeres-le-chatel, France
 ☎ +33-1-69-26-51-36

— H —

Jang-Hui **Han** (DESY Zeuthen)
jhhan@ifh.de
 Deutsches Elektronen-Synchrotron
 Zeuthen
 Platanenallee 6
 D-15738 Zeuthen, Germany
 ☎ +49-33762-77202

Yeong Jin **Han** (PAL)
hyj@postech.ac.kr
 Pohang Accelerator Laboratory
 San 31, Hyojadong, Namku
 790-784 Pohangsi, South Korea
 ☎ +82-54-279-1365
 ☎ +82-54-279-1399

Jürgen **Häuser** (NTG)
j.haeuser@n-t-g.de
 Neue Technologien GmbH & Co. KG
 Im Steinigen Graben 12-14
 D-63571 Gelnhausen, Germany
 ☎ +49-6051-6003-29
 ☎ +49-6051-6003-55

Walter F. **Henning** (GSI)
W.Henning@gsi.de
 Gesellschaft für
 Schwerionenforschung
 Planckstraße 1
 D-64291 Darmstadt, Germany
 ☎ +49-6159-712648
 ☎ +49-6169-712991

Benjamin **Höfler** (GSI)
b.hoefler@gsi.de
 Gesellschaft für
 Schwerionenforschung
 Planckstraße 1
 D-64291 Darmstadt, Germany
 ☎ +49-6151-712067
 ☎ +49-6159-712104

Tobias **Hoffmann** (GSI)
t.hoffmann@gsi.de
 Gesellschaft für
 Schwerionenforschung
 Planckstraße 1
 D-64291 Darmstadt, Germany
 ☎ +49-6159-712318
 ☎ +49-6159-712104

Eva Barbara **Holzer** (CERN)
barbara.holzer@cern.ch
 CERN Laboratory
 CH-1211 Geneve, Switzerland
 ☎ +41-22-76-72919
 ☎ +41-22-76-77740

— J —

Christophe **Jamet** (GANIL)
jamet@ganil.fr
 Grand Accelérateur National d'Ions
 Lourds
 Boulevard Henri Becquerel
 F-14076 Caen Cedex 5, France
 ☎ +33-2-31-45-47-73
 ☎ +33-2-31-45-47-28

Andreas **Jankowiak** (KPH / MAMI)
janko@kph.uni-mainz.de
 Institut für Kernphysik, Uni Mainz
 Johann-Joachim-Becher-Weg 45
 D-55099 Mainz, Germany
 ☎ +49-6131-39-26004
 ☎ +49-6131-39-22964

Ronald **Johnson** (SLAC)
ron_johnson@slac.stanford.edu
 Stanford Linear Accelerator Center
 2575 Sand Hill Road
 94025 Menlo Park, USA
 ☎ +1-650-926-8520
 ☎ +1-650-926-3800

Kevin **Jordan** (TJNAF)
jordan@jlab.org
 Thomas Jefferson National
 Accelerator Facility
 12000 Jefferson Avenue
 23606 Newport News, USA
 ☎ +1-757-269-7644
 ☎ +1-757-269-5519

Roland **Jung** (CERN)
Roland.Jung@cern.ch
 CERN Laboratory
 CH-1211 Geneva 23, Switzerland
 ☎ +41-22-76-73295
 ☎ +41-22-76-77740

— K —

Vsevolod **Kamerdzhev** (FZ-Jülich,
 IKP-COSY)
v.kamerdzhev@fz-juelich.de
 Forschungszentrum Jülich
 Leo-Brandt-Straße
 D-52425 Jülich, Germany
 ☎ +49-2461-61-6501
 ☎ +49-2461-61-2670

Alexandre **Kalinine** (ASTeC)
a.kalinine@dl.ac.uk
 Daresbury Laboratory
 Keckwick Lane
 WA4 4AD Warrington, United Kingdom
 ☎ +44-1925-603201
 ☎ +44-1925-603124

Wolfgang **Kaufmann** (GSI)
w.kaufmann@gsi.de
 Gesellschaft für
 Schwerionenforschung
 Planckstraße 1
 D-64291 Darmstadt, Germany
 ☎ +49-6159-712312
 ☎ +49-6159-712104

Klaus **Knaack** (DESY)
Klaus.Knaack@desy.de
 Deutsches Elektronen-Synchrotron
 Notkestraße 85
 D-22603 Hamburg, Germany
 ☎ +49-40-8998-3787
 ☎ +49-40-8998-4303

Jean Marc **Koch** (ESRF)
jmkoch@esrf.fr
 European Synchrotron Radiation
 Facility
 6, Rue Jules Horowitz
 F-38043 Grenoble, France
 ☎ +33-4-76-88-22-98

Markus **Körfer** (DESY)
markus.koerfer@desy.de
 Deutsches Elektronen-Synchrotron
 Notkestraße 85
 D-22607 Hamburg, Germany
 ☎ +49-40-8998-4571
 ☎ +49-40-8998-4305

Jan **Koopman** (CERN)
Jan.Koopman@cern.ch
 CERN Laboratory
 CH-1211 Geneva 23, Switzerland
 ☎ +41-22-76-74876
 ☎ +41-22-76-77740

Patrick **Krejčík** (SLAC)
pkrc@slac.stanford.edu
 Stanford Linear Accelerator Center
 2475 Sand Hill Rd
 94025 Menlo Park, USA
 ☎ +1-650-9262790

Jean-Pierre **Koutchouk** (CERN)
Jean-Pierre.Koutchouk@cern.ch
 CERN Laboratory
 CH-1211 Geneva 23, Switzerland
 ☎ +41-22-76-73230
 ☎ +41-22-76-77740

Gero **Kube** (DESY)
gero.kube@desy.de
 Deutsches Elektronen-Synchrotron
 Notkestraße 85
 D-22603 Hamburg, Germany
 ☎ +49-40-8998-3077
 ☎ +49-40-8998-3282

— L —

Dmitry **Liakin** (GSI)
D.Liakin@gsi.de
 Gesellschaft für
 Schwerionenforschung
 Planckstraße 1
 D-64291 Darmstadt, Germany
 ☎ +49-6159-712318
 ☎ +49-6159-712104

Alexei **Liapine** (TU-Berlin)
liapine@tetibm3.ee.tu-berlin.de
 Technische Universität Berlin
 Einsteinufer 17, EN2
 D-10587 Berlin, Germany
 ☎ +49-30-314-222-90
 ☎ +49-30-314-222-84

Dirk **Lipka** (DESY Zeuthen)
dlipka@ifh.de
 Deutsches Elektronen-Synchrotron
 Zeuthen
 Platanenallee 6
 D-15738 Zeuthen, Germany
 ☎ +49-33762-77280
 ☎ +49-33762-77330

Michael **Ludwig** (CERN)
Michael.Ludwig@cern.ch
 CERN Laboratory
 CH-1211 Geneva 23, Switzerland
 ☎ +41-22-76-73492
 ☎ +41-22-76-77740

— M —

Israel **Mardor** (SNRC)
mardor@soreq.gov.il
 Applied Physics Division
 Soreq Nuclear Research Center
 81800 Yavne, Israel

Christian **Magne** (CEA)
cmagne@cea.fr
 Commissariat à l'Energie Atomique
 SACM
 F-91191 Gif Cedex, France
 ☎ +33-1-69-08-64-93

Uroš **Mavrič** (I-Tech)
uros@i-tech.si
 Instrumentation Technologies
 Srebrničev trg 4a
 SI-5250 Solkan, Slovenia
 ☎ +386-5-3332300
 ☎ +386-5-3332305

Giovanni **Mazzitelli** (LNF-INFN)
giovanni.mazzitelli@lnf.infn.it
 Laboratori Nazionali di Frascati - INFN
 Via E. Fermi 40
 I-00044 Frascati (RM), Italy
 ☎ +39-69-403-2411
 ☎ +39-69-403-2256

Peter **Michel** (ELBE)
P.Michel@fz-rossendorf.de
 ELBE at Forschungszentrum
 Rossendorf e.V.
 Postfach 510119
 D-01314 Dresden, Germany
 ☎ +49-351-260-3259
 ☎ +49-351-260-3690

Velizar **Miltchev** (DESY Zeuthen)
miltchev@ifh.de
 Deutsches Elektronen-Synchrotron
 Zeuthen
 Platanenallee 6
 D-15738 Zeuthen, Germany
 ☎ +49-33762-77280
 ☎ +49-33762-77330

Istvan **Mohos** (FZJ-IKP)
i.mohos@fz-juelich.de
 Forschungszentrum Jülich GmbH,
 Institut für Kernphysik
 Leo-Brand-Straße 1
 D-52428 Jülich, Germany
 ☎ +49-2461-612629
 ☎ +49-2461-613930

Alun **Morgan** (DLS)
alun.morgan@diamond.ac.uk
 Diamond Light Source Limited
 Rutherford Appleton Laboratory
 OX11 0QX Oxfordshire, United
 Kingdom
 ☎ +44-1235-446992
 ☎ +44-1235-446967

Gerhard **Mrotzek** (DL)
g.mrotzek@dl.ac.uk
 CLRC Daresbury Laboratory
 Keckwick Lane
 WA4 4AD Warrington, United Kingdom
 ☎ +44-1925-603560
 ☎ +44-1925-602463

— N —

Graham **Naylor** (ESRF)
naylor@esrf.fr
 European Synchrotron Radiation
 Facility
 6, Rue Jules Horowitz
 F-38043 Grenoble, France
 ☎ +33-4-76-88-21-35

Ralf **Neubert** (FSU)
Ralf.Neubert@uni-jena.de
 Friedrich-Schiller-Universität Jena
 Max-Wien-Platz 1
 D-07749 Jena, Germany
 ☎ +49-3641-947425
 ☎ +49-3641-947422

Tjalling **Nijboer** (KVI)

nijboer@kvi.nl

Kernfysisch Versneller Instituut
Zernikelaan 25
NL-9747 AA Groningen, The Netherlands

☎ +31-50-363-3600

☎ +31-50-363-4003

Dirk **Nölle** (DESY)

dirk.noelle@desy.de

Deutsches Elektronen-Synchrotron
Notkestraße 85

D-22607 Hamburg, Germany

☎ +49-40-8998-2579

— O —

Patrick **Odier** (CERN)

Patrick.Odier@cern.ch

CERN Laboratory
CH-1211 Geneva 23, Switzerland

☎ +41-22-76-73817

☎ +41-22-76-77740

— P —

Andreas **Paal** (MSL)

paal@msi.se

Manne Siegbahn Laboratory,
Stockholm University
Frescativaegen 24

SE-104 05 Stockholm, Sweden

☎ +46-8-16-10-00

☎ +46-8-15-86-74

Sungju **Park** (PAL/POSTECH)

smartguy@postech.ac.kr

Pohang Accelerator Laboratory,
POSTECH

San31, Hyogok-Dong, Nam-Gu
790-784 Pohang, South Korea

☎ +82-54-279-1147

☎ +82-54-279-1399

Steve **Payne** (RAL)

S.J.Payne@rl.ac.uk

Rutherford Appleton Laboratory
Chilton

OX11 0QX Didcot, United Kingdom

☎ +44-1235-445526

Francis **Perez** (FZK)

francis.perez@iss.fzk.de

Forschungszentrum Karlsruhe
Hermann-von-Helmholtz-Platz 1
D-76344 Eggenstein-Leopoldshafen,
Germany

☎ +49-7247-826282

☎ +49-7247-826172

Andreas **Peters** (GSI)

a.peters@gsi.de

Gesellschaft für
Schwerionenforschung
Planckstraße 1
D-64291 Darmstadt, Germany

☎ +49-6159-712313

☎ +49-6159-712104

Elke-Luise **Pfaff** (GSI)

e.pfaff@gsi.de

Gesellschaft für
Schwerionenforschung
Planckstraße 1
D-64291 Darmstadt, Germany

☎ +49-6159-712384

☎ +49-6159-712039

Olivier **Pierret** (CEA)

olivier.pierret@antigone.cea.fr

Commissariat à l'Energie Atomique
Moronvilliers

F-51490 Pontfaverger, France

☎ +33-3-26-03-05-28

☎ +33-3-26-03-72-29

Dan-Ciprian **Plostinar** (UBB)

pcipri@yahoo.com

Babes-Bolyai University
Str. B.P. Hasdeu, Nr. 45, Camin 14/67
RO-3400 Cluj-Napoca, Romania

☎ +40-7228-56-530

☎ +40-2641-91-906

Eric **Plouviez** (ESRF)

plouviez@esrf.fr

European Synchrotron Radiation
Facility

6, Rue Jules Horowitz
F-38043 Grenoble Cedex, France

☎ +33-4-76-88-23-44

☎ +33-4-76-88-20-54

Michael **Plum** (LANL)

plum@lanl.gov

LANL
MS-H838
87545 Los Alamos, USA
☎ +1-505-667-7547

Patrick **Pollet** (PSI)

patrick.pollet@psi.ch

Paul Scherrer Institut
CH-5232 Villigen-PSI, Switzerland

☎ +41-56-3103286

Laurette **Ponce** (ETOILE)

ponce@ipnl.in2p3.fr

Espace de Traitement Oncologique
par Ions Legers dans le cadre
Europeen
IPNL

F-69622 Villeurbanne, France

☎ +33-4-72-44-79-77

— R —

Uli **Raich** (CERN)

Uli.Raich@cern.ch

CERN Laboratory
CH-1211 Geneva 23, Switzerland

☎ +41-22-76-72632

☎ +41-22-76-77740

Hansjörg **Reeg** (GSI)

h.reeg@gsi.de

Gesellschaft für
Schwerionenforschung
Planckstraße 1
D-64291 Darmstadt, Germany

☎ +49-6159-712447

☎ +49-6159-712104

Günther **Rehm** (DLS)

guenther.rehm@diamond.ac.uk

Diamond Light Source Limited
Rutherford Appleton Laboratory
OX11 0QX Oxfordshire, United Kingdom

☎ +44-1235-446992

☎ +44-1235-446967

Borut **Repic** (I-Tech)

borut@i-tech.si

Instrumentation Technologies
Srebrničev trg 4a
SI-5250 Solkan, Slovenia

☎ +386-5-3332300

☎ +386-5-3332305

— S —

Vahagn **Sargsyan** (DESY Zeuthen)

vsarg@ifh.de

Deutsches Elektronen-Synchrotron
Zeuthen
Platanenallee 6

D-15738 Zeuthen, Germany

☎ +49-33-76277508

☎ +49-33-76277419

Volker RW **Schaa** (GSI)

v.r.w.schaa@gsi.de

Gesellschaft für
Schwerionenforschung
Planckstraße 1
D-64291 Darmstadt, Germany

☎ +49-6159-712340

☎ +49-6159-712104

Kees Bertus **Scheidt** (ESRF)

scheidt@esrf.fr

European Synchrotron Radiation
Facility
6, Rue Jules Horowitz
F-38043 Grenoble, France

☎ +33-4-76-88-20-91

☎ +33-4-76-88-20-54

Hermann **Schmickler** (CERN)
Hermann.Schmickler@cern.ch
 CERN Laboratory
 CH-1221 Geneva, Switzerland
 ☎ +41-22-76-77078
 ☎ +41-22-76-77740

Norbert **Schneider** (GSI)
N.Schneider@gsi.de
 Gesellschaft für
 Schwerionenforschung
 Planckstraße 1
 D-64291 Darmstadt, Germany
 ☎ +49-6159-712030
 ☎ +49-6159-712104

Volker **Schlott** (PSI)
volker.schlott@psi.ch
 Paul Scherrer Institut
 WSLA/007
 CH-5232 Villigen PSI, Switzerland
 ☎ +41-56-310-4237
 ☎ +41-56-310-3383

Jürgen **Schölles** (GSI)
j.schoelles@gsi.de
 Gesellschaft für
 Schwerionenforschung
 Planckstraße 1
 D-64291 Darmstadt, Germany
 ☎ +49-6159-712312
 ☎ +49-6159-712104

Petra **Schütt** (GSI)
p.schuett@gsi.de
 Gesellschaft für
 Schwerionenforschung
 Planckstraße 1
 D-64291 Darmstadt, Germany
 ☎ +49-6159-712026

Michael **Seebach** (DESY / MDI)
michael.seebach@desy.de
 Deutsches Elektronen-Synchrotron
 Notkestraße 85
 D-22607 Hamburg, Germany
 ☎ +49-40-8998-2870

Mario **Serio** (LNF-INFN)
mario.serio@lnf.infn.it
 Laboratori Nazionali di Frascati - INFN
 C.P. 13
 I-00044 Frascati (RM), Italy
 ☎ +39-6-94032276
 ☎ +39-6-94032203

Vladimir **Skachkov** (ITEP)
skachkov@vitep1.itep.ru
 Institute for Theoretical and
 Experimental Physics
 B. Cheremushkinskaja, 25
 117259 Moscow, Russia
 ☎ +7-095-129-9494

Robert **Smith** (DL)
r.j.smith@dl.ac.uk
 Daresbury Laboratory
 Keckwick Lane
 WA4 4AD Warrington, United Kingdom
 ☎ +44-1925-603814
 ☎ +44-1925-603124

Jens **Spanggaard** (CERN)
Jens.Spanggaard@cern.ch
 CERN Laboratory
 CH-1211 Geneva 23, Switzerland
 ☎ +41-22-76-75343
 ☎ +41-22-76-77740

Till **Straumann** (SLAC/SSRL)
strauman@slac.stanford.edu
 Stanford Linear Accelerator Center
 (SSRL)
 2575 Sand Hill Rd. MS 69
 94025 Menlo Park, USA
 ☎ +1-650-926-2488

Daniel **Sütterlin** (PSI)
daniel.suetterlin@psi.ch
 Paul Scherrer Institut
 CH-5232 Villigen-PSI, Switzerland

— T —
 Jan **Timmer** (ACCEL)
timmer@accel.de
 ACCEL Instruments GmbH
 Friedrich-Ebert-Straße 1
 D-51429 Bergisch Gladbach,
 Germany
 ☎ +49-2204-84-35-08
 ☎ +49-2204-84-25-01

Gerard **Tranquille** (CERN)
Gerard.Tranquille@cern.ch
 CERN Laboratory
 CH-1211 Geneva 23, Switzerland
 ☎ +41-22-76-72554
 ☎ +41-22-76-77740

— U —
 Klaus **Unser** (BERGOZ)
unser@bergoz.com
 Bergoz Instrumentation
 Espace Allondon Ouest
 F-01630 Saint Genis Pouilly, France
 ☎ +33-4-50-42-66-42

Rok **Uršič** (I-Tech)
rok@i-tech.si
 Instrumentation Technologies
 Srebrničev trg 4a
 SI-5250 Solkan, Slovenia
 ☎ +386-5-3332300
 ☎ +386-5-3332305

— V —

Victor **Verzilov** (ELETTRA)
victor.verzilov@elettra.trieste.it
 Sincrotrone Trieste
 Area Science Park S.S. 14 km 163.5
 I-34012 Basovizza-Trieste, Italy
 ☎ +39-40-3758079

Wolfgang **Vodel** (FSU-Jena)
wolfgang.vodel@uni-jena.de
 Universität Jena
 Helmholtzweg 5
 D-07743 Jena, Germany
 ☎ +49-3641-947421
 ☎ +49-3641-947422

— W —

Hubert **Waldmann** (DESY Zeuthen)
waldmann@ifh.de
 Deutsches Elektronen-Synchrotron
 Zeuthen
 Platanenallee 6
 D-15738 Zeuthen, Germany
 ☎ +94-33762-77237
 ☎ +94-33762-77330

Udo **Weinrich** (GSI)
u.weinrich@gsi.de
 Gesellschaft für
 Schwerionenforschung
 Planckstraße 1
 D-64291 Darmstadt, Germany
 ☎ +49-6159-713858
 ☎ +49-6159-712985

Manfred **Wendt** (DESY)
wendt@ux-bello.desy.de
 Deutsches Elektronen-Synchrotron
 Notkestraße 85
 D-22607 Hamburg, Germany
 ☎ +49-40-8998-2517
 ☎ +49-40-8998-4303

Jorg **Wenninger** (CERN)
Jorg.Wenninger@cern.ch
 CERN Laboratory
 Rte de Meyrin
 CH-1211 Geneva 23, Switzerland
 ☎ +41-22-76-73715

Matthias **Werner** (DESY)
Matthias.Werner@desy.de
Deutsches Elektronen-Synchrotron
Notkestraße 85
D-22607 Hamburg, Germany
☎ +49-40-8998-2486

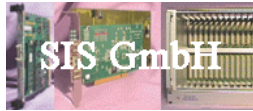
Kay **Wittenburg** (DESY)
Kay.Wittenburg@desy.de
Deutsches Elektronen-Synchrotron
Notkestraße 85
D-22607 Hamburg, Germany
☎ +49-40-8998-3956
☎ +49-40-8998-1961

— **Y** —

In Ha **Yu** (PAL)
yih@postech.ac.kr
Pohang Accelerator Laboratory
San 31, Hyojadong, Namku
790-784 Pohangsi, South Korea
☎ +82-54-279-1444
☎ +82-54-279-1399

DIPAC 2003 VENDORS

The DIPAC 2003 organizing committee appreciates the contribution of our vendors, and would like to thank and acknowledge them.



Struck Innovative Systeme GmbH



LeCroy Messtechnik



Tektronix



Hamamatsu



Canberra Eurisys



Physik Elektronik Technik -
Strahldiagnosesysteme



Agilent Technologies



National Instruments



Wiener



Telemeter Electronic



I-Tech



Bicron



Globes



Incaa Computers

Production Notes

The DIPAC2003 proceedings volume was produced using a number of *Open Software* tools and newly developed scripts.

The DIPAC2003 conference did not use a database for abstract and paper submission from the beginning. After the conference a database was introduced to organize the data at hand to ensure consistency and to facilitate the update and correction process. Starting from various input formats (*e-mails, e-mail paper submissions, Excel spreadsheets, text files*) and media, these data were written into the database using different import tools and methods.

The important fields of the database have been exported to XML with PERL, DB-, and XML-Modules, providing links to abstracts and paper files. *Important* in this context were all data necessary for the batch production of proceedings and consistent conference web pages, and therefore they comprise of abstracts for the contributions, submitted papers, affiliation data of authors, participants, and vendor lists.

The generated XML file consisted of 3240 lines of meta data describing each paper contribution. A PERL script was developed to read this XML file and transform it to `<html>`, `\pdfTEX`, and command files, providing all necessary means to generate the proceedings web site and conference proceedings.

A script run produced 449 pages for the proceedings web site (<http://bel.gsi.de/dipac2003/>). These pages consist of lists for *Sessions, Authors, Keywords, and Institutes* with all available cross links. All these pages are coded in UNICODE (UTF8), making math formulas in abstracts possible (see for example abstract PM01), as well as showing the correct writing of names like **Uršič** or **Søby**. For alphabetic sorting of author names a rule based method is used honouring accented letters, umlauts, etc.

The script generated 85 pdfTEX wrappers for each single raw pdf-file, and one for the proceedings file. Raw pdf-files are papers conforming to the JACoW (Joint Accelerator Conferences on Web) editor's guideline without page numbers, running title, and session names (see <http://www.jacow.org>). A pdfTEX wrapper transforms the raw pdf-file into one that has all hidden fields (*Title, Subject, Author, Keywords*) filled, in addition to page numbering, session names, and conference details.

No manual intervention of the script-generated pdfTEX file was necessary to achieve the printed output at hand. Embedding of division sheets between sessions, preface material, lists of authors, institutes, participants, papers, and affiliation details were configurable by means of a configuration file. The proceedings pdf-file, which can be downloaded from the proceedings web site (<http://bel.gsi.de/dipac2003/papers/proceedings.pdf>), features a completely cross-linked document with links from table of contents, list of authors, and institutes to papers.

The final version of the proceedings was made using pdfTEX (version 1.11a-2.1) with macro packages *pdfpages* (version v0.3e) and *fancyhdr* (version v2.1).

The script will be supported by the SPMS (Scientific Program Management System). It will be available from the JACoW site later this year.

February 2004
Volker RW Schaa